Lecture Notes in Mechanical Engineering

Sanjay Singh
Perumalla Janaki Ramulu
Sachin Singh Gautam *Editors*

Recent Advances in Aerospace Engineering

Select Proceedings of MRAE 2023

Springer

Lecture Notes in Mechanical Engineering

Series Editors

Fakher Chaari, National School of Engineers, University of Sfax, Sfax, Tunisia

Francesco Gherardini, Dipartimento di Ingegneria “Enzo Ferrari”, Università di Modena e Reggio Emilia, Modena, Italy

Vitalii Ivanov, Department of Manufacturing Engineering, Machines and Tools, Sumy State University, Sumy, Ukraine

Mohamed Haddar, National School of Engineers of Sfax (ENIS), Sfax, Tunisia

Editorial Board

Francisco Cavas-Martínez, Departamento de Estructuras, Construcción y Expresión Gráfica Universidad Politécnica de Cartagena, Cartagena, Murcia, Spain

Francesca di Mare, Institute of Energy Technology, Ruhr-Universität Bochum, Bochum, Nordrhein-Westfalen, Germany

Young W. Kwon, Department of Manufacturing Engineering and Aerospace Engineering, Graduate School of Engineering and Applied Science, Monterey, CA, USA

Tullio A. M. Tolio, Department of Mechanical Engineering, Politecnico di Milano, Milano, Italy

Justyna Trojanowska, Poznan University of Technology, Poznan, Poland

Robert Schmitt, RWTH Aachen University, Aachen, Germany

Jinyang Xu, School of Mechanical Engineering, Shanghai Jiao Tong University, Shanghai, China

Lecture Notes in Mechanical Engineering (LNME) publishes the latest developments in Mechanical Engineering—quickly, informally and with high quality. Original research or contributions reported in proceedings and post-proceedings represents the core of LNME. Volumes published in LNME embrace all aspects, subfields and new challenges of mechanical engineering.

To submit a proposal or request further information, please contact the Springer Editor of your location:

Europe, USA, Africa: Leontina Di Cecco at Leontina.dicecco@springer.com
China: Ella Zhang at ella.zhang@springer.com
India: Priya Vyas at priya.vyas@springer.com
Rest of Asia, Australia, New Zealand: Swati Meherishi at swati.meherishi@springer.com

Topics in the series include:

- Engineering Design
- Machinery and Machine Elements
- Mechanical Structures and Stress Analysis
- Automotive Engineering
- Engine Technology
- Aerospace Technology and Astronautics
- Nanotechnology and Microengineering
- Control, Robotics, Mechatronics
- MEMS
- Theoretical and Applied Mechanics
- Dynamical Systems, Control
- Fluid Mechanics
- Engineering Thermodynamics, Heat and Mass Transfer
- Manufacturing Engineering and Smart Manufacturing
- Precision Engineering, Instrumentation, Measurement
- Materials Engineering
- Tribology and Surface Technology

Indexed by SCOPUS, EI Compendex, and INSPEC.

All books published in the series are evaluated by Web of Science for the Conference Proceedings Citation Index (CPCI).

To submit a proposal for a monograph, please check our Springer Tracts in Mechanical Engineering at https://link.springer.com/bookseries/11693.

Sanjay Singh · Perumalla Janaki Ramulu ·
Sachin Singh Gautam
Editors

Recent Advances in Aerospace Engineering

Select Proceedings of MRAE 2023

Springer

Editors
Sanjay Singh
Amity Institute of Aerospace Engineering
Amity University Uttar Pradesh
Noida, Uttar Pradesh, India

Sachin Singh Gautam
Department of Mechanical Engineering
Indian Institute of Technology Guwahati
Guwahati, India

Perumalla Janaki Ramulu
Department of Mechanical Engineering,
School of Mechanical, Materials
and Chemical Engineering
Adama Science and Technology University
Adama, Ethiopia

ISSN 2195-4356 ISSN 2195-4364 (electronic)
Lecture Notes in Mechanical Engineering
ISBN 978-981-97-1305-9 ISBN 978-981-97-1306-6 (eBook)
https://doi.org/10.1007/978-981-97-1306-6

© The Editor(s) (if applicable) and The Author(s), under exclusive license to Springer Nature Singapore Pte Ltd. 2024

This work is subject to copyright. All rights are solely and exclusively licensed by the Publisher, whether the whole or part of the material is concerned, specifically the rights of translation, reprinting, reuse of illustrations, recitation, broadcasting, reproduction on microfilms or in any other physical way, and transmission or information storage and retrieval, electronic adaptation, computer software, or by similar or dissimilar methodology now known or hereafter developed.
The use of general descriptive names, registered names, trademarks, service marks, etc. in this publication does not imply, even in the absence of a specific statement, that such names are exempt from the relevant protective laws and regulations and therefore free for general use.
The publisher, the authors and the editors are safe to assume that the advice and information in this book are believed to be true and accurate at the date of publication. Neither the publisher nor the authors or the editors give a warranty, expressed or implied, with respect to the material contained herein or for any errors or omissions that may have been made. The publisher remains neutral with regard to jurisdictional claims in published maps and institutional affiliations.

This Springer imprint is published by the registered company Springer Nature Singapore Pte Ltd.
The registered company address is: 152 Beach Road, #21-01/04 Gateway East, Singapore 189721, Singapore

Paper in this product is recyclable.

Preface

The 2nd International Conference on Modern Research in Aerospace Engineering (MRAE 2023), hosted on September 22nd, 2023, under the auspices of the Amity Institute of Aerospace Engineering, Amity University Uttar Pradesh, Noida, India. We are delighted to announce the forthcoming publication of our conference proceedings. This compilation, titled "*Recent Advances in Aerospace Engineering*," is set to be published by Springer Nature. It stands as a testament to the collective effort and dedication of our esteemed contributors, whose work has significantly enriched the landscape of aerospace engineering with innovative research and groundbreaking discoveries.

The MRAE 2023 conference provided a vibrant platform for scholars, researchers, and industry professionals from across the globe to convene and exchange ideas at the forefront of aerospace engineering. Covering a diverse array of disciplines, our conference explored the latest advancements shaping the future of aerospace technology and innovation.

From the foundational domains of aerospace propulsion and combustion systems to the cutting-edge frontiers of electric mobility and autonomous airborne systems, our conference sessions delved into a multitude of topics, including space research, aerodynamics, computational fluid dynamics, avionics, flight mechanics, aircraft control system and stability, structural analysis, composite materials, aircraft maintenance, airworthiness, and environmental issues, artificial intelligence, unmanned aerial vehicles, and air safety. Each presentation and discussion contributed to the rich tapestry of knowledge and insight that forms the basis of this publication.

The genesis of this book stems from our collective aspiration to encapsulate the wealth of knowledge and innovation shared during the MRAE 2023 conference. It serves as a testament to our commitment to disseminating groundbreaking research and fostering collaboration within the aerospace community. By consolidating diverse perspectives and expertise, this volume aims to serve as a definitive reference for scholars, practitioners, and enthusiasts alike, offering invaluable insights into the latest developments and trends shaping the aerospace industry.

We are confident that the contents "*Recent Advances in Aerospace Engineering*" will serve as a source of inspiration for upcoming generations of aerospace professionals,igniting their passion for innovation and excellence in the field. Furthermore, we believe that the knowledge and insights encapsulated within this volume will serve as a springboard for continued innovation and propel us towards a brighter future in aerospace exploration and technology.

We extend my heartfelt gratitude to all the authors, presenters, reviewers, and organizers whose tireless efforts have made this publication possible. We extend my sincere appreciation to the editorial board, for their diligent efforts in shaping this book into its current form.

Noida, India — Dr. Sanjay Singh
ssingh10@amity.edu

Guwahati, India — Dr. Sachin Singh Gautam
Adama, Ethiopia — Dr. Perumalla Janaki Ramulu

Acknowledgements

We are thankful to the Chief guest, keynote, and invited speakers:

Dr. Prahlada Ramarao, Padma Shri-2015. Pro Chancellor S-VYASA, Director, Centre for Energy Research, Former Distinguished Scientist and CC R&D DRDO
Dr. Andrew Ooi, The University of Melbourne, Australia
Dr. Huang Weimin, NTU Singapore
Prof. Rajamohan Ganesan, Concordia University, Canada
Dr. Perumalla Janaki Ramulu, Adama Science and Technology University, Ethiopia
Dr. Parvathy Rajendran, University Sains Malaysia, Malaysia
Dr. Dinesh Bhatia, Glasgow University, Scotland
Dr. Bhargav Akkinepally, Yeungnam University, South Korea
Dr. A. K. Ghosh, Conceptual Design, Tata Aerospace and Defense, Bengaluru, India
Dr. Om Prakash, UPES Dehradun
Dr. Sachin Singh Gautam, IIT Guwahati

It would not have been possible to organize a conference without the unwavering support and expertise of these outstanding researchers and leaders.

The Conference Chair Dr. Sanjay Singh takes this opportunity to thank Patron-in-Chief Dr. Ashok K. Chauhan, Hon'ble Founder President, RBEF, and Chairman, AKC Group of companies, Patron Dr. Atul Chauhan, Chancellor, Amity University Uttar Pradesh, India and President, RBEF. Co-patron: Prof. (Dr.) Balvinder Shukla, Vice Chancellor, Amity University Uttar Pradesh, Organizing Chair: Dr. Rajesh Kumar Saluja, Amity Institute of Aerospace Engineering, Amity University Uttar Pradesh, India, Joint Organizing Chair: Dr. Neeraj Kumar Gahlot and Dr. H. Jeevan Rao, Amity Institute of Aerospace Engineering, Amity University Uttar Pradesh, India, and Financial Chair: Dr. Basant Kumar Agrawal and Dr. Narender Singh, Amity Institute of Aerospace Engineering, Amity University Uttar Pradesh, India, for their support and guidance. We also extend our gratitude to the expert Technical Chair: Dr. A. K. Ghosh, Head, Conceptual Design, Tata Aerospace and Defense, Bengaluru, India, and Dr. V. R. Sanal Kumar, Amity Institute of Aerospace

Engineering, Amity University Uttar Pradesh, India, Chairing Technical Committee. Further, we also thank the members of review committee for their valuable contributions that improved the quality of papers and made MRAE 2023 a resounding success. We would like to express deep gratitude to our publication partner Springer. No conference would be successful without excellent papers and inspiring presentations. We thank all authors, presenters, and delegates for their contribution in making MRAE 2023 a grand success.

Contents

Analytical Model of Spur Gear Tooth Crack for Evaluating the Effect of Crack Propagation Angle on Vibration Response 1
Ami Barot and Pravin Kulkarni

Predicting Air Pollution: A Smart Step in Pollution Management 13
Mitanshi Rastogi, Neha Goel, and Megha Bansal

Eduline: A Novel Edtech Platform 23
Shrey Pathak, Pratham Singh, and Purushottam Sharma

Net Quest: Networking Through Gaming 33
Rushali Salina Singh, Pankaj Bansal, Aarushi Saini, and Purushottam Sharma

Numerical Studies of Hybrid Rocket Propellant 43
Amit Kumar Thakur, Sanjivani Nikam, and Sachin Srivastava

Analysis of Code Smells Using Machine Learning Algorithms 53
Varun Jain, Rohinish Singh, Nishant Rai, and Aakanshi Gupta

Solar-Powered Fixed-Wing UAV: Fabrication Procedures with Design Methods 65
N. C. Ajay Vishwath, Payal Dhanwani, Rajeev Kumar Baghel, Ram Bendale, and Parshva Mehta

Experimental Testing of Agriculture Drone with Design Optimization 85
N. C. Ajay Vishwath, Akash R. Rajput, S. K. Shamam Gouse, Sneha Bhuva, and Upendra Pandey

Control Systems for Unmanned Aerial Vehicles: Advancement and Challenges 107
Nikhil Yogi and Niraj Kumar

A Tri-Ducted Fan Tilting VTOL UAV: Conceptual Design and Aerodynamic Analysis 119
Divij Arora, Sanjivani Nikam, Riptapan Singh, Rahul Kumar, Amit Kumar Thakur, Lovi Raj Gupta, and C. M. Bilji

Experimental and Computational Evaluation of Mechanical Properties of Glass Epoxy Composite Laminates at Different Fiber Orientations 135
K. Bhaskar Reddy, Narender Singh, Rajesh Kumar Saluja, and Neeraj Kumar Gahlot

Aging and Atomization Characteristics of Aluminum Loaded and Unloaded Ethanol Gel 147
Sankalp Jain and Rajiv Kumar

Design, Calibration, and Navigation of Bird Ambulance Drone Using APM Flight Controller 157
N. C. Ajay Vishwath, Sujeet Kumar Pandey, Vechalapu Phanendra, Kurmapu Amarnath, and Tarun Reddy

Parametric Studies of an Un-Guided Rocket Using Simple Point-Mass Trajectory Simulation Model 181
Mardav Panwar, Srinivasa Rao Gorrepati, and Manish Kumar Chauhan

Microstructural Analysis of Mg/CNT Surface Composite Using Friction Stir Processing 191
Eesha Tolety, Anmol Gupta, Narender Singh, Rajesh Kumar Saluja, and Neeraj Kumar Gahlot

Multilayer Microstrip Antenna for Broadband Monopulse Tracking Technique 199
Vrajesh Panchal, Neha Arora, and Vijay Borkar

Experimental Determination of Heat of Combustion Values, Viscosity, Surface Tension and Density for Different Jet Fuel and 2-Propanol Blending 209
Arghya Paul, Anagh Mondal, and Pratim Kumar

Non-linear Controller for a Drone with Slung Load 219
Abhishek Manalathody, Kishoor Santhana Krishnan, Jisnu Adindtra Subramanian, Sakthivel Thangavel, and Rajesh Senthil Kumar Thangeswaran

Enhancing the Performance of UAV Propeller Using Bio-Inspired Humpback Whales Tubercle—A Parametric Study at the Hub and Tip Locations 229
R. Kousik Kumaar, T. Muthuumari, and M. Kesavan

Machine Learning Assisted Development of Eight Node Hexahedral Finite Element 241
Tadala Venkata Krishna Subhash, Ankit, Dipjyoti Nath, and Sachin Singh Gautam

A Comparative Study of PID and Nonlinear Backstepping Flight Control Laws for Pixhawk-Based Multicopter 253
Divyansh Singh, Hari Om Verma, Vivek Kumar, Rajesh K. Saluja, Sanjay Singh, and Keerthana Radhakrishnan

Countering Drone Using a Mountable Net Mechanism 269
M. Rudresh, Ayush Shetty Kannoor, Gagana Babunaidu, Gnana Shibi Manoharan, Sudeep S. Bellavi, Vinayak Tsalla, and G. V. Sharath Chandra

Effect of Different Injectors on Performance of Hybrid Rocket Motor by Varying the L/D Ratio 281
Arpit Dubey, Rajiv Kumar, and Shelly Biswas

Effect of Change in Alignment of the Multiport Grain on the Performance of a Hybrid Rocket Motor 293
Gyandeep and Rajiv Kumar

Effect of Metal Addition on the Ignition Characteristics of a Pyrotechnic Igniter 303
Ritesh Dubey and Rajiv Kumar

Enhancing UAV Capabilities for Environmental Research and Rescue Missions Through Autonomous Control and Sensor Integration 311
Raahil Sheikh, Priya Gujjar, Prathamesh Minde, Himanshu Dwivedi, and Arjun Dabas

Designing and Analysis of Mild Steel Landing Gear Strut for a 3-Ton Unmanned Aerial Vehicle 325
S. M. Satheesh, N. R. Thirushah, Vishal Thirumurugan, Subramanian, and K. Vijay Anand

Comparative Study of Natural Frequency of a C-141a-il Airfoil Wing and Cantilever Beam: Simulation and Experimental Investigation 333
Madhav Sehgal, Saarthak Trikha, and Sudhanshu Tripathi

Dynamic Stall of a Pitching Airfoil: Comparative Study with ONERA and OpenFOAM 351
Sanjay Ramachandran, Arockiya Fridolin Sherbin Micheal, Gengatharan Rajarathinam, Deepak Lakshmanan, Rajesh Senthil Kumar Thangeswaran, and Sakthivel Thangavel

Conjugate Heat Transfer for a 2D Square Cylinder Using Lattice Boltzmann Method 361
Aanif Hussain and Bayram Celik

Prediction and Experimental Validation of Burst Pressure of a Gimbal Bellow Used in a Cryogenic Stage of a Launch Vehicle 373
Unnikrishnan K. R., Kodati Srinivas, Vasudevan R., and Asraff A. K.

Application of Artificial Neural Network in Impact and Crashworthiness: A Review 389
Dipjyoti Nath, Ankit, Debanga Raj Neog, and Sachin Singh Gautam

A Comparative Study of Dual Throat Nozzles for Fluidic Thrust Vectoring Applications 401
M. Siva Sakthi and Surendra Bogadi

Experimental, Theoretical and Numerical Study of Aluminum 6061–Polyurethane Foam Sandwich Composite for Space Ground System Infrastructure 415
Manish Sharma, Sreelakshmi Sandeep, Susil Kumar Nayak, S. Sankaran, C. Anil Kumar, and R. Ram Kumar

Effects of Reinforcements on Mechanical and Microstructural Properties of Aerospace Al–Li Alloy-Based Composites: A Review 427
Freedon Daniel and Gyander Ghangas

Optimization of Temperature for Synthesis of Low Molecular Weight Glycidyl Azide Polymer as Plasticizer 441
Kommajosyula Nikhil, Sarangi Prabhu Prasad, and Biswas Shelly

Studies on Curing Time and Curing Temperature of AP-HTPB-Based Composite Solid Propellant 449
Prabhat Dattakumar Phondekar and Shelly Biswas

Control Applications in Marine Robot Vehicles 463
Arun and M. P. R. Prasad

Longitudinal Static and Dynamic Stability of a Biconic Reentry Body in Subsonic Mach Number Using CFD 473
Joben Leons, M. Jathaveda, and G. Vidya

Development of a Sampling-Based UAV Path Planner for Collision-Free Navigation 485
Aliasgar S. Malik, Hari Om Verma, Vivek Kumar, and Keerthana Radhakrisnan

Design and Fabrication of Flapping-Wing UAV 497
Ashutosh Biswal, Tejas Sandeep Kapatkar, Vanshika Batosiya, Rajesh Kumar Saluja, and Hari Om Verma

Evaluation of Elastic, Mechanical, and Thermophysical Properties of Nanostructured Aluminides for Aviation Industries 507
Sudhanshu Tripathi, Devraj Singh, Rajesh Kumar Saluja, and Rashmi Vashisth

Investigation of Full-Length Aerospike Nozzle 517
Md Saquib Reza, B. K. Agarwal, and R. S. Tarnacha

Optimizing Robotic Arm Efficiency: Synergizing Aerodynamics with Arduino Control for Enhanced Six Degrees of Freedom 529
Akshay Mohan, Mohan Kumar Akurathi, Priyanka Vashisht, and Aman Jatain

Analysis of Indian Aircraft Maintenance Engineer Licensing in the Global Regulatory Framework 541
Manoj Kumar Paidisetty, V. R. Sanal Kumar, Sanjay Singh, and Deepak Chandra Chandola

Assessing the Influence of Quality Control and Assurance on Aircraft Maintenance Turnaround Time Reduction: A Regression Modeling Approach 553
Deepak Chandra Chandola, Preeti Chandola, Seema Verma, Kamal Jaiswal, Manoj Kumar Paidisetty, and Rajendra Prasad Kholiya

Recent Developments of Battle Tanks Used in Defence Applications—A Review 563
Aditya Sadhukhan, G. Srinivas, and G. T. Mahesha

An Observer-Based Solution for Structural Health Monitoring of Mechanical Systems Subjected to Unknown Inputs 585
H. Jeevan Rao, Shrishail B. Sollapur, C. Devaraj Varma, Dheeraj K. Gara, S. Singh, and Sumit Sharma

Combined Effects of External and Nozzle Exit Flows on the Jet Acoustic Power Levels of Chevron Nozzles for Transonic Aircraft 601
Arsalan Ahmad, Dekkala Vinay, Shubhangi Sundaria, Sobia Raza, Maansi Srivastasva, Tanisha Singh, Sagnik Saha, and V. R. S. Kumar

About the Editors

Dr. Sanjay Singh completed his Ph.D. in Aerospace Engineering from the Indian Institute of Technology Kanpur in 2008. He is currently a professor and director of Amity Institute of Aerospace Engineering, Amity University Uttar Pradesh, India. His research area includes flight vehicle system identification and parameter estimation, neural networks, UAV/MAV, flight and wind tunnel testing, flight dynamics, and control. He has authored several articles published in reputed journals and conferences. He is the member of review committee of many national and international journals of Aerospace field. He has supervised more than 50 UG and PG projects and dissertations. Currently, he is supervising four Ph.D. students. Dr. Sanjay Singh is currently involved in the design and development of autonomous high endurance fixed-wing UAV.

Dr. Perumalla Janaki Ramulu is the associate professor in the Department of Mechanical Engineering and acting as a director of center for Advanced Manufacturing Engineering at Adama Science and Technology University, Adama. His research interest primarily includes advanced metal joining techniques, sheet metal forming, tailor welded blanks, modeling simulation of metal forming process, material characterization, welding technologies, and different metal forming processes analysis. He specialized in experimental and modeling simulation of sheet metal with different formability tests. He has published more than 180 papers in international journal, book chapters, and conferences. He has guided 36 UG and 30 PG projects, two Ph.D., and guiding 8 Ph.D. Teaching methods have been enhanced by providing and recording the video lectures in the recent years.

Dr. Sachin Singh Gautam is currently an associate professor in the Department of Mechanical Engineering, Indian Institute of Technology Guwahati. His research interest is in computational mechanics specifically isogeometric analysis, contact problems, and GPU computing. Recently, he has started to explore machine learning applications in finite elements especially contact problems. He has published one book, 35 journal papers, five are in various stages of review, 20 books chapters, and made more than 70 conference presentations. Currently he is co-authoring a

textbook on finite elements with Prof. P. M. Dixit (Ex-Professor, IIT Kanpur). He has supervised five Ph.D.s, 22 master students, and many bachelor students. Currently he is supervising five Ph.D. students and three master students. Dr. Gautam is currently involved in development of contact and isogeometric modules for FEAST® software being developed by VSSC, ISRO.

Analytical Model of Spur Gear Tooth Crack for Evaluating the Effect of Crack Propagation Angle on Vibration Response



Ami Barot and Pravin Kulkarni

Abstract Vibration-based health monitoring is considered as an important tool since any anomaly present in the system is manifested through its own vibration signature. This vibration signature is unique in nature. This uniqueness is very well established and being utilized in industry effectively for obtaining vibration response of industrial gear boxes and this forms the basis of diagnosis of the extent to which the gears are working at the intended level of accuracy. In this study, the mathematical model is developed and based on eight degrees of freedom governing differential equations are formed consisting time varying meshing force. Further, this time varying mesh force is diffused in terms of time varying mesh stiffness. The eight degrees of freedom are four rotational and four translational. During mesh in spur gear pair, the load sharing is variable with respect to time along the line of contact and it also depends upon the number of teeth pair in contact. Different faults in gear can be enlisted as crack, spalling, pitting, etc., each contributing adversely on the system characteristics, mesh stiffness being one of those. A cracked gear tooth is attributed by many features such as crack depth, crack length, initiation zone of crack and crack propagation angle. Amidst these, the study associated with the influence of crack propagation angle on gear tooth vibrations has been undertaken and the results are presented in this paper. Time varying mesh stiffness equations are formulated based on potential energy theory and it is solved by using a MATLAB code. TVMS plot is generated to investigate the influence of propagation angle on TVMS.

Keywords Cracked tooth · Crack propagation angle (CPA) · Degrees of freedom · Differential equations · Dynamic model · MATLAB · Time varying mesh stiffness (TVMS) · Vibration

A. Barot (✉) · P. Kulkarni
PVG's COET & GKPWIOM, Pune 411009, India
e-mail: arb_mech@pvgcoet.ac.in

© The Author(s), under exclusive license to Springer Nature Singapore Pte Ltd. 2024

S. Singh et al. (eds.), *Recent Advances in Aerospace Engineering*, Lecture Notes in Mechanical Engineering, https://doi.org/10.1007/978-981-97-1306-6_1

1 Introduction

Rotating machineries are widely used in various industrial applications. Gears, shaft and bearings are the important components of rotating machinery. Failure of any rotating component causes the failure of machinery as a whole [1]. This can be avoided by replacing the components before its failure. For reliable working of mechanical systems, fault diagnosis of rotating element is the most important and crucial task [2, 3]. Vibration-based condition monitoring is a reliable method for fault identification in rotating machinery [4]. Each and every component have its unique vibration signal which is known as vibration signature. With the development of faults in rotating components, there is a change in this vibration signature and it is very conveniently used for identification of faults. Experimental-based gearbox vibration monitoring is very important in industry for maintenance. Gear faults can also be identified by developing a dynamic model of gear vibration [5, 6]. Cracks, pitting and spalling are different faults present in the spur gear pair and the pair is subjected to dynamic loading condition. Fault identification and fault severity can be detected or diagnosed by vibration-based condition monitoring. Gear tooth crack at the tooth root or fillet occurs due to fatigue load and high impact loading on gear tooth. Breakage occurs on the tooth when unexpected heavy loads are applied on the tooth. When two gears are in mesh, mesh compliance and related time varying mesh stiffness (TVMS) is an important parameter. Substantive information regarding the working state of the gears can be effectively assessed by comparing graphical impressions of earlier obtained TVMS of healthy gears. Mesh deflection of gears in mesh with rack was calculated and presented based on theoretical study [7]. While modelling mesh stiffness of gears based on analytical approach, the nature of load is assumed as concentrated load and/or uniformly distributed load based on Hertzian elastic contact theory [8–10]. The study related to the interaction of mesh stiffness and contact ratio for gear pair was presented [11]. There are different aspects of mesh stiffness in a gear pair. The effect of torsional mesh stiffness on overall TVMS was considered by Jia et al. [12]. A comprehensive study on dynamic analysis of effect of progressive crack and variation in centre distance on vibration of spur of gears is presented by Barot and Kulkarni [13]. In dynamic conditions, there are multiple ways in which the fatigue load may cause initiation of crack and further maturity of the developed crack. There is a definite sense of uncertainty involved in the overall impact which can be described as crack initiation point (at the tooth root or tip), extent of crack depth, crack length throughout the tooth width or partial (these results are presented in the earlier study [13] undertaken by the authors) and crack propagation angle (towards the tooth rim or along the tooth thickness).

In this study, the effect of crack propagation angle on the vibration response of spur gears is undertaken. The crack initiation is assumed at the tooth root and successively encompassing towards the rim. Taking into account, these considerations have ensured inclusion of all possible uncontrollable variations of crack propagation in the study.

Subsequent paragraphs, however, are indented.

2 Mathematical Model of Vibration of Spur Gear Pair in Mesh

For investigating the vibration response of a geared system, mathematical modelling is an important tool which takes into consideration several gear parameters along with working of gears under the influence of the operating conditions. The accuracy of the model is dictated by considering various aspects such as degrees of freedom (single to multi DOF), prediction of the form of the vibration pulse due to the presence of defects, incorporation of nonlinearity of elements, time varying mesh stiffness altogether or few in the model.

The purpose of designing and developing a mathematical model for vibrations of spur gear pair is to obtain, understand and analyse the response of the mechanical system to forces caused by moving parts in the machines [the forces acting along the line of action and it gives response in terms of vibration that can be displacement or velocity or acceleration]. The fatigue loading in spur gear causes development of cracks with passage of time. This will cause the nonlinear response of the machine to the forcing function. The forcing function contains frequency 1X only. However, in the nonlinear mechanical structure of the machine, the resulting vibration response will occur at 1X and multiples of this. The extent and magnitude of the harmonic content of the vibration gauges the nonlinearity of the machines. Interestingly, the internal interaction of the response occurring at 1X and its higher order harmonics (2X, 3X and so on) results in the generation of distinct sum and difference frequencies which are altogether new frequencies in the form of sidebands found in the spectrum of the defective gear pair. Remarkably, these frequencies in the response were not present in the forcing function. In case of gears, the rpm will modulate the gear mesh frequency resulting in sidebands. Modulation is always a nonlinear process.

In most of the gear pair systems, the coupling between the torsional vibration modes is controlled by mesh stiffness; therefore a 2-degree-of-freedom semi-definite mathematical model representing only the torsional vibration may yield a quite accurate result in most practical cases [14]. Zhang et al. [15] established the mathematical model of the nonlinear translational-torsional motion of spur gears using the Lagrange equation and analysed the meshing stiffness and vibration characteristics of gears and their transmission system based on gearbox. Jie et al. [16] developed a 6 degrees of freedom gear system dynamic model based on lumped parameter method to analyse the fault on vibration response.

In the present study, a nonlinear lateral-torsional model of spur gear pair with flexible support of gear pair is proposed. The model under investigation consists of two gears on two shafts, which are connected to a prime mover and an actuator. The model includes four inertias namely prime mover, pinion, gear and actuator. The torsional compliances of shafts and the transverse compliances of bearings combined with those of shafts are included in the model. Both bearing and shaft damping are also considered in the dynamic model. Lumped parameter method is used to analyse the vibration response including the effect of defects like cracks, pitting, spalling or broken tooth. Assumptions in the mathematical model are: Mass and inertia of shaft

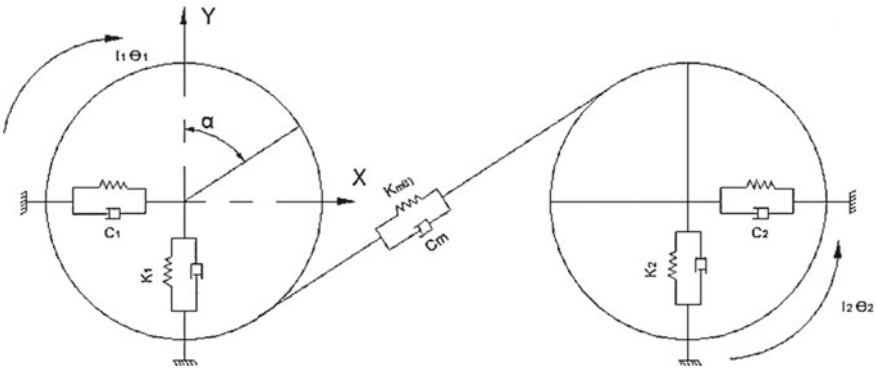


Fig. 1 8-DOF vibration model of a pair of gears meshing

are connected on the gear without considering friction between the gears and resonance of the gear. For the basic deflection of the tooth, bending, shear and compressive effects of the force components are considered and crack is throughout the length of the tooth, having uniform thickness and propagation starts at the root.

The model constitutes 8 degrees of freedom (Eqs. 1–8) which are four rotational and four translational. Rotational DOF is of the prime mover, pinion, gear and actuator. Translational are components along x and y axis of the resultant along the line of action for pinion and gear. Other important considerations in the model are inertia of prime mover and load, time varying mesh stiffness, mesh damping, torsional compliances of pinion and gear shafts, material damping in shafts (viscous), bearing compliances and damping (viscous), transverse compliances of shafts, drive torque and actuator torque (Fig. 1).

The governing equations of motion for the vibration model depicted can be written as follows:

$$I_p\ddot{\theta}_P + C_{s1}\left(\dot{\theta}_P - \dot{\theta}_1\right) + K_{s1}(\theta_P - \theta_1) = T_p \tag{1}$$

$$I_1\ddot{\theta}_1 + C_{s1}\left(\dot{\theta}_1 - \dot{\theta}_P\right) + K_{s1}(\theta_1 - \theta_P) = -F_m R_1 \tag{2}$$

$$I_2\ddot{\theta}_2 + C_{s2}\left(\dot{\theta}_2 - \dot{\theta}_A\right) + K_{s1}(\theta_2 - \theta_A) = F_m R_2 \tag{3}$$

$$I_A\ddot{\theta}_A + C_{s1}\left(\dot{\theta}_A - \dot{\theta}_2\right) + K_{s1}(\theta_A - \theta_2) = -T_A \tag{4}$$

$$m_1\ddot{x}_1 + c_1\dot{x}_1 + k_1 x_1 = -F_m \sin\alpha \tag{5}$$

$$m_1\ddot{y}_1 + c_1\dot{y}_1 + k_1 y_1 = -m_1 g + F_m \cos\alpha \tag{6}$$

$$m_2\ddot{x}_2 + c_2\dot{x}_2 + k_2x_2 = F_m \sin\alpha \tag{7}$$

$$m_2\ddot{y}_2 + c_2\dot{y}_2 + k_2y_2 = -m_2g + F_m \cos\alpha \tag{8}$$

where

T_P = Input torque of prime mover.
T_A = Output torque of actuator.
α = Pressure angle.
m_1 and m_2 = Mass of pinion and gear, respectively.
k_1 and k_2 = Bearing stiffness of pinion and gear, respectively.
c_1 and c_2 = Damping coefficient of pinion and gear, respectively.
r_1 and r_2 = Base radius of pinion and gear, respectively.
x_1 and x_2 = Displacement of pinion and gear along x axis, respectively.
y_1 and y_2 = Displacement of pinion and gear along y axis, respectively.
I_p, I_1, I_2 and I_A = Polar MoI prime mover, pinion, gear and actuator, respectively.
K_{s1} and K_{s2} = Torsional stiffness of pinion and gear shafts, respectively.
C_{s1} and C_{s2} = Viscous damping coefficients of pinion and gear shafts respectively.
θ_P, θ_1, θ_2 and θ_A = Angular displacement of prime mover, pinion, gear and actuator, respectively.

In the above equations, F_m is the time varying meshing force along the line of action and its components are considered along the X and Y direction. Time varying mesh stiffness is considered as a main influencing parameter. F_m can be expressed as,

$$F_m(t) = C_m\dot{\delta} + K_m(t)f(\delta) \tag{9}$$

where

C_m = Meshing damping of gears in NSm^{-1}
$K_m(t)$ = Time varying meshing stiffness in Nm^{-1}
δ = Relative displacement of gears along the meshing line in m.
Relative displacement of gears can be expressed as,

$$\delta = x_1\sin\alpha - x_2\sin\alpha + y_1\cos\alpha - y_2\cos\alpha + r_1\theta_1 - r_2\theta_2 \tag{10}$$

Differentiating above w. r. t., velocity is obtained as,

$$\dot{\delta} = \dot{x}_1\sin\alpha - \dot{x}_2\sin\alpha + \dot{y}_1\cos\alpha - \dot{y}_2\cos\alpha + r_1\dot{\theta}_1 - r_2\dot{\theta}_2 \tag{11}$$

By putting values of δ and $\dot{\delta}$ in Eq. (9), F_m is expressed as follows:

$$\begin{aligned} F_m(t) = {} & C_m\left[\dot{x}_1\sin\alpha - \dot{x}_2\sin\alpha + \dot{y}_1\cos\alpha - \dot{y}_2\cos\alpha + r_1\dot{\theta}_1 - r_2\dot{\theta}_2\right] \\ & + K_m(t)[x_1\sin\alpha - x_2\sin\alpha + y_1\cos\alpha - y_2\cos\alpha + r_1\theta_1 - r_2\theta_2] \end{aligned} \tag{12}$$

Time varying mesh stiffness (TVMS) is a periodic function caused by the change in number of contact tooth pairs as well as the contact positions of the gear tooth. Importantly, TVMS is one of the main sources of vibration in a gear transmission system.

3 Formulation of Time Varying Mesh Stiffness Equations

In this section, mesh stiffness formulation is presented for healthy gears and cracked tooth gears. This forms the comparative analysis for progressive condition of gears from healthy to progressive deterioration condition of gears.

3.1 Mesh Stiffness of Healthy Gears

Analytical approach has been used to calculate TVMS of two gears. Strain energy is a type of potential energy that is stored in a structural member as a result of elastic deformation. Potential energy based on theory of elasticity is considered to derive the expression of TVMS. During the transmission of forces, deformation energy in the tooth is calculated individually. Potential energy in general is given by the product of work done by gradually applied load and distance moved by it or deflection or deformation. Also, it is the product of average load and deflection.

During the evaluation of TVMS, the individual teeth is considered as cantilever beam supported at the dedendum circle with a variable cross section, where a force acts along the line of action. The deformation energy accumulated in the tooth is calculated individually for each tooth coming into an engagement. For a pair of spur gears with contact ratio lying in between 1 and 2, according to potential energy method [17–24], the total mesh stiffness K_m (in Eq. 9) can be expressed as follows:

$$K_m = \frac{1}{\frac{1}{k_h} + \frac{1}{k_{f1}} + \frac{1}{k_{b1}} + \frac{1}{k_{a1}} + \frac{1}{k_{s1}} + \frac{1}{k_{b2}} + \frac{1}{k_{a2}} + \frac{1}{k_{s2}} + \frac{1}{k_{f2}}} \tag{13}$$

subscripts 1 and 2 indicate the driving and driven gear, respectively.

where K_h = Hertzian mesh stiffness, K_a = Axial mesh stiffness, K_b = Bending mesh stiffness, K_s = Shear mesh stiffness and K_f = Fillet foundation mesh stiffness

3.2 Mesh Stiffness of Cracked Tooth Gears

For cracked tooth in a gear, crack developed at the root of tooth is considered for a single tooth of a gear. Initiation of crack takes place at the most heavily stressed

section in the material. The path of crack propagation is observed as a smooth, continuous and tend to be a straight line with slight curvature [25]. Wu et al. [26] presented method to calculate TVMS of helical gear by considering fillet foundation stiffness within multi-tooth in contact and also by considering nonlinearity. Kong et al. [27] presented analysis of time varying mesh stiffness and dynamic response of gear transmission system with pitting and cracking coupling faults.

In this study, for modelling of crack on gear tooth, the crack depth is considered as a straight line and along the whole depth of the tooth. Crack starts at the root of the driven gear and propagate as shown in Figs. 2 and 3. The crack depth is represented as C_0 and it propagates in the straight line. h_c is the initial position of crack from the centre of tooth width. The crack is assumed to be extended for the whole width of the tooth. Then the crack propagation is towards the centre line of the tooth which is at an angle α_c. This propagation angle is important and have remarkable influence on the TVMS. For crack, maximum depth of the crack can be $C_{\max}$. The tooth profile remains unaltered and the foundation stiffness is not affected. For time varying mesh stiffness calculations for cracked tooth, the mesh stiffness equation values of K_h, K_a and K_f will remain unchanged. However, bending mesh stiffness and shear mesh stiffness undergoes change due to crack on the gear tooth.

Total mesh stiffness of a pair of spur gear with cracked tooth can be expressed as follows:

$$K_m = \frac{1}{\frac{1}{k_h} + \frac{1}{k_{\text{b\_crack}}} + \frac{1}{k_{a1}} + \frac{1}{k_{s\_\text{crack}}} + \frac{1}{k_{f1}} + \frac{1}{k_{b2}} + \frac{1}{k_{a2}} + \frac{1}{k_{s2}} + \frac{1}{k_{f2}}} \tag{14}$$

The effect of crack on gear tooth is realized in Eq. 14 as compared to Eq. 13 for healthy gear.

For cracked tooth in the spur gear, initial depth of crack is C_0**,** Therefore, for any crack width C, $C = C_0 \leq C_{\max}$.

Then the effective area moment of inertia and area of cross section at the position of Y can be calculated as:

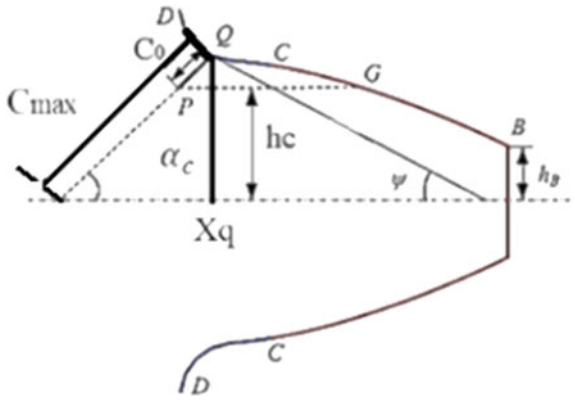


Fig. 2 Crack on spur gear

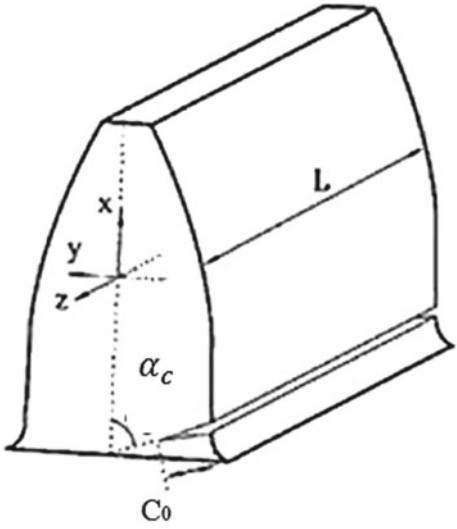


Fig. 3 Crack with constant depth

$$A = (H_c + x)L \text{ and } I = \frac{1}{12}(H_c + x)^3 L \tag{15}$$

4 Result and Discussion

As discussed in the previous section, time varying mesh stiffness (TVMS) is regarded as one of the most dominant indicators of the state of the gear under the influence of dynamic loading. For the calculation of time varying mesh stiffness of spur gear pair, analytical method is considered as an efficient and reliable method for spur gear. Depending upon the conditions of loading on a pair, the crack which is initiated at the root can propagate at an angle towards the centre of tooth thickness or rim. In following sections, results are presented for different angles of crack propagation. Based on this, significant conclusions can be drawn regarding healthy condition of gear. This is by the virtue of effect of variation of crack propagation angle on time varying mesh stiffness.

Initially, investigation of magnitude of TVMS is done for a gear tooth without crack. Successively, crack propagation angle is varied in steps and magnitude of TVMS is found for all the cases. However, variation of TVMS along the line of action is plotted graphically for some cases; healthy gear (without crack), CPA 70° and CPA 30° as shown in Fig. 4. The meshing action in a pair of gear tooth starts at the root of the driving tooth and tip of the driven tooth at the start of engagement. Successively, with the two gears rotating along their defined trajectory and the point of contact constrained to move along the pressure line at disengagement contact is at tip of driving tooth and root of driven tooth. In between these two events, some time

is elapsed corresponding to the angle of action which indicates the angle for which a tooth of driver remains in contact with the driven tooth. Accordingly, discretization of the physical phenomena of the meshing is done by considering many data points from engagement to disengagement.

Table 1 in particular shows the magnitude of TVMS for three important positions which are start of engagement, middle and disengagement. Initially, at 1000 points, the same was computed. Magnitude of TVMS is presented for three instants (at start, at middle and at end of the engagement) and for different crack propagation angles. Figure 5 shows comparative analysis of TVMS for different CPA.

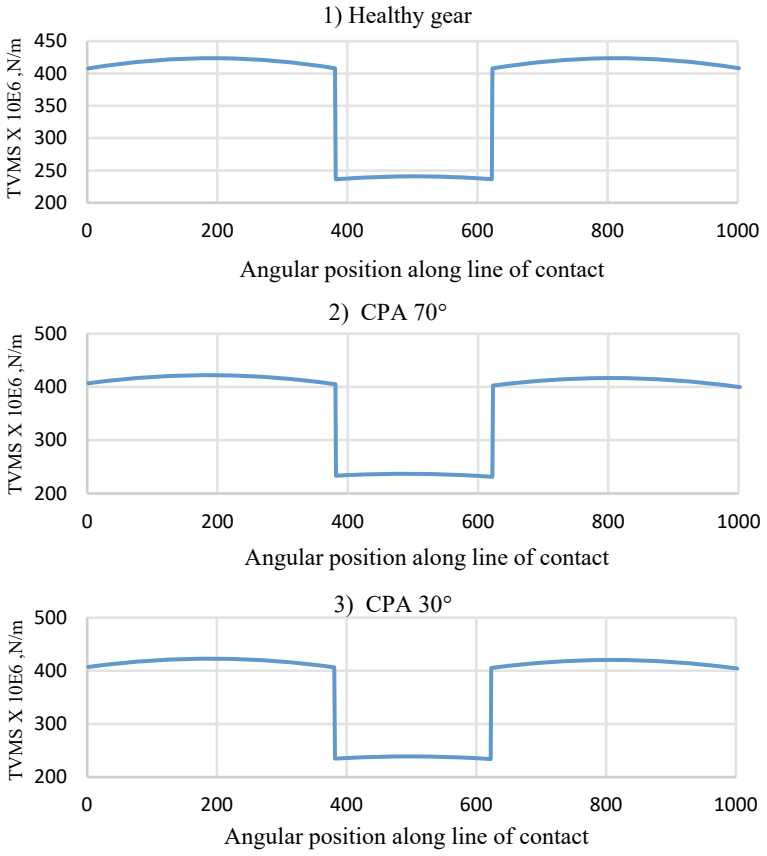


Fig. 4 Time varying mesh stiffness for healthy and crack propagation angle of 30° and 70°

Table 1 Effect of CPA on TVMS at start, middle and disengagement

CPA	Healthy	70°	30°	10°
Start	407,816,205	406,906,030	407,361,325	407,665,030
Middle	240,825,827	236,641,133	238,827,018	240,242,293
End	408,193,554	399,782,136	404,390,307	407,095,543

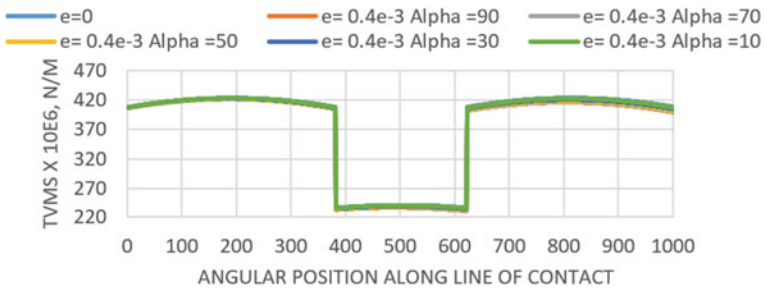


Fig. 5 Comparison of all crack propagation angle with TVMS values

5 Conclusion

As discussed in previous section, it is clear that for lower values of crack propagation angle, magnitude of TVMS is high and as angle increases, there is drop in TVMS. This indicates that drop in TVMS for higher values of crack propagation angle is associated with reduced load support. This happens due to the fact that at 90°, crack progresses towards the tooth thickness as compared to progression of crack at 10° which is the terrain of rim having massive material. This shows that, TVMS is an important indicator of development of crack on gear tooth. TVMS indicates the condition of tooth. It can be said that the way in which crack propagates on the gear tooth, have marked impact on TVMS. Moreover, it is observed based on the findings of earlier studies that the focus was on fixed crack propagation angle. This was the motivation for undertaking current study presenting results on varied crack propagation angles. The findings of this current study can be extended for evaluating the remaining life of the gear tooth with regards to variation of crack propagation angle.

Funding Not applicable.

References

1. Tandon N, Choudhury A (1999) A review of vibration and acoustic measurement methods for the detection of defects in rolling element bearings. Tribol Int 32:469–480

2. Aherwar A (2012) An investigation on gearbox fault detection using vibration analysis techniques: a review. Aust J Mech Eng 10(2):169–184
3. White MF (1984) Simulation and analysis of machinery fault signals. J Sound Vib 93(l):95–l16
4. Patel VN, Tandon N, Pandey RK (2010) A dynamic model for vibration studies of deep groove ball bearings considering single and multiple defects in races. J Tribol 132:1–10
5. Randall RB (1982) A new method of modeling gear faults. J Mech Des 104:259–267
6. McFadden PD (1986) Detecting fatigue cracks in gears by amplitude and phase demodulation of the meshing vibration. ASME transactions. J Vib Acoustics Stress Reliab Des 108:165–170
7. Weber C (1949) The deformation of loaded gears and the effect on their load-carrying capacity. Sponsored Research (Germany). Department of Scientific and Industrial Research. London. Report 3
8. Chakraborti J, Hunashikatti HG (1974) Determination of the combined mesh stiffness of a spur gear pair under load. ASME paper 74 -DET-39
9. Terauchi Y, Nagamura K (1981) On tooth deflection calculation and profile modification of spur gear teeth. In: Proceedings of international symposium on gearing and power transmission, Tokyo
10. Arafa MH, Megahed M (1999) Evaluation of spur gear mesh compliance using the finite element method. Article ARCHIVE Proc Instit Mech Eng Part C J Mech Eng Sci 1989–1996:203–210
11. Dogan O, Karpat F, Kopmaz O, Ekwaro-Osire S (2020) Influences of gear design parameters on dynamic tooth loads and time-varying mesh stiffness of involute spur gears. Sådhanå 45:258. 15 pages
12. Jia SX, Howard I, Wang J (2003) The dynamic modeling of multiple pairs of spur gears in mesh, including friction and geometrical errors, Taylor & Francis Inc. Int J Rotat Mach 9:437–442
13. Barot A, Kulkarni P (2023) Dynamic analysis of effect of progressive crack and variation in center distance on vibration of spur gears. Mater Today: Proc 77:603–613
14. Ozguven HN, Houser DR (1998) Dynamic analysis of high-speed gears by using loaded static transmission error. J Sound Vib 125(1):71–83
15. Zhang L, Chen C, Liu J, Zhao S (2018) Dynamic characteristic of spur gear with flexible support of gearbox. J Vibroeng 20(3):1530–1543
16. Liu J, Wang C, Wu W (2020) Research on meshing stiffness and vibration response of pitting fault gears with different degrees. Hindawi. Int J Rotat Mach 2020, Article ID 4176430. 7 pages
17. Wu S, Zuo MJ, Parey A (2008) Simulation of spur gear dynamics and estimation of fault growth. J Sound Vib 317(3–5):608–624
18. Ma H, Zeng J, Feng R, Pang X, Wen B (2016) An improved analytical method for mesh stiffness calculation of spur gears with tip relief. Mech Mach Theo 98:64–80
19. Ma H, Zeng J, Feng R, Pang X, Wang Q, Wen B (2015) Review on dynamics of cracked gear systems. Eng Fail Anal 55:224–245
20. Tse DK, Lin HH (1992) Separation distance and static transmission error of involute spur gears. In: 28th joint propulsion conference and exhibit. Nashville. TN, U.S.A., 9 pages
21. Yang DCH, Lin JY (1987) Hertzian damping, Tooth friction and bending elasticity in gear impact dynamics. J Mech, Trans Auto Des 109(2):189–196
22. Chen Z, Zhang J, Zhai W, Wang Y, Liu J (2017) Improved analytical methods for calculation of gear tooth fillet foundation stiffness with tooth root crack. Eng Fail Anal 82:72–81
23. Yang DCH, Sun ZS (1985) A rotary model for spur gear dynamics. ASME J Mech Trans Auto Des 107:529–535
24. Sainsot P, Valex P, Duverger O (2004) Contribution of gear body to tooth deflections—a new bidimensional analytical formula. J Mech Des 126:748–752
25. Ma H, Song R, Pang X, Wen B (2014) Time-varying mesh stiffness calculation of cracked spur gears. Eng Fail Anal 44:179–194
26. Wu X, Luo Y, Li Q, Shi J (2022) A revised method to calculate time-varying mesh stiffness of the helical gear. MATEC Web Conf 355:01005
27. Kong Y, Jiang H, Dong N, Shang J, Yu P, Li J, Yu M, Chen L (2023) Analysis of time-varying mesh stiffness and dynamic response of gear transmission system with pitting and cracking coupling faults. MDPI, Mach 11(4)

Predicting Air Pollution: A Smart Step in Pollution Management



Mitanshi Rastogi, Neha Goel, and Megha Bansal

Abstract The advancements in technology have introduced us to concepts like smart cities, smart devices, etc. A city can be considered as smart if it is liveable, inclusive, and sustainable. Other factors like building bold, strategic view for development, inclusive and accessible urban spaces, and services, having trust in government, proper waste management, and pollution management are some of the key factors which contribute significantly to making the city smart. Without oxygen, it is impossible to comprehend how humanity would survive. Modern human culture has had constant growth that has had a negative impact on the quality of the air. Daily transportation and home operations churn up dangerous pollutants in our surroundings. In the modern day, air quality monitoring and forecasting have become cumbersome tasks, particularly in developing nations like India. Managing pollution is becoming the need of the hour. This paper showcases how pollution management can be carried out with the help of machine learning techniques. A random forest algorithm has been applied to the sample data for predicting air pollution. It can be said that if air pollution is predicted at an earlier stage, it can contribute significantly to making the city smart.

Keywords Machine learning · Random forest · Air quality monitoring · Air quality index

1 Introduction

In the actions of modern humans, power consumption and its effects are unavoidable. The burning of fuel is a man-made source of air pollution, as are emissions from manufacturing facilities, automobiles, airplanes, and aerosol cans, among other

M. Rastogi (✉) · N. Goel · M. Bansal
Vivekananda Instutite of Professional Studies, Pitampura, Delhi, India
e-mail: rmitanshi@gmail.com

M. Bansal
e-mail: megha.bansal@vips.edu

© The Author(s), under exclusive license to Springer Nature Singapore Pte Ltd. 2024

S. Singh et al. (eds.), *Recent Advances in Aerospace Engineering*, Lecture Notes in Mechanical Engineering, https://doi.org/10.1007/978-981-97-1306-6_2

things [1]. The health of people is impacted by the poisonous air that makes up air pollution. Humans are more susceptible to a wide range of dangerous illnesses brought on by air pollution, including asthma, cancer, types of heart illness, and bronchitis. Scientists have discovered that air pollution has the potential to have a negative impact on various historical sites. Atmospheric emissions from industries and power plants, as well as exhausts from agriculture, are to blame for the rise in gases like CO_2, NO2, and NH_3. The greenhouse gases have a negative impact on the climate, which in turn affects how quickly plants develop [2]. The major difficulty arises while monitoring a vast number of airborne particles and numerous injurious gases. Such gases are harmful to local residents. With rising automotive and industrial growth, monitoring and forecasting AQI has become an important and difficult undertaking, particularly in metropolitan regions. To track AQI, an intelligent air purifying model is required. Even though the engrossment of the deadliest pollutant, PM2.5, is shown to be multiplied in developing countries, the majority of air quality studies and research efforts focus on these nations.

Increasing air pollution is a threat to society. A lot of work is being done in different areas to keep a check on the increasing pollution levels. IoT and machine learning are the two sustainable solutions that are helping in curbing this menace. IoT analyzes the air quality index using sensors. Sensors are further used to measure PM 2.5 which helps in monitoring AQI. In this paper, we are trying to predict air pollution with the help of machine learning that can help in adapting preventive measures well in advance. With the help of preventive methods, we can protect the environment from hazardous gases.

The next section highlights the work done in the field of air pollution monitoring. The dataset under investigation, along with feature selection and preprocessing procedures used, is all described in Sect. 3. Through data visualization, Sect. 4 discusses finding hidden patterns in the dataset. The current work comes to an end in the last segment.

2 Literature Review

In the current section, a few similar works have been done already on-air pollution by different researchers with the help of ML techniques like KNN, SVM, and LR on varied datasets using accuracy, recall, AU-ROC, $f1$-score, and precision.

Neirotti [3] briefed about the idea of a smart city as a way of improving the quality of life of pupils has become more significant recently. With the development of a taxonomy of relevant application areas, including natural resources and energy, governance, economy and people, and many more, this article offers a thorough grasp of the concept of a smart city.

Siregar [4] discussed the need for ongoing surveillance of the pollution levels in the cities. This is crucial in the context of smart cities, where environmental concerns are crucial. Technologies can be created for a hybrid pollution surveillance system using Waspmote along with wireless sensors.

Peng [5] briefed about the prevention and management of the urban environment pollution has drawn significant attention from an increasing number of individuals. To assess the current state of environmental contamination, this system employs a variety of sensor and video monitoring interfaces, and it communicates the equipment it collects through a wireless network to a central server for evaluation and planning.

Toma [6] explained the objective is to reduce hazards to one's health and to increase the awareness of the negative consequences of exposure to air pollution. This study aims to examine the main problems of a problem-solving time pollution surveillance system. In the suggested IoT solution, security is given a lot of attention. Security is the central element that drives all other system components.

Agrawal and Mohan [7] discussed the potential ways to tackle the hazardous problem caused due to air pollution. The patterns in microscopic airborne particles that were observed throughout the past year across three Indian smaller towns are presented in this research. The results are significant for developing state and local policy for dealing with the issues of contaminants in the air in urban areas.

Kumar [8] briefed about the analysis and forecast of air quality using data from 2015 to 2020 from 23 cities in India. With and without the SMOTE resampling technique, machine learning-dependent AQI prediction is conducted. GNB, KNN, RF, SVM, and XGBoost were used to carry out the analysis process. Out of all these learning algorithms, XGBoost outperformed based on n-fold cross-validation techniques.

Murali [9] focus on the adverse impact of poor quality. In this paper, the authors aim to monitor AQI in Kerala. In this paper, the authors worked on multiple regression techniques. The benefit of turning toxins into a valuable result for business sectors is examined in this investigation.

Israfil [10] illustrated unorganized growth in population, commercial garbage, and greater movement in vehicles are some of the primary factors leading to the growth in the AQI index. Of all airborne contaminants, particle size (PM) 2.5 is especially worrisome because it adversely affects people's health. With the help of the LR, the machine learning technique helps in predicting the level of PM2.5. Through the prediction, nations may reduce contaminants in the air levels to minimize the worldwide incidence of lung tumors, ischemic attacks, and chronic as well as acute respiratory diseases like bronchitis.

The literature review has helped in understanding how to improve the quality of air so the pupil can lead their life without any threat of inhaling poisonous gas. IoT and machine learning both are playing an important role in determining the quality of air prior, so preventive measures can be taken well in advance. LR clarified that there was a great need to close this gap by doing some research and AQI forecasting for India. ML models have been implemented to achieve the solution to the problem.

3 Proposed Methodology

The paper makes use of a machine learning algorithm for carrying out the analysis. The article is divided into two parts: phase one involves the learning models teaching the machines on the provided dataset. In the next phase, testing is done by implementing ML models. The workflow method is depicted in Fig. 1.

3.1 Data Elicitation and Preprocessing

Data elicitation describes the gathering of data. The test work was conducted using the dataset Air Quality Index in India from an open-source platform www.kaggle.com. The dataset consists of 6 attributes, namely: timestamp, year, month, day, hour, and PM2.5. The timeline of the dataset is from 2017 to 2022. The PM2.5 denotes the size of the pollutant particles in micrometer. At least 0.1 mm, or about the width of a fine hair, is the tiniest object that the human eye can perceive. Any given dataset is subjected to data preparation in order to improve its quality by deleting unnecessary data (Fig. 2).

Since no missing values were found in the dataset and the data is in a usable format and can be used directly for machine learning models. Thus, preprocessing was not required in this dataset.

3.2 Implementing Machine Learning Models

Machine learning algorithm has been applied to the given dataset at this step. The model will be trained and developed utilizing processed data in the present phase. The proposed model is put to the test in order to do an analysis of performance. There are numerous machine learning algorithms out of which we have opted for Random Forest because it can manage unbalanced data and is robust to outliers and nonlinear data. The accuracy, recall, and *f* 1-score were used to assess the performance. By using



Fig. 1 Workflow process

Timestamp	Year	Month	Day	Hour	PM2.5
04-06-2022 00:00	2022	6	4	0	38.8
04-06-2022 01:00	2022	6	4	1	37.94
04-06-2022 02:00	2022	6	4	2	39.91
04-06-2022 03:00	2022	6	4	3	44.31
04-06-2022 04:00	2022	6	4	4	43.65
04-06-2022 05:00	2022	6	4	5	45.31
04-06-2022 06:00	2022	6	4	6	41.89
04-06-2022 07:00	2022	6	4	7	38.34
04-06-2022 08:00	2022	6	4	8	36.63
04-06-2022 09:00	2022	6	4	9	35.84
04-06-2022 10:00	2022	6	4	10	34.71
04-06-2022 11:00	2022	6	4	11	35.89
04-06-2022 12:00	2022	6	4	12	33.83
04-06-2022 13:00	2022	6	4	13	33.05
04-06-2022 14:00	2022	6	4	14	35.29
04-06-2022 15:00	2022	6	4	15	40.67

air-quality-india

Fig. 2 Air quality in India (2017–22). *Source* https://www.kaggle.com

the values from the confusion matrix, various matrices can be computed: accurate positive (AP)–the analysis is positive and the real data is also true; accurate negative (AN)–the analysis is negative, and the real data is also false; inaccurate positive (IP)–the analysis is positive, but the real data is false, and the inaccurate negative (IN)–the analysis is false, but the real data is true. The equations used for the evaluating the performance of classification models are given below (Table 1):

$$\text{accuracy} = \frac{\text{AP} + \text{AN}}{\text{AP} + \text{AN} + \text{IP} + \text{IN}} \tag{1}$$

$$\text{recall} = \frac{\text{AP}}{\text{AP} + \text{IN}} \tag{2}$$

$$f1\text{ - score} = \frac{2(\text{Precision} * \text{Recall})}{\text{Precision} + \text{Recall}}$$

Table 1 Result analysis of random forest w.r.t accuracy, recall, and $f1$-score

Accuracy	Recall	$F1$-score
0.88	0.88	0.88

4 Results and Interpretation

In order to forecast AQI values using the contaminants in the air, this section discusses the experimental design and empirical analysis. In order to assess ML models, the air pollution dataset is divided into training (75%) and testing (25%) subsets. Python scripts have been run on the Google Colab Pro cloud platform. There are numerous data processing jobs that make use of the Python libraries like Scikit-Learn, NumPy, Pandas, Seaborn, etc.

Box plot visualizations are used to thoroughly evaluate the seasonality of the data. Box plots divide all of the data into years and months to divide it into distinct time periods. The Box plots of the summation of PM 2.5 over time, both yearly and monthly, are shown in Fig. 3. Observe how India's pollution levels decline from July to September. It can be a result of the first monsoon during this time period and a sharp increase from October to December. The fact that the median readings for 2020 and 2021 are lower than those for prior years suggests that pollution may have significantly decreased in 2020 and 2021. The obvious cause of this is that during the covid-19 pandemic, a strict lockdown stopped all human and industrial operations in India.

To find the outliers in the current dataset, a correlation-based statistical outlier was identified. All features have been used in the PM 2.5 feature's correlation heatmap analysis. PM 2.5 levels for the year, month, week, and hour are clearly displayed in Fig. 4. PM 2.5 is typically to blame for the AQI reaching higher values.

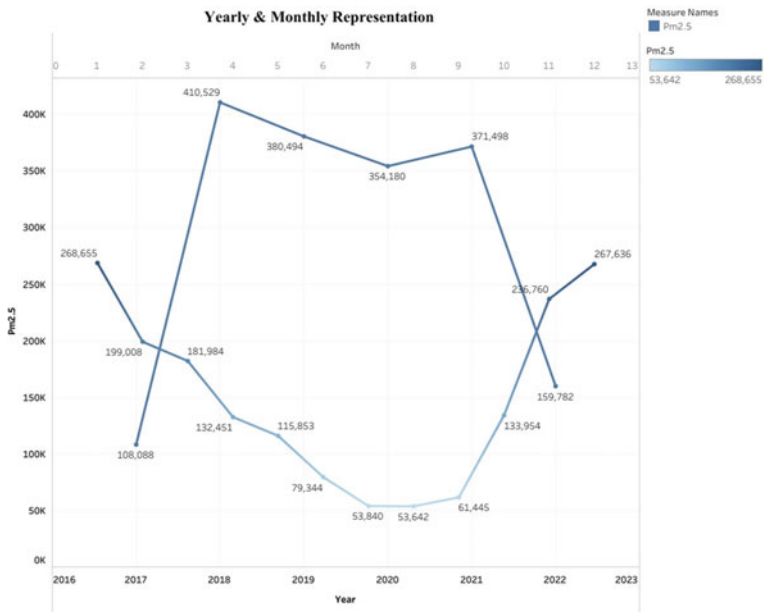


Fig. 3 Intensity of PM 2.5 represented yearly and monthly

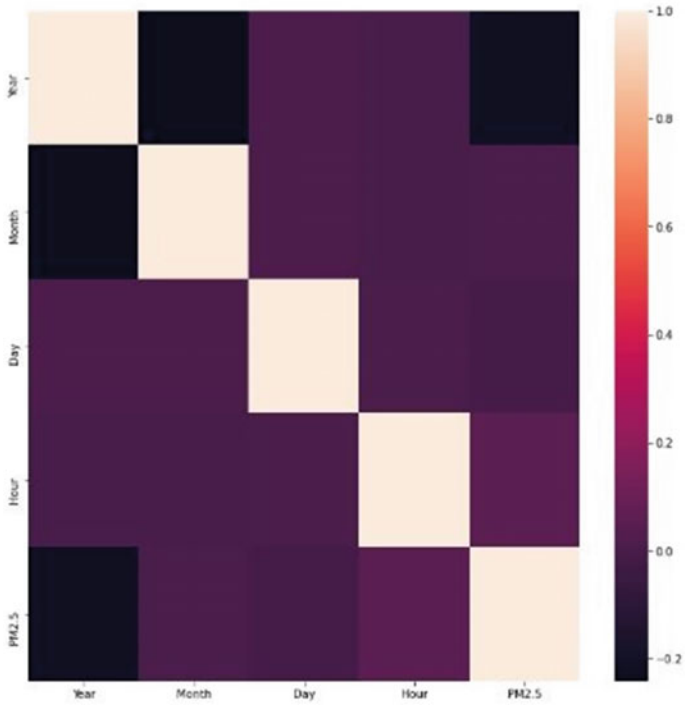


Fig. 4 Correlation heatmap analysis of PM 2.5

To establish the ideal amount of input variables for creating a predictive model, a correlation-based feature selection method has been used in the current implemented work. The algorithms for feature selection based on statistical correlation are used to determine correlations between each pair of the input variable and the target variable. The variables with the highest connection to the target variable are then selected for additional research. Any feature in the input dataset that deviates from the overall trend of the data must be identified because many machine learning algorithms are sensitive to outliers. The correlation analysis of input variable to the target variable has been shown in (Fig. 5).

5 Future Scope and Conclusion

Pollution is claimed to be a serious threat posing the lives of individuals to risk. People are suffering from breathing problems and many other different types of respiratory problems. To improve the quality of life and make the city where we are living smart, pollution management should be taken very seriously. This paper makes use of the random forest algorithm for analyzing the sample data and predicting the

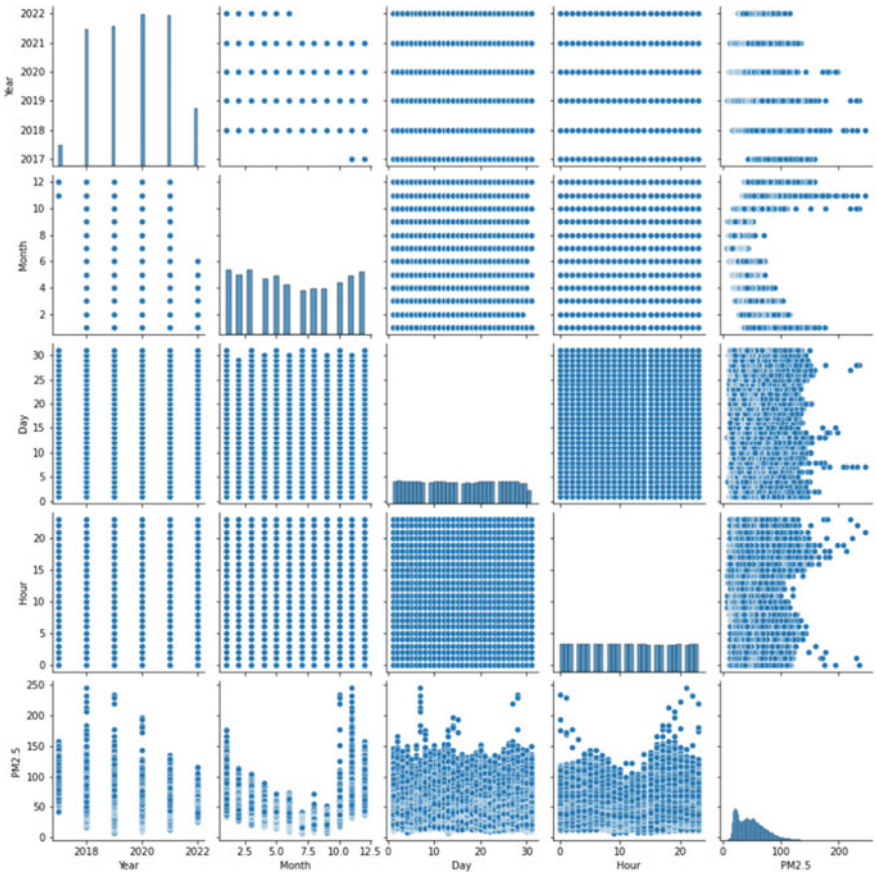


Fig. 5 Correlation analysis of input variable to the target variable

values of accuracy 88.5%, recall 88%, and *f* 1-score 0.088 which can thereby help in predicting AQI values and taking remedial measures before it is too late.

As part of future work, more machine learning algorithms can be applied to the existing dataset, and it can be checked which ML algorithm is providing more accurate results.

Funding Not applicable.

References

1. Monitoring air quality for the Arunachal Pradesh state pollution control board, Article
2. Handbook on Smart Urban Innovations (2021)
3. Neirotti P (2014) Current trends in smart city initiatives: some stylized facts. Elsevier, pp 25–36

4. Siregar B (2016) Integrated pollution monitoring system for smart city. In: 2016 international conference on ICT for smart society surabaya, pp 49–52
5. Peng H (2017) Smart city environmental pollution prevention and control design based on internet of things. In: IOP conference series: earth and environmental science
6. Toma C (2019) IoT solution for smart cities' pollution monitoring and the security challenges. Sensors
7. Agrawal G, Mohan D (2021) Ambient air pollution in selected small cities in India: observed trends and future challenges. IATSS Res 45(01):19–30
8. Kumar K (2022) Air pollution prediction with machine learning: a case study of Indian cities. Int J Environ Sci Technol
9. Murali M (2022) Prediction and analysis of air pollution using machine learning. SN Comput Sci 3
10. Israfil MA (2023) Predictive analysis of air pollution using machine learning techniques. Asia-Pacific J Res Innov 18

Eduline: A Novel Edtech Platform

Shrey Pathak, Pratham Singh, and Purushottam Sharma

Abstract After the boom, we all have seen in Educational Technologies during the pandemic times, it has now become a new and more comfortable way for students to educate and up-skill themselves. Even though this has helped a lot during the pandemic times, this way of education is harmful and not appropriate for students in the long run due to various reasons, especially in India. Eduline will provide a platform to connect educators across the globe with students willing to up-skill themselves and solve all the existing problems that are faced by students and teachers with the current platforms. Eduline does not limit itself here, as it will provide more services as the students grow. It is a way of providing fast and high-quality education, counseling, and doubt-solving to students through live sessions and not just some pre-recorded videos. A student's growth depends on quality teaching and guidance by a teacher; hence, we ensure that they learn from the top educators on our platform.

Keywords EdTech · Education · Counseling

1 Introduction

We have analyzed the issues that were faced by the students with the current platforms of EdTech. Let's divide the problems of the current Edtech platform and the solutions for them.

Present Address:
S. Pathak (✉) · P. Singh · P. Sharma
ASET, Amity University Uttar Pradesh, Noida, India
e-mail: shreypathak7@gmail.com

P. Sharma
e-mail: psharma5@amity.edu

© The Author(s), under exclusive license to Springer Nature Singapore Pte Ltd. 2024

S. Singh et al. (eds.), *Recent Advances in Aerospace Engineering*, Lecture Notes in Mechanical Engineering, https://doi.org/10.1007/978-981-97-1306-6_3

1.1 The Industry Scenario

The expansion of the online education market can be attributed to various factors, including the increasing global internet penetration and the adoption of cloud-based solutions [1]. Significant market players are investing significantly in improving the security and reliability of cloud-based education platforms, thereby driving the acceptance of these platforms among end-users [2]. Additionally, the availability of numerous service and content providers has made a considerable amount of educational content accessible online, further contributing to the market's growth.

In recent years, e-learning websites have gained popularity as they offer a wide range of online courses and educational resources to learners worldwide. Among the most prominent e-learning platforms are Udemy, Unacademy, Chegg, and Superprof, which have user-friendly interfaces and vast collections of courses. Recent statistics reveal that Udemy has over 50 million registered users and receives more than 40 million monthly visits. Similarly, Unacademy has around 100 million monthly visits, making it the most popular e-learning platform in India [3]. Chegg has over 20 million monthly visits and around 3 million subscribers, while Superprof receives over 5 million monthly visits (refer to Fig. 1 for exact figures). These figures demonstrate the significant demand for online learning and the growing popularity of e-learning platforms among students and professionals seeking to enhance their knowledge and skills.

2 Literature Review

The purpose of this literature review is to provide information that can be collected and utilized to explore the impact of technology on education, including the types of technology that are being utilized in schools today. The utilization of technology

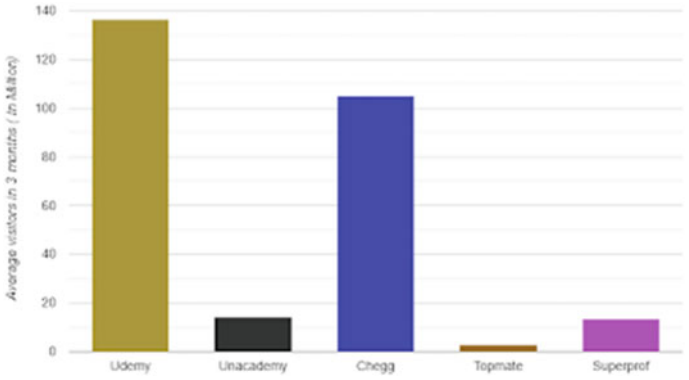


Fig. 1 Average monthly website visitors in 3 months

has changed the way students interact with their teachers [4] for help and inquiries, resulting in changes not only in the way students learn but also in the way teachers teach. This review examines the progress made in educational technology and how it has influenced students' learning methods [5]. It also provides information on the amount of time students spend using technology and the progress they have made. It acknowledges both the positive and negative perspectives on the subject as well as the ways, in which instructors are receiving support for this technology [6].

Educational institutions play a crucial role in nurturing the abilities and skills of young individuals, making it logical to introduce technology to them at a young age to aid in their development. Steven Hack Barth, in his book "The Educational Technology Handbook," defines educational technology as a methodical approach to resolving teaching and learning issues [7]. Technology has brought about a significant transformation in education through the provision of advanced tools that have impacted the entire educational system. In the past, the primary method of instruction for the general public was through professor-led lectures without any means for students to visualize information apart from the use of pen and paper [8].

3 Methodology

After successfully installing Visual Studio Code and the Python development kit on our PCs, we were able to start working on our project. This initiative would benefit e-learning. This web application is incredibly simple to use and user-friendly. The project is split into three sections:

3.1 Frontend

- This application's front end is made up of HTML, CSS, JavaScript, and ReactJS.
- HTML stands for Hypertext Markup Language, which is used to create and host simple web pages.
- Cascading Style Sheets, or CSS, are used to style HTML pages. There are several features that can be used during styling.
- JavaScript is a scripting language that enables the addition of HTML form and button functionality.
- React JS is a free and open-source JS framework for creating user interfaces. For single-page, mobile, or server-rendered applications, it can be utilized as an environment. It oversees rendering to the DOM and managing the state. Additional libraries and client-side functionality are also needed to construct React applications. JSX, a JS and XML hybrid, is used to create React JS. The elements are defined using JSX, and JS is then used to render them. React is a very declarative, effective, quick, and versatile framework [9].

3.2 Backend

- Node JS-This event-based, open-source development platform is used to run JavaScript code on the server. It is constructed using Chrome's JavaScript engine to create scalable network apps with ease [10].

3.3 Database

- MongoDB-This database management program leverages NoSQL, making it a viable substitute for conventional databases. It provides performance, high availability, and autonomous scaling [11]. Due to its flexible schema feature, it is a favorite of agile development teams.

3.4 APIs

- ZEGOCLOUD-With the help of ZEGOCLOUD's Video Call service, you can include the most feature-rich video experience into the web and mobile apps. The SDK and the UI Kit provided to us by ZEGOCLOUD provide everything we need to develop a video app in two different ways [12]. These two types of SDKs cover all phases and all of your concerns to assist you in creating the precise video app that you desire.

4 Proposed Model Eduline

Eduline provides a platform to connect educators across the globe with students willing to learn and up-skill themselves. Eduline does not limit itself here, we provide more services for the students to grow. It is a way of providing a fast and high-quality education, counseling, and doubt-solving to students by providing one-on-one live sessions. A student's growth depends on quality teaching and guidance by a teacher hence we ensure that they learn from the top educators on our platform. Figure 2 shows the flow of the web app.

By using high-end and self-maintained technology, we are building an easy, safe, and reliable one-stop platform for people who are willing to learn or up-skill themselves, irrespective of their locations. We desire to offer students the chance to receive an excellent education from renowned teachers and mentors throughout the world and to establish an environment where they may receive guidance and mentorship in order to choose the proper career path for them. Eduline is not only for students but also for educators who are willing to teach, making it easy for them and removing their work of gathering and managing the students. They can also be students who

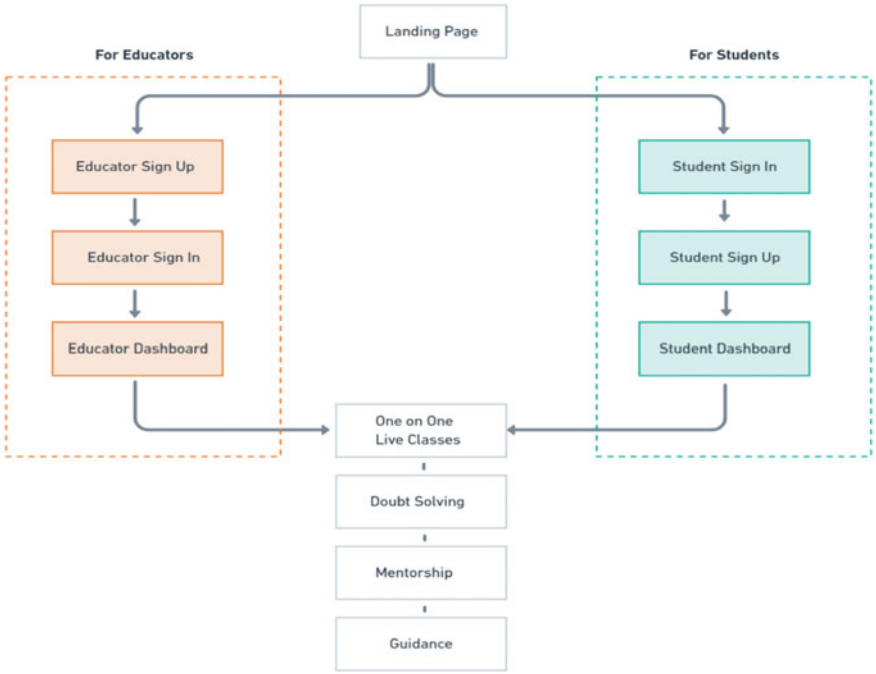


Fig. 2 Eduline workflow

want to guide their juniors to the path of success. Together working like a family, we aim to make an impact on students by providing facilities to outshine and personal growth. Along with that, we open opportunities for universities to showcase their campus on our platform and for counselors to provide their services. Keeping the spirit higher, we wish to expand globally as well.

4.1 Services

Services which Eduline would be offering to the students, educators, counselors, professionals, and universities would be the followings:

One-on-one live class

- For students: From various categories and subjects, students can choose whomsoever they want to study from (educator), on our platform
- For educators: Experts from different fields and domains can register themselves on our platform and teach the students according to their available schedules.

One-on-one doubt solving

- For students: From different categories and subjects, students can ask questions on our platform and choose from the teachers who bid to solve that question.
- For educators: They can bid on the question asked by the student, by providing their price, for solving the doubt and can solve it directly or schedule a live session, as per the student's choice.

One-on-one counseling sessions (career counseling)

- For students: Students having doubts regarding their career during the times after Class 10th and Class 12th, can have a counseling session from our top counselors and have guidance regarding what can suit them the best.
- For counselors: Counselors can register on our platform and provide paid career counseling sessions to students. Our platform will take care of everything from finding the students to getting the fees.

One-on-one counseling session (professional counseling)

- For students: Users who want to seek professional guidance like resume and portfolio reviewing or know about the industry fields and domains can schedule sessions according to their requirements from our platform.
- For counselors: Counselors and industry experts can register on our platform and provide paid Professional Counseling sessions to others. Our platform will take care of everything from finding the students to getting the fees.

Find the top 1% mentorship

- For students: Users who want to set up their start-ups and need to seek guidance or are stuck with anything, can schedule sessions according to their requirements from our platform.
- For mentors: Top mentors can register themselves on our platform and provide paid mentorship sessions to students. Our platform will take care of everything from finding the students to getting the fees.

Study abroad counseling and virtual tour of universities around the globe

- For students: Students who are looking to pursue their careers and jobs abroad can get all the necessary guidance and counseling. Apart from that, students can also get help in applying to universities in different countries and for different courses. Students can get the essence of studying in that university through our University Virtual Tour. They will get to have a tour of the campuses of the universities and the courses.
- For Counselors: Counselors in the industry of overseas education can register themselves on our platform and provide the services.
- For Universities: They can register on our platform and our platform will provide a feel of their university by giving a virtual tour and the essence of studying at that university.

4.2 Eduline in Aerospace

Eduline, with its mission to provide fast and high-quality education, counseling, and doubt-solving, can play a significant role in promoting and enhancing Aerospace in engineering and technology. By leveraging its platform and connecting educators across the globe with students who are interested in the aerospace field, Eduline can facilitate the dissemination of knowledge and skills in this specialized domain. Here are a few ways in which Eduline can contribute to the advancement of Aerospace.

- Expert Aerospace Educators: Eduline can identify and onboard top educators who have extensive experience and expertise in the aerospace industry. These educators can offer specialized courses, live sessions, and mentorship programs to students interested in aerospace engineering and technology. By learning from renowned professionals, students can gain insights into the latest advancements, industry practices, and real-world applications in aerospace.
- Comprehensive Course Offerings: Eduline can curate a diverse range of courses that cover various aspects of aerospace engineering and technology. This can include subjects like aerodynamics, spacecraft design, propulsion systems, materials science, avionics, and more. The courses can be designed to cater to different levels of learners, from beginners to advanced students, providing a holistic learning experience.
- Hands-on Practical Training: Along with theoretical knowledge, practical training is crucial in aerospace education. Eduline can collaborate with aerospace companies, research institutions, and experts to develop practical training modules. These modules can include simulations, virtual labs, and access to specialized tools and software used in the aerospace industry. By providing hands-on experience, students can develop the necessary skills required for a career in aerospace.
- Career Guidance and Mentoring: Eduline can establish a mentorship program where students aspiring to pursue a career in aerospace can connect with experienced professionals in the field. Mentors can guide students in choosing the right academic path, internships, and research opportunities, and provide valuable insights into the industry.
- Industry Collaborations and Guest Lectures: Eduline can collaborate with aerospace companies, research organizations, and industry experts to host guest lectures, webinars, and panel discussions.

Through these initiatives, Eduline can serve as a catalyst for the growth of aerospace in engineering and technology. By offering access to top educators, comprehensive courses, practical training, mentorship, and industry collaborations, Eduline can empower students to excel in the field of aerospace and contribute to its advancements in the years to come.

4.3 Validation of the Platform

Validating a proposed EdTech platform involves assessing its effectiveness, usability, and impact on learning outcomes. Here are some key aspects and methods for validating an EdTech platform.

- Pilot Testing: Conducting pilot tests with a small group of users, such as students and teachers, can help gather feedback and identify potential issues.
- User Feedback: Gathering feedback from the target users is crucial for validating an EdTech platform.
- User Experience (UX) Testing: Evaluating the user experience is essential to ensure the platform is intuitive, user-friendly, and meets the needs of its users.
- Analytics and Data Analysis: Utilizing data analytics can provide valuable insights into user behavior, platform usage patterns, and overall effectiveness.
- Expert Evaluation: Seeking input from education experts, teachers, and instructional designers can provide valuable perspectives on the quality, pedagogical approach, and alignment of the platform with educational standards.

It is important to note that the validation process should be iterative, with regular feedback collection and continuous improvement cycles. The findings and feedback gathered during the validation phase should guide refinements and updates to the platform to ensure it meets the needs of its users and enhances learning outcomes effectively.

4.4 Threats to Validity

Some of the threats that can hinder the platform development and performance can be:

- Selection Bias: If the users of the EdTech platform are not representative of the target population, it can introduce selection bias. For example, if the platform is primarily used by students with high academic performance, the results may not be applicable to the wider student population.
- Sampling Bias: When conducting studies or gathering data from the EdTech platform, the sample of users chosen may not accurately represent the overall user base. This can lead to biased findings and limited generalizability.
- Measurement Bias: Issues with the measurement tools or methods used within the EdTech platform can introduce measurement bias. This could include inaccuracies in data collection, faulty algorithms, or inconsistent grading methods.
- Social Desirability Bias: Users of the EdTech platform may provide responses or engage in activities that they believe are socially desirable or expected. This bias can impact the accuracy of self-reported data or observed behavior.
- Time Constraints: The duration of the study or evaluation period may not be sufficient to capture the long-term effects of the EdTech platform. Short-term

gains or changes may not accurately represent the platform's true impact over an extended period.

To mitigate these threats, it is important to employ rigorous research methodologies, use appropriate control groups, collect diverse and representative data, and ensure transparency in reporting results. Additionally, conducting multiple studies or independent evaluations can help validate the findings and address potential biases.

5 Conclusion

Eduline provides a platform for fast and easy communication between students and educators around the globe. This platform will be an absolute solution for nearly every aspect of the educational field. The focus of Eduline is to connect students and educators for purposes like studying, doubt-solving, counseling, mentoring, and even choosing the right colleges and universities for the student. Founded by the students themselves, we are dedicated to fulfilling all the challenges that are known and that were faced by us as students for the upliftment of the next generation. Even though e-learning is on the boom, users tend to feel that there is a lack of quick and reliable doubt-solving platforms and one-to-one live teaching. The existing platform only provides pre-recorded courses and classroom-based learning. Eduline will tackle all these problems and provide the best solution for them. We want to enable students to have an opportunity for high-quality education from top educators and mentors around the globe and create an experience for the students to make the right career choice through counseling and mentorship.

Funding Not applicable.

References

1. Research and Markets (2021) Global online education market: size, trends and forecasts (2021–2025)
2. KPMG (2017) Online education in India: 2021. https://home.kpmg/in/en/home/insights/2017/03/online-education-in-india.html
3. MarketsandMarkets (2021) Online education market by component, product, learning type, end user and region—global forecast to 2025. https://www.marketsandmarkets.com/Market-Reports/online-education-market-229410995.html
4. Inside Higher Ed (2019) Survey finds more faculty members have positive attitudes about online learning. https://www.insidehighered.com/digital-learning/article/2019/04/03/survey-finds-more-faculty-members-have-positive-attitudes-about
5. Education Week (2021) The future of classroom technology: 5 experts weigh in. https://www.edweek.org/technology/the-future-of-classroom-technology-5-experts-weigh-in/2019/11
6. Superprof (2021) About Us. https://www.superprof.com/about.html
7. Chegg (2021) About Chegg. https://www.chegg.com/aboutus/
8. Udemy (2021) About Us. https://about.udemy.com/

9. Gupta N, Sharma P, Deep V, Shukla VK (2020) Automated attendance system using OpenCV. In: ICRITO 2020—IEEE 8th international conference on reliability, infocom technologies and optimization (trends and future directions), pp 1226–1230. https://doi.org/10.1109/ICRITO48877.2020.9197936
10. Aashkaar M, Sharma P (2016) Enhanced energy efficient AODV routing protocol for MANET. In: International conference on research advances in integrated navigation systems, RAINS 2016. https://doi.org/10.1109/RAINS.2016.7764376
11. Sharma P, Saxena K, Sharma R (2016) Heart disease prediction system evaluation using C4.5 rules and partial tree. In: Behera H, Mohapatra D (eds) Computational intelligence in data mining—Volume 2. Advances in intelligent systems and computing, vol 411. Springer, New Delhi. https://doi.org/10.1007/978-81-322-2731-1_26
12. Kumar S, Viral R, Deep V, Sharma P, Kumar M, Mahmud M, Stephan T (2023) Forecasting major impacts of COVID-19 pandemic on country-driven sectors: challenges, lessons, and future roadmap. Pers Ubiquit Comput 27(3):807–830. https://doi.org/10.1007/s00779-021-01530-7

Net Quest: Networking Through Gaming

Rushali Salina Singh, Pankaj Bansal, Aarushi Saini, and Purushottam Sharma

Abstract While travelling in an airplane where one searches for something entertaining to do or watch, despite watching any movie or show or playing a game which does not contribute to an intellect of a child, one can make use of this precious time by playing this game called 'Net Quest.' While travelling via air, there is a lot of time for an individual to put his/her mind to work in a good direction and this game provides a perfect experience of educational gaming, not only proving to be fun while playing but also educative while getting to know about important concepts throughout the game. We aim to make a fun 2D platformer game educating about networking concepts using the Unity engine and inspired by AWS Cloud Quest. This game has been designed to easily learn the rules and promote cooperative and competitive learning.

Keywords STEM education · 2D platformer game · Networking

1 Introduction

Lately, gaming businesses have hiked over the market. The market size of games in 2022 is USD 220.79 billion, and in 2030, it will turn around USD 583.69 billion. To keep players engaged, modern games feature a diverse array of activities and challenges that require active exploration of the game world and the use of different problem-solving techniques [1].

Trolley problem, a prominent ethical thought experiment, was made known by a philosopher named Philippa Foot who also stated that moral judgments have a logically reasoned and perceptive foundation [2]. The concept of the Trolly problem can simply be described as that it is a decision-making skill where our decisions may either be right or wrong, basically representing us by what our point of view is, because based on our point of view we take decisions which in turn represent us.

R. S. Singh · P. Bansal · A. Saini · P. Sharma (✉)
ASET, Amity University Uttar Pradesh, Noida, India
e-mail: puru.mit2002@gmail.com

© The Author(s), under exclusive license to Springer Nature Singapore Pte Ltd. 2024

S. Singh et al. (eds.), *Recent Advances in Aerospace Engineering*, Lecture Notes in Mechanical Engineering, https://doi.org/10.1007/978-981-97-1306-6_4

The concept of the **12-year-old Kid trolley problem** (the Trolly problem was later called the 12-year-old kid trolley problem) is incorporated into the game **Fairside Justice** through a storytelling technique. The game requires players to make small decisions like the ones we make in our daily lives. These choices can result in some players gaining benefits, while others may experience losses or feel bad due to certain decisions. These seemingly insignificant decisions illustrate how even the smallest actions can profoundly impact our lives. The game does not provide any conclusive outcomes, but it does help us understand the roles we may play, whether we choose to be wise or dumb. Our perceived wisdom may vary depending on the situation, but ultimately, we are all playing a role with no perfect definition of what is right or wrong. It is up to us to choose the best course of action that leads us to the best possible outcome.

The inner aerospace experience can be made one hundred per cent more fun both through gaming and education wise with Net Quest, while children are busy watching unimportant stuff over the Internet, they can shift their mind towards a game which not only provides a good opportunity for a user to just pass from one stage to another but also provides education through the game by popping up networking concepts through the stages of the game.

This paper will explore how video game concepts can be applied in education. Specifically, in this Net Quest paper, we will introduce the concepts of networking through video games. The approach involves utilizing storytelling, networking challenges, and a reward system akin to other games to make the learning experience more engaging and interactive.

2 Literature Review

Video games are not limited to providing entertainment; they have also been found to be beneficial in education. In fact, video games can help develop valuable skills, impart cultural values, historical learning, and facilitate STEM education [3]. Therefore, video games have great potential in the field of education. We can learn so much about history in an entertaining way, e.g. let us take '**Raji: An Ancient Epic**' game into consideration. This game was released in the autumn of 2020 and is based on both Hindu mythology and Indian cultural heritage [4]. There is another set of video games that is skill based, i.e. Amazon AWS Cloud Quest. AWS Cloud Quest revamped Educate programme, which now offers new courses. This video game is intended for students and job-training participants as young as 13 who are interested in cloud computing and seeking self-guided learning opportunities. In conclusion, video games have many potential benefits for education [5], including increased engagement, improved understanding of complex concepts, and personalized learning.

Many students found learning how to code to be an intimidating prospect for which a game named 'RunJumpCode' was introduced. The aim of RunJumpCode was to teach players the fundamental principles of C# programming [6] through a

2D platformer game developed in Unity. By providing a range of challenging and puzzle-solving challenges, the game enhances the player's programming skills, to encourage players to interact with programming, a 'Code Box' was provided to them that allowed entry of predefined lines of code that changed in-game objects. The player had creative freedom to complete each level by modifying the properties of each object. The tool was vital to complete the challenges and puzzles designed. According to the findings of a pilot study, users enjoyed the game and thought it was helpful for improving their programming skills.

It is possible to predict the effect of hardware upgrades, topology changes, traffic load increases or the implementation of new applications using a simulation tool known as cisco packet tracer [7] through which a LAN Network can be developed.

Another interactive and addictive 2D platformer game known as 'Mario' matches almost all the attributes of our game like being challenging, containing an engaging storyline, and having user-friendly controls [8]. Also, the goals are same to a decent level like this game provides a chance for the user to conceive some other characteristics of variables in programming by interacting and playing the game. At the end of the proposed activities, participants will be equipped with the necessary knowledge to collaborate and design their own solutions. While in Net Quest, the user gets knowledge side to side while playing the game.

A good way to get started is to get familiarized with the basics of configuration commands. In order to make the learning of concepts enjoyable and motivating for students, creation of a computer game is a must [9]. There is a cooperative element as well as a competitive element to this game, making it interesting and educative for anyone.

3 Methodology

3.1 Game Design and Language Used

In order to make this project more user-friendly and keep a high degree of detail without losing its volume, we will combine flat art with cell shading art to create it with more warm hues. Here, we will use an iterative methodology where we first construct, then create a prototype, and last test. The project will include ongoing alpha testing. The project will include ongoing alpha testing. The programme for making art will be Adobe Photoshop and Inkscape. The game documentation management system Miro will be utilized. Additionally, the Unity game engine will be utilized, which offers excellent versatility for both the user and developer and is readily accessible on most Android devices. Additionally, it will enable the incorporation of artwork without the need for other applications. C# will be used by us in this instance. We will be able to handle objects with ease and the C# language will be adaptable for desktop apps. We will work on a basic networking model using the

Cisco packet tracer as our source of inspiration. We will gamify the networking development carried out in Cisco Packet Tracer. It will be a narrative-driven game.

3.2 Game Engine

We used Unity Game Engine, to develop this game, it easily supports 2D and 3D games, unity is specifically popular for mobile games [10]. Additionally, it supports the low-level APIs Metal on iOS and macOS and Vulkan on Android, Linux, and Windows, as well as Direct3D 12 on Windows and Xbox One. We also used Inkscape, for level designing to character designing which provides great flexibility for the creation and provides great convenience for filters that can be applied to the art [11]. We are also using Hotween v2 which is a popular animation library for Unity that allows us to easily create tweens and other animations in your game or application. It also provides a lot of flexibility in terms of how we can create the animations. It creates simple tweens with just a few lines of code, or we can use more advanced features like curves, loops, and callbacks to create more complex animations. All these software help to make our game fun and interactive, we acquired input from various games, i.e. Disney, AWS Cloud Quest, Hollow Knight, etc. (Fig. 1).

4 Major Contribution

Today, there are numerous games that support education. Disney is one platform that supports such games. It even provides preschool games through an app known as Disney Junior. Educational games for critical media literacy education are a promising approach to teaching students how to analyse and interpret media messages [12]. The Net Quest: Networking Through Games-game is inspired by ideas of the AWS Cloud quest game, Disney Games, and other above-mentioned games. When we design an educational game, many issues are faced where we want the user to play the game in a way that he/she connects real-life scenarios and makes decisions accordingly.

Creative games require observation, research and innovation [13, 14] by using a relevant structure. While other games with numerous objectives and unwanted elements may promote recall less than classical lecture-based teaching [15–18].

The main aim of Net Quest is to teach networking concepts for general education while playing the game in order to give the user a fun learning experience. The networking concepts include concepts like:

1. Local Area Network (LAN)
2. Wireless Local Area Network (WLAN)
3. Wide Area Network (WAN) (Fig. 2).

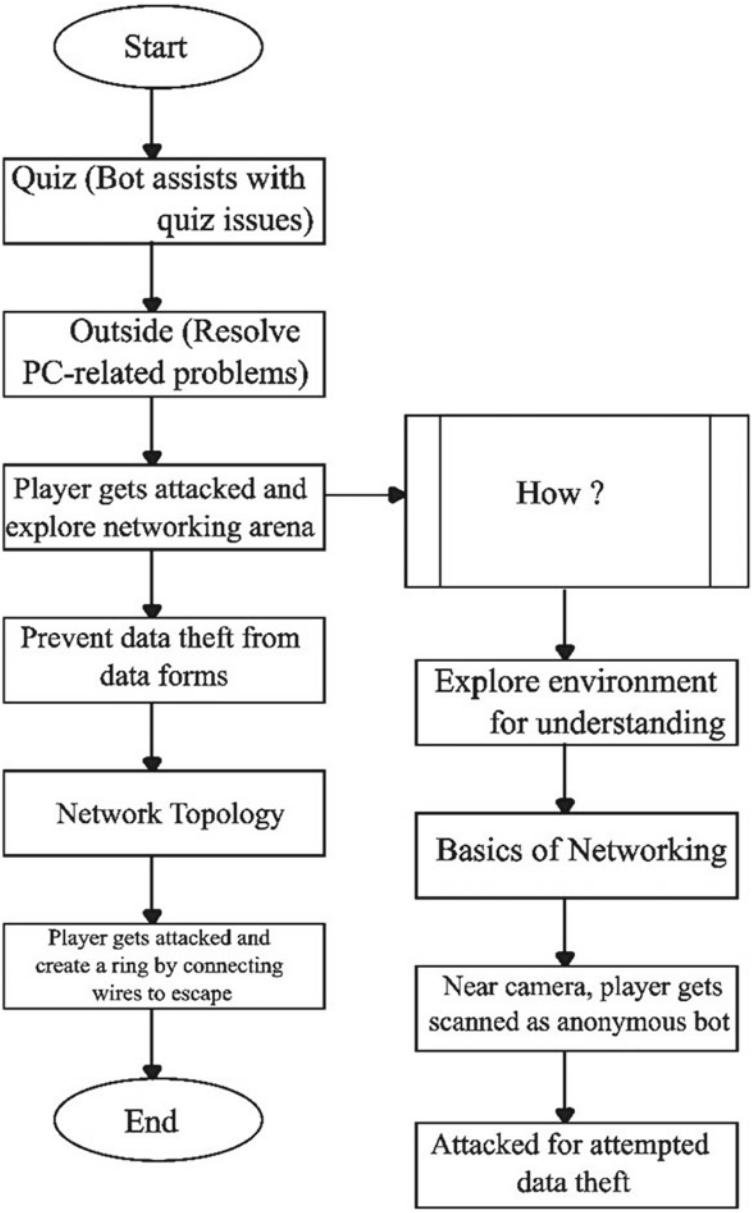


Fig. 1 Workflow of game design

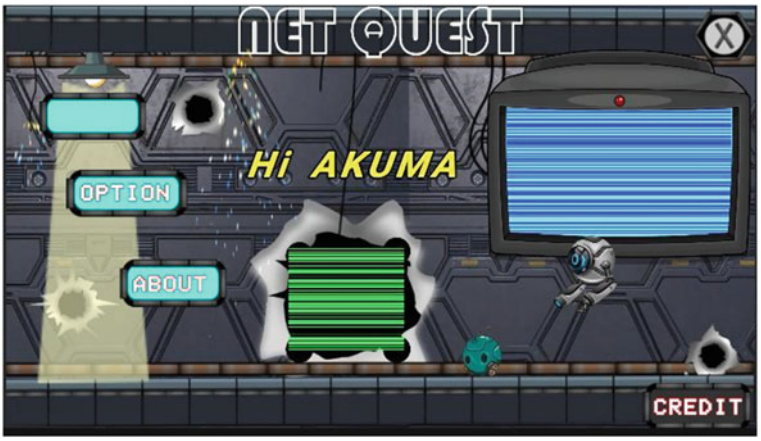


Fig. 2 Menu page

The 'Net Quest' is a 2D platformer game, which represents the interesting story of a user who is lost in a networking world full of networking problems and must figure a way out of that world by solving networking problems themselves. Whatever option the player chooses throughout the game either the right or the wrong one, the game will keep on teaching the concepts. So, players have to basically figure their way out from the networking world (Fig. 3).

Dale (The Guide) will further ask a few questions on how to deal with the issues it is facing, and then according to the user input, the game will move ahead, when this task is completed, the player will be able to see a short intro story scene as can be seen in Fig. 4.

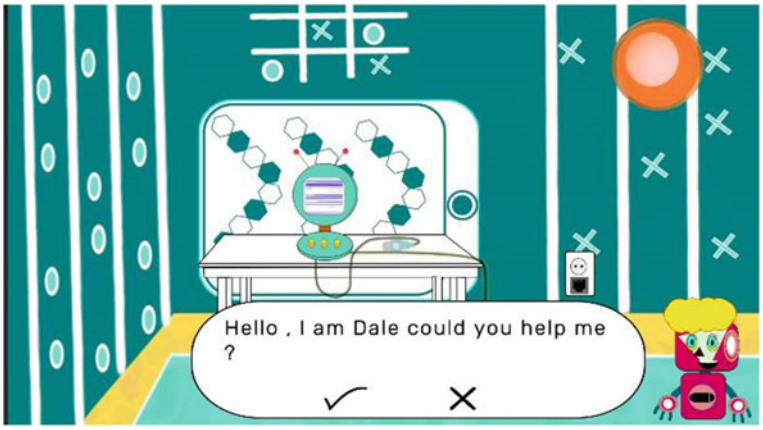


Fig. 3 First scene



Fig. 4 Story scene

After completion of the story scene, the player enters the networking realm. During his/her first phase of the networking realm, the player's identity is set anonymous following which all the doors present further in the game get locked because basically an anonymous user is seen as a threat in networking so on connecting the dots that is what is depicted through the game, now naturally when the door is locked and the player isn't able to go through the next stage it'll have to figure out another way, to cross the LAN arena. As can be seen in Fig. 5.

The player cannot move further in the game until the door is opened and the door will not open until the player does not cross the door detector, get its id as anonymous through the camera and play the game. When the player interacts with the camera, a question mark sign appears over the character as shown in figure above which depicts a sense of threat because the identity of the player is anonymous. In this stage of

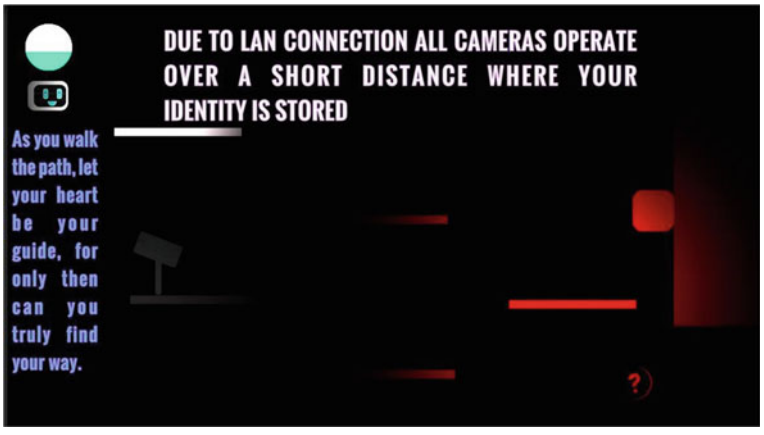


Fig. 5 LAN room

the game, we get to learn this information that due to LAN connection all camera operates over a short distance, where your identity gets stored in the camera.

Now this statement is completely like this statement that 'LAN connects computers over a relatively short distance, allowing them to share data, files, and resources. For example, a LAN may connect all the computers in an office building, school, or hospital. Typically, LANs are privately owned and managed.' which stated by IBM.

When the user passes through the door detector (placed just near the door entry) and gets detected in the camera as anonymous, then it gets a chance to skip through the bars visible in the game and reach an area above the door which gets opened for the user to go to the next level. Further in the game much more concepts of basics of networking, i.e. IP Address, Nodes (which is used in the game), Routers, Switches, Ports, Network cable and much more can be added to make it a better educational networking game.

As you can see in Fig. 6, there is a board in the scene that represents the Ring Topology. The players must solve the shown riddle of connecting wires and connect the wires according to the given topology while avoiding the laser and enemy bots. Net Quest has other typical concepts which increase the player's motivation while studying as not only the player is driven towards the game but also the player gets a boost of their intellect in the networking concepts and hence the education is made much interactive and easy to understand additionally providing a feel of playing a game.

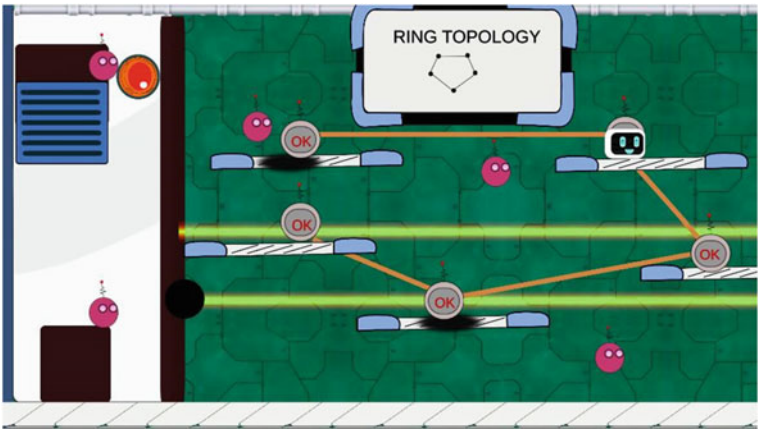


Fig. 6 Topology concept design

5 Limitations

1. Portability is the first major limitation, namely how and what can be carried in PC games teach real-world skills, which transfer to the real world which reveals weakness of PC games. It is commonplace for video games to have challenges that are based on fiction, not real-life challenges.
2. The second limitation is simplicity. In real life, complex systems defy the simple logic of PC games. Games simplify complex systems to their core and exist primarily as procedural representations of the real world.
3. The third limitation is that games lack real-life environments. After the game finishes, they are not intended to have any lasting impact on the player. Even games with a realistic goal, such as serious games or educational games, typically fail when they are applied to the real world.
4. Last limitation is about the environment where students frequently struggle to naturally draw connections between the lessons, they learn in PC games and real life.

6 Conclusion

This paper basically introduces 'Net Quest: Networking through Gaming,' a game designed to help students achieve their learning goals in a way that is more entertaining and interactive. By integrating this game into the education system, new ideas of teaching can be explored. Through this game, students are allowed to develop skills and competencies through a simulation game-based learning model, which goes beyond traditional knowledge-based objectives. However, it is more important to focus on expanding the range of concepts that students can learn from this game. There are no boundaries when it comes to extending the game. Numerous networking concepts can be added to the game in order to make it much more beneficial.

Funding Not applicable.

References

1. Stephen E (2007) Video games in the 21st century, entertainment software association
2. Misselbrook D (2021) The trolley problem, 2021 style. Br J General Pract
3. Merrilea J (2009) Video games: a route to large-scale STEM education. Rockhill Road, Kansas City, USA
4. Zeiler X, Mukherjee S (2022) Video game development in India: a cultural and creative industry embracing regional cultural heritage(s), Helsinki 00014, Finland (2022)
5. Šakić M, Varga V (2015) Video games as an educational tool. In: The sixth international, econference.metropolitan.ac.rs
6. Hinds M, Baghaei N, Ragon P, Lambert J, Dajakaruna T, Houghton T, Dacey S, Casey J (2017) Designing a novel educational game for teaching C# programming. In: McLaren BM (ed) 9th International conference on computer supported education, Porto, Portugal

7. Janitor J, Jakab F, Kniewald K (2010) Visual learning tools for teaching/learning computer networks. Košice, Slovakia
8. Theodorou C, Kordaki M (2010) Super Mario: a collaborative game for the learning of variables in programming, Greece
9. Herráez M, Gomez R, Claver J (2009) Conquer the net: an educational computer game to learn the basic configuration of networking components, Valencia, Spain
10. Patil P, Alvares R (2015) Cross-platform application development using unity game engine. Int J 3(4)
11. Sharma P, Saxena K, Sharma R (2016) Heart disease prediction system evaluation using C4.5 rules and partial tree. In: Computational intelligence in data mining—Volume 2. Advances in intelligent systems and computing, vol 411. Springer, New Delhi. https://doi.org/10.1007/978-81-322-2731-1_26
12. Bah T (2007) Inkscape: guide to a vector drawing program, 1st edn. Prentice Hall Press, Upper Saddle River, NJ, USA
13. Thevenin B (2020) Dark ride: Disneyland. Using educational games for critical media literacy education. J Media Literacy Educ 12(1):100–122
14. Gupta N, Sharma P, Deep V, Shukla VK (2020) Automated attendance system using OpenCV. In: ICRITO 2020—IEEE 8th international conference on reliability, infocom technologies and optimization (trends and future directions), pp 1226–1230. https://doi.org/10.1109/ICRITO48877.2020.9197936
15. Gee JP (2003) What video games have to teach us about learning and literacy. Palgrave Macmillan, New York
16. Betz JA (1995) Computer games: Increase learning in an interactive multidisciplinary environment. J Educ Technol Syst 24:195–205
17. Oyen A, Bebko JM (1996) The effects of computer games and lesson contexts on children's mnemonic strategies. J Exp Child Psychol 62:173–189
18. Aashkaar M, Sharma P (2016) Enhanced energy efficient AODV routing protocol for MANET. In: International conference on research advances in integrated navigation systems, RAINS 2016. https://doi.org/10.1109/RAINS.2016.7764376

Numerical Studies of Hybrid Rocket Propellant



Amit Kumar Thakur, Sanjivani Nikam, and Sachin Srivastava

Abstract Future space missions are expected to be significantly impacted by developments in hybrid rocket propellant technology. Propellants that are more effective, sustainable, and good for the environment are needed to travel to more places in space and are cost-effective. In the current scenario, it is necessary to use high-performance propellant with the least amount of fuel so that space missions can reach their orbit and accomplished their mission. Sounding rockets, experimental airplanes, and space launch vehicles are just a few of the current uses for hybrid rocket engines. Due to a better combination of fuel/oxidizer and their benefits, such as a high specific impulse, improved safety, and simpler handling compared to conventional liquid or solid fuel rockets, hybrid rockets have the potential to be used in military weapons. The effectiveness of blend metal additions in enhancing the performance of hybrid rocket propellants has been the subject of much investigation. Metal additives can improve mechanical and combustion properties. This paper evaluates fuels such as paraffin and paraffin with additives aluminum and boron and oxidizer as liquid oxygen and discusses their combustion characteristics.

Keywords Hybrid rocket engine · Hydroxyl-terminated polybutadiene · Paraffin · Chemical equilibrium applications · Liquid oxygen · Nitrous oxide

1 Introduction

The aerospace field has anticipated significant growth in recent years as a result of novel advancements that have appeared on the global market. These technologies have made it possible to commercialize a variety of uses, such as launchers for putting satellites with communications in orbit and growing interest in environmentally friendly space travel. Hybrid rocket engines (HRE) have a distinct advantage over liquid-propellant rockets and solid-propellant rockets in terms of simple design, safety, and operation. This is due to their design, which involves injecting a liquid or

A. K. Thakur (✉) · S. Nikam · S. Srivastava
Aerospace Department, Lovely Professional University, Phagwara, Punjab 144001, India
e-mail: amit.25010@lpu.co.in

© The Author(s), under exclusive license to Springer Nature Singapore Pte Ltd. 2024

S. Singh et al. (eds.), *Recent Advances in Aerospace Engineering*, Lecture Notes in Mechanical Engineering, https://doi.org/10.1007/978-981-97-1306-6_5

gaseous oxidizer into an inert solid fuel grain. Because of this design, hybrid rockets are safe and highly desirable for both military and commercial applications. In an HRE, a solid fuel grain is located at the combustion chamber of the rocket, and a liquid or gaseous oxidizer is injected into the combustion chamber at the head-end of the grain. The oxidizer then mixes with the solid fuel, causing it to burn and produce hot gases that are expelled out of the rocket nozzle, generating thrust [1].

For space missions to be successful, the performance of hybrid rocket engines is essential, and choosing the right fuel is critical to achieving high performance and cost-effectiveness. The usefulness of blend metal additions in enhancing the performance of hybrid rocket propellants has been the subject of much investigation. Metal additives can improve mechanical and combustion qualities. Various fuels and oxidizers can be used by hybrid rockets, depending on the mission's demands. Hydroxyl Terminated Polybutadiene (HTPB) [2, 5], paraffin wax [6, 8], and Poly Methyl Methacrylate (PMMA) fuels are frequently utilized as fuels in hybrid rocket engines, while nitrous oxide, liquid oxygen, and hydrogen peroxide may be employed as the oxidizer. The use of metal additions such as aluminum (Al), magnesium (Mg), boron (B), and titanium (T_i) in rocket propellants has been investigated. It demonstrates encouraging improvements in their traits and performance. Overall, the formulation and processing of the propellants must be optimized for safe and dependable operation during space missions. This study demonstrates that a hybrid rocket engine can perform better than a liquid or solid rocket engine due to certain intrinsic characteristics that researchers have investigated.

This paper [2] presents the evaluation and investigation of the propellants and their characteristics through the regression rate. To improve the regression rate and combustion characteristics, the researchers are displaying the propellant's behavior with the proper selection of fuel and their percentage with additives. The regression rate and combustion characteristics are the key constraints in the hybrid rocket engine. To enhance the regression rate of fuel, add metal additives to the solid fuel. The authors [3] of the research employed the Long Grain Centre Perforated (LGCP) idea, which uses solid fuel called HTPB that contains nano-sized particles. Although the fire duration was brief, the performance was suggestively improved by the addition of nano-sized particles to solid grain fuel. According to the authors' findings, adding the additive will cause a 120% greater probability of regression than with just HTPB.

This paper [4] shows some energetic particles, either metal or light metal hydrides in terms of regression rates. Additives such as aluminum, boron, boron carbide, tungsten, iron, carbon, magnesium, magnesium hydride, aluminum hydride, lithium aluminum hydride, ammonium perchlorate, and ammonia borane. Adding additives increases the regression rate by approximately 20–150%. This paper [5] outcomes of an organized experimental study on improving the regression rate in hydroxyl-terminated polybutadiene (HTPB) fuel utilized in an HTPB/gaseous oxygen hybrid motor are given. The significance of adding aluminum or ammonium perchlorate to the fuel, changing the oxidizer-fuel ratio, and changing the characteristic size of the fuel is are also discoursed. The ballistic evaluation of paraffin-based hybrid rocket solid fuels was presented by the authors [6], who also took into account pure wax-based fuels and fuels doped with the right metal additions. Nano-Al powders and

metal hydrides, such as lithium aluminum hydride ($LiAlH_4$) and magnesium hydride (MgH_2), were utilized as fillers in paraffin matrices. The investigation's findings demonstrate a significant relationship between the measured viscosity of the melted paraffin layer and the regression rate, with a reduction in viscosity-increasing the rate of regression. This pattern is brought on by the entrainment phenomenon of continued growth, which significantly raises the regression rate.

The goal of this work is to describe the regression rate behavior of hybrid rocket motor propellant combinations employing hydroxyl-terminated polybutadiene (HTPB) as the base fuel and hydrogen peroxide (HP), gaseous oxygen (GOX), and nitrous oxide (N_2O) as the oxidizer. A hybrid rocket motor test apparatus and a numerical simulation model are built for experimentation and simulation. Several of the firing experiments for the hybrid rocket motors using various propellant mixtures are utilized as references for numerical computations [7].

A laboratory-scale engine has been used to do experimental research on several paraffin-based hybrid rocket fuels. Three different grain shapes of paraffin wax have been created and tested with gaseous oxygen to increase the regression rate of paraffin solid fuel: cylindrical, star, and helical grain configurations. All of the test ports performed better with the helical fuel grain [8].

Aluminum can significantly improve the performance of paraffin by improving combustion efficiency, which leads to increased specific impulse and thrust. It was discovered that the mechanical properties of the paraffin/polyethylene (PE) blend had slightly improved with the addition of Al. However, it can also have an impact on the physical characteristics of the fuel, like density and viscosity, which can affect the overall performance and combustion characteristics of the rocket. To improve the formulation and examine performance under various operating conditions, more research is required, and boron enhancing ignition delay time and specific impulse. They have studied Al and B additives by 5% weight loading. The various advantages of a hybrid rocket engine over SRM and LRE, but still have not been used it. Due to its low regression rate, fluctuating in the fuel oxidizer ratio during burn time, and lower combustion efficiency. The researchers try to improve the propellant's combustion characteristics by adding metallic additives to improve the regression rate of the propellant [9].

The primary goal of this paper [10] is to increase the regression rate; as a result, pure hydroxyl-terminated polybutadiene has been tested as a baseline fuel and compared to hydroxyl-terminated polybutadiene loaded with nano- or micrometer-sized aluminum, nano-sized Viton®-coated aluminum, magnesium hydride, magnesium, nano-sized iron, and iron with magnesium. To build upon earlier work, [11] offers a lab-scale analysis of the ballistics of solid fuel formulations based on hydroxyl-terminated polybutadiene and packed with Al-based energetic additions. Tested metal-based fillers range in size from microns to nanopowders and include composites that are fuel-rich and incorporate oxidizers. An improvement in mass burning rate over the baseline of 55% ± 11% for an oxygen mass flow of 325 ± 20 kg/(m^2 s) is shown in the fuel formulation loaded with 10% nano-sized aluminum (ALEX-100), however, this performance improvement almost completely vanishes as combustion progresses.

The study discusses the creation of wax fuel grains for testing miniature hybrid rocket motors. The potential wax composition is chosen as the solid fuel, and nitrous oxide is used as the oxidizer to produce a hybrid propellant. The manufacture of wax grains and a rotary casting technology created especially for this situation are explained [12].

In this study, a novel composition for a hybrid propulsion system based on paraffin wax and HTPB fuel, loaded with nanoparticles, has been presented. Nanoparticles of magnesium hydride (MgH_2) and lithium aluminum hydride ($LiAlH_4$) have been employed as additives. Rheological, thermal, and ballistic characterization have all been done in great detail [13].

The last decades show the development in computer technology and their mathematical technique advantages. It will save us material, time, and money. Literature suggested chemical equilibrium applications (CEA) software tools developed by NASA. In this, assume boundary conditions and the software tool will evaluate the combustion characteristic. To better understand the fuel oxidizer combustion characteristics, Tables 1 and 2 are displaying the combustion characteristic of fuel and oxidizer, respectively.

To obtain all combustion characteristics such as specific impulse (I_{sp}), combustion chamber temperature (T_{cc}), characteristic velocity (C^*), coefficient of thrust (C_f), ratio of exit area and throat area, and many more relevant values by giving few assumed values like chamber pressure (P_c), oxidizer by fuel (O/F) ratio, temperature, and the ratio of the chamber to initial pressure (P_c/P_i) to software tool CEA code.

The present paper investigates the characteristics of the all above-mentioned fuels and oxidizers with and without the blend metallic additives. The following objectives followed in the present work:

- In the beginning, the HTPB and paraffin were mixed with the LOX, N_2O, and H_2O_2 at some boundary conditions (from the literature).
- Investigate the best combination of fuel and oxidizer and their combustion characteristics.

Table 1 Chemical and physical properties of fuels

Solid fuel	Formula	Enthalpy	Density (g/cm^3)	References
HTPB	$[C_{10}H_{15.4}O_{0.07}]_n$	−51.9 kJ/mol (at $n = 1$)	0.92	[14]
PMMA	$[C_5O_2H_8]_n$	−26.200 kJ/kg	1.18	[14]
Paraffin	C_nH_{2n+2}	−108.93 kJ/mol	0.89	[14]

Table 2 Chemical and physical properties of oxidizers

Oxidizers (in liquid/gas)	Formula	Boiling temperature	Density	References
Oxygen	LOX	−183 °C	1.141 (g/cm^3)	[14]
Nitrous oxide	N_2O	−88.48 °C	1.220 (g/cm^3)	[14]
Hydrogen peroxide	H_2O_2	−187.34 °C	1.4425	[14]

- Add metallic additives (Aluminum and Boron) in the selected fuel-oxidizer combination and again analyze the combustion characteristics, and validate the results with the literature.
- Conclude the percentage of additives with the fuel-oxidizer combination.

2 Methodology

To reduce the analyzing time, material, and the number of experiments, we need a capable software tool Chemical Equilibrium with Applications (CEA) code that will fulfill our desirables without compromising the performance. The procedure is to obtain the combustion properties such as specific impulse (I_{sp}), combustion chamber temperature (T_{cc}), and characteristic velocity with the help of CEA code to assume the chamber pressure (P_c) = 70 bar, oxidizer by fuel ratio, (O/F) = 1 to 13 with a 0.5 interval gap, and chamber pressure and injection pressure ratio, $\left(\frac{P_c}{P_i}\right) = 70$, select fuel as paraffin and oxidizer as liquid oxygen, and run the program.

Consider that the flow is in equilibrium. Figure 1 the specific impulse (I_{sp}) versus oxidizer by fuel ratio. It is showing that the combination of 60% of paraffin and 40% of boron with liquid oxygen gives high specific impulse than other combinations.

Figure 2 depicted the characteristic velocity (C^*) versus oxidizer by ratio (O/F). Characteristic velocity is a very important parameter in a hybrid rocket engine. The maximum characteristic velocity was obtained in the combination of 60% of paraffin and 40% of boron with liquid oxygen and it is approximately 2100 m/s.

Figure 3 displayed the combustion chamber temperature (T_{cc}) versus oxidizer by fuel (O/F). The maximum combustion chamber temperature occurred again in the combination of 60% of paraffin and 40% of boron with liquid oxygen and it is approximately 3900 K.

3 Results and Discussion

Figures 1, 2, and 3 depict the specific impulse versus oxidizer by fuel ratio, characteristic velocity vs oxidizer by ratio, and combustion chamber temperature vs oxidizer by fuel ratio, respectively. Pure paraffin combined with liquid oxygen gives a maximum specific impulse, characteristic velocity, and combustion chamber temperature is 285.1784 s, 1711.6 m/s, and 3095.21 K, respectively. When added additives aluminum with paraffin, we observed that 40 wt. % Al will give more specific impulse than 30 wt. % Al. Similarly, boron added with paraffin, 40 wt % will give a maximum specific impulse than 30 wt. %. The specific impulse, characteristic velocity, and combustion chamber temperature are 303.34 s, 1793.5 m/s, and 3445.65 K, respectively, of 40 wt. % of aluminum and the specific impulse, characteristic velocity, and combustion chamber temperature are 355.93 s, 2119.8 m/s, and 3860.4 K, respectively, of 40 wt. % of boron.

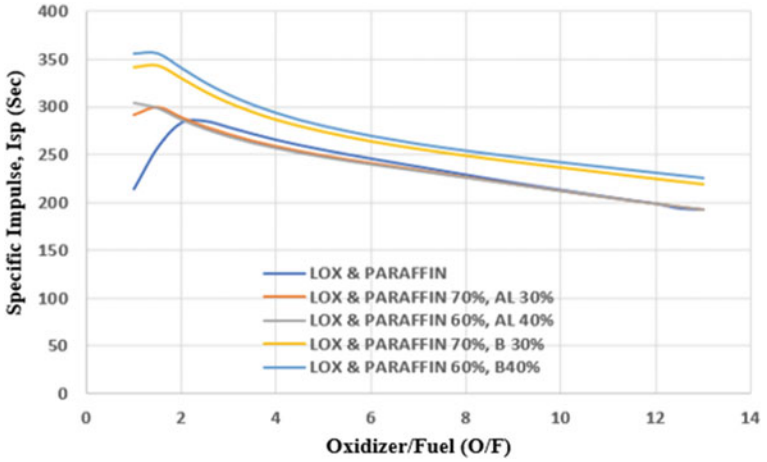


Fig. 1 Specific impulse (I_{sp}) versus oxidizer/fuel (O/F) ratio

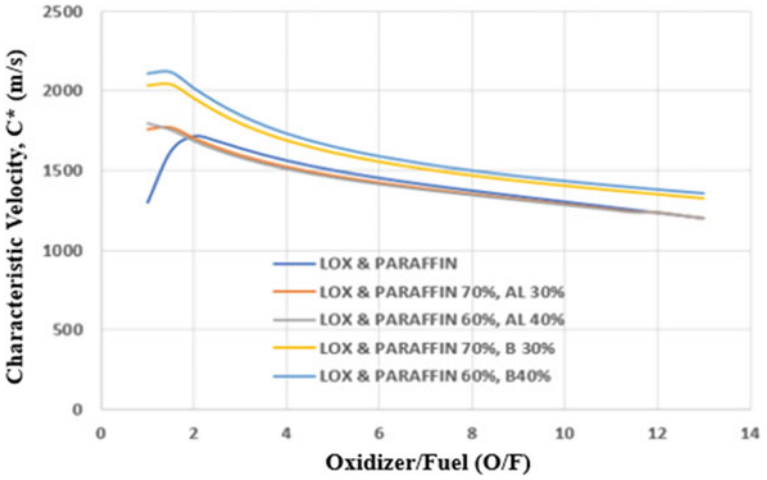


Fig. 2 Characteristic velocity (C^*) versus oxidizer/fuel (O/F) ratio

As aluminum is a metallic character and is more reactive than boron at high temperatures and aluminum oxygen is more highly stable than boron oxygen. 60 wt. % of paraffin-40 wt. % of boron is good for the environment than 60 wt. % of paraffin-40 wt. % of aluminum. The ignition of blend boron covered in a native oxide layer takes place in the first step. The second stage involves heating bare boron over the boiling point of B_2O_3 to cause it to burn, and the oxide layer is fully removed by evaporation. Therefore, it is predicted that the process of ignition and combustion will be greatly aided by the elimination of the liquid oxide layer from the surface of the boron particle. Due to boron's issues with ignition and combustion,

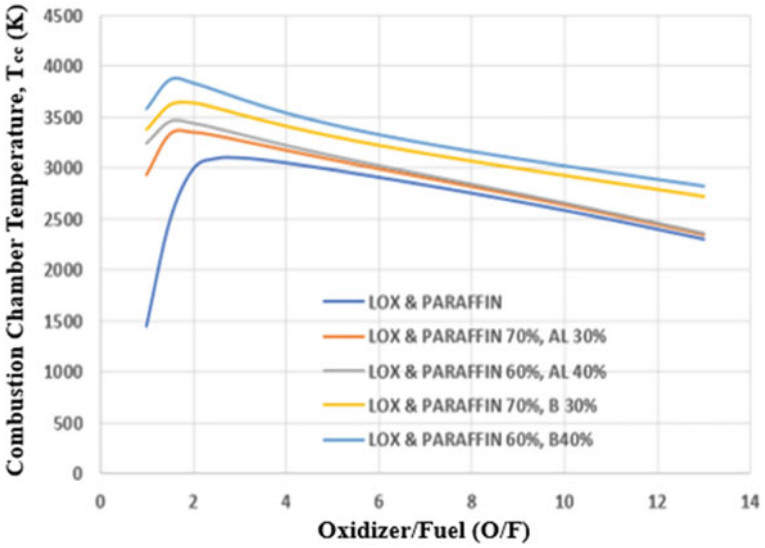


Fig. 3 Chamber temperature (T_{cc}) versus oxidizer/fuel (O/F) ratio

very few investigations have been done on it as an addition to hybrid rocket engine applications.

4 Conclusion

The current evaluation covered the preliminary investigations, including picking the best propellant combination for hybrid rocket engines and analyzing the combustion characteristics such as specific impulse, combustion chamber temperature, characteristic velocity, and many more parameters. This investigation shows that, for enhancing the combustion properties, we can add the additives in some percentages without losing the fuel properties. In this work, initialize with different fuels and oxidizers combination and then add additives and evaluate the best outcome. We analyze that liquid oxygen mixed with paraffin and additive Al gives better combustion properties than other combinations, and liquid oxygen is easily available and very cost-effective but obviously, there are some disadvantages of liquid oxygen like cryogenic behavior required insulated surface will increase the cost and for transferring oxidizer from tank to combustion chamber, need a fed system which will increase the complexity of design and weight as well as cost. Even with these disadvantages, liquid oxygen is a good choice for space missions.

5 Future Scope

The current study shows that there is a lot of scope to investigate the fuel and oxidizer combinations and also metallic blends. Mixed blend metallic with fuel and then react with oxidizer enhance the combustion characteristic which is desired. In the future, study more about the propellant and because of it, reduce the cost of the mission and enhance the performance.

Funding Not applicable.

Nomenclature

P_c	Chamber Pressure (N/m^2)
I_{sp}	Specific Impulse (Second)
C^*	Characteristic velocity (m/sec)
T_{cc}	Combustion Chamber Temperature
P_i	Injection Pressure
Δh_f	Change in Enthalpy (kj/mol)
Wt.	Weight (Newton)
LOX	Liquid Oxygen
N_2O	Nitrous Oxide
H_2O_2	Hydrogen Peroxide
Al	Aluminum
B	Boron
HRE	Hybrid Rocket Engine
CEA	Chemical Equilibrium Applications
HTPB	Hydroxyl-Terminated Polybutadiene
O/F	Oxidizer/Fuel
C_f	Coefficient of Force

References

1. Srivastava S, Thakur AK (2022) Review on hybrid rocket engine: past, present and future scenario. Int J Veh Struct Syst 14(5). https://doi.org/10.4273/ijvss.14.5.24
2. Chiaverini MJ, Serin N, Johnson DK, Lu YC, Kuo KK, Risha GA (2000) Regression rate behavior of hybrid rocket solid fuels. J Propuls Power 16 (1). https://doi.org/10.2514/2.5541
3. Risha GA, Evans BJ, Boyer E, Wehrman RB, Kuo KK (2003) Nano-sized aluminum- and boron-based solid-fuel characterization in a hybrid rocket engine. In: 39th AIAA/ASME/SAE/ASEE joint propulsion conference and exhibit. https://doi.org/10.2514/6.2003-4593
4. Akhter MZ, Hassan MA (2020) Energetic additives for hybrid rocket propulsion—review. In: 2020 Advances in science and engineering technology international conferences, ASET 2020. https://doi.org/10.1109/ASET48392.2020.9118206

5. George P, Krishnan S, Varkey PM, Ravindran M, Ramachandran L (2001) Fuel regression rate in hydroxyl-terminated-polybutadiene/gaseous-oxygen hybrid rocket motors. J Propuls Power 17(1). https://doi.org/10.2514/2.5704
6. Galfetti L, Merotto L, Boiocchi M, Maggi F, DeLuca LT (2013) Experimental investigation of paraffin-based fuels for hybrid rocket propulsion. https://doi.org/10.1051/eucass/201304059
7. Sun X, Tian H, Li Y, Yu N, Cai G (2016) Regression rate behaviors of HTPB-based propellant combinations for hybrid rocket motor. Acta Astronaut 119. https://doi.org/10.1016/j.actaastro.2015.11.015
8. Pal Y, Baskar J, Murugesan S (2012) Testing of paraffin-based hybrid rocket fuel using gaseous oxygen oxidizer. Def Sci J 62(5). https://doi.org/10.14429/dsj.62.2346
9. Pal Y, Kumar VR (2017) Physical and ballistic characterization of aluminum-loaded paraffin hybrid rocket fuels. Energy Fuels 31(9). https://doi.org/10.1021/acs.energyfuels.7b01636
10. Carmicino C, Sorge AR (2015) Experimental investigation into the effect of solid-fuel additives on hybrid rocket performance. J Propuls Power 31(2). https://doi.org/10.2514/1.B35383
11. Paravan C (2019) Nano-sized and mechanically activated composites: perspectives for enhanced mass burning rate in aluminized solid fuels for hybrid rocket propulsion. Aerospace 6(12). https://doi.org/10.3390/aerospace6120127
12. Boros C, Konecný P (2009) Development of wax fuel grain for hybrid rocket motor. Adv Milit Technol 4(2)
13. Akhter MZ, Hassan MA (2018) Characterisation of paraffin-based hybrid rocket fuels loaded with nano-additives. J Exp Nanosci 13:S31–S44. https://doi.org/10.1080/17458080.2018.1431848
14. Srivastava S, Thakur AK (2023) Comparison of propellant characteristics using paraffin and blends of aluminum and magnesium with oxidizers in hybrid rocket engine. Aerosp Syst 6(1). https://doi.org/10.1007/s42401-022-00175-5

Analysis of Code Smells Using Machine Learning Algorithms



Varun Jain, Rohinish Singh, Nishant Rai, and Aakanshi Gupta

Abstract A code smell is a sign or indication that is introduced in the source code of a software program during the design or implementation phases, which may lead to more significant problems during software maintenance. The existing methods have limitations in extracting sufficient rich information from source code, as they frequently reflect various code smells using an easy-to-understand code representation. The objective of this research is examining the code smells with machine learning classifiers. This research suggests the use of metrics extraction software named as WekaNose for the analysis of code smells and training different machine learning models for determining the efficient algorithm. In this research we have used ML algorithms like Random forest, Decision Tree, SVM, Naive Bayes and boosted algorithms such as LightGBM and AdaBoost. The proposed approach performs remarkably well in single code smell identification according to the experimental results obtained.

Keywords Software engineering · Code smells · Machine learning · Boosted machine learning algorithms

1 Introduction

Code smells are posing a significant problem in the software industry because they can lead to poor quality code, which can ultimately result in various software issues, such as bugs, crashes, and system failures. Code smells are indicators of the presence of design or implementation flaws that can make it difficult for developers to maintain and evolve software systems over time.

Code smells can also make it harder to understand code and make modifications to it, which can lead to increased development time and cost. Moreover, code smells can cause technical debt, which occurs when shortcuts are taken during development

V. Jain · R. Singh · N. Rai · A. Gupta (✉)
Amity School of Engineering and Technology, Amity University Uttar Pradesh, Noida, India
e-mail: aakankshi@gmail.com

© The Author(s), under exclusive license to Springer Nature Singapore Pte Ltd. 2024

S. Singh et al. (eds.), *Recent Advances in Aerospace Engineering*, Lecture Notes in Mechanical Engineering, https://doi.org/10.1007/978-981-97-1306-6_6

to meet deadlines, leading to code that is difficult to maintain, and requires significant resources to refactor.

Code smells can also affect the software's performance, security, and reliability. For example, long parameter lists or duplicated code can make the software slower, while complex conditional statements can make it difficult to identify and fix security vulnerabilities.

Overall, code smells can cause significant problems in the software industry, including decreased code quality, increased development time and cost, technical debt, and reduced performance, security, and reliability. Addressing code smells is critical to ensure the long-term success of software systems. Driven by the need for more accurate, efficient, and automated approaches to detect code smells. Traditional approaches to code smell detection, such as manual code reviews, can be time-consuming, expensive, and error-prone. Artificial intelligence techniques, such as machine learning and deep learning, have the potential to automate code smell detection and improve its accuracy. By training machine learning models on large datasets of code smells, AI can learn to identify patterns and features in the code that are indicative of code smells. This can enable AI to detect code smells more accurately and efficiently than traditional approaches.

In this research, we choose 3 code smells to target which occurred frequently in various software systems.

1.1 Data Class

Instead of providing any significant functionality, a data class is designed using an interface that reveals data items. Other classes in the system regularly change this data. Data and behavior are not considered within the same context, which shows a lack of data-functionality intimacy by allowing access to its confidential data to other groups.

1.2 God Class

The god class is an unnecessarily complex class that contains too much non-cohesive capability and heavily coerces data members from other classes. To address the issue of a god class in code, developers can refactor the code by breaking down the god class into smaller, more focused classes that adhere to the single responsibility principle. This can improve the code's modularity, maintainability, and testability, while reducing the risk of bugs and errors.

1.3 Long Parameter List

A method with such a large parameter list can be hard to use, and it increases the risk of erroneous mappings caused by human errors.

1.4 Contribution of This Study

In response to the needs described and with the worries about foreseeing code smells using AI techniques, a systematic review of the literature was done, and the following contributions were produced:

- Using the scientific literature being examined, presentation of research for the state of the art code smell detections which includes predictors and ML techniques being utilized.
- Recognizing the current metrics of performance being worked upon by researchers.
- Recognizing the software projects or datasets that were the source of the code smell prediction models (along with their size and other details), identifies factors that have an impact on how well code smells prediction models predict data, and makes research ideas to further the field of code smell prediction so that other academics and tool developers can build on it.

2 Background Study

See Table 1.

In Gencer and Başçiftçi [1], a systematic literature review of machine learning in software development for code smell detection, the authors conclude that machine learning has the potential to automate code smell detection and improve its accuracy, but there are still challenges that need to be addressed, such as the lack of standardization in code smell definitions, and the need for large and diverse datasets for the task of training and testing machine learning models. Another study of Cruz and Abreu [9], a machine learning approach to detect code smells demonstrates the potential of machine learning for automating code smell detection and improving the quality of software development.

AI and ML have been contributing to detection of code smell by automating the process of identifying and analyzing code smells in software systems. Traditional code smell detection methods rely on manual inspection and analysis of code by software developers, which can be time-consuming, error-prone, and subjective. AI and ML techniques can help to overcome these limitations by providing automated and objective analysis of code smells. One way in which AI and ML have been used for code smell detection is by applying supervised learning techniques to labeled

Table 1 Most related papers in the given literature

Study	Authors	Method	Findings
A systematic literature review of ML in software development for code smell detection	Gencer and Başçiftçi [1]	Study of systematic literature, identify the challenges and opportunities using ML	Potential of ML, in automating xcode smell detection and improving its accuracy
Comparing and experimenting ML techniques for code smell detection	Fontana et al. [2]	Study of 16 ML algorithms	Detecting various code smells and obtaining their metrics
Code Smells for Machine Learning Applications	Zhang et al. [3]	Model training and applying the trained model on the dataset	Using the trained model to predict the presence of code smells in new, unlabeled code
On the evaluation of code smells and detection tools	Moha et al. [4]	Working on various available tools for code smell generation	Comparing the accuracies of different techniques on few smells
On the Feasibility of Transfer-learning Code Smells using DL	Sharma et al. [5]	Train smell detection models based on CNN and RNN as their principal hidden layers	Depicts that transfer-learning is definitely feasible for implementation smells with performance comparable to direct-learning
Extracting rules for vulnerabilities detection with static metrics using ML	Gupta et al. [6]	Using 32 supervised ML algo's and J48 ML algorithm in this research	Achieved up to 96% of accurate result in vulnerability detection
A systematic literature review code bad smells in java source code	Gupta et al. [7]	Performing SLR based on the search of digital libraries	Calculated significant correlation between detection techniques
Tracing bad code smells behavior using ML with software metrics	Gupta et al. [8]	Making use of various combination of object-oriented metrics and 4 ML algo's	Demonstrated that the ML algorithms achieved high accuracy with the validation method of tenfold cross-validation

datasets of software code. These techniques involve training a machine learning model on a set of labeled data (code snippets with and without code smells) and then using the trained model to predict the presence of code smells in new, unlabeled code. Another way in which AI and ML have been used for code smell detection is by applying unsupervised learning techniques, such as clustering and anomaly detection, to identify patterns in software code that indicate the presence of code smells. These techniques involve analyzing the code without any prior labeling of code smells and identifying patterns that are not typical of well-designed code.

AI and ML techniques have also been used to develop tools that can assist developers in detecting and addressing code smells. These tools can provide real-time feedback to developers during the software development process, alerting them to potential code smells and suggesting ways to refactor the code to improve its quality. The phrase "code smell" was first used by Kent Beck, who defined it as "certain designs in the code that recommend (or sometimes shout) for refactoring." Code smells demonstrate the presence of value issues affecting numerous aspects of value of a product framework. The existence of an extreme numerous smells in a product framework makes it hard to keep up with and develop.

Smells are classified as execution, design, and design smells in light of their extension, granularity, and effect:

Execution smells are commonly restricted to a restricted extension what's more, influence (e.g., a technique). Instances of execution smells are long strategy, complex technique, long boundary list, and complex restrictive. Configuration smells happen at higher granularity, i.e., deliberations, and consequently are bound to a class or on the other hand a bunch of classes. God class, multi-layered deliberation, cyclic dependency modularization, and defiant progressive system are models of configuration smells. Along comparative lines, engineering smells length across different parts and have a framework wide effect. A few instances of engineering smells are a good part, highlight concentration, and dispersed usefulness.

A plenty of business related to code smell identification exists in programming writing. Scientists have proposed strategies for distinguishing smells that can be to a great extent separated into five classes. Metric-based smells location algorithms evaluate a series of source code measurements, create a source code representation, such as a Theoretical Punctuation Tree (ast), and apply the appropriate edges to identify smells. Rule/Heuristic-based smell location algorithms frequently use source code representations and occasionally additional programming metrics as information [4, 5, 10, 11]. When the outlined principles and heuristics are satisfied, they are able to differentiate a variety of smells. Methods for identifying smells based on history employ information about source code development. These methods extract the code's core information and how it has evolved over an arbitrary period of time.

The current study aims to address some of these research gaps by investigating the effectiveness of different machine learning algorithms and feature selection techniques in detecting a broader range of code smells in different software development contexts.

3 Methodology

The key components of our strategy, which are briefly covered below, are summarized by the following points and the flow diagram in Fig. 1.

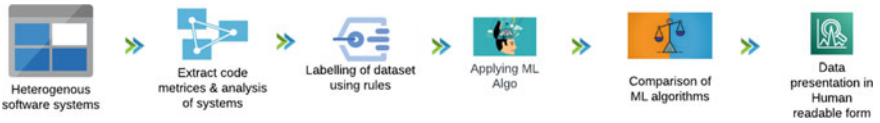


Fig. 1 Workflow diagram for the presented research

3.1 Collection of a Sizable Store of Diverse Software Systems

We used Guggulothu and Moiz [12]'s Qualitas Corpus (QC) of system data for our investigation. The corpus, and to be specific the collections being used, 20120401r, is made up of 111 Java-written systems with varying sizes and application domain affiliations. There are 70 systems that were chosen for analysis. The pick was made because the systems have to be programmable in order to calculate metrics values accurately. We carefully entered every system's missing third-party libraries, enabling the resolution of class dependencies.

It is essential to establish a machine learning approach that is independent of a particular dataset in order to generalize the outcomes that are discovered. The best that we can tell, the quantity of systems examined is the biggest number of systems that may be used for machine learning algorithms that detect code smells (or antipatterns).

3.2 Metrics Extraction and Analysis

In the machine learning method, the metrics are taken into account as independent variables. We created a significant collection of object-oriented measurements using our machine learning method, and these metrics are seen as independent variables. All 70 QC systems' metrics were computed.

The metrics which are chosen as in Gupta et al. paper are at the class, method, package, and project levels; they include measurements required by the exploited Advisors as well as common metrics that account for many facets of the code, such as complexity, cohesiveness, size, and coupling. The metrics we selected are well-known and often used in the literature [13–17]. All metrics were calculated using a program that is available online known as WekaNose. WekaNose is a tool that enables experimentation with the goal of learning how to identify code smells using machine learning methods. It helps to extract all the necessary information that is required for our experimentation.

3.3 Labeling

Following the Advisors' recommendations, the reported candidates for code smells are manually assessed and given varying degrees of gravity. A process for creating a dataset that machine learning algorithms can use to find software code smells. Advisors are employed to offer cues that a certain entity may have a code smell. The authors combine the Advisor values and set up a stratified sampling technique to construct a sizable oracle. The sampling process distributes groups of examples from different projects with varying probabilities of having a code smell with the same probability of selection. By randomly deleting negative examples from the training set until there are 1 in 3 positive and 2 in 3 negative instances remaining, the training set is then normalized in size. Code smells are classified by their level of severity using an ordinal system. Over time, software faults have been subjected to severity classification; this idea is now commonly utilized in business. To train supervised classifiers, hand labeling is used, and the best one will be chosen based on its performance (e.g., precision, recall, and learning curves).

3.4 Experimentation

By choosing a collection of appropriate machine learning algorithms to evaluate them on the created datasets, we experimented with our methodology. A dataset has been developed for each type of code smell: separate datasets for god class, data class, and long parameter list. Each row in each dataset represents an instance of a class or function and has one attribute for each measure. The label that specifies whether or not the instance is a code smell is likewise indicated by a Boolean feature. We decided to implement the Machine Learning Algorithms such as: Decision Classifier, Naive Bayes, Random Forest, AdaBoost, Support Vector Machine, and LightGBM. We have implemented these ML algorithms and compared their performance on individual types of code smells. The Weka tool has been used for applying the above-mentioned algorithms. Then, the performance metrics have been calculated. Furthermore, in the next section 'Result and Discussion' tables and graphs have been shown all the performance metrics with respect to their machine learning algorithms.

4 Results and Discussion

We have experimented with the machine learning algorithms on the category of god class, long parameter, and data class code smells and performed the analysis on the dataset to obtain the following result of performance along with the accuracy percentage for the sample datasets. Six machine learning algorithms have been

applied out of which LightGBM and AdaBoost are boosted ML algorithms on all three dataset and compared their performances.

As shown in Table 2, for the god class dataset, we could conclude the performance of LightBGM to be most effective with an accuracy of 98.80% whereas the least performed algorithm was AdaBoost which could imply an accuracy of 95.23% for the datasets.

With regard to the Long Parameter dataset as seen in Table 3, the algorithms like Decision tree, AdaBoost performed well and the highest percentage of accuracy was achieved by LightGBM which is 95.23.

Exploring the Data Class dataset, we obtained the results to be quite comparable for algorithms like Random Forest, Decision Tree, AdaBoost but the worst performer was reported by Naive Bayes with just 67.85% accuracy whereas the highest was AdaBoost with 96.82% accuracy which can be seen in Table 4.

In Fig. 2, the curves are showing accuracy for data class code smell with respect to the machine learning algorithms Random Forest, Decision Tree, and AdaBoost. The Random Forest machine learning algorithm has shown the best result for data class code smell. In Figs. 3 and 4, curves are showing the best accuracy result for code smells god class and long parameter list, respectively.

Table 2 Performance metrics for code smell god class with respected ML algorithms

	Precision	Recall	F1 score	Accuracy
Random forest	0.9667	0.9354	0.9508	0.9642
Decision tree	0.9375	0.9677	0.9677	0.9642
SVM	0.9687	1.0	0.9841	0.9880
Naïve Bayes	0.9667	0.9354	0.9508	0.9642
AdaBoost	0.9318	0.9355	0.9425	0.9603
LightGBM	0.9687	1.0	0.9841	0.9880

Table 3 Performance metrics for code smell data class with respected ML algorithms

	Precision	Recall	F1 score	Accuracy
Random forest	0.9642	0.9642	0.9642	0.9762
Decision tree	0.9629	0.9285	0.9285	0.9642
SVM	0.875	0.75	0.8076	0.8809
Naïve Bayes	0.9642	0.9642	0.9642	0.6785
AdaBoost	0.95	0.95	0.9682	0.9682
LightGBM	0.96	0.9642	0.9310	0.9523

Table 4 Performance metrics for code smell long parameter list with respected ML algorithms

	Precision	Recall	F1 score	Accuracy
Random forest	0.8421	0.64	0.7272	0.8571
Decision tree	0.8214	0.92	0.8679	0.9166
SVM	0.5937	0.76	0.6666	0.7738
Naïve Bayes	0.8421	0.64	0.7272	0.6666
AdaBoost	0.875	0.875	0.7272	0.9206
LightGBM	0.886	0.967	0.932	0.9156

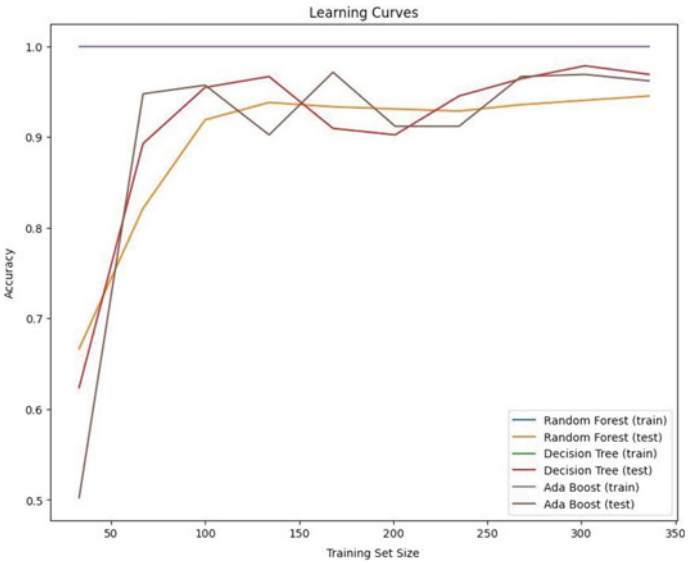


Fig. 2 For data class learning curves for best algorithms

5 Limitations

Only 70 heterogeneous systems that are open source have been taken into consideration. The link between theory and observations is the key risk associated with software engineering experimentation activity. The WekaNose tool is used in this study's setting to perform and abstract code smell measurements. WekaNose instruments exclude some smells, while other existing techniques have distinct threshold values for foul smells that could influence perceptions of foul smells. Another drawback is that we might have used deep learning, deep hybrid, and ensemble learning in this study instead of just using machine learning techniques.

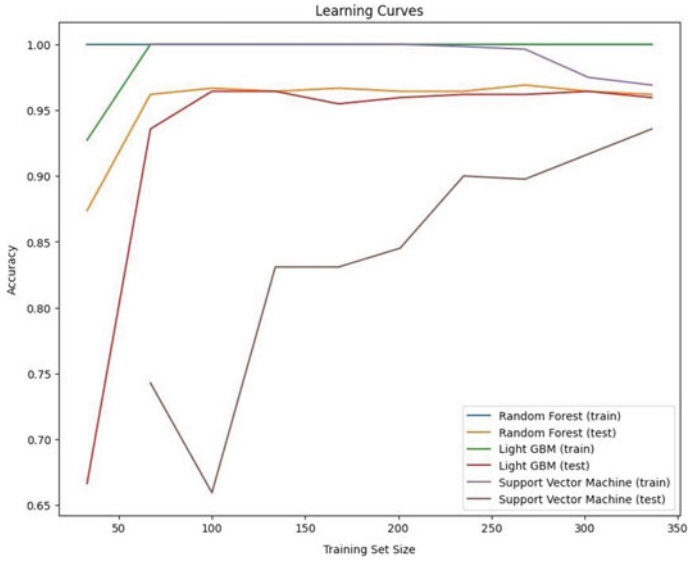


Fig. 3 Understanding the finest algorithms on the god class

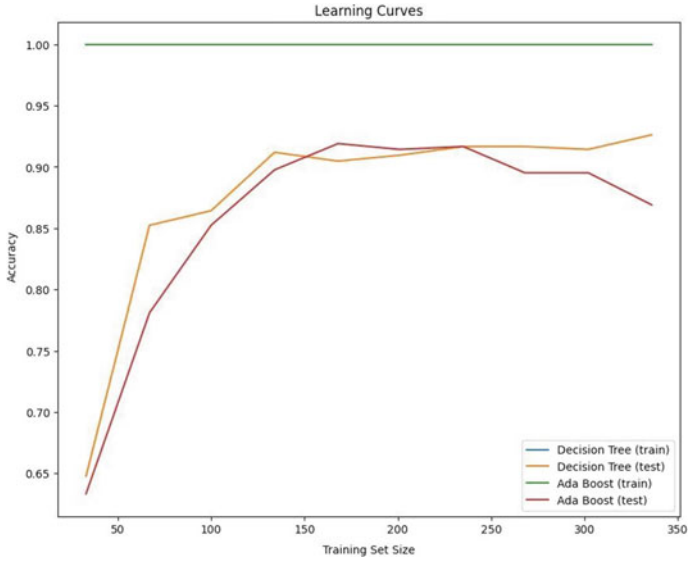


Fig. 4 Best algorithms learning curve on long parameter list

6 Conclusion and Future Work

This study outlines an approach for identifying code smells that makes use of machine learning algorithms that can adapt to fresh data. To guarantee a uniform distribution of instances and give priority to labeling cases with a greater likelihood of having code smells have an impact, the system uses stratified sampling of instances and a collection of code smell detecting tools and guidelines known as Advisors. The method was tested on three code smells using six different machine learning algorithms with comparative study of each algorithm and the accuracy being incorporated and future studies should investigate whether feature selection can improve their performance. In this paper, we have worked on only three code smells (Long parameter, God class & Data class) as these are the most occurring code smells in the codes. In the future, we can work on many other code smells which occur in the code with the help of the above 6 machine learning algorithms (Ada Boost, Decision Tree, Naive Bayes, Light GBM, Random Forest, Support Vector Machine) which we have used above in our research work.

Software is highly utilized in the aerospace sector for a number of systems, including flight control, avionics, navigation, and communication. For safety and effectiveness, aircraft software must be of high quality and maintainable. Therefore, spotting and eliminating code smells can help increase the software's dependability and maintainability in aerospace applications.

In the future, we can also concentrate on increasing the precision of machine learning approaches. Also, in the future, we can work on directly telling the code smells packages name from the code with improving the accuracy and improving the above six mentioned machine learning techniques.

Funding Not applicable.

References

1. Gencer K, Başçiftçi F (2021) Time series forecast modeling of vulnerabilities in the android operating system using ARIMA and deep learning methods. Sustain Comput: Inf Syst 30:100515
2. Fontana FA, Braione P, Zanoni M (2012) Automatic detection of bad smells in code: An experimental assessment. J Obj Technol 11(2):5:1
3. Zhang H, Cruz L, Van Deursen A (2022, May) Code smells for machine learning applications. In: Proceedings of the 1st international conference on AI engineering: software engineering for AI, pp 217–228
4. Moha N, Guéhéneuc Y-G, Duchien L, Le Meur A-F (2010) A method for the specification and detection of code and design smells. IEEE Trans Softw Eng 36(1):20–36
5. Sharma T, Fragkoulis M, Spinellis D (2016, May) Does your configuration code smell?. In: Proceedings of the 13th international conference on mining software repositories, pp 189–200
6. Gupta A, Suri B, Kumar V, Jain P (2021) Extracting rules for vulnerabilities detection with static metrics using machine learning. Int J Syst Assur Eng Manag 12:65–76. https://doi.org/10.1007/s13198-020-01036-0

7. Gupta A, Suri B, Misra S (2017) A systematic literature review: code bad smells in java source code. https://doi.org/10.1007/978-3-319-62404-4_49
8. Gupta A, Suri B, Lamba L (2021) Android smell detection using algorithms using static metrics. https://doi.org/10.1007/978-981-15-5827-6_6
9. Cruz L, Abreu R (2018) Using automatic refactoring to improve energy efficiency of android apps. arXiv preprint, arXiv:1803.05889
10. Arnaoudova V, Di Penta M, Antoniol G, Guéhéneuc YG (2013, March) A new family of software anti-patterns: linguistic anti-patterns. In: 2013 17th European conference on software maintenance and reengineering. IEEE, pp 187–196
11. Tsantalis N, Chatzigeorgiou A (2011, March) Ranking refactoring suggestions based on historical volatility. In: 2011 15th European conference on software maintenance and reengineering. IEEE, pp 25–34
12. Guggulothu T, Moiz SA (2020) Code smell detection using multi-label classification approach. Softw Qual J 28:1063–1086
13. Bansiya J, Davis CG (2002) A hierarchical model for object-oriented design quality assessment. IEEE Trans Softw Eng 28(1):4–17
14. Rawat MS, Dubey SK (2012) Software defect prediction models for quality improvement: a literature study. Int J Comput Sci Issues (IJCSI) 9(5):288
15. Chidamber SR, Kemerer CF (1994) A metrics suite for object oriented design. IEEE Trans Softw Eng 20(6):476–493
16. Lorenz M, Kidd J (1994) Object-oriented software metrics: a practical guide. Prentice-Hall, Inc
17. Aggarwal A, Jalote P (2006, September) Integrating static and dynamic analysis for detecting vulnerabilities. In: 30th annual international computer software and applications conference (COMPSAC'06), vol 1. IEEE, pp 343–350
18. Ferme V (2013) JCodeOdor: a software quality advisor through design flaws detection. Master's thesis, University of Milano-Bicocca
19. Hall T, Zhang M, Bowes D, Sun Y (2014) Some code smells have a significant but small effect on faults. ACM Trans Soft Eng Methodol 23(4):33
20. Khomh F, Vaucher S, Guéhéneuc YG, Sahraoui H (2009) A Bayesian approach for the detection of code and design smells. In: Proceedings of the 9th international conference on quality software (QSIC 2009), Jeju, Korea. IEEE, pp 305–314. https://doi.org/10.1109/QSIC.2009.47
21. Nongpong K (2012) Integrating 'code smells' detection with refactoring tool support. University of Wisconsin-Milwaukee
22. Arcelli Fontana F, Mäntylä MV, Zanoni M, Marino A, Comparing and experimenting machine learning techniques for code smell detection
23. Fontana_EMSE_2016_Comparing_and_Experimenting_Machine_Learning_Techiniques_for_Code_Smell_Detection.pdf
24. Gupta A, Suri B, Misra S, Software code smell prediction model using Shannon, Rényi and Tsallis Entropies. https://www.mdpi.com/1099-4300/20/5/372_
25. Gupta A, Gandhi R, Kumar V, Investigating bad smells with feature selection and machine learning approaches. https://doi.org/10.1007/978-3-031-05347-4_4
26. Lewowski T, Madeyski L (2022) Code smells detection using artificial intelligence techniques: a business-driven systematic review. Springer International Publishing, Cham, pp 285–319. https://doi.org/10.1007/978-3-030-77916-0_12
27. Dewangan S, Rao RS, Mishra A, Gupta M (2022) Code smell detection using ensemble machine learning algorithms. Appl Sci 12:10321. https://doi.org/10.3390/app122010321

Solar-Powered Fixed-Wing UAV: Fabrication Procedures with Design Methods



N. C. Ajay Vishwath, Payal Dhanwani, Rajeev Kumar Baghel, Ram Bendale, and Parshva Mehta

Abstract The manuscript deals with the fabrication of fixed-wing UAV or drone with solar panel on wings. The research work is to increase the endurance of the UAV using the solar power. The research work begins with a suitable methodology to design a solar UAV. Once the design phase is completed, weight estimation was performed with the available design values. The estimated weight was taken as in the input value to predict the aerodynamic forces such as lift and drag. Further thrust was estimated using a test rig and UAV experiments. These performance values are experimental which was obtained using detailed design. Further the airfoil selection and rib design were made, and finally, the structure of wing was fabricated. Similar manner tail was designed and fabricated. All the components of wings and tail were manufactured using laser cutting technology. Finally, the performance of solar cell was discussed, and their performance values are recorded.

Keywords Solar powered UAV · Design of fixed wing glider · Performance of solar powered glider · Performance of solar cells in flight applications

1 Introduction

A few years ago, the idea of a fuel-powered, sun-based aircraft with the ability to fly continuously was an incredible experiment, but today, this amazing test is possible. Military applications for UAVs primarily include confirmation, standard

N. C. A. Vishwath (✉) · R. Bendale
Department of Aeronautical Engineering, Parul Institute of Engineering and Technology, Parul University, Vadodara, India
e-mail: ajay.nc2934@paruluniversity.ac.in

P. Dhanwani
Department of Aeronautical Engineering, Bhagwan Arihant Institute of Technology, Gujarat Technology University, Surat, India

R. K. Baghel · P. Mehta
Aerospace Foundation, Vadodara, India
e-mail: rajeevkumar2505@gmail.com

© The Author(s), under exclusive license to Springer Nature Singapore Pte Ltd. 2024

S. Singh et al. (eds.), *Recent Advances in Aerospace Engineering*, Lecture Notes in Mechanical Engineering, https://doi.org/10.1007/978-981-97-1306-6_7

acknowledgment, ocean observation, and mine flight tests. Separating developments have been observed recently in the manufacturing of high noteworthiness thickness batteries and flexible solar-oriented cells. Other non-military applications include sprinkler maintenance, remote perception of rice paddies, and framework maintenance.

Other non-military applications include sprinkler maintenance, remote perception of rice paddies, and framework maintenance. The aviation industry is being forced to think of practical solutions to current advancements on a more frequent basis. Blasting jet fuel is one of the sources of carbon dioxide radiation, among others. Our analysis included a sizeable section on evaluating solar power's potential as a primary energy source. It was decided to create an RC model airplane that could be maintained by its standard battery system and controlled by sunlight as a result of this assessment and a few introductory frames.

Endurance in fixed-wing unmanned aerial vehicle is being the most crucial parameter which is limited in the electric propulsion and hydrocarbon-based fuel engines would pollute the atmosphere along with its huge cost, the demand for alternative solution increased in the market. Solar-powered unmanned transportation could improve the endurance by supplying extra power from the sunlight as well as it does not involve much additional weights. Karthik Reddy Buchireddy Sri and his team has designed 2 kg solar-powered aerial vehicle that includes payload [1].

UAVs are the type of aircraft which are generally controlled through remote controllers, and some of them even fly through the pre-programmed flight controllers. Though the UAV has wide range of applications, surveillance and aerial mapping top all of the application. The UAV which is used for the application of surveillance around international border is carried out by army soldiers. UAV could eliminate the human errors and perform better at such works. Activities like monitoring enemy and record photos and videos to secure the border area could not be done through UAV with less endurance. So solar UAV would provide better solution than conventional one due to its ability to charge from natural resources without the help of external power supply. R. Vijayanadh and his team proposed calculations and designs to generate e-aircrafts which are capable to use solar energy for their flight. The calculations and designs are also addressing the speed, range, and endurance type of performance parameters along with the usage of solar energy. This would provide security and surveillance at the borders. CATIA was used by them to model the solar UAV, and MATLAB was used by them for the image processing of images detected in borders [2].

The recent advancements in photovoltaic cells gave new wings to the unmanned industry for applications based on the solar-powered UAVs and UGVs. Cheong and Wen Rong built a solar UAV and performed the in-flight data logging. They further proceeded to obtain experimental results to achieve self-sustaining flight. The research work also included the wiring connections and mounting strategies of solar panels in the UAV. In order to meet the standard air worthiness, the electrical components used need to meet the weight and power requirements. To obtain the live data, additional in-flight telemetry and various other sensors were integrated with the

UAV in the fuselage section. Finally, the analysis was made by them to evaluate the efficiency of solar panel and the power utilized in various phases of flight [3].

Bassetti Chandrasheker and Mahesh K performed modeling and analysis of solar-powered glider to improve its endurance and thereby fabricated it. Test flight was performed with the solar cells are placed at the wing. The details and specification of the solar power were provided by them for the reader's reference. Flight mechanics calculations were made along with the aerodynamic design to enhance its efficiency [4].

In the fabrication methods, the design of the ribs for wing and tails are fabricated with the laser cutting machine that cuts the balsa wood in the airfoil shape which was designed in AutoCAD software. The ribs are then fused with the balsa wood spars, thus forming the wing structure. The styrofoam sheet is used for skin, coated with special cellulose film to reduce the skin friction drag. This method makes the fabrication and design method novel.

2 Methodology

The procedure begins with weight the estimation of the electrical and structural components of the glider. For the same design and fabrication procedure needs to be executed. Therefore, the conceptual design phase was not alone enough, which proceeds to a detailed design. The detailed design would allow one to perform weight estimation. Weight estimation is the significant input value which would allow one to estimate the aerodynamic parameters such as lift and drag values.

Lift is one of the most important aerodynamic aspects for any aerial vehicle. As a glider needs high lift to drag ratio, airfoil with maximum aerodynamic efficiency has been selected. Using assumed velocity, weight, and atmospheric conditions, wing dimensions were estimated. This will allow the designer to perform the experiments and numerical analysis to obtain the thrust required for the glider. Indeed, power required and other performance parameters could be obtained. Based on these parameters, one has to choose the motor–propeller combination. The motor and propeller combination could be found out using the experimental tests using motor thrust test rig. The results of this experiments would allow one to explore the various thrust ranges at which this motor propeller combination could produce. Based on the thrust available with the motor, motor and propeller specifications are chosen. Now based on the specification of the motor which was chosen ESCs and other electronic parts in the circuit is chosen. In order to obtain the long endurance and other mission requirements, battery matching those specifications needs to be chosen. Solar panels and MPPT have been selected on basis of the power required to fly the glider for maximum efficiency and endurance.

Based on the correct selection of components, the exact weight estimation could be obtained. Every single part in the glider subjected to gravitational force would make significant impact on the stability. Estimating location center of gravity, aerodynamic



Fig. 1 BLDC motor

center, and static margin for glider would be necessary to achieve best performance and stability of glider.

3 Weight Estimation

In order to perform weight estimation, choosing of components is an essential task. Identify the component begins with its technical specification as well as the adaptability of it in the unmanned aerial vehicle system. Based on that, here is the list of parts that need to be used along with its application and working methods.

3.1 BLDC Motor

Brushless DC motors are light in weight and give good amount of thrust which makes it more suitable in making fixed-wing UAV and multicopter UAV The BLDC motor used in RC glider is shown in Fig. 1.

3.2 Propeller

Propellers for fixed-wing UAVs are essential components that generate thrust to propel the aircraft through the air. Propellers for fixed-wing UAVs are designed to



Fig. 2 Glass fiber propeller



Fig. 3 ESC

create forward thrust and are characterized by their diameter and pitch. Two blade glass fiber propeller 14*4.7 cm is chosen for glider as shown in Fig. 2.

3.3 Electronic Speed Controller

An electronic speed control (ESC) for a fixed-wing unmanned aerial vehicle (UAV) is a device that regulates the speed and direction of the electric motor that powers the glider. Choosing an appropriate ESC ensures efficient motor performance, reliable control, and optimal flight characteristics for the fixed-wing UAV. 80 Amps 3-6S ESC has been used as shown in Fig. 3.

3.4 LiPO Battery

For fixed-wing UAVs, lithium polymer (LiPo) batteries are commonly used due to their high energy density and lightweight design. Battery in Fig. 4 is with configuration of 5200 mAh 6S 22.2v 35c has been selected.



Fig. 4 Lipo ion battery

3.5 MPPT

Maximum power point tracking (MPPT) in Fig. 5 is a technology commonly used in solar-powered UAVs to optimize energy harvesting from solar panels. MPPT controllers monitor the output of the solar panels and continuously adjust the load to operate at the maximum power point, where the solar panels generate the most power.



Fig. 5 MPPT

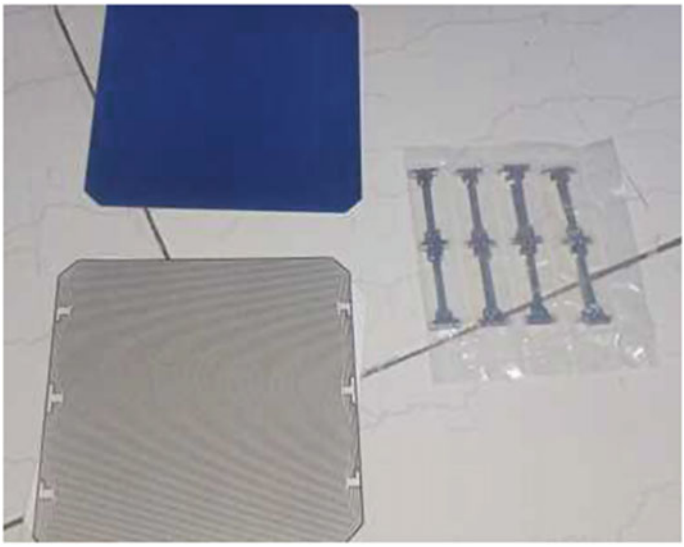


Fig. 6 Solar cells and brush

3.6 Solar Cells

C60 shown in Fig. 6, also known as fullerene or buckminsterfullerene, it is one of the types of carbon molecule with a structure similar to soccer ball.

3.7 Wings

The wing is a fundamental component of a unmanned aerial vehicle (UAV) that generates lift and provides stability during flight. UAV wings are typically designed with an airfoil shape to optimize lift and minimize drag. They are usually constructed from lightweight materials like carbon fiber or foam to ensure strength and reduce weight, and in Fig. 7, wing with solar panels mounted is shown.

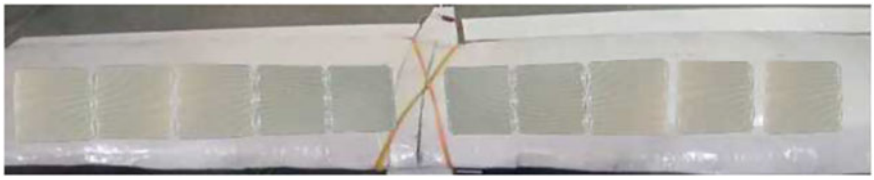


Fig. 7 Solar cells attached to wings



Fig. 8 Tail boom joining fuselage to tail

3.8 Tail Boom

The tail boom is a structural component in a fixed-wing unmanned aerial vehicle (UAV) that connects the main fuselage to the tail assembly as shown in Fig. 8.

3.9 Fuselage

The fuselage is the main body structure of a fixed-wing unmanned aerial vehicle (UAV) that houses various components and systems. It provides structural integrity and aerodynamic stability to the aircraft glider fuselage is shown in Fig. 9.



Fig. 9 Fuselage

3.10 Tail

The tail of a fixed-wing UAV is a critical component that contributes to stability and control during flight. There are mainly two types of tails which are horizontal tail. Glider horizontal as well as vertical tail is shown in Figs. 10 and 11 (Table 1).



Fig. 10 Horizontal tail

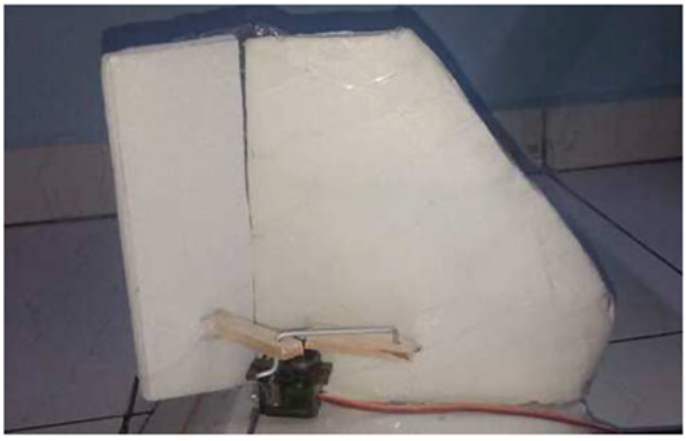


Fig. 11 Vertical tail

Table 1 Weight estimation of all the parts with their specification

Sr. No	Parts	Specification	Weight
1	BLDC electric motor	790 kV DYS D3548-6 motor	159 gm
2	LiPo battery	5200 mAh 6S 22.2v 35c	711 gm
3	ESC	80 Amps 3-6S	79 gm
4	Propeller	14*4.7 glass fiber	26 gm
5	MPPT	Genasun GV-10 lithium custom voltage MPPT	185 g
6	Solar cell	Sun Power C60 * 10	7 gm each: 70 gm
7	Wing	Balsa wood rib, carbon fiber spar, and skin-Styrofoam fused carbon fiber	635 gm
8	Tail	Tapered, balsa wood ribs, carbon fiber spar, skin styrofoam fused carbon fiber	Horizontal: 49 gm Vertical: 41 gm
10	Fuselage	Skin styrofoam fused with carbon fiber	69 gm
11	Landing gear	Conventional landing gear	110 gm
		Total weight	2734 gm

4 Lift and Drag Estimation

$$\mathrm{Re} = \frac{\rho \times V \times L}{\mu}$$

where

Re—Reynolds number

ρ—Fluid density (kg/m^3).

V—Velocity of substance (m/s)

L—Distance or length (m)

μ— Dynamic viscosity (pa $\times$ s).

Consider Reynolds number is 2.2×10^5 and for steady-state level flight, $L = W$.

So assessed that overall weight of our flight should be 2.7 kg.

The lift and drag is obtained as follows [5]:

Therefore, $L = 2.7$ kg.

We consider the wing chord length equal to 0.34 m so as to accommodate two solar panels chordwise, and also, we are taking the wing length to be 1.78 m.

By doing so we get a total wing area of 0.6052 m^2

Density of air is 1.225 kg/m^3.

$V = 27.78$ m/s.

Though for consideration we have taken this velocity, the operating ranges of velocity would be from 0 to 27.78 m/s,

i.e., $2/S = 6$.
$S = 0.6052\ \text{m}^2$.
$b = 1.78$.
Aspect ratio AR $= b^2/s$.
Therefore AR $= (1.78)^2/0.6052$.
AR $= 5.2352$.
$e = 0.94$.

$$C_L = \frac{2\boldsymbol{W}}{\boldsymbol{\rho} * \boldsymbol{v}^2 * \boldsymbol{S}} = \frac{2 * 2.7}{1.2256 * 27.7^2 * 0.6025} = 0.264.$$

$$C_{\text{L d min}} = \sqrt{\frac{\boldsymbol{C_{d0}}}{\boldsymbol{k}}} = \sqrt{\frac{0.018}{0.646}} = 0.527.$$

$$k = \frac{1}{\boldsymbol{\pi} * \boldsymbol{e} * \boldsymbol{AR}} = 0.0646.$$

$$C_d = C_{d0} + kC_L^2 = 0.018 + 0.0646 * 0.264^2 = 0.018.$$

$$D = \frac{1}{2}\rho \mathbf{v}^2 \mathbf{sc_l} = 0.5 * 1.2256 * 27.7^2 * 0.6025 * 0.018 = 0.184\,\text{N}.$$

5 Thrust Estimation

For choosing the electronics, we used the calculations of the weight and speed. Using these we came to the conclusion that we need a motor that can withstand the thrust of about 1.8 kg and a compatible esc and propeller. For these reasons, we choose the G SERIES brushless motor of 2 kg thrust. The esc used for operating the same motor was HOBBYWING SKYWALKER of 80A, and the propeller used was 14 inches long made up of glass fiber. Also, a test rig was made to check the thrust of the motor as shown in Fig. 12.

Based on the different throttle given using transmitter, thrust obtained is given in Table 2.

From Sect. 4, we can use value of lift and drag parameters to obtain thrust.

$$T = \frac{\boldsymbol{W}}{\frac{\boldsymbol{C_L}}{\boldsymbol{C_D}}} = \frac{\boldsymbol{W}}{\frac{0.264}{0.018}} = 186\ \text{g}$$

From Table 2, we could see that at full throttle, the motor with ESC and propeller combination gives maximum of 2 kg thrust.

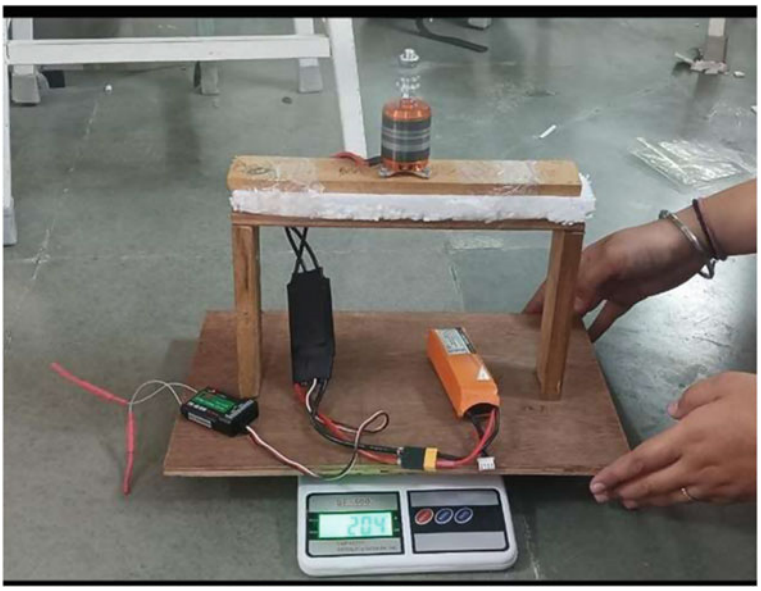


Fig. 12 Testing of motor on test rig

Table 2 Percentage of throttle with thrust obtained

Throttle (%)	Thrust (kg)
10	105
20	205
50	571
75	860
90	1169
100	2075

6 Airfoil Selection for the Main Wing

6.1 Airfoil Design

The airfoil chosen for the wing is Selig s1223 in Fig. 13 which is a highly cambered airfoil specially known for its characteristic feature of low-speed airfoil. The airfoil has its maximum thickness 12.1% at 19.8% of chord and has its maximum camber 8.1% at 49% of chord [6].

Airfoil coordinates of S1223 were taken and plotted as airfoil using laser cut technique.

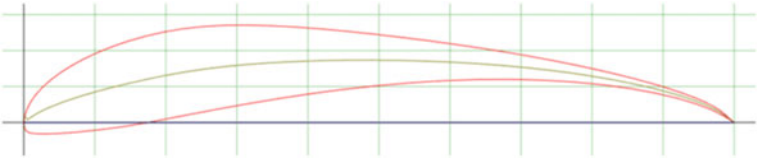


Fig. 13 Selig S1223 airfoil [7]



Fig. 14 Wing was fabricated using the styrofoam coating to provide smooth finish

7 Wing Design

The ribs made from balsa wood using laser cutting were strengthened using two spars using balsa wood material. The installation of the ribs along with the spar need uttermost care, as the improper fitting procedure would break the balsa wood ribs. The wing section so formed is then covered with 3 mm styrofoam sheet as shown in Fig. 14. This wing tends to be heavier but at the same time gives a lot more strength to the aircraft.

8 Tail Design

8.1 Horizontal Tail

Selected NACA0009, the first digit represents the zero camber which means the airfoil is symmetrical which is needed for horizontal tail.

The airfoil NACA-0009 9.0% smoothed has max thickness 9% at 30.9% chord and max camber 0% at 0% chord as shown in Fig. 15.

The cad design of the horizontal tail is shown in Fig. 16.

The weight estimation of horizontal tail is shown in Fig. 17.



Fig. 15 NACA 0009 airfoil [7]

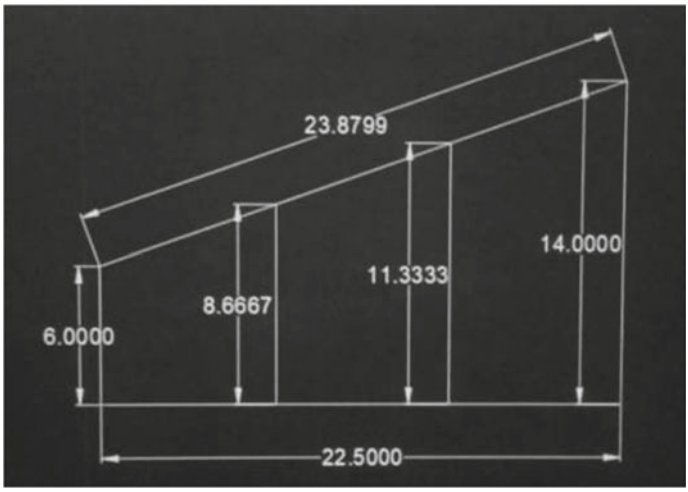


Fig. 16 CAD design of horizontal tail

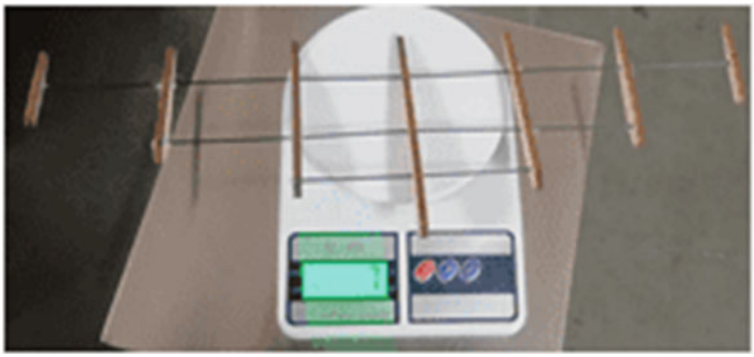


Fig. 17 Horizontal tail weight estimation

8.2 Vertical Tail Configuration

Selected NACA0009 for vertical tail, in Fig. 18 skeleton structure of vertical tail is shown.

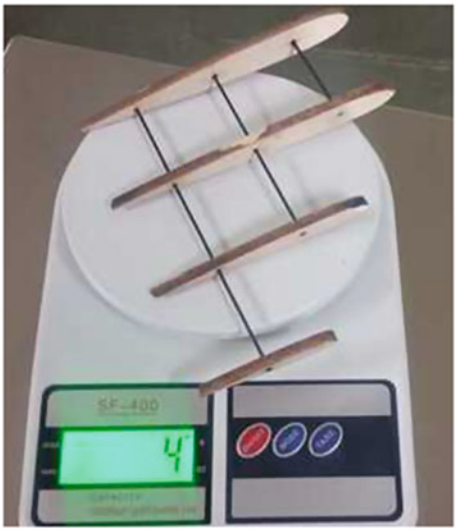


Fig. 18 Vertical tail without skin weight estimation

9 Fuselage Design

The fuselage body is made up of styrofoam so that it can carry much payload than other material. The main purpose of the fuselage is to hold all the electronic components necessary for the flight. The fuselage is made into two parts so as in one we could fit the battery, motor, ESC, MPPT, and any other components if required. Figure 19 shows the 3D model of fuselage designed in CATIA, and the structure of fuselage made by styrofoam can be seen in Figs. 21 and 22. [8].

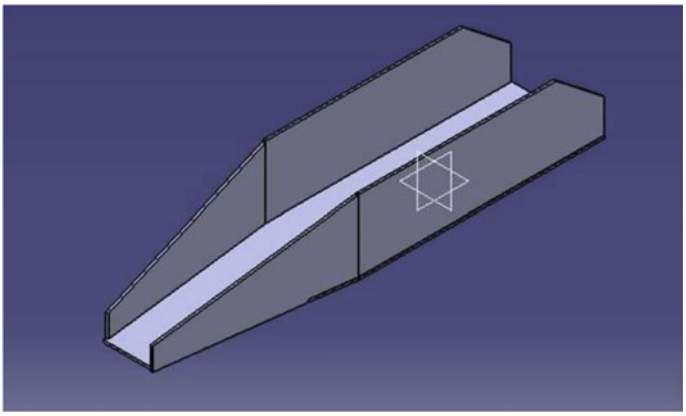


Fig. 19 Design of fuselage

10 Results and Discussions

The connections were provided successfully and tested. The connections begin with the BLDC motor which is mounted at the front of the fuselage. The BLDC motor has three terminals, namely positive, negative, and signal wires. These three need to be connected with the corresponding three terminals of ESC as shown in figure below. The other end of the ESC has two terminals red and black which is positive and negative terminals which is connected to the battery. ESC has another set of signal wires which is connected to the receiver. Battery has a terminal for recharging, which is connected to the MPPT charge controller which can manage the electric power flow, which in turn receives its power from solar panels.

Solar panel is connected to MPPT input which improvises the required voltage. Charge controller output is connected to the 6S lipo battery. When charging is completed to 11.2 V, the current drops to zero. Motor unit is connected with battery in parallel connection, and Genasun GV—10 was used in order to save the weight. Early in morning, when there is no sun, battery supplies the energy to motor, and when there is enough sunlight, the charge gets balanced naturally which provided by the charge controller. Figure 20 shows the solar glider connection.

Based on the flight time, endurance was recorded without solar energy as:

Glider without solar panels is shown in Fig. 21.

$$\text{Endurance } (E) = \frac{\text{Battery Capacity (Ah)}}{\text{Current (amps)}} = \frac{5.2}{10} = 0.52\,\text{h} = 31\,\text{min}\,12\,\text{s}.$$

Based on the flight time, endurance was recorded with solar energy as [1, 9]:

Glider with mounting of solar panels is shown in Fig. 22.

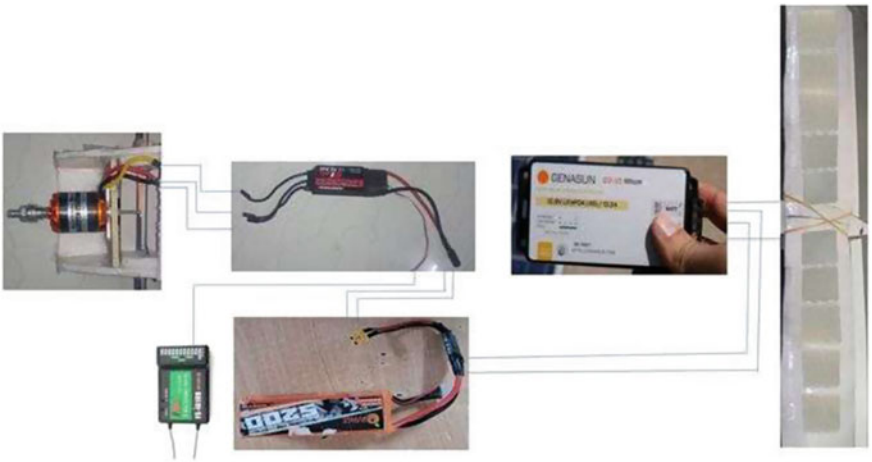


Fig. 20 Circuit connection of solar fixed-wing UAV

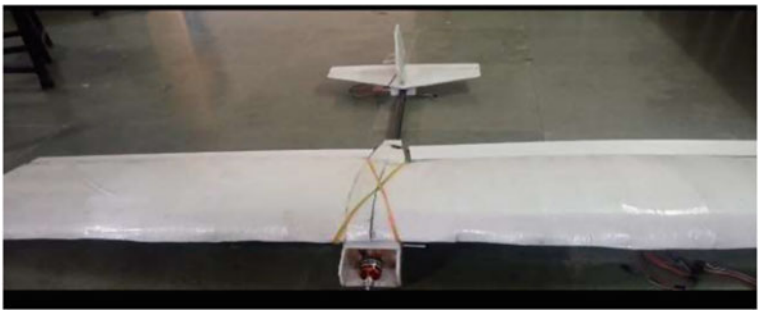


Fig. 21 Final plane without solar panel

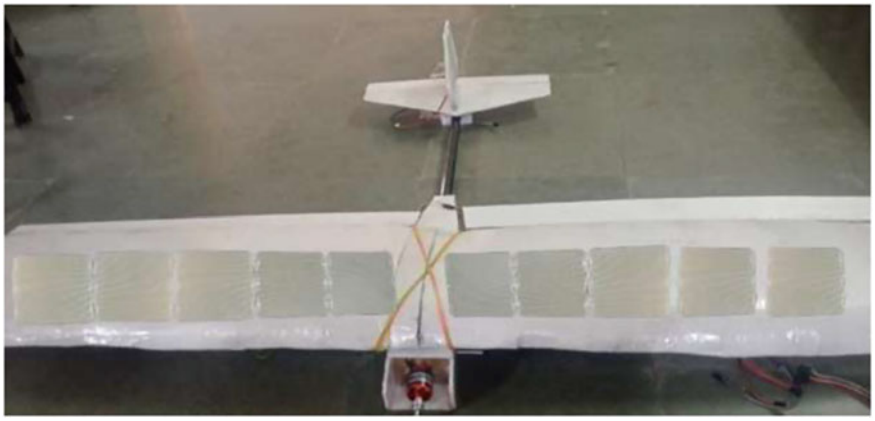


Fig. 22 Glider with solar panel

$$\text{Endurance } (E) = \frac{\text{Battery Capacity (Ah)}}{\text{Current (amps)}} = 56\,\text{min}\,13\,\text{s}.$$

11 Conclusion

The method suggested in this work provides a conceptual design that can be used to gauge general requirements and size. To improve a final unit, it is done by using basic assurance of aerodynamic characteristics of the glider and efficient solar cells, which will improve the flight performance. Wherever surveillance at low elevation or serving as a tallness correspondence stage is desired, a sun-powered aircraft with reliable flight capabilities must maintain a constant altitude.

At the end, the energy gathered during the day time from sun gives sufficient amount of energy to run and control the motor and other devices also which the battery was supplying its energy, research should be done to make solar cells give enough of energy to the circuit to fly at night as well. In future, the extended version of this research work would have the simulation and analysis of the various parts of the UAV along with flight experimental data and the data analysis of data obtained during the flight test.

Novelty of the Research Work:

In Table 3, the work that was conducted by various researchers on the similar intention was observed, and the novelty in our research work was stated after the table.

Table 3 Work done by other researchers on same intention

Design Analysis of Solar-Powered Unmanned Aerial Vehicle Published in Journal of Aerospace Technology and Management (2016) Authors: Karthik Reddy Buchireddy Sri Poondla Aneesh Kiran Bhanu M Natarajan	This study intends to stimulate research on renewable energy sources for aviation taking into account the fundamental issues for a solar-powered aircraft: operating area, energy collecting and storage, payload, and design parameters. A plane is therefore created to carry 2 kg of payload total and is examined from all angles. Additionally, the entire design is optimized for performance, from the aerofoil through the final structure
Design and Fabrication of Solar Powered Unmanned Aerial Vehicle for Border Surveillance Published in Proceedings of International Conference on Remote Sensing for Disaster Management: Issues and Challenges in Disaster Management (2019) Authors: R. Vijayanandh J. Darshan Kumar M. Senthil Kumar L. Ahilla Bharathy G. Raj Kumar	The main objectives of this paper are to make calculations and appropriate designs to create an e-aircraft model that can power its flight using solar energy, overcoming the difficulties by increasing the speed, range, and endurance of the UAV using the solar power in order to provide continuous border surveillance. CATIA V5 models the 3D solar UAV as a whole and includes theoretical design values. MATLAB has been used to complete the invaders in boundaries by image processing
Design and Development of Solar Powered Glider—part b (2016) Authors: Cheong, Wen Rong	The project focuses on producing solar cells, arranging panels on commercial UAVs, and integrating wiring connections. It plans electrical components for flightworthiness, integrates in-flight telemetry and sensors for optimal flight, and aims to produce the best solar panel fabrication solution, despite limited machinery for encapsulation

(continued)

Table 3 (continued)

Improving Endurance of a Glider by using Solar Cells Published in International Journal of Engineering Research & Technology (2020) Authors: Bassetti Chandrasheker Mahesh K	The primary goal for this study is to use solar cells to increase a glider's endurance. To do this, a prototype of this form of glider was first modeled and studied before being constructed. A section of the glider's wing that corresponds to the wing's area has solar cells covering it, and it has been tested in flight. In order to achieve the goal of this work, suitable solar cells with a decent rating were selected in accordance with the electronic requirements employed for a glider prototype. The glider's design also made sure that the aerodynamic characteristics are effective and that the flight mechanic calculations are accurate

The research was based on the construction of fixed-wing solar UAV, thereby focusing on the high endurance of the glider. As the area of concern for any aerial vehicle is weight, we have used balsa wood and carbon fiber for the skeleton of the structure. For calibrating the flight performance, we perform the thrust rig experiment for thrust estimation and used ANSYS to know the aerodynamic load on the wings. We also calibrated the required lift and thrust for the flight theoretically, which help us to select the BLDC motor required for the flight.

Funding Information Not applicable.

References

1. Sri KRB, Aneesh P, Bhanu K, Natarajan M (2016) Design analysis of solar-powered unmanned aerial vehicle. J Aerosp Technol Manag 8:397–407
2. Vijayanandh R, Darshan Kumar J, Senthil Kumar M, Ahilla Bharathy L, Raj Kumar G (2019) Design and fabrication of solar powered unmanned aerial vehicle for border surveillance. In: Proceedings of international conference on remote sensing for disaster management: issues and challenges in disaster management. Springer International Publishing, pp 61–71
3. Cheong WR (2016) Design and development of solar powered glider-part b
4. Chandrasheker B, Mahesh K (2020). Improving Endurance of a Glider by using Solar Cells. International Journal of Engineering Research & Technology (IJERT) Volume, 9.
5. Anderson JD Jr (2012) Aircraft performance and design. McGraw.
6. Eppler R (2012) Airfoil design and data. Springer Science & Business Media
7. http://airfoiltools.com/ as access on 29-06-2023 at 12:27 pm
8. Torabi HB, Sadi M, Varjani AY (2011) Solar power system for experimental unmanned aerial vehicle (UAV); design and fabrication. In 2011 2nd Power electronics, drive systems and technologies conference. IEEE, pp 129–134
9. Reddy K, Poondla A (2017) Performance analysis of solar powered unmanned aerial vehicle. Renew Energy 104:20–29

Experimental Testing of Agriculture Drone with Design Optimization



N. C. Ajay Vishwath, Akash R. Rajput, S. K. Shamam Gouse, Sneha Bhuva, and Upendra Pandey

Abstract The agriculture drone booming up in the drone industry is making a real impact in the society. However, most of the drones used for these applications are imported from foreign countries. The motive of building and testing an agriculture drone in-house makes one feel native. This research work is one with such satisfaction which includes design, building, and testing of agriculture drone with pesticide spraying techniques and equipment. Complete methodology of design and building is explained, and the exact component selection has been decoded. The method of testing motor to obtain the necessary thrust required has been demonstrated. Finally, the successful testing of agriculture drone is done, and the research values are recorded.

Keywords Agriculture drone fabrication · Unmanned aerial vehicle · Spraying system · Crop monitoring · Agriculture drone

N. C. A. Vishwath (✉) · A. R. Rajput · S. K. Shamam Gouse · S. Bhuva · U. Pandey
Department of Aeronautical Engineering, Parul Institute of Engineering and Technology, Parul University, Vadodara, India
e-mail: ajay.nc2934@paruluniversity.ac.in

A. R. Rajput
e-mail: 2203031017009@paruluniversity.ac.in

S. K. Shamam Gouse
e-mail: 2203031017008@paruluniversity.ac.in

S. Bhuva
e-mail: 200303101009@paruluniversity.ac.in

U. Pandey
e-mail: 200303101013@paruluniversity.ac.in

© The Author(s), under exclusive license to Springer Nature Singapore Pte Ltd. 2024

S. Singh et al. (eds.), *Recent Advances in Aerospace Engineering*, Lecture Notes in Mechanical Engineering, https://doi.org/10.1007/978-981-97-1306-6_8

1 Introduction

Drones have undergone remarkable development over the last 10 years. The application based on agricultural purposes with drones has received great attention over the last few decades. But these days the readily available drones are so expensive because they are mostly made by the carbon fiber material.

These days, there are much developments happen in the perfection of agriculture for improving the crop productivity. Particularly in the emerging countries like India, where more than 70% of the pastoral population rely on the agriculture fields. The farming fields face drastic losses due to the harms came from the pests and insects, which indeed decrease the yield of the crops. The fungicides are the type of pesticide like chemicals which eliminates the insects and pests and thereby improves the quality of crops. Many cases have been identified by the WHO (World Health Organization) where the humans have affected while sprinkling the fungicides in the field manually. The drones or unmanned aerial vehicles (UAVs) are therefore could be used to sprinkle the fungicides to avoid the health problems faced by humans as a result of sprinkling it manually. Drones or UAVs could be used to avoid the interaction of the humans with fungicide, where the labors may face slight difficulty to operate, but in the long run, they would learn to operate. This was briefly reviewed by U. M. Rao Mogili and B. B. V. L. Deepak in their research article [1].

Since last decades, the UAVs are put into various applications like defense, commercial, and other medical operations. But due to some of the most recent advancements in the information technology as well as sensor integrating techniques, the drones have pushed its limits and made itself available for agriculture-related applications as well. In recent days, the drones have become smarter due to its integration with several open-source technologies, advanced nanosensors, better integration techniques, improved flight time, ability to track down intruders in the field, and monitoring the wildlife and disaster-prone areas as well. Vikram Puri, Anand Nayyar, and Linesh Raja had highlighted the importance of such aerial vehicle in agriculture and had presented the list of drones that are available in the market for monitoring and observation in agriculture fields to achieve better quality of crops and protect the fields from any kind of damage [2].

The extensive use of drones in the field of agriculture gives rise to unique opportunities and challenging tasks like crop monitoring, precision distribution of agricultural chemicals and biological control agents, monitoring the health of livestock, and remote sampling are very difficult for humans to perform on daily basis. The research work by Deon vans der Merwe and his team reviewed the evolution of drone used in agriculture approaches and methods to ensure that data quality is adequate for agricultural applications and a selection of traditional and emerging agricultural drone applications [3].

Abderahman Rejeb and his team have worked on improvising the existing scientific literature and the bibliometric survey, they highlighted the current researches. To evaluate the previous researches on agricultural drones, they analyzed it and used

bibliometric techniques. The analysis concluded that remote sensing, precision agriculture, deep learning, machine learning, and the Internet of things are crucial topics for agricultural drones. They analysed over six major research works which were the first attempt to summarize the future directions of agriculture drones [4].

To reduce the cost of the drone, this research work aims to present a suitable methodology to figure out aluminum frame construction which would lower its cost and affordable in the market. The agriculture drone is unique as compared to existing drones in the market for reason carbon fiber is expensive, and Indian farmers have not yet developed to afford the high-cost carbon fiber agricultural drones. So, to address this issue, we invented a drone using an aluminum frame, which is less expensive than a carbon fiber frame.

To explain the research work carried out, with clarity, various design process and methods are elaborated in different sections. Section 2 is dedicated to the structural design of drone, which deals with the design considerations for the frame and landing gear. Electronic design for drone which deals with various components need to be used is explained in Sect. 3 in detail addressing the purposes of each part. Section 4 deals with weight estimation, Sect. 5 deals with thrust estimation, and these two sections are the major session where the actual performance of the drone was quantified. The complete circuit connection was demonstrated in Sect. 6 that would help the reader with knowing the necessary connections required to build this complex machine.

The novelty of the research work done is that the experimental testing of in-house built agricultural drone, as the frame material is unique, i.e., aluminum, design optimization is required to carry the necessary payload, as the conventional frames used in the market is carbon fiber which can carry more payload, but not reliable and affordable by most of the agriculture drone users. And the fabrication technique used here is not mentioned or practiced by any of the researchers worked on the similar works.

2 Structural Design of Drone

The complexity of design in drone is that it involves both mechanical design as well as electronics design. The mechanical design involves the geometrical dimensions and structural designs, which further deals with the various design aspects that would be helpful for design optimization.

2.1 Frame Structure

Aluminum is a lightweight, durable material that is commonly used to make a wide variety of products, including bicycles, airplanes, and other transportation machines. Frame weight is an important value which would make researchers choose

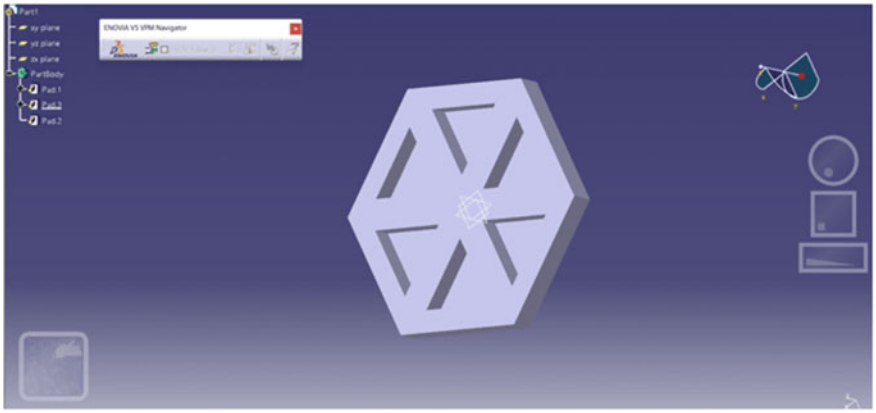


Fig. 1 Bottom plate

an aluminum frame-based product. Aluminum has higher strength to weight ratio which is why we choose aluminum as material for the drone frame. In some cases, a lighter frame may be desirable as it can improve the overall performance and handling of the product. However, depending on your use case, a heavier frame may be more stable and durable [5, 6].

The frame structure includes various parts that help in accommodating the necessary electronics to fly the drone. Frame needs to be made in such a way that it is symmetrical about all the axis or the axis where the majority of stability needs to be considered. This helps in distributing the load evenly as well as to maintain the center of gravity.

The frame has a bottom plate, design of which shown in Fig. 1, which holds the complete electronic circuits and especially the flight controller and power distribution board. It carries the load from top plate as well from the arms and transfers it to the landing gear. While fabricating the bottom plate, symmetry is expected so that the load is distributed uniformly.

The next is to design top plate of the drone. The top plate of the drone just not would cover the parts below it but also gives protection to it from top side. Another important function of the top plate is that the main battery which is the heaviest part of the drone would be carried by the top plate. So, the strength of the top plate should be enough to hold it tight as well rigid enough to distribute its weight through a column to the bottom plate (Fig. 2).

The most important part of the drone is the arm of the drone. The arm of the drone would contain the motors with the propellers on it which would be the main thrust producing system. So, the thickness of the arm needs to be enough to hold the complete system. The arm has the rectangular cross section, which is shown in Fig. 3.

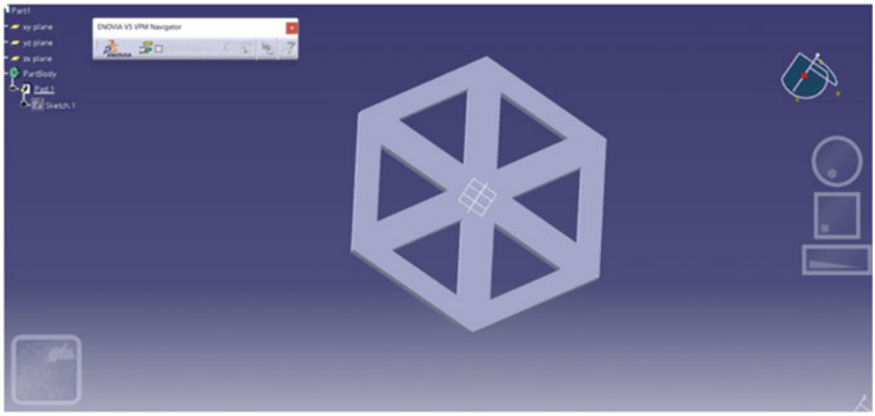


Fig. 2 Top plate

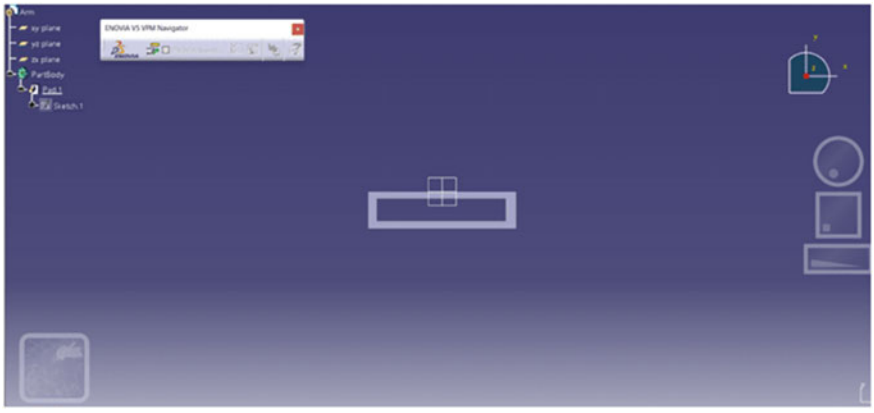


Fig. 3 Cross-sectional view of arm

The arm length is one of the most important parameters, as the arm should be lengthy enough that two propellers in consecutive arm does not collide and also has enough gap so that aerodynamics of one propeller does not affect the other (Fig. 4).

The landing gear is designed knowing the fact that it has to carry the whole weight of the drone at the time of takeoff as well as to carry the load from the drone and transfer to the ground, every time the drone lands. Another important task for the landing gear here is to hold the spraying mechanism and the tank for storing the pesticide (Fig. 5).

Assembly of drone is done and shown in Fig. 6.

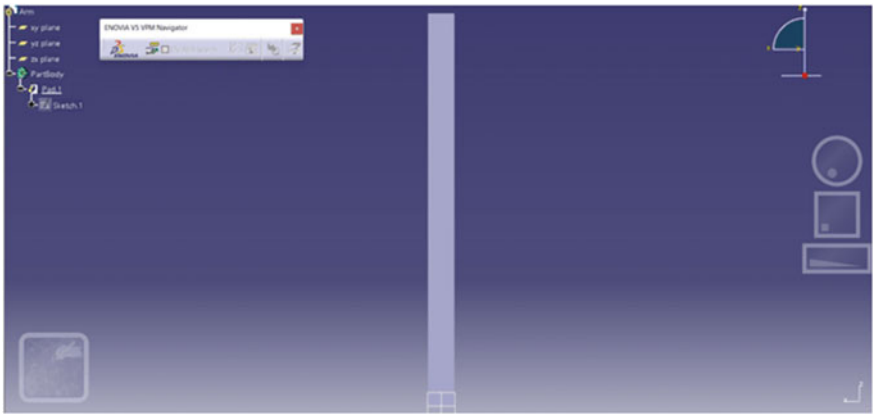


Fig. 4 Arm of the drone

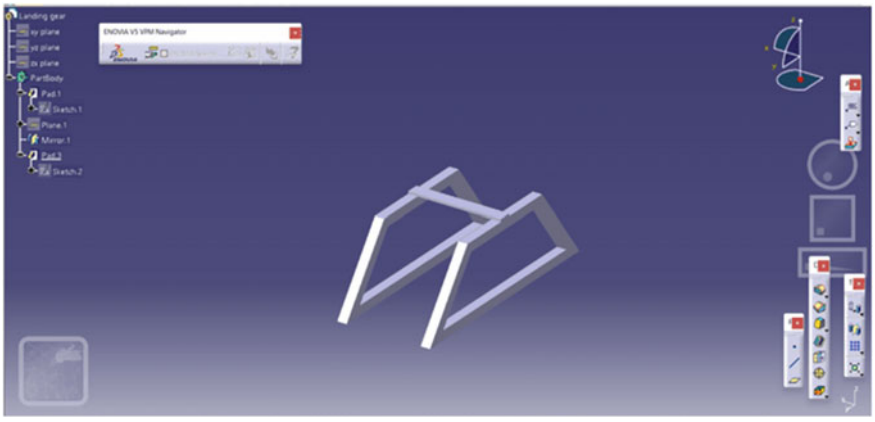


Fig. 5 Landing gear of the drone

3 Electronic Design of Drone—Component Selection

Electronic design involves the choosing the list of electronic components that suitable for building the drone as well as the circuit connection required to connect them. In this session, choosing electronic components and description about them was discussed.

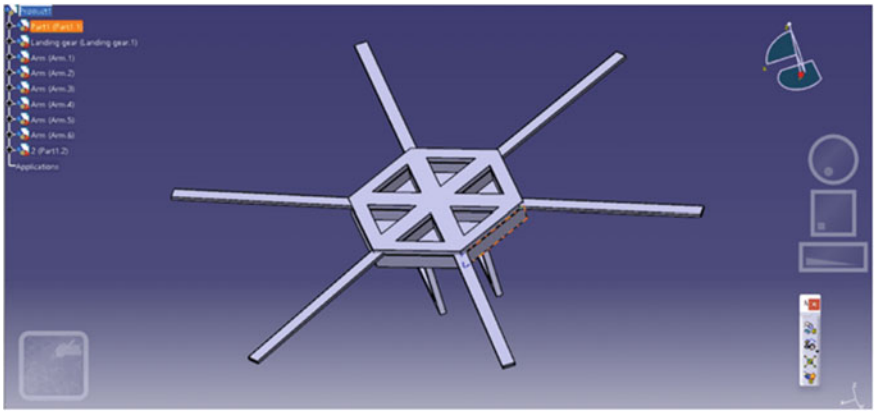


Fig. 6 Frame of the drones

3.1 High Torque Brushless DC Motor

A 350 kV high torque brushless motor is a type of electric motor that transfers power from the stator (stationary part) to the rotor (rotating part) without the use of brushes or commutators. The motor has a high torque rating, so it can provide a large amount of rotational force to turn objects or get work done. High torque: It refers to the engine's ability to deliver large amounts of rotational power or torque [7].

High torque motors are suitable for applications that require a lot of power, such as brushless: This means that the motor does not use brushes or commutators to transfer power between the stator and rotor like traditional brushed motors do. Overall, the high torque 350 kV brushless motor is a powerful and efficient motor is the correct choice as it is used in many of high-power applications, particularly in drones, electric vehicles, and industrial machinery [8] (Fig. 7).

3.2 ESC Brushless Motor Controller

A brushless ESC motor controller is an electronic device that controls the speed and direction of a brushless motor. How a brushless ESC motor controller works: The controller receives signals from the user-operated transmitter and converts those signals into signals that can control the RPM and direction of the BLDC motor. The electronic speed controller uses electric circuitry to turn power to the motor on and off at precise intervals. The controller monitors the motor current and voltage and adjusts the switching frequency and timing to maintain the desired speed and torque (Fig. 8).



Fig. 7 Brushless DC motor



Fig. 8 Brushless ESC

3.3 Pixhawk Flight Controller

The Pixhawk flight controller is a popular open-source hardware and software platform used for developing autonomous vehicles, especially in the drone and unmanned aerial vehicle (UAV) space. This is a small computer system that controls the vehicle's flight, stabilizes it, and collects and processes data from various sensors and other components of the vehicle (Fig. 9).



Fig. 9 Pixhawk flight controller

3.4 GPS Module M8N

The M8N GPS module incorporates an active antenna to ensure good signal reception even in harsh environments such as urban canyons and forests. It also features fast first time to repair (TTFF) and a low power mode, making it ideal for battery-powered applications. Overall, the M8N GPS module is a powerful and reliable GPS receiver module that provides accurate location data for various applications (Fig. 10).

3.5 Power Module

In the context of electronics, a power module is a device designed to manage and distribute power to various components or subsystems within a system. Commonly used in power electronics applications such as motor drives, inverters, and power supplies. Overcurrent protection: Many power modules have built-in overcurrent protection to prevent damage to the module and other components in your system in the event of a short circuit or other fault.

Thermal management: Power modules can generate a lot of heat, so many modules have thermal management features such as heatsinks and fans to dissipate heat and



Fig. 10 GPS module

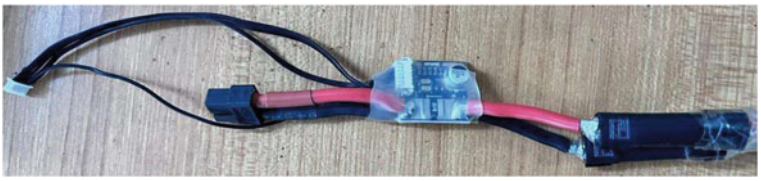


Fig. 11 Power module

prevent overheating. Overall, power modules are essential components in many power electronics applications. They provide a convenient and efficient way to manage and distribute power to various subsystems and components within a system while also providing protection against faults and other issues (Fig. 11).

3.6 Fly Sky FS-I6X

Fly Sky FS-i6X is a popular 6-channel radio transmitter widely used in RC hobby applications, such as controlling drones, RC cars, boats, and planes. It features an easy-to-use interface, ten programmable channels, and support for multiple models.



Fig. 12 Transmitter to control and command the drone

The FS-i6X also comes with a receiver that can be bound to the transmitter for wireless communication.

The FS-i6X is feature-rich and a favorite among enthusiasts. It features a large backlit LCD display that provides real-time telemetry data such as battery voltage and signal strength. The transmitter also has a built-in trainer function, allowing an experienced pilot to remotely control the model and train a less-experienced pilot.

Additionally, the FS-i6X has a wide range of customization options, including the ability to adjust stick sensitivity, trim settings, and throttle response. It can also be used in conjunction with simulators for training purposes. Overall, the Fly Sky FS-i6X is a versatile and reliable transmitter, popular with his RC enthusiasts for its affordable price and feature set [9] (Fig. 12).

3.7 Receiver

The FS-iA6B is a 6-channel receiver used for hobby radio control systems such as model airplanes.

The FS-iA6B receiver operates at a frequency of 2.4 GHz and has a range of up to 500 m in open terrain. It supports PPM, PWM, and I-BUS output modes and has a user-programmable fail-safe function.

The receiver has 6 he PWM input channels that can be bound to transmitters using buttons on the side of the receiver or via the compatible transmitter menu. FS-iA6B also features a data port that can be used to update the receiver's firmware or connect



Fig. 13 Receiver to receive the command for the drone

to other devices. Overall, the FS-iA6B is a reliable and versatile receiver that can be used in various RC applications (Fig. 13).

3.8 ESC Power Distribution Board

An electronic speed controller (ESC) power distribution board is a device used to distribute power from a battery to multiple ESCs, motors, and other electronic components in a multirotor or drone system. ESC switchboards typically have multiple power outputs designed to connect directly to the ESC that controls the speed and direction of the motor.

The main advantage of using an ESC switchboard is that it reduces the number of wires and connectors required while providing a centralized and efficient way to distribute power to all components in the system. Overall, an ESC power distribution board is an essential component in any multirotor or drone system, providing a convenient and efficient way to distribute power to the various components in the system (Fig. 14).

3.9 22000 mAh Battery

"22000 mAh 6S 25C" is a specification for lithium polymer (LiPo) battery packs commonly used in remote control (RC) vehicles, drones, and other high-power applications. Here is what each part of the specification means: 22,000 mAh: This refers to the capacity of the battery measured in milliampere hours (mAh).

In this case, the battery has a capacity of 22,000 mAh, which means it can deliver 22,000 milliamps of current per hour. 6S: This refers to the number of cells in the

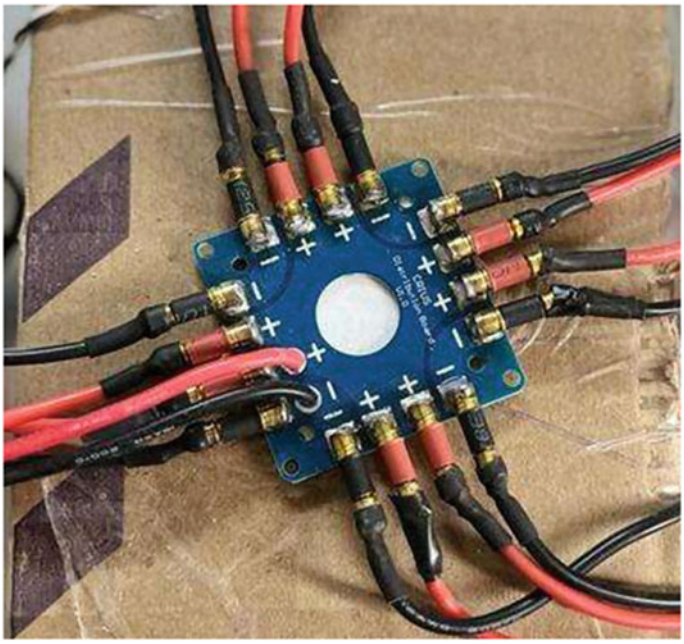


Fig. 14 ESC power distribution board

battery and how they are wired. In this case, the battery discharge rate is 25 times its capacity or 550 amps (25 × 22,000 mAh). All in all, the 22,000 mAh 6S 25C LiPo battery is a large, high-capacity battery that can provide a lot of power for your RC vehicles and other high-power devices (Fig. 15).



Fig. 15 LiPO battery

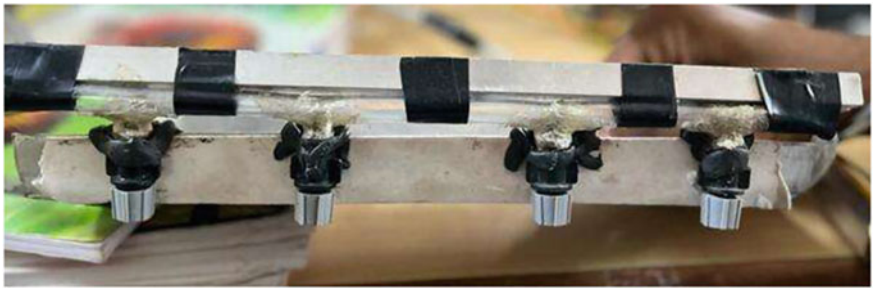


Fig. 16 Pesticide spraying mechanism

3.10 Sprinkling System

The pesticide sprinkler system is typically mounted on the bottom portion of the UAV and positioned in such a way that nozzle sprinkle the pesticide downwards. The second is the controller used to actuate the atomizer nozzle.

Pressure pump is the major part of the sprinkler system that pressurizes the flow of the pesticide out of the spraying nozzle. Performance of different spray speeds and nozzle characteristics used for spraying was designed through proper calculations [10] (Fig. 16).

The reason of choosing such high-quality motors and ESCs are that they are reliable especially when the drones are being operated for several hours continuously. The choice of battery is based on the high endurance, so to support the high endurance operations, the motors and ESCs should be in the position to work without any heating issues, and the chosen motors and ESCs are not just random but after testing several ranges of combination of motors and ESCs. The reason of choosing Pixhawk Flight Controller is that, for hexacopter and octacopter configuration, ordinary flight controllers are not efficient and give poor results in stability. Also in Pixhawk Flight Controller, the checkpoints can be given and be monitored through Mission Planner Software which would improve the yield of crops.

4 Weight Estimation

Every single part of the drone was listed with their corresponding weight in Table 1.

Table 1 Various parts of the done with their weights

Sr. No.	Name of parts	Weight per part in (g)	Weight in (g)
1	Aluminum frame	3290	3290
2	350 kV high torque brushless motor (6)	110	660
3	Brushless ESC	30	180
4	PIXHAWK flight controller	50	50
5	PIXHAWK accessories	53	53
6	GPS module	30	30
7	Power module	22	22
8	Receiver	14	14
9	Flight distribution board	36	36
10	22,000 mAh LiPO battery	2500	2500
11	Nuts, bolts, and washers	455	455
12	Landingear	258	258
13	Suction motor	560	560
14	Fertilizer with tank and tubes	1232	1232
15	Suction motor mount and fertilizer holder	186	186
16	Spraying mechanism	214	214
	Total		9710

The above weight estimation is accurate, and this forms out to be the major challenge needs to be handled. In order to lift such huge weights, normal BLDC motor will not be sufficient, and a high torque BLDC motor would be required

5 Thrust Estimation

In order to choose the right motor, all possible motors that are compatible with the drone applications and also comes under the BLDC motor category as well, needs to be tested. The exact kv of the motor needs to be known, for the same thrust of the motor need to be obtained through Test Rig. Depending on that ESC needs to be chosen as well. Also, depending on their compatibility along with range and endurance requirement, proper battery needs to be chosen [11].

The right motor can be chosen through thrust test rig setup as shown in Fig. 17. The BLDC motor with 360 kV used with 14-inch propeller. The thrust would measure the thrust produced by the motors, and this would give the idea of each motor's thrust and thereby can determine the total thrust available with the drone.

Based on the thrust rig built and the observations recorded from it, Table 2 is generated which would give the value of thrust at various speed of motor based on the amount of throttle given through the transmitter.

It can be observed that at full throttle the motor can generate up to 2.4 kg of thrust. So, if one uses the hexacopter configuration, the total thrust produced would be 14.4 kg. The total weight needs to be lifted is given on the total weight estimated

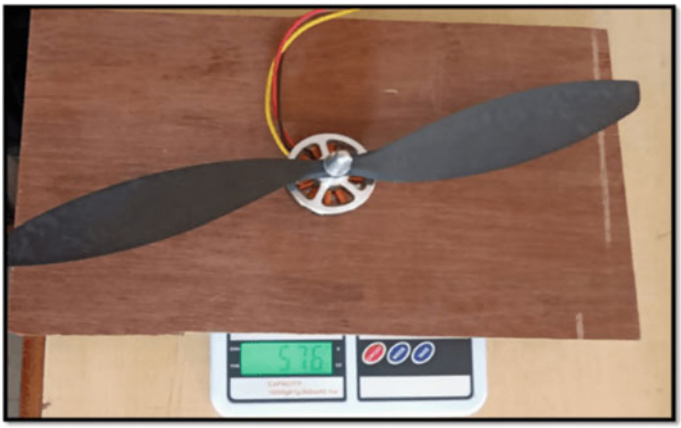


Fig. 17 Motor thrust rig setup

Table 2 Percentage of throttle with its corresponding thrust

Sr. No.	Throttle (%)	Thrust (gm)
1	10	110
2	25	220
3	50	520
4	60	920
5	75	1300
6	90	1700
7	100	2400

on previous section which is 9710 g, i.e., 9.71 kg. We can see that to lift 9.71 kg of total weight for a hexacopter it would take 1620gm of motor thrust per motor, which could be achieved in 80% of throttle.

6 Circuit Connections

The necessary circuit connections required for the agriculture drone are demonstrated in the below block diagram (Fig. 18).

The agriculture drone has hexacopter configuration so the connections need to begin with interfacing six BLDC motors with six ESCs.

The BLDC motor would have three terminals, and ESC would have three terminals. One terminal indicates positive, and one terminal indicates negative and the other one signal in both ESC as well as motor.

Though there is a lot many combinations to join the motor with ESC, preferred method is to join the middle wire of motor with middle wire of ESC and the last 2



Fig. 18 Circuit connection to control and command the drone

wires of motor could be connected to remaining 2 wires in ESC in any order, as it only changes the polarity if it was mismatched. Also changing the polarity is more important in drones as the consecutive motors need to have opposite direction of rotation.

The ESC has other end two terminals which would be of big red and black-colored wires that would get connected with the batteries. But since hexacopter needs six ESCs, a power distribution board comes in between these connections. The power distribution distributes the power from battery to the six ESCs equally.

There is another small set of wires from ESCs which would be connected to the flight controller which would have a signal pin that is for sending the signal from

flight controller to ESC. General ESC would have positive and negative wires among those small set of wires which would power the flight controller, but this ESC is not having those wires which is why necessary of power module arises.

Power module is the device that would take the power from battery and step down the supply to the flight controller to power it.

The flight controller used here is the PIXHAWK, which is the main brain of the drone, and this just not only make the control but also keeps the drone stable. The flight controller records the initial position and stores it as the equilibrium position during the calibration, and later if any disturbances occurs and the drone changes its orientation from equilibrium position, the flight controller would bring the drone to its equilibrium position.

The receiver is connected to the PIXHAWK to command the flight controller to perform the motions and calculate the disturbances caused by it using the in-built sensors it has. These disturbances are damped automatically by the flight controller based on the initial calibration performed as well as by varying the speed of each motor.

7 Results and Discussions

The agriculture drone was built successfully, and the connections are provided properly. Drones are equipped with flight control systems that include flight controllers, GPS modules, and other sensors. Agricultural drones designed for spraying applications are equipped with a spraying mechanism which would spray the pesticides effectively. The end product of agricultural drones aims to provide farmers with efficient and effective tools for crop monitoring, data collection, and targeted processing applications. Leveraging drone capabilities, farmers can improve crop management practices, optimize resource utilization, detect crop stress and disease early, and ultimately increase yields while reducing environmental impact (Fig. 19).

The agriculture drone was tested in the lawn, and its stability was good. The drone performed take off with almost 80–90% of the throttle in the transmitter which would be 1620 g to 1700 g of combined thrust by all motors together. Further at full throttle it has reached enough altitude to perform the spraying mechanism.

The drone was tested and flown at an altitude of 12–15 ft, and motion in all three axes has been done.

It was showing stable performances in both pitch and roll maneuvers with the margin of 10 to 15ft. Water sprinkling test has also been performed, and it was noted that the water gets evenly spread in targeted area with nozzle diameter of 4 mm. The spraying mechanism was using a motor regulator and servomotor which would regulate the speed of the spray while drone is flying stable above the crops across the field (Fig. 20).

To improve its efficiency, high-quality motors and ESCs could be replaced with the one suggested, along with the advanced version of the same flight controller. To



Fig. 19 Aluminum drone frame

Fig. 20 Drone flight testing



improve the payload capability, aluminum and other metals could be replaced with carbon fiber, but indeed it would increase the cost.

The frame designed and manufactured was little lengthier than the expected design as the extended arms would act as a propeller guard and prevent the damage of the propellers, thereby not losing the stability of the drone flight.

The top plate and bottom plate of the aluminum frame were protecting the electronic parts successfully, and even if the drone experiences a crash the aluminum plates would protect the electronic parts effectively. To test the same, drop test was done. Also, in the drop test the strength of the landing gear was tested, it gave a good result, and it was able to hold the complete weight of the drone and the forces imparted on it by the complete drone while it was drop under free fall subjected under the influence of earth's gravitational force.

8 Conclusion

The research work carried to build an agriculture drone with the cheapest cost possible and with sufficient efficiency that can be achieved practically. Such in-house drone products should be considered as an alternative solution for the existing luxurious and imported drone products. In future the same could be made cheaper and more efficient with advanced machining and tooling capabilities. Frame structure of the drone was made in such a way that even if it gets crashed there would be no damage to the propellers and other electrical components. Though the test results give us the satisfaction, the drone has limitation in the payload capacity it can carry, due to its heavy frame structure material weight, compared to the other conventional drones generally used in the market. Upgrading the drone by interfacing it with AeroGCS Green with a help of drone companies working on that would enhance the productivity, for the same a start-up named Aquastrobotic Aerospace Technologies Pvt Ltd has agreed to take forward this research work.

Funding Information Not applicable.

References

1. Mogili UR, Deepak BBVL (2018) Review on application of drone systems in precision agriculture. Procedia Comput. Sci 133:502–509
2. Puri V, Nayyar A, Raja L (2017) Agriculture drones: a modern breakthrough in precision agriculture. J Stat Manag Syst 20(4):507–518
3. van der Merwe D, Burchfield DR, Witt TD, Price KP, Sharda A (2020) Drones in agriculture. Adv Agron 162:1–30
4. Rejeb A, Abdollahi A, Rejeb K, Treiblmaier H (2022) Drones in agriculture: a review and bibliometric analysis. Comput Electron Agric 198:107017
5. Bright J, Suryaprakash R, Akash S, Giridharan A (2021) Optimization of quadcopter frame using generative design and comparison with DJI F450 drone frame. In: IOP conference series: materials science and engineering, vol 1012, no 1. IOP Publishing, p 012019
6. Zhafri ZM, Effendi MSM, Rosli MF (2018) A review on sustainable design and optimum assembly process: a case study on a drone. In: AIP conference proceedings, vol 2030, no 1. AIP Publishing LLC, p 020071
7. Parmar RP (2021) Decryption and design of a multicopter unmanned aerial vehicle (UAV) for heavy lift agricultural operations. In: Agricultural informatics: automation using the IoT and machine learning, pp 189–221

8. Carlier N, Desloovere M (2018) Deployment of unmanned aircraft systems as part of precision agriculture in Finland
9. Gupta C, Chutia D, Kithan M, Kesiezie AO, Saikhom V, Singh PS, Chouhan A, Sharma N, Debnath A, Handique BK, Goswami J, Goswami C, Khan AQ, Sarma KK, Raju PLN (2015) Design and integration of a lightweight multirotor unmanned aerial vehicle for remote sensing applications
10. Niemiec R, Gandhi F (2017) Multirotor controls, trim, and autonomous flight dynamics of plus-and cross-quadcopters. J Aircr 54(5):1910–1920
11. NC AV, Yadav AR, Mehta D, Belani J, Chauhan RR (2022) A guide to novice for proper selection of the components of drone for specific applications. Mater Today Proc 65:3617–3622

Control Systems for Unmanned Aerial Vehicles: Advancement and Challenges



Nikhil Yogi and Niraj Kumar

Abstract This paper presents an overview of control systems for unmanned aerial vehicles (UAVs) and explores their advancements, challenges, applications, and future trends. The introduction provides a basic understanding of control systems in UAVs, followed by a discussion of different types of control systems, including manual control, flight stabilization systems, and autonomous control systems. The paper highlights advancements in control algorithms, such as PID control, model predictive control, and adaptive control and addresses challenges related to obstacle avoidance, path planning, and sensor integration. Applications of control systems in UAVs, such as aerial photography, search and rescue missions, precision agriculture, and infrastructure inspection, are presented. The conclusion emphasizes the need for ongoing research and development to meet the evolving demands of autonomous UAV operations. This paper contributes to the understanding and advancement of control systems in the field of UAV technology.

Keywords Autonomous systems · Control systems · Unmanned systems · Feedback control · Autonomous navigation · Robotics applications

1 Introduction

Drones, also known as unmanned aerial vehicles (UAVs), have gained widespread popularity and find applications across a diverse range of industries [1]. Their increasing utilization in sectors such as aerial surveillance, agriculture, delivery services, and disaster management is attributed to their unique advantages, including remote operation, cost-effectiveness, and access to challenging locations [1, 2]. The effectiveness of UAV operations relies heavily on their control systems, which

N. Yogi (✉) · N. Kumar
Amity Institute of Defence Technology, Amity University Uttar Pradesh, Noida, Uttar Pradesh, India
e-mail: nikhil.yogi1@s.amity.edu

N. Kumar
e-mail: nkumar21@amity.edu

© The Author(s), under exclusive license to Springer Nature Singapore Pte Ltd. 2024

S. Singh et al. (eds.), *Recent Advances in Aerospace Engineering*, Lecture Notes in Mechanical Engineering, https://doi.org/10.1007/978-981-97-1306-6_9

enable precise flight paths, stability maintenance, and accurate task execution [3]. Unmanned aerial vehicles (UAVs) are aircraft that fly autonomously or remotely without an on-board human pilot. They have transformed a number of sectors by providing improved capabilities and flexibility in carrying out operations that were previously labour-intensive or difficult to do. The core of UAV operations are control systems, which provide pilots the capacity to maintain stability, manoeuvre across challenging terrain, and carry out duties precisely. The flight and behaviour of the UAV are controlled by these systems, which are made up of algorithms, sensors, and actuators. Control rules' creation and application dictate how the UAV reacts to outside stimuli, assuring its stability, manoeuvrability, and overall performance. This study aims to provide a comprehensive investigation of the advancements and challenges in UAV control systems. It begins with an overview highlighting the value and diverse applications of UAVs across various fields [1]. The subsequent section delves into control systems, offering a concise explanation of their function and the different types utilized in UAVs [2, 3]. Furthermore, the study focuses on the advancements in control systems, covering state-of-the-art control algorithms that have significantly improved UAV performance [3, 4]. It explores cutting-edge methods and tools that have enhanced the functionality and autonomy of UAVs [4]. The study also addresses the challenges involved in developing and implementing reliable control systems for autonomous platforms, emphasizing the importance of understanding these obstacles to foster further innovation in the industry [4, 5]. The applications of control systems in UAVs are extensively covered, demonstrating their effectiveness in various fields, such as aerial surveillance, agriculture, and delivery services [1, 6]. Control systems play a vital role in facilitating efficient job execution within these applications [1, 6]. Overall, this comprehensive review serves as a valuable resource for academics, engineers, and business experts seeking to enhance the performance and capabilities of UAVs [3]. The article discusses a variety of issues, such as the many types of control systems used in UAVs, the most recent control algorithms, and the obstacles involved in creating and implementing trustworthy control systems for autonomous platforms. The study also addresses UAV control system applications, proving their usefulness in domains such as airborne surveillance, agriculture, and delivery services. The research looks at a variety of UAVs, including fixed-wing, rotary-wing, and multirotor UAVs. The report also examines the difficulties of managing UAVs in various situations, such as urban, rural, and complicated terrain. By being aware of the advancements, challenges, and diverse applications of control systems in autonomous platforms, stakeholders can actively contribute to the future development and integration of these systems [3, 4].

2 Control Systems in Autonomous Platforms

2.1 Overview of Control Systems

Unmanned aerial vehicles (UAVs) depend on control systems in order to obtain desired flying paths, maintain stability, and carry out duties precisely [7]. This section gives a general introduction of UAV control systems, focusing on their core ideas and elements. Three essential parts make up a control system: the plant, the controller, and the feedback loop [8]. The UAV's propulsion, navigation, and sensor subsystems are all included in the plant's scope of the physical system under control [9]. The controller analyses data, creates control signals, and modifies the behaviour of the plant [4]. It receives input from sensors, computes control actions, and sends commands to the UAV's actuators [8]. The feedback loop continuously monitors the UAV's state through sensors and compares it with the desired state [10]. Deviations between the actual and desired states are used to adjust control signals, ensuring the UAV maintains its intended trajectory and stability [10]. Open-loop and closed-loop systems are the two basic categories into which UAV control systems may be divided [8]. Open-loop or feedforward systems rely on predetermined control inputs without taking real output or system conditions into account [8]. Although they are straightforward and computationally effective, they cannot change with the environment [8]. Sensors are used in closed-loop systems, also known as feedback systems, to continually monitor the condition of the UAV and modify the control signals as necessary [8]. The behaviour of the UAV may be controlled with improved accuracy, stability, and resilience as a result [8]. One of the fundamental equations that describe the general principles of control systems is the feedback control equation, which represents the basic concept of a control loop. This Equation [11] is often referred to as the control law and is represented as follows:

$$u(t) = K_p \cdot e(t) + K_i \cdot \int e(t)\mathrm{d}t + K_d \cdot \frac{\mathrm{d}e(t)}{\mathrm{d}t}$$

where $u(t)$ represents the control signal or the output of the control system at time t. $e(t)$ represents the error signal, which is the difference between the desired reference value and the actual value of the system at time t. K_p, K_i, and K_d are the proportional, integral, and derivative gains, respectively. These gains are adjustable parameters that determine the response of the control system and can be tuned to achieve desired performance characteristics. The control law equation combines the proportional, integral, and derivative actions to compute the control signal. The proportional term $\left(K_p \cdot e(t)\right)$ adjusts the control signal based on the current error, the integral term $(K_i \cdot \int e(t)dt)$ takes into account the cumulative error over time, and the derivative term $(K_d \cdot \frac{\mathrm{d}e(t)}{\mathrm{d}t})$ accounts for the rate of change of the error [11]. This equation represents a general form of the control law and is commonly used in various control systems, including UAV control systems. It provides a framework for designing and tuning control algorithms to achieve desired system behaviour and performance.



Fig. 1 Basic components and architecture of a control system

The input is originally received at [Start], the beginning of the control system. After processing the input, [Plant] uses the control algorithm to identify the error signal. A control signal generated by the output component is delivered to the last control element. By continuously observing the output signal, the feedback component provides information to the processing component. The control system as a whole comes to an end with the [End] (Fig. 1).

The basic components of a control system are as follows:

1. Input: The input to the control system can come from sensors, switches, or other devices that measure the process variable. The input is converted into an electrical signal that can be processed by the control system.
2. Plant: The plant of the control system compares the input signal to a desired set point or reference signal and calculates the difference between the two. This error signal is used to determine the control action that needs to be taken.
3. Output: The output component of the control system generates a control signal that is sent to the final control element, such as a valve or motor. This control signal is designed to bring the process variable back to the desired set point.
4. Feedback: The feedback component of the control system monitors the output signal and provides information to the processing component. This information is used to adjust the control action and ensure that the process variable stays within the desired range.

2.2 Types of Control Systems in Autonomous Platforms

Different types of control systems are used by unmanned aerial vehicles (UAVs) to accomplish accurate and steady flying. The most popular control system categories are shown below:

1. Manual control systems: With these, an operator controls the UAV's motions directly through the use of remote controls. They are often used in UAV applications for leisure or hobbies. Similar to manual control systems, remote control systems allow a pilot on the ground to operate an unmanned aerial vehicle. Aerial photography, surveillance, and inspection jobs all include their utilization.
2. Systems for flight stabilization: These systems utilize sensors to monitor the orientation and velocity of the UAV while making instantaneous modifications to maintain flight stability. They improve resistance to external perturbations, stability, and manoeuvrability [12]. UAVs may independently carry out planned

flying missions or follow predetermined courses with the use of autopilot technologies. For precise navigation, they integrate sensors with cutting-edge control algorithms used for goods transportation, mapping, and aerial surveying [13].
3. Intelligent control systems: These systems make use of cutting-edge methods like artificial intelligence (AI) and machine learning to help UAVs adapt to and learn from their surroundings. They perform real-time decision-making, sensor data analysis, and activities including path planning and obstacle avoidance [14, 15].
4. Cooperative control systems: These systems allow a group of UAVs to work together to accomplish a shared goal. When many UAVs are needed to complete a task, they make coordination, communication, and synchronization easier [15].

It is crucial to remember that various control system varieties are not mutually exclusive, and UAVs can combine a variety of systems depending on the demands of their missions. Hybrid architectures, which mix many control methodologies for improved performance and autonomy, are the result of advancements in control systems. Various types of conventional linear and nonlinear control strategies are given below:

1. The proportional-integral-derivative (PID) control technique is a popular linear control strategy that offers a balanced method for controlling systems. It uses proportional, integral, and derivative components to control, respectively, the error, the integral of error, and the rate of change of error. PID control provides robustness, stability, and simplicity. However, complicated nonlinear systems may be difficult for it to manage, and fine-tuning the controller settings can be difficult.
2. Using feedback of the system's whole state, state feedback control is a linear control approach. Based on the system's current state and a feedback gain matrix, it calculates the control action. Stability analysis and precision control are made possible by state feedback control. However, it depends on precise system models, which could be challenging to find in the real world. It may also be susceptible to changes in parameters and outside disruptions.
3. A specified cost function is the goal of optimal control systems like the linear quadratic regulator (LQR) and model predictive control (MPC), which also strive to meet system restrictions. These methods optimize the control actions across a limited or infinite time horizon while taking into account the dynamics of the system. Optimal control can manage complicated systems and provide superior performance. For real-time applications, it can be computationally taxing and needs proper system modelling.
4. A nonlinear control approach called sliding mode control seeks to move the system's states into a predetermined sliding surface. It does this by generating a discontinuous control action, which offers resilience against uncertainties and disruptions. Smooth performance and quick responsiveness are features of sliding mode control. Though it could display chattering, which is a quick changeover in the control signal that causes high-frequency oscillations and the possibility for actuator damage.

5. In order to respond to changing system dynamics and uncertainties, adaptive control strategies change the controller settings live. Even in the presence of unidentified or temporally fluctuating characteristics, they strive to produce high performance. Robustness may be achieved by adaptive control, which can manage system variances. On the other hand, it necessitates previous knowledge of the system's structure and is susceptible to noise and unmodelled dynamics.
6. Artificial neural networks are used in neural network control to compute the control actions and approximate complicated system dynamics. It allows for the handling of nonlinear systems without the need for exact mathematical models. Flexible and adaptable control is provided by neural networks. The accuracy of the neural network's approximation is dependent on the calibre and amount of training data, albeit training the network may be time-consuming.

The focus of the part that follows will be on current developments in control algorithms that have transformed UAV performance.

3 Advancements in Control Systems for Unmanned Aerial Vehicles

Unmanned aerial vehicles (UAVs) have improved in terms of performance, autonomy, and operational capabilities because to improvements in control systems. The development of control algorithms, enhancements to sensors and actuators, and the integration of control systems with other technologies are the main topics of this area [7, 8, 16]. The development of control algorithms has advanced significantly. UAVs can handle uncertainties and fluctuations in dynamics and environmental circumstances due to adaptive control algorithms, which continually update control parameters based on real-time feedback [8]. This enables performance and stability despite varying flying circumstances or system deterioration [7]. When a component fails, fault-tolerant control algorithms continue to maintain stable flight and control by employing fault detection and diagnostic techniques to dynamically reconfigure the control system [10]. Multiple UAVs can work together and coordinate their activities using cooperative control algorithms to complete complicated tasks that are beyond the scope of a single vehicle's capability [8]. Swarm robots, distributed sensing, and cooperative missions are made possible by these algorithms' facilitation of communication, synchronization, and information exchange [8]. UAVs can make autonomous choices using real-time inputs and mission goals using intelligent decision-making algorithms, which improves their flexibility and optimization skills [7]. UAVs can traverse surroundings that are changing dynamically and avoid obstacles while optimizing their trajectory through the use of real-time path planning algorithms [16]. These algorithms provide collision-free pathways in real time while taking into account mission goals, environmental restrictions, and UAV dynamics [17]. This increases the autonomy and effectiveness of UAVs in tasks

including airborne inspection, surveillance, and search and rescue [18]. The performance, dependability, and safety of UAVs will all increase as a result of these developments in control systems [10]. UAVs can attain increased degrees of autonomy, flexibility, and mission efficiency by adding adaptive control, fault-tolerant control, cooperative control, intelligent decision-making, and real-time path planning [7, 8, 10, 17]. These developments increase the capabilities and potential uses of UAVs, causing their fast adoption and expansion across several sectors [3, 14, 19].

4 Challenges in Control Systems for Autonomous Platforms

Despite the advancements in control systems for unmanned aerial vehicles (UAVs), ensuring the safe and efficient operation of autonomous platforms presents several challenges that need to be addressed. This section highlights key challenges faced by control systems in autonomous UAVs [8, 16], including the importance of addressing potential vulnerabilities and cybersecurity concerns. Accurate and reliable sensing and perception are crucial for autonomous UAVs to perceive their environment and make informed decisions [3, 20]. Developing lightweight, power-efficient sensors capable of providing high-quality data in various weather conditions remains a challenge [3]. Real-time processing of sensor data, particularly in complex environments, requires advanced sensor technologies and perception algorithms [9]. Furthermore, navigation and path planning pose challenges due to uncertain environments, limited information availability, and the need for real-time decision-making [3, 21]. Developing algorithms that handle dynamic obstacles, incorporate real-time sensor inputs, and optimize multiple objectives is a significant challenge, along with ensuring scalability and adaptability [9, 18]. The integration of multiple control systems in autonomous UAVs necessitates coordination while maintaining stability, performance, and safety [8]. Robust communication protocols, efficient data fusion techniques, and effective coordination strategies are needed to manage conflicting requirements, communication delays, and shared resource dependencies [10]. Furthermore, detecting and recovering from system faults or failures in real time is crucial for safe and reliable operation [8]. Robust fault detection and recovery mechanisms are necessary to identify and diagnose faults in complex control systems [10]. Together with these difficulties, it is critical to emphasize the necessity of resolving possible weaknesses in UAV control systems and maintaining cybersecurity. The prevalence of autonomous UAVs raises the possibility of cybersecurity risks. The integrity and dependability of autonomous platforms must be guaranteed by protecting control systems against unauthorized access, data breaches, and malicious assaults. For UAVs to operate safely, it is crucial to have strong cybersecurity safeguards and secure communication protocols. Ethical and legal considerations surrounding control and decision-making capabilities also arise as autonomous UAVs become more widespread [22]. Accountability, liability, privacy, and compliance with regulations need to be addressed to ensure responsible deployment [22].

Effective human–machine interaction is crucial when autonomous UAVs collaborate with human operators or operate near humans [22]. Designing user-friendly interfaces, implementing transparent decision-making algorithms, and integrating human-in-the-loop control systems enhance usability, trust, and safety [22]. Overcoming these challenges, including addressing potential vulnerabilities in control systems and ensuring cybersecurity, requires continuous research, collaboration, and advancements in sensing, perception, navigation, fault-tolerant control, and human–machine interaction [3, 8, 16, 20]. Successfully addressing these challenges will contribute to the safe, efficient, and widespread adoption of UAV technology across various domains [3].

5 Applications of Control Systems in Unmanned Aerial Vehicles

Unmanned aerial vehicles (UAVs) equipped with advanced control systems have found applications in various sectors, driven by their functionality and effectiveness. Here are some key applications where control systems play a crucial role in enabling UAV functionality: Aerial photography and Videography: UAVs with stabilized camera gimbals and advanced control systems capture high-quality aerial imagery and videos for cinematography, real estate photography, landscape mapping, and surveillance [3]. Agricultural monitoring: Control systems revolutionize agriculture by enabling UAVs to gather data on crop health, soil moisture levels, and vegetation indices. This data helps optimize irrigation, fertilization, and pest control, leading to improved crop yields and resource allocation [2, 6]. Infrastructure inspection: UAVs equipped with specialized sensors and control systems monitor the condition of structures such as bridges, power lines, pipelines, and buildings. They provide detailed inspections, reducing the need for manual inspections and improving safety and cost-effectiveness [1, 23]. Search and rescue operations: Control systems in UAVs aid search and rescue operations by enabling autonomous flight, intelligent search patterns, and real-time visual and thermal data. UAVs cover large areas quickly and assist in locating missing persons or assessing disaster-affected areas [15]. Environmental monitoring: UAVs equipped with control systems collect data on air and water quality and wildlife populations in remote or inaccessible areas. They autonomously fly predefined routes, collect data, and transmit it in real-time for analysis, supporting conservation efforts and resource management [20, 21]. Disaster management: UAVs with control systems assist in aerial reconnaissance, damage assessment, and situational awareness during natural disasters. Their precise flight control enables them to navigate challenging environments and capture critical data for emergency response teams [15]. These applications represent only a fraction of the potential uses for UAVs with advanced control systems. Further integration in sectors like delivery services,

infrastructure maintenance, environmental research, and urban planning is anticipated [24]. UAVs, combined with robust control systems, have the potential to revolutionize industries, enhance efficiency, safety, and decision-making processes [2, 23]. However, further research and development are necessary to overcome challenges and maximize the potential of control systems in UAVs [7, 14, 25].

6 Conclusion and Summary of Findings

6.1 Key Findings and Implications

Through this comprehensive exploration of control systems in unmanned aerial vehicles (UAVs), several key findings and implications have emerged. Firstly, control systems are essential components that enable the precise and stable flight of UAVs. They provide the necessary mechanisms for controlling the vehicle's attitude, altitude, speed, and navigation, ensuring safe and efficient operation. The types of control systems discussed, including manual control, remote control, and autonomous control, offer different levels of human involvement and automation, catering to diverse operational requirements. Secondly, advancements in control systems for UAVs have contributed to significant improvements in their capabilities and performance. The development of sophisticated control algorithms, such as PID, adaptive control, and model predictive control, has enhanced the autonomy, manoeuvrability, and stability of UAVs. These advancements have paved the way for a wide range of applications, including aerial photography, agricultural monitoring, infrastructure inspection, search and rescue operations, environmental monitoring, and disaster management. Moreover, the challenges associated with control systems for autonomous platforms have been identified. These challenges include ensuring robustness against external disturbances, addressing system complexity, optimizing control algorithms for efficient resource utilization, and enhancing fault tolerance and redundancy. Overcoming these challenges is crucial to unlocking the full potential of UAVs and maximizing their performance and reliability.

6.2 Limitations and Future Directions for Research

While control systems have significantly contributed to the advancement of UAV technology, there are certain limitations and avenues for future research. One limitation lies in the scalability and adaptability of control systems for UAVs. As the complexity and scale of UAV operations increase, there is a need for control systems that can effectively handle large fleets of UAVs operating in coordinated and collaborative missions. Additionally, the integration of UAVs into the existing airspace infrastructure and regulations presents challenges that require further research and

development. Another area for future research is the exploration of control systems for unconventional UAV designs, such as swarms, hybrid aerial-ground vehicles, and vertical takeoff and landing (VTOL) UAVs. These innovative designs present unique control challenges that necessitate novel control algorithms and system architectures. Furthermore, the development of control systems that can adapt to dynamic and uncertain environments is essential. The ability to handle changing weather conditions, unexpected obstacles, and unpredictable events is crucial for safe and reliable UAV operations. Research into adaptive control, machine learning, and sensor fusion techniques can contribute to the robustness and adaptability of control systems in UAVs. In conclusion, control systems play a vital role in enabling the functionality, manoeuvrability, and autonomy of unmanned aerial vehicles. Advancements in control algorithms and system architectures have expanded the applications and capabilities of UAVs across various sectors. However, challenges related to system robustness, complexity, and scalability persist. Future research should focus on addressing these challenges and exploring innovative control approaches to enhance the performance, safety, and efficiency of UAVs in both existing and emerging applications.

7 Future Trends and Directions in Control Systems for Unmanned Aerial Vehicles

The future of control systems for unmanned aerial vehicles (UAVs) is influenced by several trends and directions, driven by the need for increased autonomy, improved performance, safety, and expanded applications. Here are the key trends: Swarm intelligence: Utilizing swarm systems with multiple coordinated UAVs performing tasks collectively. Research should focus on developing control systems for efficient swarm coordination, task allocation, and adaptive behaviour. Edge computing and distributed control: Moving computational tasks closer to UAVs through edge computing to reduce latency, improve real-time decision-making, and enhance control system resilience. Distributed control architectures distribute control functions across multiple UAVs for fault tolerance and collaborative decision-making.

Machine learning and reinforcement learning: Applying machine learning techniques, including deep learning and reinforcement learning, to enhance UAV control systems. These techniques enable UAVs to learn from data, adapt to changing environments, and improve decision-making capabilities. Human–machine interaction: Designing intuitive user interfaces and tools for effective interaction between human operators and autonomous UAVs. Consideration should be given to supervisory control, interpretable explanations of UAV behaviour, and decision-making processes. Security and privacy: Developing secure communication protocols, encryption techniques, and anomaly detection mechanisms to protect control systems from unauthorized access and cyber-attacks. Privacy-enhancing technologies should also be considered to safeguard collected and transmitted data. Addressing these

future directions will enhance the autonomy, performance, safety, and usability of UAVs, enabling effective operation in complex and dynamic environments. By embracing these trends, researchers and practitioners can unlock new possibilities for UAV applications and contribute to the advancement of this rapidly evolving field.

Funding Not applicable.

References

1. Outay F, Mengash HA, Adnan M (2020) Applications of unmanned aerial vehicle (UAV) in road safety, traffic and highway infrastructure management: recent advances and challenges. Transp Res Part A Policy Pract 141:116–129
2. Kim J et al (2019) Unmanned aerial vehicles in agriculture: a review of perspective of platform, control, and applications. Ieee Access 7:105100–105115
3. Elmokadem T, Savkin AV (2021) Towards fully autonomous UAVs: a survey. Sensors 21:6223. https://doi.org/10.3390/s21186223
4. Zhang Y, Liu J, Li Y (2013) Integrating artificial intelligence and control systems for autonomous platforms: a review. IEEE Trans Industr Inf 19(6):3048–3058
5. Sun Y, Wang X (2014) A survey of decentralized control algorithms for autonomous systems. J Syst Eng Electron 25(1):65–76
6. Tsouros D, Bibi S, Sarigiannidis PG (2019) A review on UAV-based applications for precision agriculture. https://doi.org/10.3390/info10110349
7. Sutton RS, Barto AG (2018) Reinforcement learning: an introduction. MIT Press, Cambridge, MA, USA
8. Ge SS (2013) A survey of advanced control algorithms for autonomous systems. J Control Sci Eng 2013
9. Bagnell JA, How JP (2015) Real-time motion planning for autonomous vehicles using compressed Gaussian processes. In: Proceedings of the IEEE international conference on robotics and automation (ICRA), pp 1321–1328
10. Hedrick DB, Sneum AWM (2019) Robust autonomous vehicle motion planning and control. In: Robust autonomous vehicle motion planning and control. Springer, pp 1–23
11. Ogata K (2010) Modern control engineering. Pearson Education
12. Baballe MA et al (2022) The unmanned aerial vehicle (UAV): its impact and challenges. J Homepage: https://gjrpublication.com/gjrecs 2.03
13. Singhal G, Bansod B, Mathew L (2018) Unmanned aerial vehicle classification, applications and challenges: a review
14. Arafat MY, Alam MM, Moh S (2023) Vision-based navigation techniques for unmanned aerial vehicles: Review and challenges. Drones 7(2):89
15. Partheepan S, Sanati F, Hassan J (2023) Autonomous unmanned aerial vehicles in bushfire management: challenges and opportunities. Drones 7(1):47
16. Collins TJJ, Verrelli A, Tomlin CJ (2018) Advanced sensors and actuators for autonomous vehicles. Proc IEEE 106(12):2191–2213
17. Konolige K (2008) Small robots: autonomous navigation and mapping. In: Proceedings of the IEEE/RSJ international conference on intelligent robots and systems, pp 1174–1179
18. Paden B (2016) A survey of motion planning and control techniques for self-driving urban vehicles. In: Proceedings of the IEEE international conference on robotics and automation, pp 3388–3393
19. Liu Y et al (2020) Unmanned aerial vehicle for internet of everything: opportunities and challenges. Comput Commun 155:66–83

20. Hardin PJ, Jensen RR (2011) Small-scale unmanned aerial vehicles in environmental remote sensing: challenges and opportunities. GIScience Rem Sens 48(1):99–111
21. Yuan C, Zhang Y, Liu Z (2015) A survey on technologies for automatic forest fire monitoring, detection, and fighting using unmanned aerial vehicles and remote sensing techniques. Can J For Res 45(7):783–792
22. Nisser T, Westin C (2006) Human factors challenges in unmanned aerial vehicles (uavs): a literature review. School of Aviation of the Lund University, Ljungbyhed
23. Kumar V, Michael N (2012) Opportunities and challenges with autonomous micro aerial vehicles. Int J Robot Res 31(11):1279–1291
24. Shrestha R, Oh I, Kim S (2021) A survey on operation concept, advancements, and challenging issues of urban air traffic management. Front Fut Transp 2:1
25. Budiyono A (2008) Advances in unmanned aerial vehicles technologies. In: International symposium on intelligent unmanned system, ISIUS2008, Nanjing, China

A Tri-Ducted Fan Tilting VTOL UAV: Conceptual Design and Aerodynamic Analysis



Divij Arora, Sanjivani Nikam, Riptapan Singh, Rahul Kumar, Amit Kumar Thakur, Lovi Raj Gupta, and C. M. Bilji

Abstract Tilt rotor unmanned aerial vehicles (TRUAVs) are a novel technology that is gaining popularity in the modern world for a variety of applications, including surveillance, target tracking, search and rescue operations, and civil engineering. The overall dimensions, estimated weight, performance, power needs, and UAV endurance of the aircraft were all computed and assessed based on the conceptual design. An appropriate propulsion system was chosen using these computed parameters. The UAV was given a 3D CAD model. It is designed in a way that it can land on water. The selection of the airfoil for this UAV is one of the most difficult parts which requires many numerical calculations such as trial and error, wing analysis at various angles of attack, and lift estimation and finally configured with NACA6420. In this paper, we discussed the aerodynamic analysis of the UAV under various conditions and obtained the results in reference to various aerodynamic parameters, velocity, and pressure calculations attained. We assessed the obtained results with the ideal conceptual results and reperformed the analysis and optimized the results. The whole data along with graphs are presented in this paper. The contour plots were shown to analyze the pressure distribution among the UAV, and also, the velocity streamlines are also presented to observe the airflow around the UAV. To conclude, this report discusses the potential applications of this particular hybrid UAV and wholesomely presents the conceptual approach, design, and simulation of a tri-ducted tilting rotor UAV.

Keywords VTOL · Unmanned Aerial Vehicle · Fixed-wing VTOL · Tilt rotor · CFD

D. Arora · S. Nikam · R. Singh · R. Kumar (✉) · A. K. Thakur · L. R. Gupta · C. M. Bilji
Lovely Professional University, Phagwara, Punjab 144001, India
e-mail: rahul.aero001@gmail.com

L. R. Gupta
e-mail: lovi.raj@lpu.co.in

© The Author(s), under exclusive license to Springer Nature Singapore Pte Ltd. 2024

S. Singh et al. (eds.), *Recent Advances in Aerospace Engineering*, Lecture Notes in Mechanical Engineering, https://doi.org/10.1007/978-981-97-1306-6_10

1 Introduction

Since the Wright Brothers' successful completion of their very initial motorized flight tests in 1903, airplane expertise quickly advanced. Numerous airplanes of several configurations have come up during this period with usual and unusual concepts to meet a variety of conditions. Rotorcraft and fixed-wing airborne instruments have long since played crucial roles in the development of aviation as models of conventional aircraft. Fixed-wing aircraft has wings and is pushed forward by turbine jet engines or propellers. They are often used for both military and commercial applications since they have a greater range and produce a smaller amount sound, while unable to hover in one spot since the take-off environment affects their normal flight. Rotorcraft aerial vehicles, helicopters that have propellers with swashplates that move in the upward direction, can hover in one position, but cruising speed and range are reduced.

Researchers from all over the world have concentrated on airplane having both high-speed cruise and vertical take-off and landing (VTOL) capability to combine the benefits of both vehicles. Tilt rotor aerial vehicles are the result of this. It has received a lot of interest since this kind of aerial vehicle satisfies commercial requirements in addition to having cutting-edge technical features. Aerial vehicles that use both wings and rotors to generate lift are known as hybrid aircraft.

The ability of TRUAV to levitate in place similar to helicopters while traveling at far greater speeds than conventional helicopters with aviation mode is its most alluring characteristic. In conclusion, one of the best concepts for combining the advantages of fixed wings with helicopter like abilities in a range of relevance is a tiltrotor aircraft [1]. Since this concept was proposed, numerous others have emerged via various developmental endeavors during the previous century. Aside from a few hybrid aircraft designs that have been successfully placed into operation, most TRUAV development attempts have been abandoned due to financial and technological constraints, putting such breakthroughs on hold for a period. A considerable swell in significance in such UAV has, however, been observed over the past ten years on account of important scientific advances which lowered the cost of making novel concepts employing TRUAV. However, the development of vehicle is very initial stages and less in a number of areas, including design, guiding, navigation, robustness, philosophy, control, and dynamics modeling [2] (Fig. 1).

The VTOL UAV offers a broad variety of applications in the aviation sector because of its exceptional capabilities. As a consequence of a rise in VTOL UAV commercial and civilian usage, predicted to grow substantially by the next decade. Selecting a design concept for TRUAVs is crucial since it affects the whole concept. To meet design goals, the designer needs have access to the ideal TRUAV setup. To achieve this, the configuration of the concept is chosen following process outlined in References [3–7] to select of conceptual TRUAV configuration. This method employs structured design techniques to ensure best configuration is chosen that fits the design objectives. Utilization of such strategy demands the gathering of data reflecting importance of concept criterion. A bit about the modeling technique has

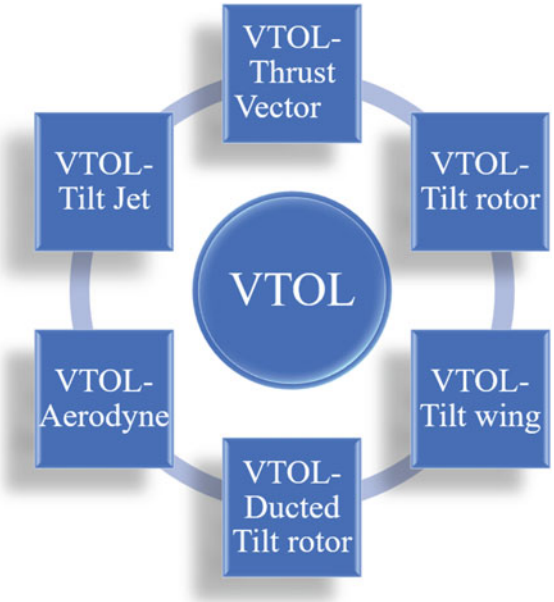


Fig. 1 Various types of TRUAV

been explained, the foundational idea for this review article, and it is time to examine how a unique conceptual approach was developed and theoretically computed to create a hybrid UAV. Within the constraints and presumptions of the research gap, the goal our project [8] is to point out the aforementioned problems, offer an answer, and offer a concept strategy for TRUAV that is following the steps. Establishing a parameters ceiling during plane is transitioning. The slightest tilting angle adjustment required for the motor to tilt, allowing the TRUAV to cruise. To allow helicopter parameters size of the TRUAV motor, rotorcraft system equations should be improved. Create concept approach which may be used as preliminary concept by merging both air1 vehicles and then combine performance criteria for the transition and the constraints.

The relationship between above-mentioned factors will be included in the recommended model chart, with the wing loading functioning as the left straight axis, rotor disc loading functioning as the right straight axis and power loading serving as the horizontal axis, respectively. The three essential phases (fixed-wing, helicopter, and transition) are taken into account when using the recommended three-step technique to measure wing area, rotor, and its disc area according to required parameters restrictions in all phases. The recommended approach is made for aircraft with a single engine that may be utilized for both fixed-wing and rotary-wing flying. Because of the challenges, the transition from the cruise to the climb or descent phase is highlighted while running flying conditions are eased in vice versa.

2 Materials and Methods

It is envisaged that one might generate a collection of twists reflecting the key execution limitations for all such forms of TRUAV using the provided procedure. Variations of the fundamental mathematical formulae used in the unconventional construct of both air vehicles are utilized to construct a mathematical approach. These calculations are then utilized to locate a point where such kinds of air vehicle forms converge, seeking toward TRUAV's optimal circumstances. Theoretical proposal for UAVs, to pick design of UAV and also reduce varied complication associated with transforming approaches, suggested configurations, have been offered and contrasted with one another. Such segment is according to findings from the already available information in order to choose the optimum design. The arrangement that was adopted, as illustrated in Fig. 2, consists of one primary surface and three ducted motor tilt arrangement and normal fixed wing with v-tail with two motors at wing tips while other motor on the V tail.

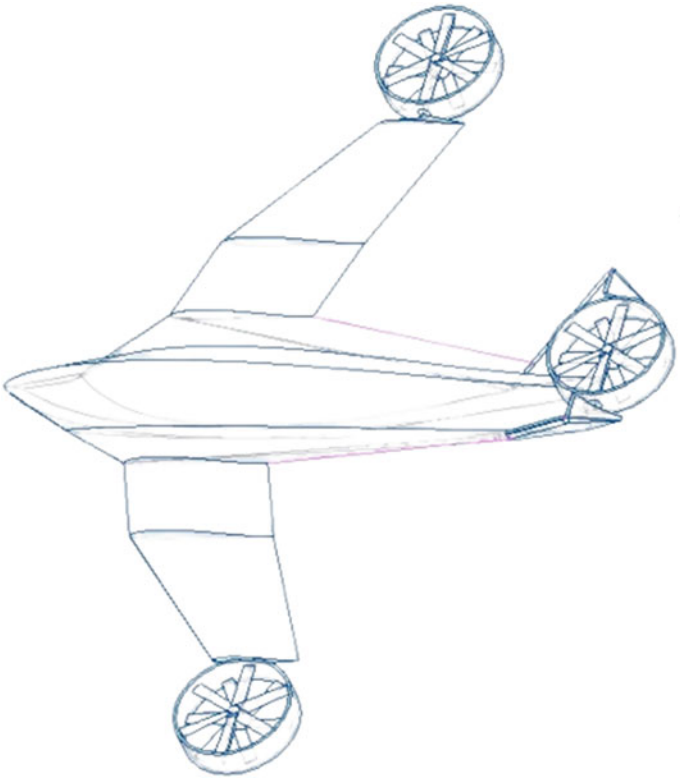


Fig. 2 Developed model—ducted tri-rotor tilt UAV

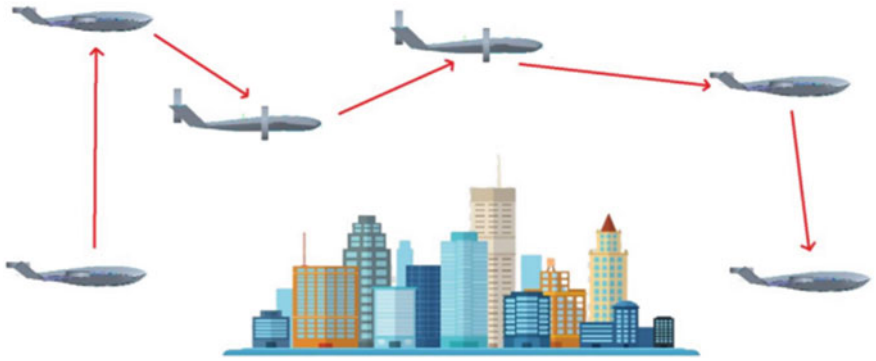


Fig. 3 Planed flight path for UAV

The design of a VTOL UAV, from the required criteria over theoretical design to building an experimental prototype for concept testing and over the steps in the analysis done on the conceptual hybrid UAV, from airfoil analysis to the final UAV analysis. The list of responsibilities the TRUAV or any other air vehicle capable of completing is throughout its entire flight known as the flight profile. During a typical operation, we took into account six stages, albeit they can be changed based on the needs of the task. In our situation, the task at hand is a cruise-type mission, designed for surveillance in a designated area while accounting for a stall speed of 9.2 m/s. The planned flying profile is shown in Fig. 3.

- The UAV ought to do an upright lift-off during the first stage and then ascend to a height of 50 m,
- Switch to airplane mode at this point,
- Then begin the cruising stage,
- After completing this phase, the vehicle should slow down in order to switch to vertical mode and
- Begin the descending phase,
- Which will ultimately accomplish the task by landing vertically.

The choice of the airfoil is the initial stage of wing design. There are two key factors that influence the choice of a profile, which are determined by the sort of mission the aircraft will have to carry out. The lift force is stabilized by the dynamic pressure ($q = 1/2V^2{}_\infty$) and the wing surface, resulting in the coefficient of lift (C_l), which is the first of these. For a certain profile, the C_l rises with the angle of attack (α). The coefficient of drag (C_d), which varies with angle of attack, is described as the drag force regularized by the dynamic pressure and the wing surface. Note that these coefficients are dimensionless and have the following mathematical definitions.

$$C_l = 2L / \rho V_\infty^2 S_w \tag{1}$$

$$C_d = 2D / \rho V_\infty^2 S_w \tag{2}$$

The tilt rotor UAV usually operates at low speeds and also small Reynolds numbers (Re). But our conceptual model is expected to operate at max speed of 35 m/s and stall speed at 10 m/s. The range of Reynolds numbers UAV will operate is between 2 × 105 and 9.93 × 105. These Reynolds number values are obtained by using the formula.

$$\mathrm{Re} = v\,1 / \nu \tag{3}$$

3 Results

3.1 Airfoil Selection and Analysis

The hybrid UAV is designed with three rotors v-tail configuration and with a high coefficient of lift. Representing that intention, five airfoils are considered and analyzed in XFLR5. The airfoils used in this study are NACA3315, NACA3618, NACA4415, NACA6420, and NACA6620.

These airfoils are analyzed in XFLR5 at Reynolds number 10 × 105, Mach number 0, and Ncrit 9. Analysis is done in sequence from α −200 to 200 at $\Delta = 1$. Two graphs from Fig. 4a, b are plotted to compare airfoils, C_l/C_d versus α and C_l versus α. The maximum relative thickness (e max) is one of the most crucial factors for the designed aircraft since the wing needs adequate room to house the servomotors for tilting.

From the above analysis, airfoil NACA6420 is chosen due to its high lift coefficient and its thickness which will be important to house servos for tilting mechanism at

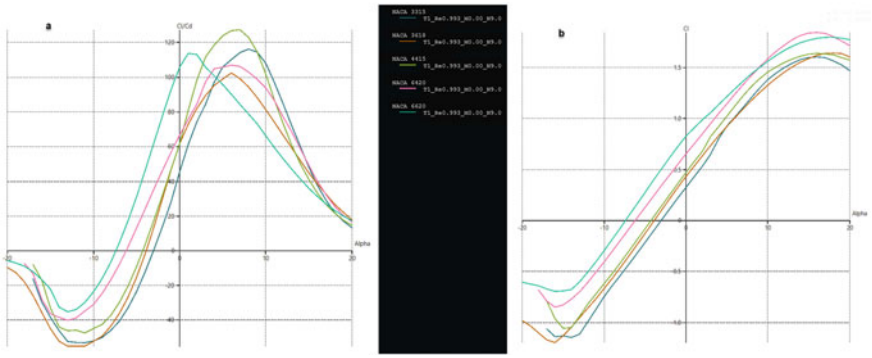


Fig. 4 **a** C_l/C_d versus α and **b** C_l versus α graph for various airfoils

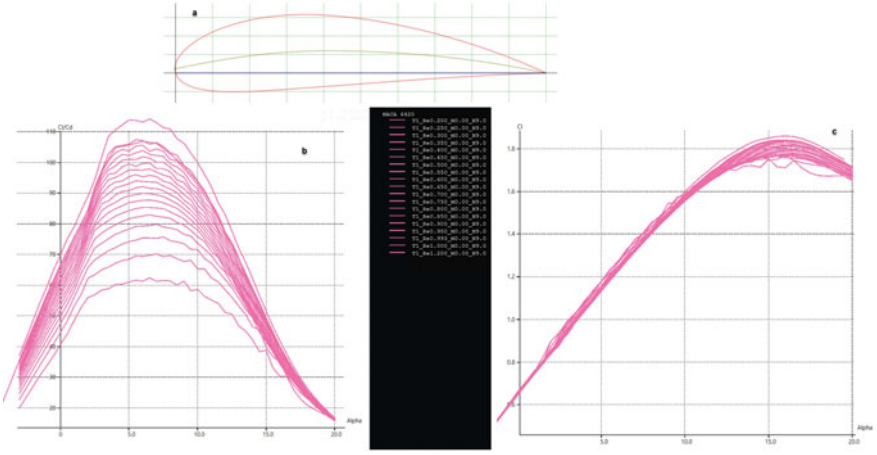


Fig. 5 **a** NACA6420 airfoil, **b** C_l/C_d versus α, **c** C_l versus α graph for various airfoil

Table 1 Design parameters of NACA6420 airfoil

Parameter	Value
Maximum camber %	6
Maximum camber position %	40
Thickness %	20

the wing tips shown in Fig. 5a and Table 1 of various parameters given below. Being a perfect balance between having good amount of thickness and high lift coefficient, NACA6420 airfoil is further analyzed in the range Reynolds numbers between 2 × 105 and 12 × 105. Two graphs from Fig. 5b, c are plotted to observe its performance in variety of Reynolds values, C_l/C_d versus α and C_l versus α.

3.2 Wing Design and Analysis

Since the airfoil is working fine in the given range of Reynolds numbers, it is further used to make a wing model in XFLR5 to analyze and calculate the coefficient of drag, lift to drag coefficient, and coefficient of lift. But first, wing model is generated in "wing and plane design" in XFLR5 the generated in shown in Fig. 6. The Tiltrotor VTOL UAV can take off conventionally as well as vertically. In order to prevent stalling in transitional modes, the VTOL UAV has been equipped with rather wide mid-wing, a more energy-efficient endurance limit, and a v-tail in place of an elevator or fins.

Now wing model is analyzed in above Reynolds number range from varying angle of attack from 00 to 100. The given analysis definition is at $v = 30$ m/s "Type-1:

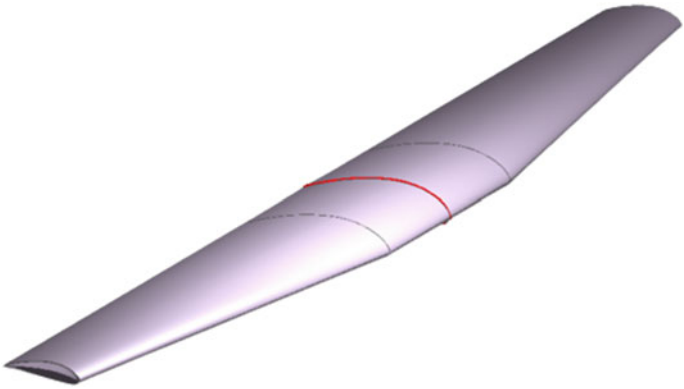


Fig. 6 Wing generated in XFLR5 to the given parameters

Fixed speed", analysis method is "Ring Vortex (VLM2)", with inertia properties plane mass = 25 kg X_CoG = 0.56 m & Z_CoG = 0 m, reference dimensions for aero coefficients are "Wing Platform projected on xy plane", at IST, i.e., $\rho = 1.225$ kg/m^3 and $\nu = 1.5\text{e}{-}05\text{m}^2/\text{s}$, and no additional drag is considered. This analysis is to determine the optimal angle of attack for the wing, and from the results presented in Fig. 7, 20 angle of attack is chosen for the current UAV. The results from the calculations are as follows $C_l = 0.396$, $C_d = 0.013$, efficiency = 1.004, $C_l/C_d = 30.603$, and $C_m = 62.713$.

The XFLR5 programme was used to do the initial calculation of the wing's $C_{l\max}$ since it is commonly utilized for initial design because it takes little time to complete, allowing for the evaluation of various airfoil ideas but lowering the accuracy of the results. To ensure more accuracy in the calculations done, the data collected with XFLR5 was verified using the more powerful CFD programme Ansys Fluent®. The purpose of this study is to propose graph between C_l versus α, to see how the boundary layer separates with various positions. A meshing approach was provided for the discretization of the issue as suitable in the areas of concern while making sure to not spend too much computing expense in order to produce accurate results. The SST (omega-k) model, which will be a reliable model suited for modeling turbulent flow, was employed to address the problem. The main drawback of this model is that it uses a lot of computer resources. The NACA6420 airfoil was calculated using a mesh of 283,444 elements, and the results show that the optimal angle of attack for this airfoil is 20, which has once again been confirmed. This resulted in Fig. 8. The pressure contours that correspond to the XFLR5 findings and their validation by Ansys Fluent are shown in this picture. The finalized angle of attack is 20 based on the direct comparison for each angle of attack.

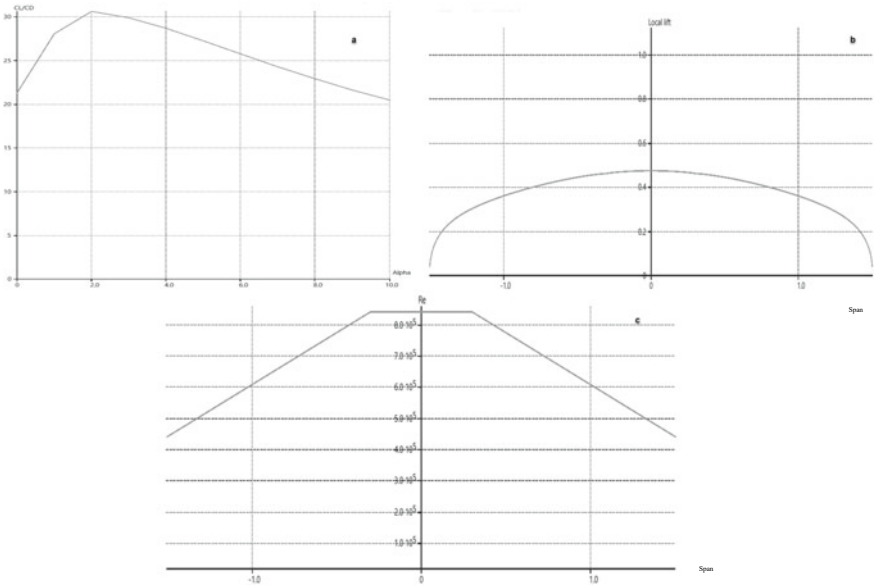


Fig. 7 **a** C_l /C_d versus alpha graph for the wing at 30 m/s, **b** Re on Y span and local lift on Y span, and **c** Local lift versus span

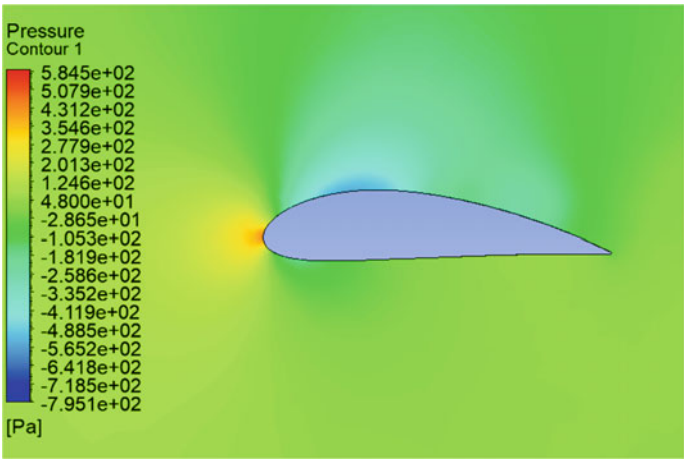


Fig. 8 Pressure contour for NACA6420 at $\alpha = 20$

4 Discussion

4.1 UAV Concept and Design

In order to carry out surveillance missions, we chose to adopt a conventional aeroplane configuration. The maximum speed of the vehicle is 35 m/s. When the wing is viewed as the primary element of the UAV that balances out the weight with enough lift, UAV is able to fly steadily. We chose a straight wing for the development of this aircraft since it is simple to manufacture and performs well at such speeds. The vertical stabilizer stabilizes the aeroplane in the yaw movement, whereas the horizontal stabilizer stabilizes the aircraft longitudinally. Since the v-tail arrangement only has two surfaces for control and stability, it has little drag than usual standard arrangement, and we chose to adopt it for the hybrid UAV under consideration.

A hybrid system known as a "ducted fan" is distinguished by enclosing the rotor blades inside a duct. By increasing the downstream flow area of this propulsion system, lift is increased while energy consumption is decreased as compared to typical rotors. Additionally, a ducted fan may reduce motor sound production while also shielding propellers. With this, we were able to create the concept aircraft depicted in Figs. 9 and 10, which was sketched using CREO PARAMETRIC software. This concept aircraft was the culmination of multiple repetitions with the initial concept and continued to final design. This idea is built according to normal aeroplane, which has mid-wing and a v-tail, and two ducted fans at the tip of the wing for vertical mode. A tilting coaxial motor located at the back of the aircraft works in conjunction with the two rotors to produce a construction recognized as a Y-4 is also a subtype of a quadcopter with four upward-directing rotors.

What is evident from the intended UAV's configuration in take-off mode is that the three rotors, which are entirely focused on supporting vertical flight, support

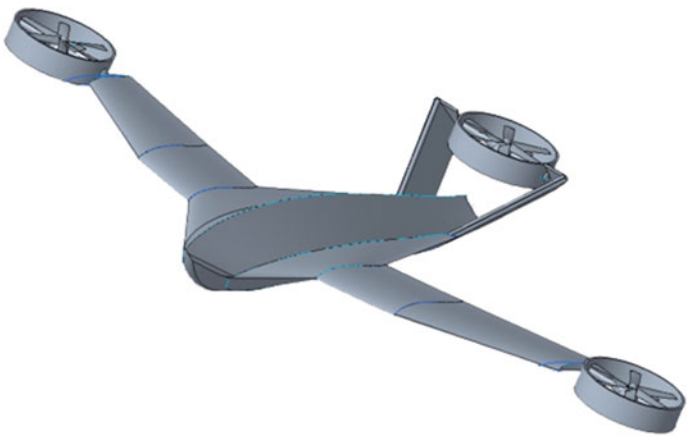


Fig. 9 Initial concept model—ducted tri-rotor tilt UAV

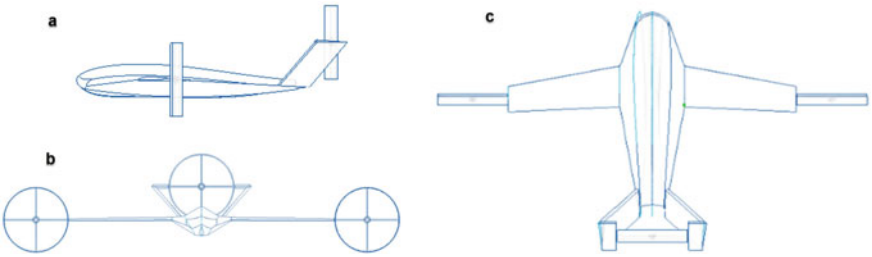


Fig. 10 Final design of the UAV a. side view, b. front view, and c. top view

the majority of the aircraft's weight. Similarly, these three motors must support the load in the take-off approach and also perform the change to the aeroplane form, the primary function of current UAV. This is done by rotating three motors by about ninety degrees, after this UAV can increase speed and reach the stall speed, as well as changing the mode to the aeroplane form. After that UAV is powered by motors.

5 Aircraft Aerodynamic Analysis/Simulation

For any aircraft to be operated as a working model, there is a series of steps to be followed from conceptual design to the working prototype. One of the major steps among those is the aerodynamic analysis which is performed in some popular simulation software like Ansys and OpenFOAM to deduce the major aerodynamic entities like lift, drag, pressure distribution, and fluid flow around the object by giving the suitable boundary conditions to observe the behavior. A number of iterations are performed to find the optimized conditions and to study the capabilities of the aircraft under critical conditions. There are many categories underlined in these analyses such as structural, mechanical, transient, fluent, and thermal. In this particular paper, we majorly concentrate on fluent which is used to primarily focus on fluid dynamics around the aircraft. Typically, aerodynamic and structural factors are combined in the design of UAVs. A UAV's ability to maneuver through the air, maintain stability, and deliver peak performance is determined by its aerodynamic design. Therefore, aerodynamic analysis or simulation aids in design optimization and design refinement for the UAV. The aerodynamic study uses computer models to forecast how the UAV will behave under various flying circumstances. It enables designers to assess the effects of various design decisions on the UAV's overall performance. Designers may optimize the performance of the UAV by fine-tuning the design by considering the drag, lift, and other aerodynamic expressions operating over device. UAV may be tested in a variety of settings, including varied wind conditions, altitudes, and temperatures, using aerodynamic modeling software, giving a more accurate picture of the actual flying circumstances. These simulations give vital insight into the UAV's

behavior and enable designers to tweak various design elements for improved performance. The next phase is to construct a prototype once the design has been improved using aerodynamic study or modeling. The findings of the real-world testing of the prototype are then compared to those obtained from the simulation. The prototype is deemed a success, and production can start if it performs as the simulation anticipated. The robust CFD software program Fluent has frequently benefited to simulation or aerodynamic analysis of CAD UAV designs. It is frequently used in the aerospace sector to assess UAV performance and improve design. Designers may easily build up and execute simulations using Fluent's user-friendly interface. It can properly forecast the airflow around the UAV and its aerodynamic forces by supporting a broad range of analytical techniques, such as potential flow, Euler, and Navier Stokes solvers. Additionally, Fluent supports a number of models of turbulence. These models can offer in-depth perceptions of the intricate flow patterns and turbulence surrounding the UAV, allowing designers to enhance the UAV's performance. Fluent offers sophisticated visualization features in addition to its robust analysis capabilities, allowing designers to see the flow patterns and aerodynamic forces affecting the UAV. These technologies can give designers insightful information on the UAV's behavior and assist them in pinpointing areas where they can make improvements. The aerodynamics of big and intricate UAV designs may be examined using Fluent, which is also very scalable. It is a flexible tool for aerospace engineers since it can be used on a variety of hardware platforms, such as workstations, clusters, and high-performance computing (HPC) systems. The geometrical setup is to import the 3D CAD model into the aerodynamic analysis or simulation software. In this, we perform dimensions check and geometry accuracy. Then we start to make the geometry ready for the aerodynamic analysis. In our case, we created an enclosure for the model with 0.5 m on each side. This enclosure acts as the environment for the model during simulation under conditions. And we have defined the inlet, outlet, and wall for the enclosure.

The boundary conditions, which specify the flow conditions at the limits of the computational domain, are a crucial component of the watertight geometry procedure. To guarantee that the simulation results are correct, the boundary conditions must be defined precisely. In this case, the boundary conditions concerned only four conditions:

- Velocity inlet: The fluid's flow rate and/or velocity when it enters the computational area are specified by the inlet boundary conditions. The inlet boundary conditions may need to be time-varying depending on the application. We have given the velocity of 30 m/sec for our model.
- Pressure outlet: At the borders where the fluid exits the computational domain, the outlet boundary conditions define the pressure and/or flow rate. Pressure boundary conditions may occasionally be replaced with outflow boundary conditions. In this case, the outlet gauge pressure is kept at 0.
- Wall: The velocity and/or temperature at the walls of the computational domain are specified by the wall boundary conditions. The parameters for the wall boundary

conditions may additionally include heat transfer coefficients. For our model, we kept the default conditions and left the temperature at 300 k.

- Symmetry: In situations when the flow is symmetric about a plane, symmetry boundary conditions are employed. According to the symmetry boundary requirements, the flow and pressure must be symmetric about the given plane. Symmetric condition is given and verified.

After completing the geometry, mesh, and physics setup, the next step in the watertight geometry process is to use Fluent to solve the fluid flow equations. The fluid flow equations are iterated until a convergent solution is attained in the solving procedure. After getting the solution, we have to study the plots and contours and reiterate the numbers until we come to an optimized solution for our model. In this solution part, we have explored our velocity streamlines, contour plots, and lift and drag plots for the model. When using Fluent to simulate a watertight geometry, the velocity streamline graph is an effective tool for visualizing the fluid flow. The fluid flow is depicted in this graph by a collection of streamlines, or lines, which display the magnitude and direction of the velocity vector at various locations within the flow field, and Fig. 11 shows the streamline of air over a model.

A watertight geometry simulation's pressure distribution within the fluid domain is graphically shown in Fluent as a pressure contour. It is a color map that utilizes a variety of hues to depict the pressure values at various locations within the flow field. The pressure contour is helpful for detecting areas of high and low pressure as well as for visualizing the pressure distribution over the body of the UAV in Fig. 12. Areas of low pressure might signify areas of flow acceleration or suction, whereas areas of high pressure could signify regions of flow separation or stagnation.

The user may see possible problem regions by examining the pressure contour, such as high-pressure zones that can weaken the UAV's body structurally or low-pressure zones that might result in instability or poor aerodynamic performance.

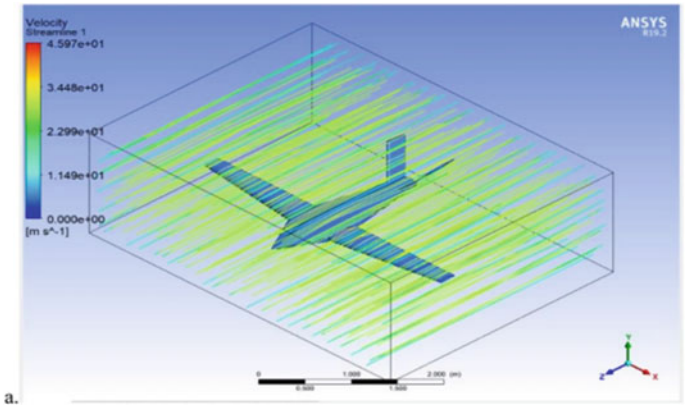


Fig. 11 **a** Streamline of air and **b** Streamline of air—front view

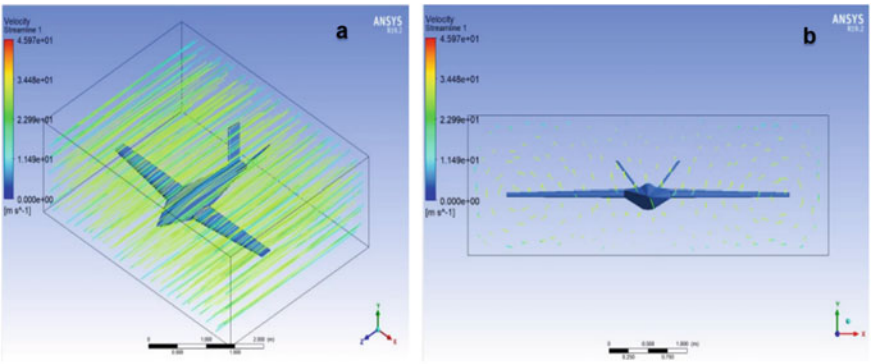


Fig. 12 **a** Pressure contour and **b** Pressure contour with streamlines

The user may determine which UAV design offers the best pressure distribution and overall performance by comparing the performance of several designs or combinations using the pressure contour.

6 Conclusion

To equip ourselves with information required with regards in creating a concept TRUAV, we have looked into historical, current, and speculative ideas. Since the conception of VTOL aircraft was first introduced, several different types of VTOL technology have been developing. The study shows that many problems with the novel idea are handled, additional concepts are improved to get intricate exhibit with a trustworthy method. The following outcomes were seen in Ansys and XFLR5 simulations of the NACA 6420 airfoil with Reynolds number 10×10^5.

- The coefficient of lift to coefficient of drag grows significantly until the alpha is 2° from −2°, after which it begins to decline until the stall angle.
- As alpha reaches angle where UAV stalls, i.e., stall angle, the coefficient of lift (C_l) likewise rises, and strangely, the drag coefficient (C_d) does as well.
- The following findings were seen in Ansys and XFLR5 simulations of NACA6420 airfoil at different Reynolds numbers in between 2 × 105 to 12 × 105.
- The coefficient of lift, C_l, proportionately rises at different Reynolds numbers
- The coefficient of draft, C_d, abruptly declines at higher Reynolds numbers, and abruptly increases at lower Reynolds numbers.
- The following is a summary of the outcomes of the aircraft's CFD simulations:
- On the front of the wing, there are higher pressure coefficients.
- A higher lift coefficient is seen with higher plane speeds.

Funding Not applicable.

References

1. Liu Z, He Y, Yang L, Han J (2017) Control techniques of tilt rotor unmanned aerial vehicle systems: a review. Chin J Aeronaut 30(1):135–148. Chinese Journal of Aeronautics. https://doi.org/10.1016/j.cja.2016.11.001
2. Kamal AM, Ramirez-Serrano A (2020) Conceptual design of a highly-maneuverable transitional vtol uav with new maneuver and control capabilities. In: AIAA Scitech 2020 forum, american institute of aeronautics and astronautics Inc, AIAA. https://doi.org/10.2514/6.2020-1733
3. Sharma S, Sharma R, Kumar V, Chandel S (2021) Analysis of a tiltrotor vertical take-off and landing unmanned aerial vehicle: CFD approach. IOP Conf Ser Mater Sci Eng 1116(1):012096. https://doi.org/10.1088/1757-899x/1116/1/012096
4. Panigrahi S, Krishna YSS, Thondiyath A (2021) Design, analysis, and testing of a hybrid vtol tilt-rotor uav for increased endurance. Sensors 21(18). https://doi.org/10.3390/s21185987
5. Çakici F, Leblebicioğlu MK (2012) Modeling and simulation of a small-sized tiltrotor UAV. J Def Model Simul 9(4):335–345. https://doi.org/10.1177/1548512911414951
6. Lee MK, Lee I (2013) Performance enhancement of tilt-rotor unmanned aerial vehicle using nacelle-fixed auxiliary wing. J Aircr 50(1):319–323. https://doi.org/10.2514/1.C031896
7. Ozdemir U et al (2014) Design of a commercial hybrid VTOL UAV system. J Intell Rob Syst Theor Appl 74(1–2):371–393. https://doi.org/10.1007/s10846-013-9900-0
8. Tarun Gopi T, Sai Shiva TP, Mohan P, Chandu Sai Nath P, Roy R, and Kumar R (2023) A review analysis of tilt rotor unmanned aerial vehicles. Mater Today Proc. https://doi.org/10.1016/j.matpr.2023.02.198

Experimental and Computational Evaluation of Mechanical Properties of Glass Epoxy Composite Laminates at Different Fiber Orientations



K. Bhaskar Reddy, Narender Singh, Rajesh Kumar Saluja, and Neeraj Kumar Gahlot

Abstract In this research, the mechanical properties of composite materials were obtained and evaluated. The combination of numerical methods and experimental techniques were used to analyze these properties. Specifically, the mechanical properties at different fiber orientation were observed and discussed. Composite material has been made with the fiber glass and epoxy resin with different orientations (i.e., 0°/45°/90°, 45°/−45°, and 0°/90°). Tensile and bending tests were performed in accordance with ASTM 3039 and ASTM 7264 standards to determine stress, strain, tensile strength, elastic modulus, and bending strength at composite failure. The study found that changes in orientation of fiber have the vital role on the strength of composite material. The fiber oriented at 0°/90° in composite has higher strength (235 MPa) compared to orientation at 0°/45°/90° (226 MPa) and + 45°/−45° (221 MPa) with 2.99% and 1.28%, respectively. The experimental analysis of the composites mechanical properties has been validated with numerical model and ABACUS model. By comparing the values obtained experimentally those from the numerical model, the authors were able to identify areas for improvement and further development in enhancing the strength of composite materials.

Keywords Composite · Fiber orientation · Mechanical properties · Glass fiber · Epoxy resin

1 Introduction

The composite materials have gained significant popularity across aviation, automotive, and marine industries due to their exceptional mechanical properties. Composites enable improved mechanical properties as well as improved materials and structures [1]. They have much higher strength, stiffness, corrosion, and fatigue resistance

K. Bhaskar Reddy · N. Singh (✉) · R. K. Saluja · N. K. Gahlot
Amity Institute of Aerospace Engineering, Amity University Uttar Pradesh, Noida, India
e-mail: ngoyat@amity.edu

© The Author(s), under exclusive license to Springer Nature Singapore Pte Ltd. 2024

S. Singh et al. (eds.), *Recent Advances in Aerospace Engineering*, Lecture Notes in Mechanical Engineering, https://doi.org/10.1007/978-981-97-1306-6_11

than standard materials, which is vital for developing aircraft components. Composite materials must be constructed such that their mechanical characteristics are adapted to the conditions of their usage or exploitation [2]. The strength of composite materials varies depending on elements such as fiber orientation, volume fraction, and layer sequence, allowing for changing mechanical qualities to suit certain applications [3–5]. The researchers studied the behavior of composites under impact loads due to their unique characteristics and increasing application in today's world. It is generally known that the aircraft sector is at the forefront of deployment of further technologies and materials, and two basic methods are applied in the growth of airframe structures [6]. The first technique, preferred by many scientists, focuses on the enhancement of current designs and materials, while the second strategy suggests the employment of recently discovered composite materials [7]. For aircraft structures, the materials should be long-lasting and sufficiently elastic to resist the expected loads. Furthermore, an accurate evaluation of composite mechanical characteristics is critical to make sure the safe and durable use of airframe structures [8]. The mechanical characteristics, including flexural and tensile strength, of natural and synthetic fiber laminate plates can be enhanced by adjusting the volume fraction and fiber orientation. So, the object of the present work is to obtain the mechanical properties of the newly designed composite laminate by altering the fiber orientation. Glass fiber composite has been selected for carrying out the research work. Because it found application as engine cover due to its ability to withstand adverse conditions and their mechanical properties. In this work, numerical simulation as well as experimental analysis of the behavior of samples under uniform load was carried out, and the most important results are summarized. The mechanical properties were obtained through tensile and flexural tests, respectively, following the standards ASTM 3039 and ASTM 7264. These experimental results were numerically validated using the ABACUS model.

2 Materials and Methods

The test specimens were made of a multi-layered composite (laminate) using glass fiber and resin. S-type glass fiber was utilized as the fiber since it has the best strength, and Ardur HY 951 epoxy was used as the resin. The most popular fiber orientation angles (0°, 45°, and 90°) have also been applied to this research. The hand lay-up approach is used throughout the entire manufacturing process. During this process, silica gel is used as a non-sticking agent while the resin is carefully placed on the sheets. After pouring the resin, the fiber sheet is positioned on top of the resin layer. A light roller is used to remove excess glue and encourage even distribution, which ensures proper adherence and prevents air bubbles. Laminate is constructed using multiple layers of fibers oriented at different angles. Once the proper number of layers has been achieved, additional silica-coated sheets are laid over the laminate. After curing for 48 h at room temperature, the mixed composition is dried. Multiple layers of fibers with varying orientation angles are utilized to create laminate. The samples were made with three distinct fiber orientation angles, 0°/45°/90°, + 45°/−5°, and

Table 1 Mechanical properties of the resin

Property	Value	Unit
Tensile strength	52	MPa
Elongation at break	11	%
Tensile modulus	2800	MPa
Hardness	85	ShoreD
Shear modulus	1230	MPa
Density	1.19	g/cm^3

Table 2 Mechanical properties of the fiber

Property	Value	Unit
Tensile strength	4600	MPa
Modulus	86.8	MPa
Density	2.46	g/cm^3
Elongation	5.4	%
Thickness of layer	0.17	mm
Surface mass	160	g/m^2

Table 3 Evaluated mechanical properties of composite

Property	Value	Unit
Tensile strength (Fc)	229	MPa
Elongation	2.9	%
Young elastic modulus (E1)	9.7	GPa
Young elastic modulus (E2)	9.7	GPa
Poisson coefficient (v)	0.25	–

0°/90°, respectively. Once the desired number of layers is achieved, additional silica-coated sheets are placed on top of the laminate. At the room temperature composite structure is left to cure for a duration of 48 h. Tables 1, 2 and 3 are used to present both the significant characteristics of composite components and the calculated properties of individual lamina.

3 Experimental Investigation

For tensile test and three-point bending test, the experimental techniques were conducted according to the ASTM 3039 and ASTM 7264 standards, respectively. The samples used had dimensions of 270 × 27 × 2.7 mm (Fig. 1) for each orientation [0°/45°/90°], [+45°/−5°], and [0°/90°]. Three samples were tested for each orientation in both the tensile and three-point bending tests. Total nine samples were

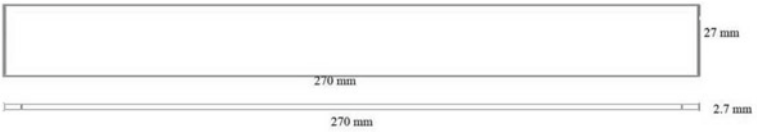


Fig. 1 Test specimen dimensions

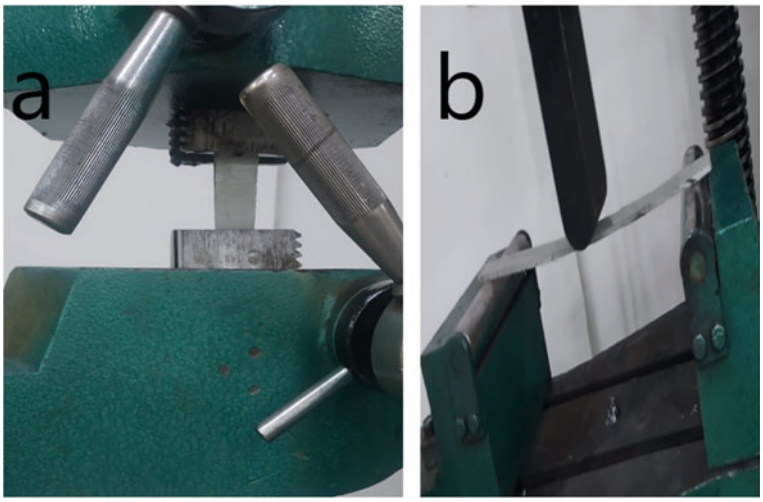


Fig. 2 Universal testing machine **a** Tensile testing, **b** Flexural testing

made for each test and were given the designations a1, a2, a3, b1, b2, b3, and c1, c2, c3.

At room temperature the tests were conducted using a universal tensile machine (Model: AMT20, max capacity:200kN, and accuracy is ± 0.05 mm) shown in Fig. 2. The force and elongation were continually recorded throughout the tests. Three replicates were utilized to determine the laminate' tensile strength, flexural strength, and modulus; the average values were then reported. For samples with fiber orientation angles of [0°/45°/90°], [+45°/−5°], and [0°/90°], mechanical characteristics from three-point bending and tensile tests were compared with numerical models.

4 Results and Discussion

Figures 3, 4 and 5 display the tensile stress–strain graphs of glass epoxy laminate composites fabricated with different fiber orientation sequences. Figure 3 displays the tensile stress–strain diagrams for the laminate with the fiber orientation [0°/45°/90°]. The laminate exhibited an average strength of 221 MPa and a strain of

2.64%. The laminate with fiber orientation [0°/45°/90°] revealed a mixed tendency, which is caused by the hybridization impact of fiber orientation, which causes varied stiffnesses with the thickness of the laminate. The pseudo-tensile behavior arises due to both the reorientation of fibers and the yielding of the matrix, allowing the laminate to accommodate extra nonlinear strains.

Figure 4 shows the tensile stress–strain graphs for a laminate with orientation [+45°/−45°]. The laminate had an in-plane shear stress that was quite high in addition to its advanced aging delamination strain [9] and noted strengths of 226 MPa and strains of 2.74. These occurrences are related to the laminate's pseudo-ductile reaction that prevents the corrosion and local delamination prior to the ultimate failure of the high-strain glass fiber [10, 11].

Figure 5 displays the tensile stress–strain diagrams for the laminate with the fiber orientation [0°/90°]. The laminate reveals a tensile strength of 235 MPa and a strain of 2.85%. With fiber orientation [0°/90°], the laminate displayed a linear elastic

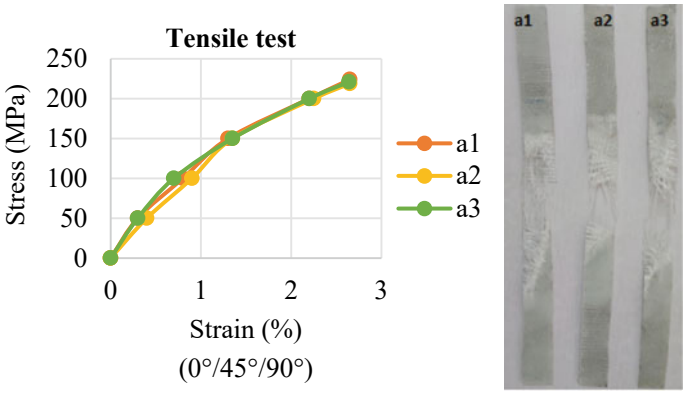


Fig. 3 Stress versus strain curve of tensile test (0°/45°/90°)

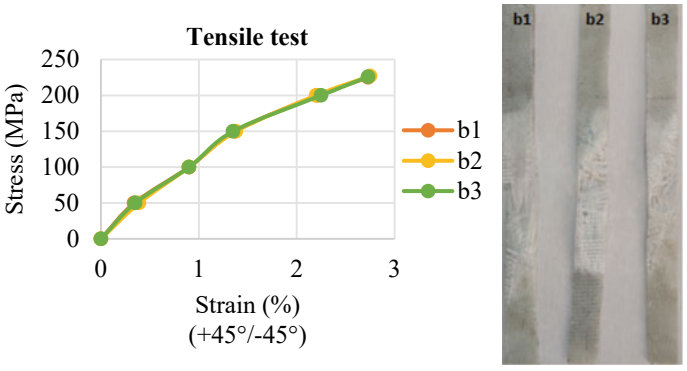


Fig. 4 Stress versus strain curve of tensile test (+45°/−45°)

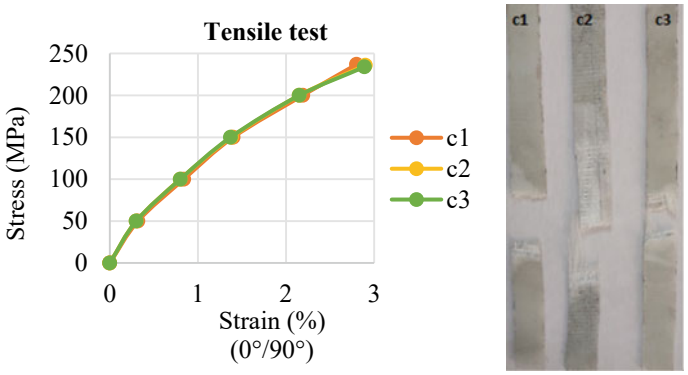


Fig. 5 Stress versus strain curve of tensile test (0°/90°)

response, and catastrophic failure was specified by a dramatic drop in stress that occurred along the laminate's breadth of the cross section. Owing to the alignment of the primary loading direction and fiber orientation, the laminate can act orthogonally, exhibiting mutually perpendicular degrees of symmetry in the material behavior. The in-plane expansive force which acts isotropically changes the deformation behavior of laminate [12, 13]. The tensile stress–strain graphs of the glass epoxy laminate composite showed that the fiber orientation [0°/90°] had the utmost tensile stress and strain, whereas the fiber orientation [0°/45°/90°] had the least tensile stress and strain. As a result, fiber orientation has a great impact on the tensile properties of the laminate.

The stress–strain diagram of a glass epoxy laminated composite that underwent flexural testing is shown in Fig. 6. The laminate with fiber orientation [0°/90°] shows the average flexural failure stress and strain of 257 MPa 3.33%, respectively. The laminate exhibited the characteristic behavior of linear elasticity in flexure until it reached a critical point without any apparent signs of damage. At this juncture, cracks began to initiate and propagate on the compressive side of the laminate causing in a gradual deviation of the load curve from its linear response [14].

Figure 7 shows flexural response of the laminate with fiber orientation [+45°/−45°]. The laminate experienced failure when subjected to an average flexural strength of 243 MPa and a strain of 3.13%. The material demonstrated a brittle response, indicated by the development of cracks in matrix under compression along the direction of the fibers. Once these cracks initiated at the highest load, they swiftly spread throughout the entire laminate.

The flexural stress–strain graphs of the laminate with fiber orientation [0°/45°/90°] are shown in Fig. 8.

The laminate exhibited strengths and strain of 236 MPa and 3.06%, respectively, laminate exhibited comparable stress–strain behaviors that were nonlinear, and significant strains leading to failure were witnessed, resulting in a pseudo-ductile behavior. In this particular scenario, the applied load exhibited a gradual increment before moderately declining subsequent to reaching the maximum load [15]. Figure 9

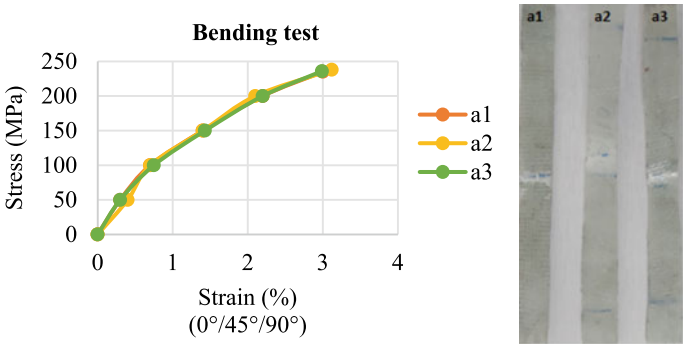


Fig. 6 Stress versus strain curve of flexural test (0°/45°/90°)

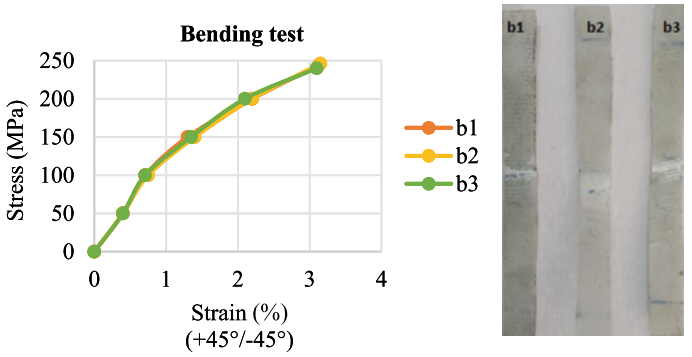


Fig. 7 Stress versus strain curve of flexural test (+45°/−45°)

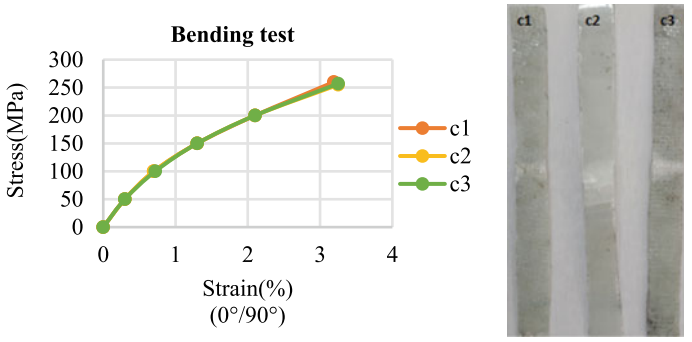


Fig. 8 Stress versus strain curve of flexural test (0°/90°)

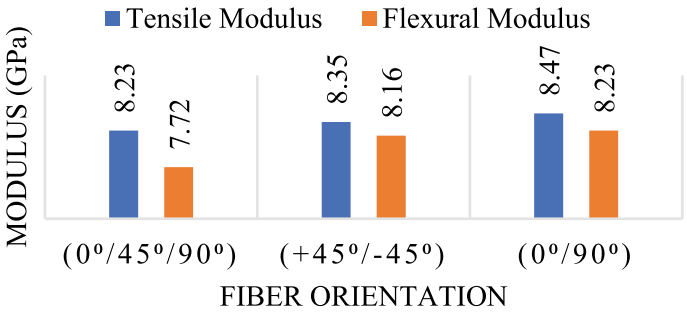


Fig. 9 Tensile and flexural modulus at different fiber orientations

displays the results obtained for the tensile modulus of laminate composites featuring various fiber orientations. Among these, the laminate with a fiber orientation of [0°/45°/90°] present the lowest values for both tensile modulus (8.23 GPa) and flexural modulus (7.72 GPa). Conversely, the laminate with a fiber orientation of [0°/90°] exhibited the utmost tensile modulus (8.47 GPa) and flexural modulus (8.27 GPa). Clearly, the orientation of the fibers significantly impacts the flexural modulus of the laminate. This effect can be attributed to off-axis phenomena, such as off-axis matrix cracking, which can adversely affect the stiffness of the laminate [16–19].

5 Numerical Simulation and Validation

Through numerical modeling with the Abaqus programme, the simulation involved conducting a tensile test on the composite structure. An Abaqus model of the structure was constructed, and all necessary analysis parameters were set up accordingly. The mesh was generated, and appropriate boundary conditions and loads were applied to the numerical model like experimental tensile test.

The matrix's tangent elastic modulus is displayed in Fig. 10a. When the tangent stiffness diminishes, plastic deformation happens, revealing the structural behavior. Figure 10b shows the presence of rupture in the simulation findings. The ruptured state is represented by the red area, which shows where the specimen was subjected to greater loads. The top and lower portions of the red sections show that there was no failure of the material. Tools for post-processing were used to generate the stress–strain graph for further analysis.

The findings from the investigation have been compared with the results from computational modeling (Fig. 11). A satisfactory fit was attained when a tensile force was applied, confirming the accuracy of the numerical model with fiber orientations.

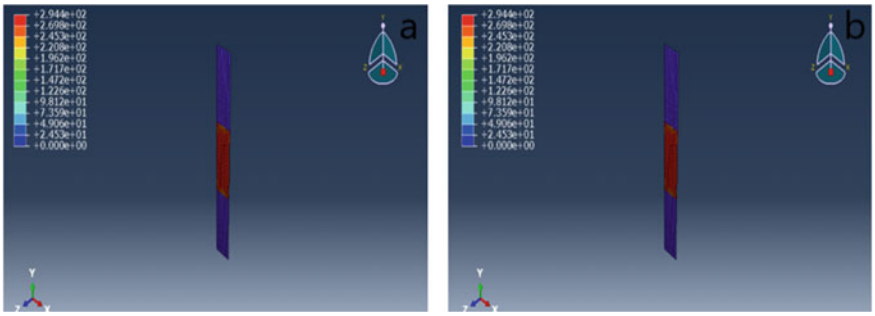


Fig. 10 Finite element analysis **a** Elastic modulus, **b** Rupture state

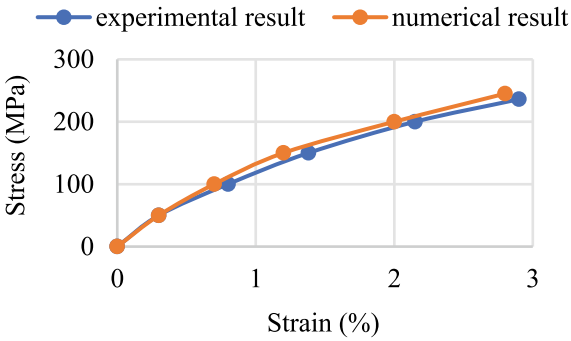


Fig. 11 Comparison of the results obtained experimentally and numerically for fiber orientation [0°/90°]

6 Conclusion

The intention of the conducted investigations was to evaluate the mechanical properties of epoxy reinforced with glass fibers using both numerical and experimental approaches, considering different orientation angles. A numerical model was created to simulate the tensile test, and its results were compared to the corresponding experimental values.

The glass epoxy laminate with a fiber orientation of [0°/90°] demonstrated the utmost recorded tensile strength of 237 MPa and modulus of 8.49 GPa. In flexural testing, the laminate with a fiber orientation of [0°/90°] exhibited the highest flexural strength of 260 MPa and modulus of 8.25 GPa. The compressive side of the laminate, with a predominance of glass fibers, absorbed most of the applied load. The findings showed promising arrangement between the numerical data and experimental data, affirming the suitability of glass fiber materials for aircraft structures. Notably, the orientation angle of [0°/90°] revealed superior strength when compared to other orientation angles. It is possible to augment the composite material mechanical properties.

Funding Not applicable.

References

1. Aleksendrić D, Carlone P (2015) Introduction to composite materials. https://doi.org/10.1533/9781782421801.1
2. Xia M, Takayanagi H, Kemmochi K (2001) Analysis of multi-layered filament-wound composite pipes under internal pressure. Compos Struct 53(4):483–491. https://doi.org/10.1016/S0263-8223(01)00061-7
3. Mylsamy G, Krishnasamy P (2023) A review on electrical properties of fiber-reinforced polymer material: fabrication, measurement, and performances. Trans Indian Inst Met 76(7):1691–1708. https://doi.org/10.1007/s12666-023-02888-3
4. Suarez SA, Gibson RF, Sun CT, Chaturvedi SK (1986) The influence of fiber length and fiber orientation on damping and stiffness of polymer composite materials. Exp Mech 26(2):175–184. https://doi.org/10.1007/BF02320012
5. Singh KK, Shrivastava R (2023) Influence of fiber orientation on thermo-mechanical response of symmetric glass/epoxy composite. J Brazilian Soc Mech Sci Eng 45(6):288. https://doi.org/10.1007/s40430-023-04228-4
6. Zolkin AL, Galanskiy SA, Kuzmin AM (2021) Perspectives for use of composite and polymer materials in aircraft construction. IOP Conf Ser Mater Sci Eng 1047(1):12023. https://doi.org/10.1088/1757-899X/1047/1/012023
7. Hashim MKR, Majid MSA, Jamir MRM, Kasim FH, Sultan MTH (2021) The effect of stacking sequence and ply orientation on the mechanical properties of pineapple leaf fibre (Palf)/carbon hybrid laminate composites. Polymers (Basel) 13(3):1–24. https://doi.org/10.3390/polym13030455
8. Budarapu PR, YB SS, Natarajan R (2016) Design concepts of an aircraft wing: composite and morphing airfoil with auxetic structures. Front Struct Civ Eng 10(4):394–408. https://doi.org/10.1007/s11709-016-0352-z
9. Wu X, Fuller JD, Wisnom MR (2020) Role of fibre fragmentation on pseudo-ductility of thin-ply [±277/0]s carbon fibre laminates with high modulus 0° plies under compressive and flexural loading. Compos Sci Technol 199:108377. https://doi.org/10.1016/j.compscitech.2020.108377
10. Fotouhi M, Jalalvand M, Wisnom MR (2017) High performance quasi-isotropic thin-ply carbon/glass hybrid composites with pseudo-ductile behaviour in all fibre orientations. Compos Sci Technol 152:101–110. https://doi.org/10.1016/j.compscitech.2017.08.024
11. Fuller JD, Wisnom MR (2015) Exploration of the potential for pseudo-ductility in thin ply CFRP angle-ply laminates via an analytical method. Compos Sci Technol 112:8–15. https://doi.org/10.1016/j.compscitech.2015.02.019
12. Abdul Majid MS, et al (2014) Stress-strain response modelling of glass fibre reinforced epoxy composite pipes under multiaxial loadings. J Mech Eng Sci 6(June):916–928. https://doi.org/10.15282/jmes.6.2014.18.0088
13. Hart-Smith LJ (1990) A new approach to fibrous composite laminate strength prediction. In: NASA. Langley research center, eighth DOD(NASA)FAA conference fibrous composite structure design. Part 2, p. p 663–693, 1990, [Online]. Available: https://ntrs.nasa.gov/search.jsp?R=19920023344
14. Pinto F, Boccarusso L, De Fazio D, Cuomo S, Durante M, Meo M (2020) Carbon/hemp bio-hybrid composites: effects of the stacking sequence on flexural, damping and impact properties. Compos Struct 242:112148. https://doi.org/10.1016/j.compstruct.2020.112148
15. Caminero MA, Rodríguez GP, Muñoz V (2016) Effect of stacking sequence on Charpy impact and flexural damage behavior of composite laminates. Compos Struct 136:345–357. https://doi.org/10.1016/j.compstruct.2015.10.019
16. Kali N, Korla R, Korla S (2023) Impact behaviour of nano-hybrid (carbon/glass) fibre metal laminates: an experimental study. Arab J Sci Eng 48(3):3881–3891. https://doi.org/10.1007/s13369-022-07317-z
17. Nega BF, Pierce RS, Yi X, Liu X (2022) Characterization of mechanical and damping properties of carbon/jute fibre hybrid SMC composites. Appl Compos Mater 29(4):1637–1651. https://doi.org/10.1007/s10443-022-10034-3

18. Katerelos DG, McCartney LN, Galiotis C (2006) Effect of off—axis matrix cracking on stiffness of symmetric angle-ply composite laminates. Int J Fract 139(3):529–536. https://doi.org/10.1007/s10704-006-0100-9
19. Agarwal P, Kumar M, Choudhary M, Sharma A, Patnaik A (2022) Experimental and numerical analysis of mechanical, thermal and thermomechanical properties of hybrid glass/metal fiber reinforced epoxy composites. Fibers Polym 23(5):1342–1365. https://doi.org/10.1007/s12221-022-4760-5

Aging and Atomization Characteristics of Aluminum Loaded and Unloaded Ethanol Gel



Sankalp Jain and Rajiv Kumar

Abstract Gel propellants, also known as gel fuels or gel-based rocket propellants, are a type of propellant used in certain rocket engines. Unlike traditional liquid or solid propellants, gel propellants have a unique consistency resembling a gelatinous substance. Characteristics of the ethanol gel changes from time to time as the ethanol starts evaporating from the gel propellant when kept in open atmosphere, thus changing the concentration of the ethanol in the gel. Thus, the aging characteristic of the ethanol plays a major role in its atomization and combustion characteristics. An experimental investigation on the aging characteristics of aluminum loaded and unloaded ethanol gel was performed. The atomization of the base gel prepared was also done through impinging jet injector for both the types of gel at varying pressures. The results of aging characteristics obtained for the loaded gel were found to be better than the unloaded ethanol gel. The trends of atomization were observed to be almost similar for both the types of gel.

Keywords Gel propellant · Ethanol · Gelling agent · Aging · Metallized gel

1 Introduction

Gel propellants are typically composed of a fuel component and a gelling agent that provides the gel-like consistency. The fuel component is usually a hydrocarbon-based substance, such as a mixture of various hydrocarbons or a specific fuel like kerosene. The gelling agent used in gel propellants serves to increase the viscosity of the propellant mixture, giving it the gel-like consistency. Various gelling agents can be used, such as nitrocellulose or other thickening agents. Gel nature of the propellant allows for improved control over the combustion process and can help prevent sloshing or separation of the propellant components during rocket flight.

S. Jain · R. Kumar (✉)
Department of Space Engineering and Rocketry, Birla Institute of Technology Mesra, Ranchi, India
e-mail: rajiv@bitmesra.ac.in

© The Author(s), under exclusive license to Springer Nature Singapore Pte Ltd. 2024

S. Singh et al. (eds.), *Recent Advances in Aerospace Engineering*, Lecture Notes in Mechanical Engineering, https://doi.org/10.1007/978-981-97-1306-6_12

Gel propellants are often used in specific applications where their unique properties are advantageous. For example, they are commonly used in certain hybrid rocket engines, where a gel as an oxidizer is combined with a solid fuel. The gel oxidizer can be more stable and easier to handle than traditional liquid oxidizers. The importance of gel fuels lies in their ability to combine the advantages of both solid and liquid fuel propellants [1]. Gel propellant has been in much more attention due to its advantages in reducing the leakage and spillage risk, adjustable thrust, being capable of multi-time ignition, and easy handling [2].

It is important to note that the specific composition and characteristics of gel propellants can vary depending on the application and the specific requirements of the rocket engine. Safety precautions and proper handling procedures are crucial when working with any type of rocket propellant. Thus, the rheological study helps to determine the viscosity at different shear rates. It also helps to understand the deformation of the gel when shear force is applied to the gel [3]. The gellant particles or molecules when dispersed into the parent liquid form a three-dimensional web-like network that transforms it into a gelled state by changing its properties from a free-flowing liquid to a thick semi-solid [4, 5].

While ethanol gel propellants have certain advantages, such as their green nature and potential for safe handling, they also present some challenges and problems. Here are a few issues associated with ethanol gel propellants.

(1) Gel Processing and Manufacturing: The production and processing of ethanol gel propellants can be complex and require specialized equipment and techniques. Gel formation, mixing of fuel and oxidizer components, and ensuring uniformity in the gel consistency can be challenging. These complexities can increase the cost and complexity of manufacturing ethanol gel propellants.
(2) Gel Stability and Shelf Life: Ethanol gel propellants can be prone to drying out or deteriorating over time, especially if not stored under proper conditions. Changes in gel consistency or drying of the propellant can affect its performance and usability. Proper storage and handling procedures are crucial to maintaining the stability and shelf life of ethanol gel propellants.
(3) Combustion Stability: Achieving consistent and stable combustion with ethanol gel propellants can be challenging. The gel consistency and combustion characteristics of the propellant can vary, leading to uneven or unpredictable burn rates. This can impact the performance and reliability of the rocket engine.
(4) Atomization: Gels typically have a higher viscosity compared to liquids, which makes it more difficult for them to flow and break up into small droplets during atomization. The thick consistency of gels can impede the atomization process, requiring more energy or specialized atomizer designs to achieve efficient atomization.

It is worth noting that ongoing research and development efforts are aimed at addressing few of the challenges associated with ethanol gel propellants. Advancements in formulation, manufacturing techniques, gel stability, and atomization characteristics may help overcome some of these limitations in the future. The present study aims to study the aging characteristics of ethanol-based gel with and without

addition of metal particles. Apart from this, atomization studies were also conducted for the prepared gel using impinging jet injector for both aluminum loaded and unloaded ethanol gel.

2 Experimental Methodology

2.1 Preparation of Loaded and Unloaded Ethanol Gel

The pure non-metalized ethanol gel was prepared using ethanol, methylcellulose, and distilled water. Firstly, distilled water was mixed with 99.9% pure ethanol. It was then stirred for a few seconds, and then, methylcellulose was added to the above solution. The mixed solution was stirred at 600 rpm for 5 min using a mechanical stirrer. The mix is then kept undisturbed for few minutes at room temperature for the gelation process to take uniformly, i.e., the formation of internal bonds between ethanol, distilled water, and HSMC takes place.

The metalized ethanol gel is prepared using ethanol, methylcellulose, distilled water, and micro-sized aluminum particles. The mixing process of the metalized ethanol gel is same as that of the non-metalized ethanol gel except the aluminum was added to the metalized gel at the end. Once the aluminum was added to the gel, it was mixed using the mechanical stirrer at 600 rpm for 5 min. The mix was then kept undisturbed for few minutes at room temperature for the gelation process to take place uniformly.

2.2 Standardization of Gels

Unloaded Ethanol Gel The amount of high substituted methylcellulose (HSMC) in the gel was changed depending on the viscosity of the gel achieved, as the goal was to get less viscosity gel for better characteristics and gel stability. Thus, the concentration of HSMC was varied from 5 to 10% as shown in Table 1. It was found that at 6.5% concentration of HSMC, the gel was showing better stability characteristics.

Loaded Ethanol Gel The amount of HSMC was varied in the gel was changed depending on the viscosity of the gel achieved to achieve less viscous gel for better characteristics and gel stability. Thus, the concentration of HSMC was varied from 4 to 5% as shown in Table 2. It was found that at 4.75% concentration of HSMC, the gel was showing better stability characteristics. Aluminum was used as a metal particle for loaded ethanol gel. The particle size of aluminum used was ranging between 10 and 40 μm.

Table 1 Composition of unloaded ethanol gel prepared for study

	Ethanol (%)	Methylcellulose (%)	Distilled water (%)	Observation
Gel 1	80	5	15	Soft gel, no separation, and flowing when kept steady
Gel 2	80	6.5	13.5	Soft gel, no separation, and not flowing when kept steady
Gel 3	80	8	12	Hard gel, no separation
Gel 4	80	10	10	Hard gel, separation

Table 2 Composition of loaded ethanol gel prepared for study

	Ethanol (%)	Methylcellulose (%)	Aluminum (%)	Distilled water (%)
Gel 1	75	4	10	11
Gel 2	75	4.5	10	10.5
Gel 3	75	4.75	10	10.25
Gel 4	75	5	10	10

2.3 Rheology

The rheology of the prepared gel is done on the Brookfield viscometer in which the dial reading of the prepared gel is observed at different RPMs which were fixed by the viscometer itself. RPMs which were taken in the consideration were 0.3, 0.6, 1.5, 3, 6, and 12. Dial reading gives out the viscosity when multiplied by the factor of the spindle used. On increasing the shear rate of the viscometer, the viscosity of the gel decreases as the movement in the gel increases.

In this experimental data, LV4 spindle was used to plot graph between viscosity and their shear stress. The rheology of the gel was performed to find the aging characteristics of the gel. The rheology of the gel was performed to find the aging characteristics.

2.4 Experimental Setup

For the atomization of the ethanol gel, impinging jet injector was selected having 45° of impinging angle and 1 mm of orifice diameter. For atomization process, setup was prepared with the goal of running the system with as little human interaction as possible. The gel was prepared and stored in a reservoir equipped with a piston that could be moved pneumatically within the assembly which is shown in Fig. 1. To expel the gel, a nitrogen gas cylinder was employed to apply pressure to the piston head. A dual pressure gauge regulator was used to regulate the nitrogen gas pressure, which was located close to the cylinder for easy control of the supply pressure. Additionally,

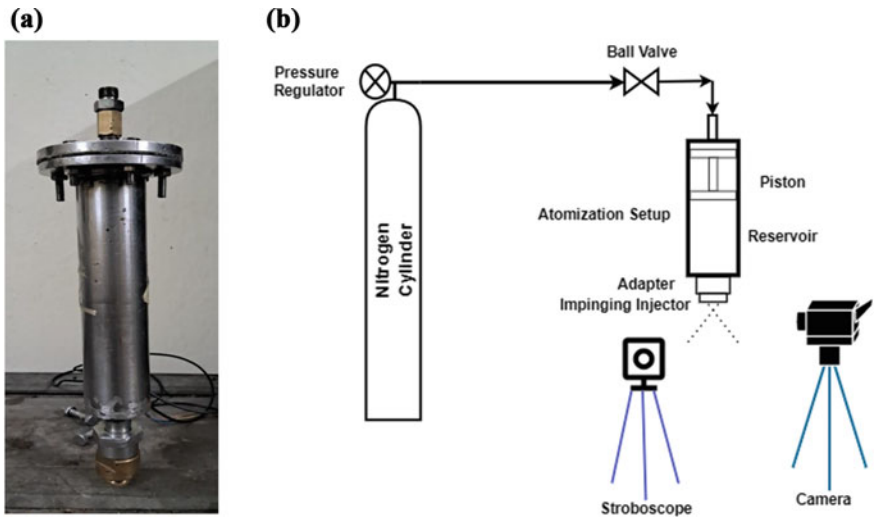


Fig. 1 **a** Gel reservoir [6]. **b** Atomization setup [7]

a solenoid valve, which was usually open, was mounted near the reservoir and acted as an actuator when the gel was pressurized.

Once the gel was prepared, it was filled in the reservoir and placed on the setup. The camera was set with the required properties at a fixed location. A stroboscope was used to make the atomization look stationary or slow. The atomization images were captured, and their image processing is done to get the required results.

3 Result and Discussion

3.1 Aging Characteristics

One of the primary aging characteristics of gel propellants is the tendency for the fuel to "creep" over time. Another aging characteristic of gel propellants is their sensitivity to temperature and pressure changes. Exposure to high temperatures or pressures can cause the gel to soften or become more viscous, which can impact its flow properties and combustion performance. Finally, gel propellants may also be susceptible to chemical degradation over time. Exposure to oxygen, moisture, or other reactive compounds can cause the gel to break down or deteriorate, potentially leading to changes in its combustion properties and performance.

Thus, to find out the aging characteristics of the loaded and unloaded ethanol gel, the gel was kept in ambient conditions of 27 °C room temperature. The viscosity of the gel was noted after every 1 h of time interval.

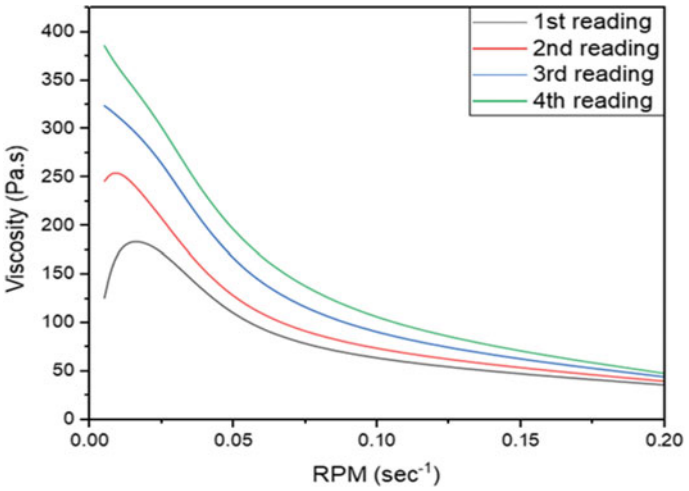


Fig. 2 Viscosity curve of non-metallized ethanol gel over each 1-h interval of time

Metalized and non-metalized ethanol gel propellants have some similar aging characteristics, such as their sensitivity to temperature changes and potential chemical degradation over time but also differ in important ways that can impact their performance over time. It is observed that the rheological property over time gets deteriorated, i.e., the viscosity of the gel was increasing over the time, when it was kept in the ambient conditions.

Figures 2 and 3 show that the viscosity of non-metalized ethanol gel was increasing more rapidly over time in comparison with the metalized ethanol gel. Both the curves show that the ambient conditions will degrade the quality of the gel. It was also observed that for non-metalized ethanol gel the viscosity was increasing rapidly in ambient conditions due to which it is only useful for 3 h after the preparation of the gel. In metalized ethanol gel, it was observed that the gel was useful for at least 6 h when kept in the ambient conditions. As a result, both types of propellants require careful storage and maintenance to ensure optimal performance.

3.2 Atomization Characteristics

Impinging jet injector was used in this study as impinging atomization is a method used to break up a liquid fuel into a fine spray of droplets. In the case of ethanol gel, impinging atomization involves forcing the gel through a small orifice or nozzle, which breaks it up into a fine mist of droplets. Impinging jet injector used in this study has 45° impingement angle and 1 mm orifice diameter.

The study of the spray characterization of the gel was carried out at different pressures for both aluminum loaded and unloaded ethanol gel. The spray images were

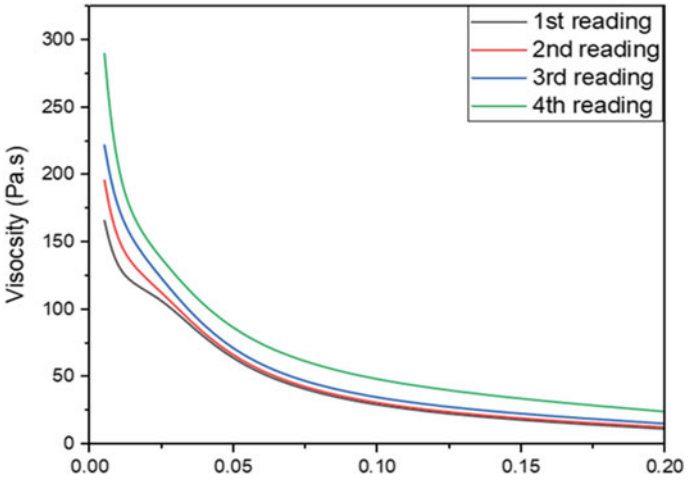


Fig. 3 Viscosity curve of metallized ethanol gel over each 1-h interval of time

evaluated using the Image J software, where data about droplet diameter, droplet area was obtained which is shown in Tables 3 and 4. Even the circularity of the particle was also obtained from the software, which depicts about the roundness of the droplets. Table 5 shows the atomization images of the gel with varying pressures.

It was observed that, as the pressure in the reservoir was increased, the atomized particles were also increasing. At 600 psi for loaded ethanol gel, it was found that the number of particles was less in number. It was due to the blockage of the impinging orifice due to larger particle size of metal particles.

The average area of droplets and mean droplet diameter of the particles was decreasing. It was also observed that the circularity of droplets was also increasing

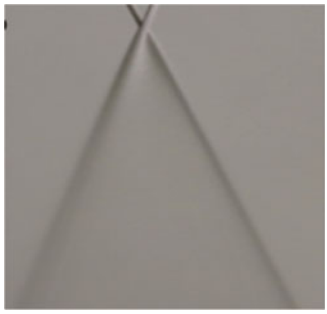
Table 3 Atomization data of non-metallized ethanol gel

Pressure	Count of droplets	Total area of droplets (mm^2)	Average area of droplets (mm^2)	Mean droplet diameter (mm)	Circularity of droplets
200 psi	2936	504.66	0.172	0.468	0.871
400 psi	3274	559.32	0.170	0.465	0.897
600 psi	3796	604.66	0.159	0.445	0.901

Table 4 Atomization data of metallized ethanol gel

Pressure	Count of droplets	Total area of droplets (mm^2)	Average area of droplets (mm^2)	Mean droplet diameter (mm)	Circularity of droplets
200 psi	1436	304.66	0.212	0.519	0.865
400 psi	1793	355.01	0.198	0.502	0.866
600 psi	1679	320.69	0.191	0.493	0.888

Table 5 Atomization of gel using impinging jet injector at varying pressures

	Unloaded ethanol gel	Loaded ethanol gel
200 psi		
400 psi		
600 psi		

which means that the atomized particles were conquering to be round in shape. These trends were almost same for both the loaded and unloaded ethanol gel.

4 Conclusions

From the present study, it can be concluded that:

(1) Both the metalized and non-metalized ethanol gel were found to have the shear thinning behavior. At low shear stresses, the gels were behaving like a thick fluid or solid, resisting deformation. However, as the shear rate was increased, the gel structure begins to break down, causing the viscosity to decrease and the material to flow more easily.
(2) Aging characteristics of the gel were studied at the ambient conditions, and it was found that non-metalized aging characteristics were poor in comparison with that of the metalized ethanol gel at the ambient conditions.
(3) The trend-line observed for the metalized ethanol gel was found to be almost similar to that of the non-metalized ethanol gel.
(4) The trends of average area of droplets and mean droplet diameter were found to be decreased with increase in the pressure exerted.
(5) The number of particles were found to be increasing with the increase in the pressure.

Atomization can be performed on both loaded and unloaded ethanol gels, taking into consideration the aging characteristics of the gels. Aging characteristics of the ethanol gel can be further tested at different temperatures and different atmospheric conditions. Atomization of the gel can also be done using different types of injectors for future study.

Acknowledgements The authors wish to express their sincere gratitude toward Space Engineering and Rocketry Department, BIT Mesra, for providing laboratory facilities for conducting the experiments on the ethanol gel propellants.

References

1. Miglani A, Nandagopalan P, John J, Baek SW (2016) Disruptive combustion behavior of gelled ethanol fuel droplets. In: ILASS-Asia, 18th annual conference liquid at spray system
2. Sun H (2022) Rheological and atomization behavior of glycyrrhizic acid based supramolecular gel propellant simulant. Colloids Surf, A 640:128460
3. Botchu J, Baek SW (2015) Formulation and comparative study of rheological properties of loaded and unloaded ethanol-based gel propellants. J Energ Mater 33(2):125–139
4. Munjal NL, Gupta BL, Varma M (1985) Preparative and mechanistic studies on unsymmetrical dimethyl hydrazine—red fuming nitric acid liquid propellant gels. Propellants, Explos, Pyrotech 10:111–117
5. Varma M, Gupta BL, Pandey M (1996) Formulation and storage studies on hydrazine based gelled propellants. Def Sci J 46:435–442
6. Behal S (2019) Rheology and Spray characterization of green gel propellant using novel injector. Thesis (MTech). BIT Mesra
7. Jain S, Kumar R (2022) Effects of gellant concentration on ethanol gel propellant characteristics. In: 4th national aerospace propulsion conference. IIT Bombay

Design, Calibration, and Navigation of Bird Ambulance Drone Using APM Flight Controller



N. C. Ajay Vishwath, Sujeet Kumar Pandey, Vechalapu Phanendra, Kurmapu Amarnath, and Tarun Reddy

Abstract The paper presents the design, calibration, and navigation of a bird ambulance drone equipped with an APM (ArduPilot Mega) flight controller. The research focuses on developing an innovative and ethical application of drone technology to rescue and assist birds and animals in distress. The study encompasses a comprehensive exploration of the drone's structural and avionics design, ensuring efficient and swift response during rescue operations. The research further demonstrates the experimental weight estimation and thrust estimation to choose the electronic components wisely. The research work proceeds to the avionic design with configuration of drone which demonstrates the detailed explanation of motions involved in the drone. Then the calibration process involves precise configuration of the APM flight controller, enabling accurate and autonomous navigation through GPS technology. The proposed bird ambulance drone represents a promising solution for wildlife conservation and rescue operations, demonstrating the ethical use of advanced technology for the benefit of all living beings.

Keywords Bird ambulance drone · APM flight controller · Navigation system · Wildlife conservation · Rescue operations · GPS technology · Autonomous flight · Flight control algorithms · Payload capacity · Safety measures · Redundant systems · Bird rescue and rehabilitation · Telemetry · Sensor integration · Remote control input

N. C. Ajay Vishwath (✉) · V. Phanendra · T. Reddy
Department of Aeronautical Engineering, Parul Institute of Engineering and Technology, Parul University, Vadodara, India
e-mail: ajay.nc2934@paruluniversity.ac.in

S. K. Pandey
Aerospace Engineering Institute of School of Engineering and Technology, Sandip University, Nashik, India
e-mail: Sujeet.pandey@sandipuniversity.edu.in

K. Amarnath
Department of Mechatronics Engineering, Parul Institute of Technology, Parul University, Vadodara, India

© The Author(s), under exclusive license to Springer Nature Singapore Pte Ltd. 2024

S. Singh et al. (eds.), *Recent Advances in Aerospace Engineering*, Lecture Notes in Mechanical Engineering, https://doi.org/10.1007/978-981-97-1306-6_13

1 Introduction

Drones have achieved a significant breakthrough in the healthcare industry by effectively transporting medicines, vaccines, and medical supplies to save human lives. Currently, researchers are exploring the development of drone ambulances for human emergencies and rescue missions. A novel and ethical application, the bird ambulance drone, aims to extend the same life-saving technology to birds and animals in distress within the same weight category. The research is based on extensive literature reviews, focusing on the use of drone technology in similar applications.

The paper proposes an emergency ambulance drone or UAV to save the birds that are injured as a viable solution to the delays faced in traditional rescue operations due to factors like traffic congestion and street blockages. With its ability to follow an aerial course, the drone can bypass ground impediments, making it the fastest option for medical care during emergencies. Piloted from a hospital control room, it can swiftly reach the desired location using the patient's GPS data obtained through a mobile application [1].

Intelligent drones prove to be a promising solution for saving birds and animals [2]. While there is significant research focused on using drone technology to save human lives, the study emphasizes that drones' small size and limited payload capacity make them suitable for bird and animal rescue [3]. The research work employed an ArduPilot Mega (APM) flight controller, known for its intelligent navigation capabilities and real-time monitoring through its own Firmware [4]. The use of APM flight controllers in bird ambulance drones is a novel and promising technique for wildlife conservation and rescue operations. These open-source flight controllers offer various functions, enabling drones to navigate accurately and autonomously. Utilizing GPS technology, the APM flight controllers precisely calculate the drone's position, altitude, and speed. Their implementation in bird ambulance drones ensures efficient and quick reactions during rescue operations [5], sophisticated flight modes, intelligent navigation skills, and redundant systems with fail-safe mechanisms, ensuring the safe return of the drone and the well-being of the birds being rescued [6]. The research is structured into various sections, detailing the components of the bird ambulance drone. The structural design and avionics design are discussed separately. Section 2 focuses on the structural design, while Sect. 3 addresses the selection of appropriate electronic components for avionics. Weight, a critical design parameter in aerospace products, is discussed in Sect. 4, where the actual weight estimation of the bird ambulance drone is provided. Section 5 is dedicated for the experimental thrust estimation of the thrusters. Avionics design has been demonstrated in Sect. 6. Motor configuration and motions of hexacopter have been explained in Sect. 7. Section 8 demonstrates the calibration methods of APM flight controller for the drone. Section 9 addresses the challenges in Wildlife Conservation and rescue operations, and Sect. 10 explains the novelty in the research work.

2 Structural Design and Development of Carbon Fiber Frame

The structural design of the bird ambulance drone prioritizes durability and performance, utilizing carbon fiber as the material of choice for its frame. Specifically, the ZD850 mm Full Carbon Fiber 850 mm Hexa-Rotor Frame Combo is selected due to its robust construction using 100% pure carbon fiber, providing exceptional strength while remaining lightweight. The 20 mm carbon fiber tube arms offer increased resistance to breakage during hard landings, ensuring the drone's reliability in demanding situations.

The hexacopter configuration offers advantages over quadcopters, with six arms providing greater power and the ability to accommodate larger batteries, leading to extended flight times. The presence of additional motors enhances the drone's stability, enabling it to land safely even with one or two motors down in case of failure. The Z850 mm frame, with its ample space for mounting essential components and accessories, is well-suited for heavy-duty applications and attaching cameras for enhanced functionality and versatility.

CATIA software was utilized for the drone's design, allowing for precise dimensions and accurate weight estimations with the application of materials. By using complete carbon fiber, the drone's individual parts and final assembly weigh significantly less than expected, enhancing its overall efficiency. Additionally, conducting structural analysis using CAD models ensures that the drone's components, particularly the arms, are adequately designed to withstand the weight of essential parts and the thrust force generated by the motor and propeller combination (Fig. 1).

The cross-section area of the arm is kept circular as shown in Fig. 2. The carbon fiber rod used for the arm has dimensions of 8.5 mm radius and 345 mm length and

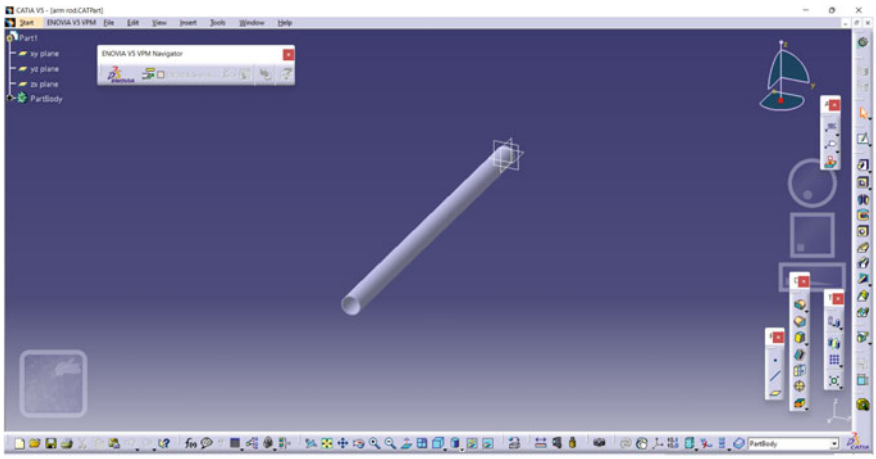


Fig. 1 Arm of the drone

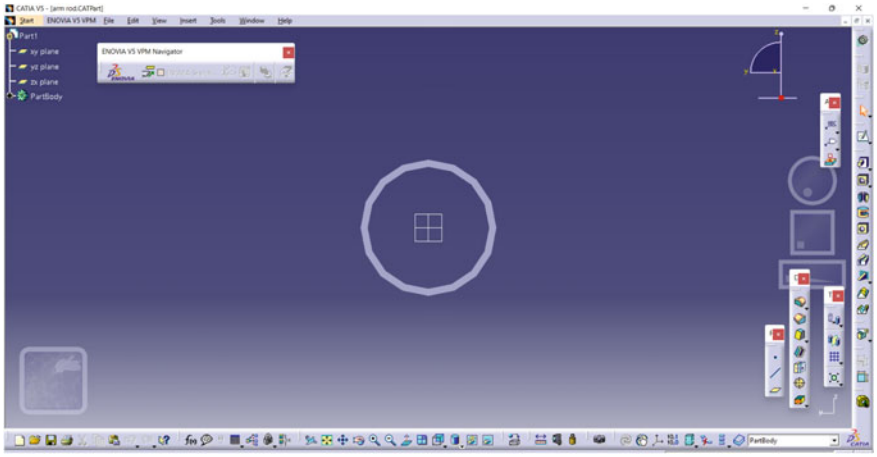


Fig. 2 Cross-section of arm of the drone

1 mm thickness. The hollow rods used would reduce the weight of the structure than the solid rod, and top of it, carbon fiber has its own strength-to-weight ratio as high as possible.

The bottom plate is the main important part of the drone which holds all the arms on it along with the complete electronic circuits on it which can be seen in Fig. 3. The bottom plate of the drone holds six arms as it is going to be the hexacopter configuration with a help of arm folding clamp. The middle of the bottom plate would be having the flight controller which is the center of gravity of the drone. The bottom plate has enough provisional space for other electronic components. Another important function of bottom plate is that it has carry all the load from top plate, arms, and the electronic parts within it to the landing gears. The bottom plate is also made up of carbon fiber material.

The next most important part of the drone is the top plate. The top plate is placed above the bottom plate and exactly resting above the arm folding clamps. The top plate holds the heaviest part of the drone, the battery. The battery would be placed in the middle of the top plate aligned with the center of gravity. The load acting on the top plate would be delivered to bottom plate through the arm folding clamp. The top plate is also made up of carbon fiber material (Fig. 4).

The arm folding clamp is the part that is used to hold the arms of the drone and rest them on the bottom plate. Also, the arm folding clamp has inbuilt spring which would enable the arms to open and close, i.e., scatter and spread or compress and shrink. This method is used to reduce the space occupied by the drone while the drone is not in operation mode. It helps users to carry drone anywhere.

The load acting on the top plate would be distributed to the bottom plate through the walls of the arm folding clamp. The clamp is having a lock mechanism at the hinge which would serve as a permanent lock during the flight operation and make sure the arm is rigid and straight at its axis. And releasing the lock would making

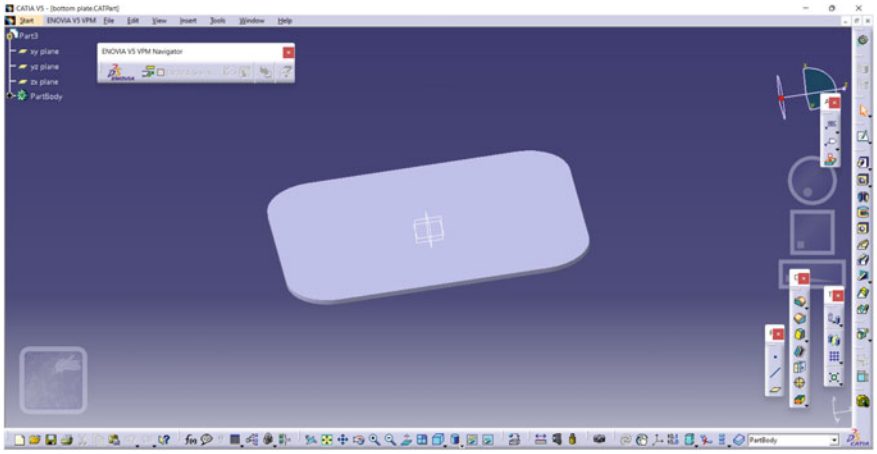


Fig. 3 Bottom plate of the drone

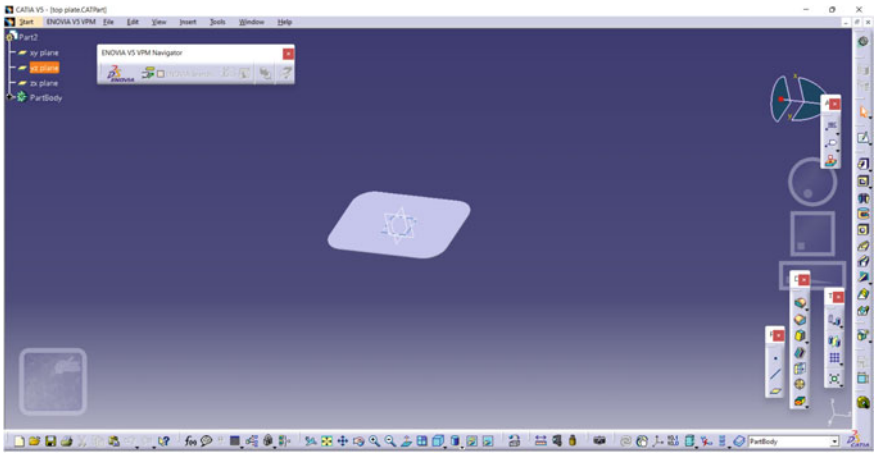


Fig. 4 Top plate of the drone

the arm free to oscillate and can be folded completely. The arm folding clamp is also made up of carbon fiber material as shown in Fig. 5.

The next part is the motor mount design, which would help in holding the motors tight along with the arms at the free end of the arms. The motor holder needs to be tight enough to hold the motors even at its maximum RPM and especially should be too rigid. The vibrations caused by the motors would be damped by the motor mount as the design is made in such a way for the same. The motor mount has a circular hole within which the circular arm would fit. The motor mount is also made up of carbon fiber material (Fig. 6).

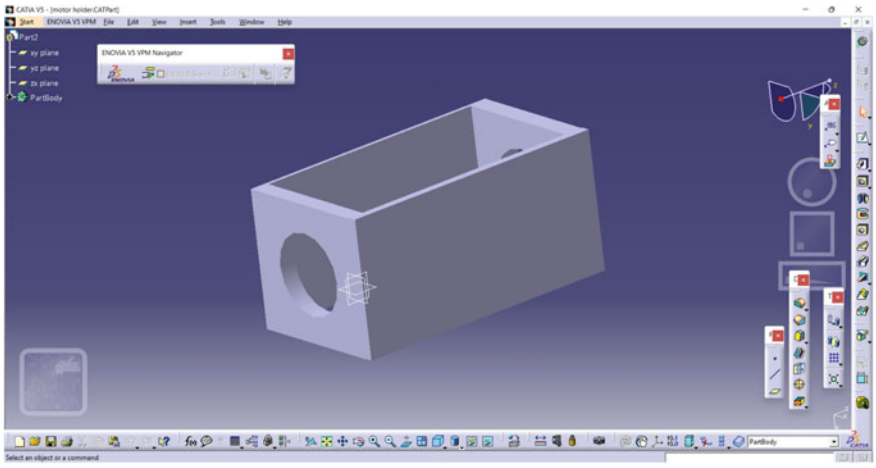


Fig. 5 Arm folding clamp

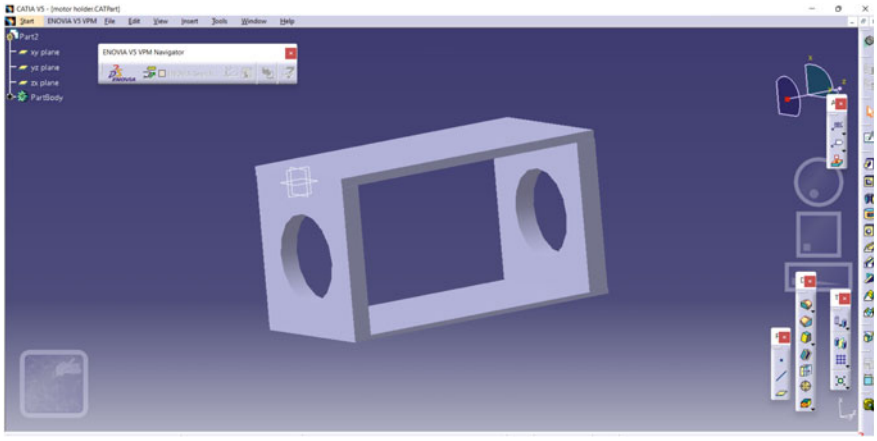


Fig. 6 Motor mount

The landing gear is designed from inspiring the helicopter skid as shown in Fig. 7. The skid-type landing gear for the drone made sure that the length of the skid at the bottom is sufficient to hold the complete drone in a small area. The landing gear is also made up of carbon fiber material. The skid is made up of solid circular rod with rubber absorbers which is having very good strength to hold the complete weight of the drone. The height of the landing gear is sufficient enough to have more ground clearance, as well as the empty space between the landing gears and bottom of the drone would be used to carry the payload, i.e., the birds and animals.

The complete drone assembly is made in CATIA as shown in Fig. 8, and the design is accurate in the measurement. They would be built using carbon fiber material.

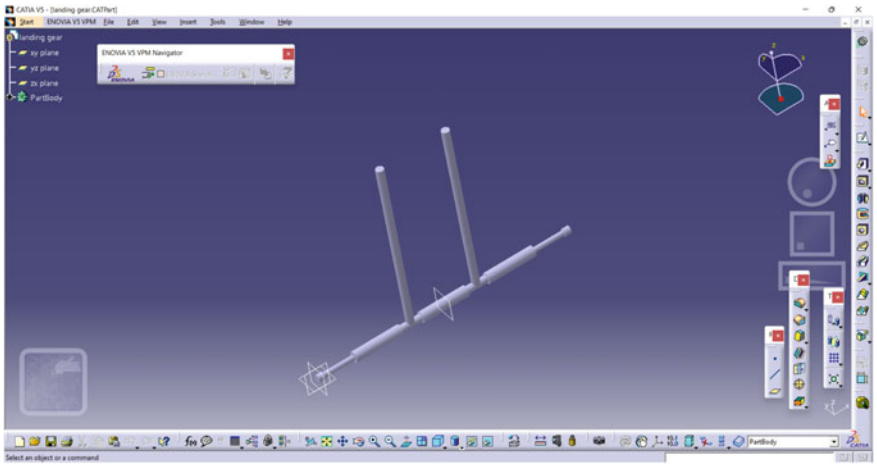


Fig. 7 Landing gear

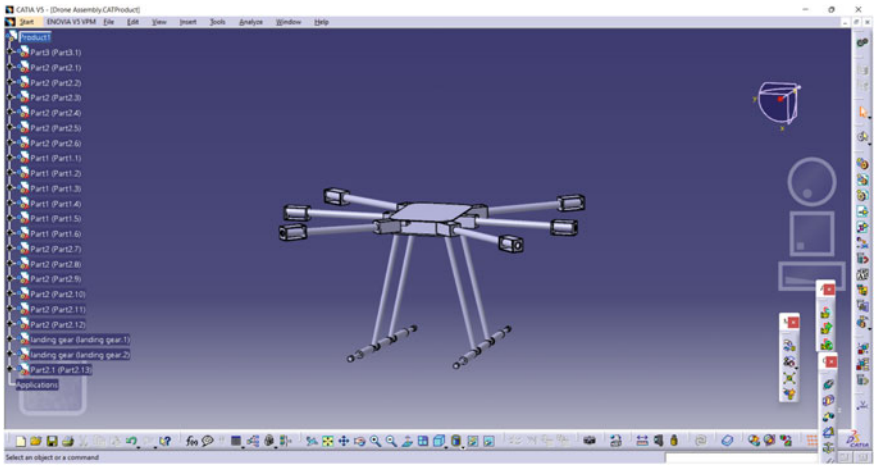


Fig. 8 Bird ambulance assembly

3 Choice of the Electronic Components

The electronic parts we choose for the drone came from a research article in which we wanted to achieve a thrust of each 600 g by taking into account the weight of 3600 g and 3000*1.2 = 3600 g. We refer to a beginner's guide for the correct selection of the drone's parts for particular purposes. The 14-inch propellers, each with total weight of 3600 g, deliver 600 g of thrust at 50% throttle and 1200 g of thrust at full throttle [7].

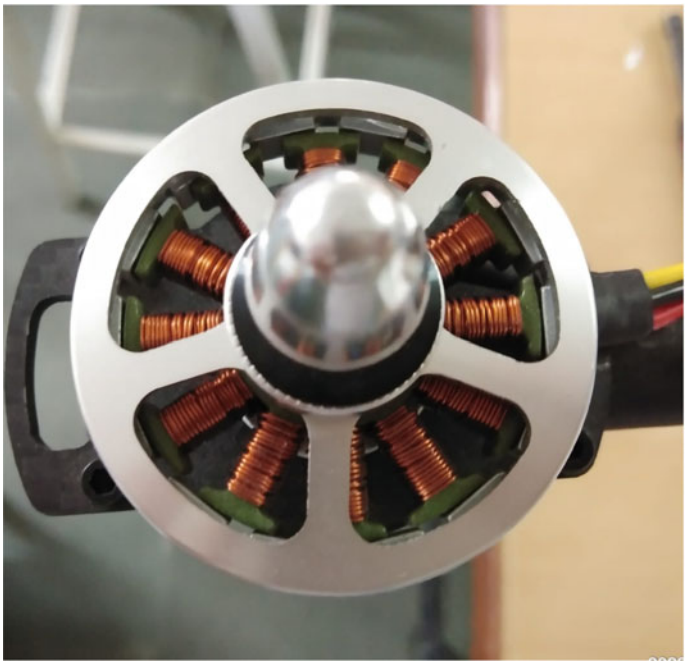


Fig. 9 BLDC motors

3.1 Motors

The motors need to be used in the drones would require characteristics like light in weight, less vibration, and less noise and also should have the ability to lift the weight of the drone along with the payload which would be bird or animal. As the type of configuration planned would be hexacopter, there would be six powerful 360 kV BLDC motors for this drone. They are in general built to deliver a lot of power, enabling the drone to carry large payloads (Fig. 9).

3.2 ESC

The electronic speed controller (ESC) is a component that regulates the motor's speed. Every motor requires one ESC to increase or decrease the speed of the motor. In response to signals from the flight controller, it modifies the motor speed. All the six ESCs would be connected in parallel to a power distribution board from, where the ESC gets its power, and also the signal is received from the flight controller through a signal pin (Fig. 10).



Fig. 10 Electronic speed controller

3.3 APM Flight Controller

Out of several flight controller used in drones, the open-source ArduPilot Mega (APM) flight controller is an autopilot system which would solve the purpose of navigation and provide stability for our hexacopter configure duration drone. It carries out flying orders and stabilizes the drone while in flight. It receives command through receiver and perform the operation as pilots order. The flight controller is responsible for all kinds of motions from takeoff to landing. At the time calibration, flight controller registers the equilibrium position or stable position. It has inbuilt sensors which would measure the real-time data of the flight. The differences made by the drone from its initial position due to the disturbances would be adjusted through the flight controller, and the drone maintains its original position. This is done by automatically varying the speed of the motor through ESC.

3.4 Receiver

A part that receives signals from the drone's remote control, the receiver enables the pilot to control the flight of the drone.

3.5 GPS Module

The GPS module gives the drone location information to the pilot or engineer in the ground control station; also, the drone can navigate to specific location on its own.

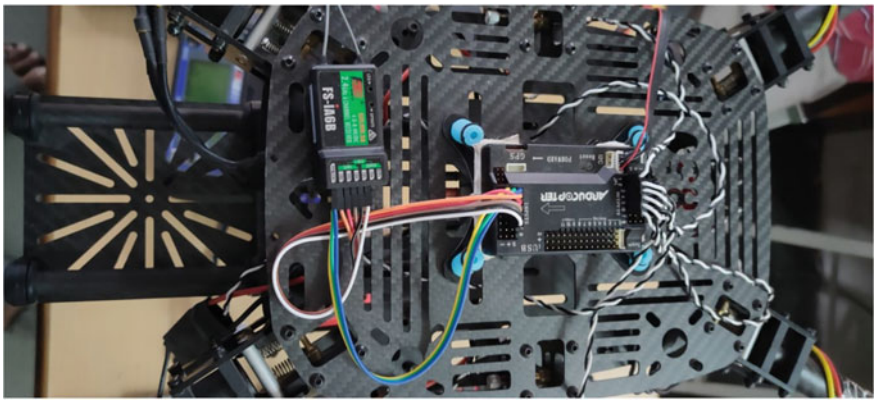


Fig. 11 APM controller, receiver, shock absorber and GPS module

3.6 Shock Absorber

A part that lessens vibrations and impacts on the drone's frame is the shock absorber. This may aid in enhancing stability and extending drone life (Fig. 11).

3.7 APM Accessories

These are extra parts that can be added to the APM flight controller to increase its capability, such as sensors and GPS modules. An additional accessory would help in getting more real-time data. It even includes telemetry devices as well (Fig. 12).

3.8 Power Module

The flight controller can keep track of the drone's power use thanks to the power module, which measures battery voltage and current (Fig. 13).

3.9 Power Distribution Board

This part of the drone transfers electricity from the battery to the ESCs and other parts via the flight distribution board (Fig. 14).



Fig. 12 APM accessories



Fig. 13 Power module

3.10 Battery

The drone is powered by this lithium polymer battery. It can supply the drone's motors with a lot of power because it has a capacity of 5200 m Ah and a voltage of 6 s (Fig. 15).

All things considered, these elements combine to provide a strong and adaptable drone that can treat injured birds in a variety of scenarios.

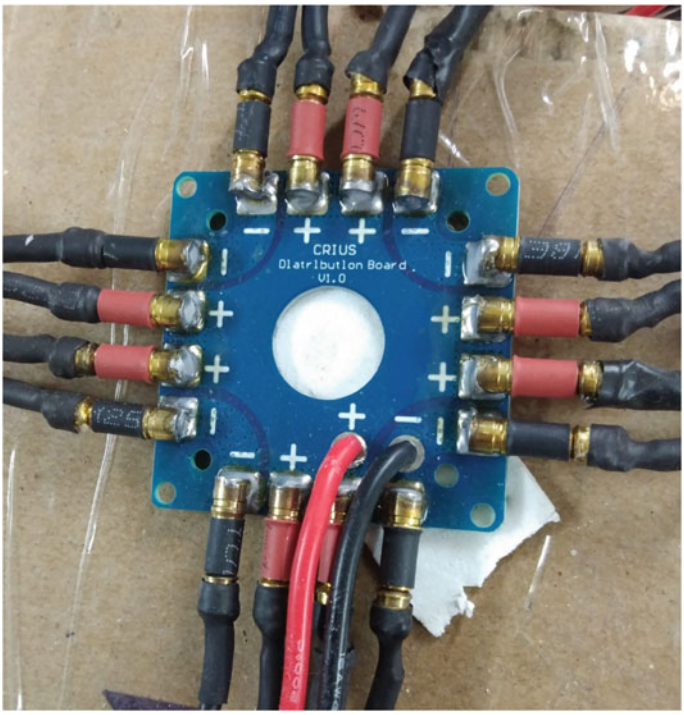


Fig. 14 Power distribution board



Fig. 15 LIPO battery

4 Weight Estimation

The weight estimation part deals with the approximate weight estimation of the drone before its flight. This is not the exact weight of the drone, but the estimation would be validated with the actual weight estimated using the actual parts in a weight machine.

Table 1 Weight of each component of the drone ambulance bird

S No	Drone parts	Weights in grams
1	Frame parts weight	1480 g
2	360 kV high torque (6 motor)	110 g * 6
3	ESC	30 g * 6
4	APM flight controller	50 g
5	APM accessories	53 g
6	GPS module	30 g
7	Power module	22 g
8	Shock absorber	14 g
9	Receiver	14 g
10	Power distribution board	36 g
11	5200 mAh 6 s battery	711 g
	Total	3250 g

In weight estimation, we initially calculated the total weight from the data of basic parts required for this category range of payloads. Frame parts weight: 1480 g, we were using 360 kV (6 motors) with high torque each weight 110 g, and we selected ESC which weights 30 g each. The APM flight controller with accessories weighs 103 g and GPS module of 30 g. The power module weighs 22 g. This Z850 mm Full Carbon Fiber 850 mm Hexa-Rotor Frame Combo is ideal for heavy-duty drone applications due to its capability of withstanding the punishing requirements of heavy-duty drone applications. It is made up of 100% 3 K TWILL carbon fiber, with 6 arms and a 20 mm carbon fiber tube for arm breakage. It has a wheelbase of 850 mm and weighs around 1210 gm, making it ideal for mounting cameras and other accessories (Table 1).

5 Thrust Estimation

In order to choose the right motor, need to test every motor that are compatible with the drone application and even in the BLDC motor category as well, the exact kv of the motor needs to be known. Depending on that ESC needs to be chosen. Also depending on their compatibility along with range and endurance requirement, proper battery needs to be chosen [7].

The right motor can be chosen through thrust test rig setup as shown in Fig. 16. The thrust would measure the thrust produced by the motors, and this would give the idea of each motor's thrust and thereby can determine the total thrust available with the drone.

The thrust measured for the given percentage of throttle is tabulated in Table 2.



Fig. 16 Test rig to check motor thrust

Table 2 Percentage of throttle with its corresponding thrust

S No.	Throttle (%)	Thrust (gm)
1	10	65
2	25	120
3	50	270
4	60	470
5	75	750
6	90	950
7	100	1300

6 Avionics Design of the Drone

The avionics component design plays a crucial role in building the drone, encompassing essential electronic components for communication and navigation. The flight controller, acting as the master controller, ensures stability, orientation, and movements of the drone using real-time data from the gyroscope and magnetometers [8, 9]. The electronic speed controllers (ESCs) regulate power to the motors, enabling control of motor speed and direction through pulse with module (PWM) signals [10]. A 5200 m Ah battery powers the distribution board, supplying current to the ESCs [11]. The receiver collects commands from the transmitter and sends them to the flight controller for motions like throttle, pitch, yaw, and roll. Additionally, an external servomotor activates the MICU bay door. The APM controller interprets commands and controls the drone's motions by varying motor speeds via the ESCs [12, 13]. An external GPS provides location data for GPS-enabled flight modes, enhancing navigation capabilities (Fig. 17).

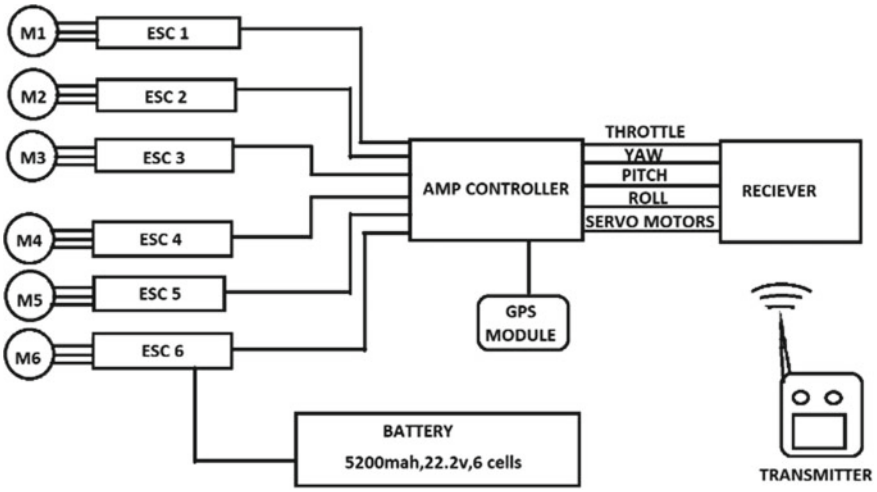


Fig. 17 Circuit connection for the complete avionics systems

7 Motor Configuration and Motions of Hexacopter

The hexacopter drone has six motors rotating the propellers to generate lift which would be sufficient to put the drone in air. All the motions of the hexacopter depend on variation of speed of each thruster (Table 3).

The motors are numbered as following in the given Fig. 18 (Table 4).

7.1 Climb and Descent

For throttle up, all motors should be in same speed and can be used to increase or decrease using a potentiometer.

So, to lift up, all the motors need to increase at a same time, and to land down, all the motors need to decrease at a same time.

Table 3 Position of motors and direction of rotation of bird ambulance drone

Motor number	Position of the motor	Direction of the motor rotation
M1	Front left motor	Anti-clock wise direction
M2	Front right motor	Clock wise direction
M3	Right motor	Anti-clock wise direction
M4	Rear right motor	Clock wise direction
M5	Rear left motor	Anti-clock wise direction
M6	Left motor	Clock wise direction

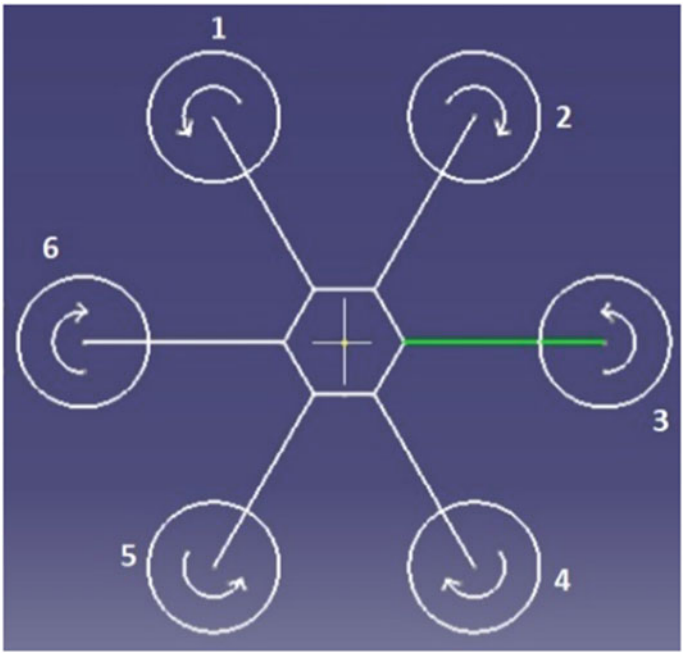


Fig. 18 Directions of the six motors

Table 4 Various propulsive movements of bird ambulance drone

Motor number	Throttle		Pitch		Roll		Yaw	
	Up	Down	Forward	Backward	Left	Right	Left	Right
M1	↑	↓	↓	↑	↓	↑	↓	↑
M2	↑	↓	↓	↑	↑	↓	↑	↓
M3	↑	↓	↑	↑	↑	↓	↓	↑
M4	↑	↓	↑	↓	↑	↓	↑	↓
M5	↑	↓	↑	↓	↓	↑	↓	↑
M6	↑	↓	↑	↑	↓	↑	↑	↓

7.2 Pitching Motion

Pitch Forward motion, i.e., When the drone needs to move forward, M1 and M2 motors should have their RPM decreased, while M3, M4, M5, and M6 motors should have their RPM increased.

Pitch Backward motion, i.e., When the drone needs to move backward, M1, M2, M3, and M6 motors should have their RPM increased, while M4 and M5 motors should have their RPM decreased.

7.3 Rolling Motion

Roll Left motion, i.e., When the drone needs to move left, M1, M5, and M6 motors should have their RPM decreased, while M2, M3, and M4 motors should have their RPM increased.

Roll Right motion, i.e., When the drone needs to move right, M2, M3, and M4 motors should have their RPM decreased, while M1, M5, and, M6 motors should have their RPM increased.

7.4 Yawing Motion

Yaw Left motion, i.e., When the drone needs to rotate about its vertical axis in left (anticlockwise turn from top view of the drone), M1, M3, and M5 should have their RPM decreased, and M2, M4, and M6 should have their RPM increased.

Yaw Right motion, i.e., When the drone needs to rotate about its vertical axis in right (clockwise turn from top view of the drone), M1, M3, and M5 should have their RPM increased, and M2, M4, and M6 should have their RPM decreased.

8 APM Flight Controller Calibration

Calibrating an APM (ArduPilot Mega) flight controller is crucial for ensuring accurate and stable performance of your drone. Below is a step-by-step guide to calibrate the APM flight controller:

1. **Connect Hardware**: First, connect the APM flight controller to your computer via a USB cable. Ensure that all other hardware components, such as motors, ESCs, and sensors, are connected properly.
2. **Install Mission Planner**: Download and install Mission Planner, which is a ground control station software for APM-based drones. It allows you to configure and calibrate the flight controller.
3. **Connect Mission Planner**: Launch Mission Planner and establish a connection with your APM flight controller by clicking on the "Connect" button in the top-right corner of the interface.
4. **Select Vehicle**: Once connected, select the appropriate vehicle type from the dropdown menu in Mission Planner. For example, choose "Hexacopter X" if you have a quadcopter.
5. **Configure Hardware**: Navigate to the "Initial Setup" menu in Mission Planner and click on "Wizard." Follow the instructions to configure your hardware, including radio control setup, accelerometer calibration, and compass calibration.

6. **Compass Calibration**: This step is crucial for accurate heading information. Choose "Compass" from the "Calibration" tab and follow the on-screen instructions to calibrate the compass. Rotate the drone in all three axes to ensure proper calibration.
7. **Accelerometer Calibration**: Accurate accelerometer calibration is essential for level flight. Select "Accelerometer" from the "Calibration" tab and follow the instructions to calibrate the accelerometer. Place the drone in different orientations during calibration.
8. **Radio Control Calibration**: Proper radio calibration ensures accurate control of your drone. Select "Radio Calibration" from the "Calibration" tab and follow the on-screen instructions to calibrate the radio control inputs.
9. **ESC Calibration**: If you are using electronic speed controllers (ESCs) for your motors, calibrate them to ensure proper throttle control. Follow the manufacturer's instructions for ESC calibration.
10. **Flight Modes**: Configure your flight modes in Mission Planner, defining the behavior of your drone in different flight modes (e.g., stabilize, loiter, and RTL).
11. **Safety Checks**: Before flying, conduct a pre-flight checklist, including verifying GPS lock, checking battery levels, and ensuring all systems are functioning correctly.
12. **Test Flight**: Perform a test flight in an open area, away from obstacles and people. Gradually test different flight modes and ensure the drone responds as expected.
13. **Fine-tuning**: After the test flight, fine-tune the flight controller parameters, such as PID gains, to optimize flight performance (Fig. 19).



Fig. 19 Bird ambulance drone side view

9 Addressing Challenges in Wildlife Conservation and Rescue Operations: The Necessity of Bird Ambulance Drone Development

The development of a bird ambulance drone is necessary to address critical challenges in wildlife conservation and rescue operations. Wildlife faces numerous threats, such as habitat loss, pollution, climate change, and human-induced accidents [14]. When animals get injured or stranded, timely assistance is crucial for their survival and rehabilitation. Traditional rescue methods often face limitations in reaching remote or challenging terrain, leading to delays and reduced chances of successful intervention [15]. The bird ambulance drone, with its unique capabilities and advancements in drone technology, offers a promising solution to overcome these challenges and effectively aid wildlife in distress [16].

9.1 Swift Response to Emergencies

One of the key reasons for developing a bird ambulance drone is its ability to provide swift responses to wildlife emergencies. Unlike ground-based rescue teams, drones can navigate through difficult terrain and bypass obstacles, allowing for faster access to the injured or stranded animals. This rapid response can significantly increase the chances of successful rescue and treatment.

9.2 Access to Remote Areas

Wildlife often gets injured or stranded in remote and inaccessible areas, making it difficult for traditional rescue teams to reach them in a timely manner. The bird ambulance drone, equipped with intelligent navigation capabilities and GPS technology, can fly to these remote locations, reaching animals in need of assistance even in challenging environments.

9.3 Ethical Treatment of Wildlife

The development of a bird ambulance drone aligns with the ethical treatment of wildlife. It emphasizes treating birds and animals equally, recognizing their pain and lives as valuable. By using technology to provide aid to wildlife, the drone ensures that injured or distressed animals receive prompt care and attention, minimizing suffering and increasing the chances of survival.

9.4 Real-Time Monitoring and Communication

The integration of APM flight controllers in the bird ambulance drone enables real-time monitoring of the drone's position, altitude, and speed. This data, coupled with video streaming capabilities, allows rescue teams to remotely assess the situation and communicate with on-site personnel to provide guidance and instructions during rescue operations.

9.5 Adaptability to Various Terrains

The bird ambulance drone's versatility allows it to operate in diverse terrains, including forests, mountains, wetlands, and urban areas. This adaptability broadens the scope of wildlife rescue operations, making it a valuable tool for conservation efforts across different ecosystems.

9.6 Cost-Effectiveness

Compared to traditional rescue methods that may involve extensive resources and personnel, the bird ambulance drone offers a cost-effective solution. It can cover large areas and respond to multiple incidents efficiently, optimizing resource utilization and reducing overall operational costs.

9.7 Data Collection and Research

Beyond rescue operations, the bird ambulance drone can serve as a valuable tool for data collection and research in wildlife conservation. Equipped with various sensors, it can gather information on wildlife populations, habitat conditions, and environmental factors, aiding conservation efforts and scientific studies.

9.8 Reducing Human Interference

Drones can minimize human interference during rescue operations, reducing stress on the rescued animals and ensuring that they can recuperate in a more natural and less disturbed environment.

10 Results and Discussion

ArduPilot Mega (APM) flight controller is an open-source software that provides GPS-based waypoint navigation, auto-stabilization, and data logging. It allows for precise and accurate navigation, real-time monitoring of the drone's location, speed, and altitude, and the ability to program custom flight paths for bird ambulance drones. Research has shown that APM is successful in navigating in difficult situations and delivering medical supplies precisely and accurately to remote locations. The bird ambulance drone is a promising technology with potential for wildlife conservation and rescue. It is equipped with a carbon fiber frame, high-torque motors, APM flight controller, GPS module, power module, shock absorbers, receiver, flight distribution board, and 5200 m Ah 6 s battery. With further research and development, it could significantly improve the success rate of bird rescue operations. The drone built and tested for this manuscript has limited payload capabilities, and further the research would proceed to the higher payload capacities to save bigger animals and birds as well.

The bird or the animal ambulance has the payload bay as mobile intensive care unit (MICU). The provision is enough to place injured birds or animals comfortable up to 5 kg. Figure 20 shows the top view of bird ambulance drone, the MICU unit has been perfectly placed within the frame of the drone. Battery has placed such that the center gravity of the drone is perfectly balanced. Carbon fiber frame is protecting the MICU unit and the electrical components.

In Fig. 21 front view of drone with payload bay open condition has been shown.

Skid-type landing gear is provided to drone's frame for safe landing and takeoff, and between this MICU unit is placed.

Though the range is limited by the transmitter, in this case the GPS guided mission using the check points in the Mission Planner Firmware would guide the guide out of range as well, provided the GPS signal does not get lost (Fig. 21).

The payload capability limitation is 5 kg, because of which only the birds and animals which are under 5 kg in total weight alone could be saved using this drone.

11 Conclusion

The APM flight control in the bird ambulance drone played the major role in navigating and stabilizing the drone completely, and data logging is also possible. The APM flight controller was configured by its own firmware which was open source that made the mission operation easy to work with. As the flight controller had inbuilt sensors with it, helped in navigating through the waypoints accurately. Also, the carbon fiber body gave the high strength-to-weight ratio, which made the drone agile. In future with huge payload capability, the application could be extended to human-based medical emergency operations as well.

Novelty in Research Work:



Fig. 20 Bird ambulance drone with MICU

This is the first time in the world a platform for birds has been designed and demonstrated for the medical purposes of birds and animals. This research work is unique, and the researchers have not attempted to build drone for such purposes.



Fig. 21 Completely built bird or animal ambulance drone

Funding Not applicable.

References

1. Das I, Roy S, Dey S, Dey T, Roy P (2022) Emergency medical assistance by ambulance drone using machine learning, light-weight cryptography and variable image steganography. In: 2022 IEEE VLSI device circuit and system (VLSI DCS). IEEE, pp 134–138
2. Sankararaman V, Suresh S (2019) Design and development of an unmanned aerial vehicle for wildlife conservation. Int J Innov Technol Explor Eng 8(8S):391–396. https://doi.org/10.35940/ijitee.K1371.0988S19

3. Abeynayake C, Jayatunga Y, Kularatne K, Jasinghe M (2019) Application of unmanned aerial vehicles in wildlife conservation: a review. Int J Sci Technol Res 8(11):3133–3141. https://doi.org/10.14257/ijast.2019.8.11.05
4. Grzonka S, Stachura K, Szeląg M (2018) Navigation of a UAV in a challenging environment using the ArduPilot platform. Appl Sci 8(8):1349. https://doi.org/10.3390/app8081349
5. Goh C, Toh Y, Tan R (2018) Autonomous delivery of medical supplies using unmanned aerial vehicles. J Intell Rob Syst 91(1):65–77. https://doi.org/10.1007/s10846-017-0731-5
6. Kumar C (2018) Design and implementation of a bird ambulance drone for wildlife conservation. Int J Sci Res Comput Sci Eng (IJSRCSE) 6(3):36–42
7. NC AV, Yadav AR, Mehta D, Belani J, Chauhan RR (2022) A guide to novice for proper selection of the components of drone for specific applications. Mater Today: Proc 65:3617–3622
8. Cheng Z, West R, Einstein C (2018) End-to-end analysis and design of a drone flight controller. IEEE Trans Comput Aided Des Integr Circuits Syst 37(11):2404–2415
9. Ebeid E, Skriver M, Terkildsen KH, Jensen K, Schultz UP (2018) A survey of open-source UAV flight controllers and flight simulators. Microproc Microsyst 61:11–20
10. Gorospe GE, Kulkarni CS, Hogge E, Hsu A, Ownby N (2017) A study of the degradation of electronic speed controllers for brushless dc motors. In: Asia Pacific conference of the prognostics and health management society 2017 (No. ARC-E-DAA-TN42858)
11. Gong A, MacNeill R, Verstraete D (2018) Performance testing and modeling of a brushless dc motor, electronic speed controller and propeller for a small uav application. In: 2018 joint propulsion conference, p 4584
12. Prakosa JA, Samokhvalov DV, Ponce GR, Al-Mahturi FS (2019) Speed control of brushless dc motor for quad copter drone ground test. In: 2019 IEEE conference of Russian young researchers in electrical and electronic engineering (EIConRus). IEEE, pp 644–648
13. Green CR, McDonald RA (2015) Modeling and test of the efficiency of electronic speed controllers for brushless dc motors. In: 15th AIAA aviation technology, integration, and operations conference, p 3191
14. Ramiro-Martinez J, Parra-Fernandez I, Oilero A (2019) An intelligent UAV system for wild bird rescue operations. J Intell Rob Syst 95(1):205–222
15. Jeong-ah K, Jin-Ho K, Yoon-Soo C (2016) Development of a rescue drone for injured birds. J Korean Soc Precision Eng (JKSPE) 33(8):653–658
16. Hemalatha N, Kalyani STMSSKK (2017) Design and development of an unmanned aerial vehicle for wildlife monitoring and conservation. Int J Sci Res Comput Sci Eng (IJSRCSE) 5(4):86–91

Parametric Studies of an Un-Guided Rocket Using Simple Point-Mass Trajectory Simulation Model



Mardav Panwar, Srinivasa Rao Gorrepati, and Manish Kumar Chauhan

Abstract In the current study, point-mass trajectory simulation model (PM-TSM) has been developed using MATLAB. Parametric studies of an un-guided rocket at user given parameters and launch conditions were performed as a part of system studies for an un-guided rocket. While conducting parametric studies, a total of 39 cases were studied for GRAD, artillery rocket with varying launch conditions. It is found that GRAD performed better than S-13 T un-guided aerial launched rocket system at 1000 and 2000-m launch altitude with launch angle of 10 and 0 degrees, respectively. The range achieved by GRAD was more than 4000 m, which is considered as the maximum range of S-13 T rockets.

Keywords Un-guided rockets · System Study · Point mass—trajectory simulation model (PM-TSM) · GRAD · S-13 T · Equations of motion for point mass model

1 Introduction

Pre-requisites to design and development for any kind of rocket lie in parametric studies that are used in order to establish performance approximations and predictions for mission objective and requirement. Among various methods to perform parametric analysis, some utilise computational methods for various system studies such as computational fluid dynamics, six degrees of freedom model and point-mass model. Among these, initial approximations are done using a point-mass model where trajectory of a rocket is plotted in a range versus altitude graph along with various plots of other variables against time which help in visualising the rocket performance as a point-mass entity.

There are many contributors in the field of parametric system studies, some of which are paper on 'Six-Degree-of-Freedom Digital Simulations for Missile Guidance, Navigation, and Control' by 'Patricia A. Hawley and Ross A. Blauwkamp', published in 2010 [1] and a paper on 'PROJECTILE MOTION USING MATLAB'

M. Panwar (✉) · S. R. Gorrepati · M. K. Chauhan
Defence Technology, Amity Institute of Defence Technology, Amity University, Noida, India
e-mail: mardav120298@gmail.com

© The Author(s), under exclusive license to Springer Nature Singapore Pte Ltd. 2024

S. Singh et al. (eds.), *Recent Advances in Aerospace Engineering*, Lecture Notes in Mechanical Engineering, https://doi.org/10.1007/978-981-97-1306-6_14

by ‘A. Clara Dhanemozhi’ published in 2015 [2]. Other work done on similar topics included thesis titled ‘Multistage 2-DOF rocket trajectory simulation program for freshmen level engineering students’, by ‘Zachery Doucet’ [3], published in ‘8-9-2019’as a part of Mississippi State University Scholars Junction, this had a script for a trajectory simulation of multistage rocket for 2-degrees of freedom, and this script played a vital role as an inspiration for writing the script in MALAB for this paper.

The equations which form the soul of this script are simplified from of equations of motion obtained in point-mass model discussed in a book titled ‘BALLISTICS Theory and Design of Guns and Ammunition’, by ‘Donald E. Carlucci’ and ‘Sidney S. Jacobson’ [4].

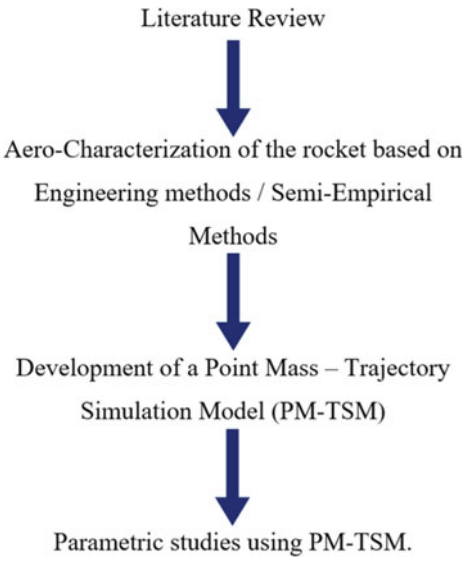
This paper aims in development of a simplified MATLAB script to perform trajectory simulation of a point mass of an un-guided rocket to get performance results of various parameters in form of 2-D plots against time and a 2-D plot of range verses altitude.

Developed in 1960s by Soviet Union, GRAD is one of the most commonly used ground launch, multiple launch rocket system across the globe and has a maximum range of 20 km. Whereas S13-T is aerial launched, un-guided rocket system of the same era and was equipped on HIND, Mi-28, Su-27 and other fighter aircrafts that were developed during that time.

Although there has been enhancement in GRAD as an enhanced range variant was developed later on to increase its range to 40 km. There were no studies or information found during the literature survey regarding the conversion of same for aerial delivered platform. Hence, the current work is focussed on the parametric studies of GRAD when it is launched from air at a certain altitude.

2 Methodology

The general methodology followed during the work for this paper can be depicted as follows.



3 Point-Mass Model

Theory behind point-mass model lies in the equations that are required to be understood and then utilised as the core of the script that will be running in the program. On one side Fig. 1 shows the motion of free-body rocket launched from the ground. Whereas using another free-body diagram of Fig. 2 helps us to understand how forces are distributed in vertical and horizontal axis which further helps us to derive the final governing equations of the point mass on which this m-script is based.

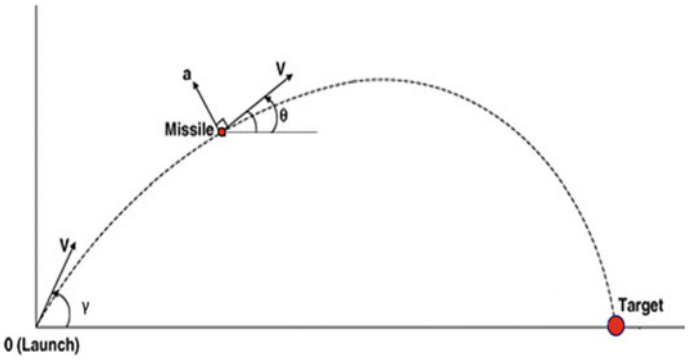


Fig. 1 Trajectory of a ground launched rocket system

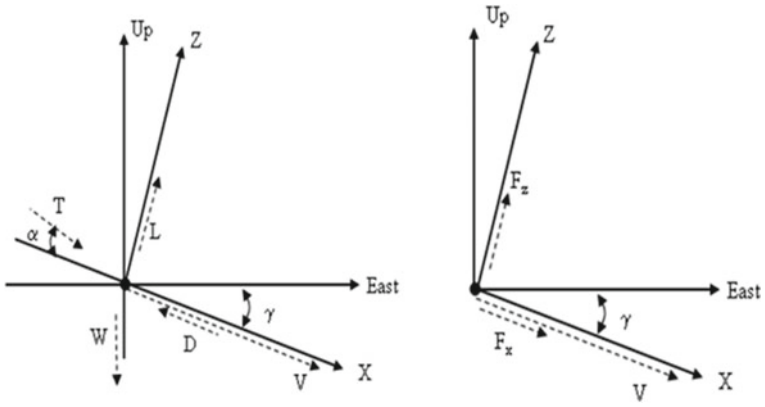


Fig. 2 Free-body diagram of a body in atmospheric free stream

After this, the equation of motion on which point-mass model is based can be written with respect to theta and velocity and continuous variables which provides an opportunity to denote the four equations as:

Equations Used

- $\dot{X} = v \times \cos\theta$
- $\dot{z} = v \times \sin\theta$
- $\dot{\theta} = -g \times \frac{\cos\theta}{v}$
- $\dot{v} = \frac{(\text{Thrust} - 0.5 \times \rho \times v^2 \times S_{\text{ref}} \times \text{Cd})}{\text{Total mass} - g \times \sin\theta}$

After understanding the equation behind the point-mass trajectory simulation model, a m-script was developed for performing parametric studies for un-guided rockets using point-mass equations. This script is used to study the performance of an un-guided rocket using 2-D plots and output of the PM-TSM model, observed as results of simulations.

4 Simulation Work

The best way to know accuracy of script is to test it, for this the method opted was to identify and tabulate parameters for the 'grad'[5] rocket system which was developed by Soviet Union in early 1960s by the use of available open-source information and then after assuming these parameters as anonymous case performing analysis for the Southern case to test performance of this system by changing launch angle and attitude for various stimulations and then using these results to check if the nominal case can provide better performance than aerial launched S-13 [6] rocket system which is of same calibre as 'GRAD' and has similar weight as well. The inputs used

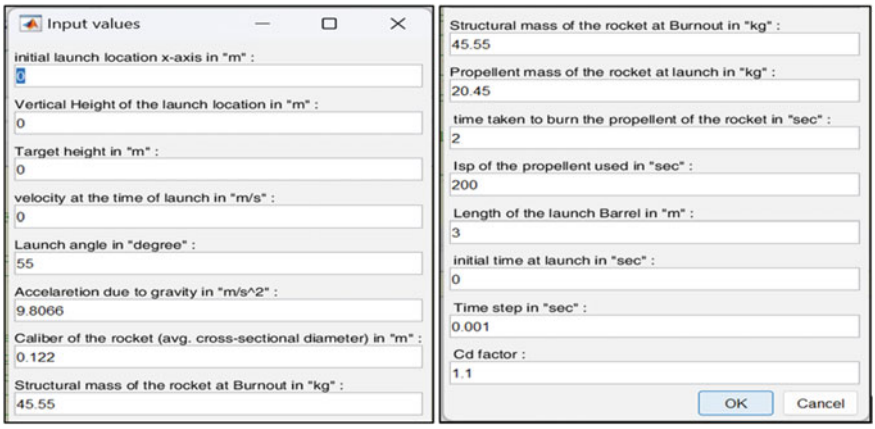


Fig. 3 Input of GRAD (original (open-source))

for 'GRAD' are discussed in Fig. 3 and are also mentioned as inputs on the right side of table one discussing the results of the nominal case.

5 Results

5.1 Parametric Study of GRAD with Data Collected Using Openly Available Sources

The results of running a case in PM TSM are opened in form of four grafts and an excel sheet, and the graphs are discussed in Figs. 4, 5, 6 and 7, where the first graph represents range versus altitude, the second graph represents time versus theta, the third graph represents time vs. velocity, and the fourth graph represents time vs Mach number.

5.2 Parametric Studies of a Nominal Case with Various Launch Angles and Altitude

For this part of the study, it is ideal to keep the rocket parameters as constant while taking multiple simulations while changing altitude and launch angles.

To do this, a nominal case has been selected to be simulated, and the results of the same are tabulated in Table 1.

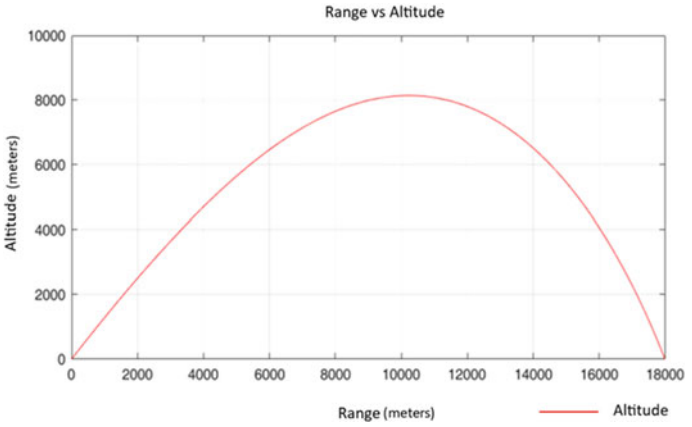


Fig. 4 Altitude variation over range

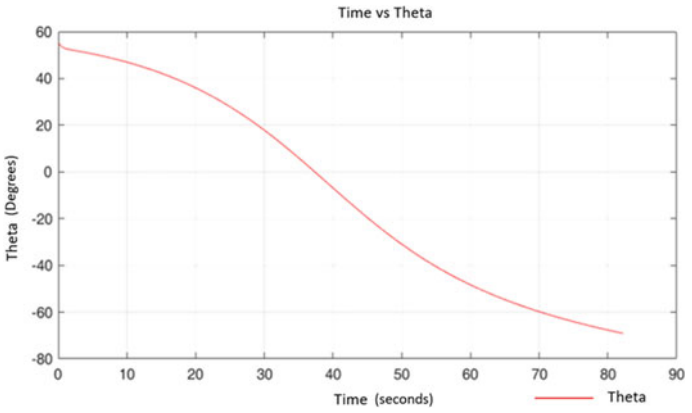


Fig. 5 Theta variation over time

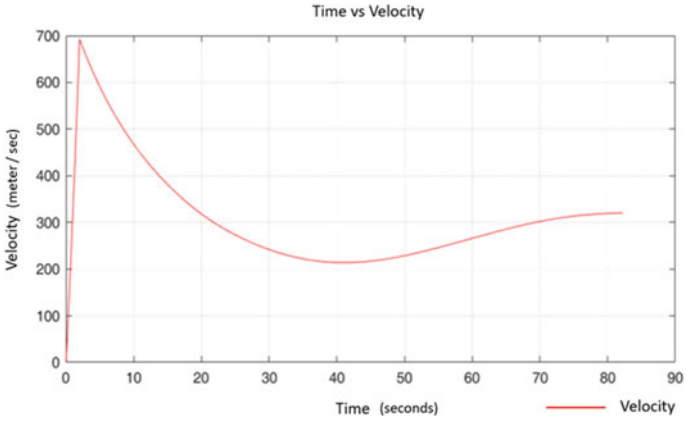


Fig. 6 Velocity variation over time

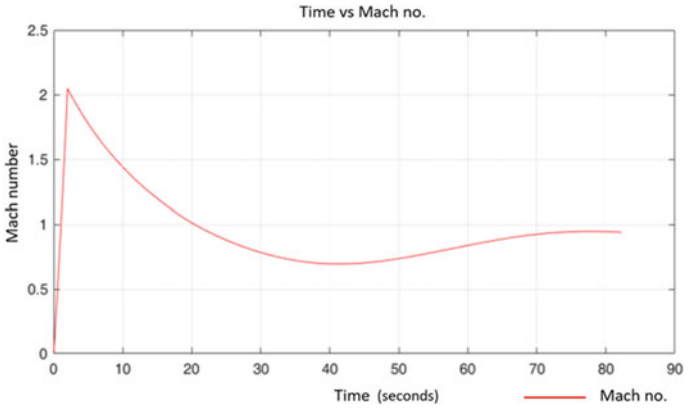


Fig. 7 Mach number variation over time

Table 1 Results of nominal case at variable altitude and launch angles

S No.	Launch altitude	Launch angle	Flight time	Range	Vertex	Peak velocity	Parameter	Value
–	(m)	(°)	(s)	(m)	(m)	(m/s)	Isp	200
a	0	55	79.477	16,408.68278	7621.5019	689.9601447	Propellent weight	20.45
1	500	− 10	2.4986	905.9549	500.0000	715.9465	Structural weight	45.55
2		0	3.1091	1362.7222	500.0000	713.3190	Total weight	66
3		10	4.7982	2497.5558	500.0001	710.3840	Cd factor	1.1
4	1000	− 10	3.9530	1766.8382	1000.0000	716.8474	Time step	0.001
5		0	5.1482	2606.3644	1000.0000	714.2094	Burn time	2
6		10	8.1647	4434.6045	1000.0001	711.2628		
7	2000	− 10	6.9227	3384.1710	2000.0000	718.5346		
8		0	9.2002	4816.3433	2000.0000	715.8766	Similar to S-13	
9		10	14.1329	7373.9863	2000.0001	712.9081		
10	3000	− 10	9.9145	4871.7955	3000.0000	720.0755		
11		0	13.1198	6725.2295	3000.0000	717.3989		
12		10	19.2964	9621.4163	3000.0001	714.4098		
13	4000	− 10	12.8665	6246.6117	4000.0000	721.4775		
14		0	16.8360	8411.2098	4000.0000	718.7835		
15		10	23.8413	11,505.7920	4000.0001	715.7754		
16	5000	− 10	15.7339	7527.9136	5000.0000	722.7479		
17		0	20.3197	9937.7357	5000.0000	720.0379		
18		10	27.9007	13,186.0060	5000.0001	717.0121		
19	6000	− 10	18.4879	8734.1091	6000.0000	723.8940		
20		0	23.5676	11,352.1100	6000.0000	721.1692		
21		10	31.5659	14,746.5658	6000.0001	718.1270		
22	7000	− 10	21.1132	9881.4614	7000.0000	724.9228		
23		0	26.5896	12,688.1662	7000.0000	722.1842		
24		10	34.9020	16,235.6976	7000.0001	719.1270		
25	8000	− 10	23.6035	10,983.2426	8000.0000	725.8412		
26		0	29.4008	13,969.5906	8000.0000	723.0900		
27		10	37.9575	17,682.2336	8000.0001	720.0189		
28	9000	− 10	25.9591	12,050.0378	9000.0000	726.6559		
29		0	32.0180	15,212.8464	9000.0000	723.8932		
30		10	40.7695	19,103.7346	9000.0001	720.8094		

(continued)

Table 1 (continued)

S No.	Launch altitude	Launch angle	Flight time	Range	Vertex	Peak velocity	Parameter	Value
–	(m)	(°)	(s)	(m)	(m)	(m/s)	Isp	200
31	10,000	− 10	28.1839	13,089.8623	10,000.0000	727.3735		
32		0	34.4579	16,429.2131	10,000.0000	724.6002		
33		10	43.3675	20,510.7362	10,000.0001	721.5047		
34	11,000	− 10	30.2847	14,108.8612	11,000.0000	728.0002		
35		0	36.7365	17,626.2837	11,000.0000	725.2173		
36		10	45.7759	21,909.2181	11,000.0001	722.1113		
37	12,000	− 10	32.2658	15,112.7187	12,000.0000	728.6144		
38		0	38.8650	18,812.0845	12,000.0000	725.8267		
39		10	48.0107	23,310.4803	12,000.0001	722.7153		

6 Conclusion

The results obtained from the system studies using PM-TSM for un-guided rockets provide the following conclusion.

Point-mass trajectory simulation model (PM-TSM) was developed for system studies for un-guided rockets, for parametric studies and analysis of performance of an un-guided rocket, and study of 39 cases was taken into consideration with various launch conditions including launch angle varying from $-10°$ to $+ 10°$ and launch altitude varying from 0 to 12000 m.

Parametric studies using point-mass trajectory simulation model (PM-TSM) were performed for un-guided GRAD, artillery launch rocket. During the parametric studies, GRAD surpassed performance of S-13 un-guided aerial launched rocket, of the same calibre as GRAD, for which, during literature review maximum range of S-13 T rocket system was found to be 4000 m, and GRAD at launch altitude of 1000 and 2000 m at launch angles $+ 10°$ and $0°$, respectively, surpassed the 4000 m mark which is the max range of S-13 T.

Funding Not applicable.

References

1. Hawley PA, Blauwkamp RA (2010) Six-degree-of-freedom digital simulations for missile guidance, navigation, and control, Johns Hopkins Apl Tech Dig 29(1)
2. Clara Dhanemozhi A (2015) Projectile motion using Matlab. Int J Sci Technol Manag 4(1)
3. Doucet Z (2019) Multistage 2-DOF rocket trajectory simulation program for freshmen level engineering students; thesis
4. BALLISTICS theory and design of guns and ammunition. In: Carlucci DE, Jacobson SS (eds) 3rd Edn

5. http://characterisationexplosiveweapons.org/studies/annex-a-122-mm-mbrl/. Last accessed 14 May 2023
6. http://roe.ru/eng/catalog/aerospace-systems/air-to-air-missile/s-13-t/. Last accessed 14 May 2023

Microstructural Analysis of Mg/CNT Surface Composite Using Friction Stir Processing



Eesha Tolety, Anmol Gupta, Narender Singh, Rajesh Kumar Saluja, and Neeraj Kumar Gahlot

Abstract The ongoing demand for lightweight materials is a more promising example of a growth trend in aeronautical and automotive uses. Recently, carbon nanotubes with better mechanical properties are highly desirable for developing some advanced composites. Magnesium has tremendous potential to improve mechanical properties when used in composites due to its wide range of lightweight material properties. Consequently, a magnesium composite was developed by adding carbon nanotubes (CNTs) as reinforcement in a magnesium matrix. A modified form of the friction stir processing (FSP) technology was used to generate the composite to improve CNT dispersion. The perforations in the structure were spaced at 10-mm and 20-mm intervals. Furthermore, the effect of carbon nanotubes was studied and validated using various characterizations. The existence of native phases of the material was confirmed by X-ray fluorescence (XRF) research. The presence of carbon, magnesium, and oxygen elements in the XRF graph indicated that CNTs were implanted during fabrication. Scanning electron microscopy (SEM) was also performed to validate the visual structure of the CNTs, and a consistent distribution was seen across the sample. The hardness test was performed, which indicated that both specimens have more microhardness than the pure Mg. As a result, it has been found that surface composites produced with a higher percentage of CNTs exhibit better microhardness.

Keywords Carbon nanotubes · Composite · Friction stir process · Morphology · Magnesium

Abbreviation

Mg	Magnesium
Al	Aluminium
MgO	*Magnesium oxide*

E. Tolety · A. Gupta · N. Singh (✉) · R. K. Saluja · N. K. Gahlot
Amity Institute of Aerospace Engineering, Amity University Noida, Noida, UP, India
e-mail: ngoyat@amity.edu

© The Author(s), under exclusive license to Springer Nature Singapore Pte Ltd. 2024

S. Singh et al. (eds.), *Recent Advances in Aerospace Engineering*, Lecture Notes in Mechanical Engineering, https://doi.org/10.1007/978-981-97-1306-6_15

Al_2O_3	Aluminium oxide
SiC	Silicon carbide
TiB_2	Titanium boride
MOS_2	Molybdenum disulphide
CNTs	Carbon nanotubes
FSP	Friction stir processing
SEM	Scanning electron microscope
XRF	X-ray fluorescence
FSW	Friction stir welding

1 Introduction

In the past few decades, the demand for the reduction of energy consumption and greenhouse gas emissions in many industries such as aerospace and automobile has increased the research of lightweight and high-strength materials [1]. Composite materials are multi-phase engineering materials developed by combining two or more different materials with dissimilar compositions and properties to create remarkable materials without affecting the chemical composition or basic identity of the primary material. As a result, rather than being the result of a chemical process, composites are the result of physically mixed materials being well fused. Metal matrix composites (MMCs), a form of synthetic composite, can meet a variety of technical requirements including high tensile strength, improved strength-to-weight ratio, high fatigue strength, and high corrosion resistance [2, 3]. Most researchers [4, 5] employ lightweight materials like magnesium (Mg) and aluminium (Al) as the metal matrix for producing efficient composites because of their superior strength-to-weight ratios. Carbon nanotubes (CNTs) have received greater attention recently because they contain a specific allotrope of carbon with a high aspect ratio and remarkable optical, thermal, electrical, magnetic, and mechanical properties [6, 7]. It first appeared as multiple layers of concentric graphitic sheet nanotubes, defined as MWCNTs. In the typical arrangement, the graphitic layer has a spacing of about 0.34 nm between the cylinders and is composed of 2–50 graphitic sheets wrapped around helical coaxial cylinders with diameters of 2–100 nm. This specific structure of carbon allocation enables unique and exceptional physical properties that encourage it to achieve superior hardness and strength. The enhancement of the properties is dependent on several factors such as uniform distribution of the reinforcement, reinforcement factor and phase, and composite porosity content and many more [8–11]. All these factors are affected by the production process. Developing a cost-effective and factors enhancement fabrication techniques is a necessary problem to be solved.

Recently, a technique for the surface modification is getting much recognition, named friction stir processing (FSP) [12]. This process is done in the same manner as the friction stir welding (FSW). In this process, there is a rotating tool which works on the sample piece and produces a highly deformed zone because of heat produced

by friction. It is known that fractioned area consists of fine grains due to the dynamic recrystallization [13, 14]. Though FSP is mainly used for grain refinement, it is also appealing process for fabrication of process. Al/SiC composite fabricated using FSP by Mishra et [15, 16] reported that there is a uniform distribution of SiC particles in the Al matrix, and the bonding was reported to be good. Eskandari et al. [17] indicated that Al alloy matrix and TiB_2 and Al_2O_3 nanoparticles as reinforcement have shown high wear resistance, high specific strength, and high elasticity on surface composite which was due to uniform distribution and bonding observed from SEM imaging. Ramesh et al. [18] based on reports, the B_4C particles' uniform dispersion enhanced the hardness of the material to 1.5 times that of the basic metal. Mahmud et al. [19] examined whether the Al_2O_3 particles were surrounded by tiny spaces and whether the reinforced particles were dispersed equally. Zadeh et al. [20] found that the top surface was discovered to be extremely smooth from the SEM pictures, and flaws like voids and fractures were not noticed. Particles of SiC and MOS_2 were discovered to be evenly distributed throughout the whole surface.

It is clear from the above discussion that limited study has been done to advance the magnesium composite. Consequently, the author interested in investigating the significant effect of CNTs on the Mg composite by potentially changing the CNT weight percentage fabricated using FSP. Further analysis included SEM, XRF, and mechanical characteristics based on macrohardness.

2 Materials and Methods

The base material used in this investigation was obtained from the NextGen industry. It is magnesium of 99.8% purity, with dimension of 10 × 10 × 100 mm. Commercially available multi-walled CNTs with the following specifications were used: length of 10 μm, inner diameter of 10–20 nm, outer diameter of 30–50 nm, and surface area of 250–300 m^2/g. The FSP device employed was constructed of tool steel and had a cylindrical shape with a shoulder (9 mm) and a pin (3 mm, length: 1.5 mm). The dimension of the device was chosen based on the existing literature. Figure 1 displays the schematic diagram for Mg, CNT, and the tool used for FSW.

The CNTs that were obtained in powder form are difficult to distribute uniformly in the matrix due to their inherent entanglement. Two different methods were used for this. As shown in Fig. 2, a circular groove with a diameter of 2 mm and a depth of 1 mm was made at a distance of 10 mm and 20 mm on the magnesium pieces. The grooves were made using the FSP tool and milling tool.

Then, the grooves were subsequently filled with CNTs, and the embedding process was completed with FSP tool and CNC machine (Fig. 3). A fixture (3 mm) is then attached to the machine and pin near the start end of the Mg piece. The tool is then programmed to rotate on a constant speed of 900 rpm and feed speed of 5 mm/min with no tool tilt angle.

The FSP magnesium samples were than polished using the same machine. The distribution of CNT amongst the samples was observed on SEM imaging (ZEISS).



Fig. 1 Raw materials used for fabrication **a** Mg, **b** CNT, and **c** FSP tool

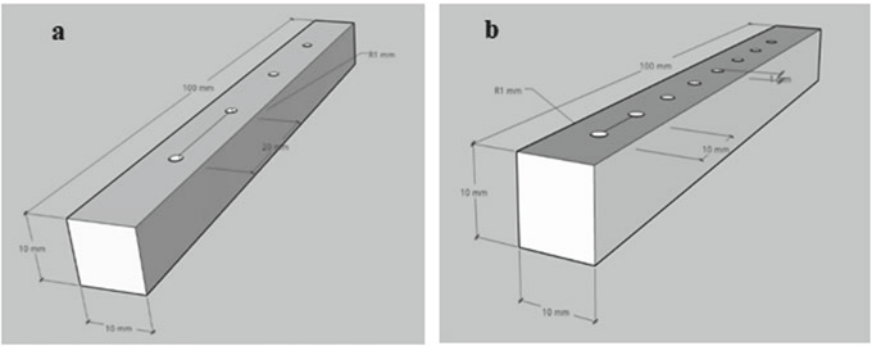


Fig. 2 Representation of specimens having **a** 10 mm, and **b** 20 mm



Fig. 3 **a** CNC machine, and **b** fabricated specimen through FSP

The evidence of the presence of and weight percentage of carbon content in the FSP samples have been obtained from the XRF analysis. These analyses were done to show that there is better mixing of CNT in the sample to produce Mg/CNT sample.

3 Results and Discussion

The graph (Fig. 4) represents the XRF analysis, conducted for two samples, one having holes at a distance of 10 mm and the other one having 20 mm. It represents the presence of carbon, magnesium, and oxygen at their respective intensities and energy levels.

Table 1 shows that the sample with grooves at a distance of 10 mm has greater content of carbon then 20-mm distanced grooves, as there is obvious more addition of CNT during the procedure. It has been observed that oxygen is present, with indications suggesting that it is likely in the form of magnesium oxide (MgO). Compound MgO is found due to environmental interaction. Some studies show that Mg interaction with environment over times causes MgO. Also, there are studies showing that MgO in the composite has not affected the strength rather has increased in some cases [20].

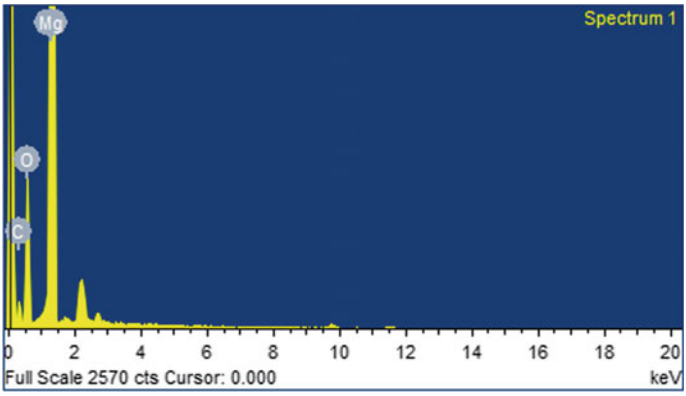


Fig. 4 XRF pattern for CNT/Mg composite

Table 1 Data obtained from XRF analysis

Element	Groove at 20 mm (Wt.%)	Groove at 10 mm (Wt. %)
C	9.63	16.44
O	28.21	24.77
Mg	62.16	58.79
Total	100.00	100.00

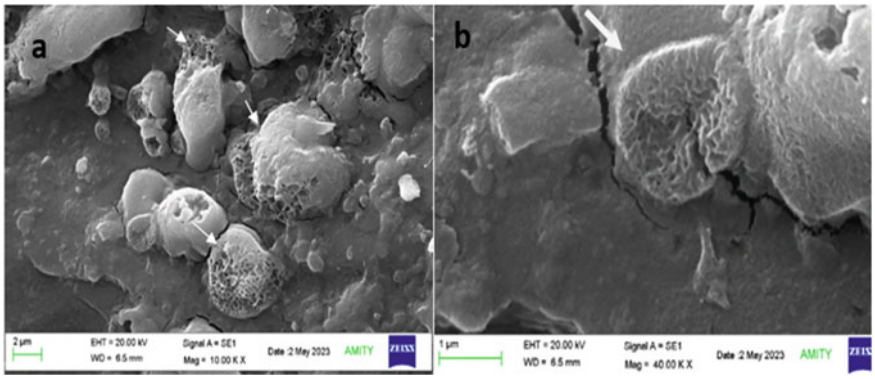


Fig. 5 SEM analysis of the specimen

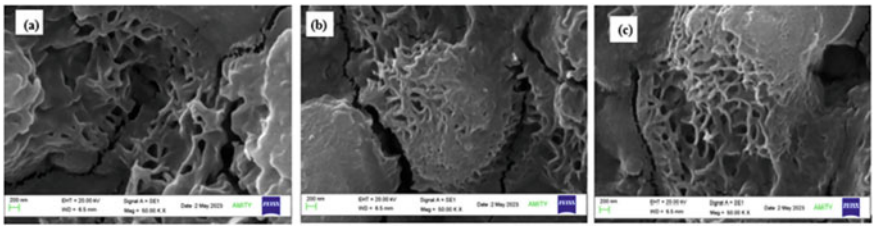


Fig. 6 Magnified image of MWCNT embedded into Mg

Figures 5 and 6 show SEM images of the samples and magnified image of MWCNT embedded into Mg, which show the dispersion of the MWCNT. From the image, it is clearly visible that tube-like structures are CNT, where half of them is embedded into Mg samples. Figure 6 shows a magnified image of MWCNT which is implanted in Mg. Figure 6 is SEM imaging at same magnification at different areas showing that the MWCNT is distributed throughout the sample uniformly. The value of the microhardness that is recorded is 48 Hv and 55 Hv, respectively, for 20 mm distance and 10 mm distance surface composites. The microhardness of the magnesium is 40 Hv without FSP. The macrohardness has been increased significantly by addition of CNT and FSP process.

4 Conclusion

The Mg/CNT surface composite was successfully produced by new and optimized FSP. The microstructure of the composite is investigated by XRF and SEM imaging. The results obtained are as follows:

- MWCNTs are dispersed into the Mg of 99.8 purity using the FSP and optimized method.
- The low travel speed of the tool aided in proper embedding of the MWCNT in Mg pieces.
- From XRF, it could be confirmed that the sample consisted of CNT by the amount of carbon. Also, we could observe that samples where the holes were made with 20 mm have more carbon content than 10 mm.
- SEM imaging could confirm that MWCNTs were in fact embedded in Mg along the length of the sample. Also, we could see the uniform distribution obtained by this FSP process.

Funding Not applicable.

References

1. Hou J, Du W, Parande G, Gupta M, Li S (2019) Significantly enhancing the strength + ductility combination of Mg-9Al alloy using multi-walled carbon nanotubes. J Alloys Compd 790:974–982. https://doi.org/10.1016/j.jallcom.2019.03.243
2. Rashad M, Pan F, Zhang J, Asif M (2015) Use of high energy ball milling to study the role of graphene nanoplatelets and carbon nanotubes reinforced magnesium alloy. J Alloys Compd 646:223–232. https://doi.org/10.1016/j.jallcom.2015.06.051
3. Wang Q, Du W, Liu K, Wang Z, Li S, Wen K (2013) Microstructure, texture and mechanical properties of as-extruded Mg–Zn–Er alloys. Mater Sci Eng A 581:31–38. https://doi.org/10.1016/j.msea.2013.05.055
4. Han GQ et al (2016) The influence of CNTs on the microstructure and ductility of CNT/Mg composites. Mater Lett 181:300–304. https://doi.org/10.1016/j.matlet.2016.06.021
5. Rashad M, Pan F, Asif M (2016) Exploring mechanical behavior of Mg–6Zn alloy reinforced with graphene nanoplatelets. Mater Sci Eng A 649:263–269. https://doi.org/10.1016/j.msea.2015.10.009
6. Barnett MR, Ghaderi A, Quinta da Fonseca J, Robson JD (2014) Influence of orientation on twin nucleation and growth at low strains in a magnesium alloy. Acta Mater 80:380–391. https://doi.org/10.1016/j.actamat.2014.07.013
7. Zhang L, Liu C-G, Wang H-Y, Nan X-L, Liu G-J, Jiang Q-C (2014) Slip-induced texture evolution of rolled Mg–6Al–3Sn alloy during uniaxial tension along rolling and transverse directions. Mater Sci Eng A 597:376–380. https://doi.org/10.1016/j.msea.2013.12.082
8. Mohan VB, Lau K, Hui D, Bhattacharyya D (2018) Graphene-based materials and their composites: a review on production, applications and product limitations. Compos Part B Eng 142:200–220. https://doi.org/10.1016/j.compositesb.2018.01.013
9. Güler Ö, Bağcı N (2020) A short review on mechanical properties of graphene reinforced metal matrix composites. J Mater Res Technol 9(3):6808–6833. https://doi.org/10.1016/j.jmrt.2020.01.077
10. Turan ME, Sun Y, Aydin F, Zengin H, Turen Y, Ahlatci H (2018) Effects of carbonaceous reinforcements on microstructure and corrosion properties of magnesium matrix composites. Mater Chem Phys 218:182–188. https://doi.org/10.1016/j.matchemphys.2018.07.050
11. Chalisgaonkar R (2020) Insight in applications, manufacturing and corrosion behaviour of magnesium and its alloys—a review. Mater Today Proc 26:1060–1071. https://doi.org/10.1016/j.matpr.2020.02.211

12. Zass K, Mabuwa S, Msomi V (2022) A review on reinforced particles used on the production of FSP composites. Mater Today Proc 56:2392–2397. https://doi.org/10.1016/j.matpr.2021.12.210
13. Sagar Å, et al (2014) Effect of tool on tensile strength in single and double sided friction stir welding 4(11):1–6
14. Mishra RS, Ma ZY (2005) Friction stir welding and processing. Mater Sci Eng R Rep 50(1):1–78. https://doi.org/10.1016/j.mser.2005.07.001
15. Puviyarasan M, Kumar VSS (2012) Optimization of friction stir process parameters in fabricating AA6061/SiCp composites. Procedia Eng 38:1094–1103. https://doi.org/10.1016/j.proeng.2012.06.138
16. Yadav P, Sharma P, Singh N (2014) Material on wire electric discharge 5(1):525–534
17. Eskandari H, Taheri R (2015) A novel technique for development of aluminum alloy matrix/TiB2/Al2O3 hybrid surface nanocomposite by friction stir processing. Procedia Mater Sci 11:503–508. https://doi.org/10.1016/j.mspro.2015.11.080
18. Gupta A, Singh P, Gulati P, Shukla DK (2015) Effect of tool rotation speed and feed rate on the formation of tunnel defect in friction stir processing of AZ31 magnesium alloy. Mater Today Proc 2(4):3463–3470. https://doi.org/10.1016/j.matpr.2015.07.322
19. Mahmoud ERI, Takahashi M, Shibayanagi T, Ikeuchi K (2010) Wear characteristics of surface-hybrid-MMCs layer fabricated on aluminum plate by friction stir processing. Wear 268(9):1111–1121. https://doi.org/10.1016/j.wear.2010.01.005
20. Alidokht SA, Abdollah-zadeh A, Soleymani S, Assadi H (2011) Microstructure and tribological performance of an aluminium alloy based hybrid composite produced by friction stir processing. Mater Des 32(5):2727–2733. https://doi.org/10.1016/j.matdes.2011.01.021

Multilayer Microstrip Antenna for Broadband Monopulse Tracking Technique



Vrajesh Panchal, Neha Arora, and Vijay Borkar

Abstract The current work proposes a single element of a microstrip patch array antenna that is performing well as a prominent radiation patch element and can be developed for monopulse tracking systems like seeker applications due to its broad bandwidth, effective directional pattern, low-profile conformal design, low cost, and ease of manufacturing. A single unit of a multilayer aperture-coupled microstrip antenna has been developed for the X-band frequency range with a bandwidth of 1 GHz. The single element of a multilayer antenna structure is designed to obtain a low return loss, wider bandwidth, better directivity, and better gain. For a multilayer microstrip antenna that operates at the center frequency of 10.9 GHz, the return loss of − 42 dB with 6.3 dBi gain, having VSWR < 1.5, has been achieved by analyzing using the CST Microwave Studio EM Simulator.

Keywords Microstrip antenna · Multilayer · Aperture coupling · Monopulse tracking · Missile seeker

1 Introduction

A microstrip patch antenna is a single unit that operates on electromagnetic wave propagation and radiation principles. It is fed an RF signal that carries the data that the antenna will broadcast or receive through a feedline. The metallic patch of the microstrip antenna is carefully selected in size and shape to resonate at a certain frequency. When an RF signal is applied to the patch, it causes it to resonate at its

V. Panchal (✉) · N. Arora
Amity Institute of Defence Technology, Amity University, Noida, Uttar Pradesh, India
e-mail: vrajeshpanchal03@gmail.com

N. Arora
e-mail: narora2@amity.edu

V. Borkar
Ex-Technology Director, Bharat Forge Limited, Hyderabad, India
e-mail: vgborkar1@rediffmail.com

© The Author(s), under exclusive license to Springer Nature Singapore Pte Ltd. 2024

S. Singh et al. (eds.), *Recent Advances in Aerospace Engineering*, Lecture Notes in Mechanical Engineering, https://doi.org/10.1007/978-981-97-1306-6_16

resonance frequency, resulting in the distribution of electric current throughout its surface. The electromagnetic field created by the microstrip patch antenna radiates outward into free space, and the antenna's radiation pattern may be modified by changing the size and shape of the patch. Microstrip patch antennas provide several benefits, such as their small size, simplicity of integration, compatibility with planar array designs, capability over a wide frequency range, and good radiation characteristics. For these reasons, they are preferred choices for monopulse tracking systems, offering a consistent and accurate angle of arrival data in a compact and cost-effective package.

Monopulse tracking is a method of radar tracking that can track a target reliably in both azimuth and elevation. Multiple receptive antennas or antenna components are employed in monopulse tracking to capture the echoes or signals reflected from the target at the same time. Typically, such antennas are organized in a specified form, like a linear or planar array. To extract useful information about the target's position and velocity, the monopulse tracking approach compares received signals from different antennas. The system can correctly estimate the angle of arrival (AoA) of the target by analyzing the phase and amplitude variations between the signals. The main idea underlying monopulse tracking is to generate two or more parallel beams that are significantly offset from one another. These beams are created by mixing signals from multiple antennas that have distinct phase relationships. These signals are then merged in a specific circuit known as a monopulse comparator to produce an error signal that may be used to track the target [1]. The error signal represents the angle difference between the target and the radar antenna's axis [2]. Monopulse tracking systems analyze incoming signals and derive angle of deviation data using advanced signal processing techniques such as fast Fourier transforms (FFT) and correlation algorithms [3]. The signals have been analyzed to produce an error signal, which is then sent to a servomotor for autonomous target tracking. The advantages of a monopulse tracking system are fast speed, high precision, and single pulse target estimate. This is often used in services like air traffic management, missile guidance, and radar-based navigation.

Monopulse tracking systems can also utilize Yagi–Uda antennas, horn antennas, and parabolic reflector antennas in addition to microstrip patch antennas. However, microstrip patch antennas are frequently employed because of their miniature size, which simplifies the construction and alignment of the linear array which may be created to give a broad bandwidth and regulate the radiation pattern by modifying the form, size, and feeding mechanisms of the patches. Multilayer microstrip patch antennas have been preferred in many situations where single-layer microstrip patch antennas may not match the needed criteria due to their better performance, miniaturization, design flexibility, integration possibilities, and high-power handling capabilities. One of the most significant drawbacks of microstrip patch antennas is their low bandwidth. This challenge is solved by the aperture-connected multilayer microstrip patch antenna [4].

A multilayer microstrip patch antenna is one having at least two dielectric layers and a radiating patch on the top layer. The antenna operates on the microstrip transmission line principle, with the patch functioning as a resonator emitting electromagnetic waves. Multilayer microstrip patch antennas outperform single-layer designs in terms of performance parameters such as greater bandwidth, increased radiation efficiency, and higher directivity. The use of a multilayer structure allows for more effective energy coupling from the feed system to the radiating element, resulting in higher directivity and higher radiation efficiency. Aperture coupling is a technique used in microstrip antennas in which the input or feed is given to the bottom or ground layer microstrip element. Because it is directly at the bottom of the main radiating patch, we will use a slot or small pin in the middle of layers as an aperture so that the energy can be coupled. One of the most notable benefits of using aperture coupling in multilayer systems is that it provides an efficient direct coupling technique for powering the radiating patch or element [5]. The feed to the patch element, positioned at top of the first substrate, is facilitated via a rectangular slot situated on the ground plane between the two substrates, with the feed element located at the underside of the lower substrate. This configuration, employing aperture coupling, demonstrates superior performance compared to a coaxial feeding. However, there are certain limitations to utilizing this feeding approach to produce an antenna, such as the slot or pin that links the energy between the feed line and the radiating element, which must be carefully inspected.

Currently, various studies and research on multilayer microstrip antennas have been undertaken. The author's research in [6, 7] depicts that the antenna, when utilized with the aperture-linked staked patch, shows the projected high gain and broad frequencies such as in L-band and C-band applications. Anandkumar and Sangeetha [8] represents that the antenna will have an advantage over the multilayered patch in that it not only enhances bandwidth but also acts as a dual band with an air gap ranging from 1 to 5 mm between the single and apertured-linked antennas. Anjaneyulu and Siddartha Varma [9] and Jothilakshmi et al. [10] show the presence of H-shaped, uneven X-shaped, and I-shaped etching slots on the ground plane which results in the energy transfer between the feed and stacked patch. Jin et al. [11] use a microstrip slot coupling feeding structure to provide monopulse performance while maintaining a low profile, compact volume, simple construction, and ease of integration. Similarly, the authors in [12] explain that it may be accomplished with a lot more investigation by employing coaxial feeding. Hemant Kumar and Kumar [13] represent the multilayer monopulse antenna array with coaxial feeding which shows that coaxial feeding can mostly use for aircraft applications that gives high gain in X-band frequency. The primary goal of this research is to explore, create, and develop with increased performance utilizing the aperture coupling feeding approach, which can also be utilized for monopulse tracking for seeker applications in radar fields.

This research work is mainly focused on the monopulse tracking technique used for missile seekers. A missile seeker is an important component of a guided missile system because it detects, tracks, and locks onto a target. Monopulse tracking is used to detect any deviations or uncertainties in the location of the target relative to the

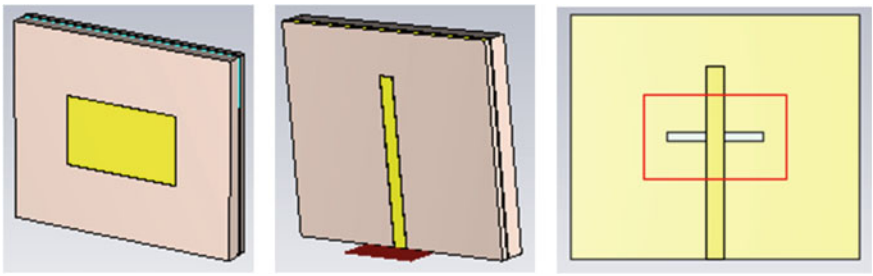
missile's line of sight [14]. This allows the missile to maintain a tight lock on the intended target throughout the engagement, increasing the chances of a successful strike. Other than missile seekers, monopulse tracking antennas are also widely used in air traffic control (ATC) radar systems for precise aircraft tracking and observation [15]. They allow for exact tracking of aircraft locations, speeds, and angles of departure from the radar's line of sight. Meteorological radar systems employ them to track and monitor weather-related phenomena such as precipitation, storms, and tornadoes [16]. They are also employed in marine navigation radars for ship traffic management, collision avoidance, and harbor monitoring [17]. They allow for vessel monitoring and give critical information for safe sailing. They are also used in space tracking systems to track satellites, space debris, and other things in space since they allow for exact monitoring of a space object's position, orbit, and attitude.

The rest of the paper is organized as follows: Sect. 2 presents the design of the proposed antenna and suggested antenna data, and simulation analyses have been provided in Sect. 3. Section 4 summarizes the proposed work.

2 Design of Antenna

The proposed multilayer single antenna element is designed for the X-band frequency range, which operates at the center frequency of 10.9 GHz and has a return loss of − 42 dB with 6.3 dBi gain and a VSWR < 1.5 with 6.57 dBi directivity with an *E*-plane beam width of 76.2° and an *H*-plane beam width of 100.8°.

The schematic diagram of the proposed multilayer antenna design is shown in the below figures. Figure 1 depicts several perspectives of the proposed multilayer microstrip antenna. The front view depicts the antenna's top layer, the radiating patch, while the rear view depicts the antenna's bottom layer, the feed line, and the rear view with the slot depicts the connection from the feed line to the radiating patch via the slot in the ground plate.



(a) Front view **(b)** Rear view **(c)** Rear view with slot

Fig. 1 Schematic diagram of the proposed antenna

Table 1 Antenna layers description

Antenna layers	Material	Dimensions (mm)
Rectangle radiating patch	Copper	$L = 5.36$ $W = 9.12$ $H = 0.035$
Radiating patch substrate	RO4003C	$L = 15.44$ $W = 18.26$ $H = 1.422$
Bond ply	RO4450B	$L = 15.44$ $W = 18.26$ $H = 0.101$
Ground plate	Copper	$L = 15.44$ $W = 18.26$ $H = 0.035$
Slot in ground plate	–	$L = 6$ $W = 0.6$ $H = 0.035$
Feed substrate	RO4350B	$L = 15.44$ $W = 18.26$ $H = 0.508$
Feed line	Copper	$L = 12.22$ $W = 1.11$ $H = 0.035$

The materials used for each layer, as well as the dimensions of the proposed multilayer microstrip antenna, have been presented in Table 1.

The initial layer of a multilayer microstrip antenna, as shown in Fig. 2, is a copper radiating patch. The second layer is the radiating patch substrate made of RO4003C material, and the third layer is the bond ply made of RO4450B material, which is utilized to bind the radiating patch substrate to the ground plate, which is made of various materials. The fourth layer is a ground plate made of copper with a slit for aperture connection. The fifth layer is the RO4350B feed substrate, used for connecting the radiating elements and the feed network. Finally, the sixth layer is a copper feed line that is utilized to transfer RF signals to the feed substrate layer.

The feeding transmission technique employed for this multilayer microstrip antenna is aperture coupling, in which the port is linked to a microstrip patch that serves as a feed line on the antenna's bottom side. To make this aperture coupling technique work efficiently and effectively and make the top layer microstrip plane radiate, a slot has been created on the ground plane between the bond ply and feed substrate, in order that the RF signal given as an input to the feed line will resonate by means of the slot to excite the radiating element.

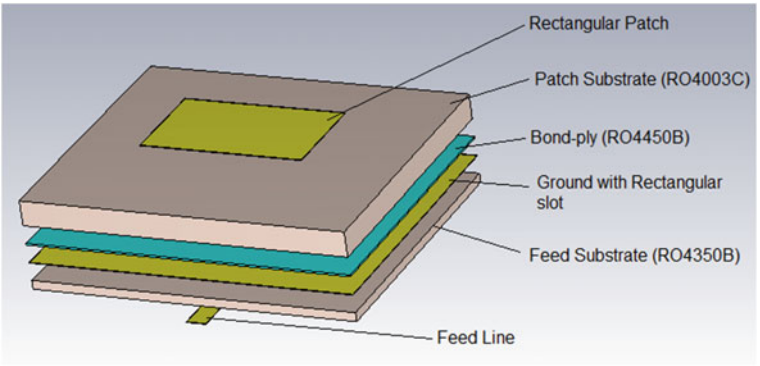


Fig. 2 Anatomy of the proposed antenna

3 Results and Discussion

The antenna performance has been examined in this section, covering the S-parameter, gain, 2-D and 3-D radiation transmission, and surface current.

A. *S*-Parameter

The proposed antenna's *S*-parameter can be obtained using CST microwave studio. Figure 3 depicts the simulated and measured S11 parameter (reflection coefficient) findings. This multilayer patch antenna has 1 GHz of bandwidth from 10.4 to 11.4 GHz and returns a loss of − 42 dB at 10.9 GHz as operating frequency by taking − 10 dB as an ideal value [13].

B. Gain

Figure 4 shown below shows the gain plot of patch antenna obtained through simulation in CST. Throughout the broad bandwidth, a good gain is achieved which is greater than 5 dBi and it has a peak gain of 6.55 dBi.

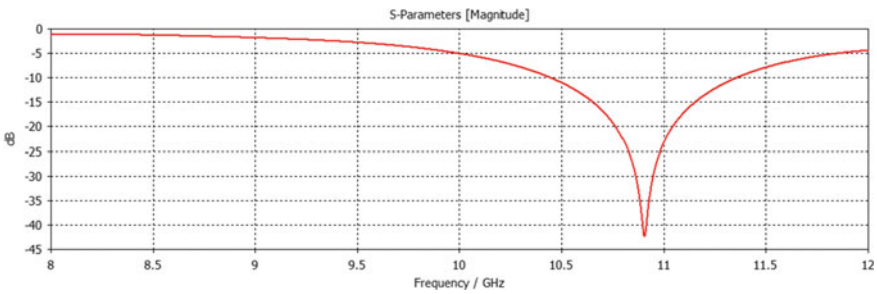


Fig. 3 S11 plot

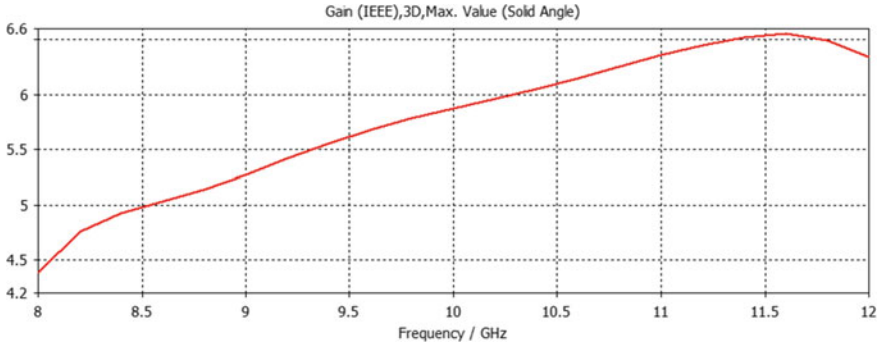
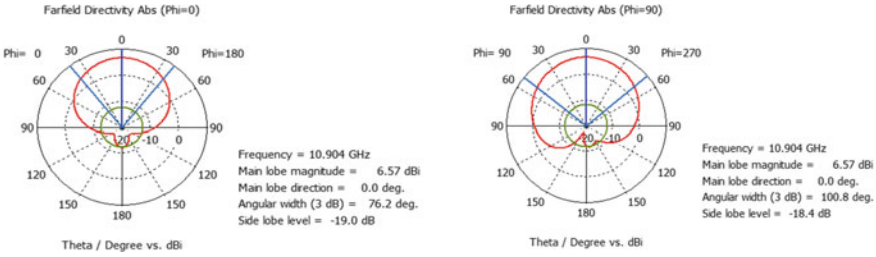


Fig. 4 Gain plot



(a) At φ = 0° **(b)** At φ = 90°

Fig. 5 2-D radiation pattern

C. 2-D Radiation Pattern

The 2-D radiation pattern, as shown in Fig. 5, represents the $\varphi = 0°$ and $\varphi = 90°$ plots, and here, it can be seen that the main lobe direction of 0° with a magnitude of 6.57 dBi, − 18.4 dB as a side lobe level has been achieved.

D. 3-D Radiation Pattern

The 3-D radiation pattern of the multilayer antenna is obtained through simulation in CST microwave studio. As shown in Fig. 6, it obtained the directional radiation pattern. This multilayer microstrip antenna provides directivity of 6.57 dBi and gain of 6.3 dBi at operating frequency of 10.9 GHz.

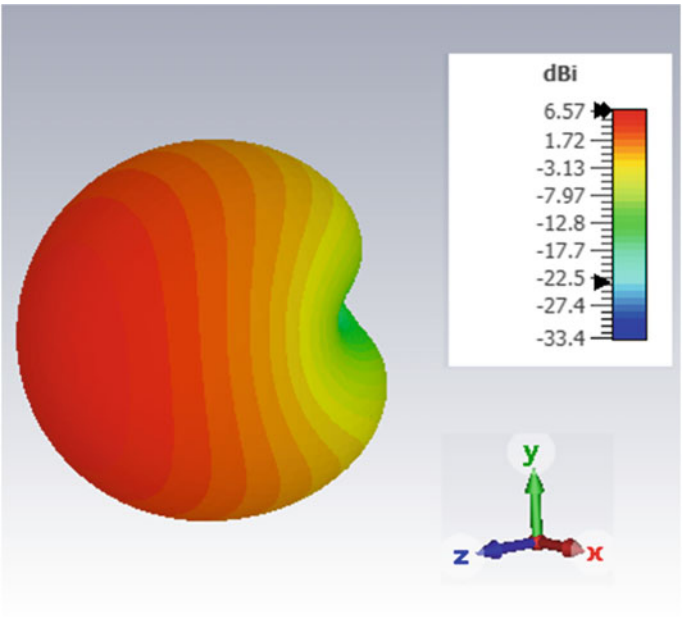


Fig. 6 3-D radiation pattern

4 Conclusion

This research work proposes a microstrip patch antenna with an aperture coupling approach that has a central frequency of 10.9 GHz and a broad bandwidth of 1 GHz and may be utilized as the central radiation patch element for an array. It is claimed that by analyzing its characteristics and optimizing the design parameters, it may be employed in monopulse tracking systems for *X*-band seeker applications due to its highly directive nature. To obtain different parameters as per the specific applications, it can be more optimized through the variations in the slot (aperture) configuration. The major performance parameters, such as antenna gain, bandwidth, and return loss, have been observed. The results indicate significant improvement in the desired performance parameters.

Funding Not applicable.

References

1. Alamdar S, Mohammadpour-Aghdam K, Khalili H, Mohammad-Taheri M (2018) A miniaturized broadband monopulse comparator with all DELTA channels nulling in Ku band. Int J Microwave Wireless Technol 10(9):1035–1041. https://doi.org/10.1017/s1759078718001071

2. Dey S, Sai Kiran N, Dey S (2020) Microstrip and SIW based monopulse comparators for microwave and millimeter wave applications. In: Proceedings of the 2020 international symposium on antennas and propagation (APSYM), Cochin, India, pp 114–117. https://doi.org/10.1109/APSYM50265.2020.9350710
3. Zhang X, Li Y, Yang X, Zheng L, Long T, Baker C (2017) A novel monopulse technique for adaptive phased array radar. Sensors 17(12):116. https://doi.org/10.3390/s17010116
4. Wang H, Fang DG (2006) Chen XG (2006) A compact single layer monopulse microstrip antenna array. IEEE Trans Antennas Propag 54(2):503–509. https://doi.org/10.1109/TAP.2005.863103
5. Lamminen AEI, Saily J, Vimpari AR (2008) 60-GHz patch antennas and arrays on LTCC with embedded-cavity substrates. IEEE Trans Antennas Propag 56(9):2865–2874. https://doi.org/10.1109/TAP.2008.927560
6. Bhattacharya S et al (2021) Aperture coupled stacked patch antenna for L-band applications. Microwave Opt Technol Lett 63(1):191–196
7. Kumar S, Dubey SK (2021) Design and analysis of a multi-layered microstrip antenna with aperture coupled feed for C-band applications. Int J Electr Commun 127:153–610
8. Anandkumar D, Sangeetha RG (2020) Design and analysis of aperture coupled micro strip patch antenna for radar applications. Int J Intell Netw 1:141–147. https://doi.org/10.1016/j.ijin.2020.11.002
9. Anjaneyulu G, Siddartha Varma J (2020) Design and analysis of slot coupled antenna on different dielectric materials. In: Lecture notes in electrical engineering, pp 409–415. https://doi.org/10.1007/978-981-15-2926-9_46
10. Jothilakshmi P, Bharanitharan J, Ramkumar V (2015) Design of multilayer aperture coupled stacked microstrip patch antenna for Wlan applications. ICTACT J Commun Technol 06(02):1105–1111
11. Jin G, Huang L, Liao S (2022) Monopulse substrate integrated waveguide collinear slot antenna array. In: Proceedings of the 2022 IEEE MTT-S international microwave workshop series on advanced materials and processes for RF and THz applications (IMWS-AMP), Guangzhou, China, pp 1–3. https://doi.org/10.1109/IMWS-AMP54652.2022.10107004
12. Karthik BR, Shanthi P (2022) Dielectric coupled microstrip patch multilayered antenna for wide scan application. In: Proceedings of the 2022 international conference on smart generation computing, communication and networking (SMART GENCON), Bangalore, India, pp 1–4. https://doi.org/10.1109/SMARTGENCON56628.2022.10083754
13. Kumar H, Kumar G (2018) Broadband monopulse microstrip antenna array for X-band monopulse tracking. IET Microwaves Antennas Propag 12(13):2109–2114. https://doi.org/10.1049/iet-map.2018.5332
14. Reddy AV, Borkar VG (2020) Design and simulation of microstrip branch line coupler and monopulse comparator for airborne radar applications. In: Advances in decision sciences, image processing, security and computer vision, ICETE, vol 2. Springer, New York, pp 10–18. https://doi.org/10.1007/978-3-030-24318-0_2
15. Bezoušek P, Schejbal V (2011) Monopulse secondary surveillance radar antenna for air traffic control. Perner's Contacts 6(4):21–28
16. Teshiba M et al (2007) A monopulse system: applications for weather radar observations. In: Proceedings of the 33rd conference on radar meteorology
17. Shirazi M, Safian R (2019) Wide-band series-fed patch antenna array with low side lobes. In: Proceedings of the 2019 IEEE international symposium on antennas and propagation and USNC-URSI radio science meeting, Atlanta, GA, USA, pp 1507–1508. https://doi.org/10.1109/APUSNCURSINRSM.2019.8888578

Experimental Determination of Heat of Combustion Values, Viscosity, Surface Tension and Density for Different Jet Fuel and 2-Propanol Blending



Arghya Paul, Anagh Mondal, and Pratim Kumar

Abstract In the present study, various samples of jet fuel blended with 2-propanol have been prepared in different ratios. All the samples were used for the determination of heat of combustion (ΔH_c, MJ/kg), and only one blending sample was chosen for determining the surface tension (σ, N/m), viscosity (μ, mmPa.s) and density (kg/m^3) values using different analytical instruments. We measured surface tension, viscosity and density and did comparison with pure jet fuel properties. Heat of combustion was measured using bomb calorimeter, surface tension was measured using stalagmometer, viscosity was measured using rotational viscometer, and density was measured using digital electronic weighing balance. All the obtained data are discussed in the form of table and graphs in the article. From the obtained results, it was observed that binary blending of jet fuel and 10% (by weight) 2-propanol is better in terms of heat of combustion values and may be utilized as alternative fuel. Some catalysts were also added in the fuels samples, but the results were not very encouraging. However, these catalysts can be used in nano-form or in gelled fuels for better results.

Keywords Heat of combustion · Surface tension · Viscosity · Jet fuel + 2-propanol · Alternative jet fuels

Abbreviations

W_1	Weight of the empty beaker
W_2	Weight of the liquid sample + beaker
V	Volume of liquid Sample
$\frac{(W_2-W_1)}{V}$	Density of liquid Sample
W_3	Weight empty + N_a drops of water
W_4	Weight of empty beaker + N_b drops of sample

A. Paul (✉) · A. Mondal · P. Kumar
Department of Aerospace Engineering of Applied Mechanics, IIEST, Shibpur, Howrah, India
e-mail: paularghya124@gmail.com

© The Author(s), under exclusive license to Springer Nature Singapore Pte Ltd. 2024

S. Singh et al. (eds.), *Recent Advances in Aerospace Engineering*, Lecture Notes in Mechanical Engineering, https://doi.org/10.1007/978-981-97-1306-6_17

W_a	Weight of water $= W_3 - W_1$
W_b	Weight of sample $= W_4 - W_1$
N_a	No. of drops of water
N_b	No. of drops of sample
Q	Heat of combustion of the sample
M	Mass of benzoic acid sample [g]
T	Temperature rise [°C]
E	Correction for nichrome wire (24 cal for 10 cm)
Jet A-1	Pure Jet fuel
J90/2-P10	90% Jet A-1 and 10% 2-propanol (by weight)
J80/2-P20	80% Jet A-1 and 20% 2-propanol (by weight)
J70/2-P30	70% Jet A-1 and 30% 2-propanol (by weight)
J60/2-P40	60% Jet A-1 and 40% 2-propanol (by weight)
J90/E10	90% Jet A-1 and 10% ethanol (by weight)
J80/E20	80% Jet A-1 and 20% ethanol (by weight)

1 Introduction

Global aviation industry is expanding at a faster rate than any other transport mode; hence, the energy demand is also increasing. In the present day, the global aviation sector devours ~ 5 million barrels of oil on a daily basis, constituting roughly 5.8% of the world's total oil consumption [1]. Projections indicate that the demand for jet fuel worldwide is expected to experience a substantial growth of 38% between 2008 and 2025, with an average annual growth rate of 1.9% [2]. As a result of this expansion, the fuel demand has increased a lot and meeting these demands is finally driving down environmental pollution. The emerging economies are the key drivers for global aviation fuel demand. Here, to meet this increasing demand, we are using fossil fuels which has pushed us toward the challenge of protecting our society from pollution and saving the biodiversity of this planet. To tackle this challenge, both the aviation industry and governments worldwide have been actively formulating pragmatic approaches by exploring non-conventional alternative jet fuels. These strategies are aimed at effectively addressing the increasing demand for aviation fuel while mitigating environmental concerns. Despite being a relatively small contributor compared to other sectors, the aviation industry is estimated to be responsible for ~ 2–3% of total CO_2 emissions and < 3% of transportation-related NO_x emissions [3]. However, it is crucial not to overlook the impact of this pollution. Aircraft engine exhaust contains similar emissions to those produced by ground transportation vehicles, including carbon monoxide (CO), carbon dioxide (CO_2), water vapor (H_2O), nitrogen oxides (NO_x), sulfur oxides (SO_x), unburned hydrocarbons (UHC) and particulate matter (PM). These emissions can be classified as greenhouse gases (GHGs), with the latter being recognized as a primary contributor to global climate change [4].

According to a study conducted by Turysbay and Toncu [5], it has been found that isopropanol exhibits remarkable characteristics in terms of emission control. Notably, it has the ability to minimize NO emissions by effectively regulating rapid heat release. The research suggests that even a slight 2° spark timing delay can result in a significant 10% reduction in NO_x emissions, along with a simultaneous decrease in HC and CO emissions. Furthermore, the implementation of isopropanol can also improve soot emissions by lowering air/fuel temperatures and preventing premature explosions. Overall, these findings highlight the potential of isopropanol as a valuable tool in reducing emissions and optimizing combustion efficiency.

Kumar and Karmakar [6] conducted a study to investigate the combustion characteristics of blends of butyl butyrate and Jet A-1 fuel. The study examined three different blends with varying butyl butyrate loading (10, 30 and 50%) under non-preheat and two preheat conditions (at 373 and 474 K) using a swirl stabilized burner. The researchers analyzed and compared various aspects of the combustion process, including qualitative information on the spray structure, true-color images of the flame, emission spectra, chemiluminescence, combustor temperature gradient, pattern factor and pollutant emissions. The findings indicated that butyl butyrate exhibits favorable physical properties for combustion, such as lower viscosity, making it somewhat superior to conventional Jet A-1 fuel. Additionally, the study suggested that blending 15–20% butyl butyrate with Jet A-1 fuel might be feasible without requiring engine modifications. This blending ratio was found to result in lower emissions of NO_x and CO, thus offering potential environmental benefits.

This paper aims to analyze the feasibility of usage of blending of alcohol and jet fuel in commercial aircraft from perspective of heat of combustion and also measure viscosity, surface tension and density. As per the report of Turysbay and Toncu [5], isopropanol is feasible as blending component of kerosene; hence, it can be used for commercial aviation fuel also, as kerosene is major component of aviation fuel. We chose isopropanol as alcohol and blended it with jet fuel at different ratios.

2 Methodology

2.1 Materials and Measuring

For experiments, jet fuel was provided by IIT Kgp for research purpose with legitimate approval. 2-propanol (99.9%) was procured from Merck Life Science Private Limited., Ethanol was procured from Changshu Hongsheng Fine Chemical Co. 2-propanol and ethanol were used as blending components, copper chromite, ferric oxide, cobalt oxide, cupric oxide all these components are used as oxidizer in the experiments, and these are available commercially. As many researchers reported, ethanol is an ideal candidate as a blending component of jet fuel [1]. So, here we have tried the blending of 2-propanol and jet fuel, and to enhance oxidation, we used

Table 1 Prepared blending composition of fuel

Serial no	Weight of jet fuel (%W/W)	Weight of isopropanol (%W/W)	Weight of ethanol (%W/W)	Weight of copper chromite (%W/W)	Weight of ferric oxide (%W/W)	Weight of cupric oxide (%W/W)	Weight of cobalt oxide (%W/W)
1	90	10	–	–	–	–	–
2	80	20	–	–	–	–	–
3	70	30	–	–	–	–	–
4	60	40	–	–	–	–	–
5	90	–	10	–	–	–	–
6	80	–	20	–	–	–	–
7	95	–	–	5	–	–	–
8	95	–	–	–	5	–	–
9	95	–	–	–	–	–	5
10	85	10	–	5	–	–	–
11	85	10	–	–	–	5	–
12	85	10	–	5	–	–	5

the above-mentioned oxidizer. We prepared four different binary fuel blends J90/2-P10, J80/2-P20, J70/2-P30 and J60/2-P40. To compare these results, we prepared two different types of binary fuel blends J90/E10 and J80/E20. We introduced three catalysts copper chromite, ferric oxide, cobalt oxide in pure jet fuel as following compositions—5% copper chromite and 95% jet fuel by weight, 5% ferric oxide and 95% jet fuel by weight and 5% cobalt oxide and 95% jet fuel by weight. Also, we performed experiments with blend fuel and catalyst. The compositions were as follows—we chose J90/2-P10 blend fuel as this shows better heating values than others. Hence, we introduced three different catalysts as 5% by weight. They are cobalt oxide, cupric oxide and copper chromite. For measuring purposes, we used digital weighing machine. We took 1 g as sample fuel and took measurement by weight (Table 1).

2.2 Combustion Using Bomb Calorimeter

To commence the experiment, an ~ 8-cm-long fuse wire with a known heat of combustion per unit length is connected to the two terminals. Subsequently, a 14-cm cotton thread is securely fastened to the fuse wire and immersed into the sample contained within the sample cup. The sample cup, along with the sample holder, is then placed into the bomb apparatus and tightly secured in place. After that, bomb is connected to the oxygen tank to pour oxygen into the bomb. We gave oxygen up to 27.2 atm. Then, the bomb was put in the can and started pouring water until the bomb was just poured. After that, the whole assembly was completed and kept in the jacket.

Temperature probe and stirrer machine were fitted into their respective positions, and microprocessor 3a was connected with the bomb to determine the rise in temperature of water. After that, the stirrer was turned on. We were waiting until the temperature came at constant. Then, through digital microprocessor, firing was done, and after 25–30 min, our experiment was completed.

2.3 Bomb Calorimeter

A well-known device to calculate heat of combustion of calorific value of a substance is bomb calorimeter. Here, heat of combustion of a substance denotes the content of energy in form of heat which is released when the substance undergoes a complete combustion. Combustion within bomb calorimeter takes place at constant volume adiabatic process because we must keep samples within a bomb (a sealed container) which is completely sealed and after that it is placed in the container filled with known amount of water. The heat liberated during the combustion is completely absorbed by the water and the calorimeter itself. For our experiment, we used microprocessor-based automatic bomb calorimeter provided by Labtronics (ISO 9001: 2008 certified), so calibration was done automatically. The water equivalent of calorimeter was obtained as 2441 cal/°C. All data were taken in triplicate and at ambient atmospheric condition. In all the cases, error was < 5%.

Heat of combustion can be calculated using the below formula [7]:

$$Q = \frac{(W \times T) - e}{m}$$

Here, Q = Heat of combustion of the sample
m = Mass of benzoic acid sample [g].
T = Temperature rise [°C].
e = Correction for nichrome wire (24 cal for 10 cm).



(a) microprocessor



(b) Automatic Bomb Calorimeter

2.4 Measurement of Viscosity

All liquid mixtures were measured by Anton Paar viscoQC viscometer [8]. It was calibrated with silicone grease in standard procedure. At first, set up the instrument at zero-level alignment with base. Then, a small cylindrical container was taken where the liquids (approx. 8 ml) were inserted. After checking the alignment of the instrument, the filled container was connected with the instrument. A rotating spindle with sensor was connected with both the instrument and cylinder. Then, a rotation speed of 150 rpm was set. All the data were taken from the instrument in triplicate at atmospheric condition. In all the cases, error was < 5%.

2.5 Measurement of Surface Tension

Using a transparent ISKO Boro 3.3 Straight Glass Stalagmometer [9], the surface tension of all liquid solutions was measured. All the experiments were performed in ambient atmospheric condition, and all the data were taken in triplicate. It was calibrated with water using standard calibration procedure. Drop weight method was applied. In this method, the weight of N liquid drops was measured while the liquid flowing through stalagmometer. At first, the measuring of pure distilled water was done, and then, the weight of the drop of sample liquid was taken. After that, by following formula, surface tension of the liquid was calculated. In all the cases, error was < 5%.

W_1 = Weight of empty beaker.
W_3 = Weight empty + N_a drops of water.
W_4 = Weight of empty beaker + N_b drops of sample.
W_a = Weight of water = $W_3 - W_1$.
W_b = Weight of sample = $W_4 - W_1$.
Surface tension of water = 0.072 N/m.
N_a = No. of drops of water.
N_b = No. of drops of sample.
Calculation

$$\text{Surface tension of sample} = \frac{W_b \times N_a \times 0.072}{W_a \times N_b}$$



(a) Anton Paar rotational Viscometer



(b) Stalagmometer

2.6 Density

The density of all liquid samples was measured analytically where we used digital analytical weighing balance, capacity 300 gm, accuracy 0.001 gm, pan size 90 mm for weight measurement of samples. At first, a definite volume of liquid solution sample was taken. Then, weight of the liquid solution sample was taken. After dividing the volume of liquid sample with its weight, we got the density of the liquid. We determined density of all samples in triplicate, and in all the cases, error was < 5%.

Weight of the empty beaker $= W_1$.

Weight of the liquid sample + beaker $= W_2$.

Volume of liquid Sample $= V$

$$\text{Density of liquid Sample} = \frac{(W_2 - W_1)}{V}$$

3 Result and Discussion

Nowadays, we all are very much concerned about pollution and global warming. Everyone is in a rush to find some sustainable solution. And fuel is one of the most crucial parts of pollution which cannot be ignored. Okoro et al. had determined heating values of blending of alcohols and pure kerosene, and they have reported only methanol and ethanol data. Here we have conducted our experiment to find the heat of combustion, surface tension, viscosity and density of blending isopropanol and jet fuel (both are commercially available). The characteristics of combustion are significantly influenced by the physical properties of the fuel. Consequently,

thorough testing of fuel properties becomes crucial, particularly when introducing a new fuel, especially one intended for use in the aviation sector as an alternative option. For better understanding and clarification, we divided our results into three sets as Set A, Set B and Set C where Set A: binary blending of isopropanol/jet fuel and ethanol/jet fuel.

Set B: Jet fuel and different catalyst mixtures.

Set C: J90/2-P10 and different catalyst mixtures.

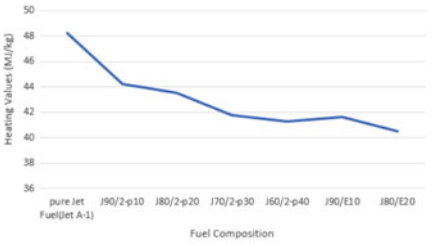
All of them are discussed below.

Set A

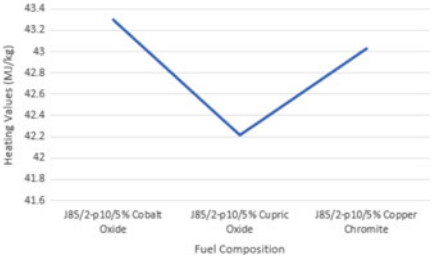
Table 2 represents the heat of combustion where the higher heating value of pure jet fuel is 48.2 MJ/kg which is the highest. Blending of jet fuel and isopropanol (2-propanol) represents as J/2-p. Blending of jet fuel and ethanol represents as J/E. The higher heating values of our prepared four different binary fuel blends are as follows: J90/2-P10 44.23 MJ/kg, J80/2-P20 43.49 MJ/kg, J70/2-P30 41.79 MJ/kg, J60/2-P40 41.27 MJ/kg. To compare these results, we prepared two different types of binary fuel blends J90/E10 41.66 MJ/kg and J80/E20 40.47 MJ/kg. As can be seen from Fig. 1a, it is a decreasing graph, and the reason behind this is the number of carbons.

Set B

We introduced three catalysts copper chromite, ferric oxide and cobalt oxide in pure jet fuel as following compositions—5% copper chromite and 95% jet fuel by weight, 5% ferric oxide and 95% jet fuel by weight and 5% cobalt oxide and 95% jet fuel by weight. All the catalysts were solid micron particles. When we mixed up the catalyst, it was not soluble in naked jet fuel, and also after combustion, it remained as it was. The higher heating values were as follows: 5% copper chromite and 95% jet fuel by weight 46.767 MJ/kg, 5% ferric oxide and 95% jet fuel by weight 42.83 MJ/kg and 5% cobalt oxide and 95% jet fuel by weight 43.79 MJ/kg.



(a) Plotting of Heat of Combustion values of Set A



(b) Plotting of Heat of Combustion values of Set C

Fig. 1 (**a**) Plotting of Heat of Combustion values of Set A (**b**) Plotting of Heat of Combustion values of Set C

Table 2 Results of heat of combustion, surface tension, viscosity and density of our blending fuel

Fuel composition	Heat of combustion (MJ/kg)	Surface tension (N/m)	Viscosity (mPa.s)	Density (kg/m^3)
Jet A-1	48.2	0.025	1.469	815.5
J90/2-P10	44.23	0.021	1.423	789
J80/2-P20	43.49	0.022	1.394	800
J70/2-P30	41.79	0.024	1.389	852.5
J60/2-P40	41.27	0.027	1.284	860
J90/E10	41.66	0.025	1.335	820
J80/E20	40.47	0.024	1.249	865
J95/5%copper chromite	46.767	–	–	–
J95/5%Ferric Oxide	42.83	–	–	–
J95/5% Cobalt Oxide	43.79	–	–	–
J85/2-P10/5%Cobalt Oxide	43.3	–	–	–
J85/2-P10/5%Cupric Oxide	42.215	–	–	–
J85/2-P10/5%Copper Chromite	43.03	–	–	–

Set C

Also, we performed experiments with blended fuel and catalyst. We chose J90/2-P10 blend fuel as this showed better heating values than others. Hence, we introduced three different catalysts as 5% by weight. They are cobalt oxide, cupric oxide and copper chromite. Here also, when we mixed up the catalyst, it was not soluble in blending jet fuel, and also after combustion, it remained as it was. The higher heating values were as follows: J90/2-P10 44.23 MJ/kg, J90/2-P10/5% cobalt oxide 43.3 MJ/kg, J90/2-P10/5% cupric oxide 42.215 MJ/kg, J90/2-P10/5% copper chromite 43.03 MJ/kg.

We also determined the surface tension, viscosity and density of pure jet fuel and binary blend of jet fuel with isopropanol and ethanol. As shown in Table 2, the dynamic viscosity decreases as the isopropanol content increases. This decrease can be attributed to the variation in viscosity and the ability of the components to wet the walls. The change in dynamic viscosity with isopropanol content is likely due to molecular rearrangement and reactions between components, particularly alkyl radicals, resulting in reduced viscosity and enhanced sliding between molecules.

This overall effect leads to improved rheological properties for the blends [5]. We did not perform the experiment of surface tension with catalyst because due to solid particle of catalyst, it got stuck in stalagmometer. Viscosity was not determined for catalyst mixed fuel, as catalyst used to settle down in the liquid fuel during viscosity measurement. This problem may be solved using nano-sized or gelled form catalyst.

4 Conclusion

We conducted our study to find out the suitability of isopropanol as a blending component with Jet A-1 fuel such that it can reduce the NOx and CO emissions than the conventional fuel (i.e., Jet A-1). We only determined the heat of combustion values, surface tension, viscosity and density. Here, in the case of binary blending J90/2-P10, which produced heat of combustion value 44.23 MJ/kg, it satisfies the ASTM standard (min. 42.8 MJ/kg) [3]. Also, it surpasses the heat of combustion values of JP-8 (43 MJ/kg) and Jet A (42.8 MJ/kg) [3]. Surpassing these standards indicates that it may have the potential to be used as alternative jet fuel. Hence, meeting these standards indicates that it can be investigated further that is it really reducing the greenhouse emissions or not. Although in a general comment, blending of alcohol with conventional jet fuel will reduce the NO_x and CO emission. Hence, this opens up the possibility of isopropanol as a suitable blending component of conventional jet fuel to use as alternative aviation fuel with the potential of mitigating pollutant emissions.

Funding Not applicable.

References

1. Okoro LN, Okwuanalu D, Nwaeburu C (2012) Calorimetric determination of energy content of alcohol fuels and blends with kerosene. Alcohol 1(3):4117
2. Chèze B, Gastineau P, Chevallier J (2011) Forecasting world and regional aviation jet fuel demands to the mid-term. Energy Policy 39(9):5147–5158
3. Zhang C, Hui X, Lin Y, Sung CJ (2016) Recent development in studies of alternative jet fuel combustion: progress, challenges, and opportunities. Renew Sustain Energy Rev 54:120–138
4. Mitigation CC (2011) IPCC special report on renewable energy sources and climate change mitigation. Renew Energy 20(11):128
5. Turysbay M, Toncu DC (2018) Preliminary experimental analysis of alcohol-kerosene blend for commercial aviation. Iran J Chem Chem Eng 37(1):131–139
6. Kumar M, Karmakar S (2023) Butyl butyrate, Jet A-1 and their blends: combustion performance in the swirl stabilized burner at different inlet air temperature. Biomass Bioenergy 168:106651
7. Kumar P, Kumar R (2020) Heat of combustion studies for carbon black mixed ADN, KDN, and AP oxidizers. Sci Technol Energ Mater 81(4):93–99
8. Chen W, Miller M, Miske I, Frederickson C (2020) Application of dielectric spectroscopy (DS) for quality control of solvent-borne conformal coatings
9. Kuznetsov G, Borisenko E, Kolesnikov N (2022) Surface tension of Cd0.9Zn0.1Te melt. Mater Lett 317:132093

Non-linear Controller for a Drone with Slung Load

Abhishek Manalathody, Kishoor Santhana Krishnan, Jisnu Adindtra Subramanian, Sakthivel Thangavel, and Rajesh Senthil Kumar Thangeswaran

Abstract This paper presents a control strategy for a quadcopter carrying a slung load. The Euler–Newton method is used for obtaining the complete non-linear model of the 6-DOF quadcopter system and a slung-load system capable of performing the swing motion along two directions. Both the system dynamics are coupled by adding the swing forces to the body forces of the quadcopter. This coupling leads to the undamped swing motion of the slung load which may cause unstable oscillations for the quadcopter, thereby degrading its performance. It is important to damp this undesired swing motion of the slung load. The objective of the controller is to allow the quadcopter to transport a slung load to the desired position without affecting flight stability. A combination of proportional-integral-derivative (PID) and non-linear PID (NLPID) controllers is used for the target position tracking control. A separate PID controller is used for damping the slung load's oscillations.

Keywords Quadcopter · Slung load · Controller · PID · NLPID

1 Introduction

The advancements of technology in the contemporary world over the past decade have resulted in the surge in popularity of Unmanned Aerial Vehicles (UAVs). UAVs are being used widely in fields such as security, surveillance, terrain mapping, logistics and transportation [1], photography and film-making, search and rescue operations [2], and precision agriculture. Amongst the various categories of UAVs, quadcopters are gaining significant popularity due to their distinctive vertical take-off and landing (VTOL) capabilities. One of the important applications of quadcopters is transportation of load using a cable. Such loads are commonly called an underslung/slung loads. The primary advantage in using a quadcopter to carry a slung load is the elimination of the need for ground-based equipment such as cranes, which can be

A. Manalathody · K. S. Krishnan · J. A. Subramanian · S. Thangavel (✉) · R. S. K. Thangeswaran
Department of Aerospace Engineering, Amrita School of Engineering, Coimbatore, Amrita Vishwa Vidyapeetham, Coimbatore, India
e-mail: t_sakthivel@cb.amrita.edu

© The Author(s), under exclusive license to Springer Nature Singapore Pte Ltd. 2024

S. Singh et al. (eds.), *Recent Advances in Aerospace Engineering*, Lecture Notes in Mechanical Engineering, https://doi.org/10.1007/978-981-97-1306-6_18

costly and time-consuming to set up. The most significant challenge is ensuring the stability and control of the quadcopter, especially when dealing with heavy loads as the slung loads may get into undamped oscillations due to various reasons like aerodynamics, elasticity of the connecting cable, and inertial coupling of the slung load and the quadcopter system. The undesired oscillation needs to be damped to ensure that the UAV can maintain its desired trajectory. Various methods are used to damp the undesired oscillations produced by the slung load. One of the widely used methods to damp the slung-load oscillations is by the controlled manoeuvering of the quadcopter. It is to be ensured that the quadcopter does not deviate from its assigned trajectory whilst performing the manoeuvers to damp the oscillations. This can be achieved by employing a robust controller for the coupled quadcopter and slung-load system.

The development of controller for a quadcopter carrying slung-load system is widely researched over the past decade. Some notable controllers developed for a quadcopter system include the model predictive controller [3], linear quadratic regulator, sliding mode controller, and PID controller [4, 5]. Feng et al. [6] considered a non-linear quadcopter setup with PID; however, the slung-load modelling was performed under linearized assumptions. From the literature, it is observed that the PID controllers do not perform efficiently for non-linear systems. Various literatures exist on the usage of NLPID over conventional PIDs and its industrial applications. Research in the field dealing with the usage of NLPID controllers for the control of the coupled system is still in its preliminary stages. Hence, a unique combination of NLPID controllers for the position response and PID controllers for the attitude and swing response is proposed to control the dynamics of the coupled system. The aim of the current study is to develop a controller for a coupled quadcopter and slung-load system. This is achieved by performing the following objectives: (i) developing a Simulink model of a quadcopter using non-linear equations of motion and subsequently developing a non-linear controller, (ii) deriving a non-linear mathematical model for a 2-DOF slung-load system and coupling it with the quadcopter Simulink model, and (iii) developing a controller for the coupled system.

2 Mathematical Modelling

This paper focuses on deriving the non-linear mathematical model of a quadcopter followed by the modelling of the slung load. The major assumptions involved in the non-linear mathematical modelling of the quadcopter slung-load system are: (i) The aerodynamic force contributed by the slung load is not considered, (ii) the slung load is modelled as a point mass. Hence the shape, size, and dimensions of the slung load and their corresponding effects on the quadcopter are not considered. (iii) The slung load is attached to the centre of gravity of the quadcopter. (iv) The cable is assumed to be rigid. Fig. 1 depicts the schematic representation of the coupled system.

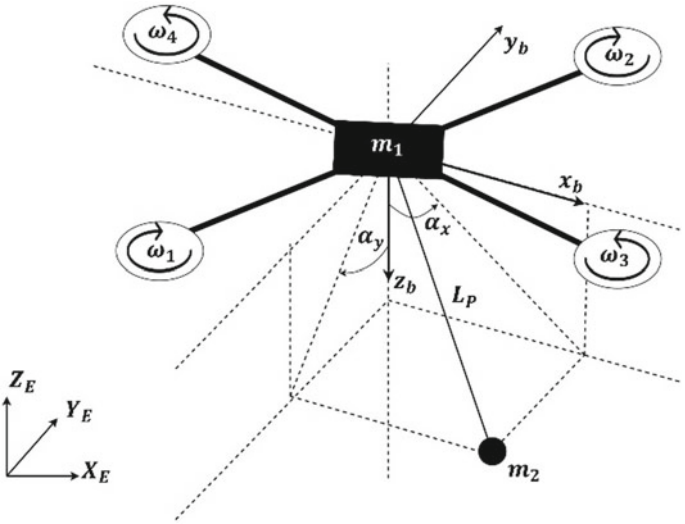


Fig. 1 Schematic representation of quadcopter carrying slung load

2.1 Non-linear Mathematical Modelling of a Quadcopter

The mathematical model of any flying vehicle consists of two parts. The first part involves the modelling of the flight dynamics of the vehicle. The second part involves the calculation of loads (aerodynamics and structural) from various components of the flying vehicle. The flight dynamic equations are derived using linear and angular momentum conservation (Newton–Euler Method) by treating the quadcopter as a rigid body (a point mass) [7]. The flight dynamic equations of the quadcopter are provided in Eqs. 1–4.

$$\begin{Bmatrix} \dot{x} \\ \dot{y} \\ \dot{z} \end{Bmatrix} = \begin{bmatrix} c_\psi c_\theta & c_\psi s_\phi s_\theta - c_\phi s_\psi & s_\phi s_\psi + c_\phi c_\psi s_\theta \\ c_\phi s_\psi & c_\psi c_\phi + s_\phi s_\psi s_\theta & c_\phi s_\psi s_\theta - c_\psi s_\phi \\ -s_\theta & s_\psi c_\theta & c_\phi c_\theta \end{bmatrix} \begin{Bmatrix} u \\ v \\ w \end{Bmatrix} \tag{1}$$

$$\begin{Bmatrix} \dot{u} \\ \dot{v} \\ \dot{w} \end{Bmatrix} = \begin{bmatrix} 0 & r & -q \\ -r & 0 & p \\ q & -p & 0 \end{bmatrix} \begin{Bmatrix} u \\ v \\ w \end{Bmatrix} + g \begin{bmatrix} -\sin\theta \\ \sin\phi\cos\theta \\ \cos\phi\cos\theta \end{bmatrix} + \frac{1}{m} \begin{Bmatrix} F_{Ax} \\ F_{Ay} \\ F_{Az} - U_1 \end{Bmatrix} \tag{2}$$

$$\begin{Bmatrix} \dot{\phi} \\ \dot{\theta} \\ \dot{\psi} \end{Bmatrix} = \begin{bmatrix} 1 & \sin\phi\tan\theta & \cos\phi\tan\theta \\ 0 & \cos\phi & -\sin\phi \\ 0 & \frac{\sin\phi}{\cos\theta} & \frac{\cos\phi}{\cos\theta} \end{bmatrix} \begin{Bmatrix} p \\ q \\ r \end{Bmatrix} \tag{3}$$

$$\begin{Bmatrix} p \\ q \\ r \end{Bmatrix} = \begin{bmatrix} \frac{I_y - I_z}{I_x} \\ \frac{I_z - I_x}{I_y} \\ \frac{I_x - I_y}{I_z} \end{bmatrix} \begin{Bmatrix} rp \\ pr \\ pq \end{Bmatrix} + \begin{bmatrix} \frac{U_2}{I_x} \\ \frac{U_3}{I_y} \\ \frac{U_4}{I_z} \end{bmatrix} \tag{4}$$

Here, position in space $\xi = [xyz]$, linear velocity $V = [uvw]$, rotational angles $\eta = [\phi\theta\psi]$, and angular velocities $\omega = [pqr]$. In the above equations, $\sin\theta$ and $\cos\theta$ are represented as s_θ and c_θ. The calculation of loads on the airframe varies with the configuration of the flying vehicle (fixed wing, helicopter, quadcopter, hexacopter, etc.). The aerodynamic loads acting on the quadcopter are represented as a function of rotor angular velocities and are shown in the following Eqs. 5–8, from Ref. [8].

$$U_1 = k\left(\omega_1^2 + \omega_2^2 + \omega_3^2 + \omega_4^2\right) \tag{5}$$

$$U_2 = kl\left(\omega_3^3 - \omega_1^2\right) \tag{6}$$

$$U_3 = kl\left(\omega_4^2 - \omega_2^2\right) \tag{7}$$

$$U_4 = b\left(\omega_2^2 + \omega_4^2 - \omega_1^2 - \omega_3^2\right) \tag{8}$$

Here, b is drag coefficient, 1 is arm length of the UAV, k is lift coefficient, ω denotes RPM of motors, where $i = 1$ to 4.

2.2 Slung-Load Modelling and Coupling of Systems

The modelling of the slung-load system is done by considering the system as a pendulum in free space with 2-DOF. α_x and α_y are the suspension angles made by the load in the x–z and y–z planes, respectively, and L_p is the length of the cable as shown in Fig. 1. The position vector of the slung load in earth fixed frame can be written as follows:

$$R = \begin{bmatrix} x + L_p \sin\alpha_x \cos\alpha_y \\ y + L_p \sin\alpha_y \\ z - L_p \cos\alpha_x \cos\alpha_y \end{bmatrix} \tag{9}$$

On solving the Lagrange equation, the equations of motion of a slung-load system can be obtained. In the current study, the slung-load dynamic equations and the forces exerted by the load on the quadcopter are derived as a function of $g, \ddot{x}, \ddot{y}, \ddot{z}, \alpha_x, \alpha_y, \dot{\alpha_x}, \dot{\alpha_y}$, and L_p. These equations are derived in earth fixed frame, and hence, the swing loads are added directly to the quadcopter's body forces.

3 Controller

Controllers are devices built to regulate the behaviour of any dynamic system by modifying the system's output. This section deals with the most basic and functional type of controller, the PID controller followed by the NLPID controller. The linear PID controllers are inefficient for non-linear systems with cross-coupling effects, and the gain scheduling process is very difficult and time-consuming. To counter the flaws of the PID controller, the NLPID controller was developed. NLPID controllers are designed with several tuning parameters providing more control over the system. However, the manual tuning of the NLPID controller is highly demanding as well as time-consuming. Though the tuning of both PID and NLPID controllers are time-consuming, NLPID is more robust whilst handling the non-linearity or cross-coupling of the system. Hence, in this paper, we have proposed a distinctive combination of PID and NLPID controllers. The NLPID controller governs the force needed to move the quadcopter to a desired waypoint or trajectory, whereas the PID controller works towards controlling the swing and maintaining the attitude of the quadcopter.

It is to be noted that quadcopters are an underactuated system, where only four control inputs are available for a 6-DOF system. The addition of the slung-load system increases the DOF of the quadcopter system to eight. The states of the quadcopter system that can be directly controlled by the system inputs are its altitude (z) and attitudes (ϕ, θ, ψ). Therefore, we need a separate treatment for other state variables such as position (x, y) and the slung-load swing angles (α_x, α_y). The proposed control strategies for the position, altitude, attitude, and slung load are discussed in this section. Figure 2 depicts the block diagram of the controller implemented in this study.

3.1 Position Controller

The altitude of the quadcopter system is controlled directly by the thrust force. The thrust requirement to attain the desired altitude can be obtained through a NLPID controller. The detailed derivation of the NLPID setup can be found in Ref. [8].

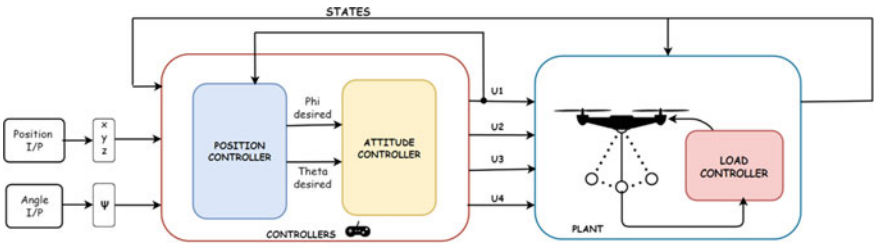


Fig. 2 Block diagram of proposed controller

However, as mentioned earlier, the quadcopter does not have direct control inputs for the motion along x and y directions. Hence, conventional control is not possible, so a pseudo-controller setup is derived as a function of heading angle and the thrust force. The position controller provides the commands as the desired roll and pitch angles. The equations are given in Eq. 10:

$$\begin{pmatrix} \cos\phi_d \sin\theta_d \\ \sin\phi_d \end{pmatrix} = \frac{m}{U_1} \begin{pmatrix} \cos\psi & \sin\psi \\ \sin\psi & -\cos\psi \end{pmatrix}^{-1} \begin{pmatrix} \ddot{x} \\ \ddot{y} \end{pmatrix} \tag{10}$$

3.2 *Attitude and Load Controller*

The attitude and slung-load controllers use a conventional PID controller. The attitude controllers directly provide the commands in terms of moments ($U2$, $U3$, $U4$) as given in the following Eq. 11:

$$U_j = K_{\gamma 1}(e_\gamma) + K_a \gamma^2 \left(\int e_\gamma dt \right) + K_{\gamma 3} \dot{e_\gamma} \tag{11}$$

Here, $j = 2, 3, 4$. e_γ is defined as $\gamma_{\text{desired}} - \gamma_{\text{actual}}$ which denotes the attitude states of the system, i.e. roll(ϕ), pitch(θ), and yaw(ψ). The K_γ terms indicate the gain parameters of the system. The slung-load oscillation is damped by setting the desired swing angle along x- and y-axes to be zero. The forces required to damp the swing angles are given in Eq. 12:

$$F = K_{\delta 1}(e_\delta) + K_a \delta^2 \left(\int e_\delta \mathrm{d}t \right) + K_{\delta 3} \dot{e_\delta} \tag{12}$$

Here, $e_\delta = \delta_{\text{desired}} - \delta_{\text{actual}}$·here, δ can be either of the swing angles.

4 Results and Discussion

This section presents the simulation results of various test cases performed using MATLAB/SIMULINK. A quadcopter model with mass of 3 kg and arm length of 0.5 m is used for this simulation. The moment of inertia of the quadcopter model is taken as 0.05 kgm^2, 0.05 kgm^2, and 0.24 kgm^2. The slung-load parameters considered for the simulation are mass of the load 0.5 kg and the cable length 0.5 m.

4.1 Quadcopter and Slung-Load System Response to Step Input

The NLPID–PID controller is tested with a series of step inputs for the above-mentioned quadcopter slung-load system. Figure 3 depicts the time response of the quadcopter slung-load system for step command in position and heading $(x, y, z, and \psi)$ using the proposed NLPID–PID controller. From position response in Fig. 3a, it is observed that the desired position (x, y) is attained within 10 s whereas the altitude (z) takes a little < 10 s to attain the commanded altitude. An overshoot of 20–30% can be seen in case of the position response. From Fig. 3b, an aggressive behaviour is observed in the pitch and roll response of the system. The pitch and roll rates at the initial stages are calculated as 4–6 rad/s, and this can arise due to the absence of velocity control on the controller. The pitch attitude in particular is observed to vary from − 30° to 45°. The same can be attributed to the larger oscillations on the slung load (60°), though it is observed to be damped out in 12 s. Due to the observed aggressive nature of the attitude of the system, large peaks are observed in the controller inputs of the system. This large peak can be reduced by: (i) providing the velocity commands to the controller, (ii) setting up of the saturation limits for the attitude angles and its rates, (iii) adding proper motor model and its corresponding angular velocity control.

4.2 NLPID–PID Versus PID

This simulation is performed for a step command along position (x, y) to demonstrate the effectiveness of the proposed non-linear controller over a complete PID controller. Figure 4 shows the time response comparison of the system for the proposed NLPID–PID and PID controllers. From Fig. 4a, it can be noted that the settling time of the PID controller is larger than that of the proposed controller. It can also be seen that the overshoot of the position response is higher than the proposed NLPID–PID controller. From Fig. 4b and c, it can be observed that initially the NLPID–PID controller shows a slight aggressive nature. The proposed NLPID–PID controller shows a better yaw performance when compared to a complete PID setup, Fig. 4d. From Fig. 4e–f, the NLPID damps the slung-load oscillations much faster than the PID controller even though the NLPID shows larger oscillation in the initial stage.

5 Conclusion and Future Scope

A non-linear mathematical model for a quadcopter and a slung-load system is developed. A unique combination of NLPID and PID controllers is developed, where the NLPID controller controls the position of the quadcopter whereas the PID controller

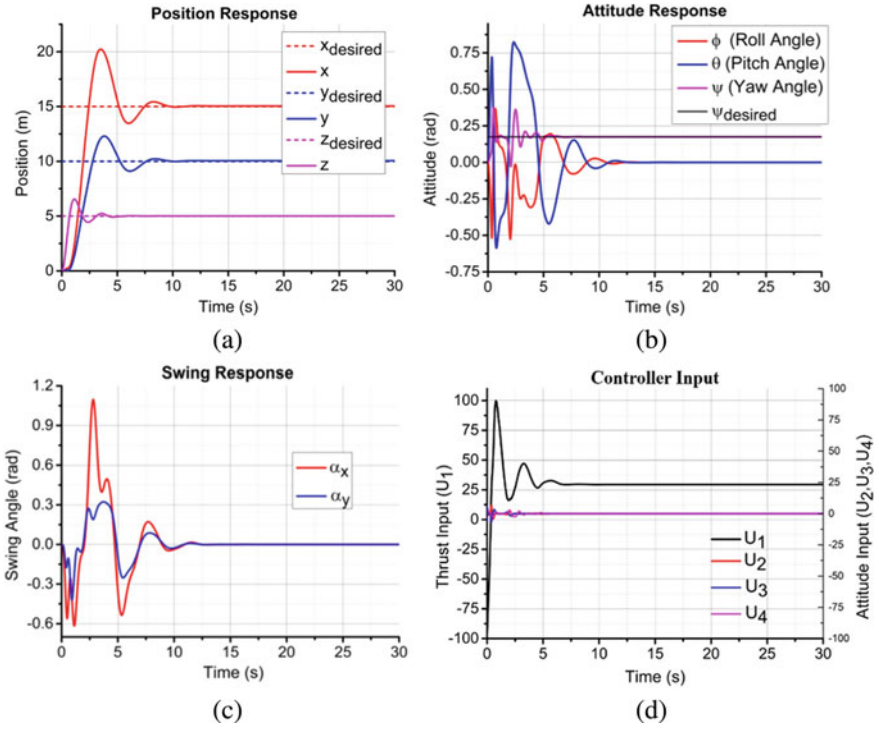


Fig. 3 Time response of coupled system to step position and heading command

controls the attitude and slung-load oscillations of the quadcopter. This approach of combining the two controllers is observed to produce better results with relatively minimal tuning parameters. From the simulation results, it can be concluded that the proposed NLPID–PID controller is working efficiently in trajectory tracking as well as in swing load damping. The observed aggressive behaviour in the attitude response can be eliminated by implementing velocity control and motor models. The controller was also simulated for trajectory, random, and real-time command cases and yielded satisfactory results. The model can be improved and simulated for payload delivery of a slung load on a moving platform. The aerodynamic effects of the slung load can be incorporated in the modelling to increase its effectiveness. Gain scheduling techniques and auto-tuning techniques can be incorporated to the proposed model to increase its robustness and efficiency.

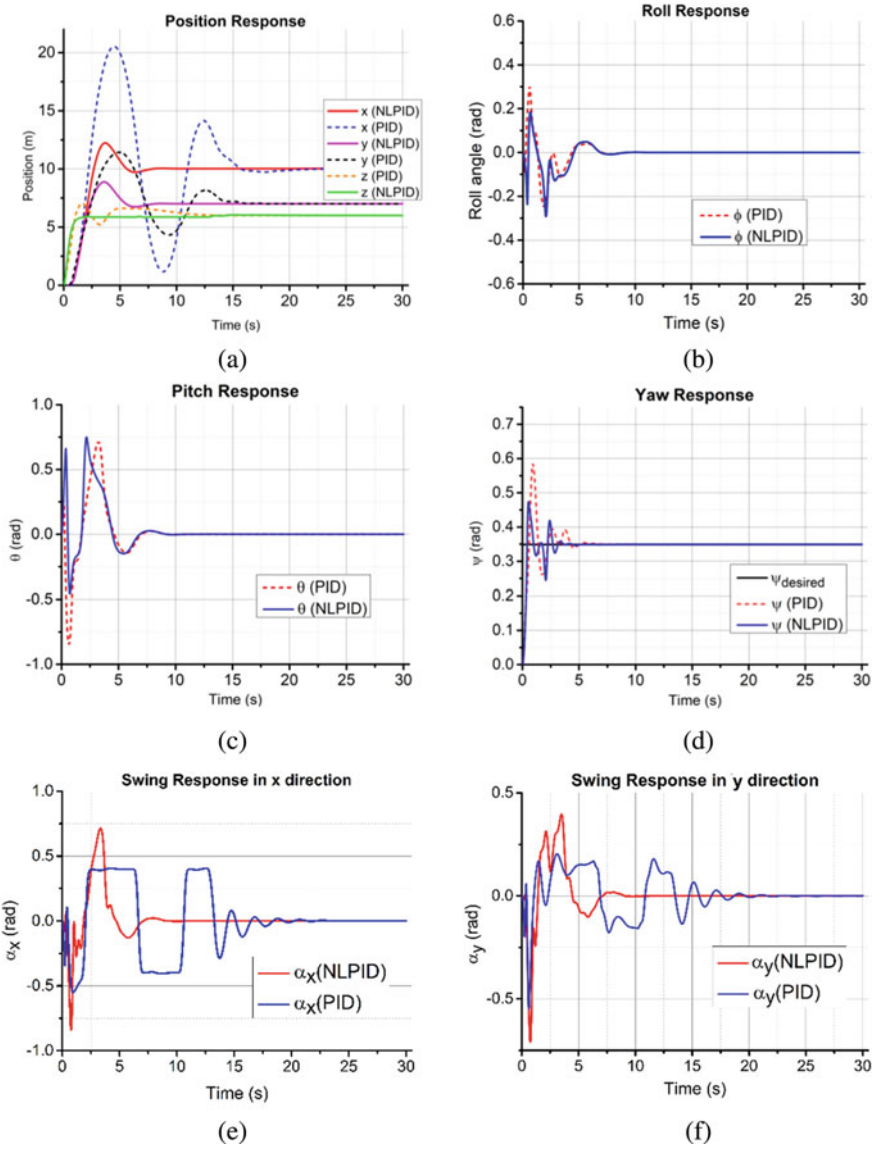


Fig. 4 Time response comparison of coupled system for NLPID and PID controllers

Funding Not applicable.

References

1. Prasad DRB, Madineni C, Kumar LT, Basumatary I, Kasyap KRP, Mohan A (2022) Simulation of an autonomous website controlled payload delivery UAV for medical emergency response. In: Proceedings of the 2022 6th international conference on computing, communication, control and automation (ICCUBEA), pp 1–5
2. Nikhil N, Shreyas SM, Vyshnavi G, Yadav S (2020) Unmanned aerial vehicles (UAV) in disaster management applications. In: Proceedings of the 2020 third international conference on smart systems and inventive technology (ICSSIT), pp 140–148
3. Ganga G, Dharmana MM (2017) MPC controller for trajectory tracking control of quadcopter. In: Proceedings of the 2017 international conference on circuit, power and computing technologies (ICCPCT), pp 1–6
4. Salih AL, Moghavvemi M, Mohamed HA, Gaeid KS (2010) Flight PID controller design for a UAV quadrotor. Sci Res Essays 5(23):3660–3667
5. Vamsi DS, Tanoj TVS, Krishna UM, Nithya M (2019) Performance analysis of PID controller for path planning of a quadcopter. In: Proceedings of the 2019 2nd international conference on power and embedded drive control (ICPEDC), pp 116–121
6. Feng Y, Rabbath CA, Su CY (2018) Modeling of the dynamics of a micro UAV with a single slung load. Springer, Cham, pp 1–19
7. Sakthivel T, Venkatesan C (2017) Flight dynamics of helicopter under steady maneuver: interesting observations. J Aircraft 54(4):1595–1604
8. Najm AA, Ibraheem IK (2019) Nonlinear PID controller design for a 6-D of UAV quadrotor system. Eng Sci Technol Int J 22(4):1087–1097

Enhancing the Performance of UAV Propeller Using Bio-Inspired Humpback Whales Tubercle—A Parametric Study at the Hub and Tip Locations

R. Kousik Kumaar, T. Muthuumari, and M. Kesavan

Abstract This study focuses on optimizing propeller design for small unmanned aerial vehicles (UAVs) to enhance their mission-specific performance. As UAVs gain prominence, there is a growing demand for improved propulsion and energy management systems. Many vertical take-off and landing (VTOL) UAVs rely on fixed-pitch propellers, leading to compromises in mission execution. To address this, the study suggests adopting variable-pitch propellers with aerofoils featuring leading edge flippers to influence aerodynamic behavior and prevent stalls. These flippers are strategically positioned at the propeller's tip and hub to enhance efficiency. Two propeller pitch configurations, 4×7 and 4×9, were examined, each with variations including no flippers, four flippers at the hub and tip, and eight flippers at the hub and tip. Through comprehensive testing, the study aimed to evaluate each design's performance in terms of propeller efficiency, thrust, and torque under specific conditions. The results indicated a significant increase in efficiency, ranging from 60 to 70%, depending on the pitch. This comparative analysis helps assess each pitch's suitability and effectiveness for UAV applications.

Keywords UAV · Propeller performance · Pitch · Flippers

1 Introduction

Efficient aircraft design demands adherence to rigorous performance standards, considering factors such as weight, volume, and component effectiveness. Propeller selection is pivotal in crafting a successful propulsion system, and access to propeller

R. Kousik Kumaar (✉)
NITTE Meenakshi Institute of Technology, Bangalore 560064, India
e-mail: kousik.kumaar@nmit.ac.in

T. Muthuumari
Nehru Institute of Technology, Coimbatore 641105, India

M. Kesavan
Nehru Institute of Engineering and Technology, Coimbatore 641105, India

© The Author(s), under exclusive license to Springer Nature Singapore Pte Ltd. 2024

S. Singh et al. (eds.), *Recent Advances in Aerospace Engineering*, Lecture Notes in Mechanical Engineering, https://doi.org/10.1007/978-981-97-1306-6_19

performance data is essential [1–5]. Propellers convert mechanical energy into thrust, propelling aircraft forward. They consist of a central hub connecting multiple blades, which, driven by the engine, create thrust akin to lift, moving the aircraft [6–10]. This operational principle ties back to Sir Isaac Newton's Third Law of motion, stating every action has an equal and opposite reaction. Propellers are key in converting engine rotational power into forward thrust by moving air behind them, propelling the aircraft.

The number of propeller blades is dictated by performance requirements and engine power. More blades are necessary for higher engine power [11–15]. Blade size, shape, and angle, combined with engine power, influence thrust production [16–20]. The era of extensive propeller-driven aircraft research was before World War II, followed by the dominance of jet propulsion. However, the rise of small unmanned aerial vehicles (UAVs) has rekindled interest in propeller aerodynamics, particularly in scenarios near the ground or closed spaces where ground and ceiling proximity significantly affects propeller performance and UAV operation, leading to changes in drone behavior and characteristics, such as drift during pesticide spraying [21–24].

2 Experimental Setup

2.1 Prototyping

Depending on the material required for the propellers, prototype propellers can be produced using conventional machining or 3-D printing. Due to its quick turnaround time, 3-D printing works best with the typically strict schedule of design iterations. For 3-D printers, an STL geometry file is typically used, as seen in Fig. 1. ABS is one of the materials available for 3-D printing propellers.



Fig. 1 File for 3-D printing the propeller and base

2.2 Testing

The chosen test stand design directly measures torque and thrust for propeller performance evaluation. It includes a tachometer, manometer, barometer, thermocouple, power supply, and speed controller alongside the sensors in Fig. 2. While sensor manufacturers offer calibrated sensors, it is advisable to verify their calibration data. Calibration is required for the torque sensor, load cell, and wind tunnel speed. The torque sensor can be calibrated by applying a known force at a specific distance, and load cell calibration is checked by applying a load. Calibration data closely match measured values, ensuring the testing instrument's accuracy. Prior to actual testing, tasks include propeller balancing, installation, wind tunnel checks, secure part connection, and software/sensor adjustment.

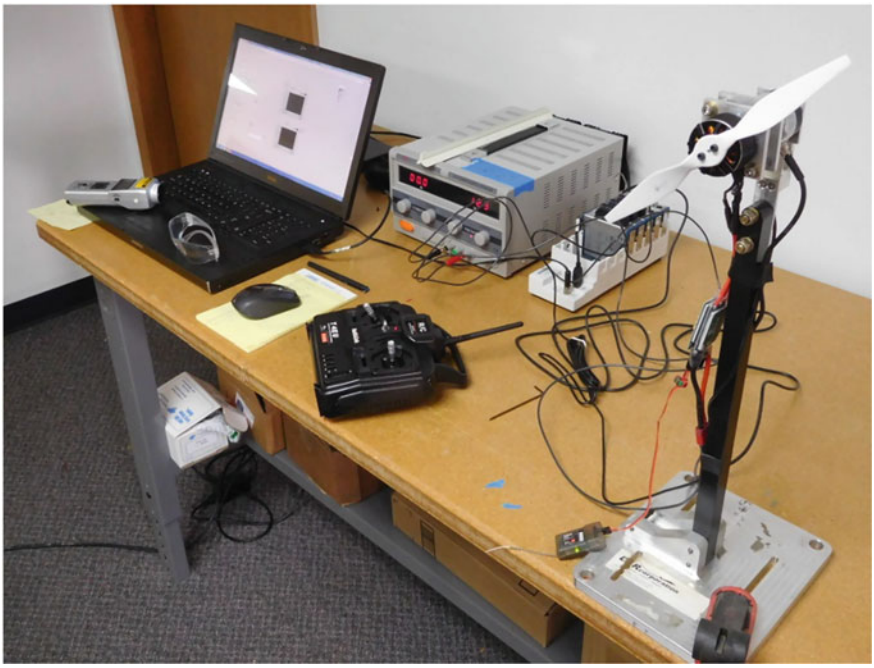


Fig. 2 Propeller test setup

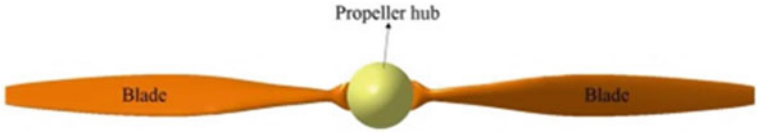


Fig. 3 Propeller without flipper

3 Design Parameters

3.1 Propeller Without Flipper

Propellers without flippers have a straightforward design consisting of a hub and blades as shown in Fig. 3. They do not feature any additional components or modifications, making them relatively easy to manufacture and maintain.

3.2 Propeller with Flipper at Tip

When flippers are placed at the tip of a propeller, they are typically referred to as small extensions or fins added to the outermost part of the propeller blades. The purpose of tip flippers is to improve the propeller's performance by reducing vortex formation, decreasing drag, and increasing overall efficiency. By adding flippers at the tip, the propeller can experience several benefits such as increased efficiency, enhanced thrust, improved stability, and noise reduction. The design and placement of tip flippers can vary depending on the specific propeller design and application which is shown in Fig. 4.

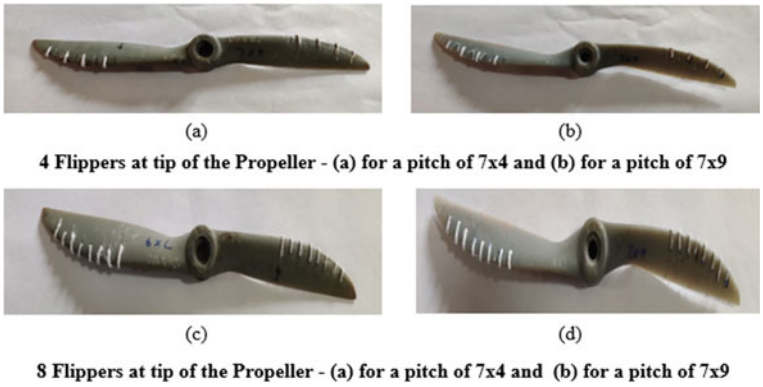


Fig. 4 Propeller with flipper at tip

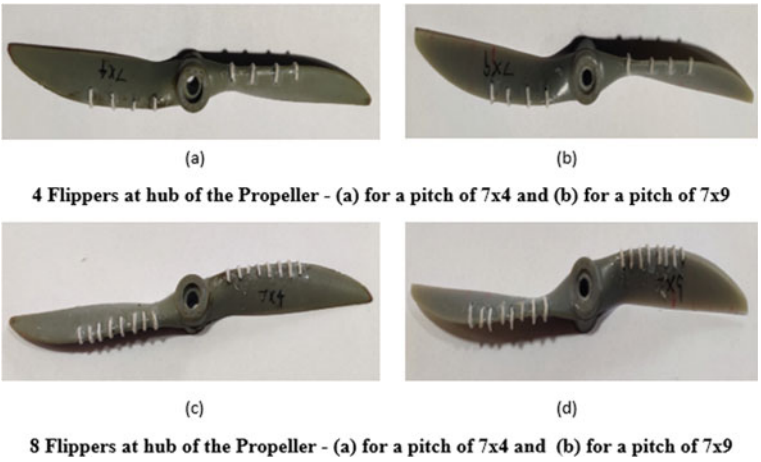


Fig. 5 Propeller with flipper at hub

3.3 Propeller with Flipper at Hub

When a propeller is equipped with a flipper at the hub, it means that a fin-like structure is added near the center or hub of the propeller blades. This flipper, also known as a hub cap or hub vortex suppressor, serves to improve the performance of the propeller in various ways. The flipper at the hub helps to reduce the formation of hub vortices.

These vortices can lead to energy losses and increased drag. By suppressing these vortices, the propeller can operate more efficiently, resulting in improved thrust production and reduced power consumption. By reducing the hub vortices, the flipper can increase the effective working area of the propeller blades. This can lead to increased thrust and torque generation, allowing for greater propulsion performance. The presence of a flipper at the hub can help improve the stability and control of the propeller which is shown in Fig. 5.

4 Result and Discussion

4.1 Propeller Speed Versus Mechanical Efficiency for 7 × 4 Pitch Propeller

In the low propeller speed region, mechanical efficiency is generally suboptimal in all cases. The inefficiency results from the propeller operating within a disruptive airflow range around the blades, leading to less effective thrust generation. As propeller speed increases, mechanical efficiency improves uniformly across all cases, primarily because the blades experience more favorable airflow, enhancing thrust generation

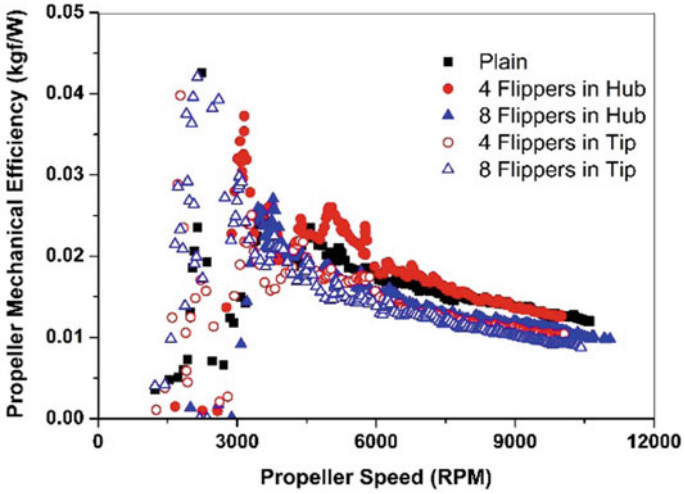


Fig. 6 Propeller speed versus mechanical efficiency for 7 × 4 pitch propeller

per unit of power input. Mechanical efficiency initially increases steadily as the propeller operates within its optimal range, efficiently converting power into thrust. At a specific propeller speed, a peak or plateau is reached, representing the maximum mechanical efficiency, the point where the propeller is most efficient in converting power to thrust. In the case with eight flippers at the tip, the maximum efficiency is achieved at 0.0449 kgf/W at 2880 rpm, showing a 28% increase in efficiency compared to the baseline propeller. Beyond this peak point, with further increases in propeller speed, mechanical efficiency may gradually decline due to increased drag and less optimal operating conditions which is shown in Fig. 6.

4.2 Propeller Speed Versus Thrust for 7 × 4 Pitch Propeller

As similar to the efficiency, thrust also varies in different stages. The thrust increases from 0 to 9000 rpm. At very low propeller speeds, the thrust generated by the propeller tends to be relatively low. The airflow around the blades may not be sufficient to produce significant thrust, resulting in lower performance. Among all the cases, the thrust is similar till 6500 rpm. As the propeller speed increases, the thrust generated by the propeller typically increases as well. The increased rotational speed allows the propeller blades to interact more efficiently with the airflow, resulting in higher thrust production. In this region, the relationship between propeller speed and thrust is generally positive, meaning that increasing the propeller speed leads to an increase in thrust output. When the speed of the propeller reaches around 9700 rpm, it attains saturation or maximum thrust region where the propeller with eight flipper at tip

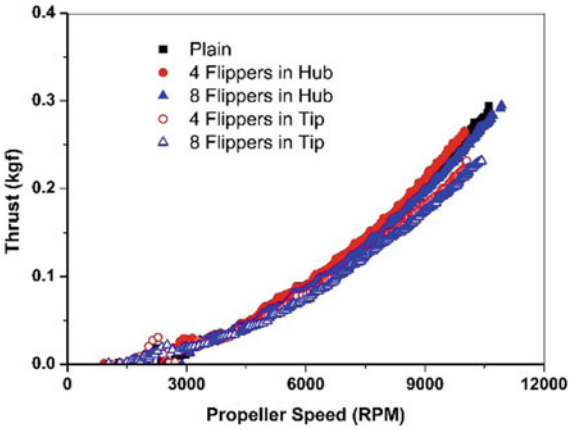


Fig. 7 Propeller speed versus thrust for 7 × 4 pitch propeller

has maximum thrust value of 0.3 kgf as compared to other cases which is shown in Fig. 7.

4.3 Propeller Speed Versus Torque for 7 × 4 Pitch Propeller

In a propeller speed versus torque graph (Fig. 8), at very low propeller speeds, the required torque is minimal because the blades encounter little aerodynamic force and low air resistance, making all propellers perform similarly. With increasing propeller speed, torque demand rises as the blades face greater air resistance, with four flippers at the tip and eight flippers at the hub exhibiting minimal oscillation at around 2800 rpm. The graph may reach a peak, representing the maximum torque required, achieved by the eight-flipper hub propeller. This point signifies the highest torque demand to overcome air resistance and maintain the desired rotational speed. The graph's shape and characteristics can vary based on factors like propeller design, blade geometry, airfoil profiles, and specific operating conditions.

4.4 Propeller Speed Versus Torque for 7 × 9 Pitch Propeller

The tested samples show a sharp oscillation in the low propeller speed region. When the speed is increased further until 2600 rpm, the propeller operates within its optimal range, which may cause the mechanical efficiency to initially increase steadily. As shown in Fig. 9, a propeller with eight flippers in the hub is performing well at this point, with an efficiency of 0.047 Kgf/W. A 7 × 4 pitch propeller exhibits a similar trend where mechanical efficiency gradually declines as speed is increased.

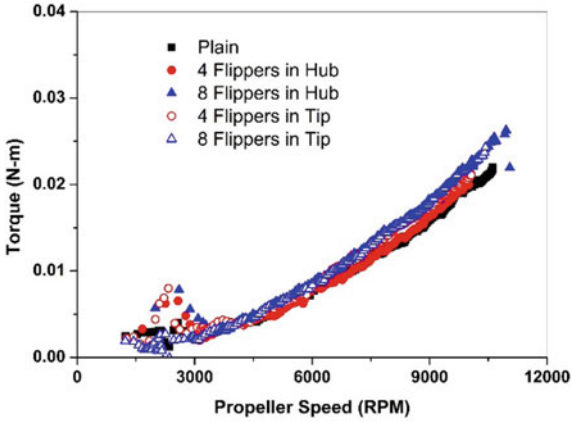


Fig. 8 Propeller speed versus torque for 7 × 4 pitch propeller

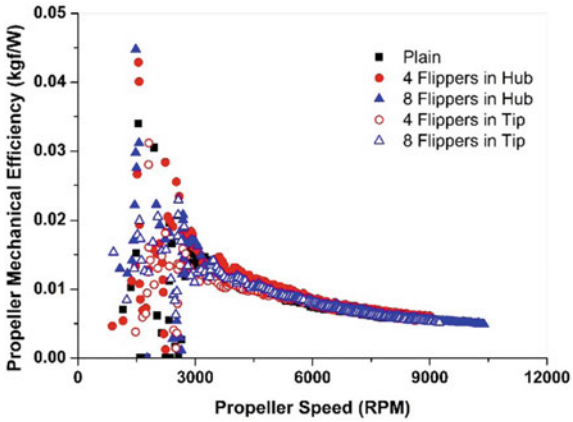


Fig. 9 Propeller speed versus mechanical efficiency for 7 × 9 pitch propeller

4.5 Propeller Speed Versus Torque for 7 × 9 Pitch Propeller

Figure 10 depicts a graph of propeller speed versus thrust showing an increase in thrust from 0 to 12,000 rpm. The thrust produced by the propeller tends to be relatively low at very low propeller speeds. At 2900 rpm, there is a slight variation in thrust for each case. The thrust is consistent across all cases as speed increases up to 9000 rpm. The propeller reaches its saturation or maximum thrust region at a speed of about 10,200 rpm. In this region, which is depicted in Fig. 10, the propeller with eight flippers at the tip has the highest maximum thrust value of 0.3 kgf compared to other cases.

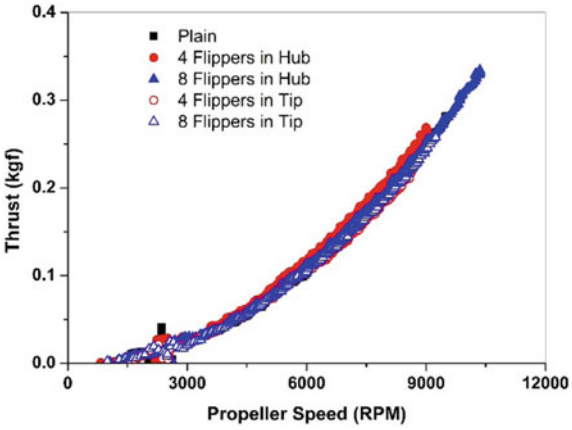


Fig. 10 Propeller speed versus thrust for 7 × 9 pitch propeller

4.6 Propeller Speed Versus Torque for 7 × 9 Pitch Propeller

At very low propeller speeds, as shown in Fig. 11 propeller speed versus torque graph, the torque needed to turn the propeller is typically low. Similar to a 4 × 7 pitch propeller, the torque needed to rotate the propeller increases as the propeller speed does. But when the speed is close to 2800 rpm, further acceleration causes slight variations in all the samples. The maximum torque of 0.06 N m, which is achieved by the propeller's eight flippers at the hub, may be represented by a peak or plateau on the graph. The propeller typically requires the most torque at this operating point to overcome air resistance and maintain the desired rotational speed.

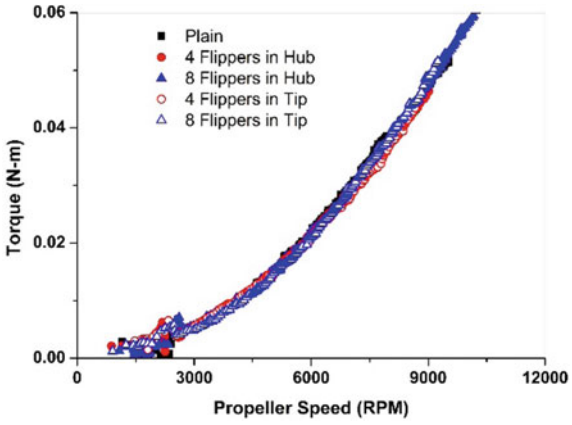


Fig. 11 Propeller speed versus torque for 7 × 9 pitch propeller

5 Conclusion

- Propeller performance is influenced by multiple factors: blade pitch, blade geometry, airfoil profiles, and operating conditions.
- The study focuses on varying blade pitch (4×7 and 4×9) and propeller profile (four and eight flippers) at the tip and hub.
- The use of flippers on the hub and tip of model propellers delays boundary layer separation and increases mechanical efficiency, thrust, and torque.
- Higher torque is crucial for enhanced thrust, especially during demanding flight conditions like take-off, climbing, and high-speed flight.
- The 7×9 pitch propeller with eight flippers at the tip outperforms other configurations.
- The optimized pitch for torque, thrust, and efficiency is found to be 7×9 with eight flippers at the tip.
- Comparing the overall results, the propellers with flippers outperformed the propellers without flippers which were considered for the base condition.

Funding Information Not applicable.

References

1. Liu X, Jawahar H, Azarpeyvand M, Theunissen R (2015) Aerodynamic and aeroacoustic performance of serrated airfoils. In: 21st AIAA/CEAS Aeroacoustics Conference, vol June, pp 1–16
2. Chong TP, Vathylakis A (2015) On the aeroacoustic and flow structures developed on a flat plate with a serrated sawtooth trailing edge. J Sound Vib 354:65–90
3. Ibrahim H, New TH (2015) Tubercle modifications in marine propeller blades. In: 10th Pacific symposium flow visual image process, vol June, pp 1–11
4. Lin SY, Lin YY, Bai CJ, Wang WC (2016) Performance analysis of vertical-axis-wind-turbine blade with modified trailing edge through computational fluid dynamics. Renew Energy 99:654–662
5. Arai T, Seiji N, Hitoshi K, Kunobu S, Araki K (2014) "Propeller type fan," CN 201410473050
6. Oerlemans S (2015) Arrangement to reduce noise of wind turbine rotor blade. CN104454379 (A)
7. Yuanjun D, Baohua L, Xingbiao Y, Changzai R, Zutao C, Linyuan Z (2015) Wind turbine blade adopting serrated blade tip tail edge structure and wind turbine. CN104948396 (A)
8. Richard WJ (2012) An Aerofoil blade with a set-back portion. GB2483059 (A)
9. Fumio K, Masashi M, Hironari F (1994) Propeller fan, JPH06173895 (A)
10. Roger GP (2003) Serrated fan blade. US2003152459 (A1)
11. Ibrahim M, Alsultan A, Shen S, Amano RS (2015) Advances in horizontal axis wind turbine blade designs: introduction of slots and tubercle. J. Energy Resour Technol 137(5):51205
12. Belamadi R, Djemili A, Ilinca A, Mdouki R (2016) Aerodynamic performance analysis of slotted airfoils for application to wind turbine blades. J Wind Eng Ind Aerodyn 151:79–99
13. Menon M, Ponta F, Sun X, Dai Q, Asce M (2002) Aerodynamic analysis of flow-control devices for wind turbine applications based on the trailing-edge slotted-flap concept. J Aerosp Eng 29(5):1–12
14. Noorazyze SN (2014) Performance evaluation of slotted and Onn Malaysia

15. Xie W, Zeng P, Lei L (2015) A novel folding blade of wind turbine rotor for effective power control. Energy Convers Manag 101:52–65
16. Yilmaz S, Erdem D, Kavsaoglu MS (2015) Performance of a ducted propeller designed for UAV applications at zero angle of attack flight: an experimental study. Aerosp Sci Technol 45:376–386
17. Finn RL, Wright D (2012) Unmanned aircraft systems: surveillance, ethics and privacy in civil applications. Comput Law Secur Rev 28(2):184–194. https://doi.org/10.1016/j.clsr.2012.01.005
18. Pajares G (2015) Overview and current status of remote sensing applications based on unmanned aerial vehicles (UAVs). Photogramm Eng Remote Sens 81(April):281–330. https://doi.org/10.14358/PERS.81.4.281
19. Kontogiannis SG, Ekaterinaris JA (2013) Design, performance evaluation and optimization of a UAV. Aerosp Sci Technol 29(1):339–350. https://doi.org/10.1016/j.ast.2013.04.005
20. Panagiotou P, Tsavlidis I, Yakinthos K (2016) Conceptual design of a hybrid solar MALE UAV. Aerosp Sci Technol 53:207–219. https://doi.org/10.1016/j.ast.2016.03.023
21. Watts HC (1920) The design of screw propellers: with special reference to their adaptation for aircraft. Forgotten Books, First
22. Wald QR (2006) The aerodynamics of propellers. Prog Aerosp Sci 42(2):85–128. https://doi.org/10.1016/j.paerosci.2006.04.001
23. Liu X, Jawahar H, Azarpeyvand M, Theunissen R (2015) Aerodynamic and aeroacoustic performance of serrated airfoils. In: 21st AIAA/CEAS aeroacoustics conferences
24. Chong TP, Joseph PF (2013) An experimental study of airfoil instability tonal noise with trailing edge serrations. J Sound Vib 332(24):6335–6358. https://doi.org/10.1016/j.jsv.2013.06.033

Machine Learning Assisted Development of Eight Node Hexahedral Finite Element



Tadala Venkata Krishna Subhash, Ankit, Dipjyoti Nath, and Sachin Singh Gautam

Abstract The finite element method (FEM) is a popular numerical technique for solving partial differential equations (PDEs) arising in computational modeling. Several engineering problems, such as those involving fluid flows, electromagnetics, heat transfer, and structural analysis, have been effectively solved using FEM. It is the most powerful tool currently in structural analysis. Recently, machine learning (ML) approaches have been used to enhance the performance of FEM. The main aim of this study is to build an artificial neural network (ANN) model using deep learning, a popular and powerful ML algorithm that can estimate the elemental stiffness matrices of 3D 8-noded hexahedral elements with very high accuracy. The performance of the model is evaluated by comparing it with Cook's beam problem. The model predicts the displacement of the beam with an error of 0.74%.

Keywords Artificial intelligence · Deep learning · Strain–displacement matrix · 8-node hexahedral element

1 Introduction

Finite element method (FEM) is a popular and the most powerful method to produce numerical solutions of partial differential equations (PDEs) over a physical field [1]. It has demonstrated efficacy across multiple fields, such as heat transfer, electromagnetics, fluid dynamics, and structural analysis. A continuum is discretized into smaller entities known as finite elements as part of the FEM procedure. A mesh—a group of discretized points within the domain—is created to do this. Then, the unknown variables like displacement, temperature, and others for the entire domain can be solved by assembling the finite elements within the mesh.

A subclass of machine learning (ML) known as "deep learning" is built on artificial neural networks (ANN) with numerous hidden layers [2]. The architecture of ANN

T. V. K. Subhash · Ankit · D. Nath · S. S. Gautam (✉)
Department of Mechanical Engineering, Indian Institute of Technology Guwahati, Guwahati 781039, India
e-mail: ssg@iitg.ac.in

© The Author(s), under exclusive license to Springer Nature Singapore Pte Ltd. 2024

S. Singh et al. (eds.), *Recent Advances in Aerospace Engineering*, Lecture Notes in Mechanical Engineering, https://doi.org/10.1007/978-981-97-1306-6_20

is loosely based on the structure of the human brain, which consists of artificial neurons, which are a collection of intricately connected nodes [3]. The previous two decades have seen a significant rise in computational capacity, which has led to the widespread application of deep learning in many computational mechanics domains, such as solving PDEs [4, 5], fracture mechanics [6, 7], fatigue [8–10], contact mechanics [11, 12], numerical quadrature [13, 14, 15], and stress recovery [16–18, 19]. More applications of ML in computational mechanics is discussed in [20].

Recently, Jung et al. [21] presented a deep-learned neural network model to generate the stiffness matrices of two-dimensional (2D) quadrilateral elements. Furthermore, Nath et al. [22] worked on the development of an ANN model that can predict the stiffness matrices of 2D finite elements, specifically the 8-node quadrilateral element. The present study extends the work of Jung et al. [21] and Nath et al. [22] to three-dimensional (3D) finite elements. Compared to the ANN model employed by Jung et al. [21], the ANN model used in this work has different activation and cost functions, while maintaining the linearly decaying learning rate. The input signal for the neural network is composed of the material properties and the elemental nodal coordinates. The ANN model estimates the strain–displacement matrix ($\boldsymbol{B}$) at the Gauss points of the hexahedral element. The predicted ($\boldsymbol{B}$) matrices by the ANN model are then post-processed to get the elemental stiffness matrices. Then, the study presents the accuracy of the ANN model in solving Cook's beam problem.

The paper first briefly discusses the finite element formulation in Sect. 2, followed by the data generation method and ANN configuration in Sect. 3. Then, it presents the results and discusses key findings in Sect. 4. Finally, the present work concludes with a comment on the applicability of artificial intelligence and ML-based algorithms in modeling finite elements in Sect. 5.

2 Finite Element Formulation

The finite element formulation for the present work is presented briefly in this section. The geometry and displacement are interpolated over an element e with n nodes as

$$\boldsymbol{x} = \sum_{i=1}^{n} N_i(\xi, \eta, \zeta)\boldsymbol{x}_i \text{ and } \boldsymbol{u} = \sum_{i=1}^{n} N_i(\xi, \eta, \zeta)\boldsymbol{u}_i \tag{1}$$

where $N_i(\xi, \eta, \zeta)$ represent the shape functions at natural coordinates (ξ, η, ζ) of the element, $\boldsymbol{x}_i$ denotes the ith nodal position vector ($i = 1, ..., n$), and u_i is the ith nodal displacement vector. The strains at the Gauss points are computed from

$$\boldsymbol{\epsilon} = \boldsymbol{B}\hat{\boldsymbol{u}}^{\boldsymbol{e}} \tag{2}$$

where $\boldsymbol{B}$ is called the strain–displacement matrix, which is obtained as the derivative of shape function matrix $\boldsymbol{N}$. . In our current work, the displacement (ue) and strain ($\boldsymbol{\epsilon}$) vectors are given as

$$\hat{\boldsymbol{u}}^{\boldsymbol{e}} = [u_1 v_1 w_1 u_2 v_2 w_2 \ldots u_n v_n w_n]^T$$

$$\boldsymbol{\epsilon} = \left[\epsilon_{11}\ \epsilon_{22}\ \epsilon_{33}\ \ \gamma_{12}\ \gamma_{23}\ \gamma_{31}\right]^{\mathrm{T}} \quad \text{with } \gamma_{ij} = 2\,\epsilon_{ij} \tag{3}$$

where u_n, v_n, w_n are the x, y, z displacements of the ith node. Following the standard finite element procedure [1], the final assembled system of equations over all the elements n_e is obtained as

$$\boldsymbol{KU} = \boldsymbol{F} \tag{4}$$

where

$$\boldsymbol{K} = \sum_{e=1}^{n_e} \boldsymbol{K}^e, \quad \boldsymbol{U} = \sum_{e=1}^{n_e} \hat{\boldsymbol{u}}^e, \quad \boldsymbol{F} = \sum_{e=1}^{n_e} \boldsymbol{F}^e, \tag{5–7}$$

are the global assembled stiffness matrix, displacement vector, and external force vector, respectively. The element stiffness matrix $\boldsymbol{K}^e$ given in Eq. (5) is obtained by $p_\xi \times p_\eta \times p_\zeta$ Gauss–Legendre quadrature rule as

$$\boldsymbol{K}^e = \sum_{\xi_i=1}^{p_\xi} \sum_{\eta_j=1}^{p_\eta} \sum_{\zeta_k=1}^{p_\zeta} w_{\xi_i,\eta_j,\zeta_k} \boldsymbol{B}^T_{\xi_i,\eta_j,\zeta_k} \boldsymbol{D} \boldsymbol{B}_{\xi_i,\eta_j,\zeta_k} J_{\xi_i,\eta_j,\zeta_k}\,, \tag{8}$$

where w_{ξ_i,η_j,ζ_k} is the weight, J_{ξ_i,η_j,ζ_k} is the determinant of the Jacobian matrix, $\boldsymbol{B}_{\xi_i,\eta_j,\zeta_k}$ is the value of strain–displacement matrix evaluated at $(\xi_i, \eta_j, \zeta_k)^{\text{th}}$ Gauss point, and $\boldsymbol{D}$ is the material constitutive matrix. In current work, $p_\xi = p_\eta = p_\zeta = 2$.

3 ANN Model

The procedure to predict the $\boldsymbol{B}$ matrix of a 3D 8-noded hexahedral element (H8) [1] for small strain elasticity with the help of a deep learning model is presented next. The detailed procedure on data generation, neural network architecture, and training the model is provided. Lastly, we show the procedure to compute the stiffness matrix from the output of the trained neural network.

3.1 Data Generation

Firstly, a huge amount of data that consists of training and testing set must be generated to ensure that the neural network model is well-trained. Random normalized data is generated to produce elements with a wide range of shapes. With eight nodes at each corner, the nth normalized geometry is a hexahedral shape. The hexahedral base is lying on the x–y plane, with node 1 at (0,0,0) and node 2 varying between (0.5, 0, 0) and (1.5, 0, 0). Nodal coordinates of node 3 $\left(x_3^{(n)}\right)$ and node 4 $\left(x_4^{(n)}\right)$ of the base of hexahedral are generated randomly such that the x range of node 3 varies from 0.5 to 1.5 and of node 4 from -0.5 to 0.5 with y range of both points from 0.2 to 1.5. The remaining four nodes of the hexahedral were generated by extruding the base of hexahedral with constant thickness ranging from 0.02 to 1.5.

In order to ensure the quality of elements in the normalized data that are randomly generated, elements with distorted shapes are excluded. Hence, the included angles of the base of the hexahedral are constrained to lie between 45° and 135°, and the edge lengths of the hexahedral excluding the distance between node 1 and node 2 are kept in the range of 0.02–2.0. In the present study, the Poisson's ratio ($\nu^{(n)}$) is sampled from a uniform distribution within the interval [0−0.499999] for each of the generated element geometries, and Young's modulus E is taken as 2.0×10^{11} units.[1]

The strain data at gauss points of each normalized element has to be generated next. For this, initially each random element from the training and testing set is discretized using a $N \times N \times N$ mesh of 8-node hexahedral elements (H8) [1] that create outer and inner nodes. Value of $N = 15$ is used in the present work. Thereafter, random displacement values are applied at all the 8 nodes of the domain of each random element in the range $[-0.25, 0.25]$ that is sampled from a uniform probability distribution. Using these displacements, the outer node element can be calculated by using the displacement interpolation as given in Eq. (1). By using the outer node displacements, the inner nodes displacements are also calculated. By utilizing the displacement values at inner and outer nodes of the discretized domain, the strain values at each Gauss point can be computed. The nth training example is formed as follows:

$$\left[v \quad \boldsymbol{X}^{(n)} \quad \boldsymbol{D}^{(n)} \quad \boldsymbol{E}^{(n)}\right], \tag{9}$$

Here, v denotes the Poisson's ratio, $\boldsymbol{X}^{(n)}$ denotes the nodal coordinates of the nth random element (17 values), $\boldsymbol{D}^{(n)}$ the random displacements applied at the 8 nodes of the nth random element ($8 \times 3 = 24$ values), and $\boldsymbol{E}^{(n)}$ the strains at all the 8 Gauss points ($6 \times 8 = 48$ values). So, the total size of one training example is $90 = (1 + 17 + 24 + 48)$.

[1] All units are normalized units.

3.2 Neural Network Architecture

The nodal coordinates $\boldsymbol{X}^{(n)}$ and the value of Poisson's ratio v are given as inputs to the neural network model as shown in Fig. 1. The output of the network is the normalized strain–displacement matrices for a nth random element at all Gauss points. The cost function used to train the ANN model in the present work is given by

$$J = \frac{1}{48M} \sum_{n=1}^{M} \sum_{\xi_i=1}^{p_\xi} \sum_{\eta_j=1}^{p_\eta} \sum_{\zeta_k=1}^{p_\zeta} \left(\boldsymbol{B}^{(n)}_{\xi_i,\eta_j,\zeta_k} \boldsymbol{u}^{(n)} - \hat{\boldsymbol{\epsilon}}^{(n)}_{\xi_i,\eta_j,\zeta_k} \right)^T \left(\boldsymbol{B}^{(n)}_{\xi_i,\eta_j,\zeta_k} \boldsymbol{u}^{(n)} - \hat{\boldsymbol{\epsilon}}^{(n)}_{\xi_i,\eta_j,\zeta_k} \right), \tag{10}$$

where M is the number of training examples, $\boldsymbol{B}^{(n)}_{\xi_i,\eta_j,\zeta_k}$, $\hat{\boldsymbol{\epsilon}}^{(n)}_{\xi_i,\eta_j,\zeta_k}$ are the normalized strain–displacement matrix and strain vector at the $(\xi_i, \eta_j, \zeta_k)^{\text{th}}$ Gauss point.

The elements obtained from the ANN model should in a rigid body motion, i.e., translation and/or rotation, produce zero strain energy. This means that the strains must be zero. So, the predicted strain–displacement matrix by the network must obey the condition as given below,

$$\boldsymbol{B}^{(n)}_{\xi_i,\eta_j,\zeta_k} \Delta \boldsymbol{u} = 0, \tag{11}$$

where $\Delta \boldsymbol{u}$ is the rigid body translation displacements vector that contains the horizontal and vertical displacements as shown in Eq. (3).

The ANN model contains 5 hidden layers as shown in Fig. 1 and Batch normalization [23] is applied to each layer before the activation function. Leaky ReLU

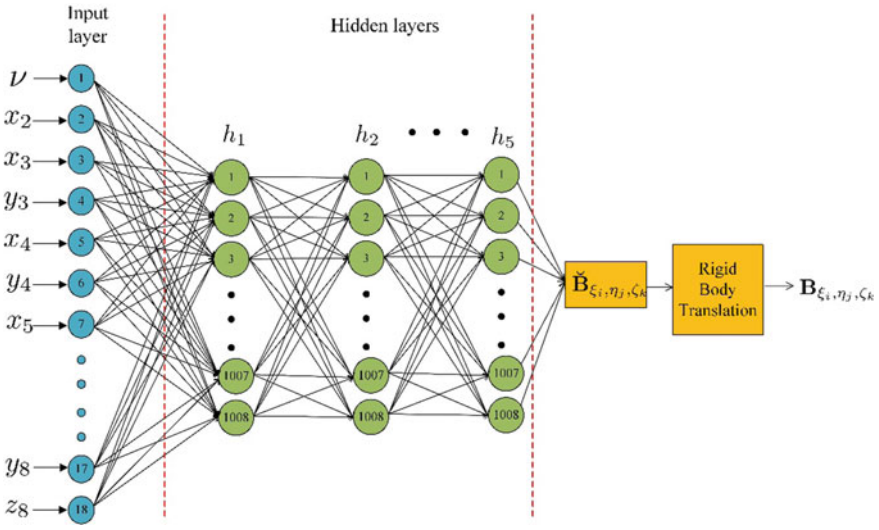


Fig. 1 Proposed neural network architecture

activation function is used in each layer. The number of neurons used in each hidden layer is 1008 ($= 8 \times 6 \times 21$), which is equal to the total number of elements in $\breve{\mathbf{B}}_{\xi_i,\eta_j,\zeta_k}$ (6×21) generated at 8 Gauss point. The 1008 outputs are reshaped to get $\breve{\mathbf{B}}_{\xi_i,\eta_j,\zeta_k}$ at each Gauss point. Finally, $\mathbf{B}_{\xi_i,\eta_j,\zeta_k}$ is obtained using Eq. (11).

For training the ANN model, $M = 100{,}000$ patterns were used and 25,000 patterns were used each for testing set. The cost function was optimized using Adam optimizer [24], and the weights of the network were randomly initialized using Xavier initializer [25]. The learning rate was decreased with increasing number of epochs using a linear decay schedule, in which the learning rate is decreased in a linear fashion from an initial value of 0.01–0. The network was trained for 12,000 epochs with the training error (mean squared error) of 2.1345×10^{-5}. The testing error is obtained as 1.3245×10^{-4}.

3.3 Stiffness Matrix Evaluation

Since normalized elements were utilized in the ANN training, pre-processing of the physical elements is required to apply the network to physical elements. As the ANN generates $\boldsymbol{B}$ matrices of normalized elements, a post-processing of the ANN output is also necessary to reconstruct the stiffness matrix of the physical elements.

In the pre-processing step, the element coordinates input for the neural network, i.e., the normalized coordinates are computed as follows:

$$\boldsymbol{X}_i = \tfrac{1}{\ell_0}\boldsymbol{R}_z^{\mathrm{T}} \begin{Bmatrix} x_i - x_1 \\ y_i - y_1 \\ z_i - z_1 \end{Bmatrix} \quad \text{where} \quad i = 1, \ldots, 8 \tag{12}$$

and

$$\boldsymbol{R}_z = \begin{bmatrix} \cos\alpha & -\sin\alpha & 0 \\ \sin\alpha & \cos\alpha & 0 \\ 0 & 0 & 1 \end{bmatrix}, \tag{13}$$

and

$$l_0 = \tfrac{\ell_{12}+\ell_{14}}{2} \tag{14}$$

where α is the angle between the side connecting node 1 and node 2 of the physical hexahedral element and the x-axis. In Eq. (14), l_{12} and l_{14} are the lengths of sides connecting node 1 with node 2 and node 4, respectively. The coordinates obtained from Eq. (12) are used to compute the input vector to the neural network $\boldsymbol{X}^{(n)}$ as shown in Eq. (9).

In the post-processing step, the $\boldsymbol{B}$ matrices at (ξ_i, η_j, ζ_k)th Gauss point of the original element are obtained from those of normalized element as given below

$$_{\text{ANN}}\boldsymbol{B}_{\xi_i,\eta_j,\zeta_k} = \frac{1}{\ell_0}\boldsymbol{T}\,\boldsymbol{B}_{\xi_i,\eta_j,\zeta_k}\,\boldsymbol{Q}^T \tag{15}$$

where $\boldsymbol{T}$ is the strain transformation matrix [1], $\boldsymbol{B}_{\xi_i,\eta_j,\zeta_k}$ is the output of the ANN, and $\boldsymbol{Q}$ represents the rotation matrix.

Then, the stiffness matrix of 8-noded hexahedral element $\left(\boldsymbol{K}^e_{\text{ANN}}\right)$ is computed by $p_\xi \times p_\eta \times p_\zeta$ Gauss–Legendre quadrature rule as

$$\boldsymbol{K}^e_{\text{ANN}} = \sum_{\xi_i=1}^{p_\xi}\sum_{\eta_j=1}^{p_\eta}\sum_{\zeta_k=1}^{p_\zeta} w_{\xi_i,\eta_j,\zeta_k}\;{}_{\text{ANN}}\boldsymbol{B}^T_{\xi_i,\eta_j,\zeta_k}\;\boldsymbol{D}\;{}_{\text{ANN}}\boldsymbol{B}_{\xi_i,\eta_j,\zeta_k}\,J_{\xi_i,\eta_j,\zeta_k}, \tag{16}$$

where w_{ξ_i,η_j,ζ_k} is the weight, J_{ξ_i,η_j,ζ_k} is the determinant of the Jacobian matrix, and ${}_{\text{ANN}}\boldsymbol{B}_{\xi_i,\eta_j,\zeta_k}$ is the strain–displacement matrix of the $(\xi_i, \eta_j, \zeta_k)^{\text{th}}$ Gauss point given by Eq. (15). In Eq. (16), $\boldsymbol{D}$ is the material constitutive matrix, which is a function of material parameters Young's modulus E and Poisson's ratio ν. In current work, $p_\xi = p_\eta = p_\zeta = 2$.

4 Results and Discussion

The efficacy of the ANN model proposed above in generating the hexahedral element namely deep-learned 8-noded hexahedral element (DH8) is assessed by validating through a patch test [21], followed by solving the Cook's beam problem [25].

4.1 Patch Test

The patch test is conducted to find out whether the element is able to correctly predict constant stress fields over the given patch of elements [1]. The patch of elements shown in Fig. 2 is used to conduct the test. The material properties are taken as $E = 3.0 \times 10^7$ units (See Footnote 1) and $\nu = 0.3$. A constant force per unit area of $q = 1.0$ units (See Footnote 1) is applied on the face BCGF in the positive x-direction. The patch of elements is subjected to constraints as follows:

1. Face ADHE in Fig. 2 is constrained in X direction.
2. Face ABFE in Fig. 2 is constrained in Y direction.
3. Face ABCD in Fig. 2 is constrained in Z direction.

The patch of DH8 elements is said to pass this test if it can simulate a constant stress field over the whole domain, i.e., $\boldsymbol{\sigma}_{xx} = 1$ (See Footnote 1) and the other five stress components are equal to zero. Table 1 presents the results of the patch test for

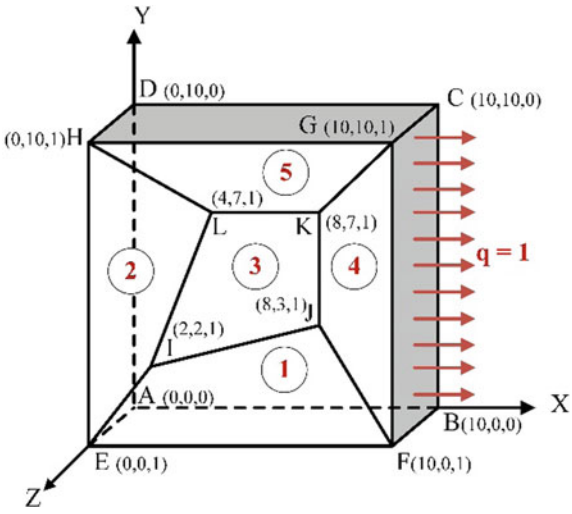


Fig. 2 Patch of elements used for conducting the patch test for DH8 element

Table 1 Stress values calculated from ANN output at all eight Gauss points (GP) of element 1 as shown in Fig. 2

GP	$\sigma_{xx}(1.0)^a$	$\sigma_{yy}(0.0)^a$	$\sigma_{zz}(0.0)^a$	$\sigma_{xy}(0.0)^a$	$\sigma_{yz}(0.0)^a$	$\sigma_{zx}(0.0)^a$
1	1.0214	0.0248	0.0248	0.0040	−0.0014	−0.0006
2	0.9838	−0.0163	−0.0163	−0.0029	0.0011	−0.0054
3	0.9941	0.0044	0.0044	0.0049	−0.0022	0.0068
4	0.9925	−0.0037	−0.0037	−0.0043	0.0016	0.0048
5	1.0192	0.0235	0.0235	0.00727	−0.0053	−0.0032
6	0.9819	−0.0168	−0.0168	0.0002	0.0039	−0.0080
7	0.9917	0.0029	0.0029	0.0083	−0.0076	0.0072
8	0.9906	−0.0042	−0.0042	−0.0010	0.0053	0.0042

The reference solution is shown in brackets
[a]All units are normalized units

element 1, as shown in Fig. 2. The results for the other elements also followed the similar trend of element 1. From Table 1, we can say that the DH8 element practically passes the patch test.

4.2 Cook's Beam Problem

The Cook's beam problem [26] (see Fig. 3) is solved using the proposed neural network to evaluate the performance of the neural network. The value of Young's modulus E is taken as 1.0 units (See Footnote 1), and the Poisson's ratio ν is taken as

0.3. A constant force per unit area of $q = 1/16$ units (See Footnote 1) is applied on the face, as shown in Fig. 3 in the positive y-direction. The domain was discretized with H8 elements. The vertical deflection at point A (v_A) is calculated after evaluating stiffness matrix using the output of the ANN. A mesh of $N_x \times N_y \times N_z = 64 \times 64 \times 4$, 20-noded hexahedral elements, was used to obtain the reference solution of $v = 23.9410$ (See Footnote 1). The results are then compared with those obtained by using H8 and 20-node hexahedral (H20) elements for different mesh sizes, as mentioned in Table 2.

Table 2 demonstrates the superior performance of the DH8 element compared with the H8 element and is converging to the solution obtained through the H20 element.

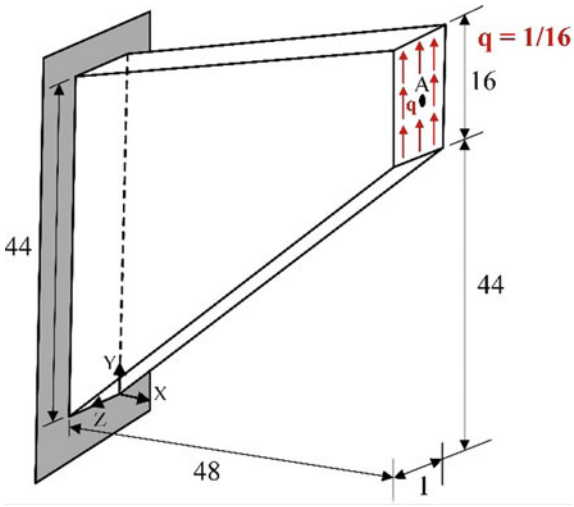


Fig. 3 Cook's beam problem

Table 2 Absolute percentage error in the y-direction displacement calculated at point A (shown in Fig. 3) [25]

Mesh	H8	H20	DH8
$2 \times 2 \times 1$	54.1493	7.1134	48.9510
$4 \times 4 \times 2$	27.5970	1.8978	25.4524
$8 \times 8 \times 2$	9.99890	0.6916	7.2841
$16 \times 16 \times 4$	3.0659	0.2606	2.1859
$32 \times 32 \times 4$	0.9121	0.0731	0.7427

5 Conclusion

In this work, a method was proposed to employ deep learning, an artificial intelligence technique, to compute the stiffness matrices of 3D solid finite elements. A deep learned 8-noded hexahedral element was developed to compute the strain–displacement matrices at each Gauss point. The training phase of the ANN is focused on the generation of normalized random element geometries, strain data generation, and optimizing the cost function. In the prediction phase, pre-processing of the inputs for the ANN model and post-processing of predicted strain–displacement matrix by the ANN model are described. By incorporating a separate layer of rigid body translation into the ANN model, the finite elements produced from it are also able to represent rigid body motions. At last, two numerical examples are also used to quantify the performance of the ANN model.

This demonstrates how 3D elasticity problems can be solved using ML by modeling finite elements. This may open the door for the use of ML-based algorithms in the future to create fast and effective FEM simulations.

Acknowledgements The authors gratefully acknowledge the support from SERB, DST under the projects IMP/2019/000276, CRG/2022/002218, and VSSC, ISRO through MoU No.: ISRO:2020:MOU: NO:480.

References

1. Zienkiewicz O, Taylor R, Zhu JZ (2013) The finite element method: its basis and fundamentals, 7th edn. Butterworth-Heinemann, Elsevier
2. Goodfellow I, Bengio Y, Courville A (2016) Deep Learning. MIT Press
3. Mitchell T (1997) Machine learning. McGraw-Hill Education
4. Lagaris IE, Likas A, Fotiadis DI (1998) Artificial neural networks for solving ordinary and partial differential equations. IEEE Trans Neural Networks 9(5):987–1000
5. Raissi M, Perdikaris P, Karniadakis GE (2019) Physics-informed neural networks: a deep learning framework for solving forward and inverse problems involving nonlinear partial differential equations. J Comput Phys 378:686–707
6. Liu X, Athanasiou CE, Padture NP, Sheldon BW, Gao H (2020) A machine learning approach to fracture mechanics problems. Acta Mater 190:105–112
7. Ozarde AP, Narayan J, Yadav D, McNay GH, Gautam SS (2020) Optimization of diesel engine's liner geometry to reduce head gasket's fretting damage. SAE Int J Engines 14(1):81–97
8. Gautam SS, Khan K (2020) Detection of fretting fatigue using machine learning algorithms. In: 3rd structural integrity conference and exhibition (sice 2020) structural integrity at multiple length scales (e-Conference), IIT Bombay
9. Nowell D, Nowell P (2020) A machine learning approach to the prediction of fretting fatigue life. Tribol Int 141:105913
10. Vithalbhai SK, Gautam SS (2021) A machine learning approach to fretting fatigue problem. In: Proceedings of the international conference on futuristic technologies (e-conference)—structural health monitoring, energy harvesting, green material and biomechanics. IIT Delhi
11. Gouravaraju S, Narayan J, Sauer RA, Gautam SS (2023) A Bayesian regularization-backpropagation neural network model for peeling computations. J Adhes 99(1):92–115

12. Oishi A, Yagawa G (2020) A surface-to-surface contact search method enhanced by deep learning. Comput Mech 65(4):1125–1147
13. Oishi A, Yagawa G (2017) Computational mechanics enhanced by deep learning. Comput Methods Appl Mech Eng 327:327–351
14. Vithalbhai SK, Nath D, Agrawal V, Gautam SS (2022) Artificial neural network assisted numerical quadrature in finite element analysis in mechanics. Materials Today: Proceedings 66:1645–1650
15. Chinchkar R, Nath D, Gautam SS (2023) Design of efficient quadrature scheme in finite element using deep learning. Advances in engineering design: select proceedings of FLAME 2022, pp. 21–29, Springer, Singapore
16. Khoei A, Moslemi H, Seddighian M (2020) An efficient stress recovery technique in adaptive finite element method using artificial neural network. Eng Fract Mech 237:107231
17. Liang L, Liu M, Martin C, Sun W (2018) A deep learning approach to estimate stress distribution: a fast and accurate surrogate of finite-element analysis. J R Soc Interface 15(138):20170844
18. Saikia BB, Nath D, Gautam SS (2023) Application of machine learning in efficient stress recovery in finite element analysis. Mater Today: Proc 78:359–363
19. Saikia BB, Nath D, Gautam S S (2024) Machine learning models for stress recovery in finite element method. In: Recent trends in computational mechanics and simulation: select proceedings of ICCMS 2022, Springer, Singapore (in press)
20. Nath D, Neog DR, Gautam SS (2024) Application of machine learning and deep learning in finite element analysis: a comprehensive review. Archives of computational methods in engineering, pp. 1–40
21. Jung J, Yoon K, Lee PS (2020) Deep learned finite elements. Comput Meth Appl Mech Eng 372:113401
22. Nath SS, Nath D, Gautam SS (2022) Design of efficient finite elements using deep learning approach. In: Biennial international conference on future learning aspects of mechanical engineering. Springer Nature Singapore, Singapore, pp 11–20
23. Ioffe S, Szegedy C (2015) Batch normalization: accelerating deep network training by reducing internal covariate shift. In: International conference on machine learning. PMLR, 2015, pp 448–456
24. Kingma DP, Ba JA (2014) A method for stochastic optimization, arXiv preprint arXiv:1412.6980
25. Glorot X, Bengio Y (2010) Understanding the difficulty of training deep feedforward neural networks. In: Proceedings of the thirteenth international conference on artificial intelligence and statistics. JMLR workshop and conference proceedings, pp 249–256
26. Cook RD, Malkus DS, Plesha ME, Witt RJ (2007) Concepts and applications of finite element analysis. John Wiley & Sons

A Comparative Study of PID and Nonlinear Backstepping Flight Control Laws for Pixhawk-Based Multicopter



Divyansh Singh, Hari Om Verma, Vivek Kumar, Rajesh K. Saluja, Sanjay Singh, and Keerthana Radhakrishnan

Abstract This paper investigates the control strategies for a quadcopter UAV controlled by a Pixhawk-based flight controller. First, the nonlinear mathematical model of a quadcopter has been derived considering its aerodynamic and rotor effects. From this model, it can be seen that the quadcopter is a nonlinear underactuated system which makes its control design challenging. Two control approaches for this quadcopter system have been chosen and analysed here, the linear proportional–integral–derivative (PID) control and the nonlinear Backstepping control approach. Both approaches were adapted for use in the PX4-Pixhawk-based controllers. Their performance was tested with a quadcopter dynamic model and the results were simulated. A comparison of the obtained results indicates that the Backstepping control technique settles > 5 times faster than the PID control and also provides more stability to the system making it the preferable control strategy for quadcopters using Pixhawk-based autopilots.

Keywords Flight control · Pixhawk · PID · Backstepping · Nonlinear controller · MATLAB–Simulink

1 Introduction

In recent years, unmanned aerial vehicles (UAVs) have seen enormous applications in various fields, from defence to commercial markets, making a strong presence, because of their mobility and ease of handling. Among the different types of UAVs, this paper focuses on quadcopters. Quadcopters have only four unique control inputs

D. Singh (✉) · H. O. Verma · V. Kumar · R. K. Saluja · S. Singh
Amity Institute of Aerospace Engineering, Amity University Uttar Pradesh, Noida, Uttar Pradesh, India
e-mail: singh2002.divyansh@gmail.com

K. Radhakrishnan
REUDE Technologies, Chennai, Tamil Nadu, India

© The Author(s), under exclusive license to Springer Nature Singapore Pte Ltd. 2024

S. Singh et al. (eds.), *Recent Advances in Aerospace Engineering*, Lecture Notes in Mechanical Engineering, https://doi.org/10.1007/978-981-97-1306-6_21

(rotor speeds) and six degrees of freedom (three translational and three rotational motions), making them underactuated systems. When we factor in the intricate aerodynamic considerations, the resulting dynamics become nonlinear too [1–4]. Quadcopters can carry out actions like vertical take-off and landing, and hovering through the highly manoeuvrable forces generated by their four rotors and propellers with varying speeds. A robust control algorithm is essential to control these rotor forces in order to ensure the stability of such a nonlinear underactuated system.

A simple but effective control algorithm can be developed by linearizing the nonlinear model with appropriate assumptions in place. However, these assumptions introduce some uncertainty into the quad model, resulting in an unpredictable response. PID and LQR are some of the linear systems for developing controls but are suitable only for simple environments [5, 6]. It is difficult for them to handle the UAV motion when uncertainties are aroused in the quad model. Hence, there is a need to find a controller scheme to make the system much more predictable and robust. For that reason, there are numerous cutting-edge control strategies developed in the past, such as the adaptive strategies and H-infinity control designs. Methodologies such as Nonlinear Feedback Linearization [5], Backstepping [7, 8] in Sliding Mode [9] command, and Adaptive Backstepping [10], etc., can be also used to design the controller.

Pixhawk flight controller is one of the most popular flight controllers to be employed on quadcopters for commercial or research purposes. This controller has a simple linear control law embedded in it that allows users to control the quadcopter motion. However, as discussed earlier, a linear control may not be effective when uncertainties arise during flight. Hence, we aim to make the controller more robust and improve its stability performance by enhancing it with a nonlinear control law.

2 Quadcopter Mechanics

Before designing the controller of any system, it is necessary to understand the kinematic and dynamic properties of the system. So, we start the analysis by introducing two operating frames. First is the inertial earth frame, E, with a NED frame orientation, and the second, the body frame, B as represented in Fig. 1. The body frame is attached to the centre of gravity of the quadcopter and moves along with it.

2.1 Quadcopter Kinematics

The kinematics of the quadcopter is established in this section using the body and inertial frames. The quadcopter's linear position and velocity in the inertial frame are defined as $X = (x, y, z)$ and $\dot{X} = (u, v, w)$, respectively. The angular position vector representing the roll, pitch, and yaw angles are defined in the body frame as $\theta = (\varphi, \theta, \psi)$, respectively, and the corresponding angular velocities are $\dot{\theta} =$

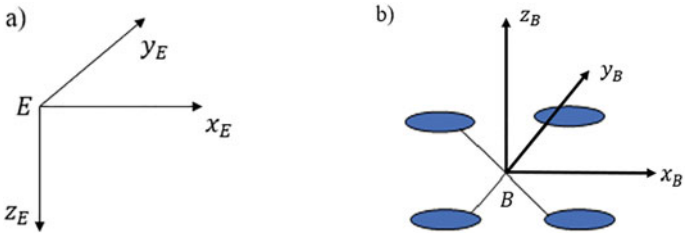


Fig. 1 **a** Earth reference frame (inertial), **b** body reference frame (noninertial)

$(\dot{\varphi}, \dot{\theta}, \dot{\psi})$. Keep in mind, though, that the inertial angular velocity vector, $\omega \neq \dot{\theta}$ since $\dot{\theta}$ is simply the time derivative of yaw, pitch, and roll angles and is in a different frame than ω. We may use the relation in Eq. (1) to translate these angular velocities into the angular velocity vector $\omega = (p, q, r)$.

$$\omega = \begin{bmatrix} p \\ q \\ r \end{bmatrix} = \begin{bmatrix} 1 & 0 & -c\theta \\ 0 & c\varphi & c\theta s\varphi \\ 0 & -s\varphi & c\theta c\varphi \end{bmatrix} \tag{1}$$

where ω—inertial angular velocity, c—cosine angle, and s—sin angle.

To relate the body and inertial frame variables, a rotation matrix **R**, as shown in Eq. 2, is used and converts the angular velocity vectors between the frames. By applying the *Z-Y-X* Euler angle conventions and 'undoing' the yaw, pitch, and roll consecutively, this matrix is created.

$$\mathbf{R} = \begin{bmatrix} c\varphi c\psi - c\theta s\varphi s\psi & -c\psi s\varphi - c\varphi c\theta s\psi & s\theta s\psi \\ c\theta c\psi s\varphi + c\varphi s\psi & c\varphi c\theta c\psi - s\varphi s\psi & -c\psi s\theta \\ s\varphi s\theta & c\varphi s\theta & c\theta \end{bmatrix} \tag{2}$$

2.2 *Quadcopter Equations of Motion*

Based on the above kinematics, two types of motion should be noted in a quadcopter, the translational and the rotational motion about the quadcopter's centre of gravity. This gives the quadcopter six degrees of freedom (6 DOFs) to move freely in space. Along with the three rotation DOFs around the *x, y,* and *z* axes, there are three translation DOFs about the three axes. These 6 DOFs can be achieved through the variation of motors' rotational speeds and thus govern the quadcopter movements. Some of the motions the quadcopter can achieve are forward, backward, lateral, vertical, roll, pitch, and yaw motions. These motions are a result of the quadcopter's rotors' reactive torque and this torque varies with respect to the rotor speed. The four

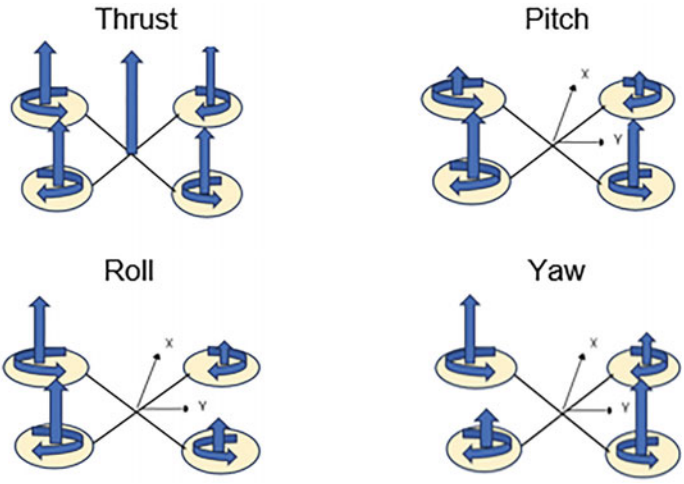


Fig. 2 Demonstration of forces acting on actuators for thrust, pitch, roll, and yaw motions

fundamental quadcopter motions determined by the rate of rotation of each propeller are shown in Fig. 2.

Figure 2 shows the quadcopter's four actuators and how these actuators work to control the angular velocity of the propeller. The arrow height represents the variation in the RPM of the propeller.

The quadcopter is thus regarded as an underactuated nonlinear system since it has four torque inputs and six DOF outputs. To simplify the quadrotor model and derive its equations of motion, we make some assumptions, including that the quadrotor body is rigid, its structure is symmetrical, and the ground impact is not considered.

The equations of motion of a quadcopter can be described using Newton's second law in the form of Euler equations as in Eqs. 3 and 4.

In the form of translation

$$ma^E = F^E \tag{3}$$

In the form of rotation

$$I\dot{\omega}^B + \omega^B \times \left(I\omega^B\right) = \tau^B \tag{4}$$

where m—mass of the quadcopter, a—acceleration, I—Inertia of the quadcopter, and τ—Moments of the quadcopter.

2.3 Quadrotor Dynamics Equation

To explain the complete dynamics of a quadcopter, we write its equations of motion in matrix form using Eqs. 5 and 6 and formulate its state space model later.

$$\begin{bmatrix} \ddot{x} \\ \ddot{y} \\ \ddot{z} \end{bmatrix} = \frac{k}{m} \begin{bmatrix} \sin\Psi\cos\Phi + \cos\Psi\sin\theta\cos\Phi \\ -\cos\Psi\sin\Phi + \sin\Psi\sin\theta\cos\Phi \\ \cos\theta\cos\Phi \end{bmatrix} F_t - \begin{bmatrix} 0 \\ 0 \\ g \end{bmatrix} \tag{5}$$

$$\begin{bmatrix} \ddot{\Phi} \\ \ddot{\theta} \\ \ddot{\Psi} \end{bmatrix} = \begin{bmatrix} \left(\frac{I_y - I_z}{I_x}\right)\dot{\theta}\dot{\Psi} \\ \left(\frac{I_z - I_y}{I_y}\right)\dot{\Phi}\dot{\Psi} \\ \left(\frac{I_x - I_y}{I_z}\right)\dot{\Phi}\dot{\theta} \end{bmatrix} + \begin{bmatrix} \frac{k}{I_x} & 0 & 0 \\ 0 & \frac{k}{I_y} & 0 \\ 0 & 0 & \frac{d}{I_z} \end{bmatrix} \begin{bmatrix} \tau_\Phi \\ \tau_\theta \\ \tau_\Psi \end{bmatrix} \tag{6}$$

where F_t is the total thrust, and τ_Φ, τ_θ, and τ_Ψ represent the moments generated for roll, pitch, and yaw angles, m—mass of the quadcopter, k—lift constant, d—drag constant, g—gravitational constant, and I_x, I_y, and I_z—moment of inertia parameters.

The primary driving force underlying all quadcopter movements is the rotors' thrust. The rotor thrust and torque are related to the square of rotor speed and can be formulated as follows:

$$T = C_t \rho A_r r^2 \omega^2 \tag{7}$$

$$q = C_q \omega^2 \tag{8}$$

where C_t—rotor thrust coefficient, ρ—density of air,A_r—propeller cross-section area, r—propeller radius, ω—rotor angular velocity, q—rotor torque, and C_q—rotor torque coefficient. The combined rotor thrust and torques are used as control inputs in the equations of motion to control the quadcopter movements and the relations in Eq. 9 provide those thrust, pitch, roll, and yaw control inputs for a quadcopter with the distance between the rotor and its centre of mass as l units.

$$\begin{aligned} F_t &= C_t\left(\omega_1^2 + \omega_2^2 + \omega_3^2 + \omega_4^2\right) \\ \tau_\Phi &= C_t l\left(-\omega_1^2 - \omega_2^2 + \omega_3^2 + \omega_4^2\right) \\ \tau_\theta &= C_t l\left(\omega_1^2 + \omega_2^2 - \omega_3^2 - \omega_4^2\right) \\ \tau_\Psi &= Cd\left(\omega_1^2 - \omega_2^2 + \omega_3^2 - \omega_4^2\right) \end{aligned} \tag{9}$$

2.4 State Space Model

The equations of motion of the quadcopter can be expressed in state space form as,

$$\dot{X} = f(X, U) \tag{10}$$

where the state vector X is,

$$X = [\Phi\theta\Psi pqruvwxyx]^T \in \mathbb{R}^{12} \tag{11}$$

and the control input vector is $U = [F_t \tau_\Phi \tau_\theta \tau_\Psi]^T$, as represented in Eq. 9

Rearranging the dynamic Eqs. 5 and 6 in state space form, we arrive at the following state equations,

$$\dot{\Phi} = p + r[\cos\Phi \tan\theta] + q[\sinh\Phi \tan\theta]$$

$$\dot{\theta} = q[\cos\Phi] - r[\sinh\Phi]$$

$$\dot{\Psi} = r\frac{\csc\Phi}{\cos\theta} + q\frac{\sinh\Phi}{\cos\theta} \tag{12}$$

$$\dot{p} = \frac{I_y - I_z}{I_X} rq + \frac{\tau_\Phi + \tau_{wx}}{I_x}$$

$$\dot{q} = \frac{I_z - I_x}{I_y} pr + \frac{\tau_\theta + \tau_{wy}}{I_y}$$

$$\dot{r} = \frac{I_X - I_y}{I_z} pq + \frac{\tau_\Psi + \tau_{wz}}{I_z} \tag{13}$$

$$\dot{u} = rv - qw - g[\sinh\theta] + \frac{F_{wx}}{m}$$

$$\dot{v} = pw - ru + g[\sinh\Phi \csc\theta] + \frac{F_{wy}}{m}$$

$$\dot{w} = qu - pv + g[\cos\theta \cos\Psi] + \frac{F_{wx} - F_t}{m} \tag{14}$$

$$\dot{x} = w[\sinh\Phi \sinh\Psi + \cos\Phi \cos\Psi \sinh\theta] - v[\cos\Phi \sin\Psi - \cos\Psi \sinh\Phi \sinh\theta] + u[\cos\Psi \cos\theta]$$

$$\dot{y} = v[\cos\Phi \cos\Psi + \sinh\Phi \sinh\Psi \sinh\theta] - w[\cos\Psi \sinh\Phi - \cos\Phi \sinh\Psi \sinh\theta] + u[\cos\theta \sinh\Psi]$$

$$\dot{z} = w[\cos\Phi\cos\theta] - u[\sinh\theta] + v[\cos\theta\sinh\Phi] \tag{15}$$

Here, each equation number presents a combination of different state equations as stated below,

2.4.3—The combination of angle rate equations.
2.4.4—The combination of angular acceleration equations.
2.4.5—The combination of velocity rate equations.
2.4.6—The combination of position rate equations.

3 Control Strategy

The developed mathematical model demonstrates that this system is underactuated, and designing a controller for this kind of system is not simple. In this thesis, we have used two control methods to regulate the quadrotor motions controlled by a PX4-Pixhawk-based flight controller, the PID control and the Backstepping control system. Since a PID system provides only a linear control, to achieve more robustness, we need to incorporate nonlinear terms in our dynamics model. To control the nonlinear dynamic model, we need to design a nonlinear controller. For this case, we have chosen one of the popular and simple techniques, the Backstepping method as our nonlinear control technique and use the Lyapunov function to define its stability conditions.

3.1 PID Control Technique

The proportional–integral–derivative (PID) technique is a control algorithm frequently used in engineering and automation systems. It aims to reach and keep our control inputs at a specified setpoint. As a result of the discrepancy between the planned setpoint and the measured process variable, the PID controller continually calculates an error signal. Then, based on three terms—the proportional term (P), the integral term (I), and the derivative term (D)—it regulates the control output based on Eq. 16.

$$u(t) = k_p e(t) + k_i \int e(t)dt + k_d \frac{de}{dt} \tag{16}$$

where $u(t)$—system output, k_p, k_i, k_d—proportional, integral, and derivative gains, and $e(t)$—error value.

In the PX4 controllers, three layers of cascade PID are used to control the quadcopter rotors. In this three-layer PID, the first layer calculates the needed velocity by taking the position error, and then in the second layer, the attitude commands

are calculated by using velocity error. In the final layer, the moments are calculated to achieve the required attitude which then becomes the control inputs for the quadcopter rotors.

3.2 Backstepping Control Technique

Backstepping is a type of control strategy in which specific states' control laws are created using a recursive control algorithm. These specific states are referred to as virtual control in our system model. While other control strategies such as feedback linearization linearize the nonlinear models, the Backstepping method does not approximate the system's nonlinear terms, thus helping the system remains stable despite external disturbances.

The Backstepping control technique is implemented in our state space model from Sect. 2.4. However, in this section, the state vector and control inputs are rewritten as in Eqs. 17 and 18.

$$X = [x_1 x_2 x_3 x_4 x_5 x_6 x_7 x_8 x_9 x_{10} x_{11} x_{12}] \tag{17}$$

$$U = \left[U_{thrust} U_{roll} U_{pitch} U_{yaw}\right] \tag{18}$$

3.3 Lyapunov Theory

Lyapunov theory is used to define the stability and behaviour of dynamical systems. Creating a scalar function known as a Lyapunov function, which measures the system's energy or potential, is the essence of Lyapunov's theory. The distance between the system's current state and its equilibrium point is measured by this function, and the stability characteristics of the system can be ascertained by looking at how this function behaves. For our nonlinear model, we use the Lyapunov functions to define our stability conditions.

3.4 Backstepping Control Law

Using the Lyapunov theory, the control laws for the roll, pitch, yaw, and attitude motions are derived to obtain a stable nonlinear flight control. Firstly, the derivation of the roll control is explained in detail from Eqs. (19)–(30).

The first two equations in the state space represent the roll angle and the roll rate. Substituting the new state space vector and control input terminologies into the state

space equations, we obtain

$$\dot{x}_1 = x_2 \tag{19}$$

$$\dot{x}_2 = c_1 x_4 x_6 - \Omega_r c_2 x_4 + d_1 U_\phi \tag{20}$$

Here, the term $\Omega_r c_2 x_4$ points to the gyroscopic precession. Gyroscopic precession phenomena happens when a rotating body's axis is moved. Gyroscopic forces on the body are dependent on the motors' inertia (Ω_r), the rate of pitch ($\dot{q}$), roll ($\dot{p}$), and the speed of each motor (ω).

Only the last term in the roll angle equations subsystem is a function of control inputs. Hence it is in a tight feedback form, a clear positive Lyapunov function.

$$v(e) = \frac{1}{2} e_1^2 \tag{21}$$

The error (difference between actual and desired value) in roll angle is e_1

$$e_1 = x_1 d - x_1 \tag{22}$$

The derivative of the above Lyapunov function 19 is

$$\dot{v}(e_1) = e_1(\dot{x}_1 d - \dot{x}_1) \tag{23}$$

Substituting from the above roll angle state space equations,

$$\dot{v}(e_1) = e_1(\dot{x}_1 d - x_2) \tag{24}$$

To define the system's stability, we use the Krasovskii–LaSalle principle. If the time derivative of the Lyapunov function becomes negative, then the system is stable. To make it negative, we assume the sign of constant:

$$x_2 = \dot{x}_{1d} + k_1 e_1 \tag{25}$$

where $k_1 > 0$

The error variable, e_2, represents the discrepancy between the current state's value and the desired value:

$$e_2 = x_2 - \dot{x}_{1d} - k_1 e_1 \tag{26}$$

Coordinate (e_1, e_2) of the Lyapunov function can be augmented as,

$$v(e_1, e_2) = \frac{1}{2}\left(e_1^2 + e_2^2\right) \tag{27}$$

Taking the time derivative of the Lyapunov function with coordinate,

$$\dot{v}(e_1, e_2) = e_1\dot{e}_2 + \dot{e}_1 e_2$$

$$\dot{v}(e_1, e_2) = e_1(\dot{x}_1 d - x_2) + e_2(\dot{x}_2 - \ddot{x}_1 d - k_1\dot{e}_1)$$

$$\dot{v}(e_1, e_2) = e_1(\dot{x}_1 d - x_2) + e_2[c_1 x_4 x_6 + d_1 U_{roll} - \Omega_r c_2 x_4 - \ddot{x}_1 d - k_1(\dot{x}_1 d - \dot{x}_1)] \tag{28}$$

$$\because e_2 + k_1 e_1 = \dot{x}_1 d - \dot{x}_1$$

Now from the above equation, we can write.

$$\dot{v}(e_1, e_2) = -e_1(e_2 + k_1 e_1) + e_2(c_1 x_4 x_6 + d_1 U_{\text{roll}} - \Omega_r c_2 x_4) - e_2(\ddot{x}_1 d + k_1(\dot{x}1 - \dot{x}1d))$$

$$\dot{v}(e_1, e_2) = e_2(c_1 x_4 x_6 + d_1 U_{\text{roll}} - \Omega_r c_2 x_4) - e_2(\ddot{x}_1 d - k_1(e_2 - k_1 e_1)) - e_1 e_2 - k_1 e_1^2 \tag{29}$$

Finally, we can extract U_{roll} from the above equation, satisfying $\dot{v}(e_1, e_2) < 0$

$$U_{\text{roll}} = \frac{1}{d_1}[e_1 - x_4 x_6 c_1 - x_4 c_2 \Omega_r - c_1(e_2 - k_1 e_1) - k_2 e_2] \tag{30}$$

Now, in a similar fashion to the roll control law derivation, we deduce the control law expressions for the pitch, yaw, and attitude control as Eqs. (31)–(33) respectively.

$$U_{\text{pitch}} = \frac{1}{d_2}[e_1 - x_2 x_6 c_3 - x_2 c_2 \Omega_r - c_3(e_2 - k_3 e_1) - k_4 e_2] \tag{31}$$

$$U_{\text{yaw}} = \frac{1}{d3}[e_1 - x_2 x_4 c_5 - c_5(e_2 + k_5 e_5) - k_6 e_2] \tag{32}$$

$$U_{\text{thrust}} = \frac{m}{\cos(x1)\cos(x3)}[e1 + g - k7(e2 + k7e1) - k8e2] \tag{33}$$

3.5 MATLAB–Simulink Controller Model

See Fig. 3.

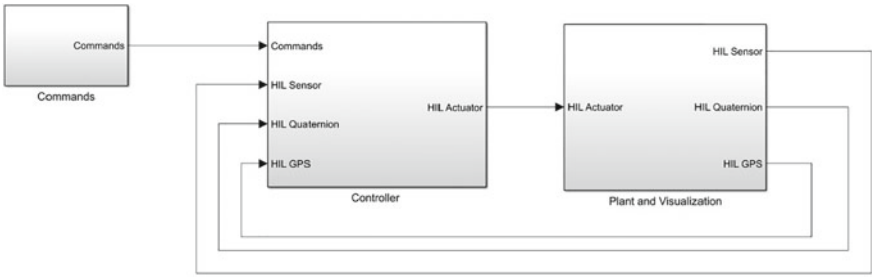


Fig. 3 Controller model designed in MATLAB–Simulink

A Simulink model was adapted from the MATLAB–Simulink PX4 system model to design our PID and Backstepping controllers and test them via software-in-the-loop (SITL) method. The model included three subsystems, the Command, Controller, and Plant and Visualization systems, each serving a specific purpose. Our quadcopter system was predefined in the Plant system and our controllers, the PID and the Backstepping, were modelled according to their control laws in the Controller subsystem, one at a time. The Command subsystem is where the desired system input commands were fed in, and the results were visualized in the Visualization subsystem. Using this Simulink model, we have obtained simulation results for a case scenario to understand the working of both the controllers and is discussed in Sect. 4.

4 Result and Discussion

4.1 Command Inputs

To summarize our work, we have chosen the Backstepping control technique to improve the PID control technique in the PX4-Pixhawk-based flight controllers. The control laws and the quadcopter dynamic model were all modelled in MATLAB/Simulink software with the desired quadcopter position and orientation as input command values. The results were simulated using the quadcopter parameters listed in Table 1 and the command values explained below. The obtained results from our simulations using both techniques are then reported in this section and are compared.

The command values that need to be fed into the controller (with the PID/Backstepping laws) are the desired drone coordinate values, x, y, z, and yaw (ψ). ψ is used here to input the drone direction. For our test case, we use the values 5 m as altitude, 3 m and 4 m for the x and y values, and 10 degrees for orientation. The gain values used to achieve the desired inputs through both the PID and Backstepping control laws are listed in Tables 2 and 3.

Table 1 Quadcopter parameters

Mass (m)	0.6 (kg)
Moment of inertia along x-axis, I_x	0.0119 (kg m^2)
Moment of inertia along y-axis, I_y	0.0119 (kg m^2)
Moment of inertia along z-axis, I_z	0.0223 (kg m^2)
Quadcopter link length, l	0.11 (m)

Table 2 PID control gains

Gains	Roll control	Pitch control	Yaw control	Altitude control
k_p	0.27	0.27	3	1
k_i	0.05	0.05	1	0.01
k_d	0.065	0.065	1.2	0.02

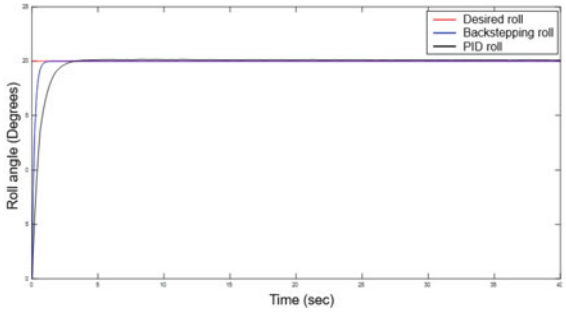
Table 3 Backstepping control gains

Gains	Roll control	Pitch control	Yaw control	Altitude control
k_1	5	5	2	5
k_2	5	5	2	4

4.2 Comparison of Simulation Results

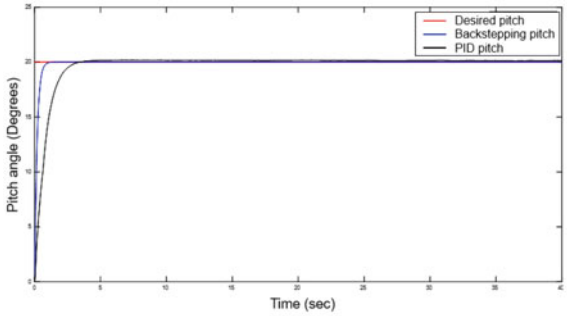
This section illustrates the roll, pitch, yaw, and altitude outputs obtained using both the controllers for our test case through Figs. 4, 5, 6 and 7 and compares the relevant performance parameters to analyse the controller abilities.

In the above graph comparisons of Backstepping simulation results with PID, by observing the rise time, the overshooting, and the settling time, we can witness that the Backstepping controller is capable of stabilizing the quadcopter faster with minimal overshoot than the PID. Analysing the most important aspect, the settling



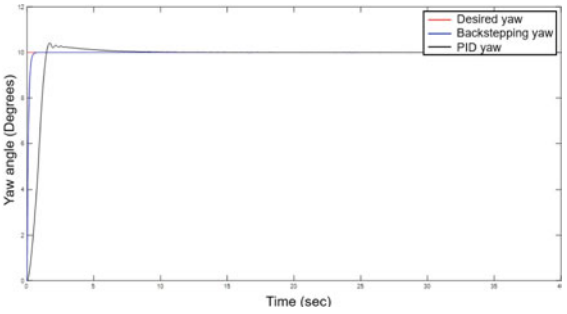
Parameters	PID	Backstepping
Rise time	1.56 sec	0.645 sec
Settling time	5 sec	0.956 sec
Overshoot	15%	3.9e-5%
Peak	21 deg	20 deg
Peak time	3 sec	1.5 sec

Fig. 4 Roll angle results obtained from PID and Backstepping control laws with resultant parameters



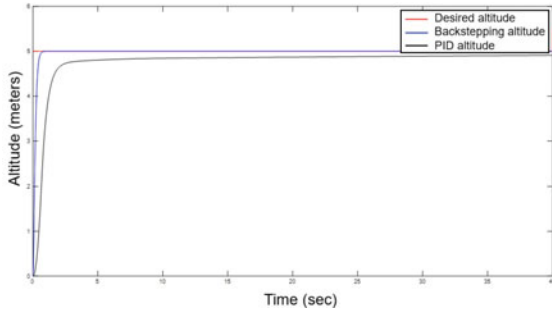
Parameters	PID	Backstepping
Rise time	1.56 sec	.745 sec
Settling time	6 sec	.956 sec
Overshoot	16%	4.9e-2%
Peak	22 deg	20 deg
Peak time	3 sec	1.6 sec

Fig. 5 Pitch angle results obtained from PID and Backstepping control laws with resultant parameters



Parameters	PID	Backstepping
Rise time	2 sec	0.745 sec
Settling time	7 sec	0.956 sec
Overshoot	16%	4.9e-1%
Peak	11 deg	10.4 deg
Peak time	3 sec	1.6 sec

Fig. 6 Yaw angle results obtained from PID and Backstepping control laws with resultant parameters



Parameters	PID	Backstepping
Rise time	1.56 sec	1.645 sec
Settling time	Not converged	2.956 sec
Overshoot	-10%	3.9e-6%
Peak	4.5 m	5 m
Peak time	NA	3.5 sec

Fig. 7 Altitude results obtained from PID and Backstepping control laws with resultant parameters

time, we see that the Backstepping controller is able to reach our desired attitude setpoint within 1 s and reach 5 m in 3 s, which is an acceptable response time for a quadcopter rather than the PID control that requires longer settling time. Also, the control logic for the Backstepping control technique detailed in this paper includes

only the attitude and altitude controllers. We can develop this control logic further by implementing a Backstepping position virtual control, and from that controller, we shall be able to find out the desired pitch and roll angle for a specific x and y value. By feeding the output roll and pitch angle into the attitude controller, we will then be able to further improve the position and attitude control of the quadcopter.

5 Conclusion

The control laws for a PX4-Pixhawk-based quadcopter have been studied in this paper. The mathematical model of the quadcopter in its three-dimensional state space form has been derived. The model is made sufficiently realistic and nonlinear by considering the effects of rotor dynamics and aerodynamics. Two types of control techniques, the PX4 autopilot–based PID technique and the Backstepping technique, have been employed here to control the quadrotor's attitude and position in 3D space specifically the roll, pitch, and yaw angles as well as the altitude since these parameters contribute directly to generating the motor thrusts of the quadcopter. An investigation of the simulation results generated from both techniques shows that in terms of rise time, settling time, and overshoot, the Backstepping controller gives a better performance compared to PID. Thus, it can be concluded that the Backstepping controller makes a Pixhawk autopilot more robust than the PID controllers.

Funding Not applicable.

References

1. Bresciani T (2008) Modelling, identification and control of a quadrotor helicopter. Master's thesis, Lund University
2. Hoffmann G, Huang H, Waslander S, Tomlin C (2007) Quadrotor helicopter flight dynamics and control: Theory and experiment. In: Proceedings of the AIAA guidance, navigation, and control conference, 2007, pp 1–20
3. de Oliveira MDLC (2011) Modelling, identification and control of a quadrotor aircraft. Master's thesis, Czech Technical University in Prague
4. Balas C (2006) Modelling and linear control of a quadrotor. Cranfield Unicersity, M.Sc. thesis, vol 2007
5. Al-Younes Y, Al-Jarrah M, Jhemi A (2010) Linear versus nonlinear control techniques for a quadrotor vehicle. In: 7th International symposium on mechatronics and its applications (ISMA), IEEE, 2010, pp 1–10
6. Bouabdallah S (2007) Design and control of quadrotors with application to autonomous flying. Ph.D. dissertation, Federal Polytechnic School of Lausanne
7. Madani T, Benallegue A (2006) Backstepping control for a quadrotor helicopter. In: 2006 IEEE/RSJ international conference on intelligent robots and systems, 2006, pp 3255–3260
8. Whitehead B, Bieniawski S (2010) Model reference adaptive control of a quadrotor UAV. In: The AIAA Guidance Navigation and Control Conference, Canada, 2010.

9. Huang M, Xian B, Diao C, Yang K, Feng Y (2010) Adaptive tracking control of underactuated quadrotor unmanned aerial vehicles via backstepping. In: American control conference (ACC), 2010, pp 2076–2081
10. Bouabdallah S, Siegwart R (2005) Backstepping and sliding-mode techniques applied to an indoor micro quadrotor. In: International conference on robotics and automation, 2005, pp 2247–2252

Countering Drone Using a Mountable Net Mechanism



M. Rudresh, Ayush Shetty Kannoor, Gagana Babunaidu, Gnana Shibi Manoharan, Sudeep S. Bellavi, Vinayak Tsalla, and G. V. Sharath Chandra

Abstract UAVs are transforming the global market as a compact, cost-effective product for various applications. These unmanned vehicles are easily accessible and gather valuable data from any desired location. However, the unauthorized use of these UAVs damages people and places' safety, security, and privacy. Demand for new technologies to counter UAVs is crucial. Counter UAS (CUAS) have evolved to nullify the threats caused by these vehicles. While most CUAS use radar to detect and jam the drone's signal, limiting the system's operation to a particular area. The purpose of our project is to study and implement a mechanism that allows flying UAVs to be tapped using a net. An effort was made to develop a compact and robust mechanism to launch a net at the enemy drone to destroy it. Testing was done with different mechanisms and finally settled on a compressed air mechanism that propels four deadweights connected to each corner of the net using a solenoid valve.

Keywords UAV · Counter UAV · Anti-drone · Net launcher · Capturing UAV

1 Introduction

In recent years, UAVs have gained significant attention for their adaptive design and wide applications. The market demand for UAVs and intelligence integration into these systems presages future problems. A CUAS can protect sensitive areas from UAV threats, such as critical infrastructure and military bases.

The expected growth in UAV traffic will bring new threats, including the possibility of rogue or malicious UAVs (mUAVs) that endanger low-level airspace operations. Unfortunately, the existing C-UAV systems must be ground-based or air-based to detect such mUAVs since they are typically inflexible and scalable [1].

M. Rudresh (✉) · A. S. Kannoor · G. Babunaidu · G. S. Manoharan · S. S. Bellavi
Department of Aeronautical Engineering, Dayananda Sagar College of Engineering, Bengaluru, India
e-mail: rudresh-ae@dayanandasagar.edu

V. Tsalla · G. V. Sharath Chandra
Tsalla Aerospace Technologies Pvt Ltd, Bengaluru, India

© The Author(s), under exclusive license to Springer Nature Singapore Pte Ltd. 2024

S. Singh et al. (eds.), *Recent Advances in Aerospace Engineering*, Lecture Notes in Mechanical Engineering, https://doi.org/10.1007/978-981-97-1306-6_22

Using computer vision to detect UAVs has been extensively researched. Sensor-based systems detect, track, and neutralize/turn off incoming UAVs autonomously. Such systems require training under different weather conditions [2]. The potential UAV misuse has led to the formation of regulations and regulatory bodies in various countries. The much-emphasized RF communication the UAV uses is the most reliable method to be deployed broadly. However, CUAS technology is still evolving when it comes to commercial UAVs [3, 4]. Nets can serve as a solution to mitigate small UAVs, which are difficult to neutralize by guns or guided missiles. Nets can be fitted with parachutes to ensure that the UAV descends safely [5, 6].

A detailed look into developing a tool to utilize these nets that can be mounted onto a UAV to catch moving targets is looked into in this paper.

2 Project Framework

The following objectives were set to achieve the project's goal.

1. To explore various counter UAV systems.
2. To investigate methods to propel a net.
3. To design and fabricate a net launching mechanism.
4. To iteratively test the mechanism under different conditions.
5. To optimize the equipment to improve upon set design parameters.

3 Design Parameters

To start with initial design process, the mission profile was drawn, depicted in Fig. 1.

The parts labeled in Fig. 1 are 101—Net basket, 102—Projectile Tube, 103—Propellant cartridges, 104—Net weights, 105—Net and 106—Target drone.

The mission profile are as follows:

1. The enemy drone will be captured within a range of 5 m from the host drone.
2. Maximum weight of mechanism should be 2 kg.

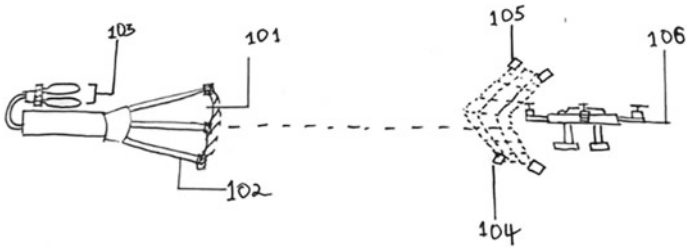


Fig. 1 Mission profile

Table 1 Comparison of different propulsion methods

Criteria	Electromagnetic	Spring	Jumper	Pneumatic
Weight	1	4	5	3
Range	5	3	5	4
Complexity	3	5	3	5
Repairability	3	2	4	5
Cost	1	3	1	1
Total	13	17	18	18

3. The net should be large enough to capture the enemy drone.
4. Effective weight of the deadweights should not exceed 100 g.

3.1 Launcher Parameters

Dimensional. The launcher must be as compact and light as possible while maximizing effective range. The dimensions would be highly dependent on the drone carrying the mechanism. An existing drone platform with a maximum weight of 2 kg and a roughly 400 × 300 × 300 mm volume was the ideal constraint considered.

Propulsion Mechanism. A propulsion method was chosen based on a relative comparison. The methods deliberated upon included electromagnetic, spring, jumper, and pneumatic propulsion. The best methods were decided as the jumper and the pneumatic propulsion based on the comparison matrix in Table 1.

3.2 Net Parameters

Material Selection. To effectively trap, the material of the net should have enough strength. The net strands should not get damaged or break when encountering the spinning propeller blades; weight is also a constraint per mission requirements. A net made of polypropylene offered a good balance of strength and weight and hence was chosen as the net material.

Area. Generally, the more the net area, the more likely it is to trap a drone within. Net area and shape will directly influence the capturability of the drone. A preliminary net size of $1m^2$ was decided on, which is large enough to capture a small-sized drone. Even if a larger drone is encountered, the net can turn off a single propeller.

Spread angle. The net spread angle was chosen based on the effective range of 5 m. The spread angle was calculated using the following:

$$\theta = \tan^{-1}\left(\frac{a}{b}\right) \tag{1}$$

where "a" is the distance between the center of the target and the outer boundary of the net. The distance between the device base and the target center is b. For our mission, considering $a = 0.707$ m and $b = 5$ m, we get $\theta = 8.05°$ [7].

4 Jumper Mechanism

A jumper mechanism is a type of release mechanism that uses structures to store energy and release it in a controlled manner to perform specific tasks [8].

The jumper mechanism consists of four carbon fiber strips, two hinges, a barrel, an aluminum latch, a motor, a servo with an arm, a deadweight, and a string. Four deadweights are attached to the net; hence, four mechanisms must be connected to a master system to propel the net out.

The sizing of CF strips was based on the material properties of commercially available materials. Various sizes and orientations of the fibers were analyzed for bending using ANSYS ACP and Static Structural analysis. Results proved that a UD strip having 5 × 0.5 mm was the most efficient dimension with a length of 100 mm. The reaction force per strip was calculated as 11.929 N with a total maximum deformation of 0.031 mm, as shown in Fig. 2.

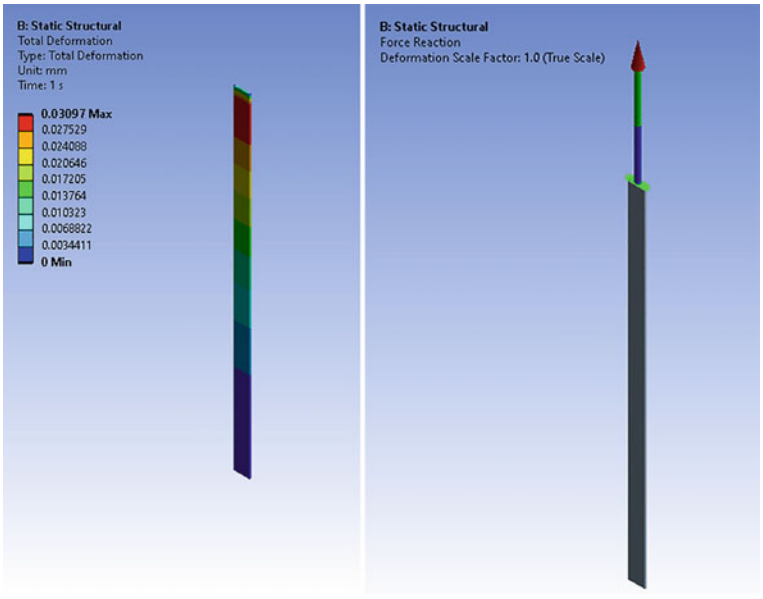
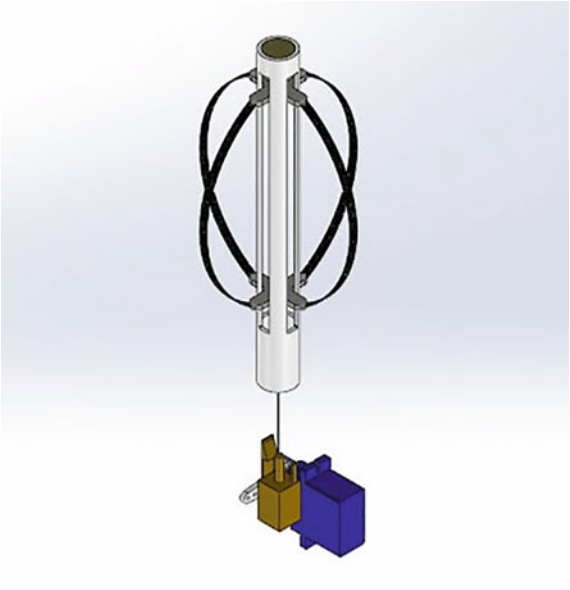


Fig. 2 Deflection and reaction of UD CF

Fig. 3 Jumper mechanism



Specific energy is the basis of Jumper. Carbon fiber and latex rubber are used to construct a hybrid compression-tension spring to maximize the specific energy [8].

CF strips are the primary energy storage device. A nylon hinge connects the four strips. While one hinge is fixed, the other moves along the barrel, stressing the CF. Hinges are connected to motor shafts by a nylon string. As the motor rotates, the string winds around the shaft, compressing the strips. Once the rated tension is reached, the string is released using an aluminum latch provided by the side of the motor. The reaction force aids in releasing the deadweight out of the barrel. In order to automate the process, a servo mechanism is used.

Though the jumper mechanism, seen in Fig. 3, offered an advantage in the range, the unavailability of unidirectional carbon fiber strips was the notable setback. Analysis showed that longer carbon fibers would be required to achieve maximum range, making the mechanism lengthy and ineffective for commercial use.

5 CO_2 Propulsion

Pneumatic propulsion uses pressurized or burning gas to provide thrust or propulsion. Gas propulsion systems offer high specific impulse, and they have relatively fewer points of failure than other propulsion systems. However, they can also be noisy and harmful to the environment if not properly controlled.

A class of carbon dioxide canisters and compressed air tanks were studied as the propellants for the system.

5.1 CO_2 Canisters

Carbon dioxide (CO_2) canisters in Fig. 4 are often used in paintball markers and air guns to propel projectiles. They are compact, easily replaceable, and portable, making them easier to carry and store. In order to achieve a range of 5 m, the pressure output of each canister is to be determined.

From, perfect gas equation

$$\mathrm{PV} = n\mathrm{RT} \tag{2}$$

Considering an ideal working temperature,
$T = 25\ ^\circ\mathrm{C} = 298.15$ K.
Mass of $CO_2 = 12$ g.
Volume of a 12 g CO_2 canister $= 14\ \mathrm{cm}^3 = 14 \times 10^{-6}\ \mathrm{m}^3$

$$n = \frac{m}{M} = \frac{\text{Mass of } CO_2}{\text{Molar Mass}} \tag{3}$$

$$n = \frac{12}{44.01} = 0.2726\,\text{mol} \tag{4}$$

Universal gas constant for CO_2 is, $R = 188.9$ J/Kg K.

$$R = \frac{(188.9 \times \text{Molar mass})}{(1000 \times \text{mass})} \tag{5}$$

$$R = \frac{(188.9 \times 44.01)}{(1000 \times 12)} = 0.693\,\text{J/mol K} \tag{6}$$

Substituting all of the above in perfect gas equation,

$$p = \frac{n\mathrm{RT}}{V} = \frac{0.2726 \times 0.69286 \times 298.15}{14 \times 10^{-6}} \tag{7}$$

$$P = 4022333.898\,\mathrm{N/m}^2 = 583.39\,\mathrm{psi} \tag{8}$$



Fig. 4 CO_2 canisters



Fig. 5 Canister casing

Converting the output pressure to equivalent force, a set of 4 canisters were used to obtain the required range.

5.2 *Conceptual Design for CO_2 Propulsion*

As canisters replaced the deadweights, an aerodynamic shape was to be incorporated to improve the mission performance, such as reducing the drag created by the canister. Inspired by the model rockets, a rocket-shaped casing around the canister was the most viable option. As shown in Fig. 5, the casing follows a reusable design wherein the canister can be replaced after each mission exercise for the next drill. As a consequence, loading time is reduced. The casing consists of a nosecone, body tube, and a tail.

Each component was designed on SolidWorks and assigned with PLA material to calculate weight and center of gravity. The Barrowman equations determined the rocket's stability.

5.3 *Performance Estimation*

Velocity of Exit Gas

$$V_e = \sqrt{\gamma \mathrm{RT}_e} = 252.32\ \mathrm{m/s} \tag{9}$$

Maximum Distance Covered by the Canister

$$H_B = \frac{T t_b^2 (M_0 - M_P)}{M_p^2} \ln\left(\frac{M_{0-} M_P}{M_e}\right) + \frac{T t_b^2}{M_p} - \frac{g t_b^2}{2} \tag{10}$$

$$H = 11.294\ \mathrm{m} \tag{11}$$

5.4 Testing

Iteration 1. There is a real need to experimentally verify the calculated range and velocity values against actual values. The test rig consists of a PVC pipe of 63.5 mm (2.5″) diameter and a simple bolt action trigger mechanism. The entire equipment can be adjusted to launch at any angle, like a mortar.

The testing was carried out for different barrel lengths and inclinations, as indicated in Table 2, to estimate the effect of barrel length and inclination on the range. The canister was unstable at low speed and tended to point toward the ground ending, its flight. Stability improvements were at the forefront of all optimizations. A fully enclosed barrel could be replaced by adopting slots within the barrel, reducing the length to establish greater accuracy, and lowering the safety latch to enable full spring compression within the trigger mechanism.

Iteration 2 and 3. After analyzing the data from the first test, it was observed that the diameter of the pipe itself, which was 63.5 mm, would contribute to building a vast structure when four were mounted on a drone.

A new constraint was set up to keep the pipe diameter at 40 mm to reduce the size of the mechanism; accordingly, the casing was reengineered. To maintain a stability caliber between 1.5 and 2d, the casing had to be more nose heavy. Additionally, the fins doubled to maintain the intended fin area, achieving stability. The components used in testing 2 are shown in Fig. 6.

Table 2 Testing results with inclination

S No.	Inclination (degrees)	Barrel (cm)	Max distance (m)	Time taken (s)
1	32	120	5.5	2
2	16	120	6.4	2
3	16	50	13.9	3

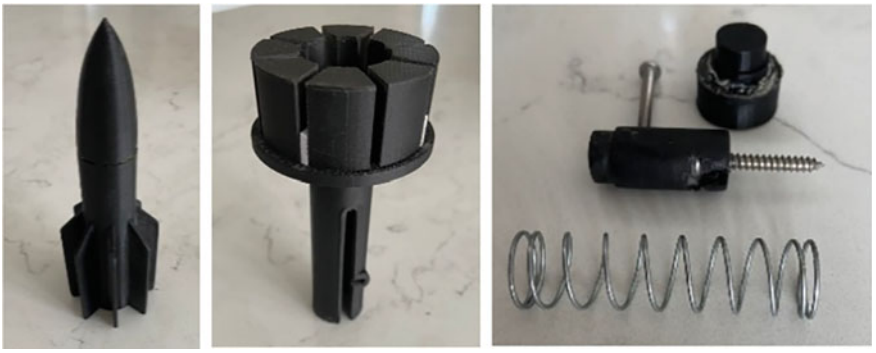


Fig. 6. 3D printed parts for testing 2



Fig. 7 Test 3 setup (left), dry ice formation upon piercing (right)

After iterative testing, it was observed that the CO_2 canisters that were bought had issues with dry ice forming upon piercing the ends to release gas for propulsion, which can be noticed in Fig. 7. The major problems were storage and supplier issues. On being stored for a long time, the canister loses its nature to release CO_2 at high pressure and instead forms dry ice. Also, the cost of refill was expensive. The next best alternative was compressed air propulsion, which was studied.

6 Compressed Air Propulsion

The prototype is made of plumbing PVC pipe rated for a pressure of 2.28 N/mm^2 (330psi). It consists of a tank body and end caps, ball valve and Schrader valve.

The end caps and tank body were sealed using CPVC cement to seal the ends from leaking air. The tank was checked for air leaks multiple times using an air compressor.

Additionally, a splitter was used to distribute the pressure to propel four deadweights. The assembly is depicted in Fig. 8.

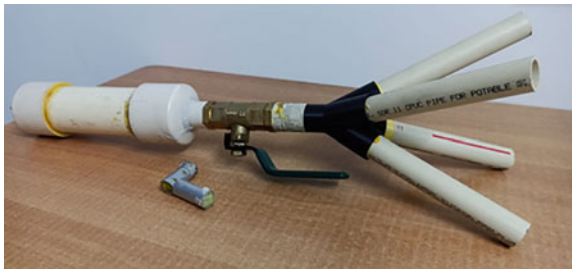


Fig. 8 Compressed air prototype 1

Table 3 Tabulation with different pressure for Iteration 1

S No.	Pressure (psi)	Pressure (N/mm^2)	Range (m)
1	90	0.62	6.4
2	100	0.69	6.3
3	105	0.72	6.1
4	110	0.76	6.3

6.1 Iteration 1

Testing was conducted at various pressure setting to check for loss and repeatability of the launch.

The test results are recorded in Table 3, proved that the launcher could consistently reach a distance of 6–8 m with all four projectiles.

A 0.3 × 0.3 m net was tested to verify the consistency of the range. Four tests at 0.72 N/mm^2 (105 psi) showed that a range of 6 m was always ensured. The opening of the net was recorded using a slow-motion camera. Launching at an angle of 15^0 ensured that the net was open by the time it reached roughly 5 m in range.

6.2 Iteration 2

The design was refined to mount the mechanism onto a drone. The goal was to reduce the weight and achieve a remote-controlled release of the deadweights.

As a result, the splitter was redesigned, and the ball valve was replaced with a 12-V solenoid valve. A net basket was also designed to enclose the net, as seen in Fig. 9.



Fig. 9 Compressed air prototype 2 along with Net basket



Fig. 10 Capturing hanging target

Table 4 Tabulation with different pressure for Iteration 2

S No.	Pressure (psi)	Pressure (N/mm^2)	Range (m)
1	80	0.55	3.3
2	90	0.62	4.2
3	100	0.69	4.5
4	105	0.72	3.5

6.3 Testing

A ground was performed on a target drone with a 100 mm^2 frontal area and weighed 150 g. This target was hung from a branch, as demonstrated in Fig. 10. Testing the mechanism in a non-windy environment yielded the results tabulated in Table 4. The net exhibits a parabolic motion and opens to its max area at a horizontal distance of roughly 4 m.

7 Conclusion

This paper proposes a system for mounting on existing drones that will solve the ground CUAS's range problem. Initial explorations of unidirectional carbon fibers proved futile. Studies of the CO_2 canisters revealed an ice formation problem; therefore, both propulsion methods faced different challenges.

The final prototype, powered by compressed air, achieved most objectives. As a result of pressure losses at pipe bends, the maximum range achieved was 4.5 m. Further studies could minimize pressure loss. The future scope involves mounting the mechanism onto a drone and testing it.

Funding Not applicable.

References

1. Brust MR, Danoy G, Stolfi DH, Bouvry P (2021) Swarm-based counter UAV defense system. Discover Internet of Things 1:1–19
2. Wagoner AR, Schrader DK, Matson ET (2017) Survey on detection and tracking of UAVs using computer vision. In: 2017 First IEEE international conference on robotic computing (IRC). IEEE Computer Society, pp 320–325
3. Chamola V, Kotesh P, Agarwal A, Gupta N, Guizani M (2021) A comprehensive review of unmanned aerial vehicle attacks and neutralization techniques. Ad Hoc Netw 111:102324
4. Klausen TA, Fossen K, Johansen TI (2018) Autonomous recovery of a fixed-wing UAV using a net suspended by two multirotor UAVs J. Field Robot 35(5):717
5. Meng X, Ding X, Guo P (2018) A net-launching mechanism for uav to capture aerial moving target. In: 2018 IEEE international conference on mechatronics and automation (ICMA), IEEE, pp 461–468
6. Goppert JM, Wagoner AR, Schrader DK, Ghose S, Kim Y, Park S, Gomez M, Matson ET, Hopmeier MJ (2017) Realization of an autonomous, air-to-air counter unmanned aerial system (CUAS). In: 2017 First IEEE international conference on robotic computing (IRC). IEEE, pp 235–240
7. Hawkes EW, Xiao C, Peloquin R-A, Keeley C, Begley MR, Pope MT, Niemeyer G (2022) Engineered jumpers overcome biological limits via work multiplication. Nature 604(7907):657–661
8. Yu D, Judasz A, Zheng M, Botta EM (2022) Design and testing of a net-launch device for drone capture. In: AIAA SCITECH 2022 Forum, p 0273

Effect of Different Injectors on Performance of Hybrid Rocket Motor by Varying the L/D Ratio



Arpit Dubey, Rajiv Kumar, and Shelly Biswas

Abstract The present study aimed to compare the effect of swirl injection on the regression rate and combustion efficiency of a hybrid rocket using two different lengths to diameter (L/D) ratios for the motor: 9.5 and 17. The fuel used was HTPB, and the oxidizer used was GOX. The significance of using a swirl injector is that it introduces an additional tangential velocity component, in addition to the axial component of conventional showerhead injectors, in the hybrid rocket motor. For the larger motor of 340 mm, it was observed that the improvement in regression rate was achieved only up to a length of 210 mm. This implies that the head end swirl injector was not capable of providing a swirling flow all the way to the nozzle end. When comparing the regression rates of the showerhead and swirl injectors for the 190 and 340 mm motors, an increase was observed in the case of swirl injection. Study revealed that in terms of combustion efficiency, the showerhead injector and the swirl injector exhibited contrasting results for the 190 mm motor. Specifically, the swirl injector demonstrated an 11% increase in combustion efficiency compared to the showerhead injector. However, for the 340 mm motor, the increment in combustion efficiency was comparatively lower at 6%.

Keywords Hybrid rocket · Swirl injector · Combustion efficiency · Regression rate · HTPB

1 Introduction

Hybrid rocket engines combine elements from both liquid and solid rocket engines, utilizing solid fuel along with either liquid or gaseous oxidizer. This unique combination offers several advantages over other types of chemical rockets, including improved safety, controllable thrust, lower developmental costs, higher reliability, and reduced complexity compared to liquid rocket engines [1]. Moreover, hybrid

A. Dubey · R. Kumar (✉) · S. Biswas
Birla Institute of Technology, Mesra, Ranchi 835215, India
e-mail: rajiv@bitmesra.ac.in

© The Author(s), under exclusive license to Springer Nature Singapore Pte Ltd. 2024

S. Singh et al. (eds.), *Recent Advances in Aerospace Engineering*, Lecture Notes in Mechanical Engineering, https://doi.org/10.1007/978-981-97-1306-6_23

rocket engines exhibit a density-specific impulse that exceeds that of a liquid-propelled rocket engine. The advantages in terms of handling, operations, performance, and manufacturing, when compared to liquid and solid rockets, have been substantiated by the research conducted by Mukunda et al. [2] and Mazzetti et al. [3]. As a result, there is a growing interest in the application of hybrid rockets in practical domains like transportation and space tourism [4, 5]. Despite these numerous merits, the practical application of hybrid rockets has been hindered by challenges associated with the low regression rate and lower combustion efficiency. Researchers have proposed numerous methods over time to address such issues. Some of the methods proposed to address these challenges include decreasing the amount of oxidizer utilized in the hybrid fuel [6], incorporating energetic particles [7], and regulating oxidizer mass flow within combustion chamber to improve mass flux near the fuel surface [8, 9]. Among these methods, the technique of controlling oxidizer flow through swirl injection [10, 11] shows significant promise.

Swirl injectors in hybrid rocket engines add tangential velocity to the conventional axial velocity of showerhead injectors. This reduces the boundary layer thickness as oxidizer moves across the fuel surface at higher velocities. The closer proximity of flame to hybrid fuel surface increases heat transfer and accelerates fuel degradation. Additionally, swirl injectors enhance the mass flux at fuel surface, improving combustion efficiency and regression rate of hybrid rocket system.

Kumar et al. noted that the existence of a swirling velocity component within flow field leads to an improved velocity magnitude, ensuring higher velocity gradient at fuel surface [12]. This heightened gradient promotes enhanced heat and mass transfer at hybrid fuel surface, therefore elevating regression rate. They also described phenomenon of swirl decay, where shear tension at fuel surface inhibits continued swirling stream of the oxidizer from motor injector side to the nozzle in motors with a L/D ratio greater than 5. As a result, the swirling velocity at the fuel surface diminishes due to these shear forces, causing the flow to transition from swirling to axial characteristics beyond a certain distance. The region close to the nozzle exhibits slower retreat compared to the spinning head end region due to the axial flow nature.

Yuasa et al. had conducted experiments on swirl injectors positioned at the head end of the grain [13]. They presented findings based on varying grain lengths, geometric turbulence factors, and the flow of oxidant. The rotation intensity and oxidant mass flow were adjusted separately during the tests. The results indicated that the regression rate achieved with swirl GOX injection was 2.7 times higher compared to axial injection of polymethylmethacrylate (PMMA). According to Carmicino et al., the injection effect becomes more significant when the impinging region's size exceeds the grain length [14]. Knuth et al. observed that the presence of a high-velocity, swirling oxidizer near the fuel surface resulted in substantial convective heat fluxes, thereby supporting the occurrence of large regression rates [15]. Pucci et al. carried out a study investigating the impact of swirl injectors on combustion instability by employing a propellant combination of nitrous oxide and polyethylene [16]. Their findings highlighted the stability achieved with 60° swirl injectors compared to radial injectors. Notably, the regression rate of the 60° swirl injector exhibited a remarkable increase of 182% when compared to both radial and axial

injectors. Summers et al. conducted research utilizing swirl injectors, oxidizer being nitrous oxide, and HTPB as fuel [17]. They varied swirl angle and swirl flow of the injectors and reported that zero-degree swirl flow injectors demonstrated regression rates 1.63 times higher than those recorded with 60° angled swirling-type injectors for same Gox. Furthermore, they emphasized vital role played by Gox and swirling flow number in improving the regression rate.

The objective of this study was to examine the influence of swirl injection on polymeric hybrid rocket fuel and to assess the efficacy of swirl in two different lengths of hybrid motors. The major challenges faced during the experimental study were related to the manufacturing of the swirl injector holes. The parameters examined in the analysis were regression rate, combustion efficiency, and swirl decay for the two distinct L/D ratio motors.

2 Experimental Procedures

2.1 Fuel and Oxidizer

In present study, the hybrid fuel used is HTPB. The fuel grain is composed of four ingredients and their details are mentioned in Table 1. Gaseous oxygen is used as the oxidizer. HTPB is selected because it is a flexible elastomer with good mechanical properties. HTPB-based fuel tends to have moderate to high regression rates, and the rate is influenced by the heat transfer from the hot gases to solid fuel surface which depends on the thermal properties of HTPB. GOX being a powerful oxidizer ensures that the combustion of HTPB is highly efficient. It can also be molded into various shapes and forms to meet specific design requirements. Before mixing, HTPB and DOA are dehumidified. HTPB, DOA, and Glycerol are then taken into required proportions in a beaker and mixed for 30 min. TDI is added at the last and the mixture is mixed for 15 min. The prepared slurry as shown in Fig. 1a is poured into mandrel, and the mold is kept inside vacuum chamber to remove air bubbles. At last, the mold was kept in oven for curing. Mold and mandrel with prepared grain is shown in Fig. 1b and c, respectively.

Table 1 HTPB fuel grain formulation

Ingredients	Chemical formula	Composition by weight (%)
Hydroxyl-terminated polybutadiene (HTPB)	$C_{7.075}H_{10.65}O_{0.223}N_{0.063}$	68
Dioctyl adipate (DOA)	$C_{22}H_{42}O_4$	24
Glycerol	$C_3H_8O_3$	2
Toluene diisocyanate (TDI)	$C_9H_6O_4N_2$	6

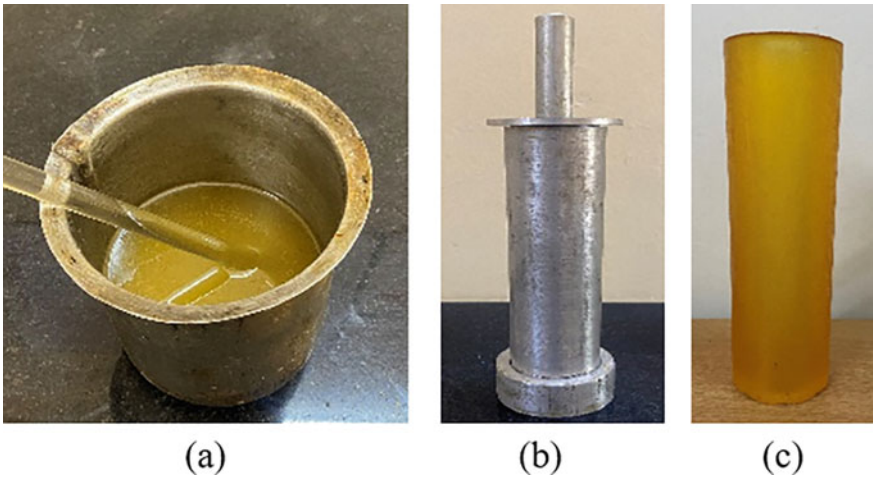


Fig. 1 **a** Prepared HTPB hybrid fuel slurry. **b** Mold and mandrel. **c** Cured HTPB hybrid fuel grain

Table 2 Dimensions of hybrid rocket motor

Geometric parameters (L/D)	9.5	17
Fuel grain length (mm)	190	340
Nozzle throat diameter (mm)	12	12
Characteristics length (m)	2.77	4.96
Initial port diameter (mm)	20	20
Fuel grain port outer diameter (mm)	50	50

2.2 Hybrid Rocket Motor

Experiments were conducted using two different motor lengths. The first motor had a length-to-diameter (L/D) ratio of 9.5 and a length of 190 mm, while the second motor had an L/D ratio of 17 and a length of 340 mm. The port diameter of the solid fuel grain was 20 mm. The hybrid rocket assemblies consisted of an injector, motor casing, and nozzle. Two types of injectors were utilized in this study: a showerhead injector and a swirl injector. The convergent–divergent nozzle was fabricated using mild steel and high-density graphite, and it had a throat diameter of 12 mm. The geometric dimensions of the two different L/D motors can be found in Table 2.

2.3 Experimental Setup

For the study, an experimental setup has been used which was already present in the Department of Space Engineering and Rocketry, BIT Mesra. It comprises of

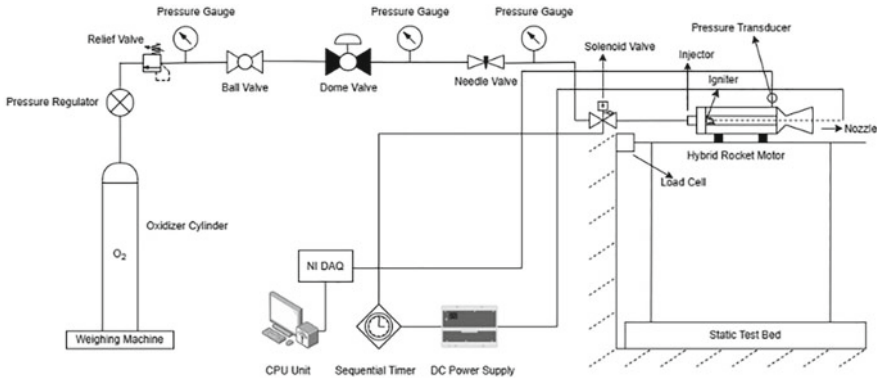


Fig. 2 Schematic diagram of experimental setup

high-pressure oxygen delivery system, DAQ system, static test bed, and a DC power supply as shown in Fig. 2. Oxygen at desired pressure is supplied to the motor through oxygen tanks. Oxygen flow is regulated using direct operated solenoid valves which are controlled by sequential timer. A composite solid propellant bead containing nichrome wire was used to fire the hybrid rocket motor. The sequential timer was used to regulate the amount of time needed to ignite the solid propellant.

2.4 Data Reduction

2.4.1 Regression Rate

The weight loss method is commonly employed in hybrid rocket systems to measure regression rate. This approach involves recording the difference in weight of the assembled motor before and after firing, which indicates the amount of fuel consumed during combustion. The resulting mass or weight loss (m_f) is then used to determine the final port diameter (d_f) using Eq. (1). Additionally, Eqs. (2) and (3) are utilized to calculate the regression rate ($\dot{r}$) and oxidizer mass flux (G_{ox}), respectively. However, in this study, a different weight loss method called the interrupted test, proposed by Kumar et al. was incorporated [18]. The interrupted test involves periodically halting the burning process at regular time intervals during the experiment. The measurement of regression rate and oxidizer mass flux in the interrupted test follows the same equations used in the weight loss method. One significant advantage of this method is that it allows obtaining four values of regression rate and oxidizer mass flux without disassembling or changing the fuel grain. The interrupted test method closely mimics the most realistic scenario in a hybrid rocket motor.

$$d_f = \sqrt{\frac{4m_f}{\pi \rho_f L} + d_i^2} \tag{1}$$

$$\dot{r} = \frac{\left(d_f - d_i\right)}{2t_b} \tag{2}$$

$$G_{\text{ox}} = \frac{\dot{m}_{\text{ox}}}{A_p} \tag{3}$$

$$A_p = \frac{\pi}{4}\left[\frac{d_i + d_f}{2}\right]^2 \tag{4}$$

2.4.2 Combustion Efficiency

The combustion efficiency is a measure of the degree of complete combustion that takes place within the combustion chamber. To determine the combustion efficiency, Eq. (5) is used, where C^*_{th} represents the theoretical characteristic velocity, and C^*_{ex} represents the experimental characteristic velocity. The NASA SP-273 (CEA) chemical equilibrium analysis software is utilized to calculate the theoretical characteristic velocity, while the experimental characteristic velocity, C^*_{ex}, is determined using Eq. (6). In Eq. (6), P_c denotes the chamber pressure obtained after each interrupted firing, A_t represents the nozzle throat area, and $\dot{m}_t$ signifies the total mass flow rate per interrupted firing. The chamber pressure is obtained by analyzing the pressure versus time plot for each firing. During combustion, a piezoresistive pressure transducer is employed to measure the chamber pressure. The analog signal from the transducer is converted to a digital signal using a National Instruments (NI) module, and it is recorded at a sampling rate of 1 kHz using LABVIEW Signal Express software.

$$\eta\% = \frac{C^*_{\text{ex}}}{C^*_{\text{th}}} * 100 \tag{5}$$

$$C^*_{\text{ex}} = \frac{P_c A_t}{\dot{m}_t} \tag{6}$$

3 Results and Discussions

3.1 Swirl Effectiveness Study

In this study, we conducted experiments with two different motor configurations: one with an L/D ratio of 9.5 and other with an L/D ratio of 17. The goal was to examine the influence of swirl injection and make a comparison with a showerhead injector. To determine regression rate, we employed the interrupted firing method, as mentioned previously. The combustion time was divided into 2-s intervals, resulting in a burn time of 8 s. Thus, we obtained 4 sets of regression rate data, as illustrated in Fig. 3.

Figure 3a presents a comparison of regression rate versus Gox for the 9.5 L/D ratio motor, considering both swirl and showerhead injectors. Similarly, Fig. 3b illustrates

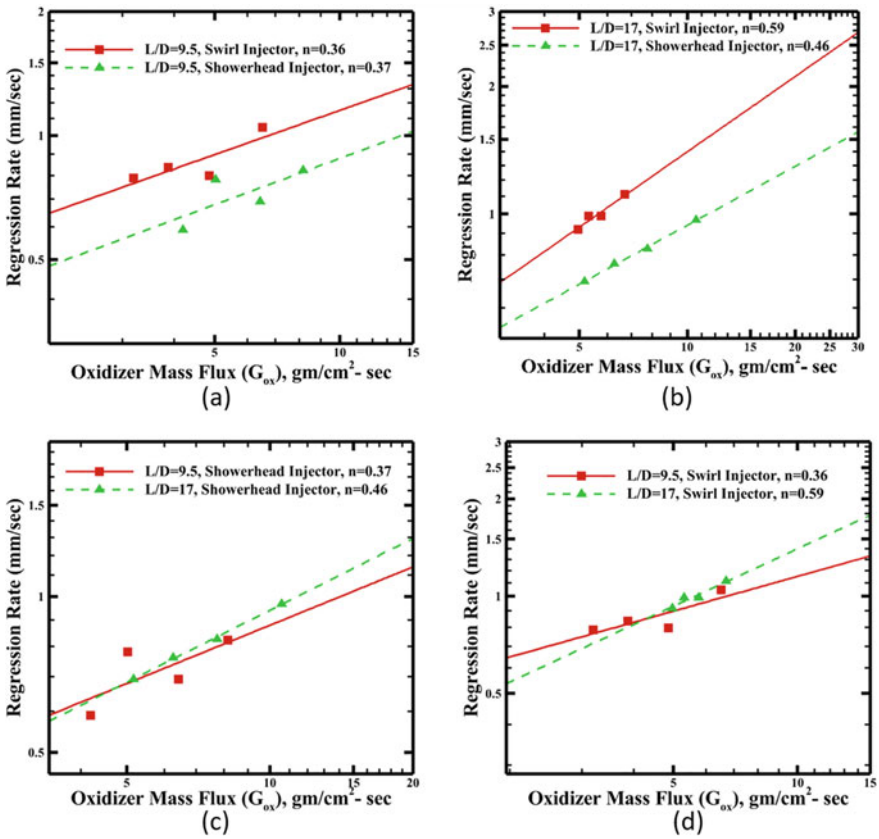


Fig. 3 Comparison of regression rate obtained with swirl injector and showerhead injector for **a** 9.5 L/D, **b** 17 L/D motor, **c** only showerhead condition, and **d** only swirl condition

the comparison for the 17 L/D ratio motor. Our findings revealed that swirl injector showed a higher regression rate than the conventional showerhead injector for both L/D ratios. Relative improvement of regression rate for 17 L/D motor shows higher than that of the 9.5 L/D motors with use of a swirl injection.

For 9.5 L/D motor with showerhead injector, regression rate exponent (n) was determined to be 0.37. This indicates a mixture ratio shift during combustion, and the value of n slightly decreased to 0.36 with the swirl injector. When n is less than 0.5, it signifies that the burning surface area increase dominates over the decrease in regression rate with burn time. On the other hand, for the 17 L/D motor, the showerhead injector exhibited $n = 0.46$, while the swirl injector had $n = 0.59$. When n is greater than 0.5, it indicates that decrease in regression rate dominates over increase in burning surface area with burn time.

Figure 3c and d compare the regression rate attained with showerhead injector and swirl injector, respectively, with change in the L/D ratio of motor. It is observed that increase in L/D ratio with showerhead gives higher regression rate compared to lower L/D ratio. This trend is different for swirl injector, where higher regression rate is observed with higher L/D ratio at higher Gox and at lower Gox, lower L/D motor gives higher regression rate. It is mainly because at lower Gox, port diameter is large and the higher L/D motor swirling effect is diminished. Also, on comparing regression rate versus Gox graph for the two cases with swirl injector, it was found experimentally that for higher Gox values, 17 L/D ratio motor showed higher regression rates. As the port diameter increases with the increase in burn time, Gox decreases and the strength of swirl also decay and regression rate decreases. On an average for the complete burn time, the regression rate of L/D 17 gave higher regression rate than 9.5 L/D.

The hybrid rocket's combustion efficiency is a crucial parameter, and therefore, it is also evaluated for both L/D of the motor. Combustion chamber pressure is measured during each interrupted firing to determine the combustion efficiency. The pressure vsrsus time plot is shown in Fig. 4. Using the average pressure value for each firing, the combustion efficiency was calculated. The data for combustion efficiency for 9.5 and 17 L/D motor is shown in Table 3.

The combustion efficiency in 9.5 L/D motor increased by 11% on switching to swirl injector from conventional showerhead injector. As shown in the Table 3, showerhead injector showed combustion efficiency of 65%, whereas for swirl injector the value is 76%. This is happening because the additional tangential component of swirling motion is providing better mixing between pyrolyzed fuel and the oxidizer. The better mixing of fuel and oxidizer is helpful in providing high performance and stable operation in hybrid rocket system. Similarly, the 17 L/D motor shows increment in combustion efficiency from 76% in showerhead injector to 82% in swirl injector. The 9.5 L/D motor showed an 11% increase in combustion efficiency, whereas 17 L/D motor exhibited only a 6% increment. It is due to the reason that as the length is increased, the turbulence level due to swirling flow was lower in 17 L/D motor than the 9.5 L/D motor. Higher the intensity of turbulence in lower L/D motor gave higher increment in the efficiency.

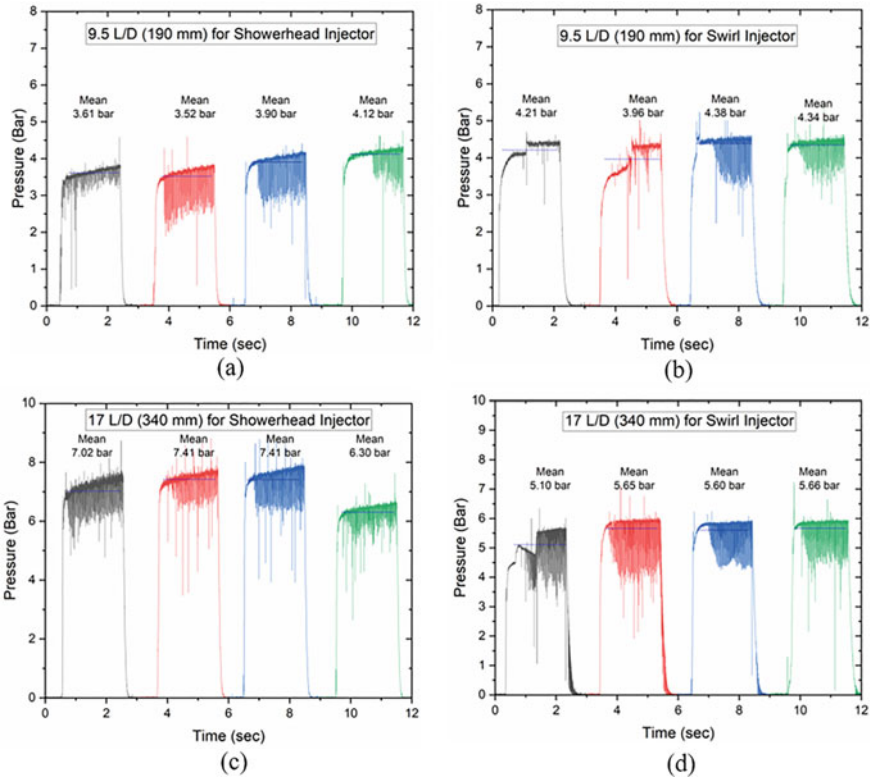


Fig. 4 Pressure versus time plot for different L/D motors with showerhead and swirl injectors

Table 3 Combustion efficiency for hybrid motors

L/D ratio of motor	Injector type	Average O/F	Average chamber pressure (bar)	Combustion efficiency (%)
9.5	Showerhead	3.06	3.79	65
	Swirl	1.93	4.22	76
17	Showerhead	1.84	7.04	76
	Swirl	1.06	5.50	82

Also, the range of combustion efficiency is lower in 9.5 L/D motor because of lower value for characteristic length (L^*) as compared to 17 L/D motor. For the 9.5 L/D motor, L^* value is 2.77 mts and for 17 L/D motor, it is 4.96 mts. It has been found that when the value for L^* grows, so does the combustion chamber pressure, resulting in an improvement in combustion efficiency. L^* is also the minimum size required for the propellant to stay long enough to react, mix, and combust properly.

3.2 Swirl Decay Study

Literature suggests that the swirl is not much effective in large L/D motor because the swirling motion cannot be sustained till the nozzle end because the boundary layer thickness was increased after the specific length from head end which led to the decrease in regression rate. Hence, an attempt has been made in this study to determine the motor length up to which the swirl injection is effective on comparison with the showerhead injector. The X-ray photography of the burnt and the unburnt grain images were compared for both the L/D ratio motors. Figures 5 and 6 illustrate X-ray images of the burnt grains, measuring 190 mm and 340 mm, respectively. From these images, it is evident that fuel regression, or the rate of fuel consumption, is higher at the head end for the swirl injector. This is attributed to the direct impact of gaseous oxygen on the fuel surface, which leads to faster heat transfer and significant erosion of the pyrolyzed fuel surface. In contrast, the showerhead injector exhibits a lower regression rate at head end region because the oxidizer flow is not in direct contact with the surface. Moving on to the 340 mm motor, the effectiveness of swirl can be observed up to a length of approximately 210 mm, beyond which the swirl behavior diminishes.

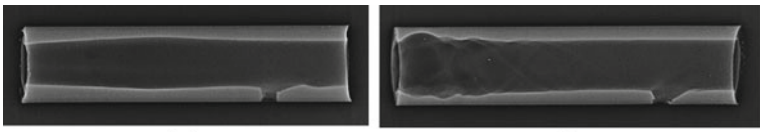


Fig. 5 HTPB 190 mm grain **a** with showerhead injector, and **b** with swirl injector

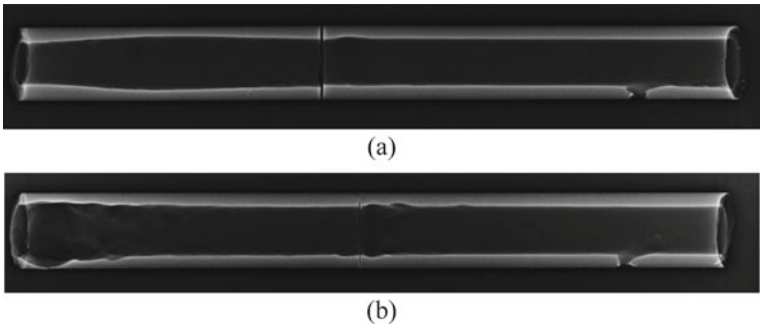


Fig. 6 HTPB 340 mm grain **a** with showerhead injector, and **b** with swirl injector

4 Conclusions

In the present study, an attempt has been made to study the effect of different injectors with varying the L/D ratio of the hybrid rocket motor. Experiments were conducted using the swirl and showerhead injector. The following conclusions have been drawn based on the experimental results.

1. The relative improvement of the regression due to use of swirl injection method was higher with the 17 L/D ratio motor compared to the 9.5 L/D motor.
2. The 9.5 L/D motor had an 11% increase in combustion efficiency, while the 17 L/D motor showed a 6% increment due to lower turbulence levels caused by swirling flow in the latter.
3. Both L/D ratio motors exhibited higher regression rates at the head end, due to direct impingement of GOX on the fuel surface using swirl injection method.
4. Swirling motion remained effective up to 210 mm in the 17 L/D ratio motor, after which it transformed into axial motion due to increased boundary layer thickness.
5. The main limitations of swirl injectors are design complexity and the need for high manufacturing precision to ensure uniformity and consistent performance. Future research potential lies in exploring multi-location swirl injections to prolong swirling motion and reduce the swirl decay factor. If successful, this approach could potentially replace liquid rocket systems with hybrid rocket systems.

Acknowledgements The authors would like to extend their appreciation to the Science and Engineering Research Board (SERB) of the Department of Science and Technology (DST) for funding the research through Sanction Order No. CRG/2021/004331. Additionally, the authors are grateful to the Department of Space Engineering and Rocketry at BIT Mesra for providing laboratory space for conducting the research.

References

1. Sutton GP, Biblarz O (2016) Rocket propulsion elements, 9th edn. John Wiley & Sons
2. Mukunda HS, Jain VK, Paul PJ (1979) A review of hybrid rockets: present status and future potential. Proc Indian Acad Sci (Eng Sci) 2:215–242
3. Mazzetti A, Merotto L, Pinarello G (2014) Paraffin-based hybrid rocket engines applications: a review and a market perspective. Acta Astronaut 126:286–297
4. Okninski A (2018) On use of hybrid rocket propulsion for suborbital vehicles. Acta Astronaut 145:1–10
5. Cai G, Zhu H, Rao D, Tian H (2013) Optimal design of hybrid rocket motor powered vehicle for suborbital flight. Aerosp Sci Technol 25(1):114–124
6. George P, Krishnan S, Varkey PM, Ravindran M, Ramachandran L (2001) Fuel regression rate in HTPB/gaseous oxygen hybrid motors. J Propuls Power 17(1):35–42
7. Sun X, Tian H, Li Y, Yu N, Cai G (2016) Regression rate behaviors of HTPB-based propellant combinations for hybrid rocket motor. Acta Astronaut 119:137–146

8. Kumar R, Ramakrishna PA (2014) Enhancement of hybrid fuel regression rate using a bluff body. J Propuls Power 30(4):909–916
9. Dinesh M, Kumar R (2019) Utility of multi-protrusion as the performance enhancer in hybrid rocket motor. J Propuls Power 35(5):1005–1017
10. Kumar CP, Kumar A (2014) Combined effect of diaphragm and oxidizer swirl on regression rate in hybrid rocket motors. Def Sci J 64(1):21–26
11. Vignesh B, Kumar R (2020) Effect of multi-location swirl injection on the performance of hybrid rocket motor. Acta Astronaut 176:111–123
12. Kumar CP, Kumar A (2013) Effect of swirl on the regression rate in hybrid rocket motors. Aerosp Sci Technol 29(1):92–99
13. Yuasa S, Yamamoto K, Hachiya H, Kitagawa K, Oowada Y (2001) Development of a small sounding hybrid rocket with a swirling-oxidizer-type engine. In: 37th joint propulsion conference and exhibit. AIAA, Salt Lake City, UT, U.S.A., pp 3537
14. Carmicino C, Sorge AR (2005) Role of injection in hybrid rockets regression rate behaviour. J propuls power 21(4):606–612
15. Knuth W, Chiaverini M, Gramer D, Sauer J (1998) Experimental investigation of a vortex-driven high-regression rate hybrid rocket engine. In: 34th AIAA/ASME/SAE/ASEE joint propulsion conference and exhibit. AIAA, Cleveland, OH, U.S.A., pp 3348
16. Pucci J (2002) The effects of swirl injector design on hybrid flame-holding combustion instability. In: 38th AIAA/ASME/SAE/ASEE joint propulsion conference and exhibit. American Institute of Aeronautics and Astronautics, Indianapolis, Indiana, pp 3578
17. Summers MH, Dennis JD, Villarreal JK (2013) Small-scale hybrid rocket test stand and characterization of swirl injectors. In: 49th AIAA/ASME/SAE/ASEE joint propulsion conference. AIAA, San Jose, CA, pp 3831
18. Kumar R, Ramakrishna PA (2013) Issues related to the measurement of regression rate of the fast-burning hybrid fuels. J Propuls Power 29(5):1114–1121

Effect of Change in Alignment of the Multiport Grain on the Performance of a Hybrid Rocket Motor



Gyandeep and Rajiv Kumar

Abstract A chemical rocket propulsion system that employs fuel and oxidizer in different physical states is known as hybrid rocket motor (HRM). HRM has some issues like low regression rate and less efficient combustion. Apart from these issues, the system has some special superiority like safest and cheaper system in comparison with other chemical propulsion system which makes it preferable for space tourism. So, diminishing this system's concern can give extra boost in the research field of this propulsion setup. The offset grains can be a revolutionary step in the HRM. They can create recirculation zones due to change in alignment, and using multiport grain with it can also enhance the regression rate due to extra surface area exposure. The result showed that the regression rate obtained with offset grains having multiport was 2–3 times higher than the normal port grains. The combustion efficiency was also 20–30% higher than the normal port grain.

Keywords Offset grains · Multiport grain · Hybrid rocket motor · Regression rate · Combustion efficiency

1 Introduction

Significant progress has been achieved in the creation of hybrid rocket motors (HRMs) since the turn of the twentieth century. An engine type known as an HRM uses propellants in various physical states and has a comparatively simple design. An HRM typically includes a solid fuel grain, an ignition system, and a pressurized tank containing either liquid or gaseous oxidizer [1]. One propellant is injected into the combustion chamber by the engine at a rapid pace, while the second propellant remains stationary. HRMs have a number of benefits, such as increased safety, less risks, a willingness to stop and restart, affordability, and simplicity when it comes

Gyandeep · R. Kumar (✉)
Department of Space Engineering and Rocketry, Birla Institute of Technology Mesra, Ranchi, India
e-mail: rajiv@bitmesra.ac.in

© The Author(s), under exclusive license to Springer Nature Singapore Pte Ltd. 2024

S. Singh et al. (eds.), *Recent Advances in Aerospace Engineering*, Lecture Notes in Mechanical Engineering, https://doi.org/10.1007/978-981-97-1306-6_24

to production and storage. Performance-wise, HRMs outperform solid and liquid rocket motors when it comes to specific impulse and density impulse, respectively [2]. The hydroxyl-terminated polybutadiene (HTPB), polymers including polyethylene and PVC-DBP, liquefying paraffin wax as fuel, and oxidizers such as di-nitrogen tetraoxide (N_2O_4), hydrogen peroxide (H_2O_2), liquid oxygen (LOX), and nitrous oxide (N_2O) are some of the types of propellants employed in HRMs.

Tian et al. [3] studied the effect of multiport grain in a hybrid rocket motor through numerical analysis, and for validating the results, they even performed experiments also. Based on the Navier–Stokes equations, a computational model was developed that took into account turbulence, chemical processes, fuel pyrolysis, and interactions at the solid–gas boundary. The propellant mixture of 98% hydrogen peroxide (HP) and hydroxyl-terminated polybutadiene (HTPB) was the main subject of the simulation. With increasing axial position, the fuel regression rates initially decline but subsequently rise. Notably, when the fuel port has the shape of a convex figure at a specific cross-section, the fuel regression rates are lower in regions with smaller arc radii. On a full-scale motor, two experiments are carried out in accordance with the outcomes of the simulation. The motor runs continuously with no obvious oscillatory combustion. In terms of fuel regression rate distributions at the cross-section, the fuel port profiles before and after the testing show good agreement with the results of the numerical simulation.

Kim et al. [4] also investigated the change in regression rate with the increment in number of the cylindrical ports in hybrid grain. An oxidizer delivery system, a multiport fuel grain, and a combustor with pre- and post-chambers were all included in the physical model. The fuels used in this experiment were PMMA and PE. Even the outcomes of end-burning were also studied. It was shown that increasing the port number causes the oxidizer-to-fuel ratio to approach its ideal value, resulting in a rise in the regression rate. This was accomplished by adjusting the oxidizer mass flux from 10 to 300 kg/m^{2}s. Regardless of particle size, the rise in regression rate diminishes after three ports. The study also showed that the radiation effect impacts polyethylene's rate of regression substantially greater than PMMA. It is also mentioned that the end-burning effect can cause large-scale grain trials to measure the regression rate inappropriately.

So this paper is about investigating an innovative technique for improvising the performance of a hybrid rocket motor. In this method of technique, the alignment of port of nozzle side grain was changed with respect to the injector side grain. The change alignment was used to create turbulent flow throughout the port length of the grain. The detailed setup would be explained in the upcoming contents of the paper. The fuel used in this experiment was made up of polyvinyl chloride (PVC) and dibutyl phthalate (DBP). Gaseous oxygen was used as the oxidizer. The experiments were done to analyze the regression rate, combustion efficiency, pressure build-up inside the combustion chamber, and the thrust generation due to the optimum expansion of hot gases.



Fig. 1 5 mm offset base and 10 mm offset multiport base (from left to right)

2 Experimental Methodology

2.1 Base, Mold, and Mandrel for the Experiment

The material used for the fabrication of the base, mold, and mandrel was aluminum. The design of each fabricated part was made on CADD software and fabricated in the departmental workshop. Two types of bases were used to cast the grain. The first one was 5 mm offset base, and the second one was the 10 mm offset multiport base. The hole of 5 mm offset base for holding the mandrel was shifted 5 mm away from the center of the whole base; same method was used for manufacturing of the 10 mm offset multiport base. The mandrel used in this investigation was having the diameter of 15 mm, and the mold was having internal diameter of 50 mm. The fabricated base is shown in Fig. 1.

2.2 Grain Preparation and Casting

As mentioned above in the introduction part, the fuel binder was polyvinyl chloride (PVC) and the plasticizer was di-butyl phthalate (DBP). The powdered PVC was mixed with the dehumidified DBP in several additions and mixed properly to get homogeneous slurry and then casted in the mold and mandrel, and after that the slurry was kept in the oven for curing process. The temperature and the time of curing were decided through iteration process for getting proper mechanical properties. In this study, four types of grain were used in which the first one was 5 mm offset port grain, the second one was 10 mm offset port grain, the third one was 30 mm normal port grain, and the last one was 10 mm offset multiport grain. After extraction of the grain, the grain was cut and casted inside the motor with use of liner. The length of each part of grain is given in Table 1. The second and the third part for both types of

Table 1 Length of each part of the grain

Type of grain	1st part	2nd part	3rd part
5 mm offset with multiport	75 mm	38 mm	75 mm
10 mm offset with multiport	75 mm	38 mm	75 mm

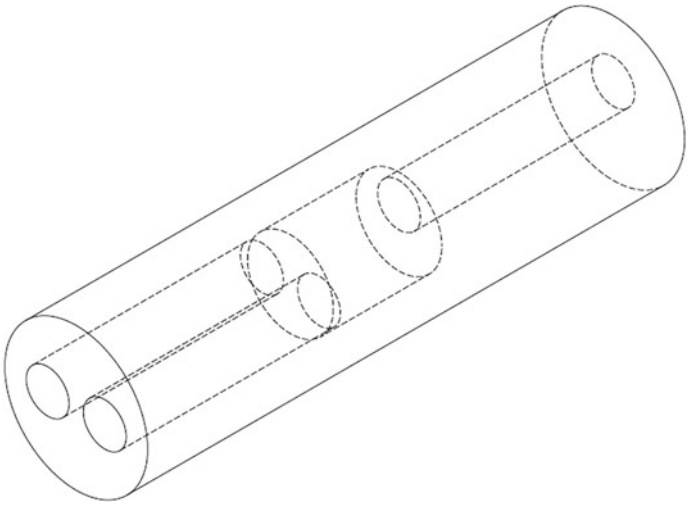


Fig. 2 5 mm offset with multiport grain

grain were same. The second part was 30 mm normal port grain which was made up PVC-DBP-chalk powder. The third part was 10 mm offset multiport grain.

For 5 mm offset case, the first part was 5 mm offset port grain, and for the 10 mm offset case the first part was the 10 mm offset single port grain. The schematic of the grains is shown in Figs. 2 and 3.

2.3 Experimental Setup

In order to calculate the mass flow rate, this study focused on doing tests using oxidizer cylinders and a weighing scale. Since gaseous oxygen is readily available and secure, it was chosen as the oxidizer. The 47-L cylinder was made of an alloy steel. To regulate the flow and pressure in the feed line, valves such the ball valve, dome valve, and solenoid valve were used. Safety precautions were taken to stop combustion in the event that the feed line system experienced any problems. With an injection pressure of 350 psi, the oxidizer flow rate was set at roughly 30 g/s. The power supply was managed by a sequential timer, which also started the combustion process inside the combustion chamber. The temperature was kept constant for igniting using a 12 V DC power supply. A system that measures pressure variations and the force applied during

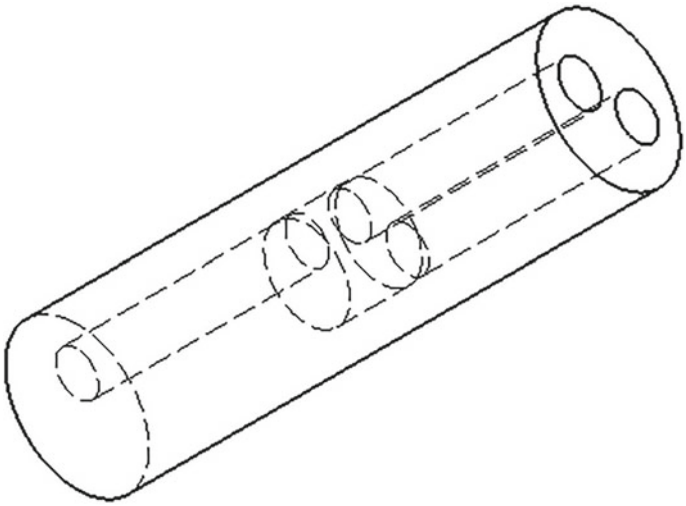


Fig. 3 10 mm offset with multiport grain

testing was used for data collecting. In order to conduct electricity and produce heat for propellant ignition and combustion in the hybrid rocket's combustion chamber, a nickel–chromium alloy wire was placed into the igniter bead, which was made of a solid composite propellant that weighed around one gram.

3 Result and Discussion

3.1 Regression Rate Analysis

There are many methods used for the calculation of regression rate. In the present study, following Eqs. (1) to (4) were used to calculate the regression rate and the oxidizer mass flux (Gox).

$$d_f^2 = \frac{4m_f}{\pi \rho_f L_g} + d_i^2 \tag{1}$$

$$\dot{r} = \frac{d_f - d_i}{2t_b} \tag{2}$$

$$G_{ox} = \frac{\dot{m}_{\text{ox}}}{A_p} \tag{3}$$

$$A_p = \frac{\pi}{4}\left(\frac{d_i + d_f}{2}\right)^2 \tag{4}$$

The regression rate was calculated through mass difference method which was obtained through the interrupted test firing of the hybrid rocket motor proposed by Kumar and Ramakrishna [5] where "d_f" and "d_i" were final and initial diameter and "$\dot{r}$" and Gox were regression rate and oxidizer mass flux, respectively. It is obtained using the equations from (1) to (4). After calculation, the graph was plotted on the Tecplot 360 software and shown in Fig. 4 where trend lines were showing the power curve. The case 1 is the 5 mm offset with multiport grain and the case 2 is the 10 mm offset with multiport grain. The base case is 15 mm normal port grain. As mentioned above, case 1 was related to 5 mm offset which is shown by red curve in the graph. The regression rate for case 1 was maximum at the Gox of 8.16 g/cm^2 s which was 1.63 mm/s. The regression rate for the case 2 which was related 10 mm offset was best at the Gox of 9.165 g/cm^2 s, and the regression rate at that particular Gox was 2.043 mm/s. The overall regression rate was observed to be higher with the case 2 due to the increased residence time of the combustion product in the combustion chamber. The value of oxidizer mass flux exponent (n) for case 1 and case 2 was 0.575 and 0.593, respectively, which shows that the regression rate would decrease a bit with increase in the oxidizer mass flux since the value was quite close to 0.5. In comparison with normal port grains, regression rate was two to three times better.

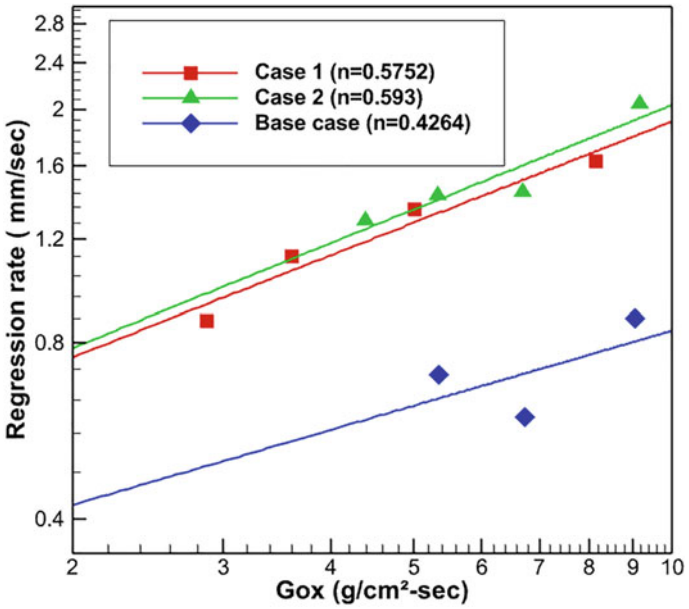


Fig. 4 Regression rate graph obtained with 5 and 10 mm offset types with multiport grain

3.2 Combustion Efficiency Analysis

The combustion efficiency is the parameter to understand how efficiently propellants combusted to generate energy. The combustion efficiency was calculated through comparing the experimental characteristic jet velocity with respect to the theoretical characteristic jet velocity. The theoretical jet velocity was calculated through the NASA CEA software with proper data. For the calculation of experimental characteristic jet velocity, formula was taken from Sutton [2] which is given as.

$$C^*_{\text{exp}} = \frac{P_c A_t}{\left(\dot{m}_f + \dot{m}_{\text{ox}}\right)} \tag{5}$$

$$\eta_{\%} = \left[\frac{C^*_{\text{exp}}}{C^*_{\text{the}}}\right] 100 \tag{6}$$

In which "P_c" was pressure build-up inside the combustion chamber, "A_t" was nozzle throat area, and in the denominator sum of the mass flow rate of the oxidizer and fuel burnt used. The combustion efficiency graph was plotted on the Tecplot software and shown in Fig. 5. The red curve was showing the 5 mm offset grain with multiport which was entitled as case 1 and the 10 mm offset was entitled as case 2 which was shown through green curve. The square box symbol was showing the combustion efficiency on that particular O/F ratio which was obtained through the calculation. The combustion efficiency of the case 1 was best observed at O/F ratio of 1.714 which was 86.55% and even showed average combustion efficiency of more than 84%. For case 2, the combustion efficiency was 79.75% at O/F ratio of 1.429, and the average combustion efficiency for this case was more than 77%. The combustion efficiency was better in the case 1 since the O/F ratio was close to stoichiometric ratio. In comparison with the normal port grain, the combustion efficiency of both cases was 50% more than the normal port grain. The combustion efficiency associated with normal port grain is shown in blue curve.

3.3 Pressure Analysis

The pressure data was collected through peizoresistive transducer during particular test firing in the form of voltage then further converted in SI units of pressure with proper calibrated equations. The data was then plotted through Origin pro software and shown in Fig. 6. The interrupted firing test was for 2 s each. Both cases are same as mentioned in the previous paragraphs. The average pressure build-up in case 1 was 8.05 bar and for the case 2 was 7.89 bar. The pressure generation was better in 5 mm offset with multiport grain since the combustion was more efficient so it generated better pressure. The pressure build-up was more in both cases with respect to normal port grain.

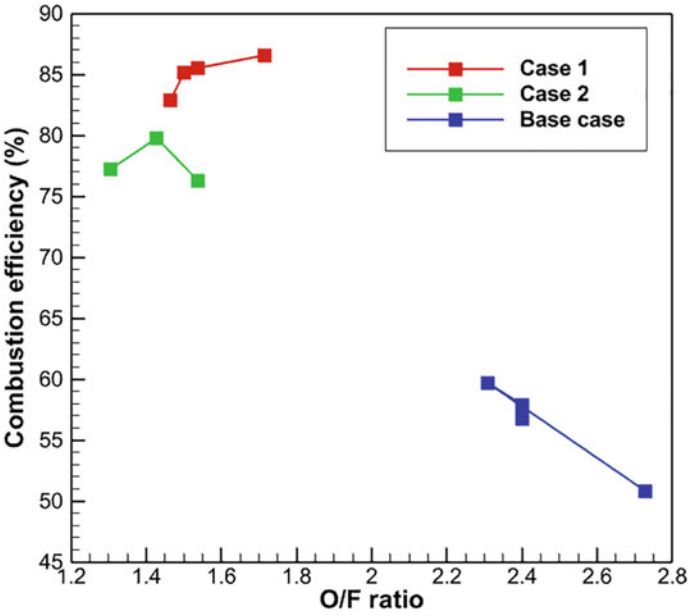


Fig. 5 Combustion efficiency comparisons with 5 and 10 mm offset types with multiport grain

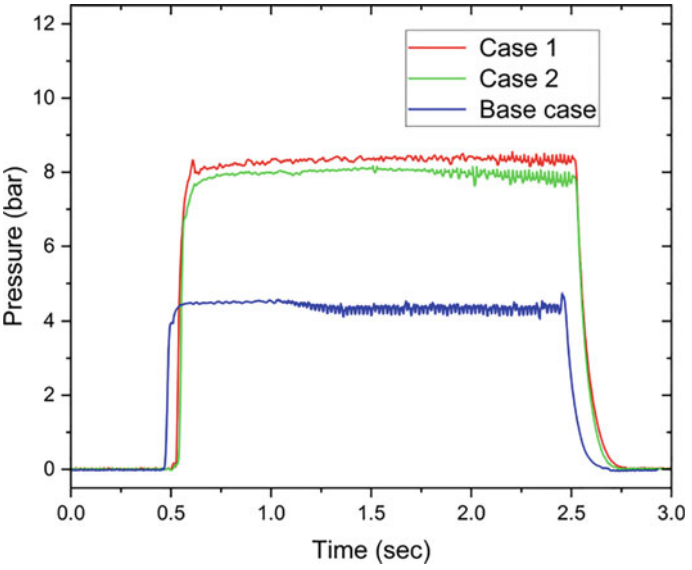


Fig. 6 Pressure comparison with 5 and 10 mm offset types with multiport grain

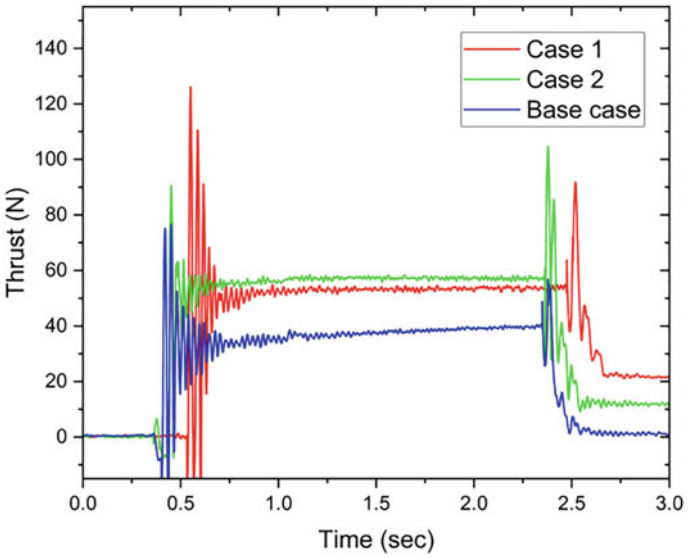


Fig. 7 Thrust comparison graph with 5 and 10 mm offset types with multiport grain

3.4 Thrust Generation Comparison

The thrust generation data was obtained using a load cell which works on Wheatstone bridge configuration. Again the data acquired was in volts and calibrated through proper equations in SI units of force. The data was plotted on the Origin pro software and the graph is shown in Fig. 7. The thrust generation was about 50.1 N for the case 1 and 55.5 N for the case 2. The force generation was better in the 10 mm offset with multiport case since the regression rate was more in that case due to which mass flow rate of propellant enhanced. The thrust generation in base case was about 37.5 N.

4 Conclusions

In this study, the efforts was made to understand the performance of a laboratory-scale hybrid rocket motor with the use of offset grains along with multiport grains. The conclusions obtained from the experimental studies are stated below:

1. The regression rate for 10 mm offset with multiport grain was higher and observed as 2.043 mm/s at Gox of 9.1 g/cm^2 s, and for 5 mm offset, it was 1.63 mm/s at Gox of 8.16 g/cm^2 s.
2. The average combustion efficiency was 84% for 5 mm offset with multiport grain and for 10 mm offset with multiport grain it was 77%.

3. The average pressure build-up was 8 and 7.89 bar for the 5 mm offset with multiport and 10 mm offset with multiport grain, respectively.
4. The thrust generation due to combustion of propellants for the 5 mm offset with multiport grain was 50.1 and 55.5 N for the 10 mm offset with multiport grain.

Acknowledgements The authors express their sincere gratitude toward Space Engineering and Rocketry Department, BIT Mesra, for providing laboratory facilities for conducting the experiments.

References

1. Ramamurthi K (2016) Rocket propulsion, 2nd edn. Trinity Press of Laxmi Publications Private Limited
2. Sutton GP, Biblarz O (2000) Hybrid propellant rockets in rocket propulsion elements. Wiley-VCH, Weinheim
3. Tian H, Li X, Zeng P, Yu N, Cai G (2014) Numerical and experimental studies of the hybrid rocket motor with multi-port fuel grain. Acta Astron 96:261–268
4. Kim S, Lee J, Moon H, Kim J, Sung H, Kwon OC (2013) Regression characteristics of the cylindrical multiport grain in hybrid rockets. J Propul Power 29(3):573–581
5. Kumar R, Ramakrishna PA (2013) Issues related to the measurement of regression rate of fast-burning hybrid fuels. J Propul Power 29(5):1114–1121

Effect of Metal Addition on the Ignition Characteristics of a Pyrotechnic Igniter



Ritesh Dubey and Rajiv Kumar

Abstract Pyrotechnic igniters are used to ignite the small solid propellant motor. The combustion of the pyrotechnic igniter plays an important role in building the pressure inside the combustion chamber of the solid rocket motor. The igniter should be able to generate pressure in the combustion chamber in a fraction of the time and should be efficient. This research paper examines the effectiveness of two metal fuels, magnesium and aluminum, in combination with potassium nitrate as an oxidizer for pyrotechnic igniters used in small solid propellant motors. The fuel-to-oxidizer ratio is maintained at 50:50. The study reveals that the Mg/KNO_3 igniter mixture outperforms the Al/KNO_3 mixture in calorific value, with a 7406.32 kJ/kg value. However, it is to be noted that the incomplete combustion of the Al/KNO_3 mixture leads to a higher gas generation compared to the Mg/KNO_3 mixture. These findings underscore the significance of selecting the appropriate metal fuel for pyrotechnic igniters to optimize performance, considering factors such as calorific value and combustion completeness. The outcomes of this research contribute to developing and improving solid rocket motor efficiency.

Keywords Pyrotechnic igniter · Solid propellant · Calorific value · Metal fuels

1 Introduction

The ignition of the propellant is a critically important phase in operating a solid rocket motor. The solid propellant fuel must be ignited in a regulated and predictable combustion reaction to reach the high temperatures and pressures necessary to provide the propelling power [1]. The igniter is used to initiate the combustion process at a predetermined rate. It releases heat and gas to raise the temperature of the propellant surface over its self-ignition threshold and to boost the pressure within the motor's free volume to a level higher than the propellant's low deflagration limit. The ignition process is complicated and requires various energy transmission processes

R. Dubey · R. Kumar (✉)
Birla Institute of Technology Mesra, Ranchi, India
e-mail: rajiv@bitmesra.ac.in

© The Author(s), under exclusive license to Springer Nature Singapore Pte Ltd. 2024

S. Singh et al. (eds.), *Recent Advances in Aerospace Engineering*, Lecture Notes in Mechanical Engineering, https://doi.org/10.1007/978-981-97-1306-6_25

between the different phases. Still, one of the most prevalent difficulties is the possibility of failing to start the rocket motor or achieving a state where it can sustain itself. To ensure the successful ignition and functioning of a solid rocket motor, it is essential to ensure that the design of the igniter is both effective and dependable [2].

Two types of igniters are pyrotechnics and pyrogen. The pyrotechnic igniter ignites the small solid propellant motor, consisting of a thin electrical resistance wire coated with ignitable squib material and enclosed in an easily ignitable substance. In practice, the small solid rocket motor is used to ignite the large solid rocket motor instead of using the igniters. The propellant used in the small motor has a very small web thickness, and the plume from this motor initiates the burning of the main motor. This small rocket motor is called a pyrogen igniter [3].

In a study that was carried out by Salma and Belal [4], the researchers compared black powder and a solution of boron potassium nitrate. Compared to black powder, they discovered that boron potassium nitrate displayed a smoother pressure–time curve and a longer igniting delay than the latter.

To generate and improve the chemical composition of spitfire powder for use in solid rocket motors, Salleh et al. [5] conducted research on the thermal combustion of the powder. They discovered that black powder has a lower temperature and an enthalpy value of 2.595 kJ/g, but spitfire powder that contains 30% thermite had a greater temperature and an enthalpy value of 7.924 kJ/g. The researchers concluded that the combustion performance of the igniter charge might be improved by adding thermite, KNO_3, and charcoal in suitable amounts. The volume of the igniter, Vi, was used to calculate the igniter's ideal weight.

Developing high-energy igniter and booster pyrotechnic compositions was the subject of research by Khan et al. [6]. The B/KNO_3, Zr/$KClO_4$, and Pb $(SCN)_2$/$KClO_3$ systems were the primary areas of emphasis for the researchers. They investigated the B/Mg/$KClO_4$ and B/Mg/$KClO_4$ combination options to develop booster formulations. Combinations of sixty percent Zr and forty percent $KClO_4$, thirty percent boron, ten percent magnesium, sixty percent $KClO_4$, and 4% extra binder were discovered to be the most effective igniters and boosters for the working of impulse cartridges.

An investigation was done by Singh et al. [7] to see how well-suited different metal-based igniter compositions were for magnesium-containing fuel-rich propellants. They measured the ignition pressure output and impetus of various igniter compositions in a closed vessel, computed the heat energy amounts calorimetrically in a closed bomb, and conducted research on vented vessel research in a test motor to assess the different igniter compositions. They concluded that the pyrotechnic composition Mg/KNO_3/EC (44:54:2) demonstrated acceptable performance at a loading density of 0.01 g/cm^3. Still, satisfactory ignition pick-up needed a priming composition with a density ranging from 0.20 to 0.30 g/cm^3.

The ignition of a solid rocket propellant is a critical phase in ensuring the successful operation of a solid rocket motor. The propellant must undergo a controlled and predictable combustion reaction to achieve optimal propulsion power. This research paper investigates the effectiveness and reliability of different igniter compositions through experiments and analyses. Existing studies on black powder and

boron potassium nitrate are compared, highlighting the latter's smoother pressure–time curve and extended ignition delay. Moreover, the addition of thermite, KNO_3, and charcoal in suitable proportions is examined to enhance the combustion performance of the igniter charge. Furthermore, novel metal-based compositions, including magnesium and aluminum with KNO_3 as an oxidizer, are explored for their ignition efficiency. The research addresses the current gaps in understanding the ignition of solid propellant rockets. By advancing knowledge in this field and optimizing igniter compositions, this study contributes to developing more reliable and high-energy igniters, ultimately enhancing solid rocket motors' overall performance and safety.

2 Experimental Methodology

2.1 Calorific of Igniter Mixture

The importance of a pyrotechnic igniter for the calorific value of solid propellants is found in its capacity to effectively start the combustion process and hence contribute to the release of greater heat energy during combustion. A small amount of igniter mixture was added to the basket, and the igniter wire was made into the circular coil and attached for the proper igniter. The basket arrangement was placed inside the bomb and pressurized using inert gas; here, N_2 was used in the study. The bomb was placed inside the distilled water bucket (2L volume). The 12 V DC supply connection was made to the bomb, and the lid was closed with the water bucket within it. A thermocouple and stirrer were inserted into the bucket to measure the temperature change and the heat transfer generated by the combustion of the igniter mixture uniformly within the water, respectively. Figure 1 shows the complete setup of the bomb calorimeter available in the department.

The temperature recorded by the thermocouple was used in Eq. (1) to get the calorific value of the igniter mixture.

$$\text{CalorificValue} = \frac{W(T_f - T_i)}{M_{ig}} \tag{1}$$

where

W = water equivalent of benzoic acid (2321.51 cal/°C),
T_f = final temperature,
T_i = initial temperature,
M_{ig} = Mass of igniter mixture.



Fig. 1 Bomb calorimeter setup (Department of Space Engineering and Rocketry, BIT Mesra, Ranchi)

2.2 Gas Generated by Pyrotechnic Igniter

In pyrotechnic devices, solid propellant burning requires the hot gas created by a pyrotechnic igniter. This hot gas acts as a heat transfer medium between itself and the propellant, elevating its temperature to facilitate combustion. When it can escape, the gas quickly expands, exposing a greater surface area for more effective burning. In general, the igniter gas is essential for starting, maintaining, and maximizing the combustion of solid propellants. The gas generated by different pyrotechnic igniter compositions is studied in a closed chamber. A bag-type igniter is a type of igniter commonly seen in solid rocket motors. To set up a bag-type igniter, as shown in Fig. 2, the materials needed include a nichrome wire having a shellac bead attached to it, a pyrotechnic substance like magnesium potassium nitrate, and a bag made of a suitable material like nylon or polyester. The pyrotechnic mixture must be finely powdered and mixed uniformly. The bag must be filled to the top with powdered pyrogen and sealed using adhesive tape.

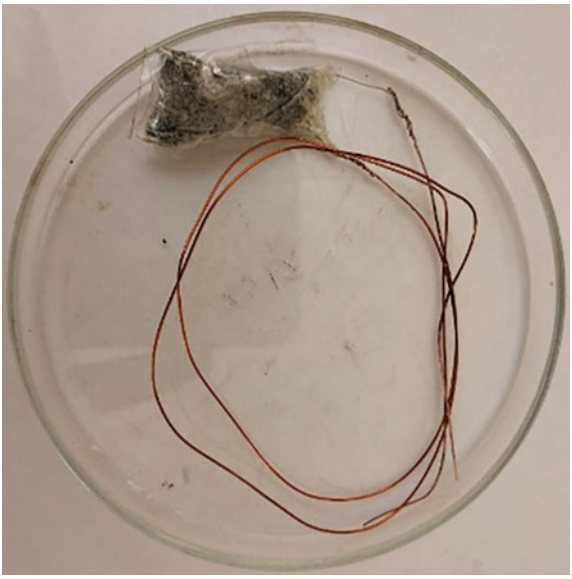


Fig. 2 Prepared bag-type igniter

3 Result and Discussion

3.1 Calorific Value of Pyrotechnic Igniters

The heat released from the igniter mixture affects the performance of the solid rocket motor. The heat of combustion studies of two different igniter combinations were done to determine the heat release from the mixture. Al/KNO_3, Mg/KNO_3 in which Mg and Al act as fuel, and KNO_3 is an oxidizer. The proportion of the fuel to oxidizer was kept at 50:50 in all combinations. The heat of combustion of shellac-based squib was also done. This squib first receives the electrical current and starts burning. The instant squib ignites, the burning of the igniter mixture continues. All this process takes place in a fraction of a second. For the study, the igniter mass is kept the same for all samples, which is 1gm. The calorific value of different igniters studied in the present study is summarized in Table 1.

From Table 1, it can be seen that the calorific value of Al/KNO_3 is higher as compared to Mg/KNO_3. This high calorific value for Al/KNO_3 is because aluminum has higher energy content than magnesium. The pyrotechnic igniter should be reliable

Table 1 Calorific value of the pyrotechnic igniter mixture

Sr. no	Igniter mixture	Calorific value (kJ/kg)
1	Shellac squib	5139.33
2	Al/KNO_3	7406.32
3	Mg/KNO_3	6858.61

and efficient in igniting the solid propellant. Al/KNO_3 igniter mixture allows the rapid ignition and combustion of the solid propellant because of the high calorific value compared to the Mg/KNO_3.

3.2 Gas Generated by Pyrotechnic Igniter

The production of heat and gas is a crucial component of a successful igniter. To compare and analyze the quantity of hot gas that the igniter combination produced due to the ignition of the igniter, an ignition delay tests were conducted. For each combination, the mass of the igniter mixture was maintained constant. The igniter was lit in a closed box, and a video was taken. The video was afterward transformed into pictures using the fps. Figures 3 and 4 show the gas generation in both Al and Mg-based pyrotechnic igniters. Each image in Figs. 3 and 4 shows the sequence of ignition from the start of ignition till the gas generation and completion.

The comparison between the Mg/KNO_3 and Al/KNO_3 pyrotechnic igniters reveals important differences in their combustion characteristics. The Mg/KNO_3 igniter, despite having a lower calorific value than the Al/KNO_3 mixture, produces a larger volume of hot gases. This can be attributed to the complete combustion of magnesium, leaving no residue behind. On the other hand, the Al/KNO_3 igniter mixture results in the formation of residue containing lumps of unburnt aluminum, as depicted in Fig. 5.



Fig. 3 Al/KNO_3 igniter burning and its gas generation



Fig. 4 Mg/KNO_3 igniter burning and its gas generation



Fig. 5 Residue of Al/KNO_3 pyrotechnic igniter after burning

This residue formation is due to the tendency of aluminum to agglomerate, leading to the creation of a layer of aluminum oxide (Al_2O_3). This layer acts as a barrier preventing the complete combustion of aluminum. In the case of the 50:50 proportion of Al/KNO_3, the ratio is not stoichiometric, meaning that the oxidizer content is insufficient for the complete combustion of aluminum. Consequently, the layer of Al_2O_3 remains intact as the temperature does not reach its melting point, leaving unburned aluminum particles unavailable for igniting the igniter main mass. The significance of this issue was explored in the context of its impact on rocket motor performance and the starting thrust transient during ignition. The presence of unburned residue and incomplete combustion was found to have adverse effects on motor performance, leading to reduced thrust output and specific impulse. Additionally, it caused irregular thrust transients during startup, potentially jeopardizing the stability and trajectory of the rocket. Furthermore, the residue particles contributed to nozzle erosion, compromising the structural integrity of the rocket motor. To enhance the efficiency and safety of chemical rockets, further research is required to understand and mitigate the consequences of incomplete combustion and unburned residues in propellant formulations.

4 Conclusions

This study focuses on the igniter and ignition characteristics for solid rocket motor applications. This study investigated the effect of different metal fuels in a pyrotechnic igniter mixture. The findings from this study have significant implications for the design and operation of solid rocket propulsion systems and the safety of personnel and equipment involved in rocket launches. The following are the conclusions drawn from the study.

1. The Al/KNO_3 igniter mixture offered a high calorific value of 7406.32 kJ/kg compared to that of Mg/KNO_3, which has a calorific value of 6858.21 kJ/kg.
2. Mg/KNO_3 pyrotechnic igniter mixture produced a large amount of hot gases compared to Al/KNO_3, which is crucial in building the chamber pressure required to ignite the solid propellant.
3. Al/KNO_3 burning left the residue of unburned aluminum, and this unburnt or agglomeration of Al occurred due to the formation of the Al_2O_3 layer.

Acknowledgements The authors express their sincere gratitude toward the Space Engineering and Rocketry Department, BIT Mesra, for providing laboratory facilities for conducting the experiments related to the present work.

References

1. Keller RB (1971) Solid rocket motor igniters. NASA SP-8051
2. Salama A, Belal H, Abdalla HM (2020) Validation of relations for the determination of pyrotechnic igniter mass. In: IOP conference series: materials science and engineering, vol 973. IOP Publishing, p 012004
3. Ramamurthi K (2010) Rocket propulsion. Trinity Press Laxmi Publications Pvt. Ltd., 2nd Edition
4. Salama A, Belal HM (2022) Experimental investigations of a pyrotechnic igniter. In: AIAA SCITECH 2022 forum, p 1480
5. Salleh Z, Hamid AHA, Mohammad WMW, Tamimi A, Sujana MJ, Ahmad KA (2021) Chemical composition of igniter for ignition system in solid rocket motor. Int Trans J Eng Manag Appl Sci Technol 12(9):1–11
6. Khan A, Malik AQ, Lodhi ZH (2017) Development and study of high energy igniter/booster pyrotechnic compositions for impulse cartridges. Central Eur J Energet Mater 14(4):933–951
7. Singh H, Somayajulu MR, Bhaskar RR (1988) Selection of an igniter system for magnesium-based solid fuel rich propellant. Propell Explos Pyrotech 13(2):52–54

Enhancing UAV Capabilities for Environmental Research and Rescue Missions Through Autonomous Control and Sensor Integration



Raahil Sheikh, Priya Gujjar, Prathamesh Minde, Himanshu Dwivedi, and Arjun Dabas

Abstract This research shall focus on the intensification of pre-existing manual drones equipping them with a variety of sensors making them autonomous, and capable, and proposing them for a variety of roles including thermal sensing, data collection, tracking creatures, forest fires, volcano detection, hydrothermal studies, urban heat, island measurement, and other environmental research. The system can function for reconnaissance, research, 3D mapping, and search and rescue missions. This study mainly focuses on automating tedious tasks and reducing human errors as much as possible by reducing deployment time and increasing the overall efficiency, efficacy, and reliability of the UAVs. Creation of a comprehensive Ground Control System UI (GCS) enabling less trained professionals to use the UAV with maximum potency. With the inclusion of such an autonomous system, artificially intelligent paths and environmental gusts can be avoided. The research paper aims to tackle and implement the above-mentioned goals.

Keywords Autonomous control · Hexacopter UAV · Forest fires

1 Introduction

Unmanned aerial vehicles (UAVs) have become increasingly popular over the years, with numerous applications in various fields such as military operations, search and rescue missions, and environmental studies. The use of UAVs has proven to be beneficial in situations where it is difficult or dangerous for human operators to carry out tasks. In recent years, UAVs equipped with thermal sensing capabilities have become essential tools for environmental monitoring and research [1]. Thermal sensing UAVs allow for the detection and measurement of thermal energy in the environment [5], which can be used to identify various phenomena such as

R. Sheikh (✉) · P. Gujjar · P. Minde · H. Dwivedi · A. Dabas
Department of Aerospace Engineering, Chandigarh University, Mohali, India
e-mail: 21BAS1114@cuchd.in

© The Author(s), under exclusive license to Springer Nature Singapore Pte Ltd. 2024

S. Singh et al. (eds.), *Recent Advances in Aerospace Engineering*, Lecture Notes in Mechanical Engineering, https://doi.org/10.1007/978-981-97-1306-6_26

forest fires, volcanic activity, and hydrothermal features. The inclusion of environmental research has allowed UAV industry to be better equipped with hazards and neighboring disasters.

The study and calibration of a multi-purpose autonomous UAV with thermal sensing capabilities are the focus of this research paper. This study aims to develop a comprehensive understanding of the capabilities of the UAV and to calibrate it for optimal performance in a range of applications. The research will involve testing the UAV in various environments and conditions to determine its effectiveness in detecting and measuring thermal energy. Furthermore, this research will explore the potential applications of the UAV in environmental research, such as tracking wildlife, mapping urban heat islands, and identifying sources of pollution. The study will also investigate the potential for using the UAV in search and rescue missions, where its thermal sensing capabilities could be used to locate individuals in remote or hazardous areas.

2 Background

Unmanned aerial vehicles (UAVs), also known as drones, have become increasingly popular in recent years due to their versatility and potential for various applications [2]. One of the most promising areas for UAV use is in environmental research and rescue missions [3]. By enhancing their capabilities through autonomous control and sensor integration, UAVs can improve the accuracy and efficiency of data collection, increase the safety of rescue operations, and provide better situational awareness for emergency responders.

Autonomous control and sensor integration has been achieved through the use of advanced software and hardware systems. For example [4], software such as Mission Planner and QGroundControl allow users to program UAVs to perform specific tasks and missions autonomously [5]. Hardware such as the Pixhawk autopilot system allows for real-time control of the UAV and the integration of different sensors. Several research studies have focused on enhancing UAV capabilities for environmental research and rescue missions. Another approach to autonomous control for unmanned aerial vehicles is with the help of MATLAB and SIMULINK in which PID controllers have been generated for various motor mixing algorithms and each sensor to be added can be calibrated with the unmanned aerial vehicle. UAVs have great potential for environmental research and rescue missions. By enhancing their capabilities through autonomous control and sensor integration, UAVs can provide more accurate and comprehensive data, increase the safety of rescue operations, and improve situational awareness for emergency responders. Ongoing research in this area will continue to improve the effectiveness of UAVs in these applications.

3 Literature Review

1. "Autonomous Navigation for Micro Aerial Vehicles in GPS-Denied Environments" by Sebastian Houben et al. examines how micro aerial vehicles (MAVs) can be used for GPS-denied environments and autonomous navigation. The challenging task of using MAVs in areas without GPS signals, like underground or inside spaces, is discussed in the study. In order to enable MAVs to navigate autonomously, the research suggests a solution to this problem that combines sensor fusion, visual odometry, and feature tracking. In order to supply the data required for autonomous navigation, the paper's proposed system uses an inertial measurement unit (IMU), a camera, and a light detection and ranging (LIDAR) sensor.
2. The research paper "Real-Time Collision Avoidance for Unmanned Aerial Vehicles" by Andreas Breitenmoser et al. illustrates the production and application of an unmanned aerial vehicle (UAV) real-time collision avoidance system. The study suggests a collision avoidance system that forecasts the UAV's future placement and any obstacles in its path using an algorithm and sensor data. When deciding to change the UAV's path or altitude to avoid a collision, the system additionally considers the UAV's speed, altitude, and direction of travel. A number of studies were conducted to test the system in both indoor and outdoor settings, with a variety of obstacle shapes and sorts. The outcomes demonstrate that the system can identify and steer clear of impediments in real-time, guaranteeing the UAV's safe and efficient operation.
3. The research paper "Autonomous Landing of Unmanned Aerial Vehicles on Moving Platforms" by Gokul Mathew discusses the development and implementation of an autonomous landing system for unmanned aerial vehicles (UAVs) on moving platforms. The paper addresses the challenge of landing a UAV on a moving platform, such as a ship or a vehicle, which requires precise control and coordination. The paper proposes a landing system that uses a combination of vision-based localization, motion estimation, and control algorithms to enable the autonomous landing of UAVs on moving platforms. The system utilizes a camera mounted on the UAV and a fiducial marker on the moving platform to estimate the position and motion of the platform in real time. The paper presents a detailed description of the algorithm and its implementation on a UAV platform.
4. In the research paper "Autonomous Unmanned Aerial Vehicle Systems for Search and Rescue Operations" by James T. Ray et al. discusses the development and implementation of autonomous unmanned aerial vehicle (UAV) systems for search and rescue operations. The paper addresses the need for rapid and efficient search and rescue operations in emergencies. The paper proposes a UAV system that uses a combination of autonomous navigation, sensor integration, and communication systems to enable efficient and effective search and rescue operations. The paper presents a detailed description of the system and its implementation in a series of experiments, including indoor and outdoor scenarios, with various search and rescue scenarios. The results show that the system can

autonomously navigate and search for potential targets with high accuracy and efficiency.

4 Methodology

To establish autonomous control of a rotor-based UAV which can be used for multiple environmental research and other processes, there are two or three major ways of carrying out this process. Firstly, if an existing model needs to be made autonomous, it can be done with the help of software like that of ArduPilot and GlobalHawk. This is a convenient method of autonomous operation since the aircraft can be fixed with flight control software through which the calibration of various sensors can be done easily. This is indeed a cost-effective mode yet requires a working model for its testing.

The model adopted for this research is done with the help of Mathswork Inc. MATLAB and SIMULINK. It is programming software that can be used to make a fixed-wing or rotorcraft autonomous with the calibration of various sensors. Since this research aims to make a hexacopter craft autonomous, we have adopted a motor mixing algorithm that is being implemented to control basic controls like pitch, roll, yaw, and thrust. All of these motions will be controlled with the help of a proportional integral derivative (PID) controller which works on a feedback control mechanism employed to repeat a particular process consecutively to make a proper mechanism. This helps in facilitating autonomous control of any RC aircraft with the insertion of a Bluetooth sensor. But the problem lies with the range and accuracy of this sensor since it cannot transmit signals to a larger distances. For small pilot drones which need to be flown in a range of 2–3 km, this solution seems feasible and effective.

MATLAB and SIMULINK have been used to automate nano (less than 250 g), micro (250 g–2 kg), and small drones (2–25 kg) for optimum usage in search missions and environmental purposes. These categories of drones can be flown conveniently and smoothly in areas that are not easily accessible like that of volcanoes and heat signature tracking of various endangered species. The methodology/flowchart for the basic flow of operations and the motor mixing algorithm is illustrated in Figs. 1, 2, 3, 4 and 5.

5 Automation of Drone Profiles

AI utilizes optimization and verification algorithms to evaluate the information it gathers from its surroundings and make decisions that are similar to those made by humans. AI-based UAVs are often utilized for both military and civilian purposes, including weather forecasting, environmental research, search and rescue missions, and climate monitoring. They offer higher performance in terms of a short path

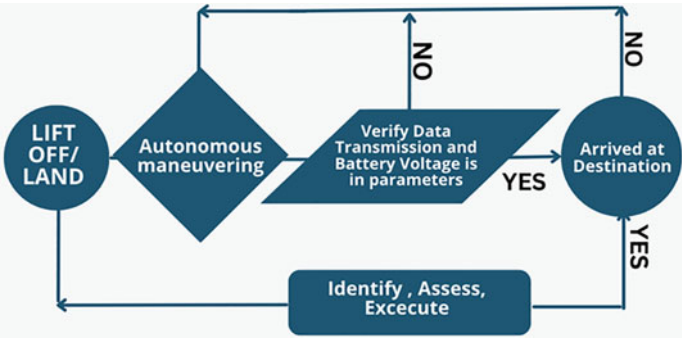


Fig. 1 Basic flowchart representation of autonomous system/process

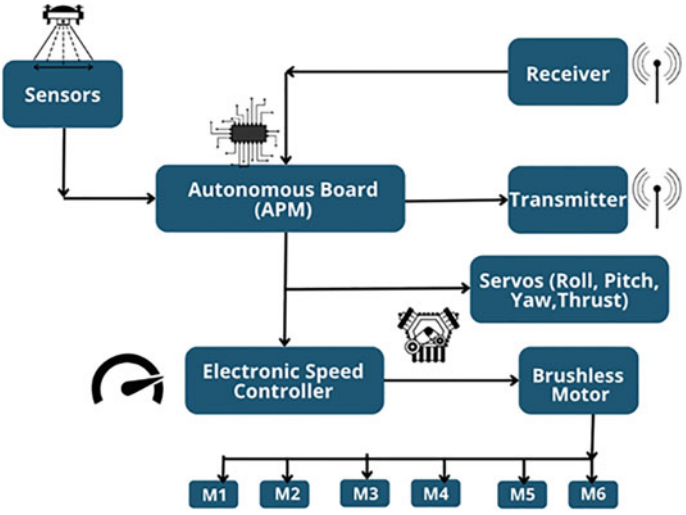


Fig. 2 Flowchart representation for the various sensors with autonomous board along with the brushless motors

length, a maximum roll angle, a minimal turning angle, and a rapid speed because of their high mobility, portability, scalability, and adaptability (Figs. 6 and 7).

For object detection: Due to its significant benefits and recent developments, target detection has attracted a lot of interest in unmanned aerial vehicles [6]. Unmanned aerial vehicles (UAVs) can be used for target tracking as well as intelligence, surveillance, and reconnaissance missions. Machine learning methods for target detection can give a highly precise result, and the model can make forecasts based on unpredictable future data. Visual recognition systems that use segmentation, localization, and categorization of images have made exceptional scientific advances. Moreover, deep learning has made significant strides in the disciplines of computer vision, image and video processing, and multimedia in resolving problems.

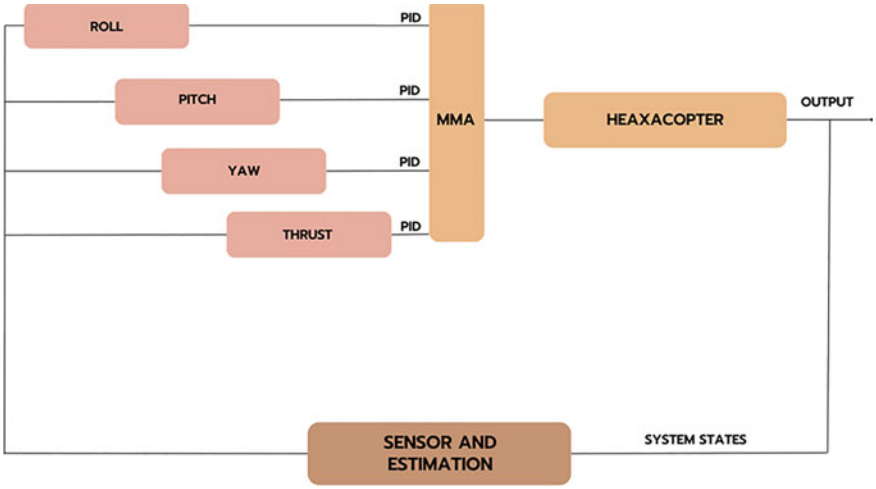


Fig. 3 Motor mixing algorithm for a hexacopter

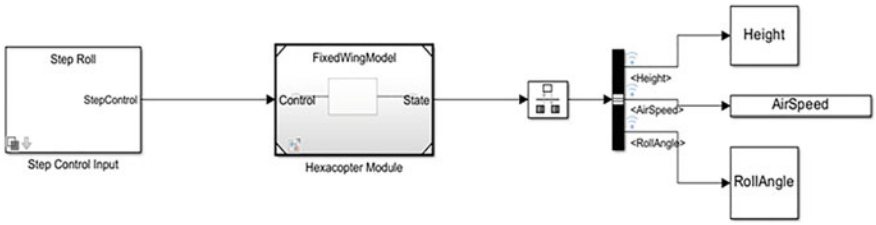


Fig. 4 For a UAV model, representation of basic control for airspeed, height, and roll angle. *Source* MATLAB

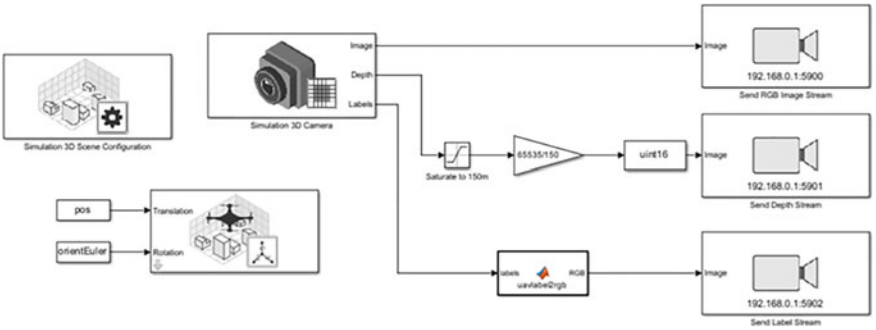


Fig. 5 Block representation of thermal imaging equipped with a camera in order to detect heat signatures in MATLAB. *Source* MATLAB

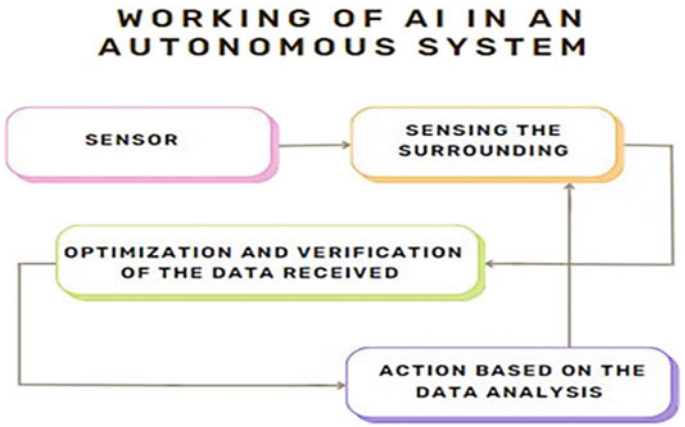


Fig. 6 Basic working of artificial intelligence in an autonomous UAV system

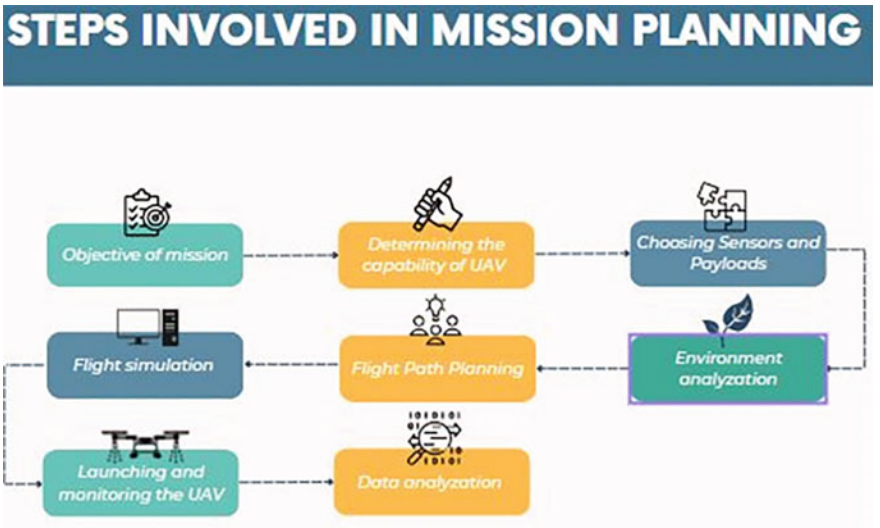


Fig. 7 Steps involved in mission planning and artificially intelligent decision making in autonomous drones

Path planning is figuring out the UAV's best and safest path from its current location to a certain destination [1]. Autonomous flights may be carried out using intelligent systems coupled with onboard sensors. The challenge of path planning is to identify a collision-free route through a scene containing both static and moving objects. One of the techniques for path planning is reinforcement learning [1], which includes teaching the UAV to find the most effective paths through trial and error using algorithms based on machine learning. This includes the sensor's data optimization and verification which is received by sensing the surroundings. Moreover, the action

is based on data analysis and mission planning, resulting in designing a flight strategy that enables the vehicle to achieve its goals.

Management of payloads: It is essential for managing payloads like sensors by adjusting the necessary parameter [7]. There are many commonly used payload algorithms such as priority-based scheduling algorithms, dynamic resource allocation algorithms, and multi-objective optimization algorithms. Multi-objective optimization algorithm takes into account a multitude of objectives, including increasing data collecting, reducing energy use, and improving flying time. The multi-objective optimization algorithm can establish the ideal balance between several objectives to efficiently and successfully optimize UAV payload management.

Control levels of autonomy are techniques for defining the degree of efficiency with which devices are capable of performing tasks, from simple to complex. There are ten different levels [2]. Here, we wish to impose the supervised automation level, which is considered to be the highest level of automation in UAVs. A supervised automation system is highly autonomous, but it is monitored by a human operator who can intervene if necessary. At this level of autonomy, the UAV may operate autonomously and can take care of all flight-related tasks, including takeoff, navigation, and landing. The UAV may also make decisions depending on the data it acquires, such as adjusting its altitudes or shifting its flight path to avoid obstructions. The human operator may still keep track of the UAV's activities in real-time and take action if necessary.

6 Specification of Mission Profile

For autonomous controlled missions, there needs to be a set of boundary conditions or pre-adjusted values which need to be inserted into the sensor configuration with the drone. These values can be used as a benchmark for the mission profile depending upon the mission profile's requirement of endurance and range. Endurance and range are critical factors for mission-designed autonomous UAVs. An autonomous UAV's endurance is its ability to stay airborne for an extended period, while range refers to how far the UAV can travel from its starting point [2]. In mission-designed autonomous UAVs, endurance and range are critical because they directly affect the UAV's ability to complete its mission. Similarly, a UAV designed for search and rescue missions may need to fly long distances to locate missing individuals or identify hazardous areas.

In addition to the mission-specific requirements, endurance and range are also critical for safety. In some cases, UAVs may need to return to their starting point for refueling or recharging, and a longer endurance or range allows them to do so without compromising the mission's success. The researchers have adopted a mission profile to carry out theoretical calculations to work with. The mission profile is incorporated in the form of an excel sheet which allows quick calculations and comparative analysis for various performance parameters (Tables 1 and 2).

Table 1 Representation of the mission requirements for the endurance, range, and minimum airspeed set for a mission profile

Mission requirements		
Endurance	8	min
Range	2	km
Stall margin	5	m/s
Min airspeed	15	m/s
Payload		
Payload weight	1	kg
Payload power	0	W
Aircraft		
Airframe weight	5	kg
Avionics power	0	W
Fuselage drag coeff	0.03	
Zero lift drag coeff	0.015	
Air density	1.225	kg/m^3

This mission profile shall allow researchers to analyze results and compare with analytical values

Table 2 Representation of the propulsion system of the motor system

Propulsion/batteries		
Battery pack capacity	27,000	mAh
Energy density	135	W–h/kg
Cell voltage	3.7	V
Cells in series (#s)	6	
Number of batteries	1	
Total battery capacity	27,000	mAh
Voltage	22.2	V
Batteries weight	4.440	kg
Total capacity used	80	%
Overall efficiency	40	%
Propulsive power	2286.43	W
Cruise current draw	102.99	A

The propulsion used is of a LiPo battery with a capacity of 8000 mAh and an energy density of 135 W h/kg

7 Results and Discussion

The researchers have implemented a path planning module in MATLAB after receiving the mission profile details. UAV scenario designer was utilized to deploy a path across the city of Manhattan. The range and endurance procured with the mission profile with a single battery has been utilized to devise the path. An algorithm has not been implemented to design these paths and would be implemented on the basis of reconnaissance and analysis path required. To avoid any obstructions during flight, a course-avoidance module is installed to detect and avoid the obstacles when a drone comes close to an obstruction. This shall help in safe maneuvers and efficient flight operations. We have chosen this path to verify our calculations and check for any percentage of error between the theoretical and analytical simulation of the mission profile (Figs. 8, 9, 10, 11 and 12).

The research implemented different modules dependent on time-responsive data with the help of MATLAB to employ a safe flight pathing for a mission profile. The mission profile can be altered to meet the designated feedback response in case of a reported disaster. The comparative study and analysis were conducted with the help of a theoretical and analytical approach for observing the time taken to complete the path. The theoretical/equation-based calculations took *0.47 h (mentioned in* Table.3*)* to complete the devised path with the prevalent parameterized mission profile. However, the analytical approach conducted on MATLAB was able to complete it in *0.502 h (Mentioned in* Fig. 11*)*. This signifies a percentage error of **6.37%** between the two methods adopted. With a meager amount of inaccuracy of flight travel, disaster and rescue-based missions can be conducted by a fast responsive system. The second stage of this research would be shifting to hardware and fabrication of

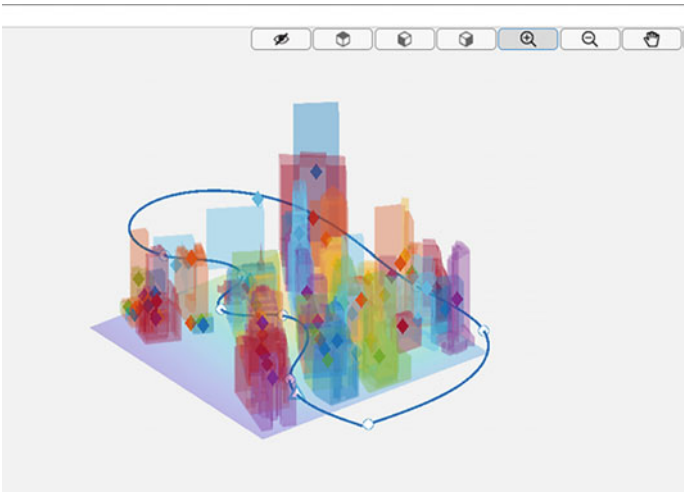


Fig. 8 UAV scenario designer used to develop the required path around the city of Manhattan [City maps imported from OpenStreet Map]. *Source* MATLAB

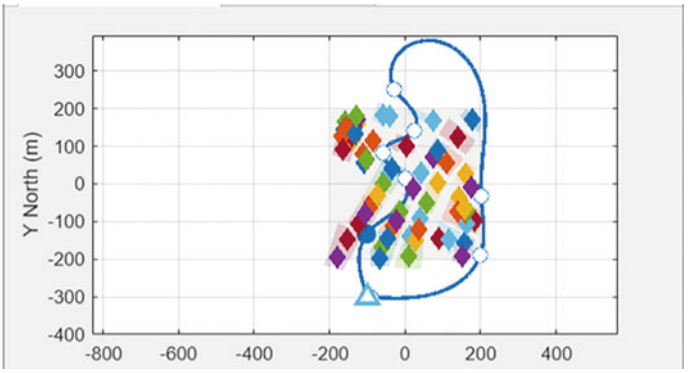


Fig. 9 UAV scenario designer used to develop the required path around the city of Manhattan {Top View} *Source* MATLAB

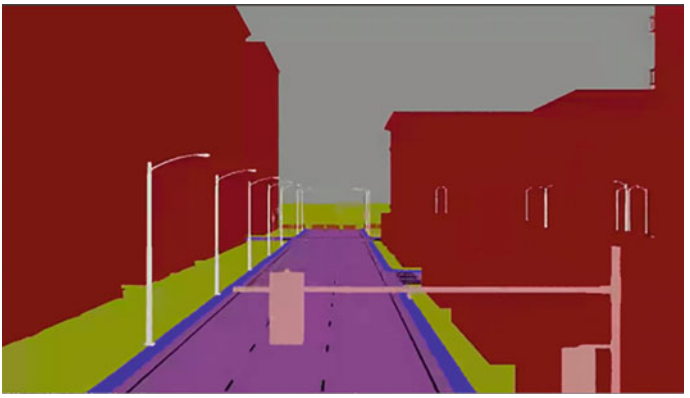


Fig. 10 Thermal imaging output in case of forest wildfires and search and Rescue missions. *Source* MATLAB

	Time (s)	X (m)	Y (m)	Z (m)	Course (deg)	Grou
1	0	-300.0000	-100.0000	0	-18.6900	
2	24.6920	-134.0000	-102.0000	0.0500	35.7400	
3	53.2230	16.0000	1.0000	0	-33.7300	
4	66.4470	83.0000	-57.0000	0	7.0500	
5	81.4490	141.0000	25.0000	0	33.5100	
6	100.3340	252.0000	-28.0000	0	-29.2000	
7	197.7480	-33.0000	201.0000	0	177.0500	
8	220.3690	-190.0000	199.0000	0	-160.0600	
9	268.0980	-301.0000	-91.0000	0	-86.9100	

Fig. 11 Tabular representation of time taken while following the projected trajectory. The overall time taken to complete the path is 0.502 h. *Source* MATLAB

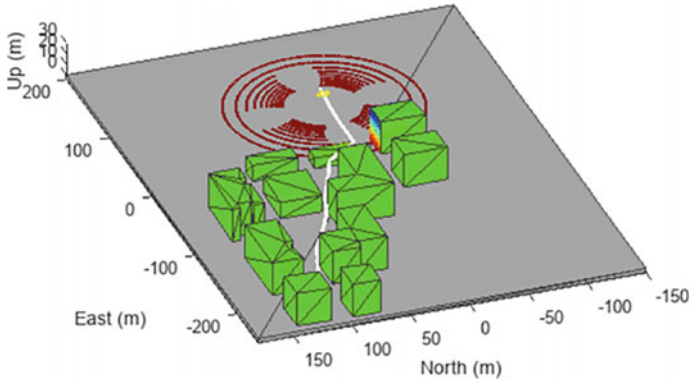


Fig. 12 Obstacle avoidance module setup through MATLAB in order to avoid collision. *Source* MATLAB

Table 3 Representation of total mass (AIRFRAME + PAYLOAD) with the mass friction, minimum frag/power/stall onset airspeed

General results						
Total mass	**10.440**	**kg**				
Mass fraction	52.11	%				
Min drag airspeed	**9.04**	**m/s**	32.53	km/h	20.21	mph
Min power airspeed	**6.87**	**m/s**	24.72	km/h	15.36	mph
Min airspeed (Stall onset)	**8.45**	**m/s**	30.44	km/h	18.91	mph
Condition results						
Cruise airspeed	25	m/s	90.00	km/h	55.92	mph
Lift coefficient	0.13		Lift		10.44	kg
Drag coefficient	0.0458		Drag		3.73	kg
Lift to drag ratio (L/D)	2.80					
Stall margin	16.55	m/s	59.56	km/h	37.01	mph
Estimated flight time	**12.6**	**min**	**0.21**	**hr**		
Estimated range	**18.9**	**km**	**11.72**	**mi**		

The bold value represents the final value received after setting the parameters and getting the results The cruise airspeed is set to be 17.5 m/s since we would be needing a lower speed for data gathering and analysis

such a methodology on drones. In future, this methodology can be incorporated into swarm technology to carry out a time-deviant and responsive system responsible for environment research and carrying out search and rescue missions.

Funding Not applicable.

References

1. Li J et al (2018) Path planning for unmanned aerial vehicles based on deep reinforcement learning. IEEE Trans Cyber 49(4):1423–1434
2. Chirici G, Giannetti F, Nocentini S, Travaglini D (2020) Assessment of a UAV-based thermal imaging system for forest fire detection. Remote Sens 12(12):2003
3. Xu Z et al (2019) Autonomous crop monitoring with UAVs: a review. Comput Electron Agric 163:104871
4. Alam MD, Oluoch J (2021) A survey of safe landing zone detection techniques for autonomous unmanned aerial vehicles (UAVs), vol 179
5. Zhang Q et al (2020) A survey on unmanned aerial vehicle applications in search and rescue operations. Int J Disaster Risk Reduct 44:101416
6. Wang H et al (2020) Real-time obstacle avoidance for UAVs using deep reinforcement learning. J Field Robot 37(1):66–81
7. Kuwata Y et al (2019) Autonomous last-mile delivery: the droid delivers. IEEE Robot Autom Mag 26(2):39–47

Designing and Analysis of Mild Steel Landing Gear Strut for a 3-Ton Unmanned Aerial Vehicle



S. M. Satheesh, N. R. Thirushah, Vishal Thirumurugan, Subramanian, and K. Vijay Anand

Abstract Fixed tricycle landing gear for 3-ton Unmanned Aerial Vehicle (UAV) with a Main Landing Gear (MLG) as a spring-leaf structure is designed. The design process is divided into specific phases: design requirements, preliminary design, detailed design, and testing. Ground load conditions are calculated in the initial design phase. The modeling begins by adding different geometries of clamping the primary strut with mild steel as the material. It is observed that the design is notwithstanding the load obtained from the ground calculations. The design is modified with clamps and connecting rods to meet the expected maximum stress during landing conditions, reducing the working stresses on the strut considerably. The stress profiles obtained from the study show that for all the models, the Mises stress observed is within the allowable stress limit. In contrast, the displacement observed is not in the allowable range, which may lead to structural damage due to a lack of shock absorption during landing.

Keywords Landing gear · Strut · Abaqus · Mises stress · Displacement

1 Introduction

The landing gear is a complex system that supports an aircraft in take-off, landing, and taxiing. Landing gear must be capable of absorbing impact loads while landing. The conventional hydraulic landing gears consume energy while retraction, and the UAV, which we considered, is used mainly for surveillance. Using spring-leaf landing gear without a retraction mechanism will increase the endurance of the UAV. The leaf spring acts as a suspension mechanism by undergoing temporary deformation and absorbs shock during landing. Numerous studies have been conducted on the

S. M. Satheesh (✉) · N. R. Thirushah · V. Thirumurugan · Subramanian
Department of Aerospace Engineering, B S Abdur Rahman Crescent Institute of Science and Technology, Chennai 600048, India
e-mail: satheesh@crescent.education

K. V. Anand
DRDO—Combat Vehicle Research and Development Establishment, Avadi, Chennai, India

© The Author(s), under exclusive license to Springer Nature Singapore Pte Ltd. 2024

S. Singh et al. (eds.), *Recent Advances in Aerospace Engineering*, Lecture Notes in Mechanical Engineering, https://doi.org/10.1007/978-981-97-1306-6_27

designing and numerical analysis of landing gear for many aircraft types to understand the stress distribution and the failure mechanism [1–5]. In the current study, a landing gear strut for a 3-ton UAV is designed optimally. The spring-leaf model is designed in 3D computer-aided design (CAD). The model is then analyzed to visualize the stress distribution through the structure and the deformation during the landing.

2 Methodology

Ground load calculations are performed analytically to estimate parameters like maximum velocity, relative drag, and inbound and outbound forces, using [6]

$$V_{\max} = \frac{(n - L/w)}{2} \tag{1}$$

$$\text{Relative drag } (D_r) = \frac{knW_L}{2} \tag{2}$$

The parameters of ground load calculation of a landing gear strut for a 3-ton UAV are finalized, referring to the estimated data corresponding to 1.5-ton UAV [7], and the parameters are listed in Table 1. C.G denotes the center of gravity, NLG denotes the nose landing gear, and MLG represents main landing gear. The three-dimensional layout design of landing gear and systems is shown in Fig. 1, schematically illustrating the parameters.

The analytical calculations for different types of landing gear used in a UAV are performed using Eqs. 1 and 2 to calculate the maximum velocity and the relative drag, presented in Table. 2, and it is found that the two-point landing gear layout

Table 1 Parameters of load calculation

Parameters	Values
Distance between C.G and NLG (a)	2532.3 mm
Distance between C.G and MLG (b)	696.48 mm
Distance between MLG and NLG (c)	3228.78 mm
Distance between MLG'S (d)	3400 mm
Landing weight (WL)	2.85 ton
Load factor (n)	3
Lift/Weight (L/W)	0.667
Descent velocity (VV)	3.05 m/s
Gravity (g)	9.81 m/s^2
Distance between C.G and NLG (a)	2532.3 mm
Distance between C.G and MLG (b)	696.48 mm

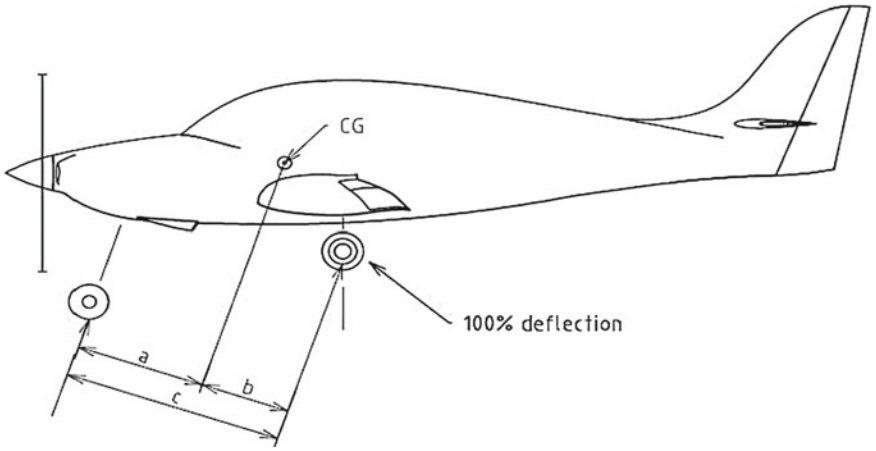


Fig. 1 Layout design of landing gear and systems [8]

Table 2 Ground load data

Types of landing	MLG		NLG		NLG considering forward CG	
	V_{max} (Kg)	D_r (Kg)	V_{max} (Kg)	D_r (Kg)	V_{max} (Kg)	D_r (Kg)
2 point	3324.52	1410.75	_	_	_	_
3 point	2476.08	1050.71	1362.03	577.97	1026.69	435.67
Tail down	3324.52	_	_	_	_	_
One point	3324.52	1410.75	_	_	_	_
Side load	1895.25	_	_	_	_	_

generated the maximum values (maximum vertical loads of 33,245 N, maximum drag loads of 14,107.5 N, and maximum side loads of 18,952.5 N). This data can be used as the applied load in the numerical analysis to visualize the stress distribution in the landing gear strut.

3 Designing and Analysis of a Leaf-Spring Landing Gear

The landing gear struts with the dimensions illustrated in Fig. 2b are designed in CREO. The three-dimensional schematic of the basic strut, considered model 1 in the current study, is illustrated in Fig. 2a. The designed structure is imported into the Abaqus package to carry out the numerical study. The material considered for the landing gear strut is mild steel [9, 10].

The sample was modeled with 6,42,860 ten-noded tetrahedral solid continuum (C3D10) elements. The three-dimensional mesh is presented in Fig. 2c, and the mesh

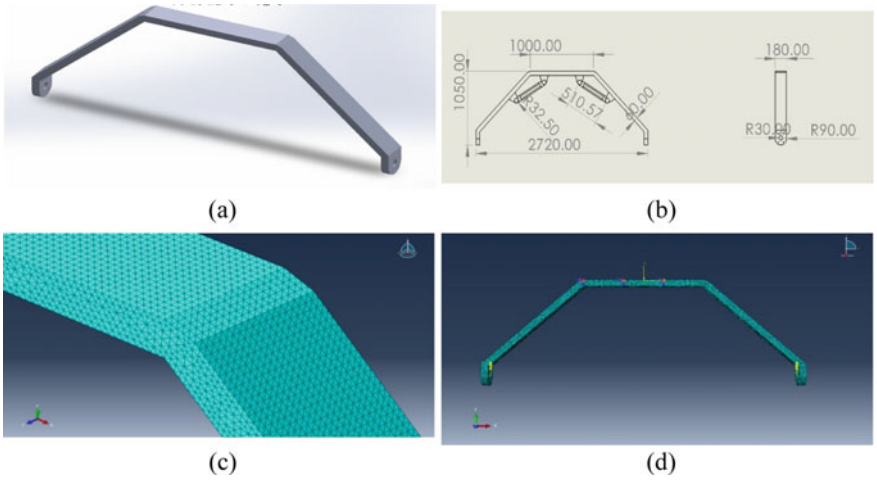


Fig. 2 **a** Three-dimensional schematic of basic strut—model 1, **b** Detailed dimension of basic strut—model 1, **c** Three-dimensional mesh for finite element analysis, **d** Schematics of applied boundary conditions

Table 3 Element type and number of elements for each model

Types of landing	Element type	Element size	Number of element
Model 1	C3D10	9 mm	6,42,860
Model 2	C3D10	9 mm	8,14,201
Model 3	C3D10	9 mm	8,32,127

details are presented in Table 3. The simulation begins with the coarse mesh in the model to identify the maximum stress location. The mesh was refined near the load application area and the area with maximum stresses. All the nodes on the top of the mesh are restricted for all translational and rotational motions. An analytically calculated load of 32,575.5 N from the ground load data is applied at the axle loading point. The boundary condition used for the model is illustrated in Fig. 2d. All the layers were assumed to be linearly elastic and isotropic with the following material properties: $E_{\text{mild steel}} = 205$ GPa, $\nu_{\text{mild steel}} = 0.29$ [11, 12].

4 Results and Discussions

The stress and displacement profile for model 1 is displayed in Fig. 3a, b. In the maximum stress profile, the maximum stresses are located at the top surface, which has fixed constraints. It is observed that the maximum stress and maximum displacement achieved are 801 MPa and 27.52 mm, respectively. The maximum allowable

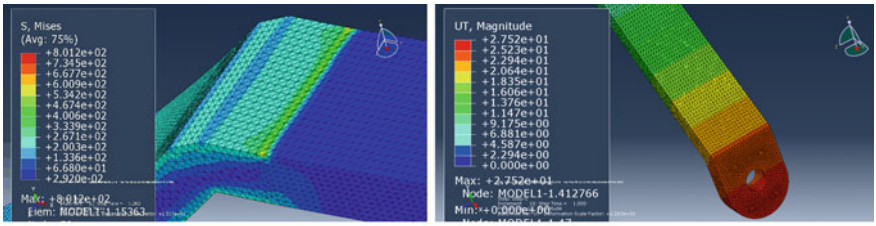


Fig. 3 **a** Mises stress profile for model 1. **b**: Maximum displacement profile for model 1

stress for mild steel is 400 MPa [13]. Since the stress calculated from the model exceeds the maximum permissible limit, the model 1 type of strut cannot be used for designing the landing gear. The existing model is then modified with additional connecting rods of different geometries (inclined and arc-shaped) to meet the strength requirements.

Inclined types of connecting rods and arc-shaped connecting rods are attached to the primary strut, as shown in Fig. 4a, c. The three-dimensional schematic and the detailed dimensions of the models with a straight connecting rod—model 2—and the model with an arc-shaped rod—model 3—are illustrated in Fig. 4a–d. The mesh size and the boundary conditions are the same as in model 1.

The stress and displacement profiles for models 2 and 3 are displayed in Fig. 5a–d. It is observed that the maximum Mises stress is reduced by 26% (591 MPa) and 40% (480 MPa) compared with model 1. It is also noted that even after modifying structures with connecting rods, the stress in the structures still exceeds the allowable stress limit of mild steel. The comparison of maximum Mises stress and the maximum displacement is given in Table 4.

The force vs displacement plot for all models 1 and 3 is presented in Fig. 6. It is seen that the presence of connecting rods not only brings down the maximum stress but also the slope by 25%. Yet, for the given dimensions of the landing gear struts, even with connecting rods, the working stress is not under the allowable stress. Hence, further studies must be conducted with composites on similar structures to meet the requirements.

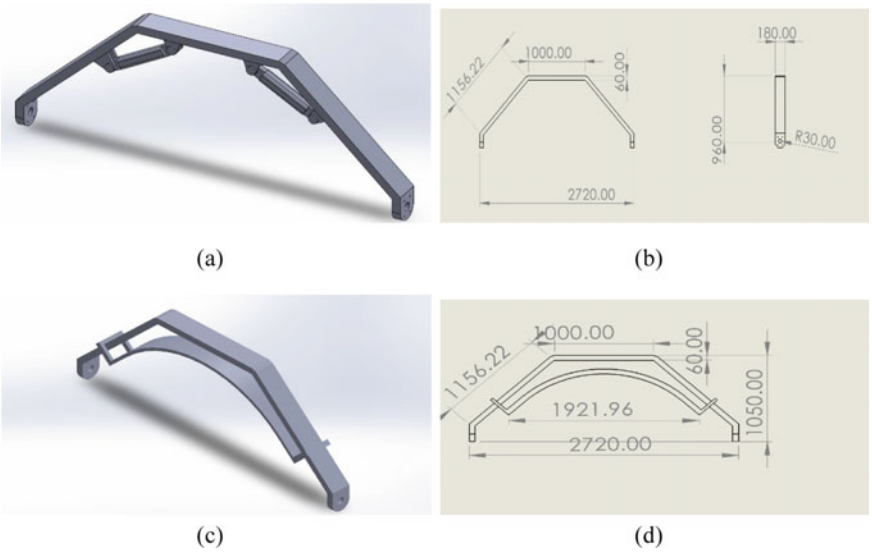


Fig. 4 **a** Three-dimensional schematic of the strut with inclined connecting rods—model 2, **b** Detailed dimension of the strut with inclined connecting rods—model 2, **c** Three-dimensional schematic of the strut with arc connecting rods—model 3, **d** Detailed dimension of strut with arc connecting rods—model 3

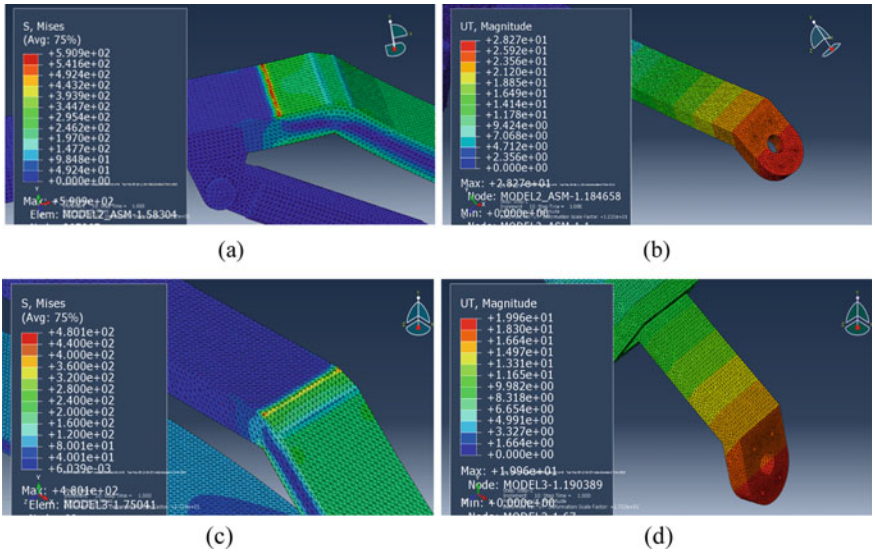


Fig. 5 **a** Mises stress profile for model 2. **b** Maximum displacement profile for model 2. **c** Mises stress profile for model 3, **d** Maximum displacement profile for model 3

Table 4 Comparison of maximum displacement and maximum stress data for various model

Models	Maximum displacement (mm)	Maximum Mises stress (MPa)
1	27.52	801.2
2	28.27	590
3	19.96	480.1

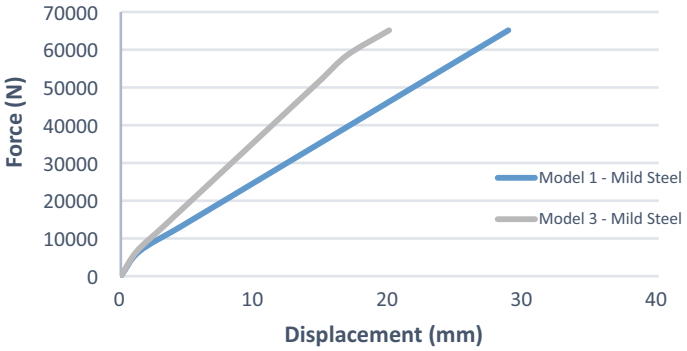


Fig. 6 Comparison of force Vs displacement plots of various models

5 Conclusion

The unmanned aerial vehicles are primarily used in surveillance and reconnaissance. These types of UAVs should have high endurance. To improve this aspect, conventional hydraulic landing gears are being replaced with leaf-spring landing gears that use spring loading to absorb shock instead of hydraulic systems. A simple strut (Model 1) for the landing gear of a 3-ton UAV is designed and analyzed with a static load of 3324.5 kg, calculated analytically, at the axle loading point. Results from the analysis (801.2 MPa of maximum Mises stress and a displacement of 27.52 mm) exceeds the maximum allowable stress (400 MPa), and hence, the leaf-spring with inclined connecting rods (Model 2) and the leaf-spring with arc-shaped connecting rods (Model 3) are designed. The models are then analyzed using the same boundary conditions and loading value, as that of model 1. The results show that the addition of the connecting rods reduces the maximum working stresses considerably yet exceeds the allowable stress limit. To achieve this, further numerical studies need to be conducted in advanced materials like composites.

Funding Information: Not applicable.

References

1. Al-banaa ASA, Ali SMJ, Pires R (2014) Stress analysis on main landing gear for small aircraft. Al-Rafadain Eng J 22(1)
2. Imran M, Ahmed RS, Haneef M (2015) FE analysis for the landing gear of test aircraft. Mater Today Proc 2(4–5):2170–2178
3. Freitas M, Infante V, Baptista R (2019) Failure analysis of the nose landing gear axle of an aircraft. Eng Fail Anal 101:113–120
4. Khatawate VH, Parikh P, Radadiya R (2021) Stress analysis of landing gear of Boeing 747–400 aircraft. In: IOP conference series: materials science and engineering, vol 1145, no 1. IOP Publishing, pp 012040
5. Pauliny J (2014) Landing gear design for single-engine four-seat aircraft. Brno University of Technology, Faculty of Mechanical Engineering: Brno, Czechia
6. Roskam J (1985) Airplane design: preliminary configuration design and integration of the propulsion system. DAR Corporation
7. Bagul P, Jenkins KW, Könözsy L (2020) Computational engineering analysis of external geometrical modifications on MQ-1 unmanned combat aerial vehicle. Chin J Aeronaut 33(4):1154–1165
8. Conway HG (1958) Landing gear design, vol 3. Chapman & Hall
9. Aerodynamics MH, Airframe structural design: practical design information and data on aircraft structures. MCY Niu. Conmilit Press Ltd
10. Sadraey MH (2012) Aircraft design: a systems engineering approach. John Wiley & Sons
11. Satish S, Alexis SJ, Bhuvendran A, Shanmugam M, Baskar S, Shaisundaram VS (2021) Design and analysis of mild steel mini truck body for increasing the payload capacity. Mater Today Proc 37:1274–1280
12. Wang XQ, Tao Z, Katwal U, Hou C (2021) Tensile stress-strain models for high strength steels. J Constr Steel Res 186:106879
13. Sonowal P, Das S, Mishra DK, Pandey KM (2020) Stress analysis of landing gear of light unmanned aerial vehicle. In: Journal of physics: conference series, vol 1455, no 1. IOP Publishing, p 012019

Comparative Study of Natural Frequency of a C-141a-il Airfoil Wing and Cantilever Beam: Simulation and Experimental Investigation

Madhav Sehgal, Saarthak Trikha, and Sudhanshu Tripathi

Abstract Vibration in a mechanical structure is of great importance as it can cause extensive damage to the structure's property if not dealt with properly, especially in the domain of aircraft and aerospace engineering. If the natural frequency of an aerospace structure becomes equal to the externally supplied vibration frequency, the structure starts resonating, which can lead to the shaking of the flying vehicle and thus the ability to change its flying path or lead to its deformation. Therefore, the vibrational and structural analysis of an aircraft wing is one of the most important components during the aircraft design process. This paper's study reports the formation and comparison of a realistic wing model of Lockheed C-140 aircraft wing that has Lockheed C-141 BL0 airfoil at its root and Lockheed C-141 BL761.11 airfoil at the tip, which is created on Autodesk Fusion 360, to that of a cantilever beam to determine its natural frequency, both by using simulation by ANSYS Workbench as well as conducting experimental testing by calculating the mode morphologies through experimentation of a scaled (1:61) 3D printed model of the wing and the beam in consideration. This study talks about vibration reduction methods to stabilize the wing using dampers or composites to structurally enhance it.

Keywords Modal analysis · Frequency analysis · Aircraft wing · Airfoil · Aircraft structure.

All authors have contributed equally to this work.

M. Sehgal (✉) · S. Trikha
Amity Institute of Aerospace Engineering, Amity University Uttar Pradesh, Noida, Uttar Pradesh 201301, India
e-mail: madhavsehgal001@gmail.com; madhav.sehgal@s.amity.edu

S. Trikha
e-mail: saarthak2trikha@gmail.com; saarthak.trikha@s.amity.edu

S. Tripathi
Department of IT and Engineering, Amity University, Tashkent City, Uzbekistan 100028
e-mail: stripathi@amity.uz

© The Author(s), under exclusive license to Springer Nature Singapore Pte Ltd. 2024

S. Singh et al. (eds.), *Recent Advances in Aerospace Engineering*, Lecture Notes in Mechanical Engineering, https://doi.org/10.1007/978-981-97-1306-6_28

1 Introduction

The majority of structural analyses are based on vibrational analysis, which is also used to determine the different frequencies of beam-like structures like trusses and columns.

The ultimate goal of vibration analysis is to, as far as possible, diverge the excitation forcing frequency from the natural frequency of the structure to prevent resonance. We discover the typical forms of the structures in this study as well. Forced and free vibrations are two different forms of vibration.

Free vibrations are those brought on by the environment, whereas forced vibrations are those that are induced artificially. Natural frequencies are those produced by unrestrained vibrations. The FEM method, in which the item is partitioned, and each section is studied separately, is the most effective approach to investigating these vibrations and frequencies.

But in order to confirm the results, we attempted to perform the modal analysis of a 3D model of the C-141a-I1 airfoil and a cantilever beam of similar dimensions and material properties using the ANSYS Workbench, both experimentally and mathematically. We discovered that the natural frequencies of the same type of beams or aerospace vehicles were coming out to be roughly the same for both types [5].

2 Vibrations

Vibrations occur wherever there are moving parts in machinery. Vibrations also occur in the structure surrounding the machinery [6]. The main causes of vibrations are:

- Unbalanced forces,
- Dry friction between two surfaces,
- External excitations,
- Earthquakes,
- Winds.

Vibrations cause uncontrolled stress, undesirable noises, and the failure of parts. The only desirable use of vibration is in the musical industry, vibrating screens, stress-relieving, etc. Resistance to these undesirable vibrations is generally referred to as damping.

3 Finite Element Method/Finite Element Analysis

The finite element approach is commonly used to compute mode shapes and natural frequencies while developing buildings to anticipate technical issues. The finite element method is similar to the building block method, where each building block's

Table 1 Deflection dependent on conditions

Condition	Deflection (X)	$\frac{dX}{dx}$	$\frac{d^2X}{dx^2}$	$\frac{d^3X}{d^3x}$
Hinged	0	–	0	–
Fixed	0	0	–	–
Free	–	–-	0	0

mass, stiffness, damping, and material properties are predicted and programmed into a finite element analysis software [8].

The finite element method is useful beyond design. The underlying frequencies and mode shapes of already-built buildings can also be determined. In general, finite element methods depict structures as discrete grid or node points connected by structural components. The finite element approach simulates the structural behavior and force and loading responses of a continuous system as a discrete representation. In Table 1, slope is represented as $\frac{dX}{dx}$, bending moment is represented by $\frac{d^2X}{dx^2}$, and shear force is represented by $\frac{d^3X}{d^3x}$.

This representation appears in the form of a mathematical model with precisely defined nodal points and discrete components connecting them [11]. If more node points are utilized to represent the structure, the solution will be more accurate. On the other hand, the model will be more rigid with fewer node points that are selected.

A typical finite element analysis requires the following:

- Spatial/Geometric location of nodal points,
- Structural components that link the nodal points and indicate the structure's stiffness,
- Mass attributes of the design,
- Structural constraints or boundary conditions
- Load operationality that may be dynamic or static.

The natural frequencies, mode forms, stress intensities, and displacements of the structure can subsequently be ascertained using the mathematical model that emerges from the research. An additional advantage of performing a finite element analysis on a specific structure is that design iterations can be easily supported, more affordably, and more quickly than by changing the actual hardware.

4 Mathematical Formulation

For the mathematical formulation, we consider some boundary conditions.

4.1 Lateral Vibrations of Beam

After equating resultant moment of any point to 0, we get a relation that [13, 14]:

$$P(x) = \frac{\mathrm{d}^2 M}{\mathrm{d}x^2}$$

$P(x)$ = Load per unit length,
M = Bending moment,
I = Moment of inertia,
E = Young's modulus.
Putting value of M in the derived equation, we get:

$$\frac{d^2\left(\mathrm{EI}\frac{\mathrm{d}^2 y}{\mathrm{d}x^2}\right)}{\mathrm{d}x^2} = P(x) = -\rho A \frac{\mathrm{d}^2 y}{\mathrm{d}t^2}$$

After solving the differential equation taking $y\,(x, t) = X(x).\, T(t)$, we get:

$$T = A\sin\omega t + B\cos\omega t$$
$$X = C_1\sin kx + C_2\cos kx + C_3\sin kx + C_4\cos kx$$

Where 'X' defines shape of normal mode of vibration termed as normal function $C_1 \ldots C_4$ are the 4 boundary conditions.

General solution:

$$y = \sum_{i=1}^{\infty} X_i(A_i\sin\omega_i t + B_i\cos\omega_i t)$$
$$X_i = C_{1_i}\sin k_i x + C_{2_i}\cos k_i x + C_{3_i} \ldots$$

4.2 Natural Frequencies of Cantilever Beam Using Governing Differential Equations (GDE)

Cantilever beam is a beam which is supported at one end and free from the other end. It is a rigid structural element whose property is to resist bending. The beam extends horizontally from a flat surface such as a wall.

Cantilever beam's length is 0.15 m, and its cross-section is 30 × 1 mm. Now, we apply the governing differential equation:

$$M = \mathrm{EI}\frac{\mathrm{d}^2 y}{\mathrm{d}x^2}$$

After applying the corresponding boundary condition on the above equation, we find out that natural frequencies for different modes of a cantilever beam are:

Mode $1 = 3.52\frac{a}{l^2}$.
Mode $2 = 22\frac{a}{l^2}$.
Mode $3 = 61.7\frac{a}{l^2}$.
where $a = \sqrt{\frac{\mathrm{EI}}{\rho A}}$.

5 Modal Analysis

The necessity of appropriate mathematical models has been demonstrated, supporting the fundamental case for the use of FEMs. This study's declared goal is to demonstrate that there is a good engineering correlation between the modes of vibration predicted by FEM and the outcomes of mathematical formulation.

The correlation between anticipated and measured vibrational modes establishes the basic validity of the models. The modes' verification further demonstrates the accuracy of the section characteristics and mass distributions. The establishment of material section properties can and should be done using static load and deflection experiments.

However, the modal analysis and testing approach takes this procedure a step further by also taking into account mass distribution. Additionally, the technique of modal analysis naturally incorporates the significance of structural elements such as nonlinear joints and structural damping.

6 Modeling Techniques

There are two ways to determine a structure's vibrational properties. The first technique is analytical modeling, which makes use of a software tool that implements the finite element approach.

Here, a "forward-type" of analyzing is used, in which the structure is divided up into elements whose mass, stiffness, and damping are determined, and the structure's mode shapes and natural frequencies are estimated from these parameters.

The stiffness and damping of the entire structure, as well as the natural frequencies and modes of vibration, may be calculated from the individual interactions at various sites [3].

7 Cantilever Beam

7.1 ANSYS Workbench Techniques Used for Modal Analysis

Dimensions

Total Length = 150 mm.
Height = 30 mm.
Breadth = 1 mm.

Boundary Condition

One end is fixed, and deflection is set to 0.

7.1.1 FEM

After the generation of geometry, we moved on to meshing. The meshing of the model was done with a minimum element size of 0.025 m and an edge length of 1 m. With high smoothing, 81 nodes are created with 40 elements. The material used was steel with an elastic modulus of 200 GPa, Poisson's ratio as 0.33, and a density of 7860 Kg/m^3 (Figs. 1, 2, 3 and 4).

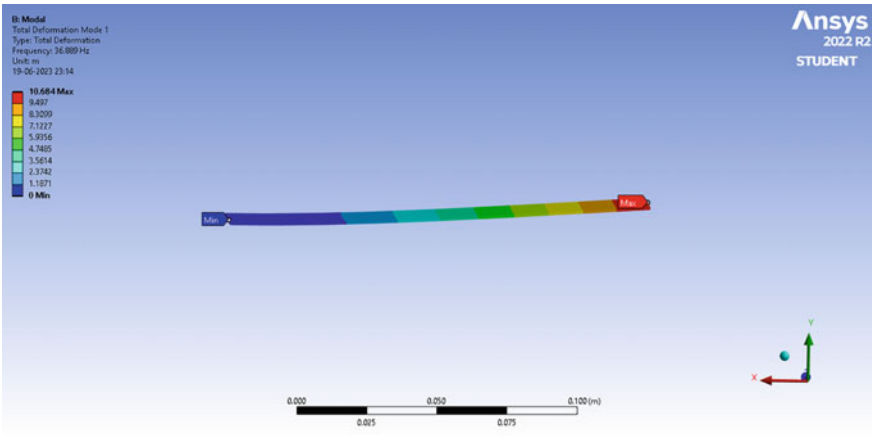


Fig. 1 First mode of cantilever beam simulation

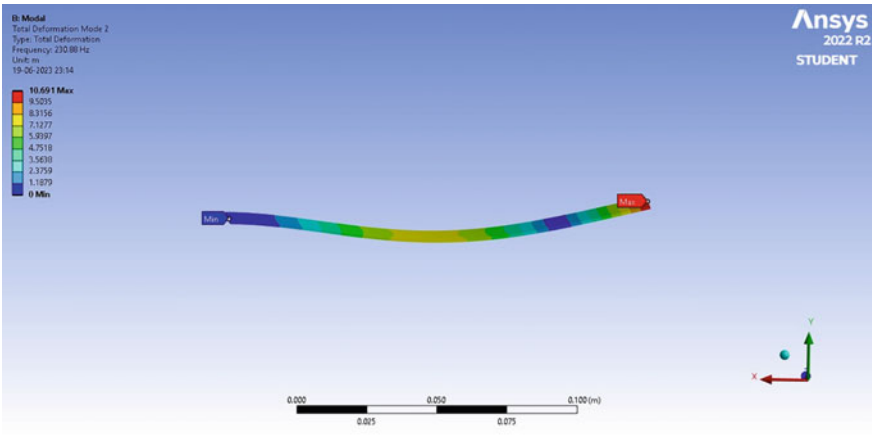


Fig. 2 Second mode of cantilever beam simulation

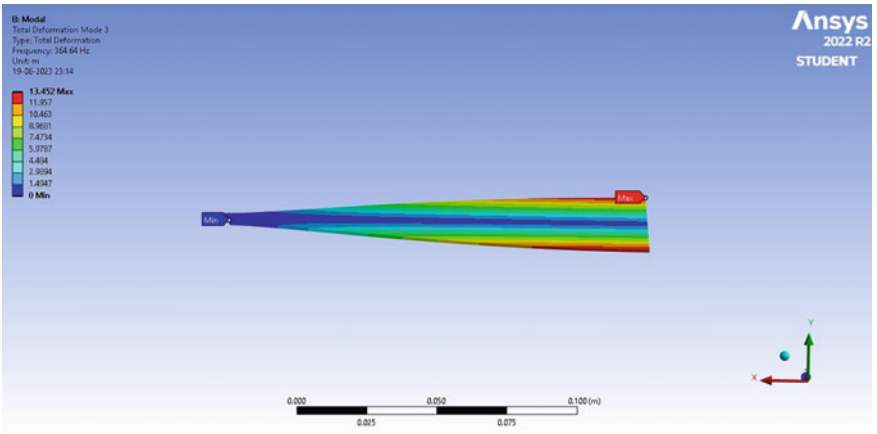


Fig. 3 Third mode of cantilever beam simulation

7.2 Experimental Data

Dimensions

Total length = 150 mm.
Height = 30 mm.
Breadth = 1 mm.

Boundary Conditions

The metal beam was fixed with the table at one side and was kept free from the other.

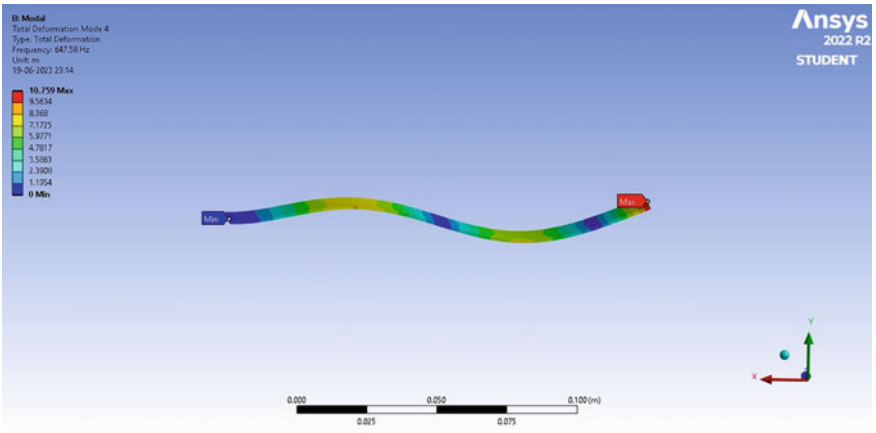


Fig. 4 Fourth mode of cantilever beam simulation

Analysis

The beam material is structural steel. It has an elastic modulus of 2e+11 Pa. The analysis was done by stroboscope tachometer.

8 Modeled Wing

8.1 ANSYS Workbench Techniques Used for Modal Analysis

A similar modal analysis is done on one-half of the wing by considering half of the wing as cantilever beam and fuselage as a fixed support point [12]. The wing is a more complicated structure as compared to beam and has an asymmetric body, but to perform a modal or structural analysis to zero error is highly unlikely. So, by considering it [1, 4] as a beam, we not only save computational power and time, but the errors produced are very few too. In order to predict the natural frequencies, we analyzed the wing by FEM. The modeled aircraft wing was developed on Fusion 360 after a close study of the wings used in Lockheed Martin C-140 which has a Lockheed C-141 BL0 airfoil at its root and Lockheed C-141 BL761.11 airfoil at the tip. The material chosen was ABS plastic, and this was done to conveniently compare the results with 3D printed model.

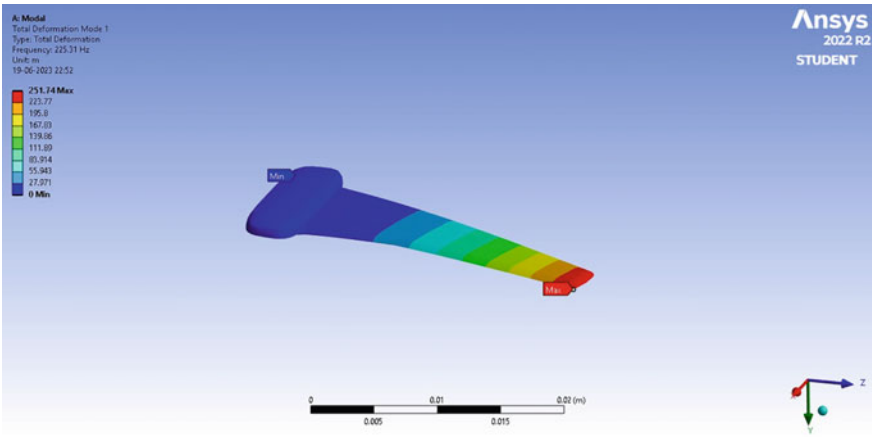


Fig. 5 First mode of ABS scaled wing simulation

8.1.1 Model Dimension

The chord length of the same was taken to be 0.07 cm at root and 0.035 m at tip with a max camber of 1.1% at tip and 1.8% at root and a max thickness of 13%. A span of 0.3 m was selected.

8.1.2 Boundary Conditions

One end is fixed, and deflection is set to 0.

8.1.3 FEM

After the generation of geometry, we moved on to meshing. The meshing of the model was done with a minimum element size, and edge length of 0.001 m. With high smoothening, 1211 nodes are created with 514 elements. The material used was ABS with elastic modulus as 1.628e+09 and Poisson's ratio as 2.978e+09, with a density of 1030 Kg/m^3 (Figs. 5, 6, 7 and 8).

8.2 Experimental Data

Model Dimensions

Chord length is variable.
Span = 300 mm.
Max. thickness = 13%.

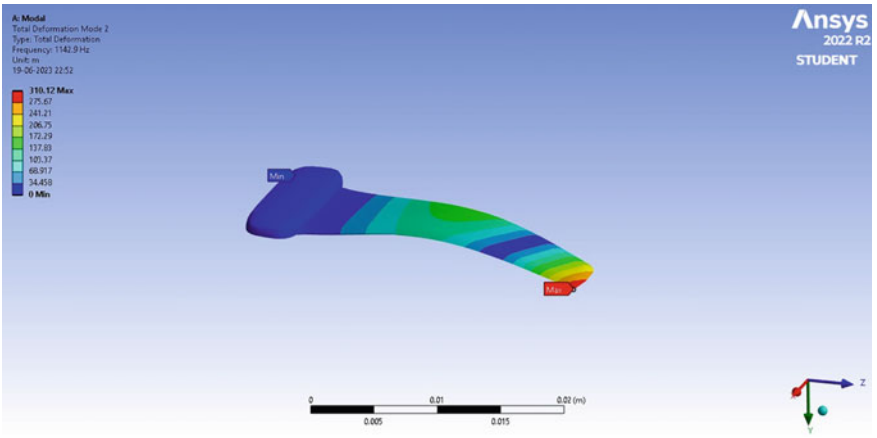


Fig. 6 Second mode of ABS scaled wing simulation

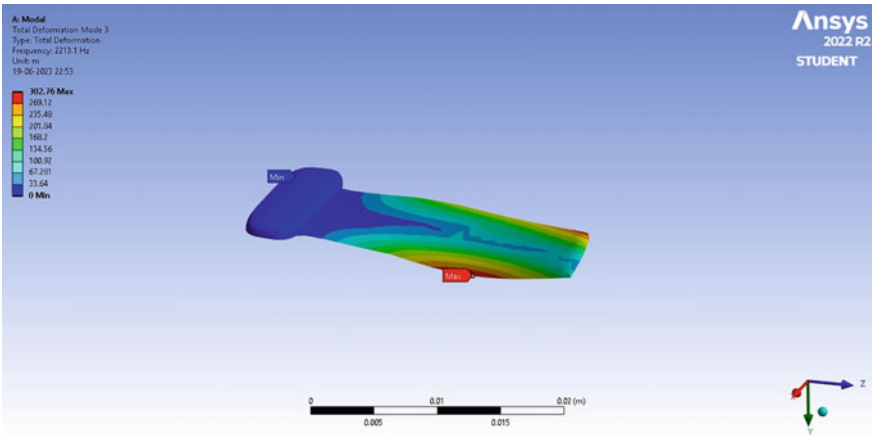


Fig. 7 Third mode of ABS scaled wing simulation

Boundary Conditions

The 3D printed wing was fixed with the table at one side and was kept free from the other.

Analysis

The material of the wing is ABS with a density of 1030 Kg/m^3 and Poisson's ratio of 2.978e+09. It has an elastic modulus of 1.628e+09. The analysis was done by the use of stroboscope tachometer (Figs. 9 and 10).

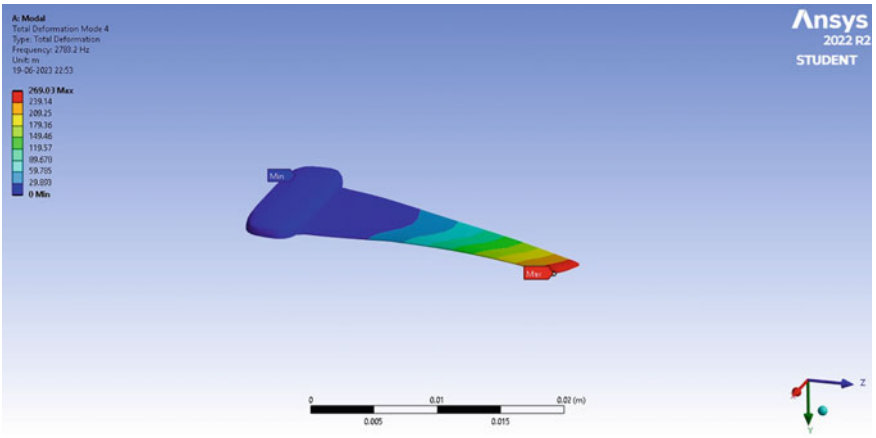


Fig. 8 Fourth mode of ABS scaled wing simulation



Fig. 9 Experimental setup of 3D printed ABS wing

9 Reduction of Vibration

Most of the vibration caused in an aircraft is due to the air resistance on the exterior of the vehicle, and mechanical vibrations caused by engine or other moving parts [7].

These vibrations can be reduced by means of dampers or changing the shape of beam, or using high quality, low-vibrating materials.



Fig. 10 Experimental setup of cantilever beam

Damper machines resist vibration. The dampers collect vibration energy and release it as heat or store it till the external pressure is off. They work like spring suspensions [9].

There are also composite materials that have been developed to absorb some of these vibrations. These materials range from rubber to asphalt-impregnated paperboard dampers. These energy-storing fibers stretch or change size to absorb energy and return to their original state.

10 Material Comparison and Modal Analysis

10.1 Aluminum 6061

A modal analysis of the modeled wing was conducted by considering it as a cantilever beam. The elastic modulus was taken as 69 GPa, density as 2713 Kg/m^3, and Poisson's ratio as 0.33. A similar approach was followed as demonstrated above, and the following data was derived (Figs. 11, 12, 13, 14, 15 and 16).

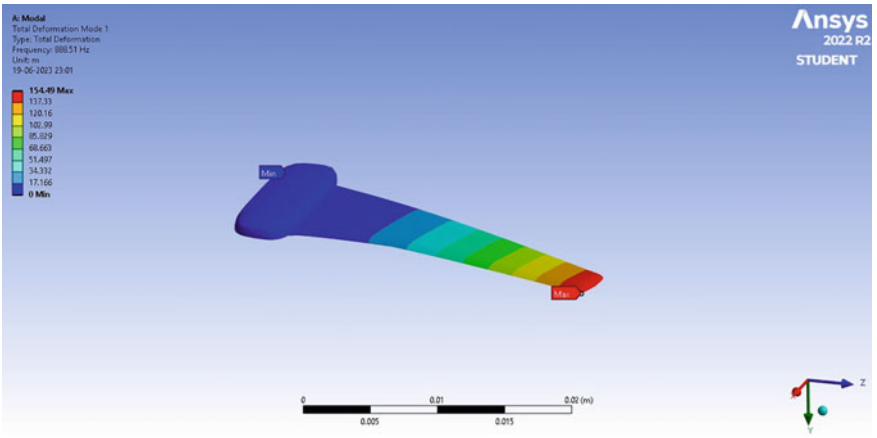


Fig. 11 First mode of aluminum scaled wing simulation

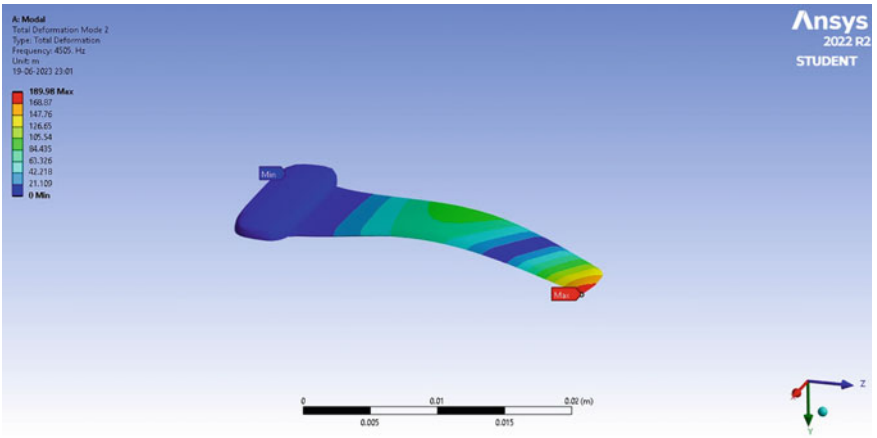


Fig. 12 Second mode of aluminum scaled wing simulation

10.2 Carbon Fiber

A modal analysis of the modeled wing was conducted by considering it as a cantilever beam. The elastic modulus was taken as 395 GPa, density as 1800 Kg/m^3, and Poisson's ratio as 0.28. A similar approach was followed as demonstrated above, and the following data was derived.

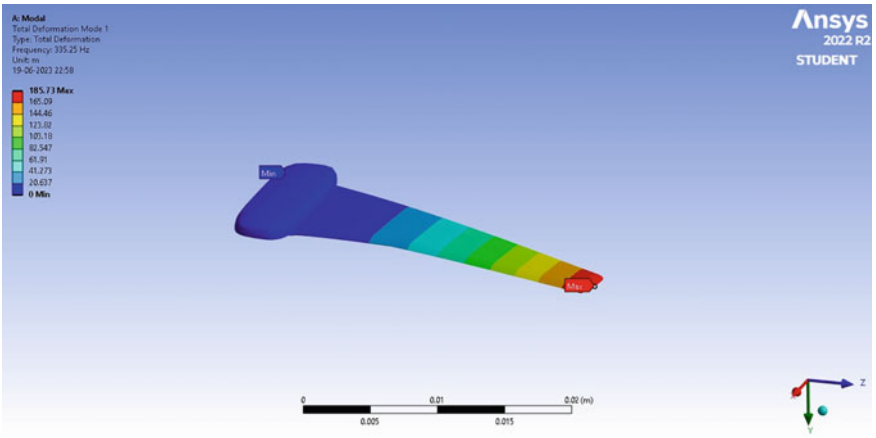


Fig. 13 Third mode of aluminum scaled wing simulation

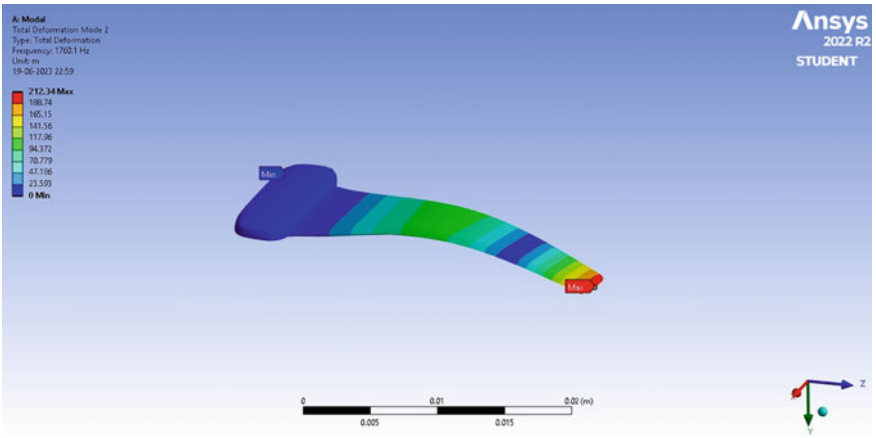


Fig. 14 Fourth mode of aluminum scaled wing simulation

11 Results and Observations

11.1 Comparison of Natural Frequencies with PLA

From the natural frequencies obtained by mathematical modeling of governing differential equations, simulation on ANSYS Workbench, and experimentation, the results can be compared as follows (Table 2).

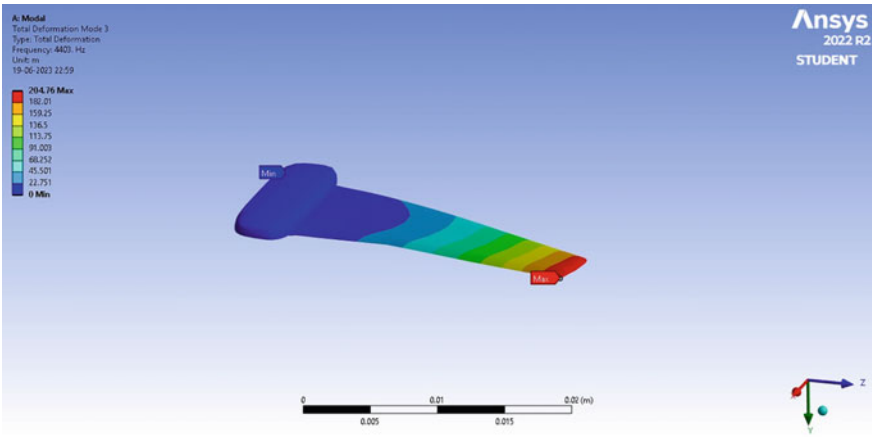


Fig. 15 First mode of carbon fiber scaled wing simulation

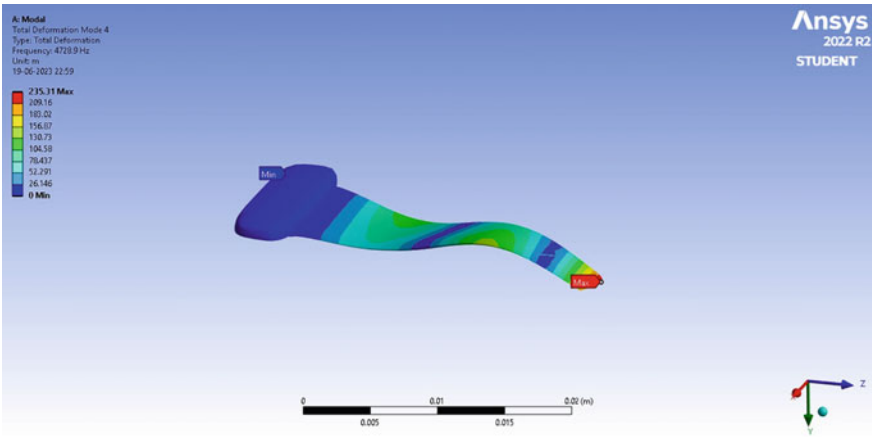


Fig. 16 Second mode of carbon fiber scaled wing simulation

Table 2 Result comparison between different methodologies

		GDE	ANSYS workbench	Experimentation
Cantilever beam	Mode 1	35.14	36.889	32.4
	Mode 2	225.5	230.88	234.34
	Mode 3	358.81	364.64	350.66
Modeled wing	Mode 1		225.31	210.15
	Mode 2		1142.9	1105.09
	Mode 3		2213.1	2212.3

Table 3 Result comparison between different materials

	Aluminum 6061	Carbon fiber
Mode 1	888.51	335.25
Mode 2	4505	1760.1
Mode 3	8972.2	4403
Mode 4	11,142	4728.9
Mode 5	12,235	5990.8
Mode 6	21,399	9373.5

11.2 Comparison of Natural Frequencies Between Aluminum 6061 and Carbon Fiber

We infer that by using aluminum we get considerably high natural frequency when compared with carbon fiber (Table 3).

12 Conclusion

In this paper, we calculated the natural frequencies for cantilever beam by mathematical formulation, ANSYS Workbench (using FEA) and experimentation. Further, we compared one-half of the wing to a cantilever beam and carried out the same analysis. We modeled an aircraft wing in Fusion 360 and calculated its natural frequencies using ANSYS Workbench (using FEA) and experimentation. The experimental method in both cases was done by making a fixed support condition at one end and letting one side be free. Then, a stroboscope was used to measure the frequency of beam and 3D printed wing.

The comparison of results were done for both the cases and natural frequencies for both cantilever beam and the wing were coming well in the error limits as can be seen in observations (Figs. 17 and 18).

One more set of modal analysis was performed on the wing by changing the materials. Firstly, Aluminum 6061 was taken and then carbon fiber was taken. This analysis was done to compare modal properties of these materials. From the comparison of natural frequencies of the wing when compared between aluminum and carbon fiber, it is seen that this material has higher natural frequencies for the same mode. A higher natural frequency indicates better stability because the chances of it getting resonate are less. From this, we concluded that aluminum may be weak in mechanical properties when compared to carbon fiber but surely has better modal properties and can absorb a large amount of vibration [2] and can be used as damping material in aircrafts.

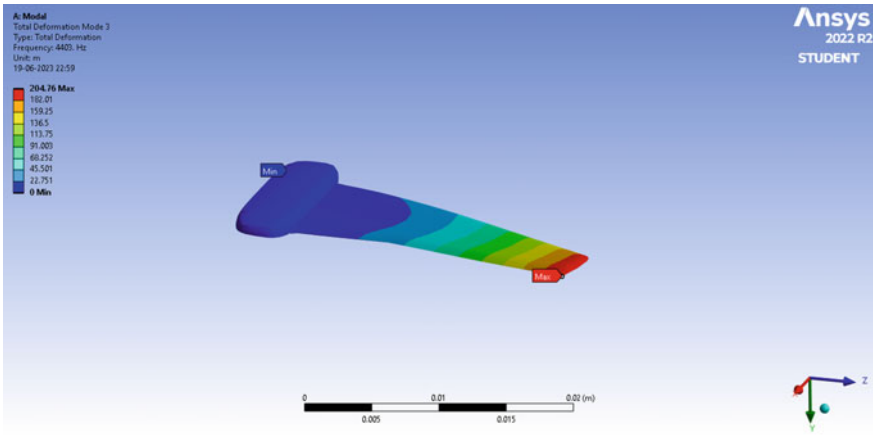


Fig. 17 Third mode of carbon fiber scaled wing simulation

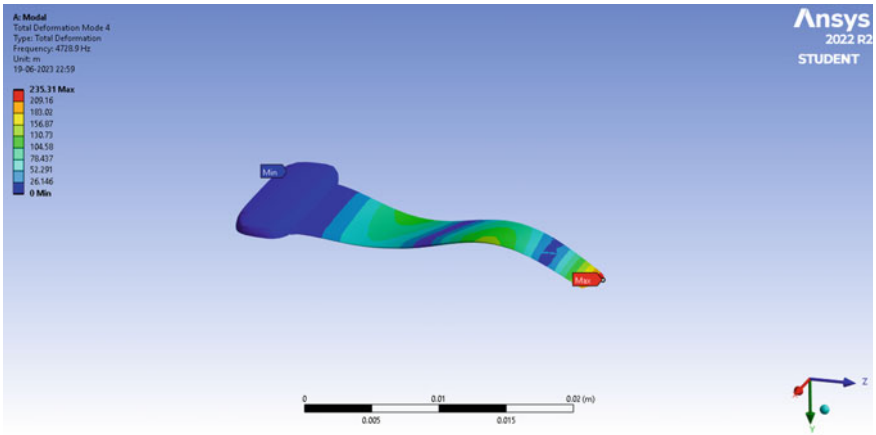


Fig. 18 Forth mode of carbon fiber scaled wing simulation

Funding Not applicable.

References

1. Koohi R, et al (2021) Modal and aeroelastic analysis of a high-aspect- ratio wing with large deflection capability—Semantic Scholar. Modal and aeroelastic analysis of a high-aspect-ratio wing with large deflection capability—Semantic Scholar. semantic- scholar.org/paper/0f175c38c1173a429b093bd86de60c57513dcb1a

2. Experimental modal analysis of an aircraft model wing by embedded fiber bragg grating sensors. Experimental modal analysis of an aircraft model wing by embedded fiber bragg grating sensors—IEEE J Mag—IEEE Xplore. https://doi.org/10.1109/JSEN.2005.854152
3. Banerjee JR (2016) Modal analysis of sailplane and transport aircraft wings using the dynamic stiffness method—IOPscience. Modal analysis of sailplane and transport aircraft wings using the dynamic stiffness method—IOPscience. https://doi.org/10.1088/1742-6596/721/1/012005
4. Rosly NA, et al (2018) Preliminary investigation on experimental modal analysis of high aspect ratio rectangular wing model—Int J Eng Technol. Preliminary investigation on experimental modal analysis of high aspect ratio rectangular wing model—Int J Eng Technol. https://doi.org/10.14419/ijet.v7i4.13.21348
5. Bogrekci I, et al (2019) Structural and modal analyses of NACA 66-206 aircraft wing model. Structural and modal analyses of NACA 66–206 Aircraft wing model—SpringerLink. https://doi.org/10.1007/978-3-030-31343-2 16
6. Grover GK, Nigam SP (2009) Mechanical vibrations. Nem Chand
7. Raffle DL (1965) Analysis and design of flight vehicle structures. Professor EF Bruhn. Tri-State Offset Co., Cincinnati, Ohio, USA. 1965. Aeronautical J 69(654):419–420
8. Tirupathi RC, Ashok DB (2016) Introduction to finite elements in engineering
9. Carrera E, Zappino E (2016) Carrera unified formulation for free-vibration analysis of aircraft structures. AIAA J 54(1):280–292
10. Coburn T (2014) Ultimate strength of aircraft structures. In: ASME international mechanical engineering congress and exposition, vol 46421. American Society of Mechanical Engineers, p V001T01A033
11. McConnell KG (2006) The elusive free-free boundary condition. Shock Vib Dig 38(6):538–540
12. Sayyad FB, Kumar B, Khan SA (2013) Approximate analytical method for damage detection in free–free beam by measurement of axial vibrations. Int J Damage Mech 22(1):133–142
13. Chaphalkar SP, Khetre SN, Meshram AM (2015) Modal analysis of cantilever beam structure using finite element analysis and experimental analysis. Am J Eng Res 4(10):178–185
14. Prashant SW, Chougule VN, Mitra AC (2015) Investigation on modal parameters of rectangular cantilever beam using experimental modal analysis. Mater Today: Proc 2(4–5):2121–2130

Dynamic Stall of a Pitching Airfoil: Comparative Study with ONERA and OpenFOAM

Sanjay Ramachandran, Arockiya Fridolin Sherbin Micheal, Gengatharan Rajarathinam, Deepak Lakshmanan, Rajesh Senthil Kumar Thangeswaran, and Sakthivel Thangavel

Abstract Dynamic stall is an inevitable complex flow phenomenon in rotorcrafts, wind turbines, supermaneuverable aircrafts and flapping- wings. Although experimental studies on dynamic stall pose difficulties, a great interest lies in understanding and mitigating its effects. Researchers opted for computational techniques and empirical/semi-empirical models for predicting the aerodynamic loads under dynamic stall conditions. The current study aims to understand the dynamic stall of an airfoil exhibiting pitching motion through numerical simulations and ONERA's semi-empirical model. The numerical simulations are carried out for different reduced frequencies of range $\kappa = 0.03,\ 0.05,\ 0.1$ and Reynolds numbers $\mathrm{Re} = 3 \times 10^4$, 3×10^5, 3×10^6. An open-source computational fluid dynamics software, OpenFOAM is used for the simulations, and the results are compared with experimental data and the ONERA model. The features of dynamic stall are examined effectively, and the results correlate well against the experimental data. With the decrease in Reynolds number, an increase in lift-curve slope is observed during the onset of dynamic stall.

Keywords CFD · OpenFOAM · ONERA model · Pitching airfoil

1 Introduction

Dynamic stall is an unsteady flow phenomenon that occurs when any lifting surface is subjected to transient motion when the angle of attack surpasses the static stall angle. The motion induces a delay in the onset of the stall, due to the formation of dynamic stall vortices. It is predominantly seen in helicopter rotor blades and wind turbines, where the angle of attack changes rapidly [1, 2]. Recently, unmanned

S. Ramachandran · A. F. S. Micheal · G. Rajarathinam · D. Lakshmanan · R. S. K. Thangeswaran (✉) · S. Thangavel
Department of Aerospace Engineering, Amrita School of Engineering, Coimbatore, Amrita Vishwa Vidyapeetham, Coimbatore, India
e-mail: t_rajesh@cb.amrita.edu

© The Author(s), under exclusive license to Springer Nature Singapore Pte Ltd. 2024

S. Singh et al. (eds.), *Recent Advances in Aerospace Engineering*, Lecture Notes in Mechanical Engineering, https://doi.org/10.1007/978-981-97-1306-6_29

mini/ micro rotorcrafts involving various flow conditions also have the possibility of dynamic stall. The aerodynamic loads during dynamic stall show severe oscillations which induce structural vibrations leading to hazardous effects.

Wind-tunnel experiments on pitching airfoils have been conducted from the mid-twentieth century to comprehend the mechanisms behind the dynamic stall and have been used for validating CFD simulations and analytical models to predict the aerodynamic loads. Major events of dynamic stall revealed by them include airfoil exceeding the static stall angle, roll up of shear layer to form a leading- edge vortex (LEV), separation of LEV causing stall onset and the formation of primary dynamic stall vortex (PDSV), complete stall and flow reattachment [3].

CFD simulations have been able to capture the flow phenomenon and reproduce equivalent results. A recent study of dynamic stall involved dynamic mesh motion, and the k-ω SST turbulence model [4] provided results with a better match to experimental data taking less computational time than any higher turbulence models. A semi-empirical model to predict dynamic stall is the ONERA model which models the dynamics of unstalled and stalled flows with a set of nonlinear differential equations. It has been used to study the aero-elastic behavior of rotor blades and wings at subsonic and transonic speeds [5]. The model was able to predict the stall phenomenon well with the lift coefficient [6]. The evolvement of the model [1], involving higher-order approximation, is used for the study and has been tuned to capture better features with the drag and moment coefficients.

The objective of the paper is to simulate the dynamic stall experienced by a pitching airfoil using OpenFOAM v10 and compare its aerodynamic hysteresis loops with the modified ONERA dynamic stall model. The model is coded in house using MATLAB version 9.13 (R2022b), and the dynamic stall cases are simulated in OpenFOAM using the k-ω SST model. The effect of reduced frequency and Reynolds number on the dynamic stall phenomenon is studied, and the flow field around the pitching airfoil is examined in detail to show the flow separation, vortex shedding, and how it affects the aerodynamic performance of the airfoil.

2 Modified ONERA Dynamic Stall Model

Petot [7] developed the ONERA dynamic stall model using differential equations and solving the unstalled lift circulation with a first-order differential equation. Laxman et al. [1] proposed the modified ONERA dynamic stall model in which a second-order differential equation is used for calculating the unstalled lift circulation shown in Eq. (2). Retaining the other equations from Petot [7], the equations of the modified ONERA model are noted in Eqs. (1–7).

$$c_l = \frac{1}{V^2}\left[sb\dot{W}_0 + \tilde{k}b\dot{W}_1 + V\Gamma_1 + V\Gamma_2\right] \tag{1}$$

$$\ddot{\Gamma}_2 + B_2\left(\frac{V}{b}\right)\dot{\Gamma}_1 + B_2\left(\frac{V}{b}\right)^2\Gamma_1 = A_3\left(\frac{V}{b}\right)^2\left[\left(\frac{\partial C_{zl}}{\partial\theta}\right)W_0 + \sigma W_1\right] + A_2\left(\frac{V}{b}\right)\left[\left(\frac{\partial C_{ZL}}{\partial\theta}\right)\dot{W}_0 + \sigma\dot{W}_1\right] + A_1\left[\left(\frac{\partial C_{ZL}}{\partial\theta}\right)\ddot{W}_0 + \sigma\ddot{W}_1\right] \quad (2)$$

$$\ddot{\Gamma}_2 + a_l\left(\frac{V}{b}\right)\dot{\Gamma}_2 + r_l\left(\frac{V}{B}\right)^2\Gamma_2 = -\left[r_l\left(\frac{V}{b}\right)^2 V\Delta C_Z + E_l\left(\frac{V}{b}\right)\dot{W}_0\right] \quad (3)$$

$$c_m = \frac{1}{V^2}[V^2 C_{m_L} + (\overline{\sigma}_m + d_m)b\dot{W}_0 + \sigma_m V W_1 + s_m b\dot{W}_1 + V\Gamma_{m_2} \quad (4)$$

$$\ddot{\Gamma}_{m_2} + a_m\left(\frac{V}{b}\right)\dot{\Gamma}_{m_2} + r_m\left(\frac{V}{b}\right)^2\Gamma_{m_2} = -\left[r_m\left(\frac{V}{b}\right)^2 V\Delta C_m + E_m\left(\frac{V}{b}\right)\dot{W}_0\right] * \boldsymbol{I}^*_{\boldsymbol{m}} \quad (5)$$

$$c_d = \frac{1}{V^2}\left[V^2 C_{d_L} + \sigma_d b\dot{W}_0 + V\Gamma_{d_2}\right] \quad (6)$$

$$\ddot{\Gamma}_{d_2} + a_d\left(\frac{V}{b}\right)\dot{\Gamma}_{d_2} + r_d\left(\frac{V}{b}\right)^2\Gamma_{d_2} = -\left[r_d\left(\frac{V}{b}\right)^2 V\Delta C_d + E_d\left(\frac{V}{b}\right)\dot{W}_0\right] * \boldsymbol{I}^*_{\boldsymbol{d}} \quad (7)$$

As the model is semi-empirical in nature, inherent uncertainties in quantification introduce complexities in predicting the accurate values for the terms. Therefore, correction factors ($\boldsymbol{I}^*_{\boldsymbol{m}}$, $\boldsymbol{I}^*_{\boldsymbol{d}}$ in Eqs. (5) and (7)) are introduced in the present study for generalization which needs to be manually tuned to reproduce experimental trends ($\boldsymbol{I}^*_{\boldsymbol{m}} = 1.87$ and $\boldsymbol{I}^*_{\boldsymbol{d}} = 1.45$ used for the cases presented). Other parameters are adopted from Laxman et al. [1]. The terms ΔC_z, ΔC_d, and ΔC_m are the difference between the linearly extrapolated static aerodynamic coefficients and the actual static coefficients during the stall, which can be influenced by chord-based Reynolds number. Therefore, the XFLR5 tool has been used to get the slopes and calculate the values of ΔC_z, ΔC_d, and ΔC_m for any particular Reynolds number.

3 Simulations of Dynamic Stall: Geometry and Computational Setup

The CFD simulations of NACA0012 are carried out with the RANS model in OpenFOAM. The turbulence model k-ω SST was chosen for the simulations as it provides good results for wall-bounded flows, and has produced computationally efficient

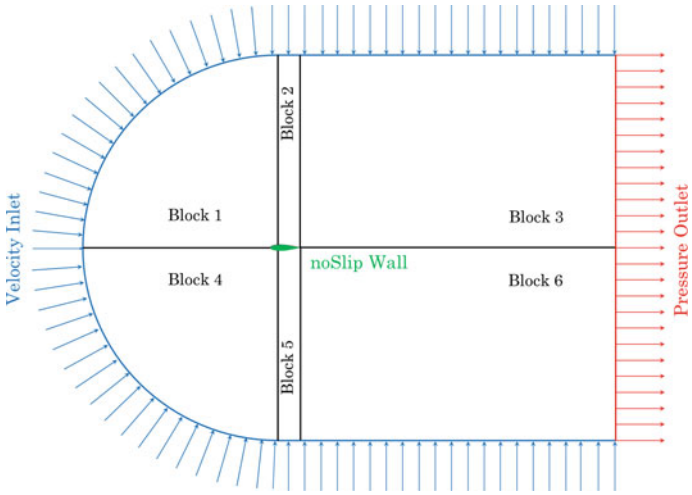


Fig. 1 Computational domain for dynamic stall simulations

results for dynamic stall with a good correlation with experimental data [4]. The dynamic mesh motion is used to represent the oscillatory motions of the airfoil similar to [8], where the mesh motion has been solved using *'interpolatingSolidBody'* method available in OpenFOAM v10. The geometry of the domain for the dynamic simulations is shown in Fig. 1. The whole domain has five patches and consists of six blocks, and a wall y^+ is equal to 5. The orientation of the airfoil is based on the mean angle of the case simulated. The airfoil's chord is 0.4 m, and the axis of the pitching motion has been fixed with the quarter-chord of the airfoil to simulate the cases in reference [1].

A grid convergence study using static simulations has been carried out, and the results are shown in Fig. 2. It is observed that the convergence in c_l and c_d is obtained at a total of 120,000 cells. This has been used for the cases of dynamic stall simulations, listed in Table 1. A parametric study on the time step, time scheme, revealed adaptive *maximum Courant number 0.9* and *Crank-Nicolson 0.5* optimal for the study. The *rhoPimpleFoam* solver is used to study the influence of reduced frequency to account for the compressibility effects, and the *pimpleFoam* solver is used for Cases-4 and 5 in Table 1.

4 Results and Discussion

The CFD simulations capture the dynamic stall events in accordance with [3], and the features of the dynamic stall observed in Figs. 3, 4, 5, 6, 7, 8, and 9 are marked in Fig. 10. After exceeding the stall angle, an increase in suction pressure causing unsteady flow in the wake is observed as revealed in Fig. 3. Figure 4 denotes the

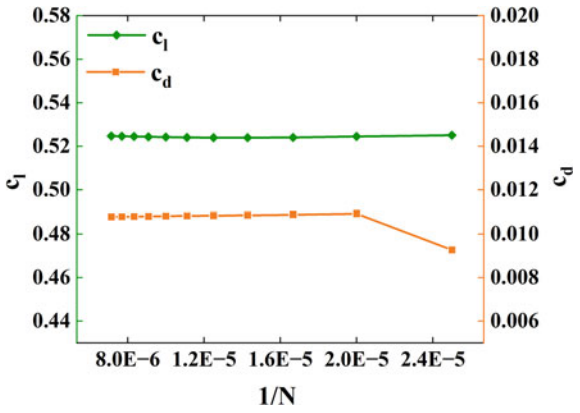


Fig. 2 Grid convergence of NACA0012 with k-ω SST model for c_l and c_d

Table 1 List of cases for dynamic simulation of pitching airfoil

Case	Mean angle θ_0 [deg]	Amplitude $\tilde{\theta}$ [deg]	Reynolds number Re [-]	Flow velocity $U\infty$ [m/s]	Reduced frequency κ [-]	Angular frequency Ω [rad/s]
1	15	10	3.0×10^6	99	0.03	14.85
2					0.05	24.75
3					0.10	49.50
4			3.0×10^5	11	0.10	5.5
5			3.0×10^4	1.09	0.10	0.545

strengthening of leading-edge vortex (LEV) causing lift slope increase shown in Fig. 10. As the flow progresses, a flow reversal is observed as shown in Fig. 5 due to which, vortices are induced inside the boundary layer causing LEV separation and the onset of dynamic stall. Then, the LEV rolls up with the shear layer forming the primary dynamic stall vortex (PDSV) and moves downstream the chord as depicted in Fig. 6. Correspondingly, stall with the lift coefficient is observed in Fig. 10, and when the PDSV separates from the boundary layer, trailing-edge vortices form as shown in Fig. 7. The trailing-edge vortices separate with opposite rotation to the LEV and are shed behind the airfoil as revealed in Fig. 8. Within this quick span of time, the airfoil completely stalls as shown in Fig. 9 and continuous vortices generate until flow settles in the unstalled regime. During the downstroke of the airfoil, since the flow is still separated, the lift contributed is lower than the upstroke motion as observed in Fig. 10. The OpenFOAM results are compared with the modified ONERA model and the experimental data from Mcalister et al [9] in Fig. 10.

Influence of Reduced Frequency: The flow contours reveal a delay for the stall phenomenon with the increase in reduced frequency (κ), as shown in Fig. 10.

Rigorous vortices are generated in the case of $\kappa = 0.03$ as it stays in the stalled angle of attack longer than the cases of $\kappa = 0.05$ and 0.1 depicted in Fig. 10.

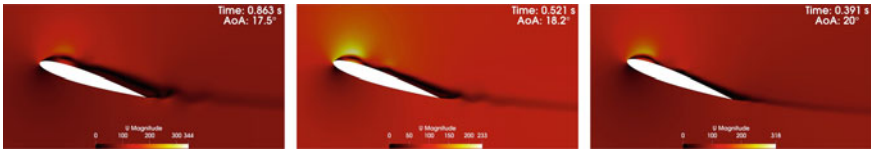


Fig. 3 Increase in suction pressure

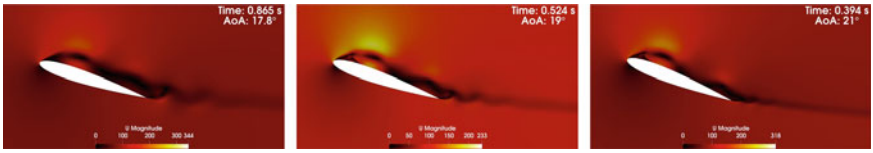


Fig. 4 Strengthening of LEV

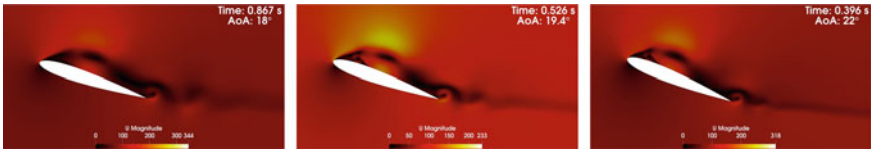


Fig. 5 Flow reversal spreads over the airfoil causing LEV separation

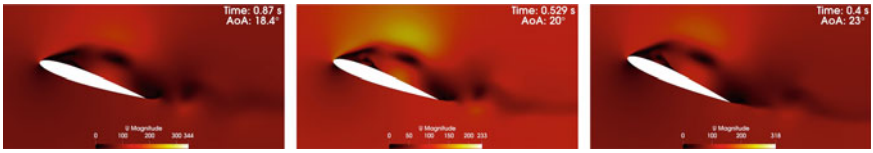


Fig. 6 Movement of PDSV downstream

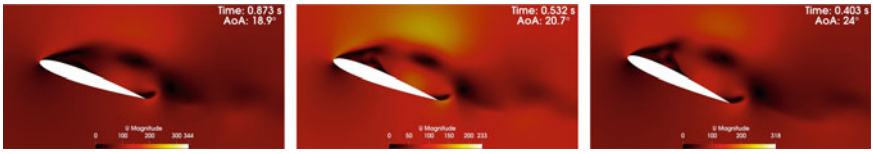


Fig. 7 Formation of trailing-edge vortices

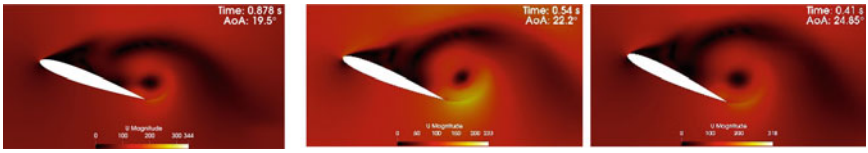


Fig. 8 Shedding of dynamic stall vortices

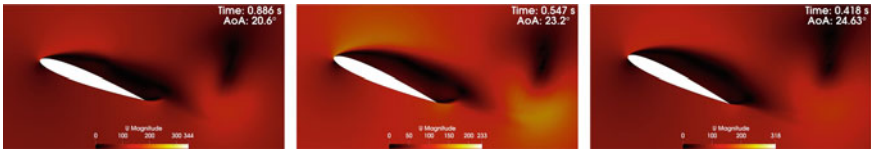


Fig. 9 Occurrence of full stall

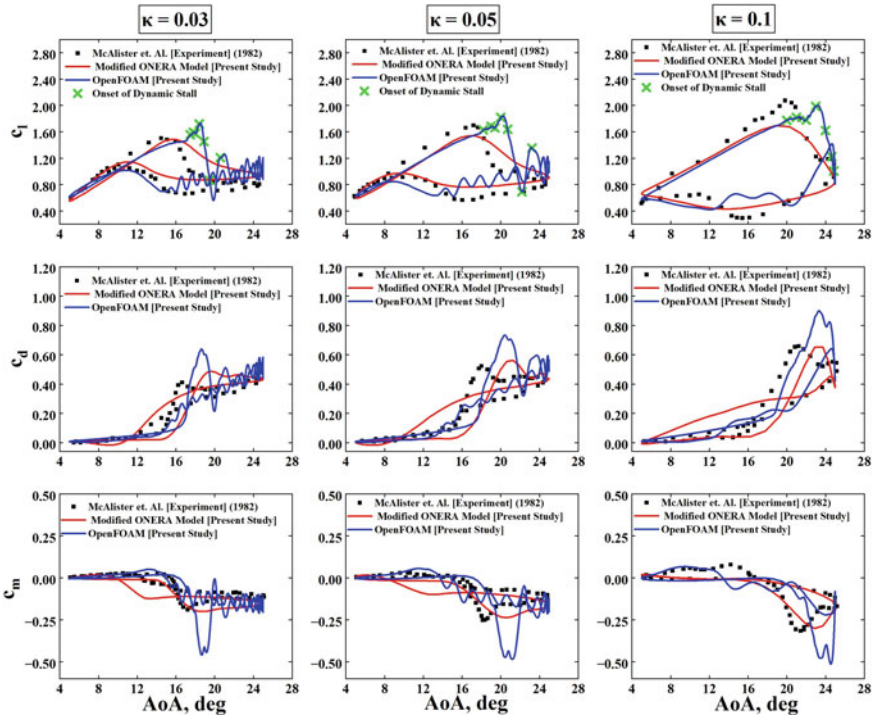


Fig. 10 Comparison of the aerodynamic hysteresis loops of pitching airfoil between modified ONERA model and OpenFOAM for Case-1, Case-2, and Case-3 (from left to right)

The OpenFOAM results for the aerodynamic coefficients show a good correlation with the experimental results except a slightly prolonged stall is seen. The results of the modified ONERA model show a similar correlation with the experimental results, but the vortex effects are not captured as the model relies on the potential flow theory, and therefore, a mean variation is predicted.

Influence of Reynolds Number: Case-4 and Case-5 have been simulated to study dynamic stall with the effects of Reynolds number as unmanned mini/ micro rotor-crafts and fixed-wing UAVs undergo various flow conditions for their specialized missions. The ONERA model is tested to analyze its predictive capabilities in these

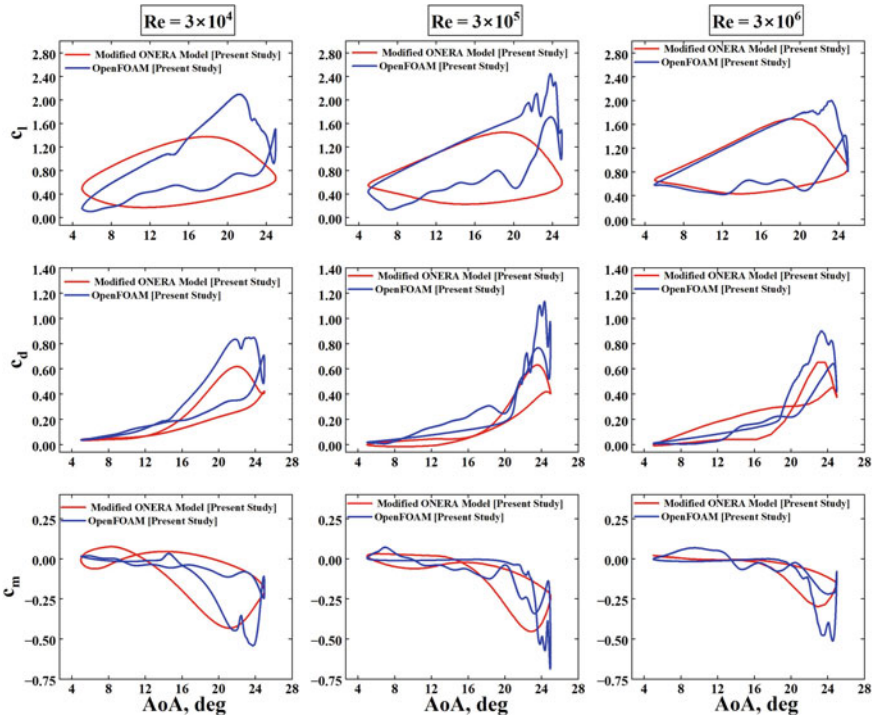


Fig. 11 Comparison of the aerodynamic hysteresis loops of a pitching airfoil between modified ONERA model and OpenFOAM for Case-5, Case-4, and Case-3 (from left to right)

Reynolds numbers, and the variations of the aerodynamic coefficients are shown in Fig. 11.

The OpenFOAM results for $\mathrm{Re} = 3 \times 10^6$ have already shown good correlation with experimental data in Fig. 10, and $\mathrm{Re} = 3 \times 10^5$ and $\mathrm{Re} = 3 \times 10^4$ show slight changes to it associated with the viscous effects. An interesting feature observed as the Reynolds number decreases, the lift-curve slope increases during the onset of the dynamic stall.

A good correlation is seen with the OpenFOAM and ONERA results in $\mathrm{Re} = 3 \times 10^6$, and the accuracy decreases with the decrease of *Re*. This is attributed to the static airfoil data, as it is not predicted the best with XFLR5 due to the increase in viscous effects. Therefore, the prediction of the modified ONERA method at lower Reynolds numbers has discrepancies. Meanwhile, CFD simulations predict the aerodynamic performance well since it relies on basic governing equations of fluid dynamics.

5 Conclusion

The events of dynamic stall captured with the OpenFOAM simulations are in accordance with the literature, and the flow features describing the aero dynamic hysteresis loops during dynamic stall have been studied. The dynamic stall phenomenon for pitching NACA0012 airfoil in successful κ shows a good correlation between the OpenFOAM CFD results, experimental data, and the modified ONERA model. Delayed stalling was observed with the increase of κ, accounted by both computational and semi-empirical results in the study. The OpenFOAM simulations for Reynolds numbers in the low range show slight changes associated with the viscous effects of the flow and an increase in the lift-curve slope with the decrease of *Re* during the onset of dynamic stall is observed. The accuracy of the modified ONERA model decreases with *Re* as the viscous effects are not properly modeled with the static data. Further studies in the static data are needed to enrich the prediction capability of the modified ONERA model in the low Reynolds number regime.

Funding Not applicable.

References

1. Laxman V, Venkatesan C (2007) Chaotic response of an airfoil due to aeroelastic coupling and dynamic stall. AIAA J
2. Valappil DK et al (2017) Influence of solidity and wind shear on the performance of VAWT using a free vortex model. Int J Renew Energy Research (IJRER) 7(2):787–796
3. Carr LW (1988) Progress in analysis and prediction of dynamic stall. J Aircr 25(1):6–17
4. Fernández F, Javier F (2022) CFD simulations of a pitching aerofoil for the study of dynamic stall
5. Boersma P (2018) A numerical flutter predictor for 3D airfoils using the ONERA dynamic stall model
6. Tang D, Dowell E (1996) Comments on the ONERA stall aerodynamic model and its impact on aeroelastic stability. J Fluids Struct 10(4):353–366
7. Petot D (1989) Differential equation modelling of dynamic stall. La Reserche Aérospatiale, 1989-5
8. https://wiki.openfoam.com/NACA0012_by_Michael_Alletto
9. McCroskey WJ, McAlister KW, Carr LW, Pucci SL (1982) An experimental study of dynamic stall on advanced airfoil sections: Volume 1—summary of the experiment; Volume 2—pressure and force data; Volume 3—hot-wire and hot-film Measurements. NASA TM-84245

Conjugate Heat Transfer for a 2D Square Cylinder Using Lattice Boltzmann Method



Aanif Hussain and Bayram Celik

Abstract In this study, we model an unsteady conjugate heat transfer problem of a solid square cylinder confined in a straight channel with adiabatic walls. In modeling of the problem, we use an in-house developed Lattice Boltzmann solver that can run on GPU. To validate the solver, we compare the obtained results with the data from two previous studies that are available in the literature by considering pressure distribution on the cylinder and spatially averaged Nusselt number along the cylinder edges. The results are in good agreement in general and promising for future studies to reveal unsteady and complex nature of the problem.

Keywords Conjugate heat transfer · Square cylinder · Lattice Boltzmann method · Unsteady flow · Corner treatment

1 Introduction

Lattice Boltzmann method, LBM has become an increasingly popular numerical method for solving complex fluid dynamics and heat transfer problems. This method was developed in late 1980s and is still progressing. LBM uses the kinetic gas model based on novel lattice gas cellular automata to simulate fluid flow. It works at mesoscopic scale to evaluate the macroscopic state variables. Values of discrete distribution functions are computed on lattice sites (nodes) that form a uniform mesh. The structure of LBM is inherently adaptable for parallel computations due to the nature of collision and streaming steps [1] which govern the core of LBM.

In single-relaxation time, SRT model, the collision operator is approximated by Bhatnagar–Gross–Krook, BGK scheme [2]. Complex problems such as conjugate

A. Hussain (✉)
Aeronautical and Astronautical Engineering Program, Istanbul Technical University, Istanbul 34469, Turkey
e-mail: hussain22@itu.edu.tr

B. Celik
Astronautical Engineering Department, Istanbul Technical University, Istanbul 34469, Turkey
e-mail: celikbay@itu.edu.tr

© The Author(s), under exclusive license to Springer Nature Singapore Pte Ltd. 2024

S. Singh et al. (eds.), *Recent Advances in Aerospace Engineering*, Lecture Notes in Mechanical Engineering, https://doi.org/10.1007/978-981-97-1306-6_30

heat transfer (CHT) and multiphase flows are convenient to solve using LBM as no additional boundary condition is required at the complex fluid-solid interfaces [3]. In LBM, heat flux, energy conservation and the local thermodynamics at such interfaces are naturally ensured [4].

In this study, the heat and fluid flow over a square cylinder that is initially at a lower temperature is confined in a straight channel with adiabatic walls. The fluid at a higher temperature enters the channel and flows over the thermally conductive square cylinder. Consideration of heat conduction besides temperature distribution makes this problem a CHT study. Depending on the Reynolds number as well as the fluid to solid conduction ratio, the considered heat and mass transfer yields steady or unsteady behavior. The conduction in the square cylinder as well as the temperature distribution are under the influence of the flow physics around the cylinder.

2 Lattice Boltzmann Method

LBM is based on the Boltzmann transport equation which uses statistical approach to represent behavior of fluid. A probability distribution function *f(r,c,t)* is used to define a collection of particles moving in space and time. Under an external force **F**, differential change in *f(r,c,t)* was given by Boltzmann as a function of collision operator Ω which is a complex function of f itself [1]. Mathematically, it is represented as:

$$f\left(\vec{r}+\vec{c}\mathrm{d}t, \vec{c}+\vec{F}\mathrm{d}t, t+\mathrm{d}t\right)\mathrm{d}r\mathrm{d}c - f(\vec{r},\vec{c},t)\mathrm{d}r\mathrm{d}c = \Omega(f)\mathrm{d}r\mathrm{d}c\mathrm{d}t \tag{1}$$

If the net external force is zero, the partial differential form reduces to:

$$\frac{\partial f}{\partial t} + c\frac{\partial f}{\partial r} = \Omega \tag{2}$$

Bhatnagar, Gross, and Krook (BGK) simplified the collision operator as a linear function [2]. This scheme is extremely fast with good accuracy. The BGK approximation is given by:

$$\Omega = \omega(f^{\mathrm{eq}} - f) \tag{3}$$

where ω is the collision frequency and f^{eq} is the local equilibrium distribution function. Using Eq. (3) in Eq. (2), the SRT-based Lattice Boltzmann equation becomes:

$$\frac{\partial f}{\partial t} + c.\nabla f = \omega(f^{\mathrm{eq}} - f) \tag{4}$$

Discretized form of Eq. (4) along specific directions (i) is used for solving fluid and heat transfer problems. Discretized Lattice Boltzmann equation is shown as:

$$f_i(\vec{r} + \vec{c}_i \Delta t, t + \Delta t) = (1 - \omega) f_i(\vec{r}, t) + \omega f_i^{\text{eq}}(\vec{r}, t) \tag{5}$$

Each time step Δt is governed by collision and streaming processes taking place at all lattice sites. During collision, the probability distributions are updated using BGK approximation as given in Eq. (6). The updated distribution functions are then streamed to adjacent lattice sites based on their lattice velocity c_i as given in Eq. (7).

$$f_i^*(\vec{r}, t) = (1 - \omega) f_i(\vec{r}, t) + \omega f_i^{\text{eq}}(\vec{r}, t) \tag{6}$$

$$f_i(\vec{r} + \vec{c}_i \Delta t, t + \Delta t) = f_i^*(\vec{r}, t) \tag{7}$$

Depending on the dimensionality of problems, different lattice models are used for modeling problems. They are identified in form *DnQm* where n is the dimension of problem and m is the number of lattice link velocities. For two-dimensional fluid flow problems, *D2Q9* is widely used as it conserves the isotropy in all directions [1]. The model is shown in Fig. 1.

Each streaming direction of f_i has a corresponding lattice speed c_i and weighting factor w_i. The values are given in Table 1.

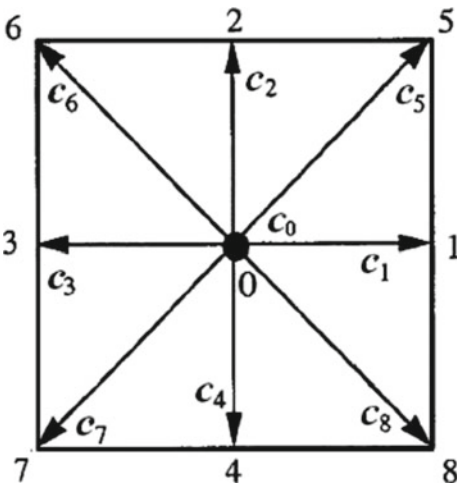


Fig. 1 *D2Q9* lattice model for 2D problems

Table 1 Weighting factors and lattice velocities for *D2Q9* lattice model [2]

Direction, i	0	1	2	3	4	5	6	7	8
w_i	4/9	1/9	1/9	1/9	1/9	1/36	1/36	1/36	1/36
c_i	(0, 0)	(1, 0)	(0, 1)	(−1, 0)	(0, −1)	(1, 1)	(−1, 1)	(−1, −1)	(1, −1)

3 Modeling Fluid Flow and Heat Transfer Equations with LBM

Equation (5) can be modeled to solve incompressible viscous flow equation and advection-diffusion equation by using two independent distribution functions f_i and g_i respectively, [3] which are given in Eqs. (8) and (9). The two Lattice Boltzmann equations are solved simultaneously for conjugate heat transfer problems.

$$f_i(\vec{r} + \vec{c}_i \Delta t, t + \Delta t) = \left(1 - \omega_f\right) f_i(\vec{r}, t) + \omega_f f_i^{\mathrm{eq}}(\vec{r}, t) \tag{8}$$

$$g_i(\vec{r} + \vec{c}_i \Delta t, t + \Delta t) = \left(1 - \omega_g\right) g_i(\vec{r}, t) + \omega_g g_i^{\mathrm{eq}}(\vec{r}, t) \tag{9}$$

The equilibrium distribution functions ${f_i}^{\mathrm{eq}}$ and ${g_i}^{\mathrm{eq}}$ are computed as weighting factors of mesoscopic quantities and fundamental state variables such as density (ρ), velocity ($\vec{V}$), and temperature (T) [3]. Equations (10) and (11) calculates the two equilibrium distribution functions ${f_i}^{\mathrm{eq}}$ and ${g_i}^{\mathrm{eq}}$ respectively.

$$f_i^{\mathrm{eq}} = w_i \rho \left(1 + \frac{\vec{c}_i . \vec{V}}{c_s^2} + \frac{\left(\vec{c}_i . \vec{V}\right)^2}{2c_s^4} - \frac{\vec{V} . \vec{V}}{2c_s^2} \right) \tag{10}$$

$$g_i^{\mathrm{eq}} = w_i T \left(1 + \frac{\vec{c}_i . \vec{V}}{c_s^2} + \frac{\left(\vec{c}_i . \vec{V}\right)^2}{2c_s^4} - \frac{\vec{V} . \vec{V}}{2c_s^2} \right) \tag{11}$$

For D_2Q_9 lattice model, c_s is the lattice speed of sound and has a constant value.

$$c_s = \frac{1}{\sqrt{3}} \tag{12}$$

Collision frequency (ω) is a significant parameter which incorporates the macroscopic property into the governing Eqs. (8) and (9). For incompressible viscous flow, collision frequency (ω_f) is related with the fluid viscosity [4] as given in Eq. (13). Similarly, for advection–diffusion problems, the collision frequency (ω_g) is related to the thermal diffusivity [4] of medium as given in Eq. (14).

$$\upsilon = \frac{\Delta x^2 c_s^2}{\Delta t} \left(\omega_f - \frac{1}{2} \right) \tag{13}$$

$$\alpha = \frac{\Delta x^2 c_s^2}{\Delta t} \left(\omega_g - \frac{1}{2} \right) \tag{14}$$

For BGK collision operator, relaxation time ($\tau = \frac{1}{\omega}$) and maximum speed $u_{\max}$ should satisfy the necessary conditions for a stable numerical solution. Based on Chapman–Enskog expansion [4], the stability conditions are given in Eqs. (15) and (16).

$$\frac{\tau}{\Delta t} \geq \frac{1}{2} \tag{15}$$

Kruger et al. [4] has shown for D_2Q_9, D_3Q_{15}, D_3Q_{19}, and D_3Q_{27} lattice models, the maximum speed should satisfy:

$$|u_{\max}| \leq \sqrt{\frac{1}{3}} \frac{\Delta x}{\Delta t} \tag{16}$$

4 Problem Definition

For this study, the dimensions of the channel and the square cylinder are shown in Fig. 2. The sizing of the domain is chosen such that the ratios of height and length of the channel to the characteristic length D are constant. Blockage ratio is taken equal to *1/4*. Length of the channel is taken as $20D$. The cylinder is placed in the channel such that the coordinates of its center from the origin (bottom left corner of channel) are ($x_c = 4D$, $y_c = 2D$). For our LBM-CHT simulations, we set the characteristic length as $D = 40$ lattice units.

The dimensionless parameters for simulating the conjugate heat transfer are taken as:

1. Reynolds number is varied in the range 10–100
2. Prandtl number = 0.71
3. Solid to fluid thermal conductivity ratio = 1.0

The initial conditions (at $t = 0$) for CHT are:

1. Inlet velocity, $u = 0.1$ and $v = 0$
2. Fluid temperature = 1.0

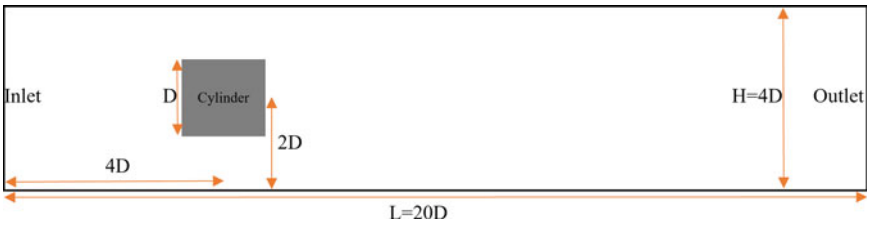


Fig. 2 Geometric details of problem

3. Cylinder temperature = 0

The boundary conditions used for flow solver are:

1. Top and bottom wall of channel have no-slip condition ($u = v = 0$)
2. Dirichlet boundary condition ($u = 0.1$, $v = 0$) at the channel inlet
3. Open boundary condition at the channel outlet
4. No-slip condition on the square cylinder faces

The boundary conditions for heat solver are:

1. Top and bottom wall of channel are adiabatic in Y-direction ($dT/dy = 0$)
2. Dirichlet boundary condition ($T = 1.0$) at the channel inlet
3. Adiabatic condition at the channel outlet ($dT/dx = 0$)

No other boundary condition for heat transfer is required at the fluid-solid interfaces. Additionally, as the cylinder is confined, the heat solver inside the cylinder naturally becomes conduction [4].

5 Boundary Conditions Implementation

In LBM, boundary conditions are applied on the unknown (incoming) distribution functions making the process non-trivial. Proper application of boundary conditions in LBM is an active research topic.

5.1 Boundary Treatment for Fluid Flow

At the no-slip wall, bounce back scheme is used. The unstreamed distributions at the boundaries are equated to the outgoing distributions which are reflected back into the fluid [4]. For Dirichlet boundary condition, a constant velocity (u_w, v_w) is enforced. At the inlet [4], for instance, the density and unknown distributions are calculated as:

$$\rho_w = \frac{f_0 + f_2 + f_4 + 2(f_3 + f_6 + f_7)}{1 - u_w} \tag{17}$$

$$f_1 = f_3 + \frac{2}{3}\rho_w u_w \tag{18}$$

$$f_5 = f_7 - \frac{1}{2}(f_2 - f_4) + \frac{1}{6}\rho_w u_w + \frac{1}{2}\rho_w v_w \tag{19}$$

$$f_8 = f_6 + \frac{1}{2}(f_2 - f_4) + \frac{1}{6}\rho_w u_w - \frac{1}{2}\rho_w v_w \tag{20}$$

For open boundaries, a zero gradient condition is employed at the outlet using a second order extrapolation scheme on the distribution functions [4] as given in Eq. (21)

$$f_i = 2f_{i-1} - f_{i-2} \tag{21}$$

5.2 Boundary Treatment for Heat Transfer

Adiabatic boundary condition is implemented using first-order extrapolation scheme. For instance on the top and bottom wall of the channel which are adiabatic in y-direction, the unknown distribution functions g_i are calculated using Eq. (22).

$$g_i((x, y), t) = g_i((x, y \pm \Delta y), t) \tag{22}$$

At the inlet, Dirichlet boundary condition for the temperature is enforced using flux conservation with T_w as the inlet temperature. The unknown distribution functions are computed [4] as shown:

$$g_1 = w_1 T_w + w_3 T_w - g_3 \tag{23}$$

$$g_5 = w_5 T_w + w_7 T_w - g_7 \tag{24}$$

$$g_8 = w_8 T_w + w_6 T_w - g_6 \tag{25}$$

5.3 Corner Treatment

At the corner lattice sites (for both channel and cylinder), it is important to ensure mass, momentum, and heat flux are properly conserved. Qisu et al. [5] has enforced a constant density ρ_{wall} to calculate the unknown distribution functions for fluid flow. For instance, at the bottom left corner, the unknown distributions are calculated as following:

$$f_1 = f_3 + \left(f_1^{\text{eq}} - f_3^{\text{eq}}\right) = f_3 \tag{26}$$

$$f_2 = f_4 + \left(f_2^{\text{eq}} - f_4^{\text{eq}}\right) = f_4 \tag{27}$$

$$f_5 = f_7 \tag{28}$$

$$f_6 = f_8 = \frac{1}{2}(\rho_{\text{wall}} - (f_0 + f_1 + f_2 + f_3 + f_4 + f_5 + f_7)) \tag{29}$$

For heat transfer case, say at the bottom left corner, simple bounce-back is used for unknown distributions g_1, g_2, and g_5. The unknown distributions g_6 and g_8 are averaged over previous time step as shown in Eq. (30). This ensures that corner nodes contribute no energy to the wall nodes after streaming [6].

$$g_6^t = g_8^t = \frac{1}{2}\left(g_6^{t-1} + g_8^{t-1}\right) \tag{30}$$

6 Results and Validation

6.1 Flow Field Results

For $10 < Re < 60$, the flow is steady and shear layers forming on the top and bottom of the cylinder yield a recirculation region behind the cylinder. As Re is increased, the recirculation region starts to extend, and finally, the balance between the two layers vanishes. Vortex shedding starts at $Re \geq 70$. For $Re = 100$, the vortex shedding becomes more pronounced with increase in shedding frequency as can be seen in the velocity contours (Figs. 3, 4, 5 and 6).

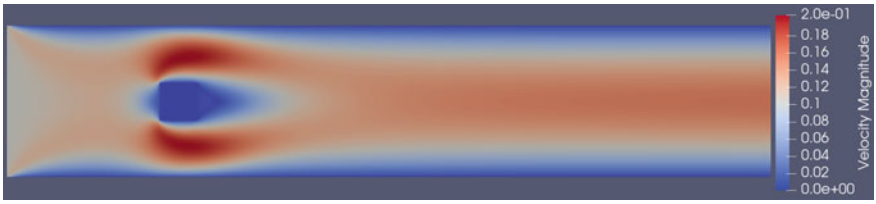


Fig. 3 Velocity contour at $Re = 10$

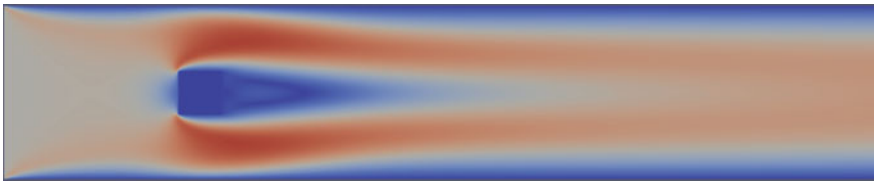


Fig. 4 Velocity contour at $Re = 60$

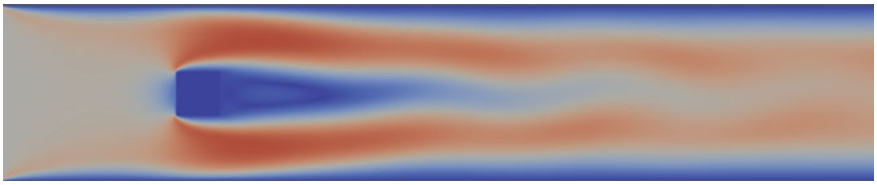


Fig. 5 Velocity contour at $Re = 70$

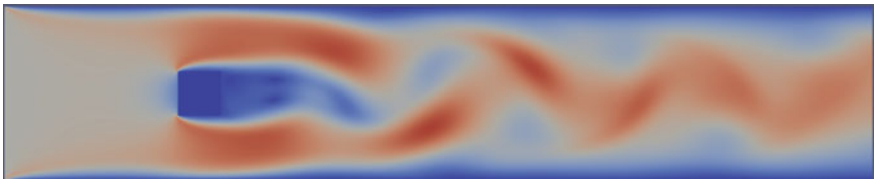


Fig. 6 Velocity contour at $Re = 100$

6.2 Thermal Field Results

As *Re* increases, the peak value of temperature rises at the leading edge (front face) of the cylinder. With the leading edge of cylinder at a higher temperature than the trailing edge, a temperature gradient develops inside the cylinder. For $Re \geq 70$, flow becomes unsteady and vortex shedding in the wake of cylinder impacts the trailing edge (rear face) which remains at a lower temperature. This implies a cooling mechanism persists at the rear face of cylinder driven by an alternating separation and reattachment of flow. The flow dynamics around the square cylinder seems to be dominant over the thermal conductivity of the cylinder at higher *Re* and therefore, affects the temperature distribution in the cylinder. Non-uniformity becomes prominent as the Reynolds number increases as can be seen in the temperature contours (Figs. 7, 8, 9 and 10).



Fig. 7 Temperature contour at $Re = 10$



Fig. 8 Temperature contour at $Re = 60$



Fig. 9 Temperature contour at $Re = 70$



Fig. 10 Temperature contour at $Re = 100$

6.3 Validation

The flow field and heat transfer results are validated by setting the blockage ratio to be *1/8* to make the geometric setting of our problem akin to previous data. Pressure distribution over square faces are compared with the experimental result from Zhou et al. [7] at $Re = 160$ and is shown in Fig. 11. As can be seen from the figure, there is a close agreement with the reference study with a mean error of 2.13%. Overall heat transfer at the fluid-solid interfaces is calculated using local Nusselt number, and the average Nusselt number for cylinder is determined by averaging the local values [8] and compared to the data by Eswaran et al. [8] as shown in Fig. 12. The averaged Nusselt number values are computed in the Reynolds number range 10–90. Again, there is a close consensus in results with a mean error of 1.21%.

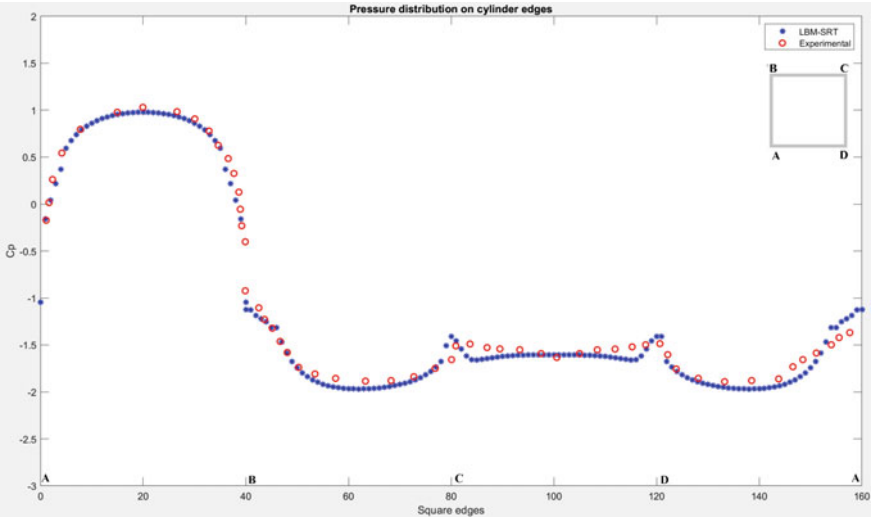


Fig. 11 Pressure distribution along the cylinder surfaces in clockwise direction

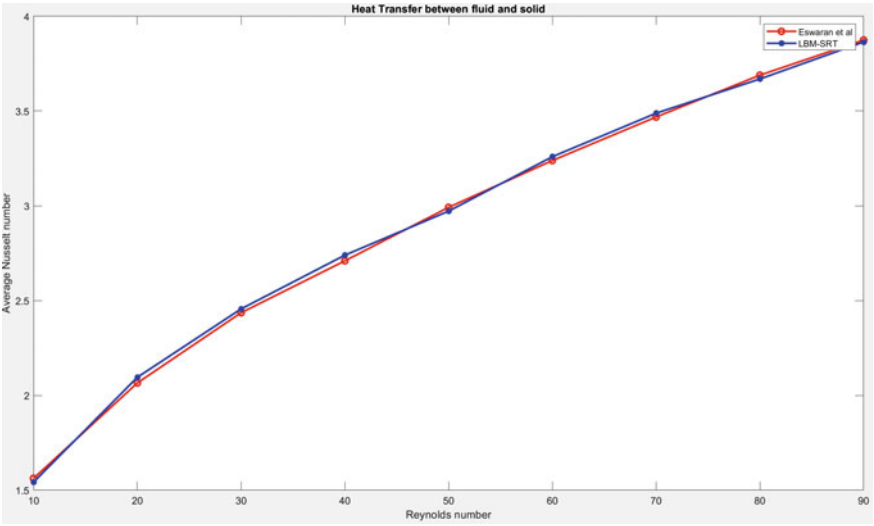


Fig. 12 Variation of average Nusselt number for cylinder with Reynolds number

7 Conclusion

This study reports the preliminary results and validation for unsteady conjugate heat transfer problem of square cylinder confined in a straight channel with adiabatic walls. These results highlight the intricate interplay between fluid flow and heat transfer in CHT scenarios, emphasizing the importance of Reynolds number in shaping the thermal behavior around solid objects. The obtained C_p distribution and the averaged Nusselt number of the solid square cylinder are in good agreement with the previously published studies available in the literature. For future studies, the problem will be discussed in detail considering various parameters that affect the flow and heat transfer physics.

Funding Not applicable.

References

1. Mohamad AA (2011) Lattice Boltzmann method: fundamentals and engineering applications with computer codes, 1st edn. Springer, London
2. Spinelli GG, and Celik B (2015) GPU accelerated multi-block Lattice Boltzmann solver for viscous flow problems. AIAC (2015), Ankara, Turkey
3. Spinelli GG, and Celik B (2017) Conjugate heat transfer computations via Lattice Boltzmann method. JAST 10(2):49–59
4. Krüger T, Kusumaatmaja H, Kuzmin A, Shardt O, Silva G, Viggen EM (2017) The Lattice Boltzmann method: principles and practice, 1st edn. Springer, Switzerland
5. Qisu Z, Xiaoyi H (1997) On pressure and velocity boundary conditions for the lattice Boltzmann BGK model. Phys Fluids 9(6):1591–1598
6. Robert SM, Robert SB, Daryl WG (1996) Boundary conditions for the lattice Boltzmann method. Phys Fluids 8(7):1788–1801
7. Zhou L, Cheng M, and Hung KC (2005) Suppression of fluid force on a square cylinder by flow control. J Fluids Struct 21(2):151–167
8. Atul S, Eswaran V (2004) Heat and fluid flow across a square cylinder in the two-dimensional laminar flow regime. Numerical Heat Transfer Part A: Applications 45(3):247–269

Prediction and Experimental Validation of Burst Pressure of a Gimbal Bellow Used in a Cryogenic Stage of a Launch Vehicle



Unnikrishnan K. R., Kodati Srinivas, Vasudevan R., and Asraff A. K.

Abstract Gimbal bellows are used in the feed systems of the cryogenic stage of an indigenously developed launch vehicle for minimizing the actuator loads as well as convey the propellants to the cryogenic engine, whilst it is gimballed. Gimbal bellow is a universal joint in which two rotational degrees of freedom with specified stiffness are provided. As a part of design qualification of the bellow duct, structural capability of gimbal bellow with respect to pressure is required to be demonstrated through a burst test. Non-linear elastoplastic stress analysis is carried out for the estimation of burst pressure of the gimbal bellow. Burst pressure is estimated based on the pressure at which deformation shows an asymptotically increasing behaviour and the analysis un-converges. The instrumentation is designed for the measurement of displacements and strains at critical locations, and burst pressure test is conducted. The predicted burst pressure of gimbal bellow through simulation is 7.46 MPa compared to the tested burst pressure of 7.89 MPa. The burst pressure and the strain/displacement values matched very well with analysis predictions. The location of failure also matched favourably.

Keywords Gimbal bellow · Finite element analysis · Burst test · Burst pressure · Strains · Stresses

K. R. Unnikrishnan (✉) · K. Srinivas · R. Vasudevan · A. K. Asraff
Liquid Propulsion Systems Centre, ISRO, Valamala, Thiruvananthapuram, India
e-mail: unnikrishnan_kr@lpsc.gov.in

K. Srinivas
e-mail: kodatisrinivas@lpsc.gov.in

R. Vasudevan
e-mail: r_vasudevan@lpsc.gov.in

A. K. Asraff
e-mail: ak_asraff@lpsc.gov.in

© The Author(s), under exclusive license to Springer Nature Singapore Pte Ltd. 2024

S. Singh et al. (eds.), *Recent Advances in Aerospace Engineering*, Lecture Notes in Mechanical Engineering, https://doi.org/10.1007/978-981-97-1306-6_31

1 Introduction

Gimbal bellows are used in the fuel and oxidizer feed systems of the cryogenic stage of a satellite launch vehicle designed by ISRO to minimize the actuator loads while gimbaling the engine. The propellant feed lines interfacing with the engine must be flexible to permit a specified angle of gimballing of the engine whilst conveying propellants to the engine [1]. To meet this requirement, three gimbal bellows are provided in each feed system near the engine interface. One of ISRO's heaviest launch vehicles highlighting its cryogenic stage is shown in Fig. 1. Figure 2 shows the gimbal bellows used in fuel and oxidizer feed systems of the cryogenic stage.

The photograph of a gimbal bellow is shown in Fig. 3. A gimbal bellow consists of bellow convolutions, two lugs welded to gimbal body, and a gimbal ring and two pairs of gimbal pins. These two gimbal bodies are connected each other through a gimbal ring using gimbal pins. The exploded view of the same with the nomenclature of the parts is shown in Fig. 4.

The burst pressure of any pressure vessel has to be evaluated to understand the maximum load it can carry before failure [2]. Finite element method is a powerful numerical method in the field of structural analysis, and the same can be used to evaluate the burst pressure of a pressure vessel [3]. In this paper, finite element



Fig. 1 Launch vehicle highlighting the cryogenic stage

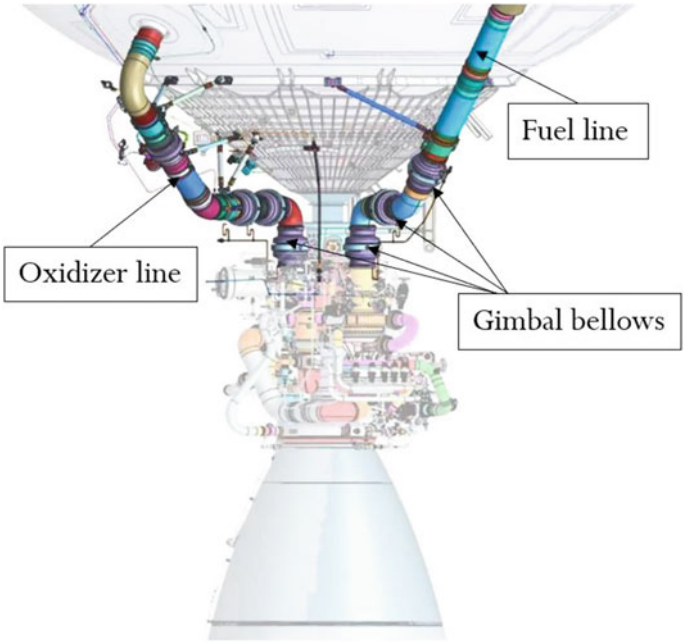


Fig. 2 Configuration of a typical propellant feed system with gimbal bellows

analysis is used to predict the burst pressure of the gimbal bellow. A pressure test is conducted to evaluate the actual burst pressure.

2 FE Model

Finite element model of the gimbal bellow is created, and elastoplastic stress analysis is carried out using commercial FE software—ANSYS/Mechanical Workbench [4]. Burst pressure, deformations and strain values are predicted. Linear 3D solid elements (SOLID185) are used to model the gimbal body, ring, closures, pin and washers. Bellow is modelled using linear shell elements (SHELL181). The total structure is modelled using 83,990 elements and 80,549 nodes. The FE model of gimbal bellow used for analysis is shown in Fig. 5. Displacements in all the three directions were arrested at the bottom of gimbal bellow, and pressure is applied inside. The loads and boundary conditions are given in Fig. 6.



Fig. 3 Photograph of the gimbal bellow

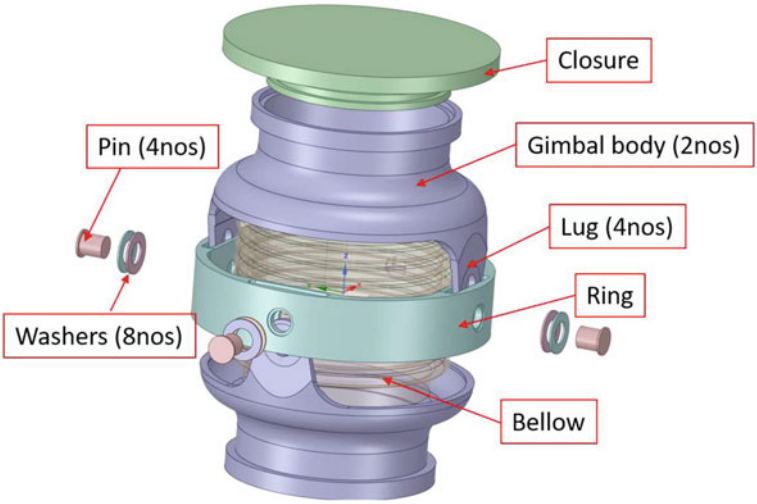


Fig. 4 Exploded view of gimbal bellow

Fig. 5 Finite element model



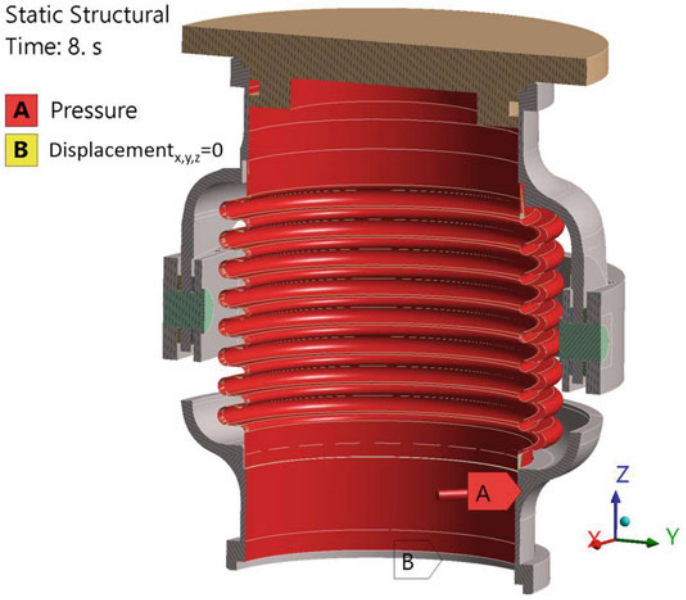


Fig. 6 Loads and boundary condition applied

Table 1 Mechanical properties of gimbal bellow materials at room temperature

Material	Young's modulus (N/mm^2)	Yield strength (N/mm^2)	Ultimate strength (N/mm^2)	Percentage elongation (%)
SS321	192,000	290	540	40
A286	192,000	660	960	15
Al–Ni Bronze	120,000	310	620	10

3 Mechanical Properties

Gimbal body, gimbal ring and bellow are made of SS321. In-house tested mechanical properties [5] of SS321 material are used for the analysis. Gimbal body and gimbal ring materials are idealized using multilinear kinematic hardening plasticity model properties, and bellow is given linear elastic properties. Pin is made of A286 stainless steel, and bilinear kinematic hardening plasticity model properties are applied. Washer is made of Al–Ni bronze, which is given only linear elastic properties [6, 7]. The mechanical properties of materials are given in Table 1.

4 Predictions from FE Simulation

The failure criterion considered whilst predicting the burst pressure from finite element analysis is "the pressure at which the deformation increases asymptotically as well as the problem execution fails to converge due to zero stiffness for the structure". Considering this, the burst pressure for gimbal bellow from the FE analysis is found to be 7.46 MPa. Region at which the gimbal bellow failed during the pressure test is at the 2 lugs. Figure 7 shows the equivalent plastic strain distribution at gimbal lug at predicted burst pressure.

From Fig. 7, it can be seen that the hole region in the lugs, where pin is engaged, has plastically deformed and failed. The peak plastic strain in the region reached 60%. Table 2 shows the maximum axial and radial deformations at gauge locations at burst pressure. Axial deformations (D1A, D2A, D3A, D4A) are measured at the top of the ring near pins. Radial deformations (D1R, D2R, D3R, D4R) are measured at the bottom side of the ring in radial direction (refer Fig. 11). Maximum axial and three-directional strains at gauge locations at burst pressure are given in Table 3. The three-directional strain gauges (three-element strain gauges) measure strain in three directions. These directions are in plane and named as X, Y, Z. The locations of these strain gauges are also shown in Fig. 11.

The axial and radial deformations of gimbal bellow at predicted burst pressure are shown in Figs. 8 and 9.

Maximum axial deformation is 60.7 mm at burst, and maximum radial deformation is 14 mm. From the figure, it can be seen that two of the lugs, which is a part of upper body, got lifted up more, whilst the lugs of bottom body are lifting very less.

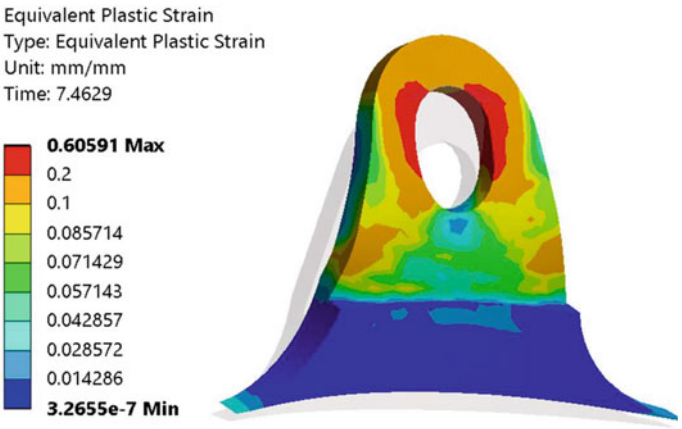


Fig. 7 Equivalent plastic strain distribution at gimbal lug at burst

Table 2 Deformation prediction at burst pressure

Sl No	LVDT location	Deformation (mm)
1	D1A, D3A (axial)	4.2
	D2A, D4A (axial)	50.3
2	D1R, D3R (radial)	− 9.7
	D2R, D4R (radial)	5.0

Table 3 Strain prediction at burst pressure

Sl No	Strain gauge location		Strain value ($\mu\varepsilon$)
1	A1, A2, A3, A4		− 18,000
2	SG1, SG2, SG3 andSG4	X	21,445
		Y	− 28,535
		Z (axial)	39,236

Similarly, from Fig. 9, it can be seen that out of the four radial locations at top of the ring near lug, two of the locations deformed radially outside (positive), whilst the other two locations deformed radially inward (negative).

5 Instrumentation and Loading

Instrumentation and the test set-up are configured based on simulation results to capture the failure of the gimbal bellow. Both ends of gimbal bellow are closed using circular closure plates, and the base of the gimbal bellow is kept on the test bed. The

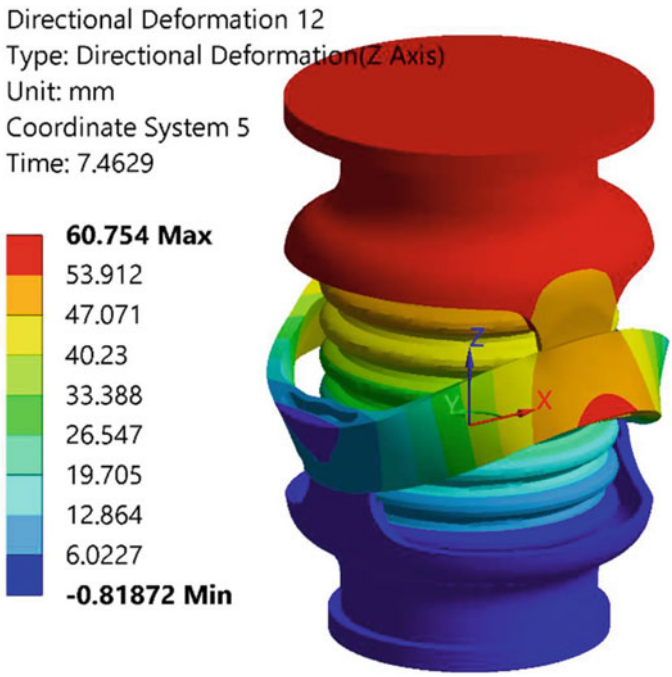


Fig. 8 Axial deformation distribution on gimbal bellow

pressure is applied inside the gimbal bellow through the tube connected from the top. The configuration of the test set-up is shown in Fig. 10.

Deformation measurements were made at eight locations. Four axial deformations were measured at the top of the ring near the lugs, and four radial deformations were measured at ring near the lugs. The rated ultimate pressure of gimbal bellow is 2.25 MPa. The LVDTs measuring deformations were removed after the ultimate pressure cycle, since it cannot be kept engaged whilst doing a burst test.

Strains were measured at eight locations. Axial strains were measured at the lugs, and three-element strain gauge rosettes were attached at the middle of the ring 45° away from pin locations. The details of displacement and strain gauge locations are shown in Fig. 11.

6 Test Results and Comparison

Burst pressure test is carried out using the pressure test fixture as shown in Fig. 10. The burst pressure of gimbal bellow from the test is 7.89 MPa. This value closely matches with the predicted value of 7.46 MPa. It is also observed that the failure of

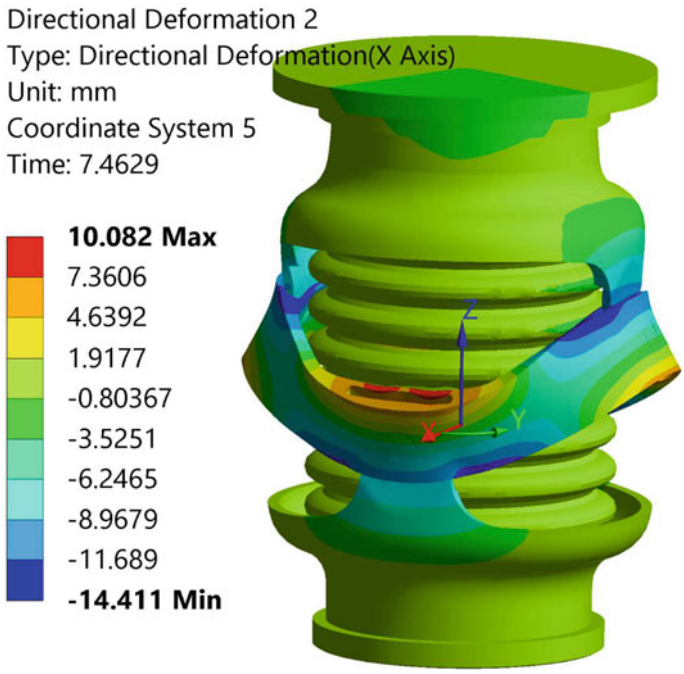


Fig. 9 Radial deformation distribution on gimbal bellow

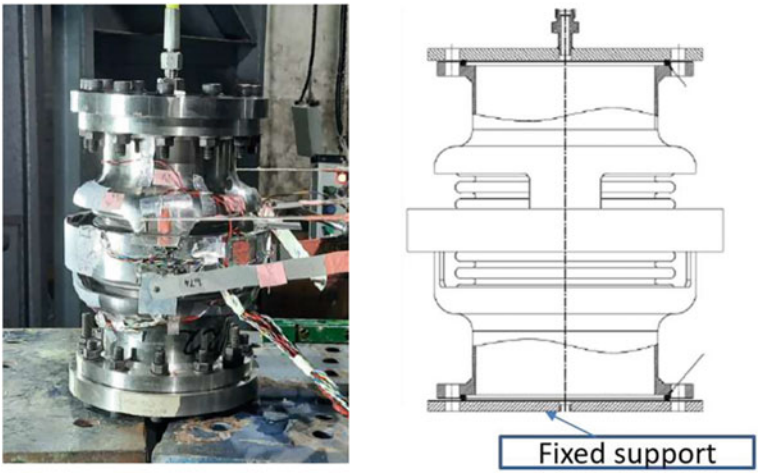


Fig. 10 Burst pressure test set-up of gimbal bellow

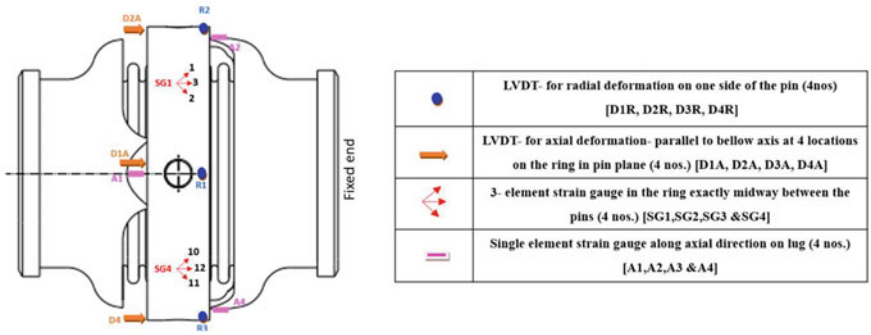


Fig. 11 Strain gauge/LVDT locations

the gimbal bellow occurs at the lugs as predicted. The failed hardware is shown in Fig. 12.

From Fig. 12, it can be observed that the deformation of gimbal bellow is similar to that in the Fig. 8 and deformation of lugs is similar to that of predicted deformed shape as shown in Fig. 7.



Fig. 12 Gimbal bellow after burst test

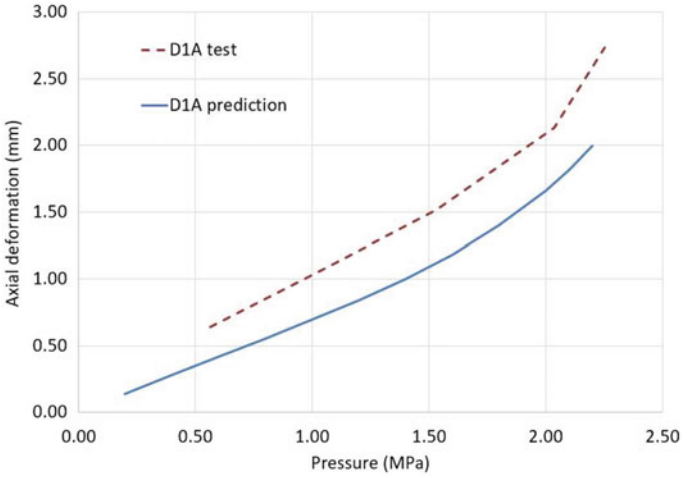


Fig. 13 Axial deformation (D1A) versus pressure comparison

6.1 Axial Deformation

During the pressure test, deformations were measured only up to the design ultimate pressure, i.e. 2.25 MPa, after which the LVDTs were removed. So, the results are compared with the corresponding values from analysis up to 2.25 MPa. From Figs. 11 and 8, it is evident that the lugs, which are at the fixed end (D2A, D4A), deflect less compared to the lugs attached to the free body of gimbal bellow (D1A, D3A). Also, variations of D1A and D3A are similar and D2A and D4A are similar. So, only D1A and D4A are considered for comparison. The variation of axial deformation with internal pressure for D1A location from test and analysis is compared in Fig. 13. The variation of D4A axial deformation with internal pressure is compared in Fig. 14.

From Figs. 13 and 14, it is observed that the test results match well with the analysis predictions for D1A location. But for D4A location (near fixed end), the test results are deviating from the prediction. This is because in this case, the deformations are very small (in the range of 140 μm).

6.2 Radial Deformation

A comparison of variation of radial deformation with internal pressure for test and analysis is shown in Figs. 15 and 16. From the deformation plot (Fig. 9) and actual deformed hardware (Fig. 12), it is seen that, out of all the radial deformation gauge locations (D1R, D2R, D3R, D4R), two of the locations (D1R and D3R) are deforming radially outwards (positive) and the other two (D2R and D4R) are deforming radially

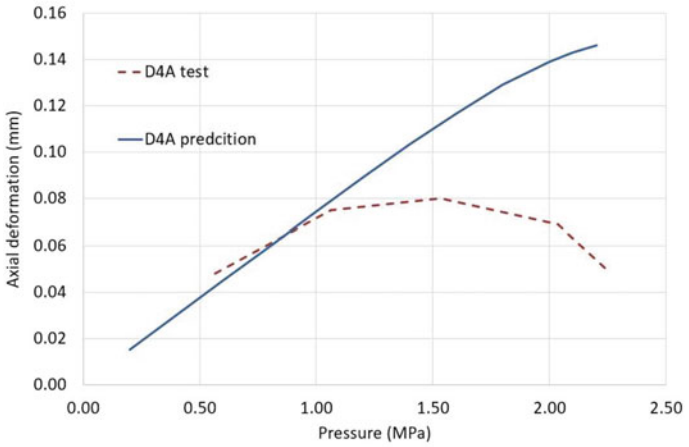


Fig. 14 Axial deformation (D4A) versus pressure comparison

inwards (negative). So, the D1R and D2R are compared with analysis results and shown in Figs. 15 and 16, respectively.

From Figs. 15 and 16, it is observed that the radial deformation from the test matches closely with the results from analysis.

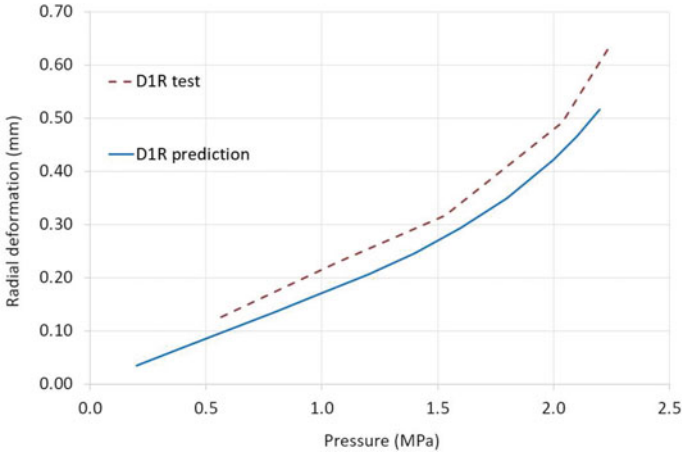


Fig. 15 Radial deformation (D1R) versus pressure comparison

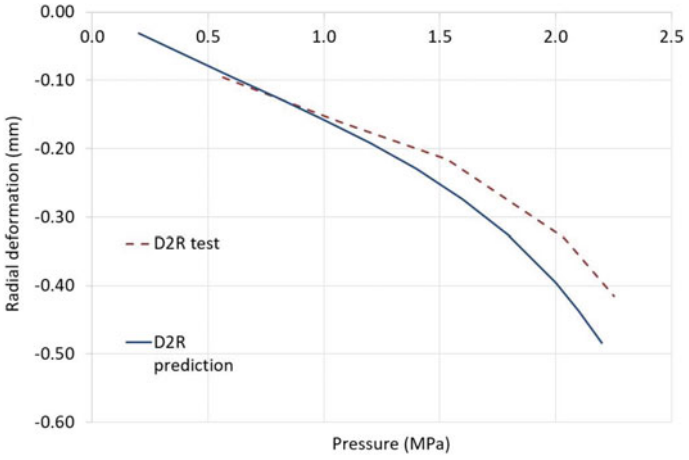


Fig. 16 Radial deformation (D2R) versus pressure comparison

6.3 Axial Strain on Lugs

Axial strain on lugs is also measured using the strain gauges, and the variation of the same with the internal pressure is compared with the prediction. The strain gauges got de-bonded after 4.5 MPa, so the test results up to 4.5 MPa is considered for the comparison with the analysis results. Also, all the four strain values are showing similar pattern. So, average value of the measurements is compared with that of prediction. The comparison of the axial strain at the lug from test and analysis is shown in Fig. 17.

From Fig. 17, it is observed that very close match between test and predicted axial strain variation up to the pressure at which the strain gauge got de-bonded.

6.4 Three-Element Strain Gauges at the Gimbal Ring

The variation of strains from three-element strain gauges with the applied internal pressure is studied and compared with the prediction. For easiness, the three strain values in the three-element strain gauges are named as follows:

1. SG1–S1, S2, S3: ($S_{1–2–3}$)
2. SG2–S4, S5, S6: ($S_{4–5–6}$)
3. SG3–S7, S8, S9: ($S_{7–8–9}$)
4. SG4–S10, S11, S12: ($S_{10–11–12}$)

Three-element strain gauges $S_{1–2–3}$, $S_{4–5–6}$ and $S_{10–11–12}$ got de-bonded at test pressure of 3 MPa and $S_{7–8–9}$ got de-bonded at 3.5 MPa. It is also observed that the strain values in same direction are following same path in all the four three-element

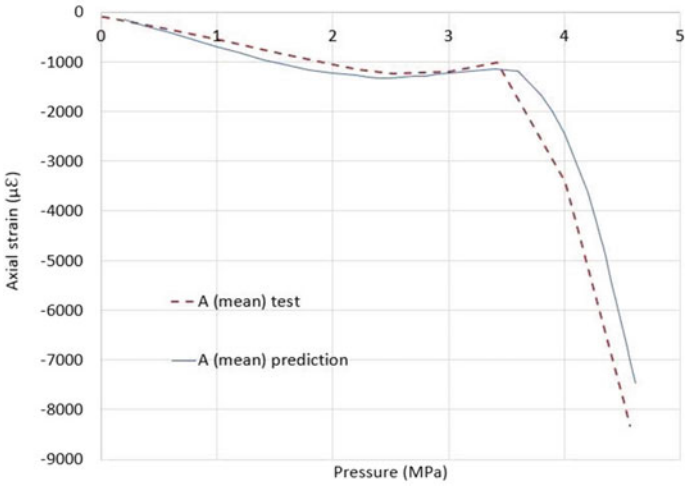


Fig. 17 Axial strain at lug versus pressure comparison

strain gauges. As the strain gauge set $S_{7–8–9}$ stayed bonded for higher pressure value, the same is considered for comparison. The variation of three-directional strain values with internal pressure till 3.5 MPa is compared in Fig. 18.

From Fig. 18, it is observed that the test results match well with the prediction.

From the comparison of the tested data with analysis results, it is observed that the deformation and strain evolution during test match well with the analysis prediction.

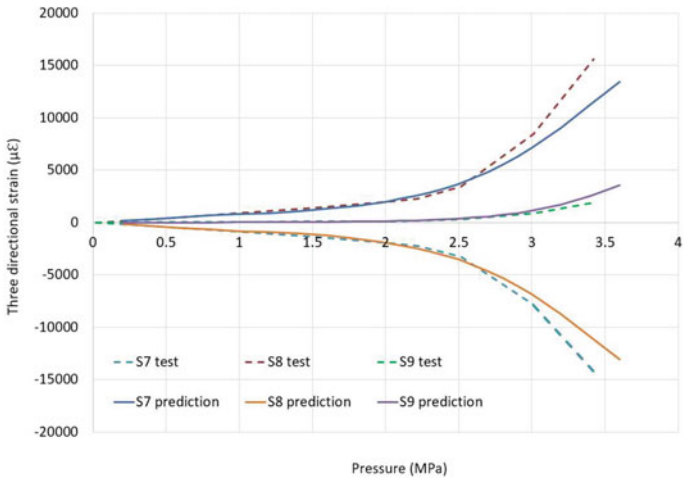


Fig. 18 Comparison of strains in gimbal ring at different pressures

7 Summary and Conclusion

Finite element analysis is performed to evaluate the burst pressure of a gimbal bellow. The variation of deformations and strains at different parts of the gimbal bellow with internal pressure is also evaluated. Burst pressure testing is carried out for validating the results from FE simulation, and the results from test and analysis are compared. From the study, the following observations are arrived at:

- The burst pressure for gimbal bellow as well as the location of failure from prediction closely matched with the actual burst pressure from test.
- Burst pressure predicted from simulation is 7.46 MPa compared to actual burst pressure 7.89 MPa.
- The variation of strains and deformations from the test also matched well with the analysis predictions.

It can thus be concluded that the FE modelling and analysis strategies adopted here are robust and accurate enough to capture the complex structural behaviour of the gimbal bellow under internal pressure undergoing very large deformations. The mechanical design of the gimbal bellow is also found to be adequate to bear the loads expected during flight of the launch vehicle.

Funding The reimbursement for attending symposia is received from my organization: Liquid propulsion system centre, ISRO.

References

1. Muller PL (1966) Propellant feed ducting and engine gimbal lines for the Saturn vehicle. No. NASA-TM-X-53532
2. Heckman D, Davis DA (1998) Finite element analysis of pressure vessels. Monterey Bay Aquarium Research Institute, Moss Landing
3. Dwivedi N, Kumar V, Shrivastava A, Nareliya R (2013) Burst pressure assessment of pressure vessel using finite element analysis: a review. J Pressure Vessel Technol 135(4):044502
4. Anonymous (2020) ANSYS theory reference. Release 2020 R2. ANSYS, Inc
5. Anonymous (2015) ASTM-E8/E8M-15a, standard test methods for tension testing of metallic materials. American Society for Testing and Materials, Philadelphia
6. FAA (2005) Metallic materials properties development and standardization: MMPDS-09. FAA, Battelle Memorial Institute, Atlantic City
7. Battelle Memorial Institute (2014) Metallic materials properties development and standardization: MMPDS-09. Battelle Memorial Institute, Atlantic City

Application of Artificial Neural Network in Impact and Crashworthiness: A Review



Dipjyoti Nath, Ankit, Debanga Raj Neog, and Sachin Singh Gautam

Abstract The paper presents an extensive review of the application of machine learning (ML) techniques, especially artificial neural networks (ANNs), in the realm of crashworthiness, hypervelocity impacts, and inverse analysis across various structural and aerospace domains. It delves into the prediction of stiffness matrices, contact stiffness, impact forces, and failure conditions, showcasing the potential of ML to streamline complex structural analysis processes. While the review highlights the predictive accuracies and computational efficiencies achieved by these methods, it also underscores the need for a more critical evaluation of model robustness, uncertainties, and real-world applicability. The review offers valuable insights into how ML can transform inverse analysis yet emphasizes the importance of addressing challenges and limitations to ensure the reliability and practicality of these innovative approaches.

Keywords Artificial neural networks · Crashworthiness · Hypervelocity impact · Inverse analysis

1 Introduction

Artificial neural networks (ANNs) are computational models inspired by the structure and functioning of biological neural networks, particularly the human brain [1, 2]. ANNs have become a powerful tool in the field of artificial intelligence, capable of learning complex patterns, making predictions, and solving a wide range of problems. ANN has revolutionized various domains, such as natural language processing,

D. Nath · Ankit · D. R. Neog · S. S. Gautam (✉)
Department of Mechanical Engineering, Indian Institute of Technology Guwahati, Guwahati 781039, India
e-mail: ssg@iitg.ac.in

D. R. Neog
Mehta Family School of Data Science and Artificial Intelligence, Indian Institute Technology Guwahati, Guwahati 781039, India

© The Author(s), under exclusive license to Springer Nature Singapore Pte Ltd. 2024

S. Singh et al. (eds.), *Recent Advances in Aerospace Engineering*, Lecture Notes in Mechanical Engineering, https://doi.org/10.1007/978-981-97-1306-6_32

computer vision, speech recognition, and data analysis [1]. Furthermore, the application of ANN can be seen in material modeling [3], damage detection [4], fatigue [5–7], stress analysis of structures [8, 9], numerical integration [10, 11], stiffness matrix computation [12–15], adhesive contact [16], etc. For more applications of ANN in computational mechanics, readers may refer to [17].

Contact mechanics overall is a broad spectrum. Areas like contact–impact, contact searching, collisions, and adhesion can be considered as various research fields inside it [18, 19]. Because of its tremendous applications and research potential in various engineering fields, research subfields like contact-impact can be further categorized based on the importance of the impactor or target body [20]. If the safety of the impactor is of prime concern, then this broad area can be termed as crashworthiness [21]. Places where the target body is important can be classified under the umbrella of ballistic impacts, for example the study of impact in bullet proof jacket design, armor designs, and in designing various protective shields [20].

In this work, we present a literature review on impact and crashworthiness analysis where ANN is used. The rest of the paper is structured as follows: Sect. 2 gives a brief introduction to ANN. Sections 3 and 4 cover the literature survey of the application of ANN in crashworthiness and hypervelocity impacts, respectively. Section 5 explores the application of ANN in addressing inverse analysis problems. Finally, Sect. 6 concludes the literature review.

2 Introduction to Artificial Neural Networks

Figure 1 shows a basic feedforward neural network with an input layer, three hidden layers, and an output layer. We consider the number of neurons in the input and the output layers as n and m, respectively. The input layer is fed with the input vector $\boldsymbol{x} = \{x_i\}(i = 1, 2, 3, ..., n)$ where x_i denotes the i th input feature. The hidden neurons in the hidden layer transform the input information through an activation function a. The activation of the hidden neurons of the l th hidden layer is given as follows:

$$\boldsymbol{h}^l = a\left(\boldsymbol{w}^{(l)}\boldsymbol{h}^{(l-1)} + \boldsymbol{b}^{(l)}\right) \tag{1}$$

Here, $\boldsymbol{w}^{(l)}$ is the weight matrix connecting the neurons in the previous $(l-1)$ th layer and the current l th layer, and $\boldsymbol{b}^{(l)}$ is the bias for the current layer. The activation of the output layer is given as follows:

$$\boldsymbol{y} = \left\{y_j\right\}_{j=1}^{m} = a\left(\boldsymbol{w}^{(L)}\boldsymbol{h}^{(L-1)} + \boldsymbol{b}\right) \tag{2}$$

Here, $\boldsymbol{w}^{(L)}$ is the weight matrix connecting the last hidden layer (L) and the output layer, and $\boldsymbol{b}$ is the bias at the output layer. To train the neural network, a loss function is defined to measure the difference between the predicted outputs $(\boldsymbol{y})$ and the true

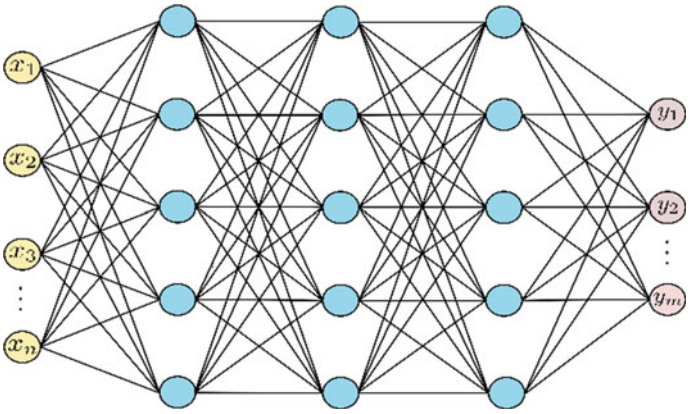


Fig. 1 ANN architecture with three hidden layers

values ($\boldsymbol{y}_{\text{true}}$). During training, the connection weights of the network get updated by minimizing the loss function.

3 Application of ANN in Crashworthiness

Crashworthiness refers to the aptitude of a structure or system in shielding occupants or payloads during a collision by adeptly absorbing and distributing impact energy. The process entails the utilization of innovative design and engineering techniques to mitigate injury and damage, thereby significantly enhancing the safety of individuals within the structure [22]. Addressing the crash phenomenon presents a formidable challenge owing to its inherently nonlinear characteristics and unpredictable nature. The need for an extensive number of simulations is imperative to accurately model a crash event within acceptable error margins. However, the substantial computational demands associated with this task, coupled with the rapid evolution of machine learning (ML) and advancements in computing capabilities, have prompted researchers to explore the integration of various ML techniques. This endeavor aims not only to diminish computational time but also to streamline and expedite the design processes inherent in crashworthiness. In this subsection, we endeavor to spotlight noteworthy research efforts undertaken by expert researchers in both the past and ongoing contexts.

In one of the earliest attempts, Omar et al. [23] implemented ANN to study the vehicular crash response. The ANN model learns to replicate the dynamic force behavior of the structures subjected to impact. Additionally, the ANN model discussed in the work of Pawlus et al. [24] gives the kinematic response like displacement, velocity, and acceleration of a vehicle undergoing a collision as the outputs. To expedite the simulation of vehicle crashes, Kohar et al. [25] introduced a framework

based on ANN. Outpacing conventional finite element simulations, this ANN-based framework accelerates the generation of deformation and force-displacement curves by the notable acceleration of 330 times for the former and 2,960,000 times for the latter.

Similarly, the ANN model used by Lanzi et al. [26] predicts the load–time curve under the crashing of various structures such as riveted tubes, honeycomb structures, and helicopter subfloor. The model predicts the load–time curve within 12% and 9% errors for the riveted and honeycomb structures, respectively. For helicopter subfloor longitudinal keel beam elements, the errors are within 8% and 9% in computing the maximum and mean force, respectively.

Convolution neural network (CNN) stands as a distinct form of ANN designed to process and analyze grid-like data, such as images or time-series data [2]. Kohar et al. [25] employed both CNN and recurrent neural network (RNN) to predict the force-displacement characteristics of tubular structures undergoing dynamic crushing. The proposed methodology enables the prediction of deformation behavior at a speed approximately 330 times faster than traditional finite element simulations.

The integration of ML techniques, such as ANN and CNN, into crashworthiness research, has shown promising results in predicting impact behavior and enhancing simulation efficiency. These approaches, exemplified by studies like Omar et al. [23], Pawlus et al. [24], and Kohar et al. [25], offer accelerated deformation predictions with reasonable accuracy, addressing the computational challenges associated with crash simulations. However, further validation and exploration of these techniques across diverse crash scenarios are necessary to establish their robustness and reliability in real-world applications.

4 Application of ANN in Hypervelocity Impact

Hypervelocity impact experiments inherently entail destruction, and the equipment employed in such experiments is notably expensive. Setting up the experimental apparatus involves a considerable financial and time investment, compounded by additional manpower costs. While numerical simulations present a potential solution by reducing the need for extensive experiments, they still incur a time cost. The evolution of computing power over recent decades has facilitated the integration of ML into the study of hypervelocity impacts. ML applications have proven effective in substantially mitigating the time and cost associated with both ballistic impact experiments and simulations, as illustrated in Fig. 2. This marks a significant research direction in the past few years, which will be elaborated upon in the following discussion.

Palleti et al. [20] conducted a study on the material response in ballistic impact events, focusing on energy-absorbing mechanisms. They combined analytical studies with experimental validation using a single-stage gas gun apparatus. Their findings revealed that different thicknesses of targets can achieve the same ballistic limit velocity due to the dominance of different energy-absorbing mechanisms.

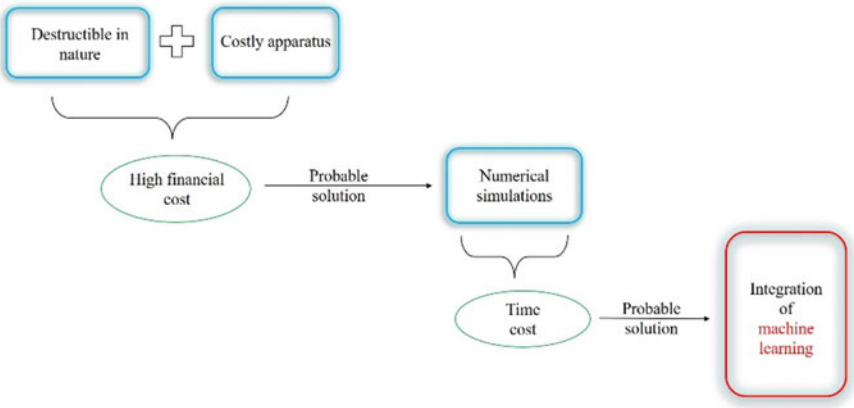


Fig. 2 Graphical representation of implementing ML in impact events

Adiabatic shear band formation, as discovered by Wingrove [27], was identified as one such mechanism for absorbing additional energy. KiliÇ et al. [28] utilized ANN to predict the ballistic limit thickness of high hardness steel armor-piercing bullets. Their ANN model demonstrated a significantly faster prediction of penetration depth compared to finite element simulations. Neto et al. [29] utilized various ANN models for evaluating mild steel plate's the mechanical response under blast loading. Their models successfully predicted maximum mid-plate displacement, charge impulse, transient mid-plate strain, and transient mid-plate displacement. In a similar vein, Bobbili et al. [30] employed an ANN model to delve into thin aluminum plates' ballistic performance. The study considered multiple factors, including plate thickness, impact velocity of the projectile, and nose shape.

Becker et al. [31] harnessed the power of ANNs to anticipate the deformation behavior of explosive reactive armor (ERA). The conventional approach of determining the optimal design for ERA by numerical simulation and experiment involves testing various impact conditions, a process that proves time-consuming. The ANN, however, efficiently predicts ERA plate deformation for specific combinations of detonation point position, plate geometry, and plate material. In a parallel context, Dennis et al. [32] implemented an ANN model to forecast the blast load generated by explosives in an internal environment. This ANN model demonstrated the capability to predict impulse loads at any points, considering the charge's size and placement. Remarkably, the ANN model exhibited a computational efficiency approximately 30 times faster than conventional numerical simulations. Additionally, Saxena et al. [33] proposed an ANN-based temperature-dependent constitutive material model for Armox 500T armor-grade steel experiencing plastic deformation at high strain rates.

Rayn et al. [34] utilized ML models, including support vector machine (SVM) [35] and ANN, to scrutinize the outcomes of hypervelocity ballistic impacts on spaced aluminum armor, with a particular focus on Whipple shields. The ML models used the input parameters, such as shield material properties, impact parameters, and

shield geometry, to predict whether the impactor would penetrate the target or not. The ANN model demonstrated superior performance, accurately classifying 96% of the impact events compared to the SVM model.

Training of any ML model requires a significant amount of data to achieve the desired accuracy. However, the data acquisition of ballistic impacts, through either FE simulation or experimentation, brings challenges in terms of cost and time. To overcome this challenge, Thompson et al. [36] used a generative adversarial network (GAN) [37] to generate sufficient additional samples to train an ML model. As a further refinement to the work, a conditional generative adversarial network (cGAN) was developed for conditioning additional information, such as class labels, apart from traditional ballistic data [38].

Furthermore, the increase in space activities in the last few decades has also increased the likelihood of impact from space debris at hypervelocity to any human space environment. Hence, the accurate detection and localization of the hypervelocity impact become significantly important for the analysis of damage and protection of any spacecraft. Bao et al. [39] used various ML algorithms to identify and locate the hypervelocity impacts from the time–frequency data extracted from the surface vibration during impact. The time–frequency data obtained from the vibration tests are used as input to the ML models. A total of nine ML models, namely decision tree, *k*-nearest neighbor, SVM, logistic regression, multilayer perceptron, random forest, extra trees, AdaBoost, and gradient boosting, are used to determine the vibration source and the vibration propagation distance [35]. The accuracy of all the ML models in identifying the vibration source was found to be more than 91%. However, the multilayer perceptron gave the best accuracy of 99.57%. On the other hand, AdaBoost performed best in propagation distance estimation with a RMSE of 2.591 cm.

Ni et al. [40] delved into the integration of ML within aerospace engineering, specifically in spacecraft, artificial satellites, and rockets. The paper explores diverse ML applications, encompassing anomaly detection, collision avoidance, attitude control, satellite communication, fault diagnosis, thermoacoustic instabilities detection, and lunar landing. The authors' conclusion underscores the significant contribution of ML to the expansion and advancement of the modern aerospace industry.

The integration of ML techniques within hypervelocity impact research has indeed exhibited remarkable potential in reducing the financial and temporal costs associated with destructive experiments. By leveraging ANN and other ML models, such as CNN and GANs, researchers have successfully expedited predictions of deformation behaviors, blast loads, and penetration depths, as well as efficiently generated training data for model development. This convergence of ML and ballistic impact studies offers a promising pathway to accelerate research in impact dynamics and spacecraft protection.

5 Application of ANN in Hypervelocity Impact

Usually, in a given structural problem, we compute the applied load and stiffness matrix as a known dataset and try to predict the deformations either with the help of conventional numerical techniques like the finite element method [41] or with relatively advanced techniques like SVM, ANN, and deep neural network (DNN) [42]. In ML, the models often function as black boxes, learning from input–output pairs to make predictions. Consequently, interchanging inputs and outputs have minimal impact on their performance. This approach, known as inverse analysis [43], involves predicting either the stiffness matrix-related features or load-related quantities for a given deformation or strain relationship.

In this section, firstly, research work associated with the prediction of stiffness matrix or quantities that can be obtained using stiffness matrix is presented. Secondly, a review of the literature that discusses the application of inverse analysis using ANN in structural health monitoring (SHM) is discussed. Thirdly, we will discuss applications of inverse analysis using ML in the field of vibration and aerospace industries. Finally, a study of the applications of inverse analysis using ANN in failure analysis is presented.

In stiffness matrix prediction, one of the earliest attempts to solve an inverse problem of detection of damage using an ANN can be traced back to Szeweczyk and Hajela [44]. They considered observable deformations of the structure under a given damage load condition as an input to ANN and predicted the components of the element stiffness matrix as output. This helped them to detect the weakest components within the structure with an approximate relative error of 10%. In elastic contact between two bodies, the estimation of normal contact stiffness is one of the key factors as it decides the level of penetration between two bodies. The higher the normal contact stiffness, the lower the penetration, but it will end up in ill-conditioning of the stiffness matrix, and lower values of normal contact stiffness result in more penetration of the bodies, which will negatively impact the physics of the problem. The ANN model proposed by Hattori and Serpa [45] predicts the normal contact stiffness. They took maximum penetration and maximum contact pressure variation as input and predicted normal contact stiffness factor as output.

Chandrashekhara et al. [46] predicted contact force in composites using given strain relations as input. They developed four different ANN models with varying parameters to test their relative performance. For training data, they considered explicit finite element codes developed using LS-DYNA3D. In the field of vibrations, measuring the dynamic response in a vibrating structure is challenging due to the presence of non-linearities. An inverse analysis approach using ML models to deal with non-linearity aspects present in vibrations can be a fruitful research area. Owing to the challenge, Hashemi and Kargarnov [47] have applied a genetic algorithm (GA) to predict the location and magnitude of impact force on a simply supported beam with a known acceleration response of a structure. Their developed model was computationally efficient and was insensitive to the location of sensors that they used to measure the responses.

Although GA can be seen as one of the commonly used tools for population search and optimization because of its adaptive nature derived from evolutionary ideas of natural genetics, there are sometimes convergence issues in solving large populations in complex problems. Owing to complexities in solving inverse non-linear problems, Yan and Zhou [48] used micro-GA to predict the location of load impact and simultaneously reconstruct impact force history. Micro-GA (GA with small populations) avoids premature convergences and also accelerates the convergence process near optimal roots. Leclerc et al. [49] applied a neural network approach to design impact detectors for a full-scale aircraft composite panel. They employed regression, classification, and a combination of both approaches to predict the impact location. In regression, they achieved training, validation, and testing errors of 0.87, 1.76, and 1.92%, respectively. For classification, the misclassification errors were 0.025 for validation and 0.032 for testing. In the combined approach, the misclassification errors in the first stage were 0.0126 for validation and 0.0253 for testing. The overall validation and test errors were 0.5 and 0.48%, respectively.

Another application of inverse analysis using ANN can be seen in failure analysis. After the failure of a structure, the data we have with us are residual plastic strain and plastic deformation, which can also be perceived as forensic signatures. In case of structural failures like crashes and pressure vessel failure, these methods can help in investigations of root causes of failures, analyzing damage conditions, and determining locations. Ren et al. [50] did a more inclusive study where they predicted conditions for damage loading, i.e., identification of amplitude, location, and duration of forces on a structure, in static as well as in dynamic loads using the forensic signatures. Their proposed model prediction accuracies for location and amplitude were well within 5% error, and for damage load prediction, errors ranged from 5 to 10%, which can still be considered a good model. Chen et al. [51] expanded upon previous research by introducing a novel deep learning model. This model was designed to predict impact load conditions (like collision velocity, location, and duration) in shell structures undergoint collision with rigid impactor. The final damaged state or permanent plastic deformation which is represented by the forensic signature, served as a key input to their innovative deep learning approach. They concluded that the proposed model was able to predict impact conditions well within 5% error, which can be considered good accuracy. Zhou et al. [52] developed a recurrent neural network to predict the impact load of non-linear structures even when the impact location is unknown. Their model comprised of one bidirectional LSTM (BLSTM) and two long short-term memory (LSTM). Use of BLSTM greatly improved the accuracy of impact load prediction. Their proposed novel RNN model was insensitive to location and number of sensors, which can be considered a significant advantage over other published methods.

The review discusses how ML-based models are used to enhance understanding of structural behaviors, reducing costs and enabling damage detection in various domains, including aerospace. These approaches contribute to reducing experimental costs and computational efforts while facilitating damage detection, impact prediction, and failure analysis.

While ML-based inverse analysis shows promise, it is crucial to acknowledge its limitations, including concerns about model robustness, data requirements, and generalizability. The review's focus on successes might downplay the trade-offs between computational efficiency and accuracy. Further research should address these challenges to ensure the practicality and reliability of ML-based inverse analysis methods.

6 Conclusion

The application of ANN in crashworthiness, ballistic impact, and inverse load analysis shows promise, reducing costs and time associated with testing. ML models accurately predict deformation behavior and evaluate crashworthiness. Techniques like ANNs capture complex relationships between parameters and responses. Inverse load analysis estimates loads based on structural responses, enabling efficient health monitoring and design optimization. ANN advancements, datasets, and computing power enhance safety and performance. Challenges remain in data availability, interpretability, and generalization. Overall, ANN is a valuable tool in structural engineering, offering innovative solutions for safety and performance improvement.

Funding The authors gratefully acknowledge the support from SERB, DST under the projects IMP/2019/000276, CRG/2022/002218, and VSSC, ISRO through MoU No.: ISRO:2020:MOU: NO:480.

References

1. LeCun Y, Bengio Y, Hinton G (2015) Deep learning. Nature 521(7553):436–444
2. Goodfellow I, Bengio Y, Courville A (2016) Deep learning. MIT Press
3. Liu X, Tian S, Tao F, Yu W (2021) A review of artificial neural networks in the constitutive modeling of composite materials. Comp B Eng 224:109152
4. Ho LV, Nguyen DH, Mousavi M, De-Roeck G, Bui-Tien T, Gandomi AH, Wahab MA (2021) A hybrid computational intelligence approach for structural damage detection using marine predator algorithm and feedforward neural networks. Comput Struct 252:106568
5. Ozarde AP, Narayan J, Yadav D, McNay GH, Gautam SS (2020) Optimization of diesel engine's liner geometry to reduce head gasket's fretting damage. SAE Int J Engines 14:81–97
6. Gautam SS, Khan K (2020) Detection of fretting fatigue using machine learning algorithms. In: 3rd structural integrity conference and exhibition (SICE 2020) structural integrity at multiple length scales (e-conference), December 14–16, IIT Bombay, Guwahati, Assam, India
7. Vithalbhai SK, Gautam SS (2021) A machine learning approach to fretting fatigue problem. In: Proceedings of the international conference on futuristic technologies (e-conference) - structural health monitoring, energy harvesting, green Material and Biomechanics, January 22–24, IIT Delhi, New Delhi, India
8. Saikia BB, Nath D, Gautam SS (2023) Application of machine learning in efficient stress recovery in finite element analysis. Mater Today Proceed 78:359–363
9. Saikia BB, Nath D, Gautam SS (2024) Machine learning models for stress recovery in finite element method. Recent Trends in Computational Mechanics and Simulation: Select proceedings of ICCMS 2022, Springer, Singapore (in press)

10. Vithalbhai SK, Nath D, Agrawal V, Gautam SS (2022) Artificial neural network assisted numerical quadrature in finite element analysis in mechanics. Mater Today Proceed 66:1645–1650
11. Chinchkar R, Nath D, Gautam SS (2023) Design of efficient quadrature scheme in finite element using deep learning. Advances in Engineering Design: Select Proceedings of FLAME 2022. Springer, Singapore, pp 21–29
12. Nath SS, Nath D, Gautam SS (2023) Design of efficient finite elements using deep learning approach. Advances in Engineering Design: Select Proceedings of FLAME 2022. Springer, Singapore, pp 11–20
13. Nath SS, Nath D, Gautam SS (2024) Efficient stiffness matrix in finite element method using deep learning for linear elasticity. Recent Trends in Computational Mechanics and Simulation: Select proceedings of ICCMS 2022, Springer, Singapore (in press)
14. Ankit, Nath D, Sauer RS, Gautam SS (2023) Evaluating the performance of different optimizers for deep learned finite elements. 6th national conference on multidisciplinary design, analysis and optimization (NCMDAO 2023). December 6–8, IIT Guwahati, Guwahati, Assam, India
15. Jung J, Yoon K, Lee PS (2020) Deep learned finite elements. Comput Meth Appl Mech Eng 372:113401
16. Gouravaraju S, Narayan J, Sauer RA, Gautam SS (2023) A Bayesian regularization-backpropagation neural network model for peeling computations. J Adhesion 99(1):92–115
17. Nath D, Neog DR, Gautam SS (2024) Application of machine learning and deep learning in finite element analysis: a comprehensive review. Arch Comput Meth Eng 1–40
18. Johnson KL, Johnson KL (1987) Contact mechanics. Cambridge University Press, Cambridge
19. Popov VL (2010) Contact mechanics and friction. Springer, New York
20. Palleti HNKT, Gurusamy S, Kumar S, Soni R, John B, Vaidya R, Bhoge A, Naik NK (2012) Ballistic impact performance of metallic targets. Mater Des 39:253–263
21. Ambrósio J (2014) Automotive structural crashworthiness and occupant protection. In: Road and off-road vehicle system dynamics handbook. CRC Press, pp 1611–1662
22. Ambrosio JAC (2001) Crashworthiness: energy management and occupant protection, vol 423. Springer, New York
23. Omar T, Eskandarian A, Bedewi N (1998) Vehicle crash modelling using recurrent neural networks. Math Comput Model 28(9):31–42
24. Pawlus W, Karimi HR, Robbersmyr KG (2013) Data-based modeling of vehicle collisions by non-linear autoregressive model and feedforward neural network. Inform Sci 235:65–79
25. Kohar CP, Greve L, Eller TK, Connolly DS, Inal K (2021) A machine learning framework for accelerating the design process using CAE simulations: an application to finite element analysis in structural crashworthiness. Comput Methods Appl Mech Eng 385:114008
26. Lanzi L, Bisagni C, Ricci S (2004) Neural network systems to reproduce crash behavior of structural components. Comput Struct 82(1):93–108
27. Wingrove AL (1973) The influence of projectile geometry on adiabatic shear and target failure. Metall Trans 4:1829–1833
28. KılıÇ N, Ekici B, Hartomacıoğlu S (2015) Determination of penetration depth at high velocity impact using finite element method and artificial neural network tools. Def Technol 11(2):110–122
29. Neto LB, Saleh M, Pickerd V, Yiannakopoulos G, Mathys Z, Reid W (2020) Rapid mechanical evaluation of quadrangular steel plates subjected to localised blast loadings. Int J Impact Eng 137:103461
30. Bobbili R, Ramakrishna B, Madhu V (2020) An artificial intelligence model for ballistic performance of thin plates. Mech Based Des Struct Mach 12:1–12
31. Becker M, Klavzar A, Wolf T, Renck M (2022) Data-driven prediction of plate velocities and plate deformation of explosive reactive armor. Def Technol 18(12):2141–2149
32. Dennis AA, Pannell JJ, Smyl DJ, Rigby SE (2021) Prediction of blast loading in an internal environment using artificial neural networks. Int J Protect Struct 12(3):287–314
33. Saxena A, Kumaraswamy A, Kotkunde N, Suresh K (2019) Constitutive modeling of high-temperature ow stress of armor steel in ballistic applications: a comparative study. J Mater Eng Perform 28:6505–6513

34. Ryan S, Thaler S, Kandanaarachchi S (2016) Machine learning methods for predicting the outcome of hypervelocity impact events. Exp Syst Appl 45:23–39
35. Murphy KP (2012) Machine learning: a probabilistic perspective. MIT Press
36. Thompson S, Teixeira-Dias F, Paulino M, Hamilton A (2022) Ballistic response of armour plates using generative adversarial networks. Def Technol 18(9):1513–1522
37. Goodfellow IJ, Abadie JP, Mirza M, Xu B, Farley DW, Ozair S, Courville A, Bengio Y (2014) Generative adversarial nets. Adv Neural Inform Process Syst 14:27
38. Thompson S, Teixeira-Dias F, Paulino M, Hamilton A (2022) Predictions on multi-class terminal ballistics datasets using conditional generative adversarial networks. Neural Netw 154:425–440
39. Bao J, Liu L, Cao J (2022) Vibration-based hypervelocity impact identification and localization. Front Inform Technol Electr Eng 23(4):515–529
40. Ni Z (2022) Reframe the field of aerospace engineering via machine learning: application and comparison. J Phys Confer Ser 2386:012031
41. Bathe KJ (2006) Finite element procedures. Klaus-Jurgen Bathe
42. Bishop CM, Nasrabadi NM (2006) Pattern recognition and machine learning, vol 4. Springer, New York
43. Roy DNG, Couchman LS (2001) Inverse problems and inverse scattering of plane waves. Academic Press, New York
44. Szewczyk ZP, Hajela P (1994) Damage detection in structures based on feature-sensitive neural networks. J Comput Civil Eng 8(2):163–178
45. Hattori G, Serpa AL (2015) Contact stiffness estimation in ANSYS using simplified models and artificial neural networks. Finite Elements Anal Des 97:43–53
46. Chandrashekhara K, Okafor AC, Jiang YP (1998) Estimation of contact force on composite plates using impact-induced strain and neural networks. Comp B Eng 29(4):363–370
47. Hashemi R, Kargarnovin MH (2007) Vibration base identification of impact force using genetic algorithm. Int J Mech Syst Sci Eng 1(4):204–210
48. Yan G, Zhou L (2009) Impact load identification of composite structure using genetic algorithms. J Sound Vibr 319(3–5):869–884
49. LeClerc JR, Worden WJ, Staszewski K, Haywood J (2007) Impact detection in an aircraft composite panel A neural-network approach. J Sound Vibr 299(3):672–682
50. Ren S, Chen G, Li T, Chen Q, Li S (2018) A deep learning-based computational algorithm for identifying damage load condition: an artificial intelligence inverse problem solution for failure analysis. Comput Model Eng Sci 117(3):287–307
51. Chen G, Li T, Chen Q, Ren S, Wang C, Li S (2019) Application of deep learning neural network to identify collision load conditions based on permanent plastic deformation of shell structures. Comput Mech 64:435–449
52. Zhou JM, Dong L, Guan W, Yan J (2019) Impact load identification of non-linear structures using deep recurrent neural network. Mech Syst Sig Process 133:106292

A Comparative Study of Dual Throat Nozzles for Fluidic Thrust Vectoring Applications



M. Siva Sakthi and Surendra Bogadi

Abstract Thrust vectoring is the technique by which the jet coming out of the nozzle is made to deflect to control the vehicle. Fluidic thrust vector control by dual throat nozzle is found to have the highest thrust efficiency with minimum pressure losses. The present study involves the design and simulation of a dual throat nozzle (DTN), a DTN with injection (I-DTN), and a bypass dual throat nozzle with a V-shaped bypass duct (V-BDTN) and with an arc-shaped bypass duct (A-BDTN). The arc-shaped bypass duct design idea is taken from the author Wu and Kim (J Mech Sci Technol 35:3435–3443, 2021). It is found that I-DTN has the highest deflection angle of 12° for NPR = 4 and the highest coefficient of the thrust of 0.96. But implementing DTN with injection has the starting problem as mentioned in the research literature. To overcome this, A-BDTN and V-BDTN are introduced. Also, A-BDTN's coefficient of thrust is very close to that of a DTN which means the thrust penalty for vectored state is negligible.

Keywords Thrust vectoring · Nozzle · Dual throat nozzle · Supersonic flow · Shock wave · Jet deflection

1 Introduction

The thrust vector control (TVC) is a method used to manipulate the exit jet in order to provide maneuverability for the aircraft. This has been utilized by various fighter aircraft, space platforms, and modern rockets. In addition to providing supplementary thrust, the TVC changes the line of thrust and allows for pitching, rolling, and yawing, stating that a fighter aircraft with TVC only needs a small aerodynamic control surface to achieve flexible control effectiveness. Two methods of thrust vectoring are fluidic thrust vector control and mechanical thrust vector control. If mechanical hardware is used in nozzles to deflect the primary exhaust flow, it is called mechanical thrust

M. S. Sakthi (✉) · S. Bogadi
Department of Aeronautical Engineering, Rajalakshmi Engineering College, Rajalakshmi Nagar, Thandalam, Chennai 602 105, India
e-mail: sivasakthi.m.2019.aero@rajalakshmi.edu.in

© The Author(s), under exclusive license to Springer Nature Singapore Pte Ltd. 2024

S. Singh et al. (eds.), *Recent Advances in Aerospace Engineering*, Lecture Notes in Mechanical Engineering, https://doi.org/10.1007/978-981-97-1306-6_33

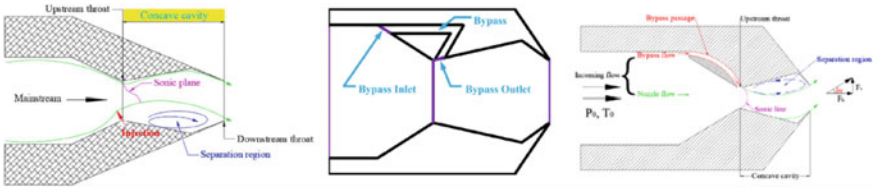


Fig. 1 Schematic of I-DTN [3] (left), V-BDTN [4] (middle), and A-BDTN [1] (right)

vectoring. But fluidic thrust vectoring methods do not use hardware and have advantages over mechanical ones [1] such as lightweight, fixed geometry, less complex, and less detectable to radar.

Fluidic thrust vectoring nozzles (FTVNs) use a secondary air source to create an off-axis deflection of the primary jet. However, in all the thrust vectoring mechanisms, the deflection is achieved by creating an asymmetric pressure distribution on the nozzle surfaces. FTVNs have been proposed and investigated since the 1990s [2]. Shock vector control (SVC), counterflow (CF), throat shifting (TS), and the dual throat nozzle (DTN) are some of the FTVNs (see Fig. 1). Each of the above methods have different desirable characteristics but at the expense of some disadvantages. For example, SVC nozzles can have large deflection angles but with loss in thrust due to oblique shocks. On the other hand, in TS nozzle, it is opposite, and it provides appreciable thrust with small deflection angles.

Dual throat nozzles are predominantly used for fluidic thrust vectoring applications. The DTN is designed with two minimum areas—an upstream minimum area and a downstream minimum area. There is a cavity called a recessed cavity in between the upstream throat and nozzle exit. Secondary air source (say bleed air from engine) is injected at particular locations in this recessed cavity to deflect the primary jet.

Recent research has identified fluidic thrust vectoring as a promising alternative, potentially lowering the overall system mass and complexity of a thrust vectoring system. Both DTN and bypass dual throat nozzle (BDTN) use the same principle except for the source of secondary jet. Unlike DTN, BDTN does not require an additional source for secondary jet; instead, the primary jet itself serves the purpose. And this eliminates the starting problem of the nozzle as discussed in the literature [5].

Author HD Kim in his latest work [1] introduced a new concept in bypass duct that used an arc-shaped bypass duct (A-BDTN) rather than a conventional V-shaped duct (V-BDTN). This type of bypass will reduce the pressure loss significantly. 2-D flow simulations were performed. In the present work, 3-D simulation is done.

2 Methodology

For the present work, the computational fluid dynamics method is used. To carry out the simulation, ANSYS Fluent R2022 module is used. Initially, the nozzle is designed (see Fig. 2). The CAD for the same is done using CATIA V5 R21, and then, it is used in ANSYS Fluent solver for further simulation. Finite volume method is utilized in the present work that uses three-dimensional, time independent, and compressible Reynolds-averaged Navier–Stokes (RANS) equations. Gravity is neglected as they do not have significant effects. The work is first validated with the data found in the literature before any further work. The simulation contours of pressure, velocity, and Mach number are extracted using post-processing features available. Data on pressure and velocity are used to find the thrust provided by the nozzle. Then, other parameters like thrust coefficient, discharge coefficient, and pressure loss are also evaluated for comparison.

2.1 Governing Equations

For the present study, the commercial software package Fluent is used which is based on a finite volume approach. The governing equations are continuity, energy, and perfect gas equation. Apart from this, some other equations are used which are discussed below.

K–ε Turbulence Model:

The standard K–ε turbulence model is used [6] which is suitable to a large number of turbulent applications.

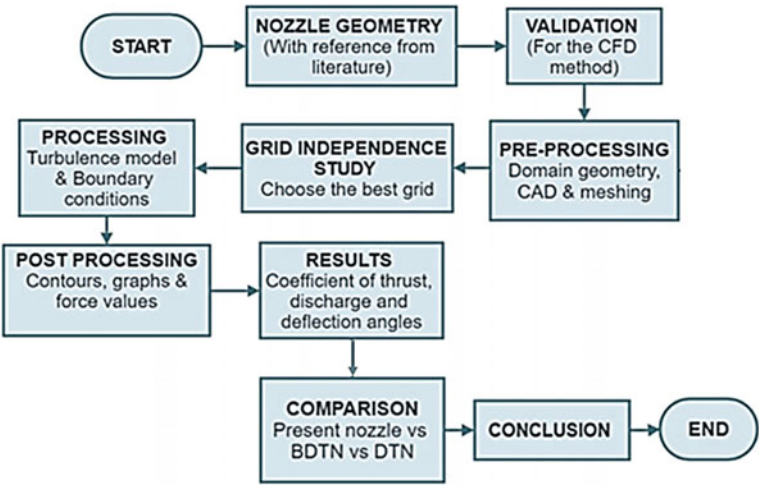


Fig. 2 Workflow chart

For turbulent kinetic energy k,

$$\frac{\partial(\rho k)}{\partial t} + \frac{\partial(\rho k u_i)}{\partial x_i} = \frac{\partial}{\partial x_j}\left[\frac{\mu_t}{\sigma_k}\frac{\partial k}{\partial x_j}\right] + 2\mu_t E_{ij}^2 - \rho\varepsilon$$

For dissipation ε,

$$\frac{\partial(\rho\varepsilon)}{\partial t} + \frac{\partial(\rho\varepsilon u_i)}{\partial x_i} = \frac{\partial}{\partial x_j}\left[\frac{\mu_t}{\sigma_\varepsilon}\frac{\partial \varepsilon}{\partial x_j}\right] + C_{1\varepsilon}\frac{\varepsilon}{k}2\mu_t E_{ij}^2 - C_{2\varepsilon}\rho\frac{\varepsilon^2}{k}$$

Sutherland Viscosity Law:

It was derived from a kinetic theory by Sutherland [4] using an idealized intermolecular force potential. The formula is specified using two or three coefficients. The equation is as follows:

$$\frac{\mu}{\mu_o} = \left(\frac{T}{T_0}\right)^{\frac{3}{2}}\frac{T_0 + S_\mu}{T + S_\mu}$$

Here, μ_0—reference viscosity, T_0—reference temperature, and Ts—effective temperature.

2.2 Validation

For any numerical simulation, the results have to be validated for the experimental data available. For validating the CFD method, a 2-D BDTN found in the literature is used [1]. The nozzle width is 88.74 mm with upstream and downstream throat diameters of 20 and 24 mm.

The diverging and converging angles of the concave cavity are $\theta 1 = 14.8°$ and $\theta 2 = 50°$, respectively. The converging angle of the upstream nozzle is $\theta 3 = 30°$. The turbulence model used is K–ε. From Fig. 3a and b, it is evident that both the Mach contours are identical. To reinforce the validation, the static pressure distribution is found in the literature from experimental data [7] Fig. 4b is compared with the pressure distribution for the HD Kim's nozzle [1] as shown in Fig. 3a. The distribution is not the same since the geometry is different, but the trend is similar representing pressure drop wherever there exists a shock. Also, the present nozzle is 3-D BDTN, whereas the one in the literature is 2-D DTN with injection.

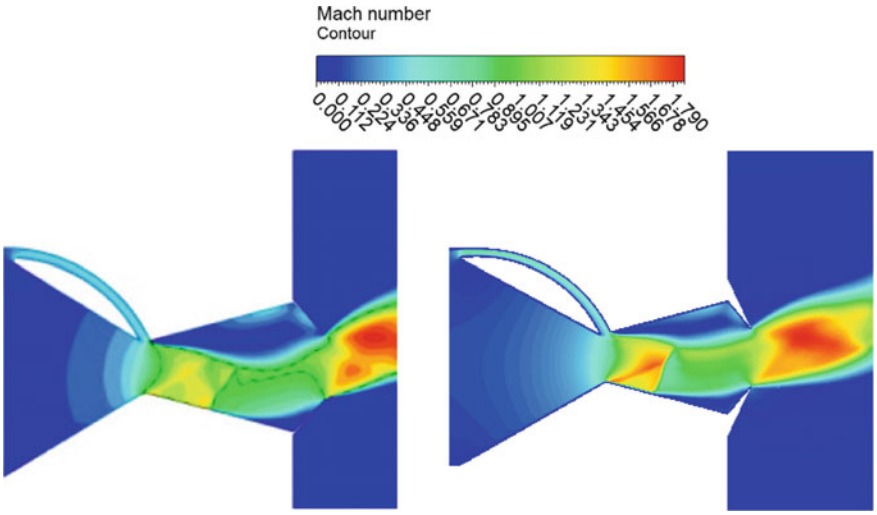


Fig. 3 **a** Mach contour in the literature [1]. **b** Mach contour from present work

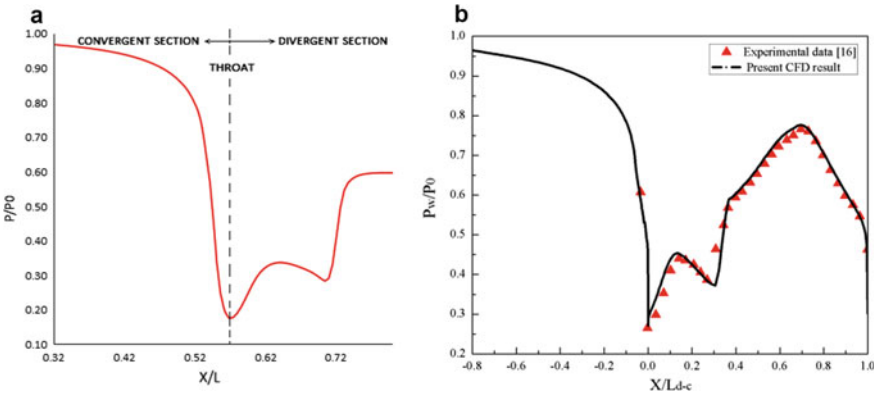


Fig. 4 **a** Static pressure distribution—present work. **b** Pressure distribution from the literature [7]

3 Simulation for the Present Work

3.1 Nozzle Description

Initially, a dual throat nozzle was designed as in Fig. 5 by referring to the literature [4, 6, 8] followed a BDTN. The divergence and convergence angle and all other dimensions are made to be in the range that is mentioned. The nozzle dimensions are the same for all the cases. Similarly, a BDTN is also designed. For any BDTN,

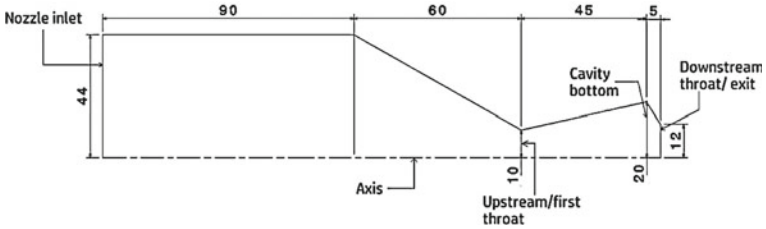


Fig. 5 Sketch of dual throat nozzle (all dimensions are in mm)

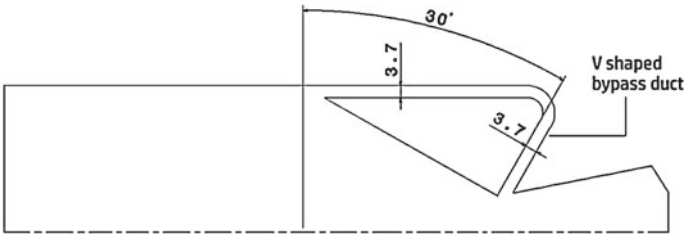


Fig. 6 Sketch of V-BDTN (all dimensions are in mm)

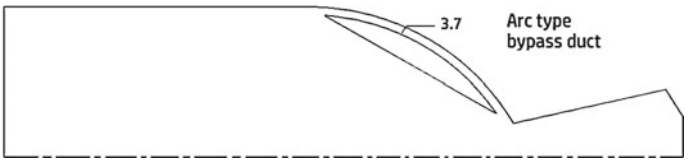


Fig. 7 Sketch of A-BDTN

the optimum width for the bypass duct is 0.185 times the throat diameter [4]. So, for the present nozzle, it is 3.7 mm (Figs. 6 and 7).

3.2 Computational Domain

A computational domain suitable to capture all flow features is considered for present simulations (as shown in Fig. 8). The domain length and width extend 30 times downstream and 20 times sideways of the throat diameter, respectively [9]. These dimensions were obtained after performing a domain independence study. The boundary conditions for present computations were considered as pressure inlet, outlet, and no-slip wall.

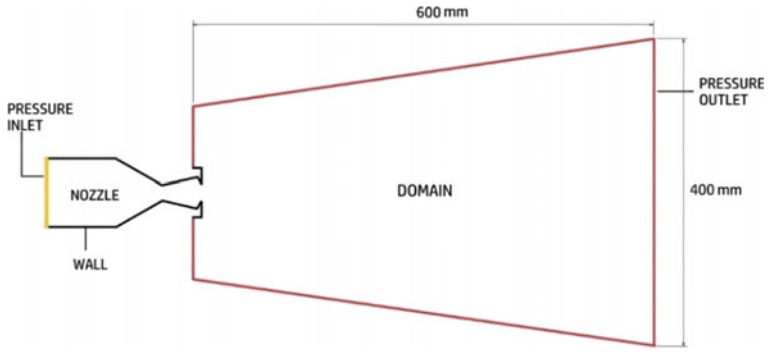


Fig. 8 Computational domain with boundary conditions for DTN

Table 1 Grid independence analysis

Grid	Nodes	Elements
Coarse	1,313,382	1,363,187
Medium	1,871,614	2,079,229
Fine	2,481,957	2,833,099

3.3 Grid Independence Analysis

A grid independent analysis was performed for the nozzle with a domain with three different grids, namely coarse, medium, and fine as shown in Table 1, aiming to find the optimum grid size.

This analysis is done so that simulation can be done with higher accuracy for the least number of elements. It is found that the pressure values for the grid with 2 million elements almost overlap with the grid with 2.8 million elements (Fig. 9). But the coarse grid with 1.3 million elements has a certain gap with the medium grid. So, for further simulation, the medium grid with 2.07 million elements is chosen as in Fig. 10. The first cell height near the wall is set as 0.01 mm. This is to ensure a maximum y^+ value approximately equal to 1 [4, 10] which will be optimum for the K–ε turbulence model [6].

3.4 Boundary Conditions

The solver uses pressure-based equations to solve the case. There are three boundaries as shown in Fig. 8. All simulations were done with a static free-stream Mach number and K–ε turbulence model [6].

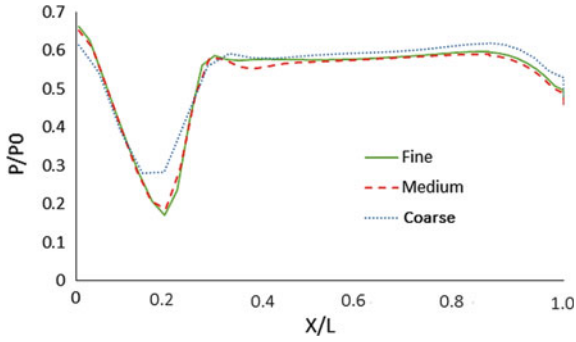


Fig. 9 Pressure distribution along the centerline

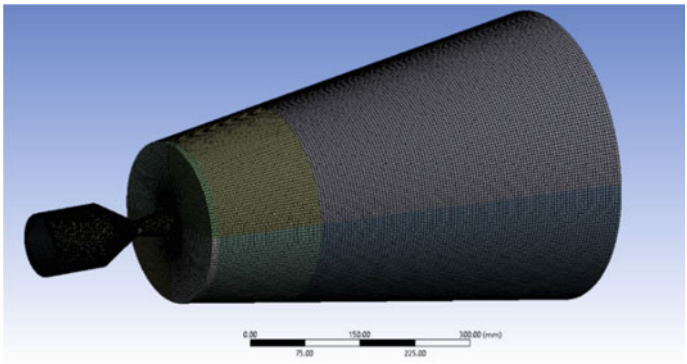


Fig. 10 Structured grid for the nozzle with the domain

The outflow of the nozzle is at the standard atmospheric conditions for which the ambient pressure (Pa) is 101325 Pa, the temperature (T_a) is 288.15 K, and the turbulent viscosity ratio is 10 [4].

The total pressure of the nozzle at the inlet ($P_{\text{in}}{}^*$) depends on the back pressure and the NPR, that is, $P_{\text{in}}{}^* = Pb \times \text{NPR}$. Since the flow at the nozzle inlet is subsonic, for computation, the value of static pressure at the inlet is set slightly lower than the total pressure. The total temperature of the nozzle inlet flow ($T_{\text{in}}{}^*$) is 288.15 K. The turbulent intensity is set at 5% [10]. Simulations are carried out for NPRs = 2, 4, 6, and 8. The wall is considered to be an adiabatic and no-slip wall.

4 Nozzle Performance Parameters

The parameters that are used to evaluate a nozzle's performance are flow deflection angle (θ), thrust coefficient (C_f), and discharge coefficient (C_d). The forces can be found from post-processing. The resultant force, F_R, can be obtained as a vector of the sum of three forces [4].

$$F_A = \int_{A_2} (\rho \upsilon_x \upsilon_x + (P - P_b))\mathrm{d}A$$

$$F_N = \int_{A_2} (\rho \upsilon_x \upsilon_y)\mathrm{d}A$$

$$F_S = \int_{A_2} (\rho \upsilon_x \upsilon_z)\mathrm{d}A$$

$$F_R = \sqrt{F_A^2 + F_N^2 + F_S^2}$$

Here, F_A, F_N, and F_S are the nozzle axial force, normal force, and side force, respectively.

The thrust coefficient is the ratio of resultant thrust to ideal thrust [1].

$$C_f = F_R / F_i$$

$$F_i = m_{\text{in}} \sqrt{\frac{2\gamma}{\gamma - 1} R T_{\text{in}}^* \left[1 - \left(\frac{P_b}{P_{\text{in}}^*} \right)^{\frac{\gamma - 1}{\gamma}} \right]}$$

Here, $P_{\text{in}}{}^*$ and P_b are the total pressure at the inlet and the back pressure, respectively.

The discharge coefficient is given by,

$$C_d = m_{\text{in}} / m_i$$

Here, m_{in} is the actual mass flow rate of the nozzle inlet and m_i is the ideal mass flow rate of the nozzle. m_i is given by:

$$m_i = \left(\frac{\gamma}{R} \right)^{\frac{1}{2}} \left(\frac{2}{\gamma + 1} \right)^{\frac{\gamma + 1}{2(\gamma - 1)}} A_1 P_{\text{in}}^* / \sqrt{T_{\text{in}}^*}$$

Here, A_1—upstream throat area

$T_{\text{in}}{}^*$—Total temperature at the inlet.

5 Results and Discussion

The effect of injection and different bypass ducts on nozzle performance for the four different nozzle configurations, namely DTN, I-DTN, V-DTN, and A-DTN, at different NPRs are investigated. All four nozzles are compared with some nozzle

performance parameters, namely flow deflection angle (θ), thrust coefficient (C_f), and discharge coefficient (C_d). The results for each nozzle are described below.

5.1 DTN Configuration

The Mach contours for the DTN for NPR 2, 4, 6, and 8 are shown in Fig. 11. The performance parameters are calculated by post-processing and are given in Table 2.

The resultant force increases with an increase in NPR. The coefficient of thrust does not follow any trend with NPR, but it varies slightly with a mean value of 0.9.

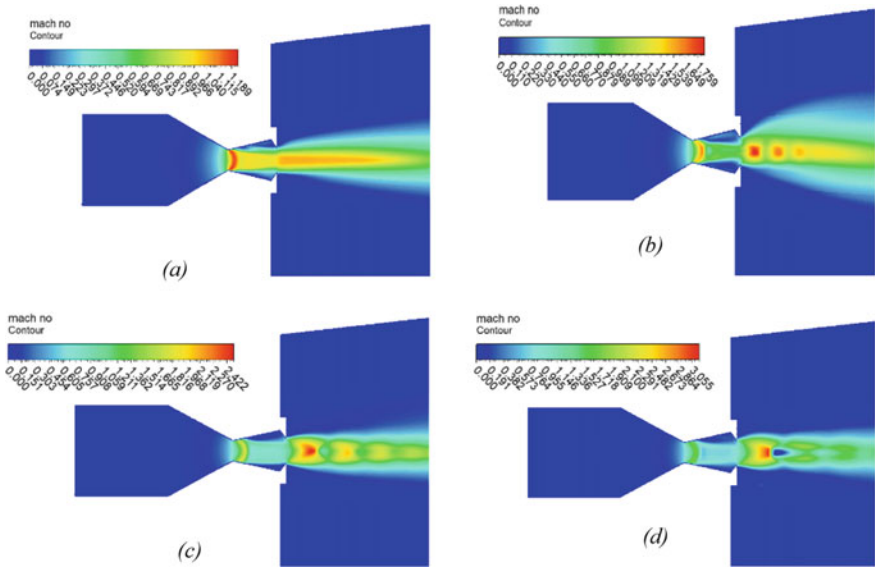


Fig. 11 Mach contour for DTN **a** NPR = 2, **b** NPR = 4, **c** NPR = 6, **d** NPR = 8

Table 2 Performance parameters of DTN for different NPRs

NPR	m_i (kg/s)	m_{in} (kg/s)	C_d	F_R (N)	F_i (N)	C_f
2	0.149	0.143	0.959732	45.65	46.7	0.977516
4	0.299	0.299	1	120	131.76	0.910747
6	0.449	0.431	0.959911	195.07	210.23	0.927889
8	0.599	0.597	0.996661	270.07	307.92	0.877078

5.2 V-BDTN, A-BDTN, and I-BDTN

Similarly, for the other three configurations, the Mach contours for NPR = 4 are depicted below in Fig. 12a–c. The calculated performance parameters are also shown in Tables 3, 4 and 5.

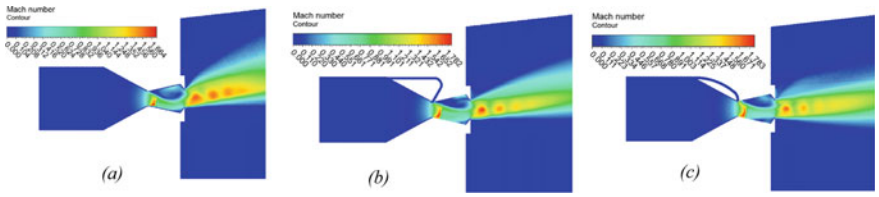


Fig. 12 Mach contour for **a** I-DTN, **b** V-BDTN, **c** A-BDTN

Table 3 Performance parameters of V-BDTN for different NPRs

NPR	m_i (kg/s)	m_{in} (kg/s)	C_d	F_R (N)	F_i (N)	C_f
2	0.149	0.142	0.95302	39.56	46.37	0.853138
4	0.299	0.284	0.949833	113.18	125.15	0.904355
6	0.449	0.428	0.953229	191.08	219	0.872511
8	0.599	0.57	0.951586	263.324	293.99	0.89569

Table 4 Performance parameters of I-BDTN for different NPRs

NPR	m_i (kg/s)	m_{in} (kg/s)	C_d	F_R (N)	F_i (N)	C_f
2	0.149	0.135	0.90604	39.815	44.08	0.903244
4	0.299	0.273	0.913043	116.4	120.3	0.967581
6	0.449	0.41	0.91314	190.079	199.98	0.95049
8	0.599	0.547	0.913189	267.48	282.13	0.948074

Table 5 Performance parameters of A-BDTN for different NPRs

NPR	m_i (kg/s)	m_{in} (kg/s)	C_d	F_R (N)	F_i (N)	C_f
2	0.149	0.141	0.946309	41.26	46.04	0.896177
4	0.299	0.283	0.946488	114.63	124.7	0.919246
6	0.449	0.425	0.946548	191.66	207.3	0.924554
8	0.599	0.568	0.948247	254.79	292.96	0.869709

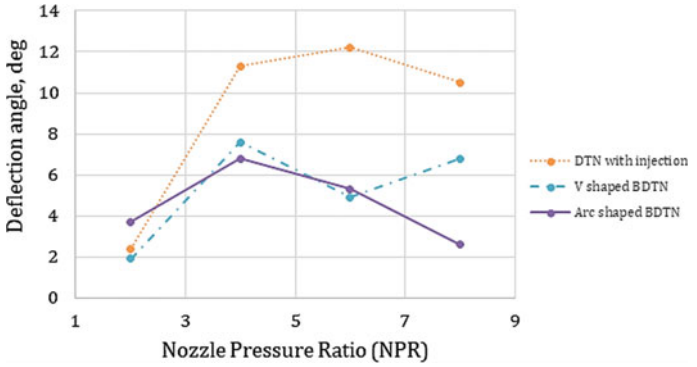


Fig. 13 Deflection angle versus NPR for different nozzles

5.3 Comparison of Nozzles for Different NPRs

Considering the deflection angle for different configurations (Fig. 13), DTN with injection has the highest deflection angle for NPR = 4, 6, and 8. And the highest has the highest deflection angle, but the same configuration performs the lowest deflection angle which is 12° for NPR = 6. But at lower NPR, i.e., for NPR = 2, A-BDTN for NPR = 8. A-BDTN and V-BDTN have similar angles except for NPR = 8.

Considering the second most important parameter, i.e., thrust coefficient (Fig. 14) for all the nozzle configurations, the C_f increases with NPR up to a certain point and then decreases. I-DTN has the highest C_f for all NPRs, and for NPR = 4, it is 0.96. However, A-BDTN and DTN have almost the same C_f for all NPRs which means A-BDTN has the least penalty in thrust and is almost equal to an un-vectored DTN.

Another parameter to be discussed is the discharge coefficient (C_d) (Fig. 15). For all the configurations, the C_d is almost constant for all NPRs. I-DTN has the lowest C_d for all NPR, and C_d for A-BDTN and V-BDTN are nearly the same (Fig. 15).

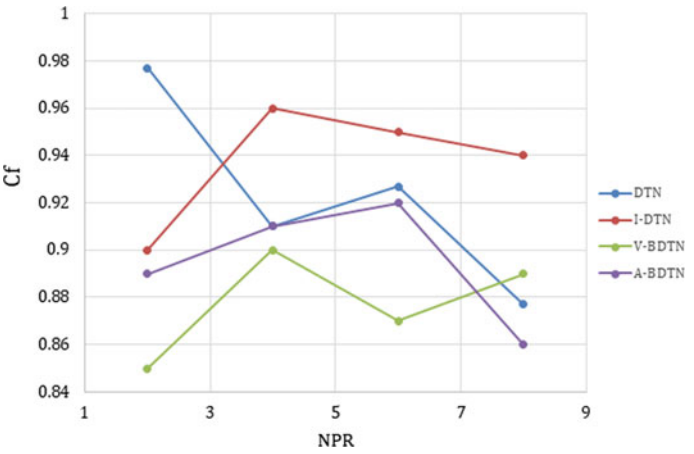
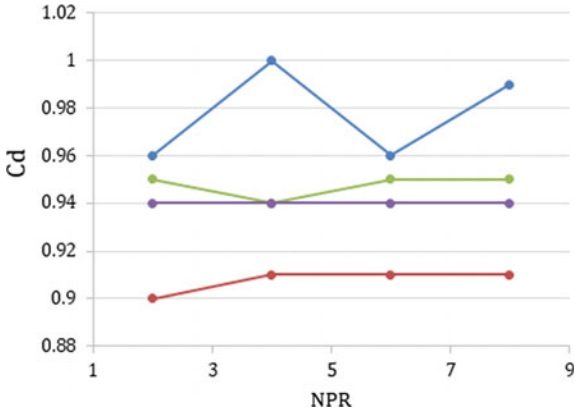


Fig. 14 Discharge coefficient versus NPR

Fig. 15 Coefficient of thrust versus NPR



6 Conclusion

In the present study, a fixed DTN with injection, a V-shaped BDTN, and an arc-shaped BDTN are numerically investigated and compared. All three nozzle's deflection angle increases with NPR up to a point and then decreases with NPR. DTN with injection gave the best result in terms of deflection angle with the highest deflection angle of 12° for NPR = 6. It is because DTN ensures that the secondary air is fed exactly perpendicular to the primary air at the nozzle throat. Similarly, it also has the highest coefficient of thrust. But implementing DTN with injection has practical difficulties and has starting problem as mentioned in the literature which can be tackled by BDTNs. Especially, BDTN with an arc-shaped bypass duct has a coefficient of thrust that is almost equal to an un-vectored DTN and also has an almost constant discharge coefficient of 0.94 for all NPRs. But for NPR = 8, it has the lowest deflection angle.

So, for lower NPRs, A-BDTN can be preferred. Also, A-BDTN will be more suitable for aerospace applications with minimal pressure losses. Otherwise, V-BDTN configuration will be a good option for a nozzle that operates at a wide range of NPR. The design of both A-BDTN and V-BDTN can be optimized to improve the deflection angles.

Funding Not Applicable.

References

1. Wu K, Kim HD (2021) A fluidic thrust vector control using the bypass flow in a dual throat nozzle. J Mech Sci Technol 35(08):3435–3443
2. Jain S, Roy S, Gupta D, Kumar V, Kumar N (2015) Study on fluidic thrust vectoring techniques for application in V/STOL aircrafts. In: SAE technical paper
3. Wu K, Kim TH, Kim HD (2021) Visualization and analysis on the thrust vectoring control in three-dimensional dual-throat nozzles. Visual Soc Jpn 24:891–915
4. Wang Y, Xu J, Huang S, Lin Y, Jiang J (2019) Computational study of axisymmetric divergent bypass dual throat nozzle. Int J Aerosp Sci Technol 86:177–190
5. Wang YS, Xu JL, Huang S (2017) Study of starting problem of axisymmetric divergent dual throat nozzle. J Eng Gas Turb Power 139(6):062602
6. Wu KX, Kim TH, Kim HD (2021) Numerical study of fluidic thrust vector control using dual throat nozzle. J Appl Fluid Mech 14(1):73–87
7. Flamm JD, Deere KA, Mason ML, Berrier BL, Johnson SK (2006) Experimental study of an axisymmetric dual throat fluidic thrust vectoring nozzle for supersonic aircraft application. In: Proceedings of the 3rd AIAA flow control conference
8. Jain S, Roy S, Gupta D, Kumar V, Kumar N (2006) Design enhancements of the two-dimensional, dual throat fluidic thrust vectoring nozzle concept. In: Proceedings of the 3rd AIAA flow control conference, AIAA 2006–3701
9. Bogadi S, Sridhar BTN (2019) Decay of supersonic rectangular jet issuing from a nozzle with diagonal expansion ramps. Therm Sci 23(6B):3929–3940
10. Wang Y, Xu J, Huang S, Lin Y, Jiang J (2019) Experimental and numerical investigation of an axisymmetric divergent dual throat nozzle. J Aerospace Eng 234:563–572

Experimental, Theoretical and Numerical Study of Aluminum 6061–Polyurethane Foam Sandwich Composite for Space Ground System Infrastructure



Manish Sharma, Sreelakshmi Sandeep, Susil Kumar Nayak, S. Sankaran, C. Anil Kumar, and R. Ram Kumar

Abstract Ground infrastructure for space launch systems is designed against thermal, over pressure, acoustic and vibration loads. This paper focuses on studying the properties of aluminum–polyurethane foam (AL-PUF) sandwich composite using experiments and computational methods for precise prediction of behavior of material for space-based applications. AL-PUF panels were subjected to quarter point loaded four-point bending test to obtain the deflection for a range of loads in order to study the mechanical properties of the material. A theoretical model of four-point bending test, its associated loads and deflections are also described in this study. A computational model (FEM) of AL-PUF specimen under four-point bending test was developed to find deflection of material under a range of loads and subsequently obtain modulus of elasticity of the material. The modulus of elasticity calculated using experimental (0.53 GPa), theoretical (0.551 GPa) and numerical data (0.553 GPa) was found to be in agreement. The core shear stress and facing bending stress were obtained to be 0.20 and 14.89 MPa respectively. Further, specimens of the material were mounted to downstream of nozzle exit of a launch vehicle stage and subjected to different heat fluxes to study the behavior of material under thermal loads. A transient thermal model of the material specimen under radiative heat fluxes was developed to numerically (CFD) predict the results of experiments, and it was found that epoxy adhesive undergoes phase change including melting, burning and material degradation. The experimental data were in agreement with the results obtained numerically using CFD.

Keywords Aluminum–PUF · Four-point bending · Thermal load · Finite element method · Computational fluid dynamics

M. Sharma (✉) · S. Sandeep · S. K. Nayak · S. Sankaran · C. A. Kumar · R. R. Kumar
Satish Dhawan Space Center, SHAR, Sriharikota, India
e-mail: manishsharma13439@gmail.com

© The Author(s), under exclusive license to Springer Nature Singapore Pte Ltd. 2024

S. Singh et al. (eds.), *Recent Advances in Aerospace Engineering*, Lecture Notes in Mechanical Engineering, https://doi.org/10.1007/978-981-97-1306-6_34

1 Introduction

Sandwich composites find a wide variety of structural applications due to low cost and high strength-to-weight ratio. Sandwich composite panels consists of two thin high stiffness face sheets, generally made of metals or composite laminates, and a thicker core, usually made of low-density materials such as honeycombs, balsa wood, cellular foams, or trusses sandwiched between face sheets using an adhesive material. The sandwiched composite thus has the properties of both the face sheets and core enabling the material to resist the load applied. Extensive computational and analytical studies on different types of sandwich composites have been conducted in the past few decades. Mohamed et al. [1] evaluated polyurethane composite structure insulated panels for domestic structural purposes. He found that vacuum-assisted resin transfer molding yielded a higher strength to composite panels. Tabatabaiefar et al. [2] studied sandwiched panels made of polystyrene/cement mixed core and cement face sheet and found that the material has high specific strength. Goettner and Reimerdes [3] studied the properties of sandwich composites with different core materials for post-impact scenarios and evaluated the decline in bending strength with crack initiation location. Fajrin et al. [4] studied the relation between theoretical and experimental four-point bending in hybrid sandwich composite structure. Balıkoğlu et al. [5] concluded that the high specific strength and corrosion restraint glass fiber/bisphenol-A epoxy resin face sheet is superior for making wind turbine blades under moist, humid and salty environment. Chuda-Kowalska et al. [6] calculated the shear rigidity of PUF and metal-sandwiched structure and developed an FEM model to validate the experimental results.

The present study is focused on AL-PUF sandwich composite consisting of aluminum 6061 face sheets and low-density polyurethane foam as the core material bonded to the face sheet using epoxy-based adhesive, as shown in Fig. 1. The properties of panels made of AL-PUF sandwich composite are studied in this paper using experimental methods and computational and theoretical models.

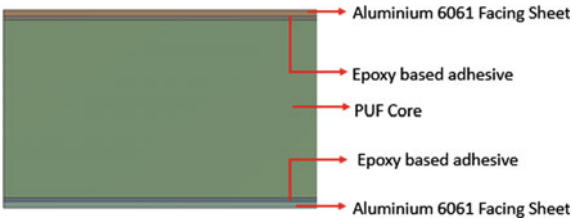


Fig. 1 AL-PUF composite

2 Theoretical Model of Deflection Under Four-Point Bending

According to ASTM C 393-00, describing the standard test method for flexural properties of sandwich constructions, the deflection at the center of sandwich panels under four-point bending test is the sum of deflection due to bending and shear. For a composite panel of bending stiffness D, and shear rigidity U with span length L, the deflection at the mid-span (δ) when a total load P is applied in a four-point bending test of quarter point loading is given by Eq. 1.

$$\delta = \frac{11PL^3}{768D} + \frac{PL}{8U} \tag{1}$$

The bending stiffness of the material is majorly contributed by the face sheet of the panel while the shear rigidity is mainly due to the core material. Hence, Eq. (1) can be written as Eq. (2) where D_f is the bending stiffness of the face sheet material and U_c is the shear rigidity of the core.

$$\delta = \frac{11PL^3}{768D_f} + \frac{PL}{8U_c} \tag{2}$$

For a composite panel specimen of total thickness d, core thickness c and breadth b, made using the same facing material of modulus E_f, the bending stiffness of the facing is calculated using Eq. (3). The shear rigidity of the core of shear modulus G for the same specimen is calculated using Eq. (4).

$$D = E_f \frac{\left(d^3 - c^3\right)}{12} \tag{3}$$

$$U = \frac{G(d+c)^2 b}{4c} \tag{4}$$

Modulus of elasticity for the composite panel is given by Eq. (5):

$$\mathrm{E} = \frac{P}{\delta} \frac{L^3}{4\mathrm{b}d^3} \tag{5}$$

Here, $\frac{P}{\delta}$ is the slope of load versus deflection graph. The schematic diagram of the bending test is shown in Fig. 2.

The core shear stress, τ, for a failure load P is calculated using Eq. (6):

$$\tau = \frac{P}{(d+c)b} \tag{6}$$

The facing bending stress, σ, for a failure load P, is given by Eq. (7):

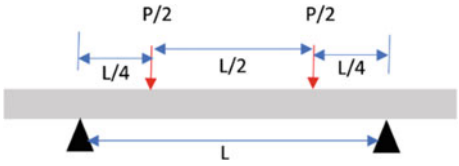


Fig. 2 Schematic of four-point bending—quarter point loading

$$\sigma = \frac{PL}{2t(d+c)b} \tag{7}$$

3 Materials and Methods for Experiments

Bending Test: Sandwich panel of AL-PUF of span length 360 mm, breadth 45 mm and total thickness 32.4 mm with a core thickness 30 mm was subjected to four-point bending with quarter point loading in universal testing machine. The applied load was increased continuously and gradually until the composite panel failed. The testing of the composite panel is shown in Fig. 3. Table 1 gives the properties of the materials used in making AL-PUF sandwich composite.

Thermal Test: AL-PUF specimen with dimension of 800 mm × 425 mm × 32.4 mm was mounted at an angle from a source of heat flux (from launch vehicle propellant

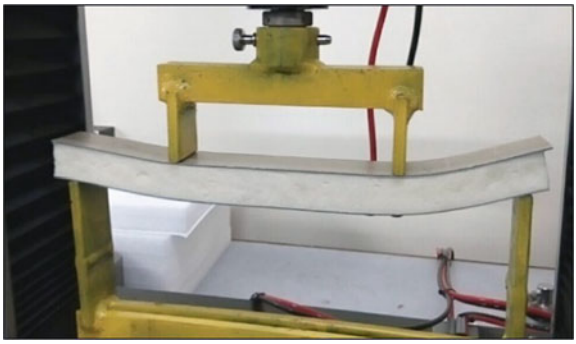


Fig. 3 Four-point bending test of AL-PUF panel

Table 1 Properties of materials

Properties	Aluminum 6061	Low-density polyurethane	Epoxy-based adhesive
Density	2750 kg/m^3	36 kg/m^3	1160 kg/m^3
Young's modulus	69 GPa	3.08 MPa	1.4 MPa
Shear modulus	27 GPa	1.34 MPa	0.5 MPa
Poisson's ratio	0.33	0.36	0.35

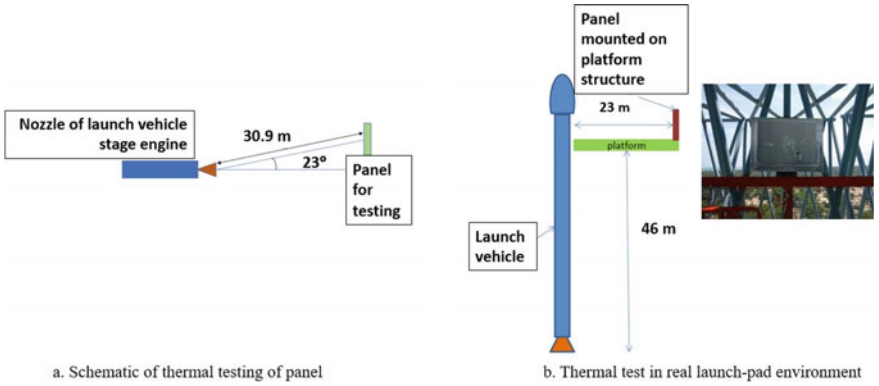


Fig. 4 Schematic of thermal tests

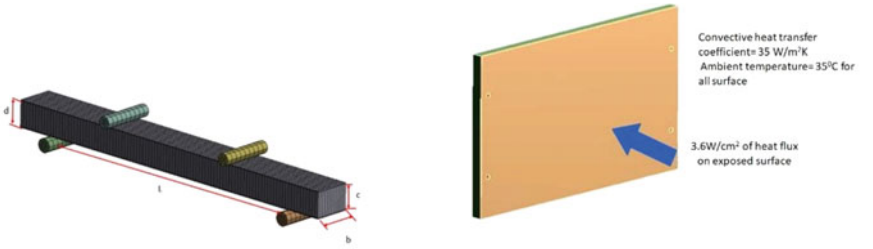
stage firing test) of 3.6 W/cm^2, as shown in Fig. 4a. The temperature at different locations was measured using thermocouples fixed at different locations. Another test was conducted at launch pad by mounting Al-PUF panel of similar dimensions on a platform which was exposed to launch liftoff. The schematic of the same is shown in Fig. 4b. A similar setup but a weaker rocket engine was used to obtain the surface temperature of AL-PUF panel when exposed to it and study the effects of exposure to weaker heat flux.

4 Computational Model

Geometry and Computational Grid: Structural analysis and thermal analysis are conducted using 3-D model with dimensions given in Table 2. Structured mesh of quadrilateral cells with cell size of 0.001 m is used for all the analyses as shown in Fig. 5

Table 2 Dimensions of the composite panel used in the analysis for various cases

SR No	Analysis	Dimensions			
		Length (L) (mm)	Breadth (b) (mm)	Total thickness (d) (mm)	Core thickness (c) (mm)
1	Four-point bending	360 (span length)	45	32.4	30
2	Thermal analysis	800	425	32.4	30



a. Dimensions marked in computational model of bending test b. Boundary conditions of computational model for thermal test

Fig. 5 Dimensions and boundary conditions for computational models

Material Modeling: Material modeling was done in ANSYS Composite PrepPost (ACP). Properties of materials are defined in Table 1. A surface was created, directional properties were defined on it, and it was meshed. Material and their singular thickness were assigned, and directions of properties were defined for each individual material. Laminates were created by defining orientation of the stacking. Properties of ply were defined, and sub-laminate was generated. Stacking different layers of sub-laminate with the defined thickness gave the layered sandwich composite with desired dimensions.

Boundary Conditions and Material Properties: A transient structural model was used for the bending tests. Load was applied on the quarter points for four-point bending tests. The failure of the composite panel was checked with respect to maximum stress, maximum strain, Tsai–Hill and Tsai–Wu criteria. The bending tests were modeled such that the 3-D composite model was placed on fixed rollers with cross-heads of constant velocity, i.e., 0.025 mm/min (as per ASTM standards). The interface of mechanical rollers and the face sheet was made frictional with the standard coefficient of 0.2 for metal-to-metal contact. The overall setup is shown in the Fig. 5. ACP and ANSYS Mechanical Transient Structural Code were coupled to run the simulations. The properties used for facing sheet, adhesive and core materials are given in Table 1, and constants used for defining failure criteria are given in Table 3. A multiphase analysis was run by coupling ACP with ANSYS Fluent for predicting the behavior of material in thermal test. Details of 3-D model and boundary conditions used to recreate the experiment are shown in Fig. 5. A transient-state model with viscous laminar flow for simulating melting and phase change was developed using the thermal properties of constituent materials as given in Table 3. Front and side faces were exposed to radiative heat transfer while all other faces exposed to the environment were subjected to convective heat transfer. Gravity and energy equation were included in the model. Pressure-based solver was used to obtain the solution. The analysis was run for 110 s.

Table 3 Properties of materials for modeling

Failure criteria constants	Aluminum 6061	Low-density polyurethane	Adhesive
Strain limits	Tensile X: 0.0244 Tensile Y: 0.0038 Tensile Z: 0.0038 Compressive: − 0.015 Compressive: − 0.0125 Compressive: − 0.0125 Shear XY: 0.015 Shear YZ: 0.012 Shear ZX: 0.012	von Mises: 0.01	
Tsai–Wu constants	XY: − 1 YZ: − 1 ZX: − 1	–	
Puck constants	Compressive Inclination XZ: 0.25 Compressive Inclination YZ: 0.2 Tensile Inclination XZ: 0.3 Tensile Inclination YZ: 0.2	–	
Thermal conductivity	202. 4 W/m K	0.04 W/m K	0.35 W/m K
Specific heat	871 J/kg K	5242 J/kg K	1812 J/kg K
Melting temperature/ phase change/ decomposition temperature	600 °C (Loses its properties at 400 °C)	230 °C (Loses its properties)	Solidus = 110 °C Liquidus = 115 °C

5 Results and Discussion

Load Versus Deflection Behavior of the Material

AL-PUF under four-point bending experiment showed a linear load versus deformation behavior until 5 mm of deformation, after which the material behaved nonlinearly. The material failure was observed at 10 mm of deformation under a load of 558 N as shown in Fig. 6. The 3-D model subjected to a four-point bending of quarter point loading is modeled computationally for a range of loads in the linear region of the material, i.e., before it fails. The deflection caused is compared with that predicted using theoretical model by Eq. 2 and experimental results. The numerical results, theoretical results and experimental data were found to be in excellent agreement as shown in Fig. 6.

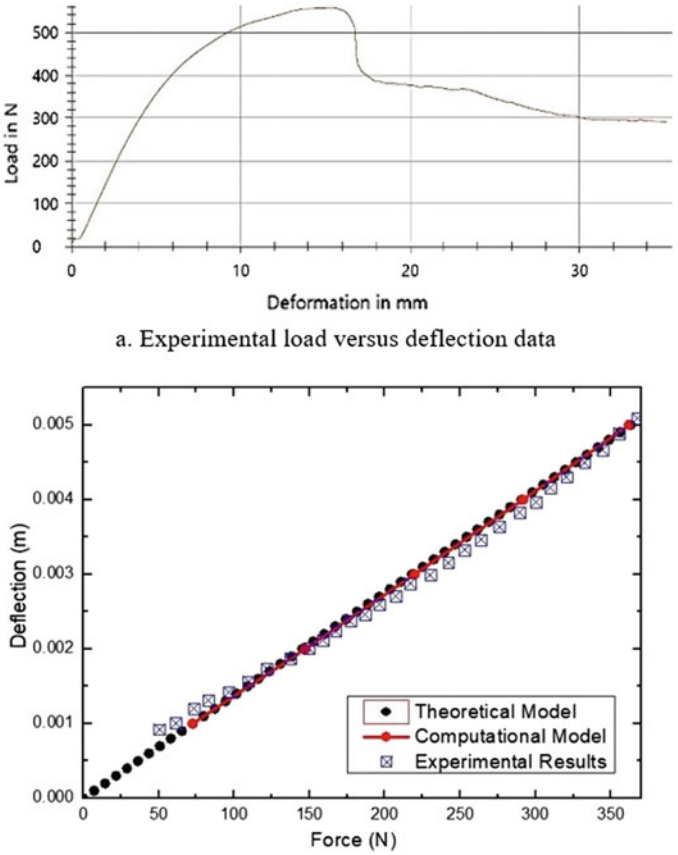


Fig. 6 Load versus deflection data for four-point bending test

Mechanical Properties of the Material

The core shear stress and facing bending stress as obtained from experimental data using Eqs. 6 and 7, respectively, were 0.20 and 14.89 MPa, respectively. The modulus of elasticity calculated using experimental (0.53 GPa), theoretical (0.551 GPa) and numerical data (0.553 GPa) as shown in Fig. 6, using Eq. 5, were seen to be in agreement.

Face Sheet Conditions and Overall Factor of Safety of the Composite

It can be seen in Fig. 7a that the stress concentration is high in the contact region and the regions between the two adjacent rollers are being affected the most. The overall factor of safety of the composite is shown in the Fig. 7b. As per NASA 5005D [7], all plastics, rubbers, composites should have a FOS of 5 on them for design load of ground systems for human space programs. Values below 5 are failed regions.

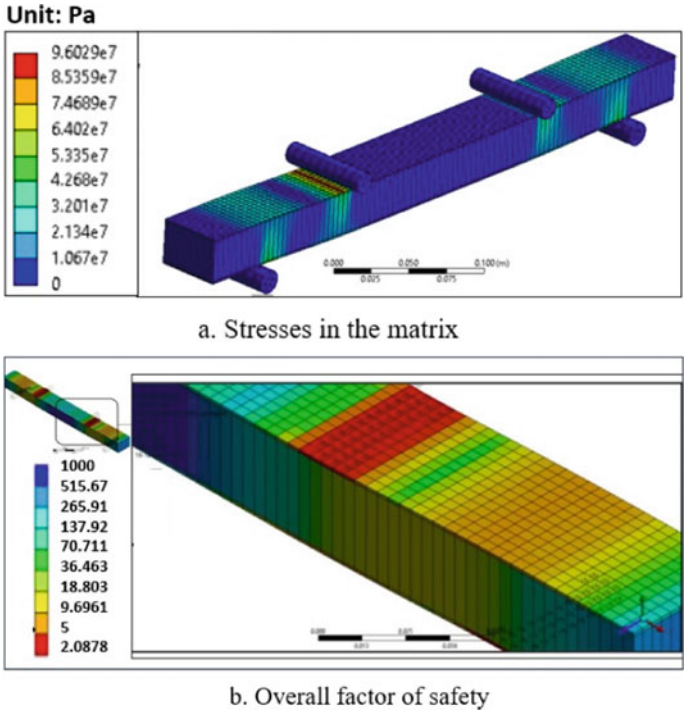


Fig. 7 Stresses in matrix and overall factor of safety

Tsai Hill and Tsai Wu Failure Criteria

Figure 8a captures the stresses due to the drastic change in the composite interfaces and initiation of delamination in the individual components such as the difference in directional strength in buildup direction and its perpendicular directions. Tsai–hill and Tsai–Wu failures are predominant if there is a difference in the directional property of the composite as in the interface. The elements/locations are highlighted with darker color in Fig. 8a. Figure 8b and c show the failure of the material according to Tsai–Hill and Tsai–Wu criteria and maximum shear criteria, respectively. Regions with values above 1 are failed.

Results of Thermal Analysis

Figure 9a shows the graph of temperature versus time obtained from CFD analysis and experiment in which the panel was exposed at an angle to the launch vehicle stage firing test. It shows a phase change in epoxy material which includes melting, burning and material degradation. The phase change started at ~ 25 s and lasted up to 65 s in the CFD analysis, and same behavior is seen in the sensor data as shown in Fig. 9a. Another test involved exposing the material to launch liftoff in launch pad. The experimental data are compared with computational results to ensure that the model is able to predict the behavior of AL-PUF panel. The front face temperature

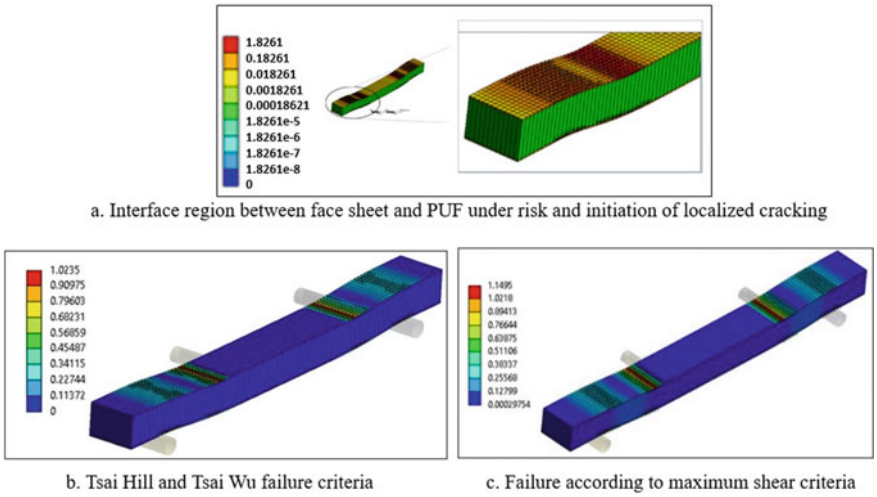


Fig. 8 Failure of the material

is shown in Fig. 9b. The peak temperature of 45 °C was achieved within 10 s of exposure to the launch. Using the thermal model, front face temperature was obtained computationally as shown in Fig. 9c which is in agreement with experimental data in Fig. 9b. The temperature distribution on the front face after completion of simulation is shown in Fig. 9d, and it can be seen that back face or the non-exposed face temperature reached 34.26 °C which is similar to experimental results. A similar experiment was conducted with the same orientation of the panel as shown in Fig. 4b, but with a weaker rocket engine gave the front face panel temperature as shown in Fig. 9e. With the same model developed for thermal test, the front face temperatures were numerically simulated. As seen in Fig. 9e, both results are consistent, proving the validity of the model.

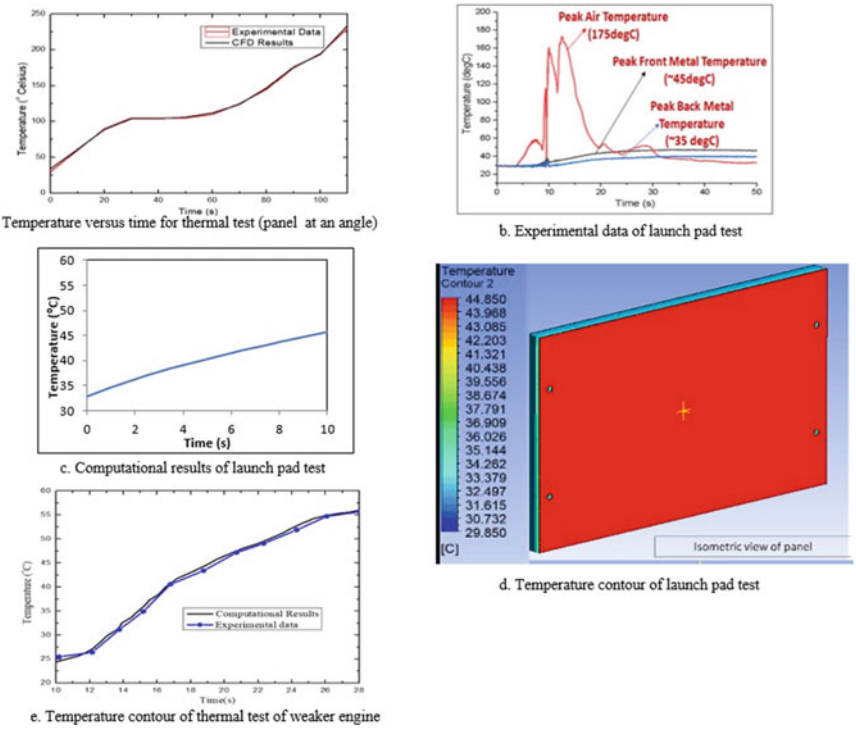


Fig. 9 Results from thermal test—experimental data and numerical analysis

6 Conclusion

To study the properties and qualify Al–PUF composite sandwiched structures for space utilization, four-point bending test was conducted. In order to validate the experiments, numerical (FEM) and theoretical analyses were performed for four-point bending tests. A 3-D model of the composite material was developed on which the structural analysis of the bending test was performed. The load versus deflection graph was studied. Moduli of elasticity obtained using experimental, numerical (FEM) and theoretical methods were 0.53, 0.553 and 0.551 GPa, respectively, and thus found to be in agreement. The failure analysis of the material using FEM was conducted using ANSYS Composite PrepPost (ACP). The results were evaluated on the basis of maximum stress, core failure, delamination, Tsai–Hill and Tsai–Wu criteria, and it was found that material failed due to delamination in the locations of maximum stresses. Overall factor of safety based on NASA Code 5005 D for launch pad application was also studied. The thermal integrity of the material was tested by subjecting AL-PUF panels to different types of intense heat fluxes from the thermal test using a launch vehicle stage. The peak temperature, material phase

change and degradation were studied. The data obtained during test were also validated with numerical study (CFD) by developing a 3-D model and providing the same boundary conditions as of the test environment.

Funding Not applicable.

References

1. Mohamed M, Hussein R, Abutunis A, Huo Z, Chandrashekhara K, Sneed L (2016) Manufacturing and evaluation of polyurethane composite structural insulated panels. J Sandwich Struct Mater 18(6):769–789
2. Tabatabaiefar HR, Mansoury B, Zand MJK, Potter D (2017) Mechanical properties of sandwich panels constructed from polystyrene/cement mixed cores and thin cement sheet facings. J Sandwich Struct Mater 19(4):456–481
3. Goettner W, Reimerdes HG (2006) Bending strength of sandwich panels with different cores after impact. In: Gdoutos EE (ed) Fracture of nano and engineering materials and structures. Springer, Dordrecht
4. Fajrin J, Zhuge Y, Wang H, Bullen F (2017) Experimental and theoretical deflections of hybrid composite sandwich panel under four-point bending load. Civil Eng Dimen 19(1):29–35
5. Balıkoğlu F, Demircioğlu TK, Işiktaş A (2021) Mechanical properties of sandwich composites used for aerofoil shell structures of wind turbine blade. Int J Surv Eng Technol 5(1):26–37
6. Chuda-Kowalska M, Pozorski Z, Garstecki A (2010) Experimental determination of shear rigidity of sandwich panels with soft core. In: Modern building materials, structures and techniques, proceedings of the international conference; vol 10. Vilnius Gediminas Technical University, Department of Construction Economics and Property, Vilnius, pp 56–63
7. NASA code of design of launch pads. NASA 5005D

Effects of Reinforcements on Mechanical and Microstructural Properties of Aerospace Al–Li Alloy-Based Composites: A Review



Freedon Daniel and Gyander Ghangas

Abstract Composites are suitable materials to fulfil the multifunctional applications for the requirements of modern industry. The composites are fabricated by combining two or more materials whilst taking benefit of their individual properties. The composites fabricated with aluminium as matrix materials are known as aluminium metal matrix composites (AMC). The physical and mechanical qualities provided by AMCs for future material applications are remarkable. As per research findings, the inclusion of reinforcements into the metal-based matrices enhances the characteristics such as strength, stiffness, wear, fatigue and creep. Generally, ceramic particles are used as inclusions to enhance the above said properties of AMCs. Addition of Li to aluminium causes a drop in density and an increase in the elastic modulus along with significant improvement in strength. Al–Li alloys attract researchers because of their excellent wettability and the ability to be hardened by precipitation hardening. When ceramic particles are included in Al–Li alloys as reinforcements, the performance limitations of the alloys present a substantial improvement. The present article attempts to give an overview of the impacts of various types of reinforcements in Al–Li alloys. The review's primary focus is to reveal the effects of different ceramic reinforcements such as SiC, B_4C, TiB_2 and Si_3N_4 on the mechanical and metallurgical characteristics of AMCs of Al–Li alloys.

Keywords Aluminium–lithium alloys · Aluminium matrix composites · Reinforcements · Characterization · Mechanical properties

F. Daniel · G. Ghangas (✉)
Department of Mechanical Engineering, SRM Institute of Science and Technology, Delhi NCR Campus, Ghaziabad 201204, India
e-mail: ghangas01@gmail.com

© The Author(s), under exclusive license to Springer Nature Singapore Pte Ltd. 2024

S. Singh et al. (eds.), *Recent Advances in Aerospace Engineering*, Lecture Notes in Mechanical Engineering, https://doi.org/10.1007/978-981-97-1306-6_35

1 Introduction

Cast aluminium alloys demonstrated good casting properties such as comparatively high strength, sufficient stiffness and lower density. These alloys are regularly utilized for automobile, aviation and naval applications because of their outstanding casting characteristics [1, 2]. These can be modified into metal matrix composites (MMCs) for high-duty applications. MMCs are also suitable for characteristics such as enhanced ratio of strength and weight, precipitation strengthening and improved corrosion resistance [3, 4].

There are four different types of MMCs, as presented in Fig. 1. To make particle-reinforced composites, melt stirring is one of the most popular and cost-effective manufacturing method, which is known as stir casting. However, many process variables need to be regulated to accomplish high microstructural integrity using stir casting [5]. When non-optimal parameters are used, the resulting microstructures may be of low density and bad quality, which may result in poor mechanical characteristics [6–8].

When aluminium alloys are used as metal matrices, MMCs are known as aluminium metal matrix composites (AMCs). AMCs achieved widespread adoption over the last 30 years for their industrial applications [9, 10]. The reinforcement types embedded into the base matrix directly impact the overall characteristics of AMCs. Because of this, the choices of reinforcements need to provide an elevated strength-to-weight proportion and a large modulus ratio in the new composite [11, 12]. Ceramic nanoparticles have exceptional properties such as good hardness, refractoriness, enhanced wear strength and good compressive strength. These are widely used as reinforcements in AMCs. Such ceramic nanoparticles include ZnO, ZrO_2, MgO, B_4C, Al_2O_3, TiB_2, SiC, Si_3N_4, graphene, titanium carbide (TiC), etc. Using nanoparticles to reinforce light metals like aluminium led to a rise in specific properties of base metal [13–16]. Matrices are typically constructed using lightweight metallic materials such as aluminium, magnesium, or titanium due to their low density [17, 18].

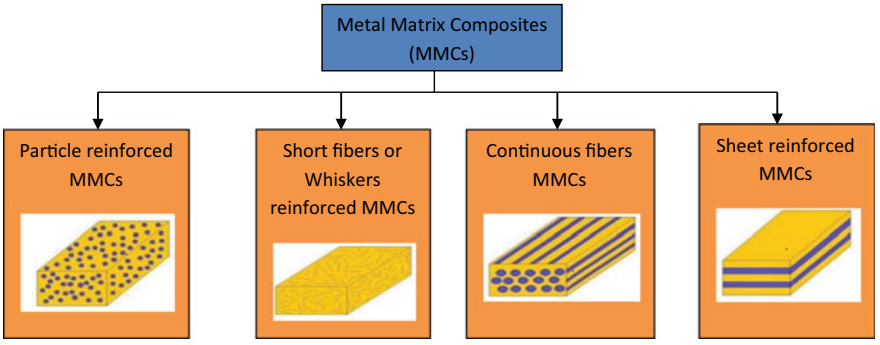


Fig. 1 Types of metal matrix composites

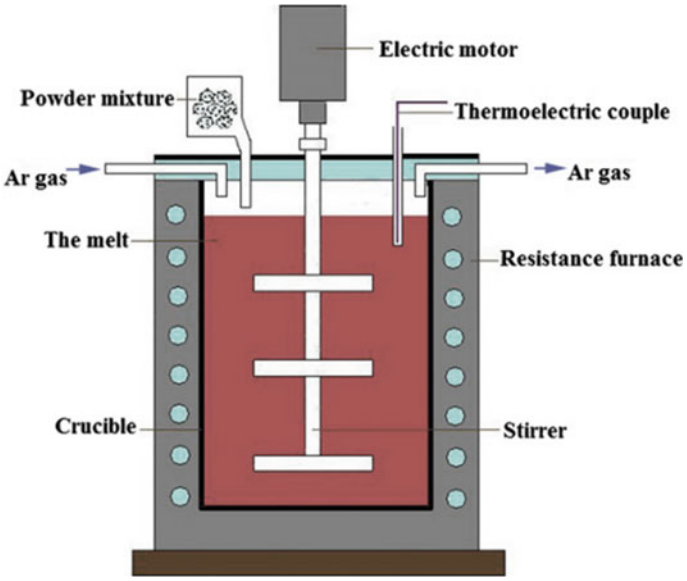


Fig. 2 Solid–liquid mixed stir casting process [3]

Stir casting, squeeze casting, powder metallurgy, compo casting and pressure infiltration process are the different casting processes that have been utilized for producing AMC. At the same time, these casting methods always form the matrix–reinforcement compounds and manoeuvres at extremely high temperatures [19–21]. Figure 2 presents the stir casting set-up.

Al–Li alloys with low density have been developed due to the ongoing need for improved fuel economy in the aeronautical and vehicle sectors. The addition of 1% Li to aluminium decreased density by roughly 3%, and elastic modulus increased by 6%. This also leads to an improvement in the material's strength and stiffness as well [22]. The fact that lithium not only lessens the density of the alloy but also adds to gains in both its strength and its elastic modulus has contributed to the rise in popularity of metals made of aluminium and lithium. This combination results in considerable gains in specific strength (calculated by dividing the total strength by the density of material) and specific stiffness (ratio of modulus of elasticity and density) [23, 24]. It is reasonable to consider the possibility of adding ceramic particles to Al–Li composites to increase the material's strength and stiffness whereas some recent researches have been conducted on materials based on Al–Li alloys [25, 26].

Extensive research work has been done in previous years on the variation of nature, types and size of reinforcements for AMCs. The researchers discovered the effects of above said parameters on the microstructure, mechanical, tribological characteristics. The literature also presented the fabrication processes, processing of AMCs, choosing of both matrix and reinforcement, techniques accessible for the characterization of AMCs. So, the current review presents effects of various ceramic reinforcements on

Al–Li alloys on microstructure, mechanical behaviour like hardness, tensile strength and wears behaviour after consolidation.

2 Literature Review

The properties of the Al–Li composites depend on various factors like fabrication process, reinforcement size and volume %, apart from the type of matrix and reinforcement employed. It can be stated by the literature survey that stir casting is most economical and most straightforward method to fabricate MMCs. The usage of Li for the fabrication of composites is quite hazardous, but a modest and low-cost experimental set-up can be utilized by transforming the old stir casting practice for the production of Al–Li-based composites [6].

2.1 Microstructure

Microstructure plays a critical part in describing the characteristics of materials and composites. The microstructure changes during the fabrication of AMCs always attract researchers for study. As per Chen et al. [27], the optical micrographs with various magnifications of the as-cast in situ TiB_2/Al–Li–Cu composite show dendritic α-Al grains with a reduction in grain size when compared to base alloy. Figure 3 shows the matrix–reinforcement interface clearly, which indicates the thermodynamic constancy of the TiB_2 elements with a strong bond between particles and matrix. Such tough interfacial matrix–reinforcement bonding leads to enhanced composite performance in relations of mechanical characteristics and load-bearing ability. Analysis using high-resolution transmission electron microscopy (HRTEM) shows that the lattice ill-match is minute with small strain at the boundary, which seems like a semi-coherent interface [28].

The microstructure of the Al–Li–SiC composites fabricated by Bauri and Surappa [6] revealed that with 8, 12 and 18 vol% SiC particles, the particle size decreased with increasing amounts of SiC content. The dispersal of SiC particles in the composites under extrusion condition is depicted in Fig. 4a–c. For MMC 8, the distribution is quite uniform, whereas for MMC 12 and MMC 18, some particle clustering is observed. On the other hand, some cracking at the interfaces in certain local locations of MMC 18 was observed. This is because of the elevated thermal stresses engendered at the interface whilst cooling due to significant variance in the temperature expansion coefficient amongst the particles and the matrix.

It is reasonable to anticipate that the more considerable volume proportion of particles to cause greater thermal stresses. In addition, a cluster of SiC particles was found in MMC 18, as mentioned previously. These clusters can potentially produce large thermal stresses, which may cause cracking at the interface [6]. The process of thermal stress relaxing at lower than room temperature for MMC made up of

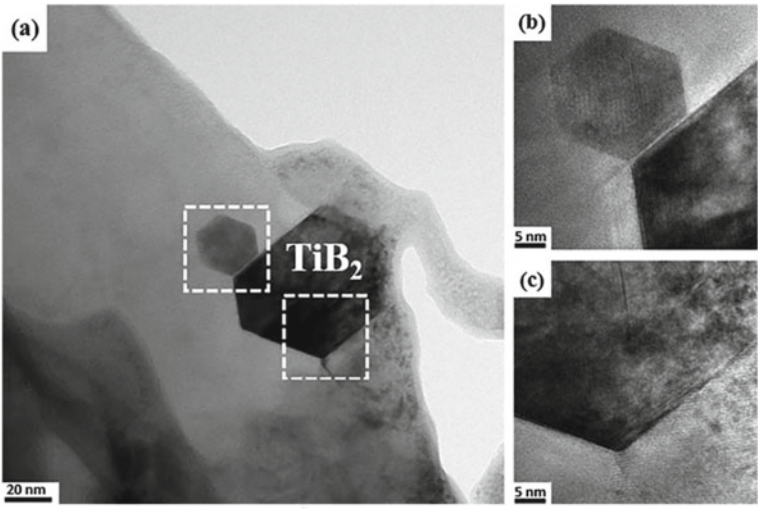


Fig. 3 Analysis of nano-scale TiB_2 particles: **a** TEM analysis at the interface, **b** and **c** HRTEM pictures TiB_2—matrix interface [28]

Al 8090 with 15% SiC was examined by Gutiérrez-Urrutia et al. [29] by using the method of internal friction. An interior friction crowning is evident, connected with the easing of thermal stresses surrounding the reinforced particles by microplastic distortion [29]. The dry sliding wear behaviour of an Al–Li–Si_3N_4 MMC was investigated by Raju and Balakrishnan [30] at a temperature of 100 °C; delamination wear with pits was revealed in the results. Fine grooves, the consequence of abrasive wear, were discovered at 200 °C. At a temperature of 300 °C, abrasive wear, as well as oxidation wear, was observable [30]. Post-fabrication of the Al 8090 + 15% SiC composite, it was observed by Rodríguez et al. [31] that the existence of lithium in the aluminium matrix enhances the strength of such substances by the precipitation of the (Al_3Li) phase within the matrix [32]. Shen et al. [33] observed that through the utilization of the controlled melt synthesis methodology, it was possible to produce the in situ TiB_2 elements reinforced Al–3.3Cu–1.0Li–0.60Mg–0.40Ag–0.14Zr matrix composite. The composite experienced a considerable reduction in its average particle size, and the emergence of the δ' (Al_3Li) phase was stimulated inside the material [34]. Microstructure of 1 wt.% of CNTs sintered Al–Li composite was studied by Jia et al. [34], and the equiaxed Al–Li alloying matrix, Al_2Cu phase on the grain boundary and needle-like Al_2Cu_4Li precipitations within the matrix were revealed [35].

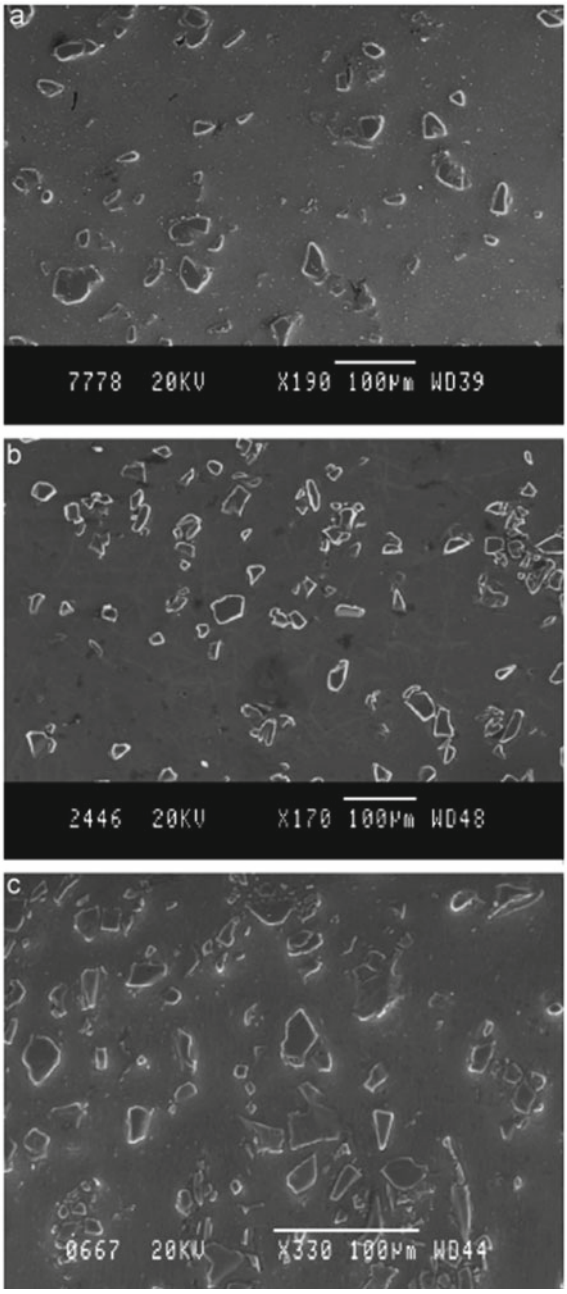


Fig. 4 **a–c** SEM micrographs of the composites in extruded condition exhibiting SiC particle distribution; **a** MMC 8; **b** MMC 12 and **c** MMC 18 [6]

2.2 Mechanical Behaviour

It was observed that in situ TiB_2 particles reinforced Al–3.3Cu–1.0Li–0.60Mg–0.40Ag–0.14Zr matrix composite manufactured using the controlled melt synthesis approach was found to exhibit a significant increase in the enhancement of its mechanical characteristics [36]. The use of ceramic materials provides advancements in mechanical characteristics, and Al/Li–SiC composite materials display a modulus of elasticity over 100 GPa with comparative densities around 2.6, which leads to 50% higher specific stiffness than that of basic Al and Ti alloys [37]. At ambient temperature, the unreinforced matrix's modulus of elasticity was around 80 GPa. Still, the ceramic reinforcements improved such level for composite up to 101 GPa. Various properties for different Al–Li composites have been tabulated in Table 1.

Hardness

Bauri and Surappa [26] examined both the as-cast and the extruded conditions of the Al–Li/SiC composite produced by the stir casting technique. They reported that the microhardness of all the composites examined was greater than that of the unreinforced matrix. Because of the inappropriate thermal expansion coefficients of the matrix and the reinforcement, composite matrices tend to have a larger dislocation density. Because of this, the composites have a greater degree of hardness. As was just said, the existence of SiC particles helps to achieve a more refined grain size [26]. Nano-indentation experiments with Berkovich tips were performed on an Al–Li 8090 + 15% SiC composite by Rodríguez et al. [35], and it was shown that the aluminium matrix hardness was greater over the alloy without reinforcement, and the measurements fell with the rise of the distance to the closest reinforcements [36]. Al–Li–SiCp composite was manufactured by Bauri and Surappa [37] through the stir casting method. Compared to the matrix without reinforcement, peak hardness in composites is much greater, and maximum aging time is significantly shorter [38]. The in situ TiB_2 particles reinforced Al–3.3Li–1.2Cu matrix composite was synthesized by Wu et al. [38] via the controllable melt synthesis route composite. A quick rise in hardness from 115 HV (as-quenched) to 141 HV after aging for 1 h and a robust age-hardening output was discovered. After ageing at 175 °C for 214 h, the material reached its maximal hardness, which was roughly twice that of the as-quenched state [39]. As per Singh et al. [39] the hardness, tensile properties of Al–SiC–B_4C hybrid composite enhance with the increase of B_4C within the matrix [40]. Al–Li cast alloy and Al–Li/B_4C composite containing 2, 5 and 10 wt.% B_4C composites were fabricated by Patil et al. [40] using modified version of conventional stir casting method. An increase up to 25 and 32% in microhardness and macrohardness values, respectively, from unreinforced alloy to 2% B_4C reinforced composite was observed [41]. Findik [41] studied the microhardness and wear properties of AA2196 alloy reinforced with B_4C and SiC reinforcements as single and hybrid ceramic composites using powder metallurgy method. The dual ceramic reinforced composites with AA2196 matrix shows superior performance compared to the

Table 1 Various properties of different composites

Fabrication method	Materials	Density (gm/cm^3)	Hardness (VHN)	Tensile/yield strength (MPa)	Compressive strength (MPa)	Elongation (%)	Modulus of elasticity (GPa)	References
Accumulative roll bonding	Al–Li/B_4C; 3 cycle	2.532		230		8.9		[33]
	Al–Li/B_4C; 6 cycle	2.542		255		10		
	Al–Li/B_4C; 8 cycle	2.547		384		10.7	87	
Stir casting method	Al 8090 alloy (extruded)	2.54	93	303	517		79	[6]
	Al 8090 + 8% SiC (extruded)	2.58	103	368	633		87	
	Al 8090 + 12% SiC (extruded)	2.6	107	326	618		90	
	Al 8090 + 18% SiC (extruded)	2.62	110	249	532		95	
Spray co-deposition method	Al 8090 alloy			537			80	[32]
	Al 8090 + 17% SiC			507			101	
Spray co-deposition method	Al 8090 T651			581			81	[36]
	Al 8090 + 15% SiC T651			568			102	
Controllable melt synthesis	Al–Cu–Li alloy	2.7	116	397		4.8	74.5	[34]
	TiB_2/Al–Cu–Li	2.76	148	469		3	83	

(continued)

Table 1 (continued)

Fabrication method	Materials	Density (gm/cm^3)	Hardness (VHN)	Tensile/yield strength (MPa)	Compressive strength (MPa)	Elongation (%)	Modulus of elasticity (GPa)	References
Stir casting method	Al 8090 alloy (extruded)	2.54	93		517	34		[38]
	Al–Li + 8% SiC (extruded)	2.58	103		633	27.2		
	Al–Li + 12% SiC (extruded)	2.6	107		618	26		
	Al–Li + 18% SiC (extruded)	2.62	110		532	25.2		

single compositions. Also an increase in hardness is recorded through dual ceramic reinforced composites [42].

Tensile/Compressive Strength

As per Bauri and Surappa [6], in comparison with the unreinforced matrix, the Al–Li–SiC composites that have a smaller volume percent of SiC display a greater ultimate tensile strength (UTS) as well as a higher 0.2% proof stress [6]. Regarding the mechanical characteristics of composites, the reinforcement–matrix contact plays a vital deciding role [31]. The key contributor to the strength of composites is the efficient transmission of stresses from the matrix to the element via boundaries. The Al–Li/ B_4C composites were fabricated by Wang et al. [42] by adopting accumulative roll bonding (ARB), which took place at room temperature. As the number of ARB cycles increased, the material strength and its ductility were enhanced concurrently. The enhanced material characteristics (UTS = 384 MPa, YS = 264 MPa and EL = 10.7%) and upgraded Young's modulus (87 GPa) were attained after eight rounds of the ARB process. Grain refinement enhancing and dislocated reinforcing contributed to the high strength of an Al/B_4C composite corresponding to eight cycles of ARB [33]. Rodríguez et al. [35] stated that the artificial ageing of Al–Li alloy and the Al–Li/SiC composite to attain the peak-aged condition leads to a higher tensile strength of the composite as associated with the alloy [36].

Bauri and Surappa [6] observed that compared to the alloy that has not been reinforced, the compressive strength and 0.2% proof stress of the corresponding SiC composites are much greater. Also, out of the stir cast Al–Li–SiCp composites with various volume percentages of SiC in the extruded state, the Al–Li–8% SiC composite demonstrates a better compressive strength than the alloy without reinforcement as well as the composites (Al–Li–12%SiC and Al–Li–18% SiC). Because Al–Li–8% SiC composite has excellent interfacial bonding, particles are distributed consistently throughout the material. In peak-aged conditions, however, the Al–Li–12% SiC composite has greater compressive strength than the Al–Li–8% SiC composite [6]. According to Medjahed et al. [43], composite strips with Al–Li–Cu–Mg–Zr alloy as matrix reinforced with titanium–carbide (TiC) microparticles which were produced through the accumulative roll bonding (ARB) process, and it was observed that the increase in TiC microparticles to 2 wt.% causes a rise in tensile strength to a peak value of 379.29 MPa [44].

2.3 Wear Behaviour

Employing a pin-on-disc machine, the dry sliding wearing behaviour of 8090Al alloy and the composites fabricated by reinforcement of SiC inclusions with a volume percentage of 8, 12 and 18% in extruded and peak-aged conditions as well were investigated by Bauri and Surappa [45] as shown in Fig. 3c and d. The alloy without reinforcement and the composites have equivalent wear rates in the mild wear regime. However, composites displayed superior wear resistance in the as-extruded form in

the severe wear regime. When it comes to severe wear, increasing the volume fraction of SiC in an extruded condition reduces the composites' wear rate. Also, the wear rate of the 8090 Al–18% SiC composite is greater than the 8090 Al–12% SiC composite [43].

The dry sliding wear behaviour of Al2024 + Li + Si_3N_4 MMC was examined by Gutiérrez-Urrutia et al. [29] at room temperatures of 100, 200 and 300 °C, and it was discovered that the resistance to wear of an Al–Li–Si_3N_4 composite rose with rising speed and temperature, even whilst the load remained the same [29].

During the analysis of dry sliding wear, Rodríguez et al. [31] observed that the reinforcing advantage in Al-8090 + 15 vol% SiCp is restricted to shifting the transition temperature to greater values which was observed for both materials. Even within the moderate wear regime, composite materials' wear rates are much greater than reinforced alloys [32]. According to del Río [46], evolution from mild to simple wear has been discovered at critical levels of pressure, temperature and slipping velocity for the 8090 Al alloy that has been reinforced with 15 vol% of SiC inclusions and without reinforcement alloy [45]. Raju and Balakrishnan [30] concluded that a composite with Li + Si_3N_4 reinforcements had a lower wear rate under conditions of higher load and sliding speed. It was also discovered that the wear rate was expressively higher when the sliding speed was lower. When the load was increased, it did not matter whether a different composite was used since a lower wear rate was recorded [46]. Okumus et al. [47] noted that the friction coefficient for SiC particle-reinforced Al–Li MMC had a greater order of magnitude, and it was hypothesized that this was due to the reason that SiC abrasive particles had penetrated deeper into the worn surfaces [47]. A study was performed by Arumugasamy et al. [48] to assess the performance of Al alloy (8090) reinforced with the fly ash and zirconia through stir casting process. The wear behaviour of ZrO_2 reinforced composites showed better results when compared to double reinforcement with fly ash [48].

3 Conclusions

Different Al–Li alloy-based MMCs have been studied with respect to various performance characteristics. A distinct trend in composite properties was observed, and the following conclusions can be drawn:

- The Al–Li alloy matrix composite reinforced with ceramics exhibits enhancement in mechanical properties such as tensile strength, yield strength, and hardness at the cost of ductility.
- Insignificant alterations were found in the rate of wear of unreinforced alloy and the composites in the mild wear regime. However, in the moderate and severe wear regions, wear rates could be observed falling over the unreinforced alloy, and an increase in wear resistance was evident with a rise in sliding speed and temperature.

- The Al–Li composites' properties depend on various factors like the fabrication process, reinforcement size and volume %, apart from the type of matrix and reinforcement employed.
- Characteristics of low-density Al–Li composites can be advantageously exploited for aerospace industry applications.

The work can be extended in the future for research on fatigue, corrosion and oxidation behaviour of the Al–Li–MMCs for the aerospace applications. More focus is required for the investigation of material properties at nanoscale level to comprehend the effects of interfacial bonding at nano-level for the improvement in the material properties.

Funding Not Applicable.

References

1. Alexopoulos ND, Pantelakis SG (2004) Quality evaluation of A357 cast aluminum alloy specimens subjected to different artificial aging treatment. Mater Des 25(5):7. https://doi.org/10.1016/j.matdes.2003.11.007
2. Ghangas G, Singhal S (2022) Influence of process parameters on mechanical and microstructural property of dissimilar friction stir welded joints of armor aluminium alloys AA7039 and AA5083. Indian J Eng Mater Sci 29(5):686–695
3. Su H, Gao W, Feng Z, Lu Z (2012) Processing, microstructure and tensile properties of nano-sized Al_2O_3 particle reinforced aluminum matrix composites. Mater Des 36:64. https://doi.org/10.1016/j.matdes.2011.11.064
4. Li X, Hao Q, Jie W, Zhou Y (2008) Development of pressure control system in counter gravity casting for large thin-walled A357 aluminum alloy components. Trans Nonferrous Met Soc China 18(4):147. https://doi.org/10.1016/S1003-6326(08)60147-8
5. Rani P, Goyat V, Dhull S, Kadiyan S, Ghangas G (2022) Multi-objective parametric optimization of FSW for mechanical properties of AA5083 joint. Mater Today Proc 65:486. https://doi.org/10.1016/j.matpr.2022.06.486
6. Bauri R, Surappa MK (2007) "Processing and properties of Al–Li–SiCp composites. Sci Technol Adv Mater 8(6):4. https://doi.org/10.1016/j.stam.2007.07.004
7. Nirala A, Soren S, Kumar N, Kaushal DR (2020) A comprehensive review on mechanical properties of Al–B_4C stir casting fabricated composite. Mater Today Proceed 21:172. https://doi.org/10.1016/j.matpr.2019.09.172
8. Dixit M, Mishra RS, Sankaran KK (2008) Structure-property correlations in Al 7050 and Al 7055 high-strength aluminum alloys. Mater Sci Eng A 478(1–2):163–172. https://doi.org/10.1016/j.msea.2007.05.116
9. Surappa MK, Rohatgi PK (1981) Preparation and properties of cast aluminium-ceramic particle composites. J Mater Sci 16(4):983–993. https://doi.org/10.1007/BF00542743
10. Coves Xamena JL (2004) Handbook of aluminum: v. 2: alloy production and materials manufacturing. Choice Rev 41(10):5929. https://doi.org/10.5860/choice.41-5929
11. Goyat V, Ghangas G, Sirohi S, Kumar A, Nain J (2022) A review on mechanical properties of coir based composites. Mater Today Proc 62:1738–1745. https://doi.org/10.1016/J.MATPR.2021.12.252
12. Singh L, Singh B, Saxena KK (2020) Manufacturing techniques for metal matrix composites (MMC): an overview. Adv Mater Process Technol 6(2):441–457. https://doi.org/10.1080/2374068X.2020.1729603

13. Alexopoulos ND, Stylianos A (2011) Impact mechanical behaviour of Al–7Si–Mg (A357) cast aluminum alloy: the effect of artificial aging. Mater Sci Eng A 528(19–20):6303–6312. https://doi.org/10.1016/j.msea.2011.04.086
14. Lai J, Zhang Z, Chen XG (2013) Precipitation strengthening of Al–B_4C metal matrix composites alloyed with Sc and Zr. J Alloys Compd 552:227–235. https://doi.org/10.1016/j.jallcom.2012.10.096
15. Zhang Q, Ma X, Wu G (2013) Interfacial microstructure of SiCp/Al composite produced by the pressureless infiltration technique. Ceram Int 39(5):4893–4897. https://doi.org/10.1016/j.ceramint.2012.11.082
16. Li GR, Zhao YT, Wang HM, Chen G, Dai QX, Cheng XN (2009) Fabrication and properties of in situ ($Al_3Zr + Al_2O_3$)p/A356 composites cast by permanent mould and squeeze casting. J Alloys Compd 471(1–2):530–535. https://doi.org/10.1016/j.jallcom.2008.04.037
17. Yar AA, Montazerian M, Abdizadeh H, Baharvandi HR (2009) Microstructure and mechanical properties of aluminum alloy matrix composite reinforced with nano-particle MgO. J Alloys Compd 484(1–2):400–404. https://doi.org/10.1016/j.jallcom.2009.04.117
18. Wang HY, Jiang QC, Wang Y, Ma BX, Zhao F (2004) Fabrication of TiB_2 participate reinforced magnesium matrix composites by powder metallurgy. Mater Lett 58(27–28):3509–3513. https://doi.org/10.1016/j.matlet.2004.04.038
19. Zhang K, Jang HW, Le QV (2020) Production methods of ceramic-reinforced Al–Li matrix composites: a review. J Compos Compd 2(3):77–84
20. Kumar KKA, Viswanath A, Rajan TPD, Pillai UTS, Pai BC (2014) Physical, mechanical, and tribological attributes of stir-cast AZ91/SiCp composite. Acta Metall Sin 27(2):295–305. https://doi.org/10.1007/s40195-014-0045-3
21. Aruri D, Adepu K, Adepu K, Bazavada K (2013) Wear and mechanical properties of 6061–T6 aluminum alloy surface hybrid composites [(SiC + Gr) and (SiC + Al_2O_3)] fabricated by friction stir processing. J Mater Res Technol 2(4):362–369. https://doi.org/10.1016/j.jmrt.2013.10.004
22. Sankaran KK, Grant NJ (1980) The structure and properties of splat-quenched aluminum alloy 2024 containing lithium additions. Mater Sci Eng 44(2):213–227. https://doi.org/10.1016/0025-5416(80)90122-6
23. Ghangas G, Singhal S, Dixit S, Goyat V, Kadiyan S (2022) Mathematical modeling and optimization of friction stir welding process parameters for armor-grade aluminium alloy. Int J Interact Des Manuf 17:1–18. https://doi.org/10.1007/S12008-022-01000-1/FIGURES/15
24. Srivatsan TS, Lavernia EJ, Eswara Prasad N, Kutumbarao VV (2013) Quasi-static strength, deformation, and fracture behavior of aluminum-lithium alloys. In: Aluminum–Lithium alloys: processing, properties, and applications. https://doi.org/10.1016/B978-0-12-401698-9.00010-0
25. Poza P, Llorca J (1999) Mechanical behavior of Al–Li–SiC composites: part I. Microstructure and tensile deformation. Metall Mater Trans A Phys Metall Mater Sci 30(3):845–855. https://doi.org/10.1007/s11661-999-0078-9
26. Bauri R, Surappa MK (2005) Investigations on serrated flow in 8090 Al alloy and 8090 Al–SiCp composites occurring during dynamic ultra low load micro hardness (DUH) indentation. Mater Sci Eng A 393(1–2):22–26. https://doi.org/10.1016/j.msea.2004.09.060
27. Chen A, Peng Y, Zhang L, Wu G, Li Y (2016) Microstructural evolution and mechanical properties of cast Al–3Li–1.5Cu–0.2Zr alloy during heat treatment. Mater Charact 114:234–242. https://doi.org/10.1016/j.matchar.2016.03.007
28. Tang Y et al (2015) Quantitative study of particle size distribution in an in-situ grown Al–TiB_2 composite by synchrotron X-ray diffraction and electron microscopy. Mater Charact 102:131–136. https://doi.org/10.1016/j.matchar.2015.03.003
29. Gutiérrez-Urrutia I, Nó ML, Juan JS (2004) Internal friction behavior in SiC particle reinforced 8090 Al–Li metal matrix composite. Mater Sci Eng A 370(1–2):555–559. https://doi.org/10.1016/j.msea.2003.07.010
30. Raju K, Balakrishnan M (2021) Statistical approach on high temperature dry sliding wear behavior of Al–Li–Si_3N_4 metal matrix composite. SILICON 14(5):2067–2078. https://doi.org/10.1007/s12633-021-00995-8

31. Rodríguez J, Poza P, Garrido MA, Rico A (2007) Dry sliding wear behaviour of aluminium-lithium alloys reinforced with SiC particles. Wear 262(3–4):292–300. https://doi.org/10.1016/j.wear.2006.05.006
32. Raju K, Balakrishnan M (2022) Dry sliding wear behavior of aluminum metal matrix composite reinforced with lithium and silicon nitride. SILICON 14(1):1–11. https://doi.org/10.1007/s12633-020-00793-8
33. Shen Y, Li X, Hong T, Geng J, Wang H (2016) Effects of TiB_2 particles on microstructure and mechanical properties of an in-situ TiB_2–Al–Cu–Li matrix composite. Mater Sci Eng A 655:265–268. https://doi.org/10.1016/j.msea.2015.12.104
34. Jia L, Liu Y, Xing Z, He G, Lu Z, Zhou Y (2022) Hot deformation behavior of CNTs/Al–Li composite prepared by powder metallurgy. Carbon Lett 32(5):1345–1354. https://doi.org/10.1007/s42823-022-00356-4
35. Rodríguez J, Garrido-Maneiro MA, Poza P, Gómez-del-Río MT (2006) Determination of mechanical properties of aluminium matrix composites constituents. Mater Sci Eng A 437(2):406–412. https://doi.org/10.1016/j.msea.2006.07.118
36. Rohatgi PK, Pasciak K, Narendranath CS, Ray S, Sachdev A (1994) Evolution of microstructure and local thermal conditions during directional solidification of A356–SiC particle composites. J Mater Sci 29(20):5357–5366. https://doi.org/10.1007/BF01171548
37. Bauri R, Surappa MK (2009) Processing and compressive strength of Al–Li–SiCp composites fabricated by a compound billet technique. J Mater Process Technol 209(4):2077–2084. https://doi.org/10.1016/j.jmatprotec.2008.04.058
38. Wu L, Li X, Han G, Deng Y, Ma N, Wang H (2017) Precipitation behavior of the high-Li-content in-situ TiB_2/Al–Li–Cu composite. Mater Charact 132:215–222. https://doi.org/10.1016/j.matchar.2017.08.015
39. Singh RLB, Jinu GR, Manoj M, Perumal AE (2022) Tribological behaviour of Al8090–SiC metal matrix composites with dissimilar B_4C addition. SILICON 14(14):8895–8908. https://doi.org/10.1007/s12633-021-01608-0
40. Patil CS, Ansari MI, Selvan R, Thakur DG (2021) Influence of micro B_4C ceramic particles addition on mechanical and wear behavior of aerospace grade Al–Li alloy composites. Sadhana Acad Proc Eng Sci 46(1):1–9. https://doi.org/10.1007/s12046-020-01543-7
41. Findik T (2023) Investigation of wear and microhardness behaviors of AA2196 matrix composite materials reinforced with ceramics produced by powder metallurgy method. Sci Sinter 01:1–30
42. Wang Y et al (2020) High-strength, ductility and modulus Al–Li/B_4C composite with near nanostructure produced by accumulative roll bonding. J Alloys Compd 834:155105. https://doi.org/10.1016/j.jallcom.2020.155105
43. Medjahed A et al (2020) Effect of TiC content on tensile properties, bend strength, and thermal conductivity of Al–Li–Cu–Mg–Zr alloy/TiC composites produced by accumulative roll bonding. J Mater Eng Perform 29(5):3253–3263. https://doi.org/10.1007/s11665-020-04809-7
44. Gu M, Wu Z, Jin Y, Koçak M (2000) Interfacial reaction and microstructure in a ZK60-based hybrid composite. J Mater Sci 35(10):2499–2505. https://doi.org/10.1023/A:1004777920804
45. Bauri R, Surappa MK (2008) Sliding wear behavior of Al–Li–SiCp composites. Wear 265(11–12):1756–1766. https://doi.org/10.1016/j.wear.2008.04.022
46. del Río TG, Rico A, Garrido MA, Poza P, Rodríguez J (2010) Temperature and velocity transitions in dry sliding wear of Al–Li/SiC composites. Wear 268(5–6):700–707. https://doi.org/10.1016/j.wear.2009.11.006
47. Okumus SC, Karslioglu R, Akbulut H (2013) A comparative wear study on Al–Li and Al–Li/SiC composite. In: AIP conference proceedings, vol 1569. https://doi.org/10.1063/1.4849294
48. Arumugasamy M, Pradha MS, Vaitheeswari V (2020) Investigation of tensile and wear properties of aluminium metal matrix composite. In: IOP conference series: materials science and engineering, vol 923. https://doi.org/10.1088/1757-899X/923/1/012060

Optimization of Temperature for Synthesis of Low Molecular Weight Glycidyl Azide Polymer as Plasticizer



Kommajosyula Nikhil, Sarangi Prabhu Prasad, and Biswas Shelly

Abstract Glycidyl azide polymer (GAP) is explored as an energetic binder/plasticizer for propellant due to its superior performance compared to hydroxy terminated polybutadiene (HTPB). GAP polymer contains an azide group which is very unstable, and at lower temperatures, the azide group tends to break making it an energetic binder/plasticizer. It can be mixed with low energetic and clean oxidizers such as AN, KN to improve the specific impulse and high energetic oxidizers such as ADN to reduce chlorine emissions for greener propulsion. The present study aimed to synthesize GAP as a plasticizer and increase the yield with an increase in temperature. The present work indicates that the increase in temperature of the aziadation process helps in increasing the yield of the GAP.

Keywords Glycidyl azide polymer · Epichlorohydrine · Dimethyleneforamide · Yield · Ethylene glycol

1 Introduction

Solid fuel is a reducing component, which on combustion results in the production of heat energy and gaseous products. The fuel component consists of a binder and plasticizer. Composite propellants require binders as a necessary component in their manufacturing. Binders make it possible to bond or form a matrix for the propellant where oxidizer and metal fuel can be embedded, also providing the necessary mechanical properties. Beginning in the late 1970s, hydroxyl-terminated polybutylene (HTPB) started to emerge as the material of choice for a wide range of space fuel binder applications. The binder influences the chemical properties of the propellant,

K. Nikhil (✉) · S. Prabhu Prasad · B. Shelly
Department of Space Engineering and Rocketry, Birla Institute of Technology, Mesra, Ranchi, India
e-mail: nikhil_k1995@yahoo.com

B. Shelly
e-mail: Shellybiswas@bitmesra.ac.in

© The Author(s), under exclusive license to Springer Nature Singapore Pte Ltd. 2024

S. Singh et al. (eds.), *Recent Advances in Aerospace Engineering*, Lecture Notes in Mechanical Engineering, https://doi.org/10.1007/978-981-97-1306-6_36

as well as the propellant processing and the ageing process. In most cases, the materials that act as binders also function as fuel, and during the combustion processes, they are oxidized. Binders such as HTPB, CTPB, and NC are utilized often. In some cases, GAP is also utilized as an energetic binder, which raises the energy density of the propellant and improves its overall performance [1, 2]. Plasticizers are the components responsible for imparting a plasticity-like quality into the propellant. The processing properties of propellant are significantly improved when plasticizer is added to the mixture. Plasticizers such as DOA, NG, are DBP are utilized often in a variety of applications [3, 4].

The traditional oxidizer used in these propellants, ammonium perchlorate (AP), has been shown to cause significant environmental concerns. To address these issues, researchers are investigating alternative oxidizers such as ammonium nitrate (AN), hydroxyl-ammonium nitrate (HAN), and high-nitrogen content compounds. These oxidizers do not contain chlorine and therefore do not have the same negative environmental impacts as AP. However, switching to these alternative oxidizers requires the use of an energetic binder or plasticizer, such as glycidyl azide polymer (GAP), to maintain the performance of the propellant [1, 2].

Glycidyl azide polymer, often known as GAP, is an energetic fuel component, when compared with hydroxyl-terminated polybutadiene (HTPB), which demonstrates superior performance. Throughout the length of the chain that makes up the polymer, GAP contains azide groups, also known as -N3 groups which increase the specific impulse. GAP in combination with oxidizers such as ammonium dinitramide (ADN), ammonium nitrate (AN), and potassium nitrate (KN) can produce chlorine-free exhaust as well as higher performance [4].

GAP has been used as a binder with AP and it was observed that when AP is added to GAP propellants, the flame structure is changed because decomposed oxygen-rich product gases from AP interact with the GAP decomposition products which are fuel rich give a gas phase heterogeneous reaction [5]. AP-based propellants using glycidyl azide polymer (GAP) have a higher specific impulse than those using polybutadiene (HTPB) when the AP content is below 85%. This is because the combustion of azide polymers is more exothermic than that of polybutadiene, leading to better performance [6].

Synthesis of GAP has been carried out using epichlorohydrin as starting material using ethylene glycol, sodium azide, and dimethylformamide at 90 °C for 15 h [7]. There are no research works available in literature on the effect of various parameters such as temperature and time of synthesis on the GAP yield. Thus, the present study attempts at optimization of yield of GAP with change in reaction temperature. The study also attempts at lowering the time of synthesis and increasing the yield by raising the temperature of azidation.

2 Experimental Methodology

2.1 Materials Required

The chemicals used are ethylene glycol (107-21-1), sodium azide (26628-22-8), dichloromethane(75-09-2), magnesium sulphate IV(7487-88-9), and epichlorohydrin. The mentioned chemicals are used in the same form as obtained from the manufacturer Sigma-Aldrich. The instrumentation used is hot plate magnetic stirrer obtained from GeNei and magnetic beads obtained from ThermoFisher.

2.2 Synthesis of GAP as Plasticizer

The chemicals required for the synthesis are epichlorohydrin (ECH), ethylene glycol (EG) which was procured from ThermoFischer, *N*,*N*-Dimethylformamide (DMF) which was purchased from Sigma-Aldrich, sodium azide which was purchased from ThermoFischer, methylene chloride (MC) purchased from Sigma-Aldrich, Magnesium sulphate purchased from Sigma-Aldrich.

The first step of synthesis is addition of weighed amount of DMF and EG which is then mixed in a beaker and then ECH is added to it. The beaker is then placed on an oil bath at 70 °C, during which sodium azide is added slowly in small batches for all the temperature case studies. This is done so that intense exothermic reactions can be kept under control. After the addition of sodium azide is completed and there is no discernible increase in temperature, the temperature of oil bath is raised to 90 °C for 15 h as base case study.

Later the oil bath temperature is raised to 100 °C, 110 °C, 120 °C, 130 °C, respectively, for a period of 5 h. Continuous stirring is required during the entire time of oil bath. After 15 and 5 h, the chemical reaction or aziadation process is complete and the mixture is brought to room temperature.

The next step involves the removal of DMF, EG, and salts from the polymer. In this step, the polymer is washed three times with distilled water at a temperature of 60 °C to remove all the salts, DMF, and EG. After washing, the polymer is added to MC solution. The polymer mixed in MC solution is now dried over magnesium sulphate taking a note of no agglomeration of magnesium sulphate. The MC solution was further filtered through a column containing silica gel.

To remove MC solution, the resultant solution with polymer was heated to 50 °C on a rotatory evaporator [7–9].

From the literature, it has been noted that the time taken for synthesis of GAP when maintained at 70 °C it takes 170 h, when maintained at 80 °C it takes 48 h and when maintained at 90 h it takes 15 h. From this data, a curvefit was drawn shown in Fig. 1 and the equation was noted which is shown below. Using extrapolation of the curve fitting, the time taken for the different temperature was developed.

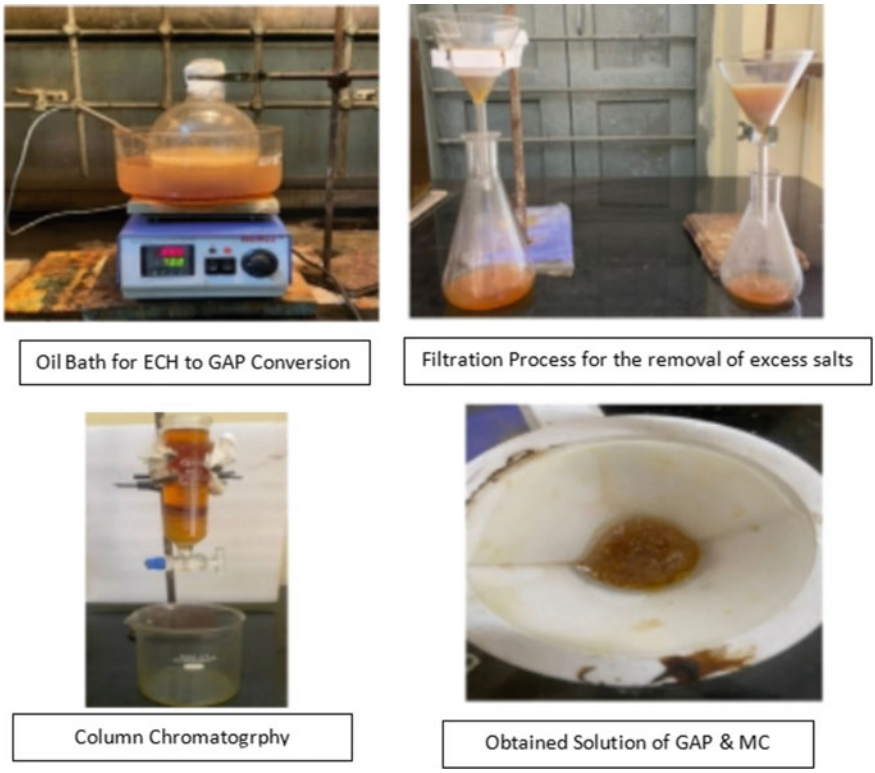


Fig. 1 Steps involved in GAP synthesis

$$y = 819139e^{-0.121x} \tag{1}$$

In the above equation, x is the temperature and y is the time taken. Mathematically, it was observed that it is futile to go beyond 150 °C. Using that equation, when synthesis was followed it has been observed that it was not appreciable and advisable to go less than 5 h as it creates almost no azidation and the yield is significantly lesser. Keeping this in mind, the synthesis time was kept at 5 h as the optimum time and for this time span remaining temperature was examined using the equation obtaied from the plot in (Fig. 2).

2.3 Fourier Transformer Infrared Spectroscopy

Fourier transformer infrared spectroscopy is a characterization technique used for determination of the characteristic group of the polymer. There has been tremendous growth in recent years, primarily because of a variety of sampling techniques and

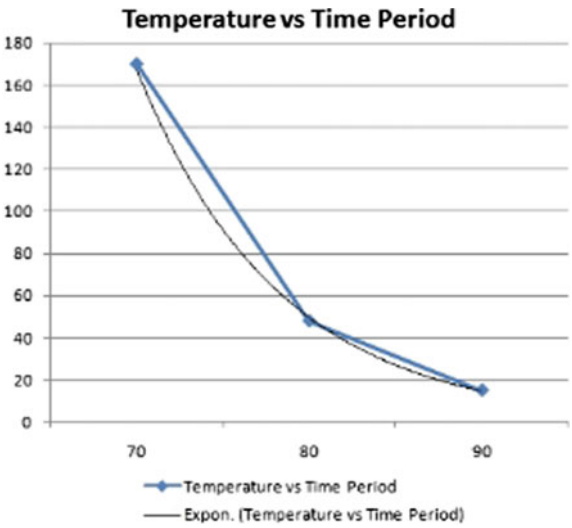


Fig. 2 Temperature vs time period plot obtained from the literature [8] with curve fit

experimentations which are available. Interaction of electromagnetic radiation with molecular vibrations gives rise to absorption bands throughout most of the IR region of spectrum. Identification of composition and morphology of polymers and their blends, curing studies, diffusion and oxidation studies, degradation of polymers, orientation of polymers, etc., are some of the areas where it finds extensive use. The Fourier transform infrared (FTIR) spectra were obtained with a Shimadzu Co, Japan; IR Presge 21 spectro-photometer in the range of 4000–400 cm^{-1} at a resolution of 4 $cm^{-1.}$

3 Result and Discussion

3.1 Effect of Temperature on the Yield of Synthesized GAP as Plasticizer

One of the primary parts of synthesized GAP is the yield obtained from the synthesis. As the temperature is increased during aziadation, the yield is also increased. Table 1 gives the effect of temperature on the yield of the synthesized GAP.

The average percentage increase from a temperature 90–130°C is 62% increase in the yield. It can also be noted that the tests are not done above 130°C due to the chemical degradation constraints.

The above obtained GAP is tested for its density, and it is found to be 1.3 g/ml. The density measurement was carried out for the span of 1 month and it is found to remain constant.

Table 1 Effect of temperature on the yield percentage of synthesized GAP

S. No.	Temperature (°C)	Yield percentage	Increase in yield (%)
1	90	50	–
2	100	62	12
3	110	71	19
4	120	78	27
5	130	82	32

3.2 FTIR of Synthesized GAP

From Fig. 3, a peak at 2135 cm^{-1} was obtained for the GAP which represents the azide group. In the pre-polymer ECH, a distinct peak C-Cl_2 at 747 cm^{-1} but this peak completely disappears in the GAP sample which clearly indicates the replacement of chlorine by azide group. The peaks at 2949 cm^{-1} show that C–H stretching vibration and peak at 3485 cm^{-1} shows the OH group vibration. These typical peaks confirm the formation of GAP in the synthesis process.

There is a strong peak of azide group at 2100 cm^{-1} for the oil bath temperature of 110 °C. This is because of the complete azidation reaction of ECH which results in the high yield of the synthesized GAP.

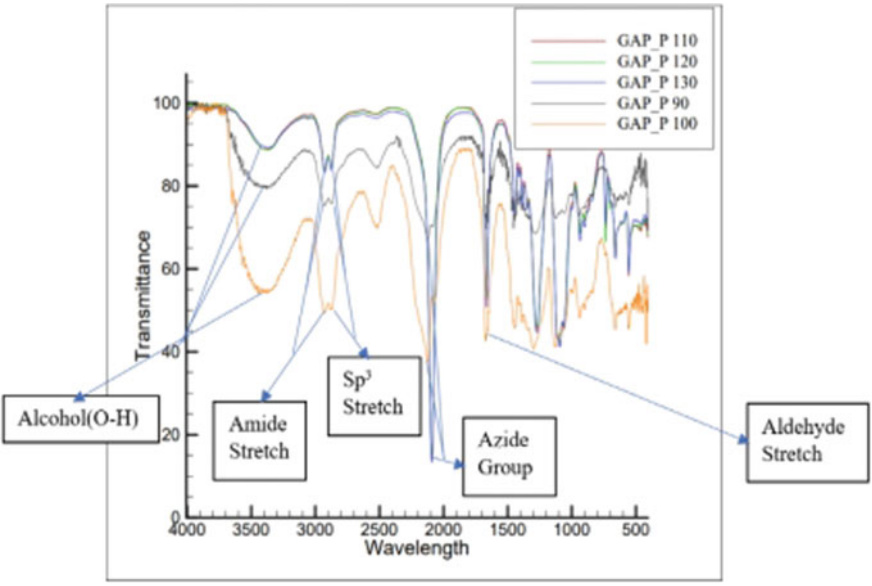


Fig. 3 FTIR plot of different oil bath temperature for GAP synthesis

4 Conclusions

Form the present study, it can be concluded that:

- The yield obtained from the synthesized GAP increases with an increase in temperature by 32% at 130 °C reaction temperature.
- The results obtained from the FTIR support that the synthesis of GAP has been achieved at different temperatures.
- At high oil bath temperature of the synthesis, there is a strong peak of azide group in the FTIR results. This signifies the complete azidation of the ECH.
- As the oil bath temperature increases, the yield percentage also increases. Since the amount of ECH and sodium azide is equimolar in amount, the yield obtained depends on the ECH conversion to GAP.

Acknowledgements/Funding Information The authors wish to express their gratitude towards Central Instrumentation Facility (CIF), BIT Mesra for carrying out the FTIR analysis of synthesized GAP.

References

1. Nazare AN, Asthana SN, Singh H (1992) Glycidyl azide polymer (GAP)-an energetic component of advanced solid rocket propellants—A review. J Energ Mater 10(1):43–63
2. Jain SR (2002) Solid propellant binders. J Sci Ind Res 61:899–911
3. Ramamurthi K (2016) Rocket propulsion. Trinity Press
4. Mishra DP (2017) Fundamentals of rocket propulsion. CRC Press
5. Kubota N, Sonobe T (1988) Combustion mechanism of azide polymer. Propel Explos Pyrotech 13(6):172–177
6. Yoshino O, Nagayama K (1997) Development of high burn rate azide polymer propellant. J Energ Mater 15:59–69
7. Eldsäter C, Malmström E (2014) Binder materials for green propellants. In: Green energetic materials, pp 205–234
8. Ahad E (1990) U.S. Patent No. 4,891,438. U.S. Patent and Trademark Office, Washington, DC
9. Kasztankiewicz A, Kogut A, Jankiewicz M, Maksimowski P (2018) Synthesis of high-energy polymer–glycidyl azide polymer (GAP). Problems of Mechatronics. Armament Aviation Saf Eng 9(2):59–72

Studies on Curing Time and Curing Temperature of AP-HTPB-Based Composite Solid Propellant



Prabhat Dattakumar Phondekar and Shelly Biswas

Abstract The curing process plays a crucial role in solidifying composite propellants, which consist of hydroxyl-terminated polybutadiene (HTPB) as a binder and ammonium perchlorate (AP) as an oxidizer. This paper examines and discusses the impact of curing time and temperature on solid propellant samples, considering factors such as burn rate, mechanical properties, FTIR characterization, and thermal decomposition analysis. Through experimental methods, it was observed that all the aspects were positively influenced. Specifically, increasing the curing temperature led to an enhanced propellant burn rate. Similarly, the mechanical properties such as Young's modulus, hardness, and elongation at break for the sample with 60 and 70 °C curing temperature lie in the standard range, whereas the rest of the samples are beyond the range due to a higher curing temperature which makes the sample brittle. FTIR analysis revealed changes in the strength of the isocyanate functional group, indicating the formation of allophanate linkage at a curing temperature of 100 °C. Moreover, the thermal decomposition of samples with 60, 70, 80, and 90 °C curing temperatures indicated three major peaks, but in the sample with 100 °C curing temperature, one more peak was detected at around 370 °C shows that the decomposition process of oxidizer and binder has divided into two different peaks. Considering the overall perspective, it was evident that an increase in curing temperature significantly affected the propellant and its burn rate, mechanical properties, FTIR analysis, and thermal decomposition.

Keywords Mechanical properties · FTIR · Ammonium perchlorate · HTPB · Thermal decomposition

P. D. Phondekar · S. Biswas (✉)
Birla Institute of Technology, Mesra, Ranchi, Jharkhand 835215, India
e-mail: shellybiswas@bitmesra.ac.in

© The Author(s), under exclusive license to Springer Nature Singapore Pte Ltd. 2024

S. Singh et al. (eds.), *Recent Advances in Aerospace Engineering*, Lecture Notes in Mechanical Engineering, https://doi.org/10.1007/978-981-97-1306-6_37

1 Introduction

Ammonium perchlorate (AP) and hydroxyl-terminated polybutadiene (HTPB) are two common components used in the formulation of solid rocket propellants. Ammonium perchlorate is an oxidizer that provides the necessary oxygen for the propellant to burn. Hydroxyl-terminated polybutadiene (HTPB) is a synthetic polymer that serves as the fuel component in the solid propellant. HTPB undergoes combustion reactions with AP to produce large amounts of gas and heat [1, 2]. The curing time and curing temperature of an HTPB-based solid propellant can vary depending on the specific formulation and desired properties of the propellant. Generally, HTPB-based propellants are cured at elevated temperatures to promote cross-linking between the polymer chains and create a more stable and durable solid. Typical curing temperatures can range from around 60 $\pm$ 2 °C, although some formulations may require higher temperatures. The curing time can also vary depending on the temperature and specific curing agent used in the formulation. Some propellants may require several hours or even days of curing time at the specified temperature to fully cross-link and cure. During the curing process, the propellant is typically cast into a desired shape or mold and then heated at the specified temperature for the desired curing time. After curing, the propellant can be inspected and tested for various properties, such as density, mechanical strength, and burn rate, to ensure it meets the desired specifications [3, 4].

The curing temperature can significantly affect the mechanical properties of a solid propellant made with HTPB [5]. Generally, higher curing temperatures lead to a stronger and more durable propellant, but there are limitations to this effect. At low curing temperatures, the cross-linking between the HTPB polymer chains may not be sufficient, resulting in a weaker and less stable propellant. On the other hand, if the curing temperature is too high, the polymer chains break down and degrade, leading to a propellant with reduced strength and increased brittleness. Therefore, the curing temperature is crucial to achieve a desired balance between cross-linking and degradation. Typically, the optimal curing temperature for a particular propellant formulation is determined through testing and experimentation. In addition to strength and durability, the curing temperature can also affect the mechanical properties of the propellant, such as elasticity, ductility, and toughness [6]. There is very limited work that shows the effect of curing time and curing temperature on various properties of composite solid propellant. So, this study tries to find the effect of curing on ballistic properties, mechanical properties, and thermal decomposition of AP/HTPB solid propellant. The main objective of the present study is to reduce the curing time to increase the productivity of propellants and the effect of curing temperatures and curing time on mechanical properties, ballistic properties, FTIR characterization, and thermal decomposition of the propellant.

2 Material and Methods

2.1 Preparation of Propellant Samples

The ingredients used in this work consist of ammonium perchlorate (AP) (80%) as an oxidizer, hydroxyl-terminated polybutadiene (HTPB) (13.6%) as a fuel binder, dioctyl adipate (DOA) (4.32%) as a plasticizer to make it flexible and easier to process, Toluene diisocyanate (TDI) (2%) as curing agent to harden the HTPB binder and create a solid propellant and glycerol (0.2%) as a bonding agent to promote a good bonding between oxidizer and binder.

The manufacturing process of HTPB-based solid propellant typically involves the following steps, the propellant formulation is prepared by mixing HTPB binder, AP, DOA, TDI, and glycerol in a specific ratio with the solid loading of 80%. The mixture is then homogenized to ensure uniform distribution of ingredients as shown in Fig. 1. The second is casting, the mixed propellant is transferred into the casting unit, which is typically made of aluminum or other suitable materials, as shown in Fig. 2. The casting unit is then vibrated to remove any air bubbles from the mixture, which can cause defects in the propellant. Third is curing, the casting unit is transferred to a curing oven, where the propellant is heated at a specific temperature for a specific time to cure the propellant.

The curing temperature and time depend on the specific formulation and the desired properties of the propellant. The standard curing temperature of AP/HTPB-based propellant is 60 °C for 6 days. To study the effect of different curing conditions, four different cases have been carried out as 5, 4, 3, and 2 days at curing temperatures of 70 °C, 80 °C, 90 °C, and 100 °C, respectively, as given in Table 1.



Fig. 1 Preparation of propellant slurry



Fig. 2 Plating of propellant slurry

Table 1 Relation between curing times and cure temperatures

Sample No.	S_1	S_2	S_3	S_4	S_5
Curing time (days)	6	5	4	3	2
Curing temperature (°C)	60	70	80	90	100

2.2 Burn Rate Studies and Density Measurement

The Crawford Bomb Strand Burner Setup is a laboratory-scale device used to measure the burning rate of solid propellants under various pressure ranges such as 14.69 psi (1 atm), 200 psi, and 400 psi in a nitrogen atmosphere. The burning rate is calculated based on the time it takes for the burn front to travel a known distance. The strand dimensions are, length of 100 mm and cross-sections of 6 mm × 6 mm. The burn rate has been calculated by using the following eq. no. 1.

$$\dot{r} = \frac{(\text{Distance between the fuse wires (length of the strand)}\,\frac{\text{mm}}{\text{s}}}{(\text{the output of the timer (burn time)}} \tag{1}$$

The volume displacement technique was used to calculate the density of the propellant samples. The propellant samples were submerged in the measuring liquid which is distilled water (specific gravity 1.002). By measuring the amount of water displaced and considering the mass of the sample, the density of propellants was computed.

The density of the propellant samples was considered using their respective mass and volume. The formula for calculating the density is by using Eqs. 2 and 3.

$$\text{The volume of a propellant} = \text{New water level} - \text{Original water level} \tag{2}$$

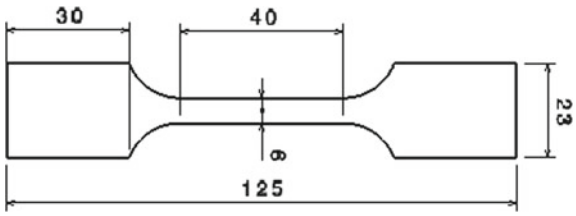


Fig. 3 Dimensions of specimen for mechanical properties

$$\text{Density of the propellant} = (\text{mass of a propellant}))/(\text{volume of a propellant}) \quad (3)$$

2.3 Study of Mechanical Properties

Universal Testing Machine (UTM) is commonly used to test the mechanical properties of materials, including propellants. Propellants are often subjected to mechanical testing to determine their strength, stiffness, and other properties that are critical for their performance in rocket engines. The standard dimension of the specimen (in mm.) for mechanical testing is shown in Fig. 3.

2.4 FTIR Studies

Fourier transform infrared (FTIR) analysis is commonly used to detect functional groups in a propellant sample based on the way it absorbs infrared radiation. The greater the amount of a functional group in a sample, the higher its absorbance peak will be. The present study involves the FTIR characterization of AP/HTPB-based all the propellant samples S_1, S_2, S_3, $\underline{S}_4$, and S_5.

2.5 Thermal Decomposition Studies

A thermal decomposition study is used to understand the effect of reactions and changes in the mass of the propellant sample with the temperature change. It includes DSC and TGA studies, and Differential Scanning Calorimetry (DSC) is a widely used technique to analyze the thermal behavior of materials.

3 Equipment

The equipment used to achieve the objective of this work consists of a Crawford Bomb Strand Burner Setup for studies of burn rate at higher pressure range, a Universal Testing Machine (Instron3366) has been used for measuring the mechanical properties of all the given samples, and Fourier Transform Infrared Spectroscopy (FTIR) study has been carried out on FAR-MID-NIR-FTIR Spectrometer instrument of Perkin Elmer, USA. It shows the graph of absorbance or transmittance vs wave number.

Thermo Gravimetry (TG) and Differential Scanning Calorimetry (DSC) investigations of all given propellant samples are covered in this work. A simultaneous thermal analyzer (STA Model 409 PG Luxx) of NETZSCH has been used for the study. All the tests were carried out at a heating rate of 10 $Kmin^{-1}$.

4 Results and Discussions

The performance and mechanical properties result for the standard condition (60 °C in 6 days curing) was carried out. Also, the performance and mechanical properties results for the new conditions for 5, 4, 3, and 2 days curing on 70, 80, 90 and 100 °C curing temperatures, respectively, as formulated in Table 1 were carried out.

4.1 Burn Rate Studies and Density Measurement

A burn rate and density measurement study has been carried out for all five propellant samples with various curing conditions. The results of burn rate and density are formulated in Table 2.

Table 2 gives the results of burn rate testings and density measurements of all the propellant samples. It clearly indicates that as the curing time increases, the burn rate increases, and the density of the propellant samples decreases. The density of samples

Table 2 Burn rate and density measurement data of all propellant samples

Sample No.	Burn rate (mm/s)			Density (gm/cm^3)
	14.69 psi	200 psi	400 psi	
S_1	3.92	10.12	12.92	1.34
S_2	3.95	10.35	13.05	1.32
S_3	4.1	10.46	13.23	1.31
S_4	4.34	10.82	13.76	1.30
S_5	5	11.01	13.39	1.28

S_2, S_3, S_4, and S_5 decreased by 1.49%, 2.23%, 2.61%, and 4.10%, respectively, as compared to standard sample S_1. It indicates that the propellant becomes brittle at higher curing temperatures, so it shows positive effects on burn rate and negative effects on packing density. From the above results, the optimized propellant sample is S_2 with 70 °C curing temperature due to a lower decrease in density compared to the standard curing condition.

4.2 Study of Mechanical Properties

The cured dog bone sample has been tested under a Universal Testing Machine (UTM) to determine all possible parameters. A durometer instrument is used to calculate the hardness of all given samples after being cured. Figure 4 shows the samples of specimens during the tests. It indicates the breaking point at the maximum stress point. Table 3 gives the results of the mechanical properties of all given formulations.

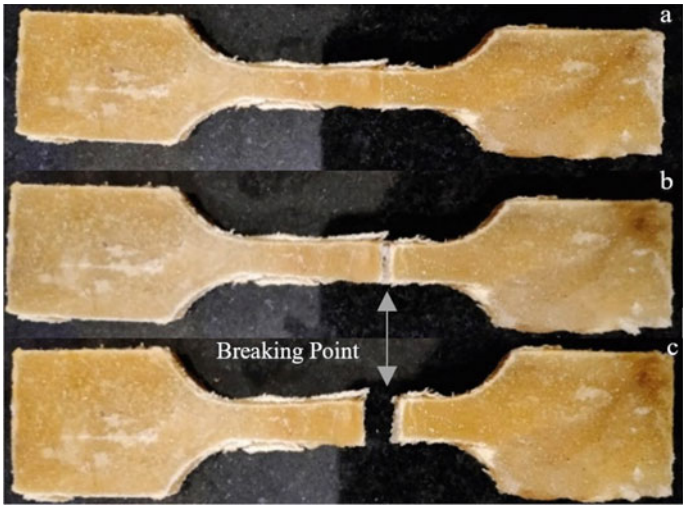


Fig. 4 **a** Specimen before testing, **b** specimen during testing, **c** specimen after testing

Table 3 Results of mechanical properties of samples

Sample	Young's modulus (MPa)	Elongation at break (%)	Hardness (shore A)
S_1	32.70 ± 2.3	11.73 ± 1.2	74
S_2	39.83 ± 1.6	9.93 ± 2.2	75–79
S_3	46.45 ± 4.5	5.40 ± 0.6	75–81
S_4	52.21 ± 6.2	3.17 ± 1.1	78–82
S_5	73.17 ± 5.2	1.51 ± 0.8	78–86

The mechanical properties such as Young's modulus, elongation at break, and hardness have been formulated in Table 3. It shows that Young's modulus and hardness of propellant sample increase with increasing curing temperature, whereas the standard range of Young's modulus and hardness (shore A) for composite materials is 30–40 MPa and 60–80 shore A, respectively [7]. At the same time, the elongation at the breakpoint decreases with increasing the curing temperature, and the standard range of elongation at the breakpoint of composite material is 6–25% [7].

The above results indicate that Young's modulus and elongation at break for samples S_1 and S_2 lie in the standard range, whereas S_3, S_4, and S_5 are beyond the range due to the formation of brittle nature. The hardness property of samples S_1 and S_2 lies perfectly in a standard range of composite materials but for samples S_3, S_4, and S_5, it goes beyond the range. It is because the composite propellant is getting harder and more brittle at high temperatures, so the range of hardness becomes wider on increasing the curing temperature.

4.3 FTIR Studies

FTIR studies have been carried out for all five samples S_1, S_2, S_3, S_4, and S_5 of AP/HTPB-based propellant, under a nitrogen atmosphere at 30 °C and 2 mbar pressure. The results in Fig. 5 indicate the functional groups, and their corresponding compounds present at different stages. The peak intensity of each functional group shows its relative concentration in the sample. The functional group with the strongest peak represents the highest concentration of that group in the sample.

It was observed in the first four cases for samples S_1, S_2, S_3, and S_4 that the prime components are CO, CO_2, –CH_2, –CH_3, CH_4, C_2H_4, C_4H_6, CONH, NO_2, N_2O, NH_3, NCO, HCl, and H_2O seen at their respective ranges of wave number in the samples as per the literature [8]. In the fifth case, the strength of the isocyanate group (–NCO) has been found in the range of 2000–2300 cm^{-1}. It clearly shows (Fig. 5e) the presence of formation of allophanate linkages (–NHCOOCONH) at high curing temperatures.

The reaction between hydroxyl-terminated polybutadiene (HTPB) and toluene diisocyanate (TDI) is the process for the production of polyurethane materials. This reaction results in the formation of a polyurethane polymer. HTPB is a type of polymer that contains hydroxyl functional groups (–OH) at its terminals. TDI is an aromatic diisocyanate compound with two isocyanate functional groups (–NCO). When HTPB and TDI react, the isocyanate groups of TDI react with the hydroxyl groups of HTPB through a process called urethane linkage formation or polyurethane cross-linking.

The reaction can be represented by the following generalized Eq. 4

$$\text{HTPB}\ (-\text{OH})\ +\ \text{TDI}\ (-\text{NCO})\ \rightarrow\ \text{Polyurethane} + \text{By - products} \qquad (4)$$

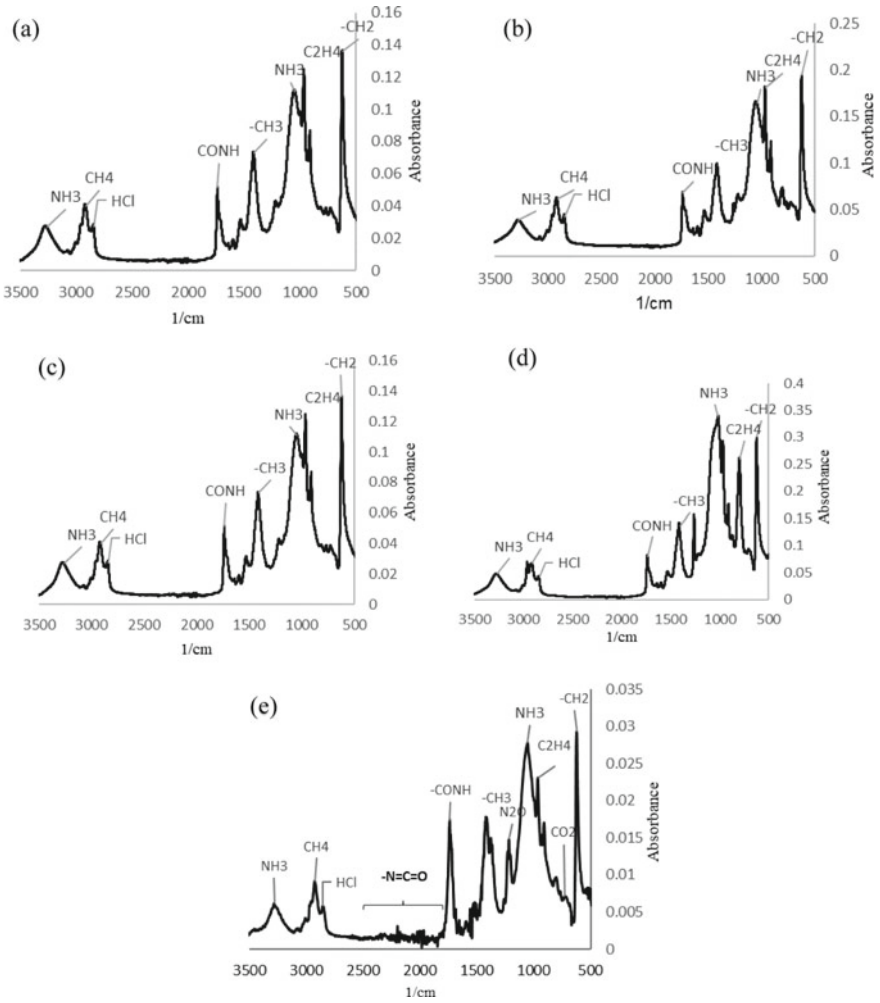
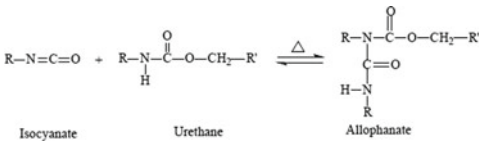


Fig. 5 FTIR curve of a propellant sample. **a** S_1, **b** S_2, **c** S_3, **d** S_4, **e** S_5

In this reaction, the isocyanate groups (–NCO) react with the hydroxyl groups (–OH) to form urethane (or carbamate) linkages (–NHCOO–), resulting in the formation of a three-dimensional network structure. The resulting material is a polyurethane polymer, which possesses a range of desirable properties such as flexibility, durability, and chemical resistance. As temperature increases, the reaction between TDI and HTPB continues, leading to the formation of allophanate linkages. In this step, the reaction occurs between the remaining isocyanate groups of TDI and the urethane groups (–NHCOO–) formed in the previous step [9].



(5)

The allophanate formation reaction involves the reaction between the isocyanate groups (-NCO) and the urethane groups (-NHCOO-) as mentioned in Eq. 5. This linkage has been clearly identified due to FTIR characterization studies. Figure 5e clearly shows that at high temperatures such as 100 °C, the strength of the isocyanate functional group has been found because of the formation of allophanate linkage. So, these allophanate linkages showed some positive effects on burn rate, tensile strength, etc., but it showed some negative effects on propellants such as brittle nature and over-curing.

4.4 Thermal Decomposition Study

The thermal decomposition analysis has been carried out for the solid propellant samples S_1, S_2, S_3, S_4, and S_5 to understand the decomposition mechanism of it. The DSC curve and TG of all the prepared samples are formulated in Figs. 6 and 7, respectively. The endothermic and exothermic peaks with respect to the temperature for the various propellant samples are presented in Table 4. For the analysis, a heating rate of 10 $Kmin^{-1}$ was examined in a nitrogen environment. The temperature range tested was ambient to 800 °C under nitrogen flow at a rate of 60 $mLmin^{-1}$.

The TG curve of all the propellant samples indicates the mass degradation with respect to temperature as shown in Fig. 7. Whereas the DSC curve of propellant

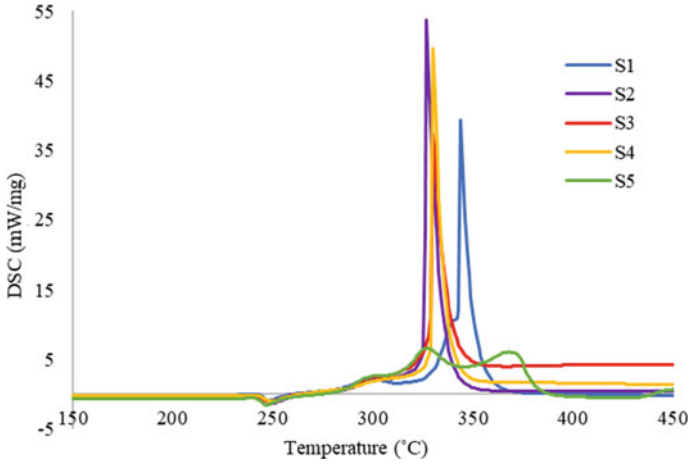


Fig. 6 DSC curve of the propellant samples

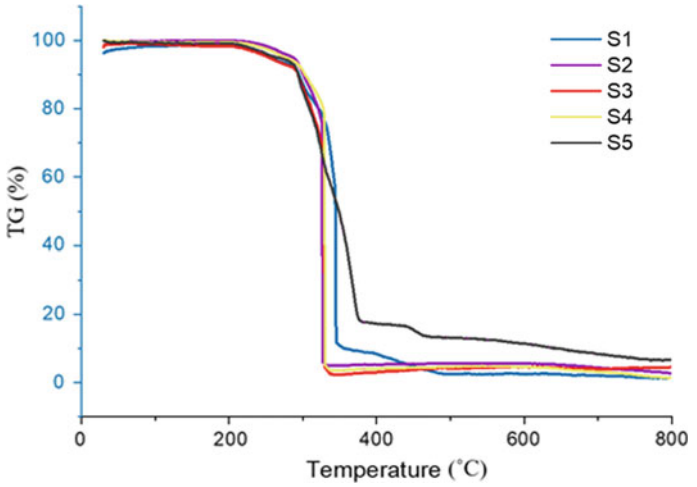


Fig. 7 TG curve of the propellant samples

Table 4 Peaks obtained from the DSC curve of the propellant samples

Sample	Peak at temperature (°C)	Peak types
S_1	249	First endothermic
	299	First exothermic
	344	Second exothermic
S_2	249	First endothermic
	299	First exothermic
	327	Second exothermic
S_3	250	First endothermic
	300	First exothermic
	330	Second exothermic
S_4	250	First endothermic
	300	First exothermic
	330	Second exothermic
S_5	250	First endothermic
	299	First exothermic
	327	Second exothermic
	370	Third exothermic

samples S_1, S_2, S_3, S_4, and S_5 shows three major peaks: the first peak indicates a phase change of AP from orthorhombic to cubic endothermically in the range of 249–250 °C. The second peak indicates the starting of the decomposition of AP in the range of 299–300 °C exothermically and the third peak indicates the evolution of multiple gases due to the decomposition of oxidizer and binder exothermically between the

range of 327–344 °C, but in sample S_5, one more peak has detected at 370 °C shows that the decomposition process of oxidizer and binder has divided into two different reactions. The above results clearly show that at higher curing temperatures, the propellant decomposition process takes place with an extra reaction. It means the chemicals take extra energy to break down into exhaust gases which might indicate the negative effect of allophanate linkage.

5 Conclusion

The present study attempts to reduce the curing time of composite solid propellants without compromising ballistics and mechanical properties. Based on the above results, the following conclusions are obtained:

1. The burn rate and density studies indicate that as the curing temperature increases, the burn rate and density are increased due to the brittleness and formation of allophanate linkage. It shows a positive effect on these properties at high temperatures.
2. The mechanical properties such as Young's modulus, elongation at break, and hardness for samples S_1 and S_2 lie in a standard range of composite propellant whereas, for samples S_3, S_4, and S_5, it goes beyond the limit due to brittleness.
3. The FTIR studies for a sample with 100 °C curing temperature show the strength of the isocyanate group (–NCO) due to the formation of allophanate linkage at high curing temperatures, whereas in the rest of the samples, this group has not been identified.
4. The thermal decomposition of samples S_1, S_2, S_3, and S_4 indicated three major peaks but in sample S_5, one more peak was detected at around 370 °C showing that the decomposition process of oxidizer and binder has divided into two different peaks which might indicate the negative effect of allophanate linkage.

The above conclusions indicate that propellant samples with a curing temperature of 70 °C have perfectly satisfied the ballistics, mechanical, and thermal decomposition analysis. It can be used for future applications to increase the productivity of HTPB-based solid propellant with a decrease in one day of the curing time.

References

1. Jacobs PWM, Whitehead HM (1969) Decomposition and combustion of ammonium perchlorate. Chem Rev 69(4):551–590
2. Naseem H, Yerra J, Murthy H, Ramakrishna PA (2021) Ageing studies on AP/HTPB based composites solid propellants. Energetic Mater Front 2(2):111–124
3. Prasad CH, Arunachalam V, Ranganathan V (2014) Effect of the formulation of ingredients and the process parameters on the fracture toughness of HTPB-based composite Solid propellant. J Energy Chem Eng 2(3):94–105

4. Smith T (1960) Solid propellants... elastomeric-binder and mechanical-property requirements for solid propellants. Ind Eng Chem 52(9):776–780
5. Shekhar H (2011) Effect of temperature on mechanical properties of solid rocket propellants. Def Sci J 61(6):529–533
6. Nagmeldin M, Elamin, Abuuznien MHM (2007) Effect of the decreasing of curing time on the performance and mechanical properties of HTPB/AP composite propellants. J Karary Univ Eng Sci (2007)
7. Mukunda HS (2017) Understanding aerospace chemical propulsion. I.K. International Publishing House Pvt. Limited, India
8. Wang YW, Liu LL, Xiao LY, Wang ZX (2015) Thermal decomposition of HTPB/AP and HTPB/HMX mixtures with low content of oxidizer. J Therm Anal Calorim 199:1673–1678
9. Ezzati N, Asadi E, Abdouss M, Kowsari E (2021) Polyurethane. In: Functionalized polymers. CRC Press, pp 208–234

Control Applications in Marine Robot Vehicles



Arun and M. P. R. Prasad

Abstract This research paper focuses on the application of Model Predictive Control (MPC) on a 3-degree-of-freedom (DOF) Marine Robot (USV). Marine Robots are multivariable, nonlinear, and coupled systems. Controlling these vehicle trajectories is a challenging task for the researchers. The MPC control algorithm is designed such that USV can track a desired reference point. The efficiency of the MPC control algorithm on the USV is examined in the MATLAB environment. Using the MPC control method, results demonstrate that the USV can successfully track the desired reference point.

Keywords Model Predictive Controller (MPC) · Marine robotics · Unmanned Surface Vehicle (USV) · Coupled system · Degree of Freedom (DOF)

1 Introduction

Marine robotics is a fast-developing field that entails the development and deployment of autonomous or remotely controlled vehicles in aquatic environments. These robots are made to handle a variety of jobs, such as data collection, monitoring, and maintenance underwater. Marine research, environmental monitoring, and undersea infrastructure inspection are just a few of the areas in which they are essential contributors. Marine robots provide many benefits, including improved operational performance, cost-effectiveness, and less human risk in risky underwater situations [1].

Control systems play a crucial role in the functionality of marine robots, enabling them to carry out tasks with precision and efficiency within dynamic and unpredictable marine environments. These systems are responsible for ensuring stability,

Arun (✉) · M. P. R. Prasad
National Institute of Technology, Kurukshetra, Haryana, India
e-mail: arunbibyan987@gmail.com

M. P. R. Prasad
e-mail: mprprasad@nitkkr.ac.in

© The Author(s), under exclusive license to Springer Nature Singapore Pte Ltd. 2024

S. Singh et al. (eds.), *Recent Advances in Aerospace Engineering*, Lecture Notes in Mechanical Engineering, https://doi.org/10.1007/978-981-97-1306-6_38

precise maneuverability, and effective response to external disturbances or fluctuations in environmental conditions. They provide the necessary mechanisms for navigation, obstacle avoidance, path planning, and the ability to maintain desired positions or trajectories. Moreover, control systems facilitate the integration of sensor data, decision-making algorithms, and actuator control, making them an indispensable component for the overall functionality and performance of marine robots [2].

Model Predictive Control (MPC) [3] is an innovative control approach that leverages a mathematical representation of the controlled system for optimizing future control actions. In contrast to conventional control techniques that rely on predetermined control policies, MPC employs predictions of the system's future behavior to compute control inputs that optimize a predefined objective function. By considering system dynamics, constraints, and prediction horizons, MPC enables the generation of optimal control strategies. This predictive capability empowers MPC to effectively address complex and nonlinear systems.

The implementation of Model Predictive Control (MPC) in marine robots offers numerous notable benefits. Firstly, MPC enables precise control and maneuverability, empowering marine robots to execute intricate tasks with exceptional accuracy and efficiency. It facilitates robust control even in the face of disturbances, external forces, and uncertain environmental conditions. MPC also presents a systematic framework to effectively manage constraints inherent in marine robotics, including vehicle dynamics, actuator limitations, and collision avoidance. Additionally, MPC's capacity to incorporate future predictions enhances adaptability, making it well-suited for dynamic marine environments characterized by rapid changes in conditions.

Path following is one of the major tasks for a USV. The adaptive control technique reported in [4] is used to follow a straight line. A conventional LOS method is reported in [5].

The research objective of this study is to examine the utilization of Model Predictive Control (MPC) in marine robots and evaluate its performance in comparison to traditional control methods. The purpose of the study is to design an MPC-based control system for a particular marine robot platform, taking into account the dynamics, sensor integration, and actuator capabilities of the platform. The research will primarily focus on evaluating the effectiveness of MPC in terms of accuracy, efficiency, stability, robustness, and adaptability across various marine scenarios. The scope of the study will encompass activities such as mathematical modeling, implementation of control algorithms, and performance evaluation of the marine robot platform's MPC-based control system.

Prototype

The USV depicted in "Fig. 1" is a prototype made of fiberglass and features a twin hull configuration [6]. It was developed by VantTec, a student group from Tecnológico de Monterrey. The twin hull design offers stability for a camera that is mounted on the deck, while the superstructure on the deck accommodates the necessary electronics and other equipment. For propulsion, the USV is equipped with two rear



Fig. 1 Vantec prototype navigating on a pool [6]

Table 1 Parameters of the prototype [6]

Parameter	Values
Length overall (L)	1.01 m
Length on the water's edge	0.93 m
Draft (T)	0.09 m
Beam overall (B)	0.75 m
Beam on the water's edge	0.61 m
Side hull separation (centerline to centerline)	0.41 m
Individual hull beam (B_{Hull})	0.27 m
Longitudinal center of gravity (LCG)	0.45 m
Mass (m)	30 kg
Length-to-beam ratio	2.47 m

thrusters, enabling movement in three dimensions: surge, sway, and yaw. "Table 1" presents comprehensive information regarding the physical parameters of the vehicle, encompassing dimensions, weight, and power source.

2 Modeling

This section presents the mathematical model of a three-degree-of-freedom (3-DOF) unmanned surface vehicle (USV). Previously, [6, 7] explained the VTec S-III USV's dynamic model and the notations proposed by Fossen [1] are utilized. The inertial and body-bound reference frames are depicted in "Fig. 2", along with the variables η and v. The vector $\eta = [x, y, \psi]^{\mathrm{T}}$ represents the x, y coordinates and yaw angle (ψ) in the inertial frame, while the vector $v = [u, v, r]^{\mathrm{T}}$ represents the surge, sway velocities, and yaw rate in the body-bound reference frame. Hence, the equations of motion can be expressed as Eqs. (1) and (2).

$$\tau = M(v) + C(v)v + D(v) \tag{1}$$

$$\dot{\eta} = \mathcal{I}(n)v \tag{2}$$

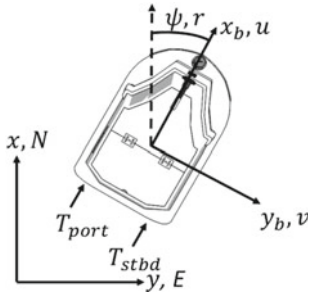


Fig. 2 USV's body bound and inertial reference frames (N and E represent north and east directions) [7]

The symbol "*M*" represents the inertia matrix, as stated in Eq. (3), which characterizes a submerged or floating object in the water. This matrix is composed of two parts: the rigid body mass matrix, which accounts for the mass distribution and moments of inertia around the object's principal axes, and the added mass matrix, which incorporates the impacts of hydrodynamics resulting from the object's motion in water.

$$M(v) = \begin{bmatrix} m - x_{\dot{u}} & 0 & -my_G \\ 0 & m - Y_{\dot{v}} & mx_G - Y_{\dot{r}} \\ -my_G & mx_G - N_{\dot{v}} & I_z - N_{\dot{r}} \end{bmatrix} \tag{3}$$

The symbol "*C*" represents the Coriolis matrix, denoted as $C(v)$, as provided in Eq. (4). This matrix comprises two components: the standard Coriolis rigid body matrix and an added mass matrix. The Coriolis matrix "*C*" establishes a relationship between the angular velocity and linear velocity of a moving rigid body, and it is utilized to compute the forces and moments exerted on the body.

$$C(v) = \begin{bmatrix} 0 & 0 & -m(x_G + v) \\ 0 & 0 & -m(y_G - v) \\ m(x_G + v) & m(y_G - v) & 0 \end{bmatrix} + \begin{bmatrix} 0 & 0 & 2\left(Y_{\dot{v}} v + \left(\frac{Y_{\dot{r}} + N_{\dot{v}}}{2}\right) r\right) \\ 0 & 0 & -X_{\dot{u}} u \\ 2\left(-Y_{\dot{v}} v - \left(\frac{Y_{\dot{r}} + N_{\dot{v}}}{2}\right) r\right) & X_{\dot{u}} u & 0 \end{bmatrix} \tag{4}$$

The incorporation of a factor of 2 in Eq. (4) is necessary to account for the vessel's catamaran configuration and ensure that it aligns with the specific parameters of the experiment.

The drag matrix, denoted as $D(v)$, is presented in Eq. (5) and encompasses both linear and nonlinear drag effects by utilizing two distinct drag matrices. By combining these matrices through summation, the equation effectively characterizes the total drag experienced by the body.

$$D(v) = \begin{bmatrix} X_u & 0 & 0 \\ 0 & Y_v & Y_r \\ 0 & N_v & N_r \end{bmatrix} + \begin{bmatrix} X_{u|u|}|u| & 0 & 0 \\ 0 & Y_{v|v|}|v| + Y_{v|r|}|r| & Y_{r|v|}|v| + Y_{r|r|}|r| \\ 0 & N_{v|v|}|v| + N_{v|r|}|r| & N_{r|v|}|v| + N_{r|r|}|r| \end{bmatrix} \quad (5)$$

An inertial reference frame is created by transforming the velocity vector from a reference frame attached to the body by the transformation matrix, denoted as $\mathcal{I}(n)$ and specified in Eq. (6). This transformation makes it possible to depict the velocity vector with an outside, fixed frame of reference.

$$\mathcal{I}(n) = \begin{bmatrix} \cos\varphi & -\sin\varphi & 0 \\ -\sin\varphi & \cos\varphi & 0 \\ 0 & 0 & 1 \end{bmatrix} \quad (6)$$

The vector of forces and moments produced by the two thrusters on the vessel is shown in Eq. (7) by the symbol τ. Specifically, these thrusters are referred to as the port and starboard thrusters, and their combined effects are encapsulated in the τ vector. The vector τ represents both the linear forces and rotational moments produced by the thrusters.

$$\tau = \begin{bmatrix} \tau_x \\ \tau_y \\ \tau_z \end{bmatrix} = \begin{bmatrix} \tau_{\text{port}} + \tau_{\text{starboard}} \\ 0 \\ (\tau_{\text{port}} - \tau_{\text{starboard}})/B/2 \end{bmatrix} \quad (7)$$

The constant hydrodynamic coefficients are presented in "Table 2," which provides the specific values assigned to these coefficients.

3 Controller Design

Model Predictive Control (MPC) [3] is a control technique widely used in various industries, including marine robotics, to achieve precise and efficient control of dynamic systems. MPC operates by utilizing a dynamic model of the system to predict its future behavior over a defined time horizon. By considering these predictions, MPC formulates an optimization problem to determine the optimal control actions that meet desired performance criteria. "Fig. 3" shows the MPC's basic control loop.

One of MPC's key advantages is that it can deal with system constraints. These constraints can include physical limitations on the system, safety requirements, or operational bounds on inputs and outputs. By incorporating these constraints into the optimization problem, MPC ensures that the control actions generated are feasible and within the defined limits. This capability is particularly valuable in marine robotics applications, where there may be constraints on actuator capabilities or safety limits that need to be respected.

Table 2 Hydrodynamic coefficients

Coefficients	Values
X_u	25
Y_v	0.5
Y_r	3
$X_{\dot{u}}$	− 2.25
$Y_{\dot{v}}$	23.13
$Y_{\dot{r}}$	− 1.31
N_v	0.06
N_r	0.02
$N_{\dot{v}}$	− 16.41
$N_{\dot{r}}$	− 2.79
$X_{u\|u\|}$	− 70.92
$Y_{v\|v\|}$	99.98
$Y_{v\|r\|}$	− 5.48
$Y_{r\|v\|}$	− 5.48
$Y_{r\|r\|}$	− 8.9
$N_{v\|v\|}$	− 5.48
$N_{v\|r\|}$	− 8.9
$N_{r\|v\|}$	− 8.9
$N_{r\|r\|}$	− 3.50

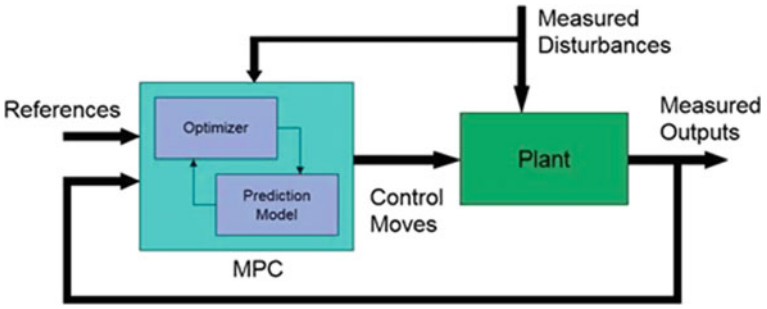


Fig. 3 MPC basic control loop [3]

MPC's predictive nature enables it to make proactive control decisions. By considering the future behavior of the system, including potential disturbances or changes in the environment, MPC can anticipate and react to these events in advance. This proactive approach improves system performance by enabling better tracking accuracy, trajectory following, and disturbance rejection compared to reactive control techniques.

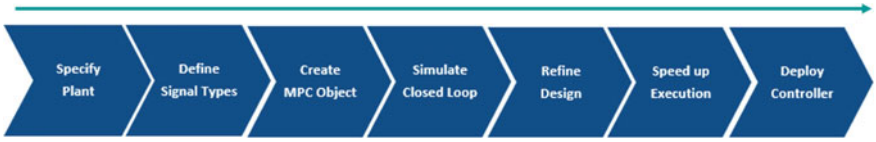


Fig. 4 MPC design workflow

Moreover, MPC provides flexibility in terms of objectives and performance criteria. The optimization problem formulation allows for the incorporation of various objectives, such as minimizing energy consumption, optimizing trajectory tracking, or achieving specific system behaviors. This flexibility enables customization of the control algorithm to meet specific requirements and operational goals in marine robotics applications.

One other benefit of MPC is its capacity to handle time-varying and nonlinear systems. By employing a dynamic model of the system, MPC can accurately predict the system's behavior even in the presence of nonlinearities and time-varying dynamics. This capability makes MPC suitable for controlling complex marine robotic systems that may exhibit nonlinear and time-varying characteristics.

Overall, MPC is a powerful control technique for marine robotics that leverages a predictive model of the system to optimize control actions over a defined time horizon. It offers the ability to handle constraints, proactive decision-making, flexibility in objective formulation, and the capability to handle nonlinear and time-varying systems. These advantages make MPC a valuable tool for achieving precise and efficient control in marine robotic applications.

"Fig. 4" shows the usual workflow to design an MPC controller in traditional, or linear, MPC.

The prediction and control horizons are taken as 70 s. and 1 s., respectively, while the sampling time is taken as 0.03 s. The weight vectors assigned to the Manipulated Variables (MV), Manipulated Variables rate (MV Rate), and output variables (OV) are [0 0 0], [9 8 3], and [15 20 25], respectively.

4 Results

In this section, we present the results of the step response analysis of each variable (Surge, Sway and Yaw rate) conducted on the system under MATLAB environment as shown in Fig. 5. The reference for surge and sway variables is taken as $+1$, while for the yaw rate, it is -1.

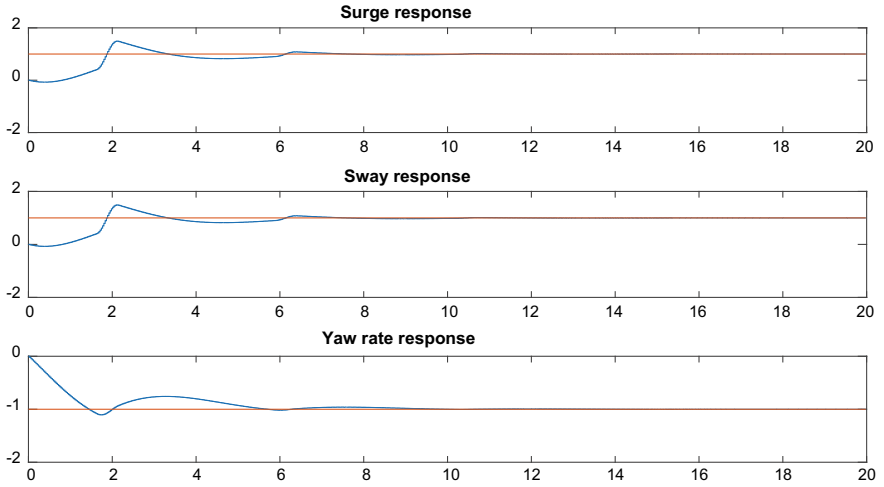


Fig. 5 Step responses of surge, sway, and yaw rate variable using MPC technique

5 Conclusion

The Model Predictive Control (MPC) algorithm is effectively used to control Unmanned Surface Vehicles (USVs) in the MATLAB environment. The step response analysis of the surge, sway, and yaw rate variables demonstrated the effectiveness of the MPC algorithm in accurately tracking the desired reference trajectories. The reference values for surge and sway were set as $+1$, while for yaw rate, it was set as -1. One notable finding is that all three variables exhibited approximately similar settling times of 5.5 s, indicating that the MPC algorithm achieved precise and timely control for each output variable. This observation highlights the ability of the MPC-based control system to regulate the USV's movement along the surge, sway, and yaw axes, ensuring alignment with the desired reference trajectories. The similar settling times across the three variables also indicate the robustness and adaptability of the MPC algorithm in handling multiple control objectives concurrently. The successful tracking of the desired references for all three variables underscores the potential of MPC in improving the control performance of USVs. By utilizing predictive models and optimizing control actions over a finite time horizon, the MPC algorithm effectively accounts for system dynamics, constraints, and disturbances, resulting in accurate and adaptive control.

Funding Information Not Applicable.

References

1. Gonzalez-Garcia A, Castaneda H (2021) Guidance and control based on adaptive sliding mode strategy for a USV subject to uncertainties. In: IEEE J Ocean Eng 46(4):1144–1154
2. Fossen TI (2011) Handbook of marine craft hydrodynamics and motion control. Wiley, Hoboken, NJ
3. Gonzalez-Garcia, Castaneda H (2019) Modeling, identification and control of an unmanned surface vehicle. In: Proceedings of AUVSI XPONENTIAL 2019: all things unmanned
4. Liu Z, Zhang Y, Yuan C, Luo J (2021) Adaptive path following control of unmanned surface vehicles considering environmental disturbances and system constraints. In: IEEE Trans Syst Man Cybern Syst 51(1):339–353
5. Fossen TI (2019) Handbook of marine craft hydrodynamics and motion control. Wiley
6. Wang L, Cao Y (2013) Control system design for an autonomous underwater vehicle. Int. J. Control Autom Syst 11(1):162–172
7. Camacho EF, Bordons C (2004) Model predictive control. Springer

Longitudinal Static and Dynamic Stability of a Biconic Reentry Body in Subsonic Mach Number Using CFD



Joben Leons, M. Jathaveda, and G. Vidya

Abstract Reentry from orbit is a critical phase in the entry trajectory. For a non-propulsive ballistic entry, static and dynamic stability plays an important role in the trajectory, especially for the safe deployment of parachutes, typically at high subsonic Mach numbers. Static stability of flight vehicles is being estimated through empirical methods, CFD and experiments. Longitudinal static and dynamic stability of a typical reentry body for subsonic Mach number of 0.6 is predicted using commercial software CFD + + and presented here. Steady state simulations are carried out for low angle of attack at $\alpha = 0$ and 2° on an unstructured grid using SST k-ω model. Transient simulation using forced oscillation method is used to compute pitch damping derivatives. Results for transient simulations are validated against test data.

Keywords Bi-conic reentry body · CFD · Subsonic · Static stability · Pitch damping

1 Introduction

Returning from space is the critical task which involves hitting the atmosphere at the precise flight path angle and velocity. Without exceeding thermal and structural limits, it is necessary to dissipate the kinetic and potential energy of re-entry object from Earth orbit and recover it on the ground. These constraints can be met either through aerodynamics or propulsion or both. The entry can be semi-ballistic, ballistic, or lifting entry. Other than the mass and entry flight path angle, in a non-propulsive

J. Leons (✉)
ACE College of Engineering, Trivandrum, India
e-mail: joben.leons@gmail.com

M. Jathaveda · G. Vidya
Indian Space Research Organisation, VSSC, ADSG, Trivandrum, India
e-mail: mjveda@yahoo.co.uk

G. Vidya
e-mail: g_vidya@vssc.gov.in

© The Author(s), under exclusive license to Springer Nature Singapore Pte Ltd. 2024

S. Singh et al. (eds.), *Recent Advances in Aerospace Engineering*, Lecture Notes in Mechanical Engineering, https://doi.org/10.1007/978-981-97-1306-6_39

ballistic entry, stability is the important aerodynamic parameter that influences the trajectory design. The determination of the static and dynamic stability parameters is important for trajectory design/ analysis. The static stability parameters can be estimated from either wind tunnel or CFD methods, whereas the dynamic stability primarily has been estimated from wind tunnel testing through forced oscillation, free oscillation, and aero-ballistic range tests [1–3]. Due to the advances in the CFD, the estimation of the dynamic stability derivatives has been carried out through CFD [4]. A compilation of the observations in the literature to date related to brief background, experimental and computational techniques for measuring pitch damping, and the effect of vehicle and operational variables on dynamic stability characteristics are given in [5]. The dynamic stability of the Orion capsule was analyzed, using the forced oscillation method through CFD techniques [6]. A 1:10 scale model of a typical ballistic reentry vehicle [7] is considered for the current study. Static stability is computed through the steady state simulations and dynamic stability using the forced oscillation technique and presented in this paper.

2 Configuration and Setup

Figure 1 shows the study configuration, sign convention, and coordinate system. The base diameter of the configuration is D. The model is a sphere–cone–flare configuration. The body mesh and the four parts, namely nose, midsection, flare, and base, are marked in Fig. 1.

An unstructured grid of 38 million is used [8]. The enclosure for the mesh used is a cuboid. Domain size is approximately 74D as shown in Fig. 1 (where *D* is the base diameter taken as reference length), considering subsonic flow conditions. Prism layers are generated from the surface of the configuration to capture the viscous flow physics. CFD simulations are carried out using commercial package CFD++ [9], with SST-k-ω model. Steady state CFD simulations are carried out low angle of attack of $\alpha = 0$ and 2° for NAL wind tunnel conditions corresponding to Mach number 0.6. Forced oscillation technique is employed for the same case with amplitude of $\pm$ 2°.

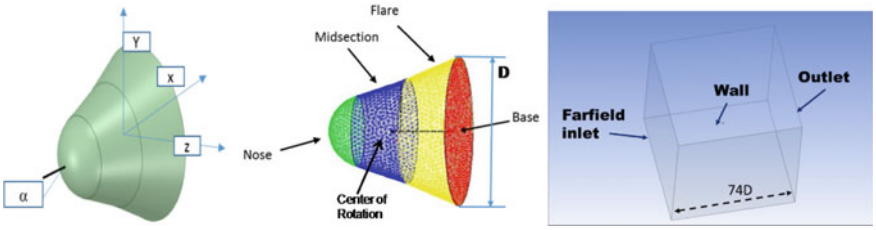


Fig. 1 From the left: configuration, sign convention, body mesh and domain

The center of rotation is located near the end of the midsection as we can see in the Fig. 1. It is about this point that the body will be oscillated for the dynamic condition.

3 Solver Theory

3.1 Governing Equations

Continuum fluid flow is governed by conservation of mass, momentum, and energy. The Solver is based on the Reynolds-averaged Navier–Stokes equation (RANS equations). RANS is a common turbulent modeling approach and is based on the statistical treatment of the flow. The variables that govern the flow are divided into a time averaged component of the flow and a fluctuating component that represents the deviation from the mean flow. The equations for a compressible fluid can be written as follows:

$$\frac{\partial \rho}{\partial t} + \frac{\partial}{\partial x_j}\left[\rho u_j\right] = 0 \tag{1}$$

$$\frac{\partial}{\partial t}(\rho u_i) + \frac{\partial}{\partial x_j}\left[\rho u_i u_j + p\delta_{ij} - \tau_{ji}\right] = 0 \tag{2}$$

$$\frac{\partial}{\partial t}(\rho e_0) + \frac{\partial}{\partial x_j}\left[\rho u_j e_0 + u_j p + q_j - u_i \tau_{ij}\right] = 0 \tag{3}$$

3.2 Turbulence Model

The equations governing turbulent flows can be solved directly only for simple cases of flow. CFD simulations use turbulent models to predict the evolution of turbulence for most real-life turbulent flows. Turbulence modeling is the construction and use of a mathematical model to predict the effects of turbulence. These turbulence models are simplified constitutive equations that predict the statistical evolution of turbulent flows.

The SST k-ω turbulence model, used in this study, is a two-equation eddy viscosity model. The formulation of shear stress transport (SST) model combines the best of two worlds. The SST k-ω model can be used as a low-Re turbulence model without any extra damping functions due to the use of a k-ω formulation in the inner parts of the boundary layer which makes the model directly usable all the way down to the wall through the viscous sub-layer. Outside the boundary layer, SST formulation also switches to k-ε behavior and thereby the common k-ω problem that the model

is too sensitive to the inlet free-stream turbulence properties is avoided. This model is useful in cases of separating flow and adverse pressure gradients.

3.3 Forced Oscillation Method

Forced oscillation technique is used for the simulations for the dynamic derivatives by providing input oscillation as cosine function. Time step for the transient simulation is chosen so that it is good enough to capture the flow physics. Simulation is carried out for 8 cycles. Steady state results are taken as the initial conditions for the transient simulation.

This method works by forcing a body to oscillate with a constant magnitude of angular displacement around its center of gravity. Simple harmonic oscillation (SHO) method is one of the simple displacement methods that can be used. By forcing the body to oscillate with simple harmonic motion around its center of gravity, the unsteady aerodynamics calculated with CFD tools can be used to obtain the dynamic stability derivatives. The dynamic stability derivatives that can be acquired through this method are C_{m_0}, C_{m_α} , and $(C_{m_q} + C_{m_{\dot{\alpha}}})$. Besides C_{m_0} and C_{m_α}, , the longitudinal pitch damping derivatives always comes in its coupled forms of $(C_{m_q} + C_{m_{\dot{\alpha}}})$ because the change in angle of attack is related to its alpha changing rate and pitching.

For the forced oscillation method, there are three modes of simple harmonic oscillation: plunging mode, pitching mode, and flapping mode. These modes have different inputs or combined inputs in *xyz* axes. Pitching mode is used in this study. In this mode, the object is oscillated about the *z* axis (Fig. 1 for axes).

For pitching moment, oscillation is made by defining a constant sinusoidal angular pitching velocity. This is given as follows:

$$\theta(t) = \theta_a \sin(\omega t) \tag{4}$$

$$\alpha(t) = \alpha_0 + \alpha_a \sin(\omega t) \tag{5}$$

$$q = \dot{\theta} \tag{6}$$

$$\theta_a = 2^\circ \tag{7}$$

Combining Eqs. 4–6, we get:

$$\dot{\theta}(t) = q(t) = \dot{\alpha}(t) = \alpha_a \omega \cos(\omega t) \tag{8}$$

The mathematical expression of the forces and moments for the longitudinal moment coefficient calculation can be obtained by a Taylor series expansion, and the linearized equation may be rewritten for the aerodynamics moment coefficient for

the unsteady analysis as

$$C_m(t) = C_{m_0} + C_{m_\alpha}(\alpha - \alpha_0) + C_{m_{\alpha^\circ}} \frac{\alpha^\circ k}{\omega} + C_{m_q} \frac{qk}{\omega} \tag{9}$$

Using non-dimensionalized aerodynamic time parameter and substituting (5), in the Eq. (6) becomes:

$$C_m(t) = C_{m_0} + C_{m_\alpha}\alpha_a \sin(\omega t) + \left(C_{m_q} + C_{m_{\dot{\alpha}^\circ}}\right)\frac{d}{v}\alpha_a \omega \cos(\omega t) \tag{10}$$

Since a periodic pitching motion is prescribed to the body, the forces can be expected to be periodic. The frequency of the forces should be the same as that of the prescribed motion. Thus, the moment coefficient can also be expressed in the following form.

$$C_m(t) = C_{m_0} + C_{m_{1s}} \sin(wt) + C_{m_{1c}} \cos(wt) \tag{11}$$

Comparing Eqs. (7) and (8), it can be observed that

$$C_{m_{1c}} = \left(C_{m_q} + C_{m_{\dot{\alpha}}}\right)\frac{d}{v}\alpha_a \omega \tag{12}$$

The first harmonics for the pitching moment coefficient can be calculated as

$$C_{m_{1c}} = \frac{\sum C_{m_i} \cos(\omega t_i)}{\sum \cos(\omega t_i)\cos(\omega t_i)} \tag{13}$$

The summations are done over one complete period.

4 Results and Discussion

4.1 Steady State Condition

The residual plot for steady state simulations is shown in Fig. 2. Residual plot indicates good convergence of the mass, momentum, and energy.

Figure 3 shows the C_p palette for $\alpha = 2°$, and Fig. 3 shows the Mach palette for steady state simulation for $\alpha = 2°$. Large subsonic pocket with suction pressure in the wake region can be seen in Fig. 3. High pressure stagnation region is visible (region 1) in Fig. 3. Region 2 in the leeward side of the nose indicates expansion and a drop in pressure. From the Mach palette, a decrease in Mach number is seen at the stagnation point. Mach number increases continuously along the vehicle length. A discontinuity in Mach number variation occurs at the cone junction due to curvature

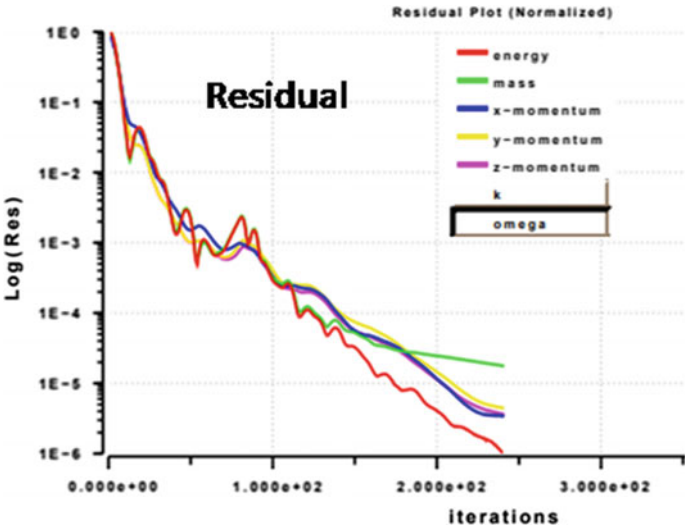


Fig. 2 Residual plot at Mach 0.6, $\alpha = 2°$ showing convergence

change. A large region of low-speed base flow is seen aft of flare, which contributes to the base drag.

Figure 4 for $\alpha = 2°$ indicates that the normal force coefficient is increasing from nose to base indicating that all parts of the body contribute toward the normal force coefficient. Both midsection and flare contribute equally, to 75% of the total value and nose contributes to 25% of the total. The contribution of the base to the normal force coefficient is insignificant, as expected. The plot for $\alpha = 0°$ indicates that normal force coefficient is 0, as expected.

The plots for $\alpha = 0°, 2°$ in Fig. 5 merge with each other, indicating the axial force coefficient is similar at these angles of attack. Referring to Fig. 5, the nose cap contributes 15% to the total axial force coefficient, followed by similar contribution

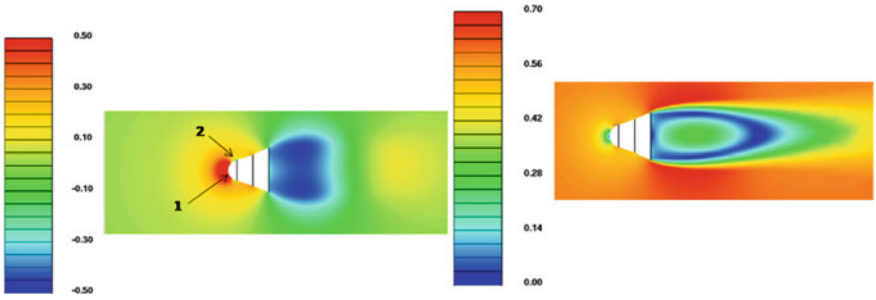


Fig. 3 From the left: **1.** C_p palette at Mach 0.6, $\alpha = 2°$, **2.** Mach palette at Mach 0.6, $\alpha = 2°$

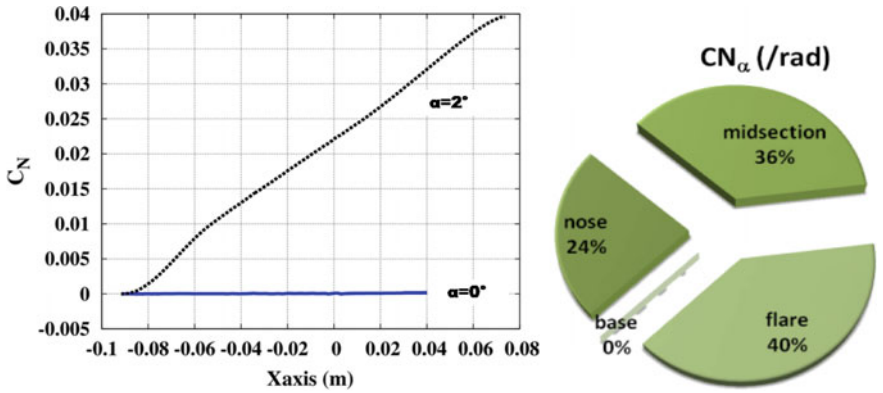


Fig. 4 From the left: **1.** Cumulative normal force coefficient for $\alpha = 0$ and 2°, **2.** Normal force coefficient—Component breakup

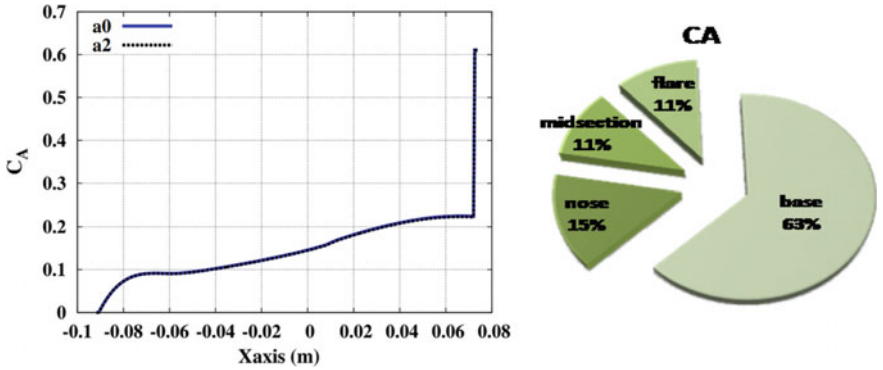


Fig. 5 From the left, **1.** Cumulative axial force coefficient for $\alpha = 0$ and 2, **2.** Axial force coefficient—Component wise breakup

by the midsection and flare 11% each. Base contribution is the highest at 63% due to the suction pressure prevailing in the base region [10, 11].

Pitching moment coefficient for $\alpha = 2°$ is negative indicating a pitch down (restoring moment). Table 1 shows the comparison of the static coefficients with the experimental results. Percentage difference between the test and CFD is shown for C_A and $C_{N\alpha}$.

4.2 Dynamic Stability

The forced oscillation technique is used for computing the dynamic stability derivatives. Based on the earlier experience, time step for the transient simulation with dual

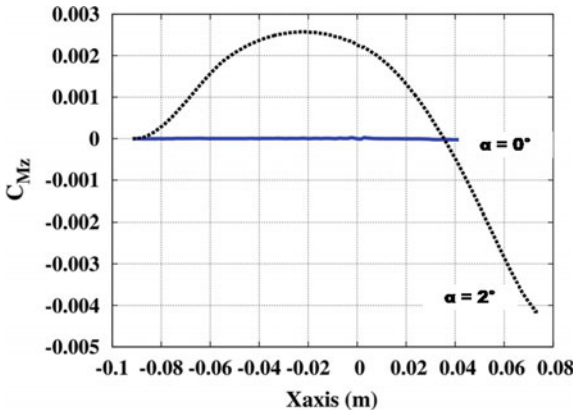


Fig. 6 Cumulative pitching moment coefficient

Table 1 Static aerodynamic coefficients

M	C_A(Test-CFD)	$C_{N\alpha}$(/rad) (Test – CFD)	XCP (in terms of D from CR)
0.6	− 13.81%	6.79%	0.105

time stepping is chosen so that there are 1000 points in a single cycle. Simulation is carried out for 8 cycles. Steady state results are taken as the initial conditions for the transient simulation. In these simulations, the body is forced to oscillate around its center of rotation with an input oscillation as cosine function. For this simulation, the oscillation/motion is imposed on the whole of the grid. Figure 7 shows residual drop for inner iteration. One order drop is seen in the inner iterations.

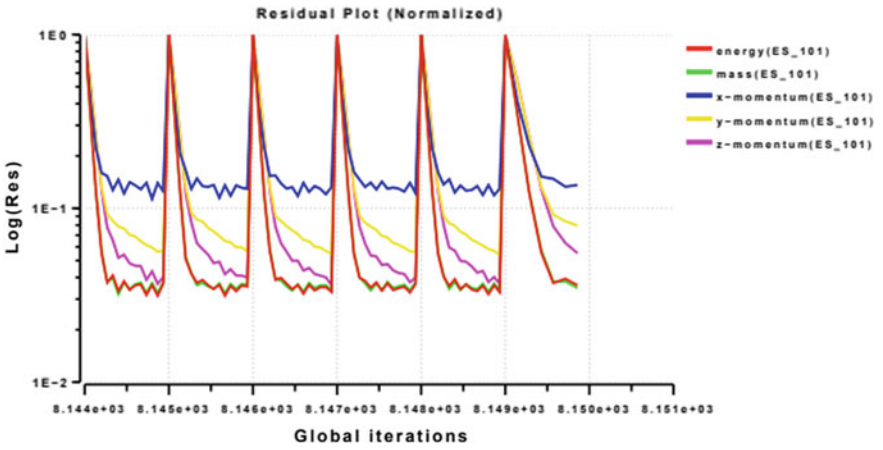


Fig. 7 Inner iteration residual drops by 1 order

The grid is oscillating instead of the body; hence, the positive amplitude of theta would mean negative angle of attack for the body. The grid is oscillated with a sinusoidal motion resulting in the oscillatory pitching moment response. The C_p palettes in the Fig. 8 correspond to certain time instances in the cycle of oscillation indicated in Fig. 8. Initially the alpha is negative which results in the stagnation region getting shifted to the upper region of the body. Instances 1 and 4 are for the two extreme conditions of the oscillation.

The nature of the curve for C_A is different from that of the C_{mz} and C_N (Fig. 9). The plot for C_N versus time (Fig. 9) starts with negative lift as the grid oscillates with a positive amplitude first. This causes the body to have a negative angle of attack (pitch down) which results in the negative lift. The net effect of the lift and the axial force is that it results in a pitch up moment for a positive theta which is restoring in nature.

Pressure probes have been used in the transient condition to get the variation of pressure at the different points in the model. This was done to check the lag in the

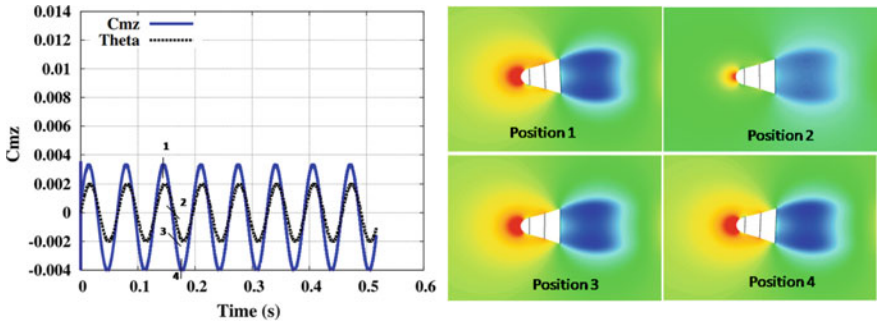


Fig. 8 From the left, **1.** Cmz and Grid angle (θ) versus time for $M = 0.6$, **2.** C_p palettes for different positions in the wave

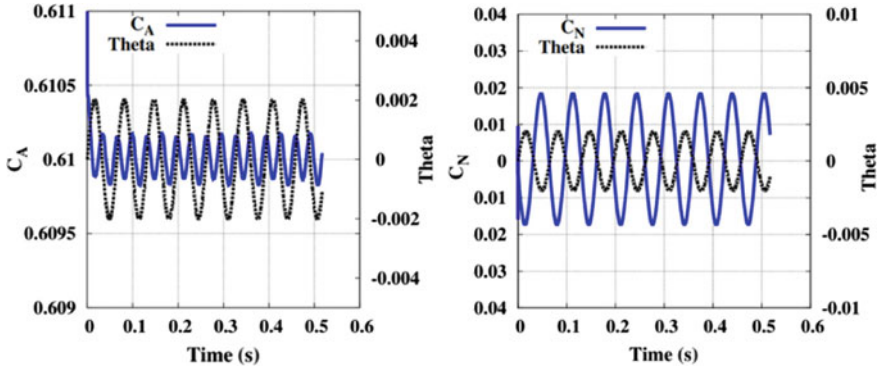


Fig. 9 From the left, **1.** CA and Grid angle (θ) versus time, **2.** CN and Grid angle (θ) versus time

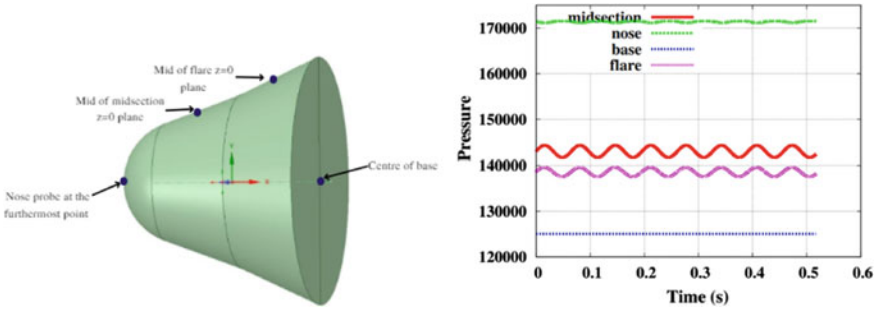


Fig. 10 From the left, **1.** Probe points location, **2.** Pressure versus time (at probe points)

variations of pressure downstream and how one component is affecting the other. The probe positions are given in Fig. 10.

Looking Fig. 10, it can be noted that the pressure variations for probes on the midsection and flare are in phase as they are on the same side of the body. Since both are in the top side of the body, they have an increase in pressure as they are facing the wind when α is negative for the body. The base probe has no variation in pressure, probably because the point selected is in the center of the base. Points in the wake shear layer can be monitored in future. The nose on the other hand has very small variation that occurs because of the probe moving while the body oscillates.

Pitch damping derivatives are obtained by processing the Cmcg data obtained after neglecting the first cycle of oscillation (initial transient). The result obtained is -0.39. The result is negative in sign, indicating positive pitch damping and has 16.32% difference when compared with the test data showing a good comparison.

5 Conclusion

Longitudinal static stability and dynamic stability for a typical reentry body are assessed at subsonic Mach number of 0.6 using commercial software *CFD++*. Steady state simulations are carried out for $\alpha = 0$ and 2° on an unstructured grid of size 38million, to compute the static stability of the configuration. Static aerodynamic parameters of C_{A} and $C_{\mathrm{N}\alpha}$ are compared with the test data. Transient simulation using the forced oscillation technique is performed for 8 cycles considering the steady state solution as initial solution. Pitch damping derivatives are computed by processing the moment coefficient data obtained from the transient simulation. The pitch damping derivative obtained is negative in sign indicating positive pitch damping, and the match with test data is good at this subsonic Mach number.

6 Future Work

Effect of grid, time step, inner loop iteration, cycle averaging change, turbulence model, and sting on the results shall be studied in the future. Simulation for different Mach numbers can also be done.

Acknowledgements Authors thank to ISRO for providing access to specific data, archives, or resources that contributed to the research and Mr. M Jathaveda and Mrs G Vidya – Employees of ISRO,VSSC.

Authors thank Shri K Srinivasan, Head, WTDD, for sharing the NAL wind tunnel test data report.

Funding Not applicable.

References

1. Samardzic M et al (2018) A forced oscillation system for damping derivative measurement in the T-38 trisonic wind tunnel. Sci Tech Rev 68(3)
2. Saravanan R et al (2915) Pitch damping characteristics of a typical crew return module using freeoscillation technique in Hypersonic Mach number, SAROD 2015
3. Bandyopadhyay P et al (2013) Development of a methodology for estimation of aerodynamic parameters from the aero-ballistic test data, SAROD 2013
4. Ma Y, Lv M, Su C. Numerical simulation of pitch- damping dynamic derivatives. In: 8th European conference for aeronautics and space sciences (EUCASS). https://doi.org/10.13009/EUCASS2019-78
5. Kazemba CD et al (2017) Survey of blunt-body supersonic dynamic stability. J Spacecr Rockets 54(1)
6. Potturi AS, Peroomian O (2016) Dynamic stability analysis of the orion crew module through computational fluid dynamics. In: AIAA AVIATION forum 13–17 June 2016
7. Subramoniam A et al. Space Capsule recovery experiment project—Mission overview, IAC-07:D2.2.04
8. Balasubramanian S, Vidya G (2019) Base flow characterization of blunt cone-flare configuration at various mach numbers. In: FMFP-19 conference, PSG College
9. Metacomp CFD++V20.1
10. Moore FG, Hymer TC (2001) Improved power-on, base drag methodology for the aero prediction code. NSWCDD/TR-00/67, May 2001
11. Butsko JE. Prediction of the subsonic base drag of hypersonic re-entry vehicles. AIAA paper 66-991

Development of a Sampling-Based UAV Path Planner for Collision-Free Navigation



Aliasgar S. Malik, Hari Om Verma, Vivek Kumar, and Keerthana Radhakrisnan

Abstract Unmanned aerial vehicles (UAVs) have become immensely popular in various applications, from surveillance, monitoring to package delivery, search, and rescue missions. Efficient path planning is a crucial aspect of UAV operations to ensure safe and optimal navigation in complex environments. Given its efficient detection of ideal paths, the A* algorithm has drawn considerable interest in the world of path planning. This paper presents an extensive investigation of the A* algorithm and its application in UAV path planning. The objective of this investigation is to analyze the performance of A* in terms of path optimality and versatility across various test cases. The paper provides a comprehensive overview of the algorithm, including its underlying principles and heuristic search strategy. Through the means of this, we have tested the proposed algorithms on various test cases and obtained collision-free traversal.

Keywords UAV · Path planning · Autonomy · Navigation · Obstacle avoidance

A. S. Malik (✉)
Amity Institute of Aerospace Engineering, Amity University Uttar Pradesh, Noida, India
e-mail: ali.malik@s.amity.edu

H. O. Verma · V. Kumar
Faculty of Engineering, Amity Institute of Aerospace Engineering, Amity University Uttar Pradesh, Noida, India
e-mail: Hoverma@amity.edu

V. Kumar
e-mail: vkumar13@amity.edu

K. Radhakrisnan
Reude Technologies, Chennai, India
e-mail: keerthana_asn@reude.tech

© The Author(s), under exclusive license to Springer Nature Singapore Pte Ltd. 2024

S. Singh et al. (eds.), *Recent Advances in Aerospace Engineering*, Lecture Notes in Mechanical Engineering, https://doi.org/10.1007/978-981-97-1306-6_40

1 Introduction

Path planning is an essential component of UAV motion planning, enabling autonomous vehicles [1, 2] to navigate through complex environments efficiently. The purpose of path planning is to find an optimum path that allows a UAV to move from its current location to a goal location while avoiding obstacles and ensuring smooth, continuous motion. In robotics, path planning algorithms are used to find out the robot's trajectory [3] from its current location to a desired end location [2, 4]. The trajectory must be collision-free and satisfy certain constraints, such as minimizing the time taken [5] or energy consumed (Fig. 1).

Unmanned aerial vehicles (UAVs), also known as drones, have become extremely popular in recent years, both in the commercial and in military sectors. In the case of UAVs, path planning involves selecting a flight path that meets mission objectives, while ensuring safe and efficient operation [6]. The path needs to be feasible and collision-free, and it must take into account the UAV's dynamics, such as its speed, altitude, and payload.

Path planning in UAVs is a challenging task due to the unpredictable nature of the environment. Obstacles such as buildings, trees, and power lines can pose a significant challenge to UAV navigation [4]. Furthermore, factors such as wind speed, turbulence, and air pressure can affect the UAV's flight trajectory and path planning.

Path planning in UAVs involves the utilization of algorithms that rely on mapping the surrounding environment, in some cases through sensor information, to determine the most optimal route. Some of these algorithms are A* (A-star) [2], Dijkstra's algorithm [7], rapidly exploring random trees (RRT) [7], etc. A* is a well-known algorithm that employs a heuristic search to identify the shortest path between two points. It finds extensive application in real-time path planning scenarios, such as drone racing, and search and rescue missions. On the other hand, Dijkstra's algorithm is a classical approach that determines the shortest path between two nodes on a graph. It constructs a tree of shortest paths originating from start to every other point in the

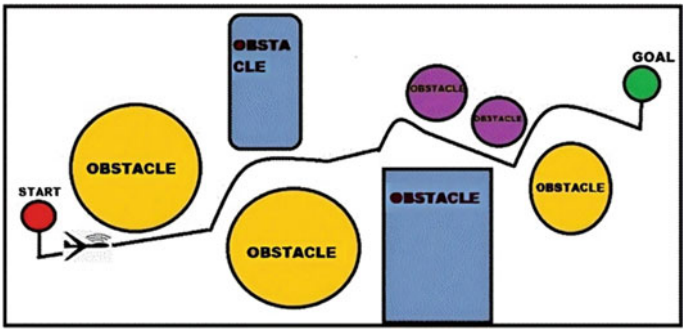


Fig. 1 Autonomous path planning in UAVs

graph. Meanwhile, RRT is a probabilistic algorithm [4] that generates a random tree comprising feasible paths and selects the path that exhibits the closest proximity to the destination.

One of the most widely used path planning algorithms in robotics is the A* algorithm, which is a heuristic search algorithm used for finding the shortest path between two points [5]. A* uses a heuristic function to estimate the distance between the current location and the desired location. The algorithm then selects the next location that minimizes the cost function, which is the sum of distance already covered and the anticipated remaining distance.

The study at [4] presents the two most popular graph-based and sampling-based techniques compared with regard to 3D UAV path planning in a complicated environment. The most popular algorithms, RRT for sampling-based methods and A* for graph-based methods, are evaluated in the same circumstances and subjected to the same performance metrics. Comparatively speaking, the A* algorithm produces shorter pathways than the RRT algorithm. While the RRT algorithms uniformly search the space, the A* algorithm only explores the volumes necessary for path construction. Hence, A* was chosen as the algorithm to be employed for this research.

2 Problem Statement

The autonomous navigation of UAVs poses significant challenges that require efficient and accurate path planning and obstacle avoidance techniques. Despite its popularity, several critical issues persist in the application of path planning algorithms, limiting their effectiveness in real-world scenarios.

Firstly, the UAV may encounter difficulties when confronted with environments characterized by intricate structures, multiple obstacles, and dynamic changes [8], where the generated paths may not be truly optimal due to limited consideration of the surrounding context. Additionally, the applied algorithm may struggle to adapt to real-time updates, such as the appearance of new obstacles or changes in the environment, which can compromise the safety and efficiency of autonomous systems.

Another key challenge is the computational complexity of the algorithm used by the UAV when dealing with large-scale environments. As the size and complexity of the search space increase, the algorithm's performance deteriorates, leading to longer computation times and increased resource consumption resulting in delay. This limitation hampers the real-time capabilities of UAV's autonomous navigation systems and restricts their deployment in time-sensitive applications.

Moreover, the algorithm [6, 9, 10] may not adequately handle situations involving uncertain or incomplete information. When facing ambiguous or incomplete maps or sensor data, the algorithm's reliance on precise heuristic estimations may lead to suboptimal path choices or even failures in finding viable paths.

The performance of UAVs must be improved by addressing these issues and strengthening the A* algorithm's efficacy and efficiency in path planning and obstacle

avoidance. Therefore, this research aims to investigate and propose novel approaches, algorithms, or modifications to the existing A* algorithm to overcome the limitations mentioned above and enable more reliable and efficient autonomous navigation in complex environments.

3 Methodology

3.1 A Path Planning*

A* is a path planning algorithm that is utilized extensively in a variety of fields, including robots, video games, and GPS navigation [11, 12] systems. The optimum route between a starting point and a destination on a graph or map is identified using a heuristic search method. The A* algorithm selects the best node to explore next by weighing the total distance traveled from the starting node (g-score) and the anticipated distance to the goal node (h-score).

$$f(n) = g(n) + h(n) \tag{1}$$

The algorithm starts by considering the starting node and adds it to the "open set" of nodes to be visited. The lowest f-score node is then selected and added to the "closed set" of visited nodes. The f-score is calculated by adding the g-score and the h-score together. The method keeps expanding nodes in this way until it either reaches the target node or runs out of nodes to explore without coming up with a path. [4, 11].

The A* algorithm is highly effective due to its utilization of the estimated distance to the goal node as a heuristic for guiding the search process. This heuristic, which can be the Manhattan distance [2, 9] or the Euclidean distance [9], is determined by calculating the distance between the current node and the target node. By employing this heuristic, the algorithm can efficiently navigate toward the goal while avoiding unnecessary exploration of irrelevant paths. To apply the A* algorithm in UAVs for path planning, it is crucial for the UAV to possess a map or a graph representing the environment it operates within. A complete description of the terrain, any obstacles, and the exact positions of the start and end positions should all be included on this map. By utilizing the A* algorithm, the UAV can determine the shortest path between the two points while effectively circumventing any obstacles encountered along the way.

The A* algorithm can be further optimized using various techniques, such as the use of a priority queue or the implementation of a bidirectional search. The priority queue can help to speed up the search by choosing the nodes with the lowest f-score more efficiently, while the bidirectional search [1, 13] can reduce the search space by starting the search from both the start and end nodes [9]. Overall, the A* algorithm is a powerful tool for path planning in various fields, including UAVs and robotics.

Its effectiveness lies in its ability to use a heuristic to guide the search and to quickly find the optimal path to the goal while avoiding obstacles [6, 7].

3.2 A Algorithm Pseudo-code*

```
function A_star(start, end):
    // Create a start node with the desired input start position
    start_node = Node(None, start)
    // Create an end node with the desired input end position
    end_node = Node(None, end)
    // Initialize the open list and add the start node to it
    open_list = [start_node]
    // While there are nodes in the open list
while open_list is not empty:
        // Get the node with the lowest f-value from the open list
       current_node = node in open_list with the lowest f-value
       // Move the current node from the open list to the closed list
        remove current_node from open_list
        add current_node to closed_list
        // If the current node is the goal node, a path is found
        if current_node == end_node:
       return reconstruct_path(current_node) // Helper function to
backtrack and return the path
        // Generate children nodes for the current node
        children = generate_children(current_node)
        // For each child node
        for child in children:
           // If the child node is in the closed list, skip it
           if child is in closed_list:
               continue
        // Calculate the g, h, and f values for the child node
        child.g = current_node.g + cost of moving from current_node
to child
       child.h = heuristic function to estimate the cost from child
to end_node
        child.f = child.g + child.h
// If the child node is already in the open list and has a higher g-
value, skip it
        if child is in open_list and child.g > open_list[child].g:
              continue
        // Add the child node to the open list
        add child to open_list
   // If the open list is empty and the goal node is not found, no path
exists
      return no path found
```

The provided code demonstrates the implementation of the A* algorithm for autonomous path planning and obstacle avoidance in a three-dimensional environment. The A* function takes the environment, start position, and end position as inputs. Here, the environment is defined as a three-dimensional array, representing a

grid of cells. Each cell can be either 0 (representing an empty space) or 1 (representing an obstacle).

The code begins by defining a Node class, representing each node or cell in the environment map. Each node has a parent, a position, and three parameters: g, h, and f values. The f value is the total of the g and h values, and the g value indicates the cost from the start node to the current node. The h value is a heuristic estimate of the cost from the current node to the end node.

It initializes the start and end nodes with their respective positions and sets their g, h, and f values to 0. It also initializes two lists: an open list to keep track of nodes to be evaluated, and a closed list to store nodes that have been evaluated. The start node is added to the open list.

Once the open list is empty, the algorithm exits the while loop. The node with the lowest f value is chosen from the open list and designated as the current node inside the loop. If the current node is the final node, the algorithm verifies this. If so, it reverses through the parent nodes to reconstruct the path from the end node to the start node and then returns the path. The algorithm creates the child nodes if the current node is not the end node. It takes into account any and all movements that could be made in the three-dimensional space, including combinations of movement in the x, y, and z axes. The algorithm determines whether or not the created child node is inside the environment's limits.

The Algorithm then checks if the child node is already in the closed list (nodes that have been evaluated). If it is, the algorithm continues to the next child node. If not, it determines whether the child node is already in the open list. If so, the algorithm moves on to the next child node if the child's g value is higher than the g value of the node in the open list. The process continues until all of the children have been reviewed if the child node passes every test and is added to the open list. Until the shortest path is discovered or there are no more nodes to explore, this loop iterates.

Robot Movement

The algorithm takes into account 26 possible positions that the robot could move to in a single step and uses these positions to generate the children nodes of a particular node. These positions are defined in the following format: (x, y, z), where x, y, and z represent the changes in the robot's position along the three spatial dimensions. For example, (0, − 1, 0) represents the position one step left along the y-axis, and (−1, − 1, − 1) denotes the diagonally up-left-backward in 3D.

These positions allow the robot to navigate in three dimensions, enabling it to move horizontally, vertically, and diagonally in all possible directions within the given environment. It's important to note that not all of these positions may be applicable or valid depending on the specific environment. The algorithm checks for the validity of each position before considering it as a potential movement option. Obstacles or boundaries in the environment may restrict the robot's movement in certain directions, as indicated by the code snippet where it checks if the node position is within the bounds of the environment and if the position is obstructed by an obstacle.

3.3 Sample Space

An example of the Environment array used in our algorithm to represent the 3D environment space in which the UAV path obtained by the algorithm is tested is given in Eq. 2. It is a nested list containing multiple layers, each representing a 2D grid of the environment. Each element in the grid is a list of numbers, where 0 represents an open path or empty space, and 1 represents an obstacle or a building.

$$
\begin{aligned}
\textbf{Environment} = [&[[0,\ 0,\ 1,\ 0,\ 0,\ 0],\\
&[0,\ 0,\ 0,\ 0,\ 0,\ 0],\\
&[1,\ 0,\ 0,\ 0,\ 0,\ 0],\\
&[0,\ 1,\ 0,\ 0,\ 0,\ 0],\\
&[0,\ 1,\ 1,\ 1,\ 0,\ 0],\\
&[0,\ 0,\ 0,\ 0,\ 0,\ 0]],\\
&[[0,\ 0,\ 1,\ 0,\ 0,\ 0],\\
&[0,\ 0,\ 0,\ 0,\ 0,\ 0],\\
&[1,\ 0,\ 0,\ 0,\ 0,\ 0],\\
&[0,\ 1,\ 0,\ 0,\ 0,\ 0],\\
&[0,\ 1,\ 1,\ 1,\ 0,\ 0],\\
&[0,\ 0,\ 0,\ 0,\ 0,\ 0]],\\
&[[0,\ 0,\ 1,\ 0,\ 0,\ 0],\\
&[0,\ 0,\ 0,\ 0,\ 0,\ 0],\\
&[1,\ 0,\ 0,\ 0,\ 0,\ 0],\\
&[0,\ 1,\ 0,\ 0,\ 0,\ 0],\\
&[0,\ 1,\ 1,\ 1,\ 0,\ 0],\\
&[0,\ 0,\ 0,\ 0,\ 0,\ 0]]]
\end{aligned}
\tag{2}
$$

Here is a breakdown of the structure:

- The array has six layers, which can be accessed using indices 0–5.
- Each layer is a 2D grid with dimensions 6×6, representing a 6×6 grid.
- Each element of the grid is a list with six numbers (0 or 1), representing the cells of the grid.
- Each grid block along axes x, y, and z are of length 50 m where x and y represent lateral and longitudinal travel, whereas z represents the height of the obstacles.

4 Results and Discussion

4.1 Results

Test Case 1

The 1st test case parameters were set up such that the UAV starts its journey from the point with coordinates (1, 1, 1) and reaches its destination at the point with coordinates (5, 5, 5). The start point represents the initial position of the UAV, and the end point represents its desired final destination. Several obstacles are placed in the UAV's environment that the UAV needs to avoid during its flight. These obstacles were represented by the three-dimensional coordinates (3, 5, 4), (4, 5, 3), (3, 1, 4), (2, 4, 3), (2, 5, 3), (1,3,4). The 3D environment with the obstacles created for this test case and the path generated by the A* algorithm can be viewed in Fig. 2 with the generated path following the coordinates (1, 1, 1), (2, 2, 2), (3, 3, 3), (4, 4, 4), (5, 5, 5) sequentially to reach its destination while avoiding obstacles.

Test Case 2

In the 2nd case, as demonstrated in Fig. 3, the start point of the UAV was set to (1, 2, 1) and its destination point as (3, 5, 5), whereas the obstacles in this test case were represented by the coordinates (1, 5, 4), (2, 5, 2), (3, 5, 2), (4, 4, 4), (1, 4, 4), (4, 3, 4).The path that the algorithm produced for the UAV to transverse obstacle-free and reach its destination was (1, 2, 1), (2, 3, 2), (3, 4, 2), (3, 5, 4), (3, 5, 5).

Test Case 3

Finally, a 3rd case was tested in which the UAV starts at (6, 4, 5) and ends at (2, 5, 3) with the obstacles positioned at coordinates (3, 6, 4), (4, 2, 4), (2, 3, 4), (2, 6, 4) (4,

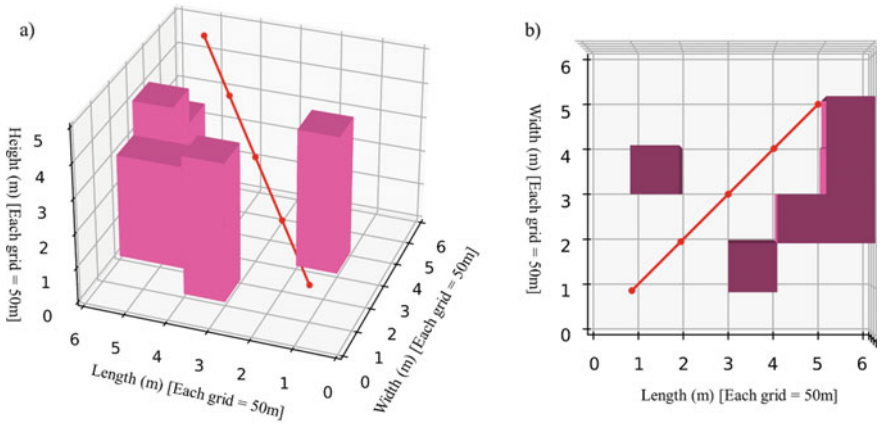


Fig. 2 3D Environment showcasing the obstacles and the UAV path traversal for test case 1 in **a** isometric view, **b** top view

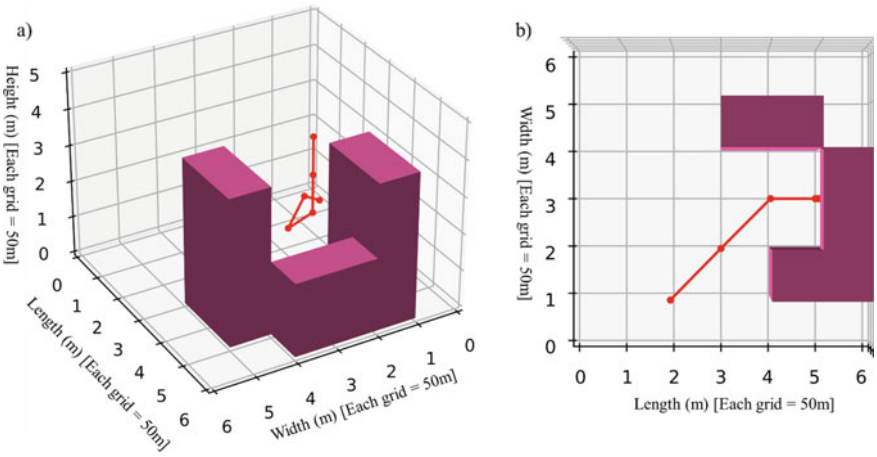


Fig. 3 3D Environment showcasing the obstacles and the UAV path traversal for test case 2 in **a** isometric view, **b** top view

3, 4). The resultant environment and the generated obstacle-free path are depicted in Fig. 4. The planned path coordinates calculated were (6, 4, 5), (5, 5, 4), (4, 5, 3), (3, 5, 3), (2, 5, 3).

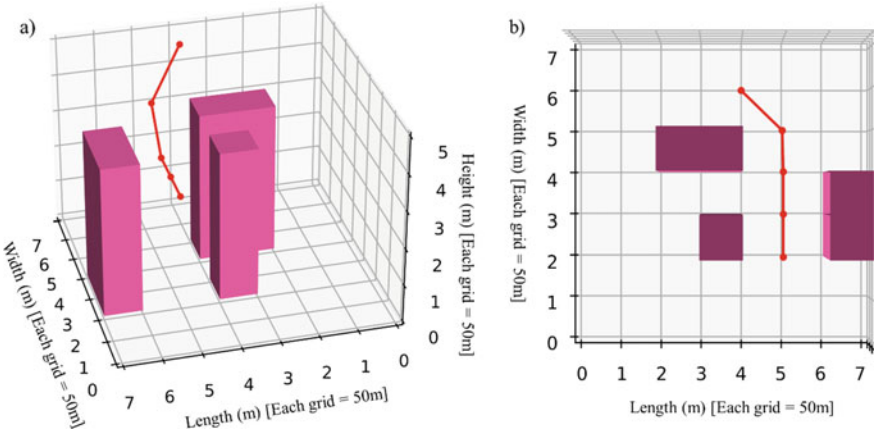


Fig. 4 3D Environment showcasing the obstacles and the UAV path traversal for test case 3 in **a** isometric view, **b** top view

4.2 Discussion

From the results obtained, we observe that the proposed A* algorithm strikes a delicate balance between optimality and computational efficiency. By evaluating potential paths and employing a combined cost function ($f = g + h$), the algorithm intelligently explores the search space while prioritizing nodes with lower costs and heuristic estimates. This approach allows the algorithm to converge toward the optimal path, effectively navigating through complex environments and avoiding obstacles. The resulting path, represented as a sequence of positions, offers a reliable route for the UAV, optimizes its navigation, and maximizes overall efficiency. The algorithm's superiority lies in its ability to leverage a heuristic function and estimate the distance to the goal, which guides its decision-making process and significantly reduces the computational effort.

5 Conclusion

In conclusion, the A* algorithm proposed is a powerful approach in path planning, to find the best path between two points efficiently. This unique combination of factors allows the UAV to make informed decisions, efficiently navigating through complex environments. One of the algorithm's main advantages is its capacity to strike a balance between exploration and exploitation. This method gives higher priority to nodes that are more likely to lead to the ideal path by using the heuristic function, which offers an estimation of the distance still to travel. This allows the algorithm and in turn the UAV to avoid unnecessary exploration and focus on promising areas of the search space. This ensures that algorithm can find an optimal or near-optimal solution while minimizing the computational resources required. Furthermore, its ability to adapt to different problem settings and its ability to handle various types of graphs, and test cases can result in it becoming a valuable tool for path planning in diverse environments/conditions.

Acknowledgements I would like to thank Ms. Keerthana Radhakrisnan and *Reude Technologies, Chennai,* for their continuous support and guidance throughout the duration of this research. I would further like to thank Dr. Hari Om Verma, Mr. Vivek Kumar, and *Amity Institute of Aerospace Engineering, Noida,* for providing me with the opportunity, means, and support to conduct this research.

Funding Information Not Applicable.

References

1. Kevin D, Delphine R, Inkyung S, Peter N (2019) Comparison of path-planning algorithms for unmanned aerial vehicle deployment under threats. IAFC Paper Online 52–13:1978–1983

2. Al Gburi Hussein Q, Al-Baiati AE. Path-planning dynamic 3D space using modified A* algorithm. In: 2020 IOP conference series: materials science and engineering, vol 928, p 032016
3. Mickel SP, Inna S. Sampling-based A* algorithm for robot Path-Planning. Int J Robot Res 33(13):1683–1708
4. Han J (2019) An efficient approach to 3D Path-Planning. Inf Sci 478:318–330
5. Zhangjie F, Jingnan Y, Guouw X, Yiming C, Yuanhang M (2018) A heuristic evolutionary algorithm of UAV path-planning. Hindawi Wirel Commun Mob Comput Article ID 2851964
6. Jinchao C, Li M., Zhengu Y (2020) An improved A* algorithm for UAV path-planning problems. In: 2020 IEEE 4th information technology, networking, electronics and automation control conference (ITNEC 2020)
7. Wang X, Liu Z, Liu J (2023) Mobile robot path planning based on an improved A* algorithm. In: Proceedings of SPIE 12604, international conference on computer graphics, artificial intelligence, and data processing (ICCAID 2022), 23 May 2023, p 1260449
8. Akshay Kumar G, Himansh A, Parsediya DK (2018) Time-efficient A* algorithm for robot path-planning. In: 3rd International conference on innovations in automation and mechatronics engineering. ICIAME 2018
9. Stefan H (2008) 3D Path-planning and stereo-based obstacle avoidance for rotorcraft UAVs. In: 2008 IEEE/RSJ international conference on intelligent robots and systems, Nice, France. 22–26 Sept 2008
10. Al Rashan M, Al Kurd A (2022) UAV path-planning using genetic algorithm with parallel implementation. Int J Comput Sci Inf Technol (IJCSITY) 10(2)
11. Jeauneau V, Jouanneau L, Kotenkoff A (2018) Path-planner methods for UAVs in real environment. IFAC Papers On Line 51–22:292–297
12. Mohanraj S (2019) Performance of buckets versus min-heap in the A* search algorithm. Dissertation. University of Windsor
13. Jongho P, Youdan K (2015) Collision avoidance for quadrotor using stereo vision depth maps. IEEE Trans Aerospace Electron Syst 51(4)

Design and Fabrication of Flapping-Wing UAV



Ashutosh Biswal, Tejas Sandeep Kapatkar, Vanshika Batosiya, Rajesh Kumar Saluja, and Hari Om Verma

Abstract Related to high-performance flapping micro-air vehicles (MAVs) or unmanned air vehicles (UAVs) has a significant impact on flight performance and mission capabilities, so the development of lightweight, compact, and energy-efficient flapping mechanisms is important. The substantial design validation and performance assessment are very much required for the realization of such a flexible as well as intricate flapping mechanism with the extra capability of producing thrust levels that bound to cruising forward flight and vertical take-off and landing (VTOL) situations. The development of a robotic bird still faces substantial challenges in simulating a bird's periodic main wing action to produce lift and propulsion. The processes like flapping, folding, bending, and twisting make up the major wing action sequences. Bird flight served as the model for the artificial bird's initial design, which was based on decomposing that intricate motion into a simple mechanism. The design made explicit use of the Festo Corporation's existing and distinctive "Smart Bird" flapping-wing unmanned aerial vehicle (UAV). In this paper, I and my colleagues design a version of flapping-wing UAV or an ornithopter and then fabricate it into a fully functional flying mechanical bird.

Keywords Ornithopters · Flapping-wing UAV · Unmanned aerial vehicles (UAV)

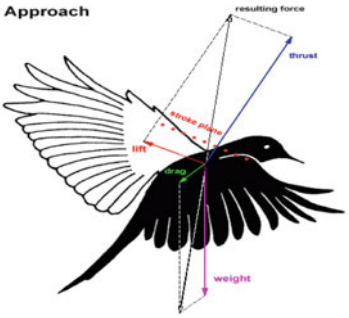
1 Introduction

The flapping of wings, their folding and all these phenomena led the human minds to incorporate that distinct design in making objects fly. This discovery leads back to nearly 1920s when scientists started getting the taste of this wonderful mechanism and that led to the curiosity of us of ways to use the flapping mechanism to our advantage in various fields across the globe.

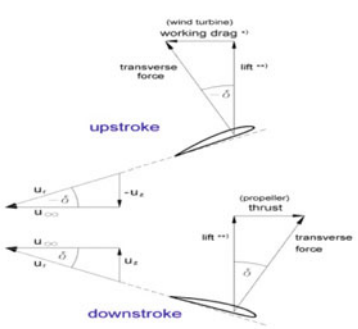
A. Biswal (✉) · T. S. Kapatkar · V. Batosiya · R. K. Saluja · H. O. Verma
Amity Institute of Aerospace Engineering, Amity University Uttar Pradesh, Noida, UP, India
e-mail: ashubiswal4@gmail.com

© The Author(s), under exclusive license to Springer Nature Singapore Pte Ltd. 2024

S. Singh et al. (eds.), *Recent Advances in Aerospace Engineering*, Lecture Notes in Mechanical Engineering, https://doi.org/10.1007/978-981-97-1306-6_41



A.
Free body diagram of an ornithopter [16]



B.
Up-stroke and down-stroke action [17]

Leonardo da Vinci started researching avian flying in 1485. He understood that people are too bulky and weak to fly with just wings linked to the arms. He consequently drew a design for a machine that required the pilot to lie down on a board and operate two sizable, membranous wings with the use of arm cranks, shift paddles, and a set of pulleys. The very first ornithopters with wings were built in France. In 1871, Jobert utilized an elastic band to propel a miniature bird model. Tatin's ornithopter was reportedly the inspiration for a commercial toy and was maybe the first to incorporate active twisting of the wings [1]. Around 1884 onwards, Lawrence Hargrave constructed many ornithopters that were propelled by springs, rubber bands, water vapor, or compressed air [2]. He pioneered the use of tiny flapping wings to power a larger fixed wing, doing away with the necessity for gear reduction and streamlining the structure. Percival Spencer successfully piloted several unmanned ornithopters with wingspans up to 8 feet in the early 1960s. The study was primarily driven by the desire to comprehend coupled bending and torsional motion effectively and to enhance it for possible technological implications. The study centered on developing ultra-lightweight UAVs that can fly more effectively and covertly as well as innovative and fascinating ways of providing thrust. Additionally, it was observed that the UAV would be constructed using materials that were economical and highly accessible on the market.

Rotating-wing, flapping-wing, and fixed-wing vehicles are the three main types of aerial vehicles present in the world. They have been utilized in accordance with their benefits and drawbacks. Fixed-wing MAVs have been employed often for surveillance because they can stay in the air for longer, which is necessary for a long-distance mission with careful preparation [3].

However, due to their ability to hover and land vertically, rotary-wing MAVs have been widely utilized in aerial imagery and delivering packages [4]. When the model is shrunk, it has been shown both fixed-wing and rotary-wing designs suffer from reduced aerodynamic performance [5]. The fact that fixed-wing MAVs have a poor lift-to-drag ratio and sub-optimal flight control has been noted [6].

Compared to rotary-wing MAVs, the FW-MAVs are well-known for their effective and smooth flight performance and remarkable hovering abilities [7]. Due to their

compact size, FW-MAVs are able to operate in limited spaces. They also make less noise than rotary-wing aircraft, which makes them less detectable and ideal for surveillance missions [8].

Researchers have been looking for inspiration from nature's greatest flyers, including tiny birds and insects like the common house/fruit fly, due to the strong demand for such enhancements. The primary concept for the research was how efficiently birds fly and how their wing mechanisms impact their capacity to sustain aerodynamic advantage and acquire air supremacy.

Collis [9] has compiled a thorough survey of early research on flowing fluid, its characteristics, and active flow control. Ornithopters are the name given by scientists or aircraft designers to flying objects with flapping wings. The gear system and battery power of the ornithopter allow it to raise the number of flaps. We are working to create a great real-time system using the specs of various birds. In order to comprehend the flapping process, the fundamentals of aviation have been investigated. Thus,

- lift force upwards must equal weight force downwards for an aircraft or bird to maintain a constant altitude, and
- thrust force forward must equal the opposing force of drag for an aircraft or bird to maintain a constant speed.

Flapping Wings Methodology

Considering constraints of weight, structural strength, and mechanical intricacy, the flapping wings and their propulsion in the air are made to generate as much lift as possible. Due to its greater mobility and related uses, such as surveillance, scouting, and search and rescue operations, the flapping devices have attracted a lot of interest and attention over the last few years. A review of the extensive academic research on the structural-fluid interaction, unsteady flow models [11, 15], quasi-steady models, aero elasticity, and the study of aerodynamics of flapping wings [10–15] reveals that there is a dearth of information on how to design and create effective and lightweight flapping mechanisms. The mechanism is achieved by undergoing the extensive process of Biomimicry. The practice of trying to replicate a live thing in nature's greatest traits is known as Biomimicry. In general, airplanes use the fluid flow around their airfoil-shaped wings, and they can only significantly alter the stream under high-speed conditions (high Reynolds number range).

Bird aviation, often referred to as ornithopter flight, has just two degrees of freedom (DOF), the first of which is the primary flapping mechanism and the second of which is the tiny divergence from the stroke vector (out-of-plane flapping motion). The flight mechanism of insects comprises of three degree-of-freedom, the third one being the active wing rotation that is replaced by the passive wing rotation mechanism in ornithopters that is called "feathering." The bulk inertial stress of the wings while flapping is what causes passive rotation. As a result, the kinematics of ornithopter flying are made simpler since it seems as though the wing rotation is automated. To get efficient angles of attack in relation to the flapping wing leading edge in 2D airfoil instances, wing rotation is also known as "pitching."

1.1 Contribution of Flapping Wings Kinematics

The flapping wings have been studied over the years and the contributions toward fluid-kinematics is immaculate. A tabulation of the contributions is as below:

Force	Model used	Motion	Contribution
Lift	General bird	Flapping	Lift force is almost independent of flapping frequency for low flapping frequency
		Pitching, flapping and pitch-flap	Lift force is dominantly produced by pitching motion
		Flapping	Moderate increase of AOA is advantageous to average lifting force production
		Flapping	Lift augmentations due to flapping motion were found to decrease exponentially as advance ratio increases
Thrust/ propulsive efficiency	General bird	Flapping	The average thrust value increases with respect to flapping frequency
		Flapping	Thrust and power increase with increasing flapping frequency
		Flapping	Increasing frequency will result in more thrust coefficient (higher wing torsional stiffness)
		Pitching, flapping pitch-flap	Thrust force is dominated by flapping motion
		Flapping	Moderate increase of AOA is advantageous to average thrust force production
		Flapping	Thrust generated due to flapping motion would decrease monotonically with increasing orientation angle
	Flap airfoil	Flapping	Propulsion velocity increases with both flapping frequency and amplitude
Drag	Flap airfoil	Flapping	If flow is subjected to drag forces, it will have friction wake shape downstream of body
	Gen. bird	Pitching, flapping pitch-flap	Drag force is dominated by flapping motion

The ornithopters are usually man-made using the resources like gears, gear train/ drive mechanisms, wings, battery to power it, motors, and various other electrical and mechanical components.

2 Calculations.

2.1 Lift Calculation for the Ornithopter

The lift force produced by the wings of an ornithopter is given by the following formula:

$$\mathbf{L = 1/2 \times C_L \times \rho \times A \times V^2}$$

where L is the lift force (N) produced, C_L is the Coefficient of lift, ρ is the density of air $\left(\frac{kg}{m^3}\right)$. The density of air is taken as 1.225 $\left(\frac{kg}{m^3}\right)$. The area of the wing chosen is approximately 0.09 (m^2), this area was chosen as my ornithopter is inspired by a bird named "The Blue Jay" that has a wing span of (32–45) cm and body length of (22–30) cm. We have chosen "The Blue Jay" bird as a reference for our studies because it is a very aggressive and intelligent bird that is known for mimicry. It also has one of most aerodynamic torsos as well as a good wing span to body ratio that can fly quite far in a single flight. It being also being a small bird kind of helped us replicating its dimensions. The air speed is taken as 10 $\left(\frac{m}{s}\right)$. Coefficient of lift for low Reynolds number regime is 0.8.

Hence, after putting all the values of the individual quantities in the formula and computing it, we get that the lift produces is approximately **5N**

2.2 Gearing Ratio and Flapping Frequency

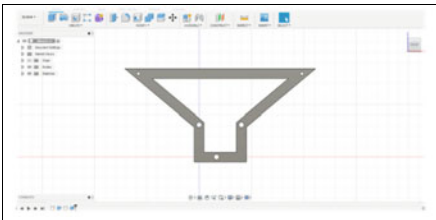
The required number of flaps or the flapping frequency of a standardized ornithopter or flapping-wing UAV or MAV is 4–6 flaps per sec. Hence, the flapping frequency of the ornithopter is an average of 5 flaps per sec. Accordingly, we will calculate the gearing ratio of the gears. The gearing ratio is given by the following formula:

$$\textbf{Gearing ratio (GR)} = (\textbf{(kv or rpm) of BLDC} \times \textbf{LiPo battery voltage}) / (\textbf{flapping frequency} \times \mathbf{60})$$

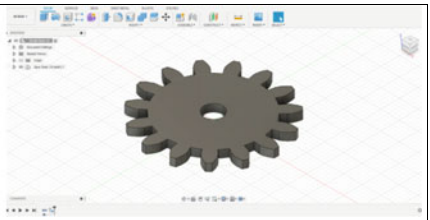
Now, in the ornithopter, we have used a 1400 kV BLDC (Brushless DC) motor and LiPo battery of voltage 7.4–8 V. After applying all values and calculating, we get the GR (gearing ratio) as 34.33. Now, the nearest actual gearing value is 32 hence, accordingly, we have designed the gears and their arrangement for the ornithopter.

3 Flapping Mechanism and Design

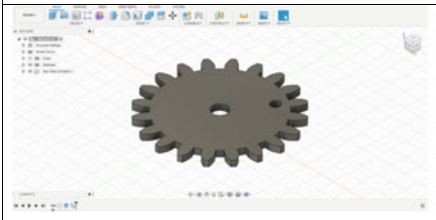
The design of the ornithopter was inspired by the bird "Blue Jay." The components as well as the assembly of my ornithopter was designed in the computer software ***Fusion 360***. Then, these components were 3D printed using the material of polylactic acid (PLA) that ranks as one of the top contender filaments for 3D printing.



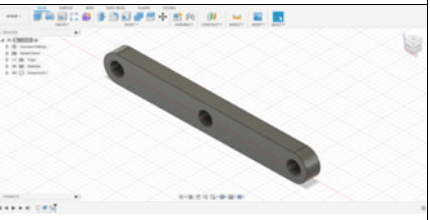
Mount of the Ornithopter



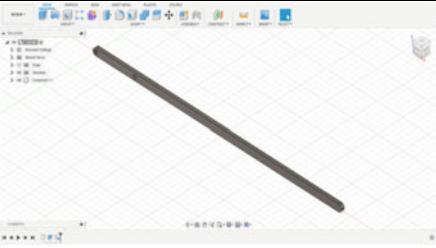
Small Gear - 15 teeth, hole radius-5mm, module-2, thickness-2mm



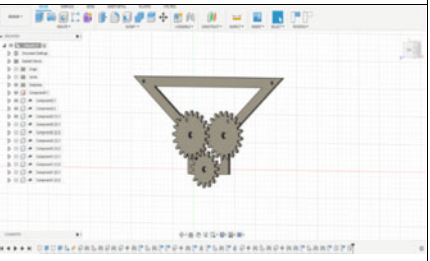
Big Gear - 20 teeth, hole radius-5mm, module-2, thickness-2m



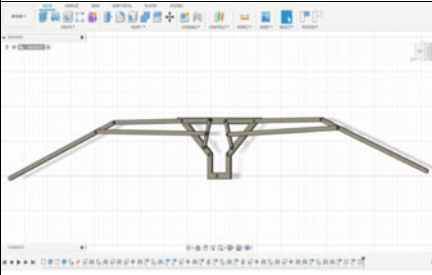
Connecting Rod



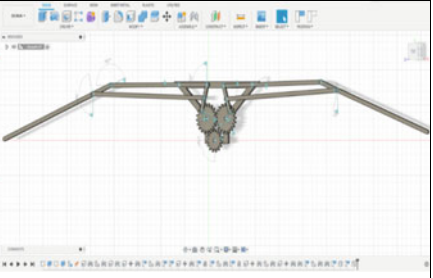
Rod



The whole gear assembly on the mount

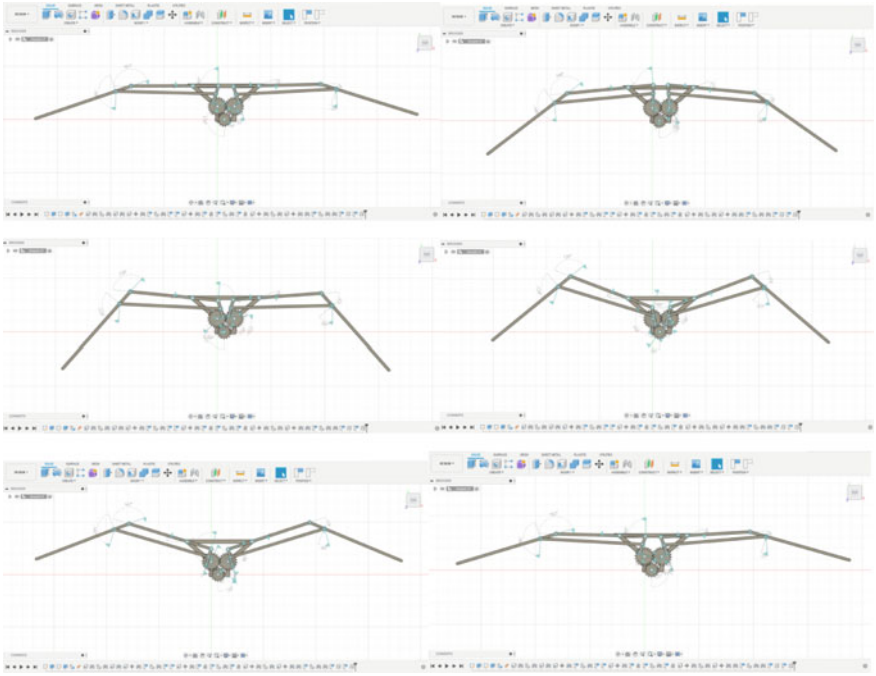


Rod assembly on mount



The whole skeleton of ornithopter

After assembling the ornithopter, we can introduce **as built** and **revolute** joints in their connections to make them move and fully function in a simulative way. We can view this as below in a series of pictures/slides to understand the flaps.



One flap of the ornithopter in slides

We have used various electrical components in my project. Some notable components used in the ornithopter are as follows:

Battery The motor and other DC components used in the UAV are powered by a 2 s LiPo Battery. The max voltage of a LiPo cell is 8 V.

Servo These are small and intricate devices that help in movement of tails, rudders, stabilizers, ailerons, etc. These are connected to channels that are connected to receiver and transmitter, hence get governed accordingly.

ESC and Receiver Electronic speed controller (ESC) is like a control panel made out in a small circuit that helps monitor and regulate the speed or rpm of the DC motor used in the ornithopter, that in turn helps regulate the flapping frequency or flaps.

Receiver is a device with antennas that receives the signals sent by the transmitter and works like a couple. It channels the signals to ESC and servos to move and provide the rpm as given by the user on the other end.

Transmitter Transmitter is nothing but the module where we directly give our command as to what amount of rpm to be released or what amount of rotation is to be done a servo.

Hence, all these components were used in the device after fabrication together with wires and other connecting components to finalize the ornithopter.

4 Uses and Future

Flapping wings, as shown through birds, may be more versatile and energy-efficient than fixed-wing aviation and added to that they may even allow for vertical take-off and landing (VTOL). Although it has been hypothesized that these benefits are most effective at tiny sizes and low flight velocities, but only the complicated non-linear character of such unstable flow separations makes it difficult to establish a unified explanatory theory of flapping. The flapping wings may theoretically be adjusted to have zero angle of attack while being on upstroke, allowing it to glide through the air with ease. The features inducing drags are kept to a minimum since flapping airfoils often create both lift and push. These key aspects may enable a high level of efficiency.

There are a vast number of practical applications of unmanned aerial devices like mechanical birds or ornithopters. Some of the most widely discussed applications of flapping-wing UAVs can be noted as:

1. Western countries have implemented ornithopters using the factor of resemblance to real birds to monitor various other birds especially endangered species in zoos and wildlife parks without scaring the birds, thus saving them from being hunted or exploited. Another example is that an artificial hawk remotely controlled by officials enables them to keep the grouse on ground so they can be captured for study.
2. Again, due to their huge resemblance to natural birds and insects, these are widely used by military for aerial reconnaissance over various territories like, places that cannot be easily reached on foot, surveillance on places occupied by militants without alerting them, and many more.
3. Now a days, a lot of science fiction movies include the concept of flapping-wing aircrafts; hence, many models of such custom UAVs are being made widely to be incorporated in movies, documentaries, etc.
4. Another very interesting application is that scientists have made hyper-realistic flapping devices resembling exactly to birds and incorporating them near airports to scare away or distract birds or animals that might cause damage to airplane engines.

There are many more applications of this technology. Now talking about the future human is never fails to surprise with the amount of creativity. There are already

studies on progress to make human ornithopters so that humans can fly. But realistically also, researchers and developers desire to eliminate the use of gear mechanisms by intricately bio-mimicking animal flight muscles. Georgia Tech Research Institute's Robert C. Michelson is also developing a reciprocating chemical muscle to be used in flapping-wing MAVs. Michelson uses the term "entomopter" for this type of ornithopter. Another instance is an organization named SRI International is developing a type of polymeric artificial muscle that might be used for flapping wings.

As cool and intriguing this mechanism and technology adaptation seems but it also has negatives. History is provident of the numerous accidents and deaths caused due to directly trying to build human ornithopters and so. We now have better safety and security but still these technologies are also being used in harmful means to people, military, and other targets.

5 Conclusion

Hence, the design and fabrication of flapping-wing UAV or ornithopter is completed. The model inspired by the bird "Blue Jay" with above-mentioned specifications is laid down. This topic or mechanism or technology any term we give is very promising and futuristic, but we also need to watch that we do not step out of our boundaries on the wheels of curiosity and sacrifice ourselves or harm others. The more evolved mechanisms show more promised results and higher levels of efficiency on success of various missions like surveillance and others. Some limitations of our work could be summarized as:

- The ornithopter is quite unstable and difficult to maintain in the right direction during flight.
- Our ornithopter has very limited payload capacity due to the energy requirements for flapping flight.
- They require regular maintenance to ensure their proper functioning.
- The materials and electronic used in making the ornithopter are fairly expensive.

In this flapping-wing device, we designed and made from scratch while taking inspiration and studying various research papers and experiments, watching various guidance videos and mentoring from my mentor we could successfully design this ornithopter that produces lift of approximately **5N**, with a near about **32** gear ratios, equipped with a **1400 kV** Brushless DC motor, and servo for various operations within the device and wholly controlled by a transmitter and receiver couple.

Funding Information Not applicable.

References

1. Chanute O (1894) Reprinted 1998. Progress in flying machines. Dover. ISBN 0-486-29981-3
2. Hudson Shaw W, Ruhen O (1977) Lawrence Hargrave: explorer, inventor & aviation experimenter. Cassell Australia Ltd. pp 53–160
3. Tang J, Sun J, Lu C, Lao S (2019) Optimized artificial potential field algorithm to multi-unmanned aerial vehicle coordinated trajectory planning and collision avoidance in three-dimensional environment. Proc Inst Mech Eng Part G J Aerosp Eng
4. D'Andrea R (2014) Guest editorial can drones deliver? IEEE Trans Autom Sci Eng 11:647–648
5. Nakata T, Liu H, Tanaka Y, Nishihashi N, Wang X, Sato A (2011) Aerodynamics of a bio-inspired flexible flapping-wing micro air vehicle. Bioinspir Biomim 6:045002
6. Armanini SF, De Visser CC, De Croon GCHE, Mulder M (2015) Time-varying model identification of flapping-wing vehicle dynamics using flight data. J Guid Control Dyn 38:526–541
7. Armanini SF, Caetano JV, De Croon GCHE, De Visser CC, Mulder M (2016) Quasi-steady aerodynamic model of clap-and-fling flapping MAV and validation using free-flight data. Bioinspir Biomim 11:046002
8. Mwongera VM (2015) A review of Flapping Wing MAV modelling. Int J Aeronaut Sci Aerosp Res 2:27–36
9. Collis SS, Joslin RD, Seifert A, Theofilis V (2004) Issues in active flow control: theory, control, simulation, and experiment. Prog Aerosp Sci 40(4):237–289
10. Ellington CP (1999) The novel aerodynamics of insect flight: applications to micro-air-vehicles. J Exp Biol 202:3439–3448
11. Ho S, Nasseh H, Pornsinsirirak N, Tai YC, Ho CM (2003) Unsteady aerodynamic and flow control for flapping wing flyers. Prog Aerosp Sci 39:635–681
12. Lin CS, Hwu C, Young WB (2006) The thrust and lift of an ornithopter's membrane wings with simple flapping motion. Aerosp Sci Technol 10:111–119
13. Yang LJ, Hsu CK, Ho JY, Feng CK (2007) Flapping wings with PVDF sensors to modify the aerodynamic forces of a micro aerial vehicle. Sens Actuators A 139:95–103
14. Tsai BJ, Fu YC (2009) Design and aerodynamic analysis of a flapping-wing micro air vehicle. Aerosp Sci Technol 13:383–392
15. Wu JH, Sun M (2004) Unsteady aerodynamic forces of a flapping wing. J Exp Biol 207(7):1137–1150
16. http://www.ornithopter.de/english/principle.htm
17. Jagadeesh R, Madhu Mathi S, Vijayaraja K (2019) Design and analysis of flapping wing unmanned aerial vehicle. Int J Eng Res & Technol (IJERT) 8(4)

Evaluation of Elastic, Mechanical, and Thermophysical Properties of Nanostructured Aluminides for Aviation Industries

Sudhanshu Tripathi, Devraj Singh, Rajesh Kumar Saluja, and Rashmi Vashisth

Abstract Intermetallic-based alloys due to their unique material properties are considered as most suitable modern engineering materials. The present study depicts the elastic, mechanical, and thermophysical properties of aluminides at nanoscale using ultrasonics non-destructive evaluation (NDE) technique. Ultrasonic method is one of the popular methods used widely to characterize the microstructural properties at bulk as well as nanoscale. To evaluate ultrasonic and thermophysical properties, the second-order elastic constants (SOECs) obtained via application of using the Coulomb–Born–Mayer interaction potential for the chosen material. The mechanical parameters have also been evaluated based on obtained SOECs. It is found that Young's modulus for nanostructured aluminides matches with the reported range of 180–281 GPa. The better ductile behavior of nanostructured NiAl in comparison with nanostructured FeAl is confirmed by Pugh ratio. The ultrasonic velocity has been further utilized to find out the lattice thermal conductivity. All the computed parameters have been utilized to find out the thermal relaxation time, Debye temperature, and acoustic coupling constants for nanostructured aluminides. The ultrasonic theoretical model with well-established relations has been utilized to characterize the nanostructured aluminides. MATLAB as a simulation tool has been utilized to obtain the material characteristics.

Keywords Nanomaterials · Elastic constants · Mechanical properties · Ultrasonic properties

S. Tripathi (✉)
Department of IT and Engineering, Amity University, Tashkent, Uzbekistan
e-mail: stripathi@amity.uz

D. Singh
Rajju Bhaiya Institute of Physical Sciences for Study and Research, V.B.S. P. University, Jaunpur, UP, India

R. K. Saluja · R. Vashisth
Amity Institute of Aerospace Engineering, Amity University Uttar Pradesh, Noida, India

R. Vashisth
Amity Institute of Information Technology, Amity University Uttar Pradesh, Noida, India

© The Author(s), under exclusive license to Springer Nature Singapore Pte Ltd. 2024

S. Singh et al. (eds.), *Recent Advances in Aerospace Engineering*, Lecture Notes in Mechanical Engineering, https://doi.org/10.1007/978-981-97-1306-6_42

1 Introduction

B-2 structured transition aluminides, namely NiAl and FeAl, exhibit high melting point, high temperature strength, low specific gravity, thermal conductivity, and corrosion resistance at higher temperature [1–3]. However, low ductility and poor strength reported at room temperature [4] limits their wide-scale industrial applications. The temperature-dependent study on 'elastic and mechanical properties' of NiAl and FeAl at bulk scale using first principle [5] indicates that elastic anisotropy of NiAl and FeAl shows reverse characteristics with growing temperature. The bcc Fe/NiAl interface segregation tendency has been studied using the first principle [3]. Further reported in literatures [6] that for the B-2 transition metals and alloys the reduction in grain size up to the nanoscale has relevant consequences on the material properties. Recently molecular dynamics simulation-based studies report the material properties at nanoscale. Sutrakar et al. [7] reported the super elastic behavior of B2-NiAl nanowires with crystalline phase to amorphous phase transformation. Ni_3Al-based intermetallics have shown their effective application as compressor and turbine blades in aircraft engine.

The evaluation of ultrasonic properties is essential for study of solid-state attributes of materials, e.g., 'the crystal energy density', 'specific heat', 'thermal conductivity', and 'the thermal relaxation time' [8, 9]. The determination of numerous mechanical and elastic parameters such as 'Young's modulus', 'shear modulus', 'Poisson's ratio', 'bulk modulus', and Pugh's indicator predicts the nature and crystal's quality under the influence of external stress [10, 11]. The elastic constants are well related to the anharmonic and mechanical properties of the materials. Thus, the determination of higher-order elastic constants up to the second and third order with varying physical constraints provides better understanding of materials dynamic thermophysical characteristics. Elastic properties analysis offers information regarding their empirical interatomic potential, atomic bonding characteristics, nonlinear performance, and mechanical strength [12]. The lack of information regarding X-Al (X=Fe, Ni) nanostructures elastic, thermal, and ultrasonic properties under variant physical condition motivated the present study. The important property of ultrasonic method is its non-destructive behavior, makes it better in comparison with the other techniques. The theoretical study determines the mechanical, elastic, and thermophysical properties of nanostructured X-Al (X=Fe, Ni) using simple interaction potential model at room temperature (i.e., at 300 K).

2 Theory

The ultrasonic NDE theoretical approach has been employed to characterize the nanostructured aluminides. The elastic constant of higher order signifies the attributes of the types of the forces within the crystalline material and is the bridge between materials mechanical dynamic thermophysical properties. The elastic constants of

second order (SOECs) have been discovered employing the Coulomb and Born–Mayer potential following Brugger's definition [13].

According to the Brugger's definition, the interionic potential depends on electronic charge, hardness parameter, nearest neighbor distance, and other physical parameters. The detailed expression for the derivation of elastic constants of higher order and its relation to physical parameters are obtained from the literature [14, 15]. The material's elastic energy density (F) is described in relation to the strain tensor components η_i (i *or* $j = x, y, z$) along different axes given as

$$F = f\left(\eta_{xx}, \eta_{yy}, \eta_{zz}, \eta_{xy}, \eta_{yz}, \eta_{zx}\right) \tag{1}$$

Here, x, y, and z represent three axes, and η_{ij} (i or $j = x, y, z$) are six strain components due to crystal symmetry. The SOECs are defined as second-order strain derivative of elastic energy density given as

$$C_{IJ} = \frac{\partial^2 F}{\partial \eta_I \partial \eta_J} \tag{2}$$

Here, subscript I, J denotes the atom in the basal plane and above/below the basal plane. The parameters I, J having values in the range 1–6 reliant on even nature of the crystal lattice. The B2-structured materials lead three SOECs ($C_{11,}C_{12,}C_{44}$) and six TOECs due to crystal symmetry. The anharmonic theory of lattice dynamics [16] describes the temperature-dependent formulation for elastic constants as the addition of static component and vibrational components given as

$$C_{IJ}(T) = C_{IJ}^{s} + C_{IJ}^{\text{vib}} \tag{3}$$

$$C_{IJK}(T) = C_{IJK}^{s} + C_{IJK}^{\text{vib}}$$

Here, subscript I, J, K denotes the atom in the basal plane and above/below the basal plane, terms s, vib signifies the static component of elastic constant computed at 0 K, and the vibrational component computed at any temperature T K. The parameter C_{IJ}^{s} is constant evaluated at 0 K, while the parameter C_{IJ}^{vib} is variable due to dependence of free energy density on the physical parameter variations, e.g., temperature, pressure, etc. These static and dynamic parameters can be determined using the formulation given as [15, 16]

$$\left.\begin{aligned} C_{11}^{0} &= \frac{3}{8}\frac{e^2}{r_0^4}S_5^{(2)} + \frac{3\phi(r_1)}{br_0}\left(\frac{1}{\sqrt{3}r_0}+\frac{1}{b}\right) \\ &\quad + \frac{2\phi(r_2)}{br_0}\left(\frac{1}{2r_0}+\frac{1}{b}\right) \\ C_{12}^{0} = C_{44}^{0} &= \frac{3}{8}\frac{e^2}{r_0^4}S_5^{(1,1)} + \frac{\phi(r_2)}{br_0}\left(\frac{1}{2r_0}+\frac{1}{b}\right) \\ C_{IJ}^{\text{vib}} &= \left\{ l_1 k_{\text{B}} \left|\frac{\partial C_{IJ}^{0}}{\partial r}\right|_{r=r_0} + \frac{f_{IJ}^{\text{vib}}}{TV_{\text{C}}} \right\} \end{aligned}\right\} \tag{4}$$

Here terms $\phi(r_1)$, $\phi(r_2)$ represent the interaction potential among central atom and atoms up to second nearest neighborhood. r_1, r_2, are the nearest neighbor distance of the first and second nearest atoms with the central atom related to r_0 as $r_1 = \sqrt{3r_0}$, $r_2 = 2r_0$. The parameters $S_5^{(2)}$, $S_5^{(1,1)}$ are the lattice sum with the values 0.35419, 0.346708, respectively. $V_{\text{C}} = 4r_0^3$ signifies the elementary volume of the unit cell. f_{IJ}^{vib} represents vibrational energy for each unit cell, the parameter l_1 depends on nearest neighbor distance and potential function, and k_{B} is Boltzmann constant. The evaluation of mechanical properties for aluminides is of great importance for industrial applications. Fe–Al combination is very important for tailoring purpose, and thick layer of Fe–Al intermetallic is formed at joint. The joint's mechanical properties are well influenced under thermophysical conditions. Thus, it is customary to determine the mechanical properties of the aluminides at nanoscales. The mechanical properties of the materials are well related to SOECs, and thus, the SOECs has been utilized to obtain the mechanical constants such as 'Young's modulus' (Y), 'bulk modulus' (B), 'shear modulus' (G), 'Poisson's ratio' (σ), 'Lame modulus' (λ), and 'the Pugh's indicator', i.e., (B/G ratio) is used for determination of materials mechanical strength under varying constraints. The 'bulk modulus' of the material (B) shows its ability to resist volume deformation under the external stress. Similarly, shear modulus (G) signifies the materials ability to resist shear deformation, and the stiffness of the material is predicted by the computation of 'Young's modulus'. The mathematical expressions for computation of these mechanical properties in relation with the SOECs are [17–19] given as

$$\left.\begin{aligned} B &= \frac{C_{11}+2C_{12}}{3};\ Y = \frac{9GB}{G+3B} \\ G &= \frac{C_{11}-C_{12}+2C_{44}}{8} + \frac{5[(C_{11}-C_{12})C_{44}]}{[8C_{44}+6((C_{11}-C_{12}))]} \\ \sigma &= \frac{3B-2G}{6B+2G};\ \lambda = \frac{Y\sigma}{(1+\sigma)(1-2\sigma)};\ \mu = \frac{Y}{2(1+\sigma)} \end{aligned}\right\} \tag{5}$$

The ultrasonic wave as it propagates through the material leads to the knowledge about crystallographic texture information and various other thermal phenomenon related to crystal lattice at microscale as well as at nanoscale. The weighted average of three different form of ultrasonic wave velocities [1, 2] explicitly 'shear wave

velocity', (V_{T2}), 'quasi-shear wave velocity', (V_{T1}), and 'longitudinal wave velocity' (V_L), alongside the crystallographic paths <100>, <110>, and <111> provides the Debye average velocity (V_D) [3] given as

$$V_D = \left[\frac{1}{3}\left(\frac{1}{V_L^3} + \frac{1}{V_{T1}^3} + \frac{1}{V_{T2}^3}\right)\right]^{-1/3} \tag{6}$$

The Debye temperature (T_D) is another crucial thermophysical factor which needs to determine as it describes the thermodynamic behavior of the material and is strongly affected by V_D. T_D [4] is the temperature for greatest frequency of phonons which can transfer via single crystal. The equilibrium of thermal phonon distribution gets disturbed during ultrasonic wave propagation through a material [3]. The thermal conductivity of nanostructured aluminides obtained via Morelli and Slack approach [20, 21] given as

$$\kappa = \frac{A' M_w T_D^3 \delta^3}{\gamma^2 T n^{2/3}} \tag{7}$$

where δ^3 is volume per atom, γ is Grüneisen parameter, and A' is the constant which depends on Grüneisen parameter given as

$$A' = \frac{2.43 \times 10^{-8}}{1 - 0.54/\gamma + 0.228/\gamma^2} \tag{8}$$

3 Result and Discussion

The higher-order elastic constants for nanostructured NiAl and FeAl are evaluated using the method described in theory section. The lattice parameters for the materials under study are 2.87 Å and 2.85 Å, respectively [22]. Figure 1 shows the nanostructured NiAl, FeAl with BCC lattice crystal structure. The nonlinearity parameters 'b' are computed under minimum energy condition and are 0.312 Å and 0.188 Å for NiAl and FeAl at nanoscale, respectively.

The material density and SOECs are calculated using Eqs. (1)-(4) and compared with available data in literature shown in Table 1, respectively. The elastic constants provide the information about material stiffness and durability. The obtained values of C_{11} are higher than that of C_{44}. C_{11} provides the information about resistance toward linear compression while C_{44} gives information about hardness of the material. Thus, the elastic constants are estimated up to the substantial statistics which approximates the values in the literatures [5, 23–25]. The deviation in the present investigation at the nanoscale observed from the values reported at bulk scale. The direct values of SOECs are not available for comparison at nanoscale; however, when it is compared

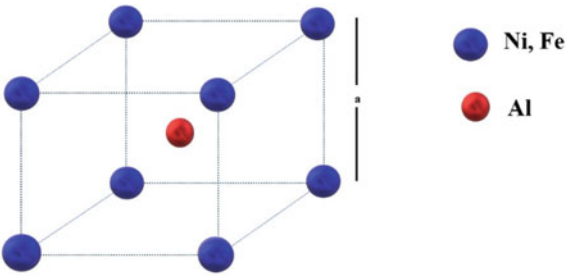


Fig. 1 NiAl and FeAl nanostructure with BCC lattice with parameter *a*

with the SOECs values obtained at bulk scale, the significant difference is observed due to the difference in the mechanical properties at nanoscale. The TOECs values for nanostructured aluminides have been evaluated using the formulation available in literature [14, 26, 27], in relation to as described by Eq. (3). The TOECs data of nanostructured aluminides for direct comparison of the results obtained is not available in literatures. However, for CsCl structured material, the C_{111} value is negative as depicted in Table 2, also for Al negative values of C_{111} were reported experimentally. Hence, our theoretical methodology for the estimation of nonlinear elastic constants B2-structured aluminides at nanoscale is justified.

Table 3 depicts the mechanical properties of the nanostructured aluminides computed using SOECs in relation as descried in Eq. (5). The obtained SOECs values and the computed values of B satisfy the Born stability criteria $C_{11} + 2C_{12} > 0$, $C_{44} > 0$, $C_{11} - C_{12} > 0$, and $C_{11} > B > C_{12}$, for nanostructured aluminides. The parameter B signifies the materials resistance to break while the parameter G denotes the resistance to plastic distortion. The Pugh ratio B/G measures the material ductile/brittleness behavior [28, 29]. As it is clear from Table 3 that nanostructured NiAl is ductile while FeAl is brittle at room temperature. The previous study reports that the Young's modulus value for NiAl at nanoscale should lies in between 180 and 281

Table 1 Lattice parameter, density, and SOECs of nanostructured NiAl and FeAl at 300 K

Material		a (Å)	d (gcm^{-3})	C_{11} (GPa)	C_{12} (GPa)	C_{44} (GPa)
NiAl	Present	2.872	6.004	211.1975	113.9685	117.5842
	[6]	2.901		203.14	131.69	112
FeAl	Present	2.852	5.927	282.3585	107.1525	117.438
	[6]	2.895		266.42	133.07	142.01

Table 2 TOECs (GPa) of nanostructured NiAl and FeAl at 300 K

Material	C_{111}	C_{112}	C_{123}	C_{144}	C_{166}	C_{456}
NiAl	− 1896.9	− 950.70	− 795.4	− 579.8	− 630.26	− 776.7
FeAl	− 1578.1	− 478.9	− 408.8	− 315.6	− 370.4	− 409.5

Table 3 Mechanical properties of nanostructured NiAl and FeAl at 300 K

Material	B (GPa)	G or μ (GPa)	B/G	Y (GPa)	λ (GPa)	σ
NiAl	144.91	79.05	1.83	200.67	92.20	0.26
FeAl	163.89	102.93	1.59	255.35	95.27	0.24

Table 4 Ultrasonic velocities (Kms^{-1}) of nanostructured NiAl and FeAl at 300 K

Material	Direction	V_L	V_{T1}	V_{T2}	V_D
NiAl	<100>	5.93	4.42	4.42	4.75
	<110>	6.83	4.42	4.02	4.64
	<111>	7.10	4.29	4.29	4.74
FeAl	<100>	6.90	4.45	4.45	4.88
	<110>	7.25	4.45	5.43	5.29
	<111>	7.37	4.80	4.80	5.26

GPa [30], which is similar to our findings as depicted in Table 3. The low value of the Young modulus for NiAl reveals that NiAl ais softer than FeAl at nanoscale.

The SOECs have also utilized to obtain the ultrasonic velocity for longitudinal (V_L), quasi-shear (V_{T1}), and shear mode (V_{T2}) along <100>, <110>, and <111> directions at 300K as depicted in Table 4. The Debye average velocity is computed as weighted average of these three ultrasonic velocities. It is noticeable from Table 4 that V_D for NiAl is highest along <100> direction whereas for FeAl, along <111> direction. The highest values along these directions reveal materials hardness is much prominent along these directions. The V_D obtained for these materials may be further utilized for thermophysical and losses computation in the material. The thermal conductivity of the NiAl and FeAl has been calculated using Eq. (7). The obtained value of thermal conductivity for NiAl is 9.69 W/cmK and for FeAl is 2.94 W/cmK. The high value of thermal conductivity makes NiAl thermally stable and suitable for wide-scale industrial applications.

4 Conclusion

The Born–Mayer and Coulomb interaction potential model has been employed to figure out the elastic and thermophysical properties of nanostructured aluminides, using ultrasonic theory. The higher values of SOECs for FeAl obtained at 300K indicate that it has better elastic properties in comparison with NiAl. The mechanical stability principle is satisfied by aluminides at nanoscale, revealing their mechanical stability. The Pugh indicator shows that NiAl is ductile in nature, whereas FeAl is brittle in nature at room temperature. The material anisotropic characteristics are obtained via evaluation of ultrasonic velocity at room temperature. The

aluminides elastic and thermophysical properties have been introduced at nanoscale, and obtained results deliver better understanding of these material and may be utilized for further research investigation and industrial applications.

Funding Information Not applicable.

References

1. Lazar P, Podloucky R (2006) Ab initio study of the mechanical properties of NiAl microalloyed by X=Cr, Mo, Ti, Ga. Phys Rev B 73:104114
2. Kaplanskii YY, Loginov PA, Korotitskiy AV, Bychkova MY, Levashov EA (2020) Influence of heat treatment on the structure evolution and creep deformation behavior of a precipitation hardened B2-(Ni,Fe) Al alloy. Mater Sci Eng A 786:139451
3. Gao X, Wang H, Ma C, Lv M, Ren H (2021) Segregation of alloying elements at the bcc-Fe/B2–NiAl interface and the corresponding effects on the interfacial energy. Intermetallics 131:107096
4. Hu X-L, Zhang Y, Lu G-H, Wang T, Xiao P-H, Yin P-G, Xu H (2009) Effect of O impurity on structure and mechanical properties of NiAl intermetallics: A first-principles study. Intermetallics 17:358–364
5. Liu L, Wu X, Wang R, Li W, Liu Q (2015) First principle study on the temperature dependent elastic constants, anisotropy, generalized stacking fault energy and dislocation core of NiAl and FeAl. Comput Mater Sci 103:116–125
6. Park HS, Zimmerman JA (2006) Stable nanobridge formation in <110> gold nanowires under tensile deformation. Scripta Mater 54:1127–1132
7. Sutrakar VK, Pillai ACR, Mahapatra DR (2014) Orientation, size, and temperature dependent ductile brittle transition in NiAl nanowire under tensile loading-a molecular dynamics study. Defence Sci J 64
8. Jozwik P, Polkowski W, Bojar Z (2015) Applications of Ni_3Al based intermetallic alloys—Current stage and potential perceptivities. Materials (Basel). 8(5):2537–2568
9. Li X-H, Xing C-H, Cui H-L, Zhang R-Z (2019) Elastic and acoustical properties of Cr_3AlB_4 under pressure. J Phys Chem Solids 126:65–71
10. Shafiq M, Arif S, Ahmad I, Asadabadi SJ, Maqbool M, Aliabad HR (2015) Elastic and mechanical properties of lanthanide monoxides. J Alloy Compd 618:292–298
11. Al-Qaisi S, Abu-Jafar MS, Gopir GK, Ahmed R, Omran SB, Jaradat R, Dahliah D, Khenata R (2017) Structural, elastic, mechanical and thermodynamic properties of Terbium oxide: first-principles investigations. Results Phys 7:709–714
12. Iqbal R, Bilal M, Jalali-Asadabadi S, Rahnamaye Aliabad HA, Ahmad I (2018) Theoretical investigation of thermoelectric and elastic properties of intermetallic compounds ScTM (TM=Cu, Ag, Au and Pd). Int J Mod Phys B(32):1850004
13. Brugger K (1964) Thermodynamic definition of higher order elastic coefficients. Phys Rev 133:A1611
14. Yadav RR, Pandey DK (2005) Size dependent acoustical properties of bcc metal. Acta Phys Pol A 107:933–946
15. Yadav CP, Pandey DK, Singh D (2019) Elastic and ultrasonic studies on RM (R=Tb, Dy, Ho, Er, Tm; M=Zn, Cu) compounds. Zeitschrift für Naturforschung A 74:1123–1130
16. Leibfried G, Hahn H (1958) Zur Temperaturabhängigkeit der elastischen Konstanten von Alkalihalogenidkristallen. Z Phys 150:497–525
17. Tripathi S, Agarwal R, Singh D (2019) Nonlinear elastic, ultrasonic and thermophysical properties of lead telluride. Int J Thermophys 40:1–18
18. Tripathi S, Agarwal R, Singh D (2020) Size-dependent ultrasonic and thermophysical properties of indium phosphide nanowires. Zeitschrift für Naturforschung A 75:373–380

19. Singh D, Kaushik S, Tripathi S, Bhalla V, Gupta AK (2014) Temperature-dependent elastic and ultrasonic properties of berkelium monopnictides. Arab J Sci Eng 39:485–494
20. Gray DE (1972) American institute of physics (AIP). Handbook. McGraw-Hill, New York
21. Morelli DT, Slack GA (2006) High lattice thermal conductivity solids. In: High thermal conductivity materials. Springer, pp 37–68
22. Bukreeva KA, Babicheva RI, Dmitriev SV, Zhou K, Mulyukov RR (2013) Inhomogeneous elastic deformation of nanofilms and nanowires of NiAl and FeAl alloys. JETP Lett 98:91–95
23. Truell R, Elbaum C, Chick BB (2013) Ultrasonic methods in solid state physics. Academic Press
24. Singh DJ (1992) Electronic structure, magnetism, and stability of Co-doped NiAl. Phys Rev B 46:14392
25. Connétable D, Maugis P (2008) First principle calculations of the κ-Fe_3AlC perovskite and iron–aluminium intermetallics. Intermetallics 16:345–352
26. Pandey DK, Yadav RR (2009) Temperature dependent ultrasonic properties of aluminium nitride. Appl Acoust 70:412–415
27. Tripathi S, Agarwal R, Vashisth R, Singh D (2021) Diameter dependent ultrasonic investigation of SiC nanowires. Innovative applications of nanowires for circuit design. IGI Global, pp 71–100
28. Frantsevich IN (1982) Elastic constants and elastic moduli of metals and insulators. In: Reference book
29. Pugh SF (1954) XCII. Relations between the elastic moduli and the plastic properties of polycrystalline pure metals. Lond Edinburgh Dublin Philos Mag J Sci 45:823–843
30. Hu W, Li M, Fukumoto M (2008) Preparation and properties of HVOF NiAl nanostructured coatings. Mater Sci Eng, A 478:1–8

Investigation of Full-Length Aerospike Nozzle

Md Saquib Reza, B. K. Agarwal, and R. S. Tarnacha

Abstract The aim of the paper is to design the aerospike nozzle and analyse the flow over it for various conditions by carrying out flow simulations in software. Contour was obtained with the help of a MATLAB Code. Effect of different atmospheric pressure, varying with altitude, in correspondence with the design pressure has been studied through numerical simulations in order to understand the performance of the aerospike nozzle in conditions categorized as over-expansion, optimum and under expansion (Nazarinia et al., Design and numerical analysis of aerospike nozzles with different plug shapes to compare their performance with a conventional nozzle [1]).Also, how the changes in various parameters impacts the performance is studied. Thrust is a very important parameter in gauging the functionality and capability of the aerospike nozzle. The overall thrust generated is calculated with the help of the MATLAB code generated for 100% length spike. Overall thrust is a combination of the thrust that is generated due to that of the chamber force and the one due to the flow of the gases over the spike (Besnard et al., Design, manufacturing and test of a plug nozzle rocket engine [2]). The program build helps in quickly obtaining the thrust values for different conditions imposed. The outcomes of the analysis depict how the aerospike showcases good performance even during its operation at altitudes other than the optimum altitude.

Keywords Aerospike · Thrust · Expansion · Mach number · Supersonic

Nomenclature

θ_t	Throat angle
P_a	Ambient Pressure

M. S. Reza (✉) · B. K. Agarwal
Amity Institute of Aerospace Engineering, Amity University Uttar Pradesh, Noida, India
e-mail: saquibreza87@gmail.com

R. S. Tarnacha
Amity Institute of Technology, TATA Technologies, Amity University Uttar Pradesh, Noida, India

© The Author(s), under exclusive license to Springer Nature Singapore Pte Ltd. 2024

S. Singh et al. (eds.), *Recent Advances in Aerospace Engineering*, Lecture Notes in Mechanical Engineering, https://doi.org/10.1007/978-981-97-1306-6_43

P_c	Chamber Pressure
T_c	Chamber Temperature
NPR	Nozzle Pressure Ratio
γ	Specific Heat Ratio
E	Expansion Ratio
A_t	Throat Area

1 Introduction

Nozzle is a very essential component in the operation of aircrafts or rocket. It provides the thrust that is important for the forward motion of the vehicle. As compared to the conventional nozzles, like the bell nozzles, the aerospike nozzles have much more efficiency, but it surely comes with some penalty.

One of the features of the aerospike nozzle that makes it stand out is "Altitude Compensation." In the case of the conventional nozzles it is seen that, it gives its best performance only at its optimum/design altitude and at rest of the altitudes it doesn't operate at its best efficiency and has to suffer some loss of thrust. This problem can be ruled out to a much greater extent in case of the aerospike nozzle due to its capability of altitude compensation. It increases the nozzle area ratio and because of this it is able to keep up the aerodynamic efficiency as the altitude goes on increasing along its path, thus ensuring high efficiency and good operation at most of the conditions. Unlike the bell nozzle, the aerospike nozzle doesn't have any wall or shroud within which the flow of the gases is being contained. The atmosphere around the spike acts as the outer wall whereas the ramp of the spike behaves as the inner wall. The hot gases approach from an annulus that is sited at some radial interval from the spike and the gases are then headed towards the spike. Then, expansion of these gases is what helps in the development of thrust. Flow around the spike greatly varies when it is operated under different conditions. In case of the optimum expansion, the flow forms a columnar shape; in case of the over expansion, the flow is more closely aligned towards the centreline of spike body; and lastly during under expansion, it can be seen that flow tries to expand itself and starts functioning in a similar way to that of the bell nozzle, however maintain its aerodynamic efficiency.

As mentioned, these advantages do come up with some penalties like weight, heating problems, etc. But its exceptional features have also attracted scientists and researchers to study and learn about it.

Despite its project Single Stage To Orbit SSTO [3] being scrapped off by NASA, it has again become prominent in the field of research in Europe and Japan.

Since 1997, scientists have been actively engaged in researching in the field of aerospike nozzles. Their efforts have encompassed various aspects, including the design and optimization of nozzle contours, conducting hot-firing and cold-flow tests, and employing numerical simulations [4]. Moreover, they delved into the analysis of flow fields, the behaviour of the nozzle base [5], and the influence of freestream

conditions on flow fields and nozzle performance, using a combination of experimental and numerical approaches with inclusion of shrouded nozzle [6]. In this present study, we focus on the design of the aerospike nozzle contour along with performance validation at different altitudes.

2 Geometry

2.1 Contour Designing

There are various approaches of designing the contour of an aerospike nozzle. The method chosen in this research paper is Methods of Characteristics [7]. A MATLAB code was generated using the input parameters [8]. It uses Prandtl–Meyer function and isentropic relations for calculation of the coordinates of the spike. The full-length spike is generated for analysis. The flow properties along the nozzle wall are found using the isentropic flow relations at each axial and radial coordinate. The design input parameters and output values are listed in the Tables 1 [8] and 2. Using these axial and radial coordinates, a spike was created, as shown in Fig. 1.

Table 1 Input parameter for the MATLAB Code

Parameters	Symbol	Values	Units
Throat angle	θ_t	67.84	Degree
Design altitude	–	15,544.8	m
Ambient pressure	P_a	11,028.11	Pascal
Chamber pressure	P_c	2,068,000	Pascal
Chamber temperature	T_c	3200	K
Nozzle pressure ratio	NPR	187.5	–
Specific heat ratio	γ	1.4	–
Expansion ratio	E	12.35	–
Throat area	A_t	5.025×10^{-5}	m

Table 2 Output parameters obtained from MATLAB Code

Parameters	Value	Unit
Exhaust Mach no.	4.15993	–
Cowl separation	0.286798	m
Length	0.283847	m

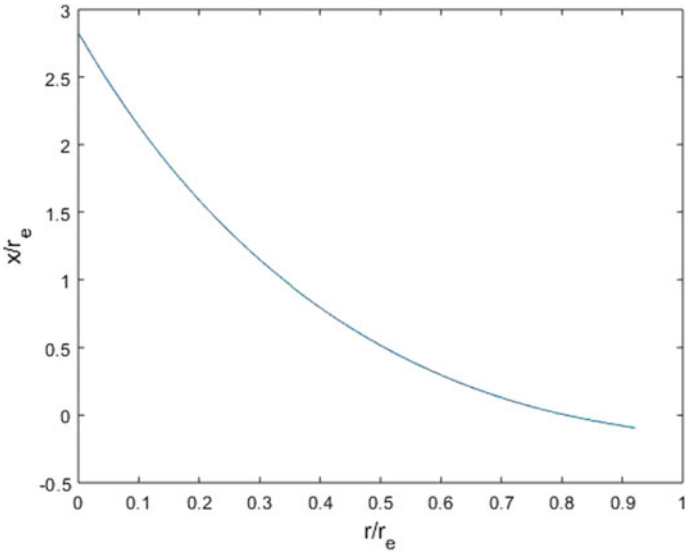


Fig. 1 Upper half of the spike obtained from MATLAB code

2.2 Part Naming

The coordinates obtained were imported in Computational Fluid Dynamics tool (ICEM-CFD) where the geometry was built [9]. The most important portion is the creation of the throat/ thruster angle since the flow is directed towards the spike through this angle.

The far field was constructed very large in comparison with the spike so as to study the complete flow over it and to impose the conditions at boundary as shown in Fig. 2a.

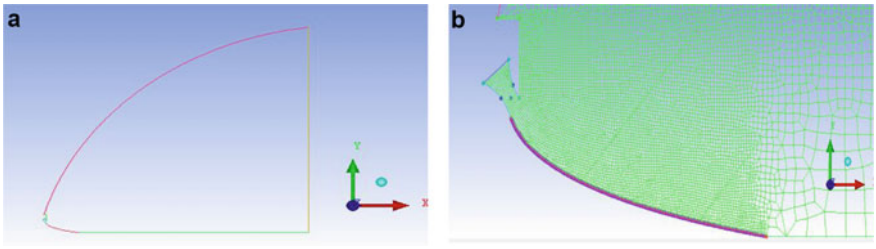


Fig. 2 **a** Aerospike geometry with far field **b** meshed geometry with far field

Table 3 Grid comparison

S. no.	Cells	Pressure at the nozzle exit (Pa)
1	125,000	115,390.000
2	140,366	111, 560,344
3	142,400	111, 658,360

2.3 Grids

The aerospike assembly comprises of the full-length spike, cowl wall, throat, axis-symmetry, pressure inlet, pressure outlet and far field.

Geometric variation near the throat spike and cowl wall is complex; therefore, it makes it nearly impossible to generate a mesh of acceptable quality using structured grids [10], due to this, the solution domain was discretized using all "quad "unstructured grids as shown in Fig. 2b.

We carried out simulations on aerospike using three distinct meshes to assess their results. During the mesh generation process within the domain, we compared the non-dimensional wall pressure at the exit. This comparison, shown in Table 3, examines the parameters at the nozzle exit with respect to the number of grids cells. Notably, it was observed that all parameters exhibited close proximity, with only a negligible difference between 1, 40,366 and 1, 42,400. As a result, 1, 40,366 computations have been performed to reduce the time.

3 Simulation and Analysis

To perform the analysis in FLUENT software, an input file geometry with far field Fig. 4a and mesh Fig. 4b was created. An inviscid, density-based solver, steady time state setup, 2D space (axis symmetric) was used. The compressibility effect has been considered, Calorically perfect gas ($\gamma = 1.4$) [11] was selected with implicit formulation approach and first-order upwind discretization scheme. Courant number used was 1 [8]. Mach number contour generated based on the discussed setup as shown in Fig. 3.

3.1 Thrust Calculation

The major parameter for performance evaluation of a nozzle is the thrust it produces. The thrust for the aerospike nozzle is calculated on the basis of three categories namely:

1. Thrust due to the thrusters or the combustion chamber.
2. Thrust due to the centre body or the spike.

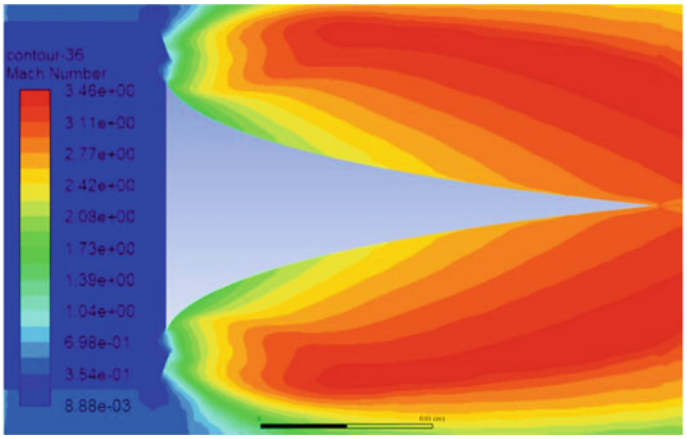


Fig. 3 Flow simulation around aerospike nozzle at 15,544.8 m

3. Thrust due to base (due to the truncation, there is recirculation of flow that generates a component of thrust called base thrust) [12].

In case of a 100% plug nozzle the third component of thrust, i.e. thrust due to the base is zero as there is no base radius and so no base pressure is generated.

Therefore, the thrust for a full spike is summation of only thrust due to thrusters and the thrust produced by the centre body [2].

4 Comparison of the Results

The results obtained from the simulations are summarized in Table 4. In Table 5, a comparison is presented between the thrust calculated numerically and the thrust calculated analytically during the simulation. Additionally, Table 6 provides a comparative analysis of the exit Mach number and thrust calculations from a reference research paper, validating the results obtained in this study (Fig. 4).

Table 4 Validation

NPR		% error
From reference paper	Calculated value	
187.5	187.5208	0.0111

Table 5 Comparison of the numerically and analytically obtained thrust

Thrust calculated numerically	Thrust obtained analytically	% error
616.519	616.5125	0.0011

Table 6 Comparison of NPR ratio

Exit match no.			Calculated thrust		% error	Coefficient of thrust
Value from reference paper	Calculated value	% error	Thrust from reference paper (N/m)	Calculated value of thrust (N/m)		
3.46	3.40	0	625.4	616.267	1.4604	1.682

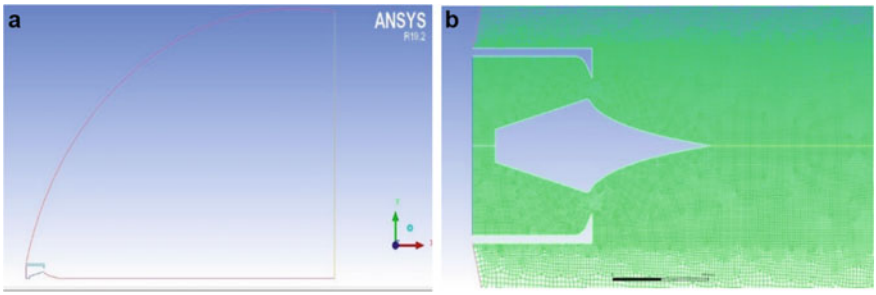


Fig. 4 **a** Aerospike geometry with far field **b** meshing done in the aerospike geometry

5 Results and Discussions

After validating the results for the full spike, a new geometry was designed in order to study the variation in its performance for different condition. The design altitude for this geometry was 12,950 m [7].

The three cases as shown below in the figures depict the flow simulation of 100% length full spike at different altitudes. These cases correspond to the cases of its flow at optimum altitude, altitude greater than the optimum altitude and altitude lower than the optimum altitude [13, 14].

Table 7 shows different values of thrust obtained.

5.1 Case 1: Over-Expansion

This is the case when the external pressure or the ambient pressure is greater than that of the exit pressure of the aerospike nozzle.

Table 7 Thrust obtained at different altitude

S. no.	Performing condition	Exit Mach number	Thrust (N)
1	Over-expansion	2.35	835.75
2	Optimum expansion	2.98	5254.5
3	Under expansion	3.20	6248.7

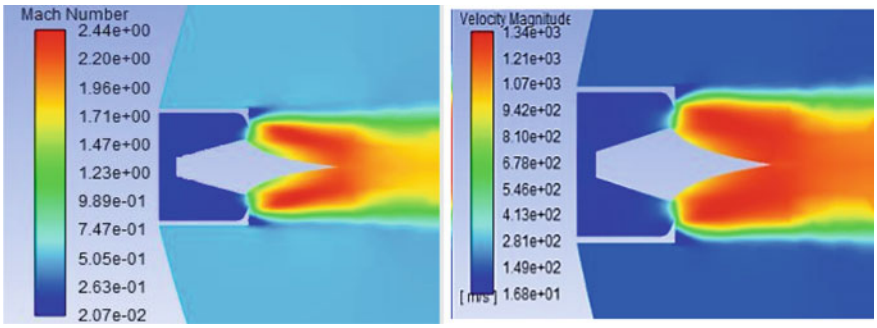


Fig. 5 Contours for over-expansion: **a** Mach contour **b** velocity contour

This operation is at an altitude less than the optimum altitude. Due to the high ambient pressure, the flow around the nozzle is pushed more towards the centreline of the spike, i.e. the flow remains more closely to the spike and this can be seen in Fig. 5

The pressure ratio for this case = 6.137.

5.2 Case 2: Optimum Expansion

This is the case when the external pressure or the ambient pressure in which the aerospike nozzle is operating is same as that of the exit pressure of the nozzle. At this altitude, the aerospike nozzle gives its best performance and also the flow maintains a columnar shape around the spike, and this can be seen in the case of Fig. 6

The pressure ratio for this case = 1.

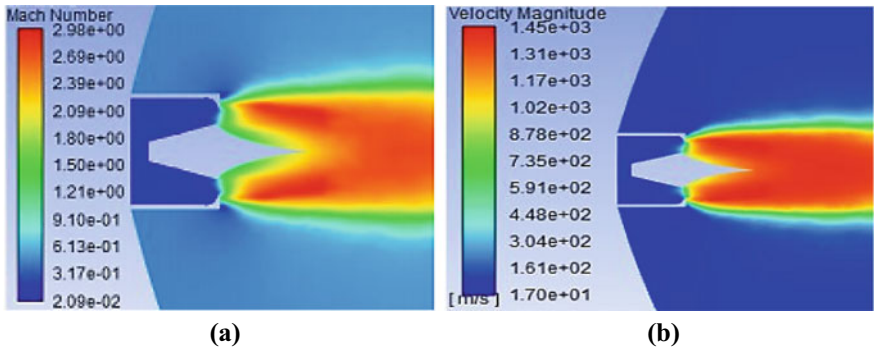


Fig. 6 Contours for optimum expansion: **a** Mach contour **b** velocity contour

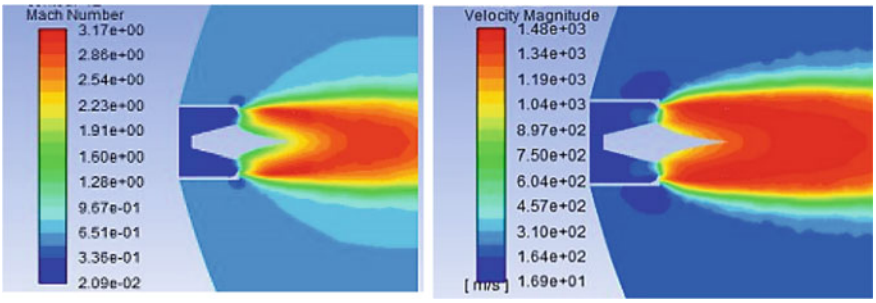


Fig.7 Contours for under expansion: **a** Mach contour **b** velocity contour

5.3 Case 3: Under Expansion

This is the case when the external or the ambient pressure is less than that of the exit pressure of the aerospike nozzle. This operation is at an altitude greater than the optimum altitude.

Even though in this case, the aerospike starts to behave like a bell nozzle but due to its ability of altitude compensation, the aerodynamic efficiency is maintained. In this, the flow expand outwards and this can be seen in Fig. 7.

The pressure ratio for this case = 0.0611.

Also it has been observed that in this case an improved thrust coefficient is being obtained [8]

Given below are the results of simulation showcasing all the above-mentioned cases of optimum expansion, under expansion and over-expansion and how the flow varies due to all the conditions exposed.

6 Conclusion

The purpose of the research paper was to study and analyse the aerospike nozzle at different altitudes. Contour as per the design was obtained from the MATLAB code, and further the geometry was created using ICEM-CFD software. A refined mesh was created so that more accurate results can be obtained. The prime area of concern was the throat and the spike, and to get more accurate results for those zones, mesh was more refined or dense in those areas as compared to the other zones.

The overall thrust for the full aerospike nozzle was calculated taking in consideration the chamber force and the thrust due to the centre body. The thrust value obtained from the MATLAB code in comparison with that of the one in the reference paper [11] had very minimal percentage of error.

The research has investigated three distinct operational scenarios for aerospike nozzles. Case 1, termed "over-expansion," occurs when external or ambient pressure surpasses the nozzle's exit pressure, typically at lower altitudes and Case 2 represents "optimum expansion," where the external pressure matches the exit pressure of the nozzle. This condition is typically achieved at the ideal altitude for the aerospike nozzle's best performance and produces better performance than case 1. Case 3, known as "under expansion," occurs when the external or ambient pressure is lower than the exit pressure of the nozzle, often at altitudes beyond the optimal range. While in this case, the aerospike nozzle begins to resemble a bell nozzle, its unique altitude compensation feature preserves aerodynamic efficiency and improved thrust coefficient and performs better than Case1 and Case 2 as shown in Table 7.

The study's simulation results provide valuable insights into how these expansion cases and varying flow conditions affect aerospike nozzle performance, yet gives good performance due to its altitude compensating feature to maintain the aerodynamic efficiency.

Even though there are some disadvantages, overcoming those shortcomings can prove it to be a boon to the propulsion sector.

7 Conflicts of Interest

I, Md Saquib Reza, as a corresponding author, on behalf of all other authors hereby states that there is no conflict of interest.

References

1. Nazarinia M, Naghib-Lahouti A, Tolouei E (2005) Design and numerical analysis of aerospike nozzles with different plug shapes to compare their performance with a conventional nozzle. In: AIAC-11 Eleventh Australian International Aerospace Congress
2. Besnard E, Chen HH, Mueller T, Garvey J (2002) Design, manufacturing and test of a plug nozzle rocket engine. In: 38th AIAA/ASME/SAE/ASEE Joint Propulsion Conference & Exhibit, p 4038
3. Kornuta JA, Performance comparison of the aerospike & de Laval nozzles
4. Liu Y, Zhang GZ, Dai WY etal, Experimental investigation on aerospike nozzle in different structures and working conditions
5. Wang CH, Liu Y (2005) Studies on base pressure model of aerospike nozzle. Chinese J Aeronaut 26(1)
6. Nair PP, Suryan A, Kim HD (2019) Study of conical aerospikenozzles with base-bleed and freestream effects. J Spacecr Rockets 56:4
7. Denton BL (2008) Design and analysis of rocket nozzle contours for launching Pico-Satellites
8. .Khan S, Khan A, Munir AJSV (2014) Design and analysis approach for linear aerospike nozzle 20(2):25–37
9. Kumar KN, Gopalsamy M, Antony D, Krishnaraj R, Viswanadh CB (2017) Design and optimization of aerospike nozzle using CFD. IOP Conf Series: Mat Sci Eng 247(1):012008
10. Levaka VK, Reddy S, Design and flow simulation of truncated aerospike nozzle

11. Naghib-Lahouti A, Tolouei E (2006) Investigation of the effect of base bleed on thrust performance of a truncated aerospike nozzle in off-design conditions. In: European Conference on Computational Fluid Dynamics
12. Korte J et al (1997) Multidisciplinary approach to aerospike nozzle design
13. Shahrokhi A, Noori SJJC et al (2018) Favorable plug shape of an aerospike nozzle in design, over and under expansion conditions 8(1):1–14
14. Imran S, R. Publications (2016) Introduction to aerospike and its aerodynamic features 6(5)

Optimizing Robotic Arm Efficiency: Synergizing Aerodynamics with Arduino Control for Enhanced Six Degrees of Freedom



Akshay Mohan, Mohan Kumar Akurathi, Priyanka Vashisht, and Aman Jatain

Abstract The combination of robotics and aerodynamics has proven to be an interesting field of study, leading to advances in many fields. This brief presents a new approach to the design and control of a robotic arm that focuses on aerodynamics. The robotic arm uses an Arduino microcontroller for simplicity and ease of use. The aerodynamic design of the robot arm is designed to increase efficiency and effectiveness by reducing weight and improving lift. By using the aerodynamic structure, the structure of the arm is streamlined to reduce air resistance, resulting in more fluid and clear power. The choice of heavy and durable materials further contributes to the aerodynamic performance. The control of the robotic arm is used by the Arduino microcontroller, which provides various platforms to work and interact with various sensors and actuators. Control algorithms include real-time feedback from position and force sensors to make precise and responsive movements. Aerodynamic design principles are incorporated into the controller, which can adjust the configuration of the robotic arm according to atmospheric conditions. This research contributes to the field of robotics by demonstrating the benefits of integrated aerodynamics and Arduino-based control in the creation of human arms. These findings lead to the development of more efficient robotic systems and provide valuable insights for future research at the intersection of robotics and aerodynamics.

Keywords Arduino · D-O-F · End effector · Robotic arm · Aerodynamics

A. Mohan · M. K. Akurathi · P. Vashisht (✉) · A. Jatain
Department of Computer Science & Engineering, Amity University Haryana, Gurgaon, India
e-mail: pvashisht@ggn.amity.edu

A. Jatain
Manav Rachna University, Faridabad, India

© The Author(s), under exclusive license to Springer Nature Singapore Pte Ltd. 2024

S. Singh et al. (eds.), *Recent Advances in Aerospace Engineering*, Lecture Notes in Mechanical Engineering, https://doi.org/10.1007/978-981-97-1306-6_44

1 Introduction

Robotic arms have gained significant attention in various industries due to their ability to perform complex tasks with precision and efficiency. With the advent of open-source hardware platforms like Arduino, the development and implementation of robotic systems have become more accessible and cost-effective [1]. This research paper aims to explore the design and control of a 6-degree-of-freedom (6-DOF) robotic arm using Arduino, investigating its potential applications and demonstrating the feasibility of utilizing this platform for robotics research and development [2].

The 6-DOF robotic arm possesses six independently controllable joints, allowing it to perform a wide range of movements in three-dimensional space. Its versatility makes it suitable for tasks such as pick-and-place operations, assembly, welding, and even surgical procedures [3]. The integration of Arduino, a popular microcontroller platform, provides an opportunity to develop a low-cost and customization solution for robotic arm control [4].

The paper focuses on the design aspects of the robotic arm, discussing the mechanical structure, choice of actuators, and sensor integration. It explores different kinematic models to establish the relationship between joint angles and end-effector position [5]. The forward and inverse kinematics calculations play a crucial role in mapping desired end-effector positions to corresponding joint angles and vice versa. By leveraging Arduino's computational capabilities, these calculations can be performed in real time, enabling precise control of the robotic arm [6].

In addition to the mechanical design, the paper investigates the control strategies implemented using Arduino. It discusses the selection and programming of appropriate control algorithms, such as proportional–integral–derivative (PID) control, to regulate joint motions and achieve desired end-effector trajectories [1]. Furthermore, the research explores the integration of sensors, such as encoders and force sensors, to provide feedback and enable closed-loop control, enhancing the arm's accuracy and robustness [6, 7].

The Arduino platform offers several advantages for developing robotic systems. Its ease of use, vast online community, and extensive library support make it an attractive choice for researchers and hobbyists alike [8]. Moreover, its compatibility with various communication protocols allows for seamless integration with external devices, such as cameras or wireless modules, facilitating advanced functionalities like vision-based control or remote operation [9].

To validate the feasibility and performance of the Arduino-based 6-DOF robotic arm, experimental results are presented. The paper demonstrates the arm's capabilities by executing tasks such as object manipulation, trajectory tracking, and obstacle avoidance [10]. The obtained results provide insights into the arm's accuracy, speed, and reliability, showcasing the potential of Arduino as a viable platform for robotic arm development [11].

2 Literature Review

Bhargava [12] inspects a robotic arm controlled by an Arduino. The robotic system of five degrees of freedom (DOF) is used in his work. An Arduino Uno is used to control it. A microcontroller is a device that receives input signals from the stoner. Using a potentiometer, the arm is made up of four corridors. In addition, the effect ends, the joints rotate, and when there is gyration, a servo motor is used to give it. Each link has been strictly drafted. The SolidWorks distance metalworking toolbox was used first, followed by the 2 mm thick aluminium distance used in fabrication. Consequently, the legs are used to assemble the servomotors and liaison. The final arm shape has been created. The Arduino has been programmed to give a gyration to each servo commensurable to the gyration of the potentiometer shaft. The nature of the relative movements of the links that make up the robot makes it possible to characterize it. In a study by Pohlmeyer et al. [13], a BCI system was used to control a prosthetic arm. The study involved using 96-channel EEG signals to track prosthetic arm movements. The study showed that the system achieved 85 delicacies for the actors [13]. Rahul Gautam's review of the development of artificial robotic arms calls for this type of picky robotic control to break problems similar as placing or removing objects from workers. The robot arm has been successfully produced because the movement of the robot can be precisely controlled. Since string relief is veritably precious, it should be designed to reduce disunion on the table in order to protract service intervals. In a review by Lebedev and Nicolelis, colourful studies on the BCI system were anatomized [14]. The review shows that non-invasive BCI systems can achieve 70–80 delicacy in controlling robotic arm movements [15]. Ashraf Elfasahany has delved, designed, and developed a competitive low-cost robotic arm with four degrees of freedom. This study presents the design, development, and perpetration of a robotic arm able of performing simple tasks similar as handling feather light accoutrements. Tempera material is used to design and manufacture the robot arm, where a servomotor is used to make the connection between the arms. The encoder in the servomotor eliminates the need for a regulator. Still, the range of gyration of the motor is lower than 180 degrees, limiting the area the arm can reach and the positions it can take [15]. In a study by Müller- Putz et al. five actors with quadriplegia used the BCI to control a robotic arm performing functional tasks similar as drinking from a mug. Actors reported a high position of satisfaction and perceived control with the system [16]. Mahanta G.B et al. have presented the use of soft computational styles to determine the rear kinematics of the Kawasaki RS06L 6- DOF robotic regulator for pick-and-place operation. Comprehensive analysis was conducted between ways similar as artificial bee colony (ABC), firefly algorithm (FA), invasive weed optimization (IWO), and seed mass optimization for confirmation and corroborates the effectiveness of the proposed styles (PSO) [17]. Before the factual trials, detailed analysis was performed in the simulation terrain to determine the inverse kinematics of the proposed system, and the results were fed into the Kawasaki regulator to elect and place the work, evidence. demonstrate effective reversibility. exploration by Liu

et al., experimenters used the BCI system to control a robotic arm performing pick and place tasks [18].

3 Problem Statement

The following are the project's problem statements:

1. A robot is a sophisticated system. The mathematical modelling reveals a higher order, requiring the derivation of large equations. As a result, a CAD model can be employed as a different technique [2].
2. Linear controllers must be linearized before being used in robot systems, and the controller does not account for parameter uncertainty [5, 9]. To address this issue, a nonlinear controller will be utilized.
3. The hybrid controller comprising two nonlinear controllers, the fuzzy and neural-network controller, can improve the nonlinear controller's transient response and steady-state response [8].

4 Scope

CAD-designed model and controller for six (6) degrees of freedom of industrial robots. The development of the controller will be based on the Arduino controller. The simulation platforms will be MATLAB/Simulation, Ansys, and SolidWorks.

5 Methodology

As given in the diagram (Fig. 1), we can see the working principle of six-DOF robotic arm.

1. Begin with a literature review to study previous papers and come up with a problem statement.
2. Secondly, design the CAD model until the desired position and orientation are achieved [2].
3. Then the CAD model is converted to a physical model by using SimMechanics Simulink.
4. In the fourth stage, Arduino is programmed next, and observation of the result is done through a simulation study [4].

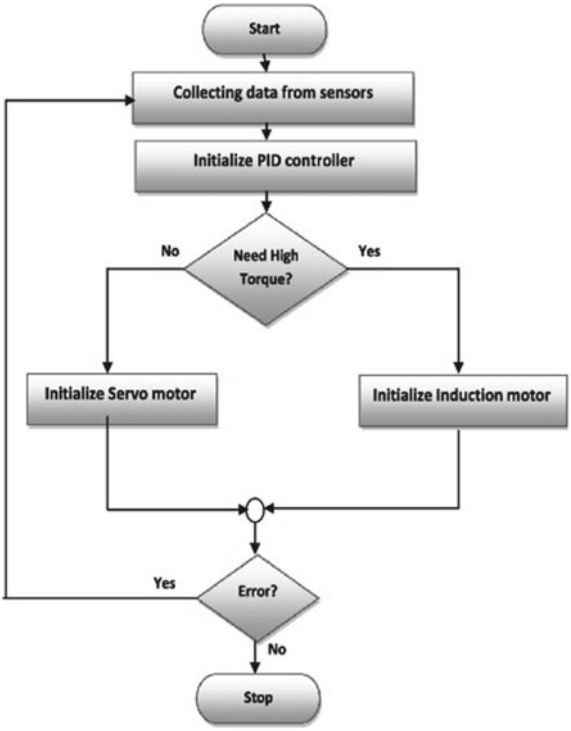


Fig. 1 Working process of the robotic arm

5.1 Design of CAD Model

Computer-aided layout (CAD) is the orientation, manipulation, analysis, or optimization of valuable resources in the layout using computer models [9]. CAD software is used to improve garment production quality, decorate with beautiful patterns, improve communication through data, and generate production data. CAD output is usually in the form of digital files for printing, machining, or different manufacturing processes [8]. The CAD model is created using SolidWorks (Fig. 2), and the SolidWorks assembly window can be viewed in Fig. 1. Creating a CAD model in the assembly window ensures each part's position and orientation are correct [10].

6 Working Principle

The working principle of the robotic arm with Arduino includes aerodynamics revolving around the optimization of the arm to reduce wind resistance and allow efficient operation [3]. The structure of the arm is designed to be aerodynamic shapes found in nature, like the wings of birds. Arms reduce overall weight by using heavy

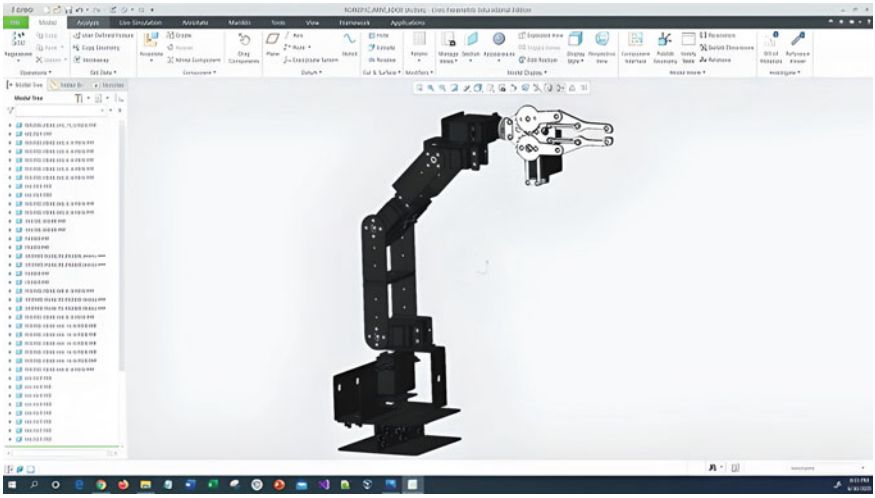


Fig. 2 Window of SolidWorks

equipment, which increases mobility and reduces the energy required for movement. The arm has many joints or parts that allow it to follow the range of motion found in aerodynamic systems. Sensors such as accelerometers and gyroscopes collect real-time data about the position and direction of the arm, while the Arduino microcontroller processes the data. The microcontroller runs control algorithms that interpret the sensor data, allowing the arm to be tuned for optimal aerodynamic performance [6]. The actuators of the arm, such as servos or stepper motors, are controlled by the Arduino, which adjusts their speed and position according to the instructions it receives. This control arm holds steady, reduces drag, and maximizes its travel for aerodynamic efficiency.

In terms of use, the robotic arm using Arduino and aerodynamics can be used for activities that have a clear and effective interaction with the surrounding air. For example, in air tunnel testing, a lever can be used to control the pattern and measure the power and airflow patterns [3]. The design of the arm is inspired by the aerodynamic shape that makes it less influenced by wind flow to ensure the measurement is accurate and reliable. Additionally, in the assembly of drones or other aircraft, robotic arms can be used to precisely position and handle food, considering aerodynamic considerations [7]. By optimizing its motion based on aerodynamics, the robotic arm can help improve the overall performance and performance of the aircraft assembly.

Continuous improvements in control algorithms, body inertia, and other aerodynamic functions demonstrate the robotic arm's performance in various aerodynamic applications, helping to improve performance quality and accuracy in tasks related to the surrounding air [8].



Fig. 3 Mechanical gripper

7 Components

7.1 Mechanical Gripper

The mechanical gripper (Fig. 3) is used to grip and hold objects while moving them from one place to another. The gripper has a built-in micro servo that opens and closes its jaws for material picking. The model is made of acrylic using a laser cutting program [1, 4].

The servo shaft extends to the end of the first jaw and engages with the gear of the second jaw. The force rotates as the motor rotates, and when the forces intertwine, the jaws open and close to release or hold the material. The servomotor is connected to a gear linkage that links with other gear linkages to provide smooth motion for a wide range of objects of all sizes [7].

7.2 Base with Bearing

The base is designed to support the entire assembly while balancing the centre of gravity of the entire arm. The base allows the arm to optimally move in the desired direction, allowing the arm to occupy the entire hemisphere volume [2]. The bed is attached to the box spring and supports the full load of the box spring; it also provides rotation from the base to the robot arm.

7.3 Servomotor

The robot arm has three main servomotors: one for the base movement, the two sides of the base plate, and the movement to send multiple links to the arm [3]. The servomotor is fixed on the base plate, which makes it stable and prevents them from vibrating during use.

The rotary actuator consists of a motor and an input field. It also requires a complex controller, which is usually a separate module designed specifically for servomotors [3, 4].

7.4 Connectors

Electrical equipment is a device used to connect electrical devices and generate electrical energy. These are electrical accessories consisting of male and female plugs and jacks. This connection can be temporary, as for mobile equipment, or it can be a permanent electrical connection between two cables or equipment that requires the use of a brake tool for assembly and disassembly [1]. Only male-to-male connectors or plugs for connection in our project.

7.5 Lagrange's Equation of Motion

Lagrange's equation of motion is a powerful tool for deriving the equations that describe the motion of a mechanical system. In the case of a 6-degree-of-freedom (DOF) robotic arm, we can use Lagrange's equations to obtain the equations of motion for each joint.

Let us assume that our robotic arm has six revolute joints, numbered from 1 to 6, and the generalized coordinates representing the joint angles are q_1, q_2, q_3, q_4, q_5, and q_6. We can denote the mass of each link as m_1, m_2, m_3, m_4, m_5, and m_6, respectively. The lengths of the links can be represented as L_1, L_2, L_3, L_4, L_5, and L_6.

The kinetic energy T of the robotic arm can be expressed as the sum of the kinetic energies of each link:

$$T = 0.5 \times \left(m_1 \times L_1^2 \times q_1^2 + m_2\right) \times \left(m_2 \times L_2^2 \times q_2^2 + m_3 \times L_3^2 \times q_3^2\right) + \left(m_4 \times L_4^2 \times q_4^2 + m_5 \times L_5^2 \times q_5^2\right) + m_6 \times L_6^2 \times q_6^2)ma^2$$

where $\dot{q}_1$, $\dot{q}_2$, $\dot{q}_3$, $\dot{q}_4$, $\dot{q}_5$, and $\dot{q}_6$ represent the time derivatives of the joint angles.

The potential energy U of the robotic arm is the sum of the potential energies of each link due to gravity:

$$
\begin{aligned}
U = {} & m_1 * g * L_1 * \sin(q_1) + m_2 * g * (L_1 * \sin(q1) + L_2 * \sin(q_1 + q_2)) \\
& + m_3 * g * (L_1 * \sin(q_1) + L_2 * \sin(q_1 + q_2) + L_3 * \sin(q_1 + q_2 + q_3)) \\
& + m_4 * g * (L_1 * \sin(q_1) + L_2 * \sin(q_1 + q_2) \\
& + L_3 * \sin(q_1 + q_2 + q_3) + L_4 * \sin(q_1 + q_2 + q_3 + q_4)) \\
& + m_5 * g * L_1 * \sin(q_1) + L_2 * \sin(q_1 + q_2) + L_3 * \sin(q_1 + q_2 + q_3) \\
& + L_4 * \sin(q_1 + q_2 + q_3 + q_4) + L_5 * \sin(q_1 + q_2 + q_3 + q_4 + q_5) \\
& + m_6 * g * L_1 * \sin(q_1) + L_2 * \sin(q_1 + q_2) + L_3 * \sin(q_1 + q_2 + q_3) \\
& + L_4 * \sin(q_1 + q_2 + q_3 + q_4) + L_5 * \sin(q_1 + q_2 + q_3 + q_4 + q_5) \\
& + L_6 * \sin(q_1 + q_2 + q_3 + q_4 + q_5 + q_6))
\end{aligned}
$$

where g represents the acceleration due to gravity.

The Lagrange L of the system is the difference between the kinetic energy T and the potential energy U:

$$L = T - U$$

Using Lagrange's equations of motion, we can obtain the equations that govern the dynamics of each joint. The general form of Lagrange's equation for a generalized coordinate q can be expressed as:

$$\mathrm{d}/\mathrm{d}t(\partial L/\partial(\dot{q})) - \partial L/\partial q = \tau$$

where τ represents the generalized force acting on the joint.

By applying this equation to each joint of the robotic arm, we can derive a set of six equations of motion, one for each joint (Fig. 4).

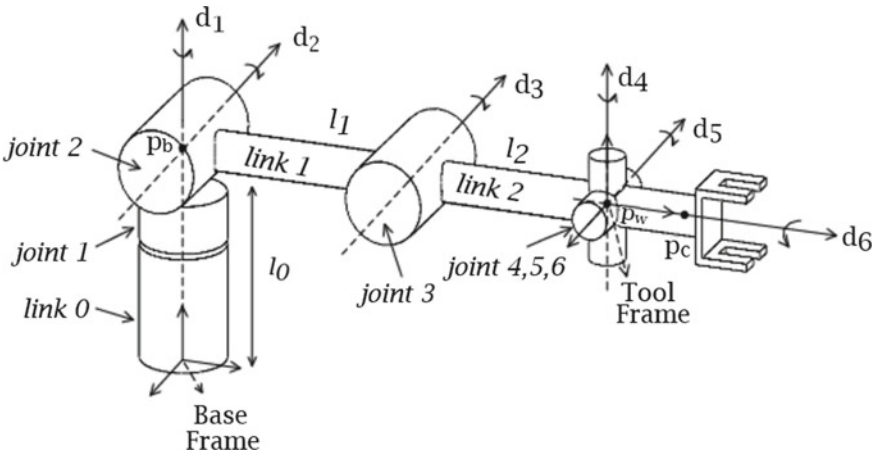


Fig. 4 Joints and links of robotic arm

8 Mechanical Links

The differential link transmits motion from the servomotor to the tool holder assembly or gripper. Connection is designed to transfer power with minimal load on the servomotor.

Using the equipment correctly, the connection model is very heavy. The main idea of using pods instead of hard parts is to save energy by reducing the amount of energy needed to power the arm [9].

9 Result and Discussion

In our research paper on a 6-degree-of-freedom (6DoF) robotic arm using Arduino, we conducted a workspace analysis to determine the reachable volume and limitations of the robotic arm's mechanical design. The workspace analysis is crucial for understanding the arm's capabilities and potential applications.

We calculated the boundaries of the arm's workspace using geometric modelling and kinematic equations. Our results indicated that the robotic arm's reach was sufficient to cover a significant volume within its operational range. However, we observed certain limitations near the arm's joint limits and mechanical constraints. We generated a three-dimensional representation and presented it graphically to visualize the workspace. The visualization demonstrated the arm's capabilities in reaching various points within its workspace, highlighting areas where it excelled and identifying regions that required further optimization.

These findings provide valuable insights for the selection of tasks and applications suitable for the robotic arm. Understanding the limitations of the workspace helps in avoiding situations where the arm might experience collisions or reduced performance due to its mechanical constraints. Furthermore, it serves as a foundation for future improvements in the arm's design and expansion of its operational envelope.

10 Conclusion

Combining the principles of aerodynamics with an Arduino-powered robotic arm opens up exciting possibilities to make it more efficient and effective in a variety of applications. By designing the arm's model to follow the aerodynamic pattern, using deep and integrated components with real-time feedback, the arm can optimize road motion to reduce weight and increase manoeuvrability. The use of servo or stepper motors controlled by the Arduino board allows accurate processing and adjustments based on sensor data, making the arm more stable and working with better performance. Continuous optimization, including airflow patterns, friction, and other aerodynamic factors, can improve the performance of the robotic arm.

Combining robotics and aerodynamics with Arduino, the robotic arm offers great opportunities for high performance and productivity in areas such as wind tunnel testing, drone assembly, and manufacturing.

Acknowledgements We consider it a privilege to have undertaken this endeavour with the motivating guidance of Dr. Priyanka Vashisht, Associate Professor, ASET, Amity University Haryana, our project's supervisor. We would want to use this time to offer our heartfelt thanks to them for all their invaluable advice and helpful feedback during this project, as well as for critically guiding us through the whole development period. We are grateful to you for believing in me.

Funding Information Not applicable.

References

1. Katal G, Gupta S, Kakkar S (2013) Design and operation of synchronized robotic arm. IJRET Int J Res Eng Technol 1163–2319
2. Omijeh BO, Uhunmwangho R, Ehikhamenle M (2014) Design analysis of a remote controlled pick and place robotic vehicle. Int J Eng Res Dev 10(5):57–68
3. Nishar KD, Sekar I (2015) Vision assisted pick and place robotic Arm. Adv Vis Comput An Int J 2(3):9–18
4. Nair SR (2012) Design of an optically controlled robotic arm for picking and placing an object. Int J Sci Res Publ 173
5. Elfasakhany A, Yanez E, Baylon K, Salgado R (2011) Design and development of a competitive low-cost robot arm with four degrees of freedom. Mod Mech Eng 1(02):47–55
6. Quigley M, Asbeck A, Ng A (2011) A low-cost compliant 7-DOF robotic manipulator. In: 2011 IEEE international conference on robotics and automation. IEEE, pp 6051–6058
7. Patel HK, Verma P, Ranka S (2011) Design and development of co-ordinate based autonomous robotic arm. In: 2011 Nirma University international conference on engineering. IEEE, pp 1–6
8. Gunasekaran K (2015) Design and analysis of articulated inspection arm of a robot. Int J Trends Eng Technol 5(1)
9. Dhote PK, Mohanta JC, Nayab Zafar M (2012) Motion analysis of articulated robotic arm for industrial application
10. Clothier KE, Shang Y (2010) A geometric approach for robotic arm kinematics with hardware design, electrical design, and implementation. J Robot
11. Oliveira LA, Costa JJ, Carvalho MG, Gerhardt HJ, Kramer C (1991) On aerodynamic sealing for industrial applications. J Wind Eng Ind Aerodyn 37(3):255–268
12. Bhargava A, Kumar A (2017) Arduino controlled robotic arm. In: 2017 International conference of electronics, communication and aerospace technology (ICECA), vol 2. IEEE, pp 376–380
13. Pohlmeyer EA, Mahmoudi B, Geng S, Prins NW, Sanchez JC (2014) Using reinforcement learning to provide stable brain-machine interface control despite neural input reorganization. PLoS ONE 9(1):e87253
14. Lebedev MA, Nicolelis MA (2006) Brain–machine interfaces: past, present and future. TRENDS Neurosci 29(9):536–546
15. Pawar V, Bire S, More S, More K, Mule R (2018) Review on design and development of robotic arm generation-1. Int J Innov Sci Res Technol 3(3)
16. Müller-Putz G (2021) Invasive BCI approaches for restoration of upper extremity movements. In: Neuroprosthetics and brain-computer interfaces in spinal cord injury: a guide for clinicians and end users. Springer, Cham, pp 217–232
17. Mahanta GB, Deepak BBVL, Dileep M, Biswal BB, Pattanayak SK (2019) Prediction of inverse kinematics for a 6-DOF Industrial robot Arm using soft computing techniques. In: Soft computing for problem solving: SocProS 2017, vol 2. Springer, Singapore, pp 519–530

18. Du G, Yao G, Li C, Liu PX (2021) An offline-merge-online robot teaching method based on natural human-robot interaction and visual-aid algorithm. IEEE/ASME Trans Mechatron 27(5):2752–2763

Analysis of Indian Aircraft Maintenance Engineer Licensing in the Global Regulatory Framework

Manoj Kumar Paidisetty, V. R. Sanal Kumar, Sanjay Singh, and Deepak Chandra Chandola

Abstract The demand of aircraft maintenance engineers (AMEs) is significantly increasing year by year as the growth of aviation industry is rapidly growing worldwide. The regulatory bodies have to ensure adequate training is provided to the prospective AMEs and licensed timely. The International Civil Aviation Organization (ICAO) stipulates the framework for its member states in regards to the civil aviation which includes AME's and Air Crew's licensing and further guides the states for mutual acceptance of licenses of member states. Still, it is found that the acceptance of Indian AME license holders by other regulatory bodies like FAA and EASA is found challenging due to lack of harmonization of licensing procedures, soft skills, and practical experiences. This paper aims to identify the challenges and the feasibility of Indian AMEs in the international aviation industry by analyzing the regulations stipulated by the ICAO and other prominent states. Based on the study, an economical solution is recommended that complies with international regulations and DGCA requirements.

Keywords License · Aircraft maintenance engineer · ICAO · EASA · DGCA

M. K. Paidisetty (✉) · V. R. Sanal Kumar · S. Singh
Amity Institute of Aerospace Engineering, Amity University Uttar Pradesh, Noida, Uttar Pradesh, India
e-mail: m.k.paidisetty@gmail.com

V. R. Sanal Kumar
e-mail: vrskumar@amity.edu

S. Singh
e-mail: ssingh10@amity.edu

D. C. Chandola
Banasthali Vidyapith University, Jaipur, India

© The Author(s), under exclusive license to Springer Nature Singapore Pte Ltd. 2024

S. Singh et al. (eds.), *Recent Advances in Aerospace Engineering*, Lecture Notes in Mechanical Engineering, https://doi.org/10.1007/978-981-97-1306-6_45

1 Introduction

With the increasing demand of aircraft for the passenger travel, the demand of qualified AMEs is on the raise globally. The AMEs Licensing in India is stringent process and is monitored under the surveillance of the Directorate General of Civil Aviation (DGCA). Article 33 of Chicago Convention states that the license issued by the member states should be accepted by the rest of the member states [1]. However, EASA member states were found to be not accepting licenses issued by the non-EASA member state. Further, this is not in compliance with the Chicago convention Article 33 [2].

Despite the high standards of educating with theoretical and practical trainings, Indian AME license holders face challenges in finding acceptance of their license in other countries. This paper's focus is to analyze the current trainings and licensing process for AMEs in India, detailed study of the existing regulations, industry requirements, and suggest improvements to increase the acceptance of Indian DGCA's AME licenses internationally. Hence, it is salient to collaborate with the International Civil Aviation Organization (ICAO) and other prominent regulatory bodies in order to identify opportunities for enhancing the regulations of the Indian DGCA. This collaboration will help strengthen the acceptance and recognition of the Indian DGCA AME License on an international scale. This process of reviewing and comparing the AME regulations, trainings, and licensing processes of Indian DGCA with international regulatory bodies; along with the expert opinions could led to develop an efficient roadmap for increasing the recognition and acceptance of Indian AME licenses globally.

2 Background

One of the major contributors for any Nation's growth is infra-structure along with connectivity, for which the Civil Aviation plays a vital role. The advanced aircraft technologies demand technically qualified AMEs for manufacturing/maintenance [3]. India is producing qualified and well-trained AMEs for production and maintenance of the advanced aircraft. However, it has been noted that some countries currently do not recognize the Indian DGCA AME License holders [2]. Therefore, it is crucial to proactively identify any potential areas of improvement and address them [4]. This will contribute to enhancing aviation safety by ensuring that highly qualified AMEs are entrusted with advanced aircraft maintenance tasks, and it will facilitate the global employment opportunities for Indian AMEs.

2.1 Objective

The objective of this paper is identifying means to address the international requirements to accept the Indian DGCA AME license and to increase the probability of employment of the Indian AMEs globally.

2.2 Need of Study

Eighty-five percent of aircraft accidents are occurring due to human errors [5], and 12% of the same in the twentieth century was due to maintenance and inspections [6]. Present aircraft is with the advanced technologies to ensure safe flying by strengthening complex and redundant aircraft systems [7]. With the growing Indian population, it is the crucial to find the avenues for the AMEs to identify various job opportunities for better standard of living.

2.3 Scope of Study

This study is based on the review of research papers, requirements of various regulatory bodies, accidents, and incidents reports of the various regulatory bodies. The primary scope of this study is to identify the areas of improvement in the Indian DGCA Regulations pertaining to AME licensing, in order to increase the employment globally.

2.4 Limitation

This is limited to the analysis of the current regulations and training processes for AMEs in India and the comparison with those followed by other countries.

3 Literature Review

This is an essential segment for this study to identify the possibilities of increasing the acceptance of Indian DGCA AME license holders in the international aviation market. Several regulatory documents and research articles have been referred to, including DGCA Civil Aviation Requirements 66, International Civil Aviation Organization Annex 1, European Union Aviation Safety Agency Part 66, Federal Aviation Authority Requirements - CFR Part:65—Subpart/Appendix: Subpart D and E, and

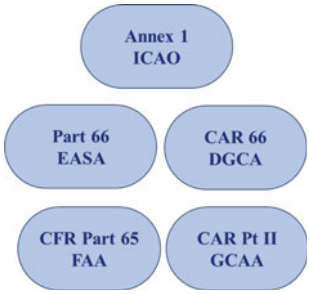


Fig. 1 "Prominent regulatory bodies"

General Civil Aviation Authority of UAE—CAR Part II Chapter 7—CAR 66 Aircraft Maintenance Engineer Licensing. These are the guidelines for their state in regards to the licensing to the qualified personnel for aircraft maintenance, as per their state's requirements (Fig. 1).

DGCA Civil Aviation Requirements 66 is a comprehensive document that provides the regulatory framework for AME licensing and training in India. It outlines the eligibility criteria, training requirements, examination procedures, and other aspects related to AME licensing [8, 9]. This document is crucial in understanding the regulatory framework for AMEs in India and the standards set by the DGCA. Annex 1 of ICAO is a global standard that specifies the requirements for personnel licensing in civil aviation [10]. This document covers various aspects related to AME licensing, including the competency-based training, skill tests, and medical requirements. Understanding the standards set by the ICAO Annex 1 is crucial to identify the possibilities of accepting the Indian DGCA AME license holders in the international aviation market. The European Union Aviation Safety Agency (EASA) Part 66 is a regulatory framework that covers the licensing requirements for maintenance personnel in the European Union [11]. This document specifies the knowledge, skills, and experience required for obtaining an AME license in the EU. This document is crucial in understanding the standards set by the EASA and the possibilities of accepting Indian DGCA AME license holders in the global aviation Industry.

4 Research Methodology

The research methodology adapted for this paper is the comparative analysis of the prominent civil aviation regulators and ICAO. In addition, the experts in the industry were interviewed for this paper.

4.1 Comparative Analysis

This is to compare the AME training and licensing process in India with that of other countries to identify similarities, differences, and areas with potential for further enhancement. The methodology involves examining the AME training and licensing process with the prominent regulatory bodies. The data for the comparative analysis collected through a comprehensive literature review of relevant published civil aviation regulations, manuals, and reports. The findings from the comparative analysis have offered valuable insights into areas of opportunity for further enhancing the Indian AME training and licensing process, particularly in terms of strengthening the global acceptance of the AME license.

Eligibility
The regulatory bodies require applicants to be at least 18 years of age, as stipulated by the International Civil Aviation Organization (ICAO) and the Directorate General of Civil Aviation (DGCA) in India. The European Union Aviation Safety Agency (EASA), the Federal Aviation Administration (FAA) in the United States, and the General Civil Aviation Authority (GCAA) in the United Arab Emirates. However, each regulatory body has its own additional specific eligibility criteria. DGCA India requires applicants to have passed the 10 + 2 examination in Physics, Chemistry, and Mathematics from a recognized board or university or its equivalent. The FAA focuses on language proficiency, requiring applicants to be able to read, write, speak, and understand the English language [12]. If an applicant is employed outside of the United States by a U.S. air carrier and does not meet the English language requirement, their certificate may be endorsed as "Valid only outside the United States." The GCAA in the UAE has its own set of specific eligibility criteria. Applicants must either be a UAE/GCC national, a legal employee of a UAE approved organization with proper justification for the need to hold a UAE GCAA license, or a graduate of a GCAA CAR 147 approved basic aircraft maintenance training organization [13]. Despite these differences in requirements, all regulatory bodies share a common goal of ensuring the highest standards of safety and competence in the aviation industry [14]. By setting minimum age limits and specific eligibility criteria and requiring proficiency in areas like language and academic qualifications, they help ensure that aircraft maintenance engineers are well-trained, knowledgeable, and prepared to meet the needs of the industry.

Knowledge Requirements
ICAO, DGCA India, EASA, FAA, and GCAA all require applicants for aircraft maintenance engineer's licenses or mechanic certificates to pass written tests covering various topics related to aircraft maintenance and engineering. ICAO states that the applicant must pass exams on air law and airworthiness requirements, natural science and aircraft general knowledge, aircraft engineering, aircraft maintenance, and human performance. DGCA India mandates written tests on electrical fundamentals, electronic fundamentals, digital techniques/electronic instrument systems, materials and hardware, maintenance practices, basic aerodynamics, human factors,

aviation regulations, aircraft, and various engines with propellers [8, 9]. Similarly, EASA and GCAA require all the topics mandated by DGCA India and include mathematics and physics [11, 13]. FAA requires each applicant to pass a written test covering the construction and maintenance of aircraft appropriate to the rating sought and relevant regulations. Overall, while there are some differences in the specific topics covered in the written tests, all the aviation authorities mentioned require applicants to pass written exams covering a broad range of knowledge related to aircraft maintenance and engineering.

Experience

The requirements for aircraft maintenance engineer licenses can vary depending on the country and regulatory authority involved. However, in general, experience in the inspection, servicing, and maintenance of aircraft or its components is required. The amount of experience required depends on the category and subcategory of the license being sought. For example, according to ICAO, for the issue of a license with privileges for the aircraft in its entirety, at least four years of practical aircraft maintenance experience on operating aircraft is required. However, if the applicant has satisfactorily completed an approved training course, the requirement is reduced to two years.

According to EASA, for category A, subcategories B1.2 and B1.4 and category B3, either three years of practical maintenance experience on operating aircraft, completion of relevant technical training, or completion of an approved basic training course are required. For category B2 and subcategories B1.1 and B1.3, either five years of practical maintenance experience on operating aircraft, completion of relevant technical training, or completion of an approved basic training course is required. For category C with respect to complex motor-powered aircraft, three years of experience exercising category B1.1, B1.3, or B2 privileges on complex motor-powered aircraft or as support staff according to point 145.A.35, or a combination of both; or five years of experience exercising category B1.2 or B1.4 privileges on complex motor-powered aircraft or as support staff, or a combination of both are required. For category C with respect to other than complex motor-powered aircraft, three years of experience exercising category B1 or B2 privileges on other than complex motor-powered aircraft are required. Experience requirements of DGCA India and GCAA are similar to EASA [8, 11, 13].

FAA mandates the applicant to have at least 18 months of practical experience with the procedures, practices, materials, tools, machine tools, and equipment generally used in constructing, maintaining, or altering airframes, or powerplants appropriate to the rating sought or at least 30 months of practical experience concurrently performing the duties appropriate to both the airframe and powerplant ratings [12].

The experience requirement of one year could be reduced by the regulatory bodies for the applicants who have satisfactorily completed training in an approved training organization or who have acquired a degree in an allied field of engineering from a recognized university.

Skill

The International Civil Aviation Organization (ICAO), the Directorate General of Civil Aviation (DGCA) in India, the European Aviation Safety Agency (EASA), the Federal Aviation Administration (FAA), and the General Civil Aviation Authority (GCAA) have all established requirements for obtaining and maintaining aircraft maintenance licenses or certificates. ICAO requires applicants to demonstrate the ability to perform functions related to the privileges they are seeking, without specifying any examination or certification process [10].

DGCA India requires applicants to demonstrate their aircraft maintenance skills for each category or subcategory of license or specific type of aircraft. It stipulated guidelines for practical training and experiences requirements for the endorsement of an aircraft in license [8, 9].

EASA requires applicants to pass an examination demonstrating their level of knowledge of the appropriate subject modules, with the examination to be conducted by an approved training organization [11].

FAA requires applicants to pass an oral and practical test on the rating they are seeking, with the tests covering the applicant's basic skill in performing practical projects related to the subjects covered by the written test for that rating. Applicants for a powerplant rating must also demonstrate their ability to make satisfactory minor repairs and alterations to propellers [12].

GCAA requires applicants to demonstrate their level of knowledge in the appropriate subject modules through an examination. This applies to both applicants for an aircraft maintenance engineer's license and those seeking to add a category or subcategory to an existing license [13].

Overall, while all these organizations have established requirements for aircraft maintenance licenses or certificates, there are some differences in the specific requirements and examination or certification processes they use.

4.2 Expert Interviews

A questionnaire was sent to the industry experts regarding the potential growth of the aviation industry in India and its impact on the demand for aircraft maintenance engineers (AMEs). The responses revealed that growth in the aviation industry will increase the demand for qualified and skilled AMEs, but the longevity and sustainability of players in the industry will determine the manpower requirements and job stability. However, it is worth noting that there are variations in the training and certification procedures for AMEs in India when compared to other countries. These differences encompass educational qualifications, practical training, examination processes, as well as duration and quality of training. Furthermore, the current limited acceptance of Indian AME license holders in other countries is primarily attributed to the need for greater harmonization, recognition, and adherence to international regulations and standards, as well as government policies. Recognizing and

addressing these areas for improvement will contribute to fostering a more globally aligned and recognized AME licensing system for India. The strengths and weaknesses of DGCA regulations for AMEs were also highlighted, with strengths including harmonization with EASA regulations and alignment with international requirements. However, there were certain areas that were identified as opportunities for improvement within the Indian DGCA's training and licensing process for AMEs. These include enhancing the understanding and practical implementation of regulations and expanding the scope of training organizations. The comments made by the experts examined with respect to the facts available on the ICAO Web site regarding the effective implementation of regulations, and it is found that DGCA's effective implementation is much above than the global average in all areas of aviation [15]. Further, since DGCA has adapted the EASA system, therefore its regulations are in harmonization with the EU regulations.

In order to address suggestions made by the experts, such as implementing more stringent requirements for instructors, improving online resources, expanding training opportunities, and simplifying the licensing process, these improvements may contribute to strengthening the training and licensing framework for AMEs under the Indian DGCA, ensuring a more effective and streamlined process for the benefit of all stakeholders involved.

5 Identification of Gaps and Improvements

Based on the analysis of the various regulations and the expert interviews, some of the topics which can be discussed for further improvement are as follows:

5.1 Lack of Harmonization

The common goal of the regulatory bodies is to ensure the highest standards of safety and competence in the aviation industry. Even though, there are still differences in eligibility criteria, knowledge requirements, and experience requirements. These differences can make it difficult for aircraft maintenance engineers to obtain licenses or certificates in different countries. One possible improvement could be greater harmonization of requirements across regulatory bodies to reduce barriers to mobility and facilitate the recognition of qualifications across borders.

5.2 Lack of Emphasis on Practical Experience

The practical experience for the AMEs in the inspection, servicing, and maintenance of aircraft varies depending on the category and subcategory of the license

being sought. Furthermore, some regulatory bodies provided reduction of practical experience requirements if an applicant has completed an approved training course. One possible improvement could be to place greater emphasis on practical experience requirements and to ensure that approved training courses include sufficient practical training.

5.3 Lack of Emphasis on Soft Skills

While all regulatory bodies require applicants to demonstrate knowledge of various topics related to aircraft maintenance and engineering, there is less emphasis on soft skills such as communication, teamwork, and problem-solving. However, these skills are crucial for ensuring the safe and efficient operation of aircraft, especially in high pressure situations. One possible improvement could be to include soft skills training in approved training courses and to assess soft skills as part of the licensing or certification process.

5.4 Lack of Emphasis on Continuing Education

While regulatory bodies require applicants to pass written exams covering various topics related to aircraft maintenance and engineering, there is less emphasis on continuing education and ongoing professional development. However, the aviation industry is constantly evolving, and it is essential for aircraft maintenance engineers to stay up-to-date with the latest developments and best practices. One possible improvement could be to require regular continuing education or professional development for licensed or certified aircraft maintenance engineers.

6 Future Direction

This paper has discussed and evaluated the regulations of ICAO, EASA, DGCA, FAA, and GCAA. However, there are numerous other civil aviation regulatory bodies, and the study on these could extract some perspectives in this area.

7 Conclusion

The aviation industry is one of the fastest-growing industries in the world, and the demand for skilled aviation professionals is on the rise. Aircraft maintenance engineers (AMEs) play a crucial role in ensuring the safety and reliability of aircraft,

making them an integral part of the aviation industry. However, Indian AMEs face challenges in obtaining international recognition and acceptance of their licenses, which limits their job opportunities and career growth. This study highlights the key issues faced by Indian AMEs in the international job market and provide recommendations to address these issues. The DGCA may work toward harmonizing Indian AME license requirements with international standards, those set by the International Civil Aviation Organization (ICAO). The DGCA could establish mutual recognition agreements (MRAs) with other countries to recognize Indian AME licenses. The DGCA can consider opportunities for Indian AMEs to gain international exposure, such as internships and exchange programs. Indian AMEs may undergo additional training and certification to meet international standards, such as the European Aviation Safety Agency (EASA) Part-66 certification. The DGCA can collaborate with Indian aviation companies to actively promote the employment of Indian AMEs and facilitate their participation in international projects. By fostering such partnerships, the DGCA can create avenues for Indian AMEs to gain valuable experience and exposure on a global scale. Additionally, this will provide the job opportunities to the various prospective engineers and can provide a means for their livelihood. This proactive approach will not only benefit the AMEs by offering them international opportunities but also contribute to the overall growth and reputation of the Indian aviation industry.

References

1. ICAO. Doc 7300 convention on international civil aviation convention
2. Yadav DK (2010) Licensing and recognition of the aircraft maintenance engineers—A comparative study. J Air Transp Manag 16(5):272–278. https://doi.org/10.1016/j.jairtraman.2010.03.005
3. Chandola DC, Verma S, Jaiswal K, Chandola P, Goyat M, Narvekar N (2023) An exploratory study on the significance and challenges of aircraft base maintenance engineering in the aviation industry. In: 2023 International conference on computational intelligence and knowledge economy (ICCIKE). https://doi.org/10.1109/ICCIKE58312.2023.10131844
4. Chandola DC, Chandola P, Verma S, Jaiswal K (2023) An exploratory study to evaluate significance of maintenance planning in reducing aircraft maintenance turnaround time within airlines industry. In: 2023 International conference on computational intelligence and knowledge economy (ICCIKE). https://doi.org/10.1109/iccike58312.2023.10131888
5. Matthews S (2003) The potential for improving aviation safety and reducing the accident rate. In: AIAA\ICAS international air and space symposium and exposition: the next 100 years. American Institute of Aeronautics and Astronautics Inc. https://doi.org/10.2514/6.2003-2796
6. Trifonov-Bogdanov P, Vinogradov L, Shestakov V (2013) Civil aviation accidents and incidents classified according to groups of aviation specialists. Aviation 17(2):76–79. https://doi.org/10.3846/16487788.2013.805861
7. International Civil Aviation Organization (2010) Annex 8 to the convention on international civil aviation, airworthiness of aircraft, no July 2010
8. DGCA CAR 66
9. DGCA Appendix I to AMC for CAR-66
10. ICAO Annex 1 to convention on international civil aviation. Personnel Licensing 13th edition, July 2020

11. EASA (2021) Easy access rules for continuing airworthiness (Regulation (EU) No 1321/2014) Annex 1, 2021. Available https://www.easa.europa.eu/document-library/easy-access-rules/online-publications/easy-access-rules-continuing-airworthiness?page=5#_Toc256000023
12. FAA advisory circular certification of a repairman (general)
13. GCAA CAR Pt II Ch 7-CAR 66 aircraft maintenance engineer licensing
14. Chandola DC, Jaiswal K, Verma S, Singh B (2023) Aviation MRO: a comprehensive review of factors affecting productivity of Aircraft Maintenance Organization. In: 2022 Advances in science and engineering technology international conferences (ASET). https://doi.org/10.1109/ASET53988.2022.9734808
15. Safety audit results: USOAP interactive viewer. https://www.icao.int/safety/Pages/USOAP-Results.aspx. Accessed 15 July 15 2023

Assessing the Influence of Quality Control and Assurance on Aircraft Maintenance Turnaround Time Reduction: A Regression Modeling Approach



Deepak Chandra Chandola, Preeti Chandola, Seema Verma, Kamal Jaiswal, Manoj Kumar Paidisetty, and Rajendra Prasad Kholiya

Abstract The aircraft maintenance turnaround time is critical to airlines' operational efficiency and profitability. This paper summarized the significance of quality control (QC) and quality assurance (QA) processes on aircraft maintenance turnaround time. The paper adopts a mixed-methods approach that combines a literature review and quantitative data analysis from a large-scale survey of maintenance personnel working in the aircraft maintenance domain within the airline industry. The results show that QC has a comparatively higher impact on lowering turnaround time of aircraft maintenance. The paper also identifies some best practices for improving QC and QA in the aircraft maintenance industry, such as standardization, automation, collaboration, training, and regulation. Conclusions in the paper include recommendations for improving aircraft maintenance quality and efficiency.

D. C. Chandola (✉) · P. Chandola · S. Verma
Banasthali Vidyapith, Tonk, India
e-mail: deepak.chandola@outlook.com

P. Chandola
e-mail: preeti.chandola@outlook.com

S. Verma
e-mail: Seemaverma3@yahoo.com

K. Jaiswal
Higher Colleges of Technology, Abu Dhabi, UAE
e-mail: kjaiswal@hct.ac.ae

M. K. Paidisetty
Amity Institute of Aerospace Engineering, Amity University Uttar Pradesh, Noida, Uttar Pradesh, India
e-mail: manojphd2023@gmail.com

R. P. Kholiya
Swiss Business School, Kloten, Switzerland
e-mail: rajendrrakholliya@outlook.com

© The Author(s), under exclusive license to Springer Nature Singapore Pte Ltd. 2024

S. Singh et al. (eds.), *Recent Advances in Aerospace Engineering*, Lecture Notes in Mechanical Engineering, https://doi.org/10.1007/978-981-97-1306-6_46

Keywords Aircraft maintenance management · Quality control · Engineering · Airlines management · Quality assurance · Compliance monitoring · MRO management

1 Introduction

Aircraft maintenance ensures safety, performance, and availability through various activities such as inspections, repairs, modifications, and troubleshooting. However, the involvement of multiple trades makes it complex and time-consuming. Minimizing turnaround time is crucial for operational efficiency, profitability, and customer satisfaction, but it requires balancing quality and time. Quality control (QC) and quality assurance (QA) processes monitor, verify, and improve maintenance work. QC involves inspections, tests, measurements, and feedback, while QA includes policies, procedures, standards, documentation, and reviews. Inadequate quality control or assurance can lead to rework and delays, while excessive processes can also cause turnaround time delays. This research investigates the impact of QC and QA on turnaround time and proposes strategies to optimize the balance between quality and time in aircraft maintenance.

1.1 Objective

The key objective of this research article is to feature the impact of quality control and quality assurance in the aircraft maintenance turnaround time and to drive mathematical equations to measure.

1.2 Need and Scope of Study

Airlines aim to boost profits through time and cost savings. This paper highlights the quality function's role in cutting aircraft maintenance turnaround time based on a thorough review of research papers, industry expert insights, and a questionnaire-based survey.

1.3 Limitation

This study focuses on quality control and assurance as an operating function within airlines and is restricted to the Asian region only.

1.4 Problem Statement and Research Gap

This paper evaluates the quality function's role in decreasing aircraft maintenance turnaround time in aviation. Unlike previous studies centered on optimization models, this research addresses the importance of quality control. It provides comprehensive data for the aircraft maintenance industry.

1.5 Background of Study

Airlines worldwide adhere to two EASA-driven regulations, Part-M and Part-145 (see Fig. 1). These regulations, supported by acceptable means of compliance and guidance materials [1], require implementing quality control and quality assurance frameworks. Part-M organizations, also called continuing airworthiness management organizations (CAMO) [1], are governed by these regulations.

Similarly, Part-145 organizations are known as aircraft maintenance organizations (AMO) or maintenance repair and overhaul organizations (MRO). CAMO organizations mainly define the work scope being executed by MRO organizations to ensure aircraft airworthiness [2]. This relationship is depicted in Fig. 2.

Considering the organization's approval and capabilities, aircraft maintenance is divided into line and base maintenance, as illustrated in Table 1.

Line maintenance implies minor work which does not demand a hangar. On the other hand, base maintenance requires hangar access to perform all major work [3]. While performing aircraft maintenance activities, quality control and quality assurance are effectively applied to maintain continuing airworthiness. This research paper



Fig. 1 Types of regulation used in aircraft maintenance management

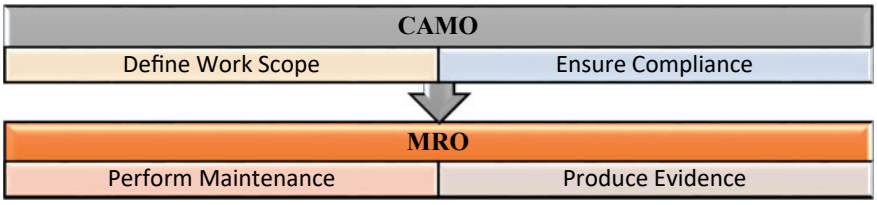


Fig. 2 Relationship between CAMO and MRO

Table 1 Types of aircraft maintenance capabilities

Aircraft maintenance capabilities	
Line maintenance	Base maintenance
LRU replacement, minor inspection, minor troubleshooting, and other minor work	Base maintenance, major inspection, major assembly change, aircraft jacking, and aircraft stripping

shall analyze the impact of quality control and assurance on aircraft maintenance turnaround time.

2 Literature Review

Quick aircraft maintenance turnaround is essential for optimal availability and minimal disruptions. Quality control and assurance are vital in upholding standards and minimizing maintenance errors. This study evaluates their impact on turnaround to boost operational efficiency [4]. Quality control stands as the sentinel of elevated standards, meticulously upholding precision while diminishing errors and amplifying the efficiency of the maintenance process. It serves as the vigilant guardian, detecting and rectifying deviations and latent issues in their nascency, thus mitigating errors during operational checks and aircraft's return to service [5]. The strategic core of quality control resides in the seamless orchestration of procedures, erasure of redundancies, and the finesse of workflow optimization—all converging to expedite task fulfillment and usher in a diminished turnaround time [6]. The aviation industry prioritizes safety; quality control ensures safe operations while ensuring least possible aircraft maintenance turnaround time. Rigorous inspections, adherence to regulatory standards, and safety protocol compliance are integral to quality control and may adversely affect aircraft maintenance turnaround time, and airlines are experiencing it a challenging task as the number of aircraft and its operations increase [7]. High-quality levels minimize safety risks, leading to fewer safety-related issues and smoother maintenance processes [8]. This contributes to a safer operational environment and facilitates quicker turnaround times. Quality control practices also address safety-related issues that may cause delays during maintenance [9]. Safety ratings on maintenance job cards raise awareness among engineers, addressing concerns [10]. In essence, robust quality control practices enhance efficiency, safety, and expedited aircraft maintenance turnaround [8]. Quality assurance certifies educated, trained, and authorized maintenance personnel through a single-window authorization system, which includes unique numbers with validity periods. Additionally, quality assurance performs scheduled and surprise audits to verify conformity with standards and regulations as outlined in the maintenance organization exposition (MOE) [11]. Standardized procedures, guidelines, and protocols

are established by quality assurance for maintenance tasks [12]. This standardization promotes consistent execution, reducing errors caused by inconsistent practices. Streamlining operations, eliminating redundancies, and improving efficiency are achieved by following established processes, leading to shorter turnaround times [13]. Compliance with regulatory requirements is ensured through comprehensive quality assurance frameworks [14]. This minimizes the risk of delays or penalties due to non-compliance, resulting in smoother and more efficient maintenance operations. Continuous improvement is a vital aspect of quality assurance [15]. Airlines are experiencing challenges in monitoring performance metrics, identifying areas for enhancement, and implementing corrective actions, which enable organizations to optimize maintenance turnaround time [16]. This approach enhances efficiency, reduces errors, and facilitates faster turnaround times. The significance of quality control and assurance in aircraft maintenance cannot be overstated, as they assume a pivotal role in curtailing maintenance timelines [17]. These practices assume foundational importance by engendering proactive quality control measures, eliminating redundant and ineffective quality control processes, enhancing quality assurance methodologies, and erecting a rigorous quality assurance framework. Within this framework of comprehensive quality measures, the aviation sector gets empowered to intricately refine maintenance operations intricately, yielding not only cost efficiencies but also the unwavering preservation of heightened standards in safety and service [17].

3 Research Methodology

The paper's research methodology (Fig. 3) involves defining the problem statement, a thorough literature review, designing a survey, and collecting and analyzing data. A nine-question survey evaluates quality control and assurance's role in minimizing downtime of aircraft maintenance.

The survey was distributed to aviation experts, and electronically collected data was analyzed to inform insights and a statistical model. Both qualitative and quantitative techniques are gauged to evaluate quality management's importance. A Google Forms questionnaire, distributed among aircraft maintenance professionals, is presented in Table 2. Five of the nine questions, detailed in Table 2, acted as dependent and independent variables on a linear scale.

Demographic queries, shown in Figs. 4 and 5, ensured respondent authenticity. Data collection and analysis adhered to ethical standards, upholding data integrity.



Fig. 3 Research methodology framework

Table 2 Statistics of questionnaire

#	Statistics of research questionnaire	
	Description	Quantity
1	Number of questions included in the study survey	9
2	Survey distributed to aircraft maintenance industry individuals employed by airlines	5000
3	Number of responses received from participants	4651
4	Response rate from airlines professionals	93.02%

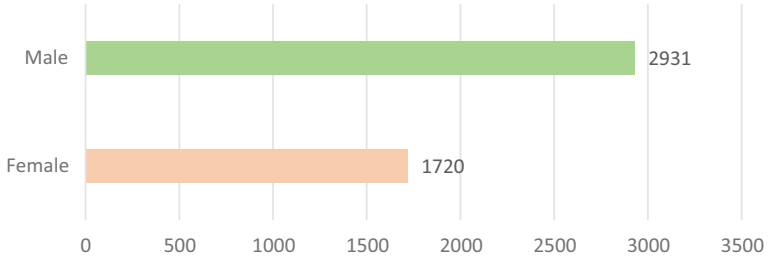
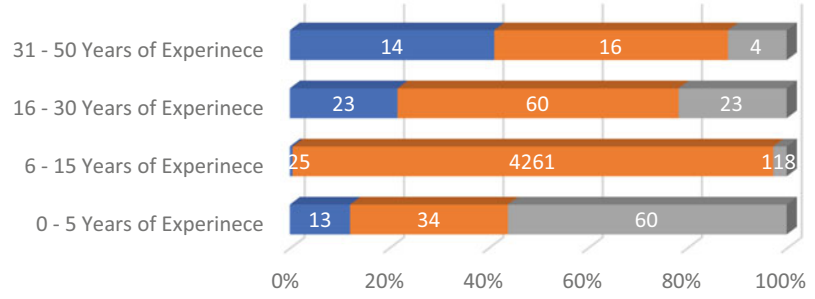


Fig. 4 Gender of respondents



	0 - 5 Years of Experinece	6 - 15 Years of Experinece	16 - 30 Years of Experinece	31 - 50 Years of Experinece
Senior Leadership	13	25	23	14
Management	34	4261	60	16
Worker	60	118	23	4

Fig. 5 Hierarchical level and experience of respondents

Referring to Fig. 5, the majority of respondents possess 6–15 years of work experience and holding managerial roles.

4 Investigation Results

The study comprises five key phases (Fig. 6), initiating with a response review. Subsequently, Microsoft Excel's data analysis feature conducts multiple regression and quantifying outcomes.

Table 3 outlines the independent and dependent variables (IVs and DVs) employed, with one DV and four IVs discerned from the literature review.

Regression facts revealed some remarkable actualities, as shown in Table 4. Adjusted R-square value 0.6249 from the model summary shown that the regression of independent variables describes 62.49% of the change of dependent variable.

A review of the ANOVA summary (Table 5) directs that the regression model is extremely significant with an F value of 1937.5782, $P < 0.01$. It proves that quality control and assurance are crucial in lowering maintenance turnaround time.

Table 6 presents the regression coefficient summary, demonstrating a strong interrelation among all variables. The coefficient for proactive quality control (QC) shows the highest value of 0.513, indicating its significant influence on reducing aircraft maintenance turnaround time.



Fig. 6 Steps followed during data analysis

Table 3 Variables used in questionnaire

#	Details of variables used in the research questionnaire	
	Description of variables	Variables
1	Reduction of turnaround time	Dependent
2	Proactive quality control	Independent
3	Inefficient quality control processes	Independent
4	Quality assurance methodologies	Independent
5	Quality assurance framework	Independent

Table 4 Outcome of regression statistics

#	Regression statistics	
	Description	Value
1	Multiple *R*	0.7907
2	*R*-square	0.6252
3	Adjusted *R*-square	0.6249
4	Standard error	0.2556
5	Observations	4651

Table 5 Outcome of ANOVA summary

#	ANOVA summary					
	Description	df	SS	MS	*F*	Significance *F*
1	Regression	4	506.1788	126.5447	1937.5782	0.0000
2	Residual	4646	303.4338	0.0653		
3	Total	4650	809.6126			

Table 6 Regression coefficient summary

#	Regression coefficient summary						
	Description	Coefficients	Standard error	*t* Stat	*P*-value	Lower 95%	Upper 95%
1	Intercept	0.192	0.054	3.540	0.000	0.086	0.299
2	Proactive quality control	0.513	0.021	24.343	0.000	0.472	0.554
3	Inefficient quality control processes	0.238	0.018	13.281	0.000	0.203	0.273
4	Quality assurance methodologies	0.099	0.022	4.475	0.000	0.055	0.142
5	Quality assurance framework	0.110	0.019	5.748	0.000	0.072	0.147

Data explanation of the coefficient summary helps in developing a model Eq. (1) and shows the significance of QC and QA in aircraft maintenance downtime reduction.

$$y = 0.513x_1 + 0.238x_2 + 0.099x_3 + 0.110x_4 + 0.192 \tag{1}$$

Expressed by Eq. (1), x_1 signifies the influence of proactive quality control in diminishing rework and turnaround duration. Meanwhile, x_2 underscores the importance of addressing inefficient quality control processes for enhancement, while x_3 emphasizes the value of quality assurance methodologies. Furthermore, x_4 underscores the role of quality assurance frameworks in abating aircraft maintenance turnaround time. Data interpretation unequivocally underscores that prioritizing quality control and assurance can markedly truncate aircraft maintenance downtime. However, a collective quality control score is comparatively higher than quality assurance.

5 Discussion and Recommendations

The data analysis yielded unequivocal findings: quality control and assurance are pivotal factors in curtailing turnaround time and augmenting an organization's profitability. Consequently, management and executive leadership are urged to implement the ensuing recommendations to optimize aircraft maintenance turnaround time.

Initiating with Proactive Quality Control Cultivating a proactive ethos among quality control professionals through cultural investment will substantially reduce rework instances and elevate aircraft maintenance turnaround efficiency.

Redesigning the Quality Control Process Deliberate consideration by the leadership team to overhaul the existing quality control process, underpinned by a comprehensive evaluation of its efficacy, promises to foster enhanced effectiveness, and streamlined operations.

Enhancing Quality Assurance Methodologies Organizations catering to aircraft maintenance must proactively enhance their prevailing methodologies. This necessitates a continuous cycle of evaluation to ensure ongoing relevance and efficacy.

Reassessment of the Quality Assurance Framework By thoroughly examining the existing framework, organizations can identify and bridge existing gaps. Furthermore, benchmarking the quality assurance framework against industry standards could usher in substantial improvements and heightened performance.

By diligently adhering to these recommendations, organizations can chart a course toward optimized aircraft maintenance turnaround times, fostering greater operational efficiency and bolstering overall profitability.

6 Conclusion

This research revealed that the quality system could be improved greatly by reexamining proactiveness, a process in practice, methodologies, and frameworks. It will help airlines to reduce the aircraft maintenance turnaround time.

Acknowledgements The research received uninterrupted support from Banasthali Vidyapith University (India). The researchers are grateful for the valuable support provided by respondents who participated in the survey.

Funding Information Not applicable.

References

1. Alomar I, Yatskiv I (2023) Digitalization in aircraft maintenance processes. Aviation 27(2):86–94. https://doi.org/10.3846/aviation.2023.18923
2. Chandola DC et al (2023) An exploratory study on the significance and challenges of aircraft base maintenance engineering in the aviation industry. In: 2023 International conference on computational intelligence and knowledge economy (ICCIKE), May 2023. https://doi.org/10.1109/iccike58312.2023.10131844
3. Chandola DC, Chandola P, Verma S, Jaiswal K (2023) An exploratory study to evaluate significance of maintenance planning in reducing aircraft maintenance turnaround time within airlines industry. In: 2023 International conference on computational intelligence and knowledge economy (ICCIKE), May 2023. https://doi.org/10.1109/iccike58312.2023.10131888
4. Dmitriev S, Burlakov V, Popov O, Popov D (2015) Technological processes and quality control in aircraft engine maintenance. Aviation 19(3):133–137. https://doi.org/10.3846/16487788.2015.1107306
5. Chandola DC (2019) Reducing cost through long term schedule maintenance planning in aircraft maintenance industry. Int Res J Adv Eng Technol 5:4503–4509. http://www.irjaet.com/Volume5-Issue-5,6/paper4.pdf
6. Chandola DC et al (2023) Statistical analysis of production planning impact on aircraft maintenance turnaround time by exploring challenges during work package preparation. Tuijin/Jishu J Propuls Technol 44(2):422–433. https://doi.org/10.52783/tjjpt.v44.i2.202
7. Latorella KA, Prabhu PV (2000) A review of human error in aviation maintenance and Inspection. Int J Ind Ergon 26(2):133–161. https://doi.org/10.1016/S0169-8141(99)00063-3
8. Gerede E (2015) A qualitative study on the exploration of challenges to the implementation of the safety management system in aircraft maintenance organizations in Turkey. J Air Transp Manag 47:230–240. https://doi.org/10.1016/j.jairtraman.2015.06.006
9. Chan WT-K, Li W-C (2022) Investigating professional values among pilots, cabin crew, ground staff, and managers to develop aviation safety management systems. Int J Ind Ergon 92:103370. https://doi.org/10.1016/j.ergon.2022.103370
10. Shanmugam A, Paul Robert T (2015) Ranking of aircraft maintenance organization based on human factor performance. Comput; Ind Eng 88:410–416. https://doi.org/10.1016/j.cie.2015.07.017
11. Bogdane R, Gorbacovs O, Sestakovs V, Arandas I (2019) Development of a model for assessing the level of flight safety in an airline using concept of risk. Procedia Comput Sci 149:365–374. https://doi.org/10.1016/j.procs.2019.01.150
12. Albakkoush S, Pagone E, Salonitis K (2021) An approach to airline MRO operators planning and scheduling during aircraft line maintenance checks using discrete event simulation. Procedia Manuf 54:160–165. https://doi.org/10.1016/j.promfg.2021.07.024
13. Chandola DC et al (2023) Analyzing the statistical impact of supply chain management on aircraft maintenance turnaround time within the MRO industry. Eur Econ Lett 13(3):1959–1969. https://doi.org/10.52783/eel.v13i3.603
14. Kasava NK, Yusof NM, Khademi A, Saman MZ (2015) Sustainable domain value stream mapping (SDVSM) framework application in Aircraft maintenance: a case study. Procedia CIRP 26:418–423. https://doi.org/10.1016/j.procir.2014.07.075
15. Bugaj M, Urminský T, Rostáš J, Pecho P (2019) Aircraft maintenance reserves—New approach to optimization. Transp. Res Proc 43, 31–40. https://doi.org/10.1016/j.trpro.2019.12.016
16. Chandola DC, Jaiswal K, Verma S, Singh B (2022) Aviation MRO: a comprehensive review of factors affecting productivity of Aircraft Maintenance Organization. In: 2022 Advances in science and engineering technology international conferences (ASET), pp 1–7. https://doi.org/10.1109/ASET53988.2022.9734808
17. Abramovici M, Gebus P, Göbel JC, Savarino P (2018) Semantic quality assurance of heterogeneous unstructured repair reports. Procedia CIRP 73:265–270. https://doi.org/10.1016/j.procir.2018.03.334

Recent Developments of Battle Tanks Used in Defence Applications—A Review



Aditya Sadhukhan, G. Srinivas, and G. T. Mahesha

Abstract This review paper focuses on the technological developments taking place in the battle tanks used in defence technology. Battle tank is the primary offensive weapon. A tank must have high firepower to destroy enemy target with self-protection and mobility. To achieve these performances the design of a battle tank plays an important role. Various challenges need to be addressed during the development of battle tanks include protection, armament and firepower design, vibration control, providing necessary crew comfort, ammunition safety, gun barrel, suspension, and track design. Design constraints puts limitations for the realization in their development. These constraints are weight capacity, performance, and transportability. The objective is to review the design process parameters and how these are realized during a battle tank manufacturing.

Keywords Ammunition · ERA (Explosive Reactive Armour) · Firepower · Gun barrel · Gun control system · Main Battle Tank (MBT) · Mobility · NBC protection · Protection · Suspension

Paper Objective In this paper, the primary focus is on proposing and exploring innovative concepts, principles, and methodologies related to the design of a battle tank. The paper deals with the theoretical aspects of the design domain and provides a comprehensive overview of existing literature, established theories, and relevant information about the battle tank design. Furthermore, the paper discusses the theoretical underpinnings of various design decisions, considering factors like user experience, functionality, aesthetics, and sustainability. By analysing and synthesizing theoretical knowledge, the paper contributes valuable insights to the design community and serves as a foundation for further studies and practical applications in the field.

A. Sadhukhan · G. Srinivas · G. T. Mahesha (✉)
Department of Aeronautical and Automobile Engineering, Manipal Institute of Technology, Manipal Academy of Higher Education (MAHE), Manipal, Karnataka 576104, India
e-mail: mahesh.gt@manipal.edu

© The Author(s), under exclusive license to Springer Nature Singapore Pte Ltd. 2024

S. Singh et al. (eds.), *Recent Advances in Aerospace Engineering*, Lecture Notes in Mechanical Engineering, https://doi.org/10.1007/978-981-97-1306-6_47

1 Introduction

1.1 Battle Tanks

A battle tank is a combat vehicle which has high firepower, mobility, and equipped with protective armour. It moves with the caterpillar tread and has a powerful engine. A battle tank, often simply referred to as a tank, is a heavily armoured and tracked military vehicle designed for frontline combat in land warfare. Tanks are powerful machines that play a crucial role in ground-based military operations. They are typically equipped with a large-calibre cannon as their primary weapon, along with secondary machine guns for anti-infantry or anti-aircraft purposes. The main features of a battle tank include:

Armour Tanks have thick steel or composite armour that provides protection for the crew and vital components against small arms fire, shrapnel, and even some anti-tank weaponry.

Armament The primary armament of a tank is usually a large, high-velocity cannon capable of firing armour-piercing rounds to engage and destroy enemy tanks and fortified positions. Some tanks may also have a coaxial machine gun alongside the main cannon for engaging infantry.

Mobility Tanks are equipped with tracks instead of wheels, which allow them to traverse rough terrain and move effectively in difficult conditions, such as mud, snow, or sand.

Crew The typical crew of a tank consists of three members: the driver, who operates the vehicle; the gunner, who aims and fires main weapon; and the commander, who oversees the overall operation and targeting of the tank.

Fire Control System Modern tanks are equipped with advanced fire control systems, including rangefinders, laser target designators, and computerized aiming systems, to improve accuracy and targeting speed.

Engine Tanks are powered by powerful engines, often running on diesel fuel, to provide the necessary speed and manoeuvrability. Tanks have evolved significantly since their introduction in World War I, and they continue to be an essential component of armoured warfare. They have played crucial roles in numerous military conflicts and have adapted to meet the challenges of modern warfare. The constant development of new technologies, such as composite armour, active protection systems, and digital communications, ensures that tanks remain formidable assets on the battlefield.

2 Firepower

2.1 Ammunition

The characteristic design of 120 × 570 mm tank ammunition cartridges particularly focused on operation and safety of the ammunition during handling. Clearance around the cartridge case inside the cartridge chamber may exceed 2 mm along the diameter. In majority of the cases, the length of the cartridge does not touch the cartridge chamber walls. Combustible material (composition of nitrocellulose, cellulose, and other components) is used to make the cartridge case which consisting of a one or two parts bonded together. These are generally wet milled, compressed, impregnated, and varnish coated. The ignition risk is reduced, by sealing the NC cartridge cases from above with a case adapter, which prevents it from the ignition. Case adapter is made of either cellulose or plastic. When the cartridge is fired, it is incombustible [1]. Reduction in procurement cost and improvement of the high explosive anti-tank (HEAT) training round is a major priority. It can be done by improving the launch dynamics of the projectile, projectile position in the forcing cone, sealing abilities of the sealing ring and obturator, and reducing the wear of the tubes. The test was carried out on computer simulation as well as real-time experimental setup on M831A1 HEAT training round which is used in the 120-mm M256 gun system of the M1 tank. As the launch cycle proceeds, the balloting effect results flexing in the steel nose spike during launch. It can produce negative effect on the gun tube shape [2]. The major characteristics for NC or HTPB-based gun propellant are thermochemical characteristics, chemical stability, explosion heat, impact, and friction sensitivities. These properties are determined by various instrument such as differential scanning calorimetry–thermogravimetric analysis, vacuum stability tester, bomb calorimeter (BC), BAM fall hammer, and BAM friction tester, respectively. NC or HTPB-based gun propellant has better stability. It also has lower impact and friction sensitivities than M1 SBP. Experiments are carried out with NC/HTPB-based gun propellant using CL-20, RDX, or TKX-50 [3].

2.2 Turret

MATLAB-based MPC toolbox is used to improve the operating system of a turret to avoid the obstacle which is present on the vehicle platform. It also provides stability and clearance with reference to the hull. The deck clearance for tank turret stabilization can be modelled using MATLAB-based MPC toolbox. MPC controller stabilizes weapons while operating [4]. Turret of a tank is a complex geometry as it experiences various complex loading. For optimization, FEA can be done on turret structure. This experiment is carried out on a 1/5th scale model using SAP IV by strain gauge method. FEM gives stresses and deflections at various location if the turret structure. It can also use to analyse the structure of any fighting vehicle hulls and turrets [5].

2.3 Gun Barrel

By using internal ballistic theory, convective heat transfer coefficient of the gun barrel wall temperature can be measured. Axis symmetric unsteady heat transfer mode (1D) can solve heat transfer in gun barrel [6]. During shooting, the gun barrel subjected to vibration and bending which reduces its accuracy. The vibration can be reduced by reducing the mass at the frontal part. Stiffens is an important property of gun barrel which is improved by using carbon fibre. It also reduces the mass of the barrel. Lifespan of gun barrel can be improved by using "carbon fibre layer" as reinforcement [7]. Peeling of the chromium layer on the surface of the bore leads to bore matrix softening of a gun barrel, and as a result, failure occurs to the gun barrel. This is occurring along the length of the gun barrel. Peeling changes to wearing from the tail of the gun to the muzzle. Damage rate is maximum at the muzzle and gun tail compared to the middle portion of gun barrel. As the temperature increases, the bore matrix becomes soft, and plastic deformation occurs. It causes increase in bore diameter and decrease in gun accuracy. Cr layer completely peels off in the gun tail. Where in the middle part Cr layer peels off in a small amount. So, the damage rate is very small in the middle part of gun barrel. The muzzle also experiences a high damage rate as the Cr layer completely worn off in the line of the muzzle. After shooting, the bore surface becomes soft due to the high pressure and temperature. The hardness is less in the tail part compared to both the middle part of the barrel and muzzle as the gun tail is subjected to very high temperatures [8]. The spin rate of the projectile and muzzle velocity reduces due to the inner wall wear in the gun barrel. It also reduces the accuracy and shooting power. It has been found that the wear of the barrel increases with the angle of attack of the projectile. When the number of shots reaches 4300, then maximum angle of attack reaches, i.e. 0.106 rad. At the end of the barrel life, the projectile muzzle spin rate lowers about 57.5% [9]. Gun barrel subjects to catastrophic fatigue failure due to cyclic loading. It occurs due to high pressure and temperature combustion gas. This may produce crack in inner wall. The fatigue failure of gun barrel avoided by monitoring the external surface strains. The maximum stress has the major influence in the fatigue property. As the pressure increases, the fatigue life decreases. Cracks are mainly induced by the erosion, and then, it propagates in radial direction and reduces both strength and toughness [10]. Gun barrel erosion occurs under various conditions, and propellant gas plays a major role in this. Propellant gas reacts with the gun barrel material, and it produces an inner layer which may melt at a lower temperature than the actual gun barrel material and weaken the mechanical property. The physical properties of Tantalum result in greater erosion than chromium. Additionally, CO dissociation can occur, which can be prevented by treating the surface with nitrogen or nitriding [11]. To understand the temperature distribution within a gun barrel, it is crucial to grasp the heat transfer that occurs during internal ballistics. The thermal behaviour of the system is primarily influenced by thermophysical properties such as the position of the projectile, its velocity, the temperature of the gas inside the barrel, the volume behind the projectile, and the mass fraction during interior ballistics. Maximum wall

temperature is achieved after 3 ms from the fire. Compared to the temperature of the burned gases, the convective heat transfer coefficient inside gun barrel has a greater impact. Convection coefficient has major influence inside barrel [12]. Gun tube erosion can happen in various conditions, but the most severe case is when the melting temperature of the gun steel surpasses that of the tube's inner surface. Tantalum is more susceptible to erosion compared to chromium due to its specific physical properties [13]. Jump firing data and tube curvature data are mainly used to compare tank guns for their accuracy and dynamic behaviour. Tube curvature has the most influence on jump error [14]. "Tube flexure" during dynamic testing of a MBT is carried out with the help of instrumentation. Fire control design is a part of tube dynamics which improves the delivery accuracy. The jump of a projectile can be influenced by the bore when it travels down [15]. Ceramic gun barrels have long life while reducing the weight. But it is difficult to machining the ceramic for rifling the land and groove in the inner surface. It is also difficult to maintain the twist rate of rifling. Gun barrel can be made of ceramic by powder injection moulding. Advance ceramic materials such as silicon aluminium oxynitride, zirconia, and silicon nitride can be used for gun barrel manufacturing. But these are limited for small calibre gun barrel [16]. The gun barrel's muzzle generates a significant amount of smoke, and the level of smoke is measured by a characteristic quantity known as characteristic quantity of muzzle smoke (CQMS), which is defined according to the Beer–Lambert law. CQMS is employed to evaluate the potential hazard level of the smoke generated by the propellant charge. Muzzle smoke is a significant cause of pollution on the battlefield, as it can have an adverse impact on the health of soldiers [17]. Gun barrels are exposed to high temperatures and pressures that can cause ablative damage and stress concentration. The rifling profile of a gun barrel may take on different shapes, such as rectangular, trapezoidal, multiarc, and multilateral-arc. The friction that occurs between the projectile and the gun barrel wall surface can be calculated using the shear-slip friction theory. Multiarc and multilateral-arc rifling result in fewer stresses compared to rectangular and trapezoidal rifling. As a result, gun barrels with multiarc and multilateral-arc rifling profiles are more resistant to impact than those with rectangular and trapezoidal rifling [18]. Performance of a gun barrel depends on the thermal behaviour of the material and also some other parameters such as effect of maximum bore temperature, cook-off temperature, active cooling, and heat transfer phenomenon. With the aid of external jacket water cooling, a 155 mm gun barrel can fire total 56 rounds at a rate of three rounds per minute continuously without reaching cook-off temperature. The gun will cook off after 1132 s, and it reaches the temperature of 388 K with forced water cooling of 1.23 kg/s of flow at external gun barrel surface [19].

2.4 Gun Control System

Turret traverse and gun elevation is an important phenomenon for MBTs. The gun can be coupled to two different types of electric motors, such as DC motor and

an induction motor. In this experiment, the mechanical system has been modelled in MATLAB and Simulink together for the turret traverse and gun elevation. Both DC and AC motor can be used for both the turret and gun elevation. It has been found that, in real-life dynamic application, AC motor has superior performance at higher operating speeds [20]. To improve the electric drive's performance of MBT turret, the polarizing relay has been used. It has designed based on the electronic optimal regulation theory. The major advantage is the volume and price both are less. The turret which uses control system with polarized relay and amplidyne motor which can be replaced by this electrical system [21]. By utilizing an adaptive control scheme with full state feedback, the turret-gun control system can be significantly enhanced, leading to improved stabilization accuracy and elimination of high-gain feedback issues. In addition, the servo performance can also be improved. The active disturbance rejection adaptive control (ADRAC) controller is a motion controller that offers exceptional precision and can be utilized effectively in tank turret-gun systems. This controller can manage both parametric uncertainties and disturbances due to its control scheme with full state feedback [22]. Tank fire control system and autoloader subjects to various difficulties and sudden failures. This can be minimized by implementing a real-time monitoring unit to check the status and store the data of the gun control system and autoloader. By comparing and analysing this test data, the problem can be rectified which will further help for eliminating the sudden failures of gun control system and autoloaders. Test data can be exported and backed for long-term use. It must have high measurement speed and detection accuracy [23].

3 Protection

3.1 Structure

A combat platform comprises a range of essential components, including weapons, guns, fire control systems, power packs, automatic transmission systems, hydro-pneumatic suspensions, crew comfort systems, and more. The utilization of modelling, simulation, and impact analysis tools enhances design process of combat vehicle [24]. Track geometry, suspension system, and the hull are important structures to survive from crash. It has carried out by experimental simulation using LS-DYNA and LS-OPT. Shock impulse is an important parameter for the tracked military vehicle structure [25]. MBTs are made of rolled homogeneous armour (RHA). The interior of the driver cabin and control room is constructed using medium carbon steel, employing a dissimilar metal joining process. Typically, the methods employed for this purpose include manual metal arc welding, gas metal arc welding, or gas tungsten arc welding. However, it is important to note that these techniques can result in certain challenges, such as hydrogen-induced cracking, elevated levels of residual tensile strain, and softening of the heat-affected zone (HAZ). This can be avoided by solid-state friction welding between medium carbon steel and RHA. It does not

have any macro-level defect. The grain size within the heat-affected zone closely resembles that of the base metals. The tensile strength of the dissimilar joints is slightly reduced by 3.6% compared to the medium carbon steel base metal, while maintaining a joint efficiency of 96%. It also has high impact toughness and hardness [26].

3.2 Armour

Discarding sabot (ADS) projectile has high kinetic energy and brittleness which generates high shearing stresses due to impact against steel slab. It causes "plugging" effect due to penetration. The DS projectile possesses the capability to penetrate an armour plate with a thickness of 20 mm [27]. Active protection system (APS) increases the protection capability of MBTs without reducing the mobility. APS reduces excessive weight while electric armour technology and high energy laser weapons provide more interception modes of APSs [28]. Ceramic protection and ERA has efficient armour protection HEAT ammunition. The use of multi-layered armour protection incorporates passive armour modules (PAM). Furthermore, an intelligent dynamic armour module is added as an additional layer to counteract specific kinetic energy projectiles, while bulging armour modules are employed to counter the effects of HEAT ammunition. Additionally, an active protection system is implemented to safeguard against HEAT ammunition, strategically positioned on both the turret top and sides of the hull [29]. Composite armour systems are still developing and improving. Efficiency of kinetic ammunition is comparatively high against the composite armours of a combat vehicle [30].

3.3 ERA

To defeat an ERA protected combat vehicle, TandEM warhead can be used fitted with precursor. It can neutralize the ERA either by detonation or without detonation. Non-initiating precursor (NIP) strongly depends upon the ERA and angle of attack. NIP technique can be used to defeat a specific ERA without detonation. Detonation takes place due to inhomogeneity in the ERA explosive cassette. Inhomogeneity occurs due to hand mixing of RDX and hydroxyl terminated polybutadiene (HTPB) which makes it more sensitive [31]. The sandwich reactive armour may be flat or V-shaped configuration. In flat reactive armour configuration, the penetration depth is observed to decrease by 55–75% when impacted obliquely. However, when utilizing a V-shaped configuration, the penetration depth of the projectile is reduced by 90% compared to the flat configuration. V-shaped angle has little effect on the penetration depth [32]. Explosive reactive armour (ERA) is employed in main battle tanks (MBTs) to counter both kinetic and chemical munitions. The effectiveness of the ERA system is influenced by several factors, including the sand-off distance, detonation

delay, and angle of impact variability. The penetration depth of the plate decreases as the sand-off distance increases. The residual penetration of the projectile is primarily influenced by the delay in detonation. Maximizing the stand-off distance is crucial for effective interaction between the flyer plates and the projectile during impact, necessitating the installation of ERA at this distance [33]. An external steel enclosure is employed to safeguard ERA against accidental activation. An increase in plate thickness leads to a decrease in penetration into the target. Explosively formed projectiles (EFPs) possess enough energy to activate the ERA sandwich once they penetrate the covering plate. Covering plate also alters the shape of the EFP's nose. As inclination angle rises, the target's penetration decreases [34]. ERA consists of front and back plate made of steel with SX2 and Prima sheet 1000 fillings having good impact velocity for detonation [35].

3.4 NERA

Steel plates having sandwiched rubber layer, i.e. laminated steel-elastomer armours are the non-explosive reactive armour (NERA). It has an advantage known as "bulging effect". Upon collision, the side steel plates undergo deformation in opposing directions, leading to the disruption of the kinetic energy of the projectile. To stop kinetic energy (KE) projectile, one can utilize an RHA steel block, although it necessitates a thickness like the length of the projectile. This increased thickness subsequently adds weight to the combat vehicle. Alternatively, employing non-explosive reactive armour (NERA), a sandwiched rubber material deforms internally, causing bulging to occur in the front and back steel plates. As the rubber recoils, it envelops and stabilizes the rod positioned between the side steel plates, which deform in opposing directions. Consequently, the rod initiates bending and ultimately fractures into multiple pieces due to the armour penetration [36]. The major parameters of NERA are "response to hits" and "orientation of the NERA plates" against shaped charge warhead and the composition of the intermediate layer of NERA. NERA is comparatively efficient than to SLERA and NxRA. NERA also has excellent multiple hit capability and good survivability than NxRA. NERA is safer and light than ERA because it consists of non-explosive energetic interlayer. NERA is dependent on panel orientation [37].

3.5 Nuclear–Biological–Chemical (NBC) Protection

To operate in nuclear scenario, MBTs are provided with special radiation protection lining materials inside in sheet form. There are three distinct types known as PE(M)SE, PEC-ISE, and PEC-IISE. These types are characterized by their polymer matrix, specific fillers, and anti-ageing additives. The evaluation of NBCs involves assessing their resistance to neutron and gamma radiation, both primary

and secondary [38]. PEC-ISE is utilized in integrated combat vehicles (ICVs), while PE(M)SE finds its application in the T-90 tanks. Mechanical protection is affected by the chemical, biological, and radiological contamination. Passive, active, and hybrid (passive-reactive) cassettes increase the ballistic protection but reduce the susceptibility against decontamination. Sealing material (elastomer) and protecting cap (steel or aluminium sheets of 1 mm thickness) can reduce contamination of the cassettes. The material must have low absorption or resistant to contamination absorption. The cassettes must be designed in such a way so that it can be easily dismantle for disinfection [39]. The tank crew must be protected with nuclear**–b**iological**–c**hemical (NBC) protective clothing. Protective clothing must have good breathability and comfort. The following test is carried out for NBC protective clothing, i.e. water vapour resistance test, air permeability test, liquid chemical agent challenge, vapour challenge, HD-BTT test, mandrel test, expulsion test, and inverted expulsion test [40].

4 Mobility

4.1 Manoeuvrability

Track is mainly used to distribute the pressure equally on a road which has low load-bearing capacity. Soil property is an important parameter for track design. The mobility is influenced by several factors, including the soil's load-bearing capacity, the track's adhesion to the ground, and the resistance encountered during turns. When the tracked vehicle turns on an irregular surface, wear occurs on the double or single load-bearing wheels. It can be reduced by mounting the wheels on suspension rocker arm [41]. Sinkage is the most important design parameter for the track vehicle. Power and fuel consumption of a tracked vehicle follows cubic power law with sinkage. Ground pressure is also an important parameter where the pressure above 0.9 da-N/cm2 must be avoided. It can be minimized by increasing the track length or track width. "Duckbill extensions" can be done to the outside part of the shoe which was used in "Sherman Tank". Shoes can be made of 300 M high strength nitride steel. Increasing the wheel diameter and width improves the off-road or cross-country performance. The CG should be kept slightly rearward [42].

4.2 Steering

Tracked vehicle performance affected in the loose terrain and sloped terrain. The performance of slope steering depends on slope angle and ground characteristics [43].

Steering stability depends on the minimum steering radius, centroid speed, maximum circumferential velocity of the sprocket, and maximum sideslip angle.

Steering dynamics depends on the track slip with respect to ground, vehicle lateral slip, and the centrifugal force [44].

4.3 Transmission

A high-performance electric transmission with 1300 horsepower "gas-turbine" engine and a 200HP supercharged diesel engine is used. Driving sprockets are mounted on the output shaft. This is run by an electric motor. Dynamic performance is achieved by an IGBT, i.e. insulated gate bipolar transistors and AC motor (inverter controlled). Diesel engine has low fuel consumption. It helps to achieve maximum torque. Increasing the power of the powertrain improves the survivability and tank mobility in the warzone. If traction motor is placed into the frontal part, it will increase the protection from the frontal part [45]. Hybrid electric combat vehicles have good drivability due to optimal operation of internal combustion engine (ICE) and high fuel efficiency. It also comprises with regenerative braking and silent operation capability. Hybrid electric combat vehicles require silicon carbide power electronics and energy efficient batteries. The components must survive in high temperature [46].

4.4 Suspension

Multi-cylinder hydro-pneumatic suspension system is useful for tracked chassis. Performance of a "hydro-pneumatic suspension" varies according to the variation of diameters and damping pipe lengths and initial gas volumes. Increasing the diameter of the damping pipe within a certain range enhances the performance of hydro-pneumatic suspension [47]. Magnetorheological fluid dampers play a crucial role in enhancing the stability and ride comfort of vehicles. By implementing the continuous skyhook control law, the vehicle's stability and ride comfort are further improved. This control law effectively decreases the vertical displacement and vertical velocity amplitudes of the vehicle body's centre of gravity, resulting in a smoother ride. Additionally, it significantly reduces the time required to reach equilibrium and achieves stability without excessive oscillations. In modern MBTs, this suspension system can replace "torsion bars with spiral spring" [48].

4.5 Track

Wear and hysteretic heat loss affect the rubber components of the "M1 Abrams Tanks". Titanium backer pads can be used to reduce the wear. This is manufactured by electron beam melting (EBM) additive manufacturing process with Ti-6Al-4 V powder. Fatigue property of the backer pads is directly depending on the displacement

during compression [49]. Rubber components such as road wheel tyre and track link have high nonlinear dynamic response. Nonlinearities for rubber components are occurred due to elastic and viscoelastic characteristics of material [50].

5 Miscellaneous Design Parameters

5.1 Simulator

MBT gunner's target tracking tasks can be simulated, under the whole-body vibration conditions. The software displays sight points and target. Afterwards, it receives the turret pointing command via the gunner's handle joystick [51]. MBT simulator is used for training and educational purpose. It provides virtual representation of MBT fire controls [52]. MBT gunner station control can be simulated which help for training. Further it can simulate the controller which manages the trajectory of the primary cannon projectiles [53].

5.2 Vibration Control

Tracked vehicle experiences high-frequency (HF) vibration which is proportional to the speed, and it produces polygon and rolling effect between the track and wheel. To reduce the vibration, an elastic track tensioning device with a damper can be used as cushion between the chassis and idler [54]. Detection and monitoring of a tracked military vehicle can be done by information extraction of ground vibration which is generated by the military vehicle. The peaks are clearly identified with the frequencies which are associated with distance between the nearest wheel axes and vehicle speed and track periodicity [55]. Modal tests are performed to identify the mode shape of natural vibration, and frequency occurs in tracked vehicle structure. Hull vibration is experimented by modal hammer testing method [56].

5.3 Crew Comfort

Ride comfort of crew depends on the seat location and seat suspension system [57].

5.4 Fuel Tank

In a battlefield, military vehicle's fuel tank is targeted by the enemy due to which fuel tank is ignited and destroy the vehicle. PTFE/Al/Bi_2O_3 reactive material or aluminium or steel projectile impacts the fuel tank, and these projectile fragmentations have excellent ignition ability. But the ignition of fuel tank depends on velocity of impact. Ignition ability are as follows of three materials, i.e. PAB > AP > SP [58].

5.5 Effects on Soil

MBT produces a long-term negative environmental impact on the land. MBT produces more damage on wet soil [59].

5.6 Acquisition

Acquiring defence equipment requires efficient economic analysis of costs and benefits with acquisition alternative of that weapon. There are three possible options for acquiring assets: development, technology adoption, and purchase. It is crucial to compare the benefits and benefit–cost ratios of these alternatives. The primary goal of defence procurement is to conduct value analysis during project decision-making. The second objective involves analysing the project's value and adjusting the acquisition strategy accordingly. Finally, the defence management team verifies the actual valuation [60].

5.7 Dust

Large amount of dust is raised by the military vehicle in the battlefield. The dust raise phenomena depends on the wind speed, travelling speed, mass flow rate, and wind direction. Mass concentration of dust plumes reduced due to front wind. When wind speed exceeds 4 m/s, the reduction rate decelerates [61].

5.8 Periscope

A periscope is an optical device which helps sighting of objects when there is no direct (LOS) line of sight with the observer. It contains light reflective walls and tube.

Reduction in size of a periscope can be achieved by utilizing a mirror waveguide with an appropriate angle to transmit the image [62].

5.9 Air Filter

Dust trap produces several problems in engine efficiency. Dust is continuously removed by ejection suction. Dust concentration in sandy or desert terrain is of 1 g/m^3.Multi-cyclone air filter is used in MBTs with 1 g/m^3 dust concentration. It retains more than 1500 g of dust. In second separation stage, it uses filter paper [63].

5.10 Future Combat System

The future combat system (FCS) of an MBT consists of primary and secondary armament system. Primary armament system involves with main gun armament, and secondary armament system involves highly energetic and direct-projection laser gun. The main gun may be conventional solid propellant (SP) or electro-thermal chemical (ETC) gun or electromagnetic (EM) automatic cannon [64]. Solid propellant (SP) guns can be altered by liquid propellant (LP) gun propulsion technology or electrothermal-chemical (ETC) guns or electromagnetic (EM) railguns in future combat system MBTs. Liquid propellant (LP) gun propulsion technology can be the alternative to solid propellant (SP) guns. Currently in the experimental phase, electrothermal-chemical (ETC) guns employ a chemically energetic (reactive) working liquid as opposed to solid propellant. On the other hand, electromagnetic (EM) railguns, also referred to as coil guns or pulsed-power EM guns, can launch lightweight projectile measuring 30-60 mm in diameter, achieving hyper velocities ranging from 4000 to 8000 m/sec [65].

6 Research Gap and Analysis

Table 1 refers to the existing research gap and corresponding analysis of the existing battle tank technology. It is an analysis where current research has not adequately addressed on this specific research gap and has left questions unanswered. Here identified research gap has been described and analysed to define the scope and direction of new research endeavours.

Table 1 Research gap and analysis

Research gap	Analysis
Autonomous and unmanned systems integration	Research could focus on how to integrate advanced autonomous and unmanned technologies into battle tanks, allowing for improved reconnaissance, decision-making, and potentially reducing the need for human crew members
Advanced armour and defensive systems	Developing novel armour materials and designs that provide enhanced protection against a wider range of threats, such as advanced kinetic penetrators, chemical energy munitions, and directed energy weapons
Hybrid propulsion and energy efficiency	Investigating ways to improve the energy efficiency of battle tanks through hybrid propulsion systems, energy recovery mechanisms, and advanced power storage solutions to extend operational range and reduce logistical challenges
Crew ergonomics and human–machine interface	Enhancing the ergonomic design of tank interiors and optimizing the human–machine interface to reduce crew fatigue, improve situational awareness, and enable more effective operation in complex and high-stress combat environments
Network-centric warfare integration	Exploring methods to integrate battle tanks into broader network-centric warfare systems, allowing for seamless communication, data sharing, and coordination with other military assets
Countermeasures against weapons	Developing effective countermeasures against precision-guided weapons, such as anti-tank guided missiles, including advanced active protection systems, decoys, and electronic countermeasures
Urban warfare capabilities	Adapting battle tanks for urban warfare scenarios by improving manoeuvrability, situational awareness, and minimizing collateral damage to civilian infrastructure
Environmental adaptability	Researching technologies that allow tanks to operate effectively in diverse environments, from extreme cold to desert heat, and in various terrains, including mud, sand, and rocky landscapes
Sustainability and logistics	Investigating methods to reduce the logistical burden of maintaining and operating tanks, such as through improved maintenance practices, modular designs for easier repair, and more sustainable fuel options

(continued)

Table 1 (continued)

Research gap	Analysis
Decision support	Exploring ways to use artificial intelligence and machine learning to provide real-time analysis of battlefield data, offer decision support to tank crews, and enhance the overall effectiveness of decision-making
Lethality and firepower	Researching advanced weapon systems, ammunition types, and targeting technologies to improve the tank's lethality against a wide range of targets, including both armoured and soft targets

7 Future Scope

7.1 Autonomous and Unmanned Systems

The incorporation of autonomous and unmanned technologies was a growing trend. Future tanks might have the capability to operate with varying degrees of autonomy, reducing the risk to human operators and allowing for more complex manoeuvres.

7.2 Advanced Armament

Future tanks could feature improved main guns, such as electromagnetic railguns or advanced energy-based weapons, offering enhanced range, accuracy, and firepower.

7.3 Active Protection Systems (APS)

APS is designed to detect and intercept incoming threats like missiles and rockets before they can hit the tank. These systems were being developed to provide better protection against anti-tank guided missiles and other modern threats.

7.4 Advanced Armour and Materials

The quest for lighter yet stronger armour materials continued. This could improve tank protection while allowing for greater mobility.

7.5 Sensor Integration

Future tanks might feature advanced sensors, improved night vision, thermal imaging, and other detection technologies to enhance situational awareness and targeting capabilities.

7.6 Hybrid Propulsion Systems

To develop hybrid or electric propulsion systems for tanks, aiming to improve fuel efficiency and reduce the thermal and acoustic signatures of the vehicles.

7.7 Modularity and Upgradability

Designing tanks with modular components would allow for easier upgrades and adaptations to changing battlefield requirements.

7.8 Stealth and Signature Reduction

Reducing a tank's acoustic, thermal, and electromagnetic signatures could make it harder for adversaries to detect and target them.

7.9 Directed Energy Weapons

The integration of directed energy weapons, such as lasers, for defence against drones, missiles, and other threats was a topic of research.

7.10 Human–Machine Teaming

Future tanks might involve a higher level of integration between human operators and AI systems, allowing for more efficient decision-making and operation.

It is important to note that the future of military technology is highly influenced by geopolitical and strategic factors, as well as advances in civilian technology that can be adapted for military use.

8 Conclusions

The conclusion of a battle tank design typically summarizes the key findings and outcomes of the design process. Based on the literature review carried out on "Study of Battle Tank", the following conclusions are drawn-

8.1 Effectiveness

Evaluate how well the tank design fulfils its intended role on the battlefield. Assess its capabilities in terms of firepower, mobility, protection, and situational awareness.

8.2 Technological Advancements

Highlight any innovative or cutting-edge technologies incorporated into the tank design that provide an edge over existing or potential adversaries.

8.3 Operational Versatility

Discuss the tank's adaptability to different terrains and operational environments. A versatile tank should be able to perform effectively in various scenarios.

8.4 Crew Safety and Comfort

Consider the protection and well-being of the tank crew. A comfortable and safe working environment can enhance the crew's performance and mission success.

8.5 Logistical Considerations

Analyse the ease of maintenance, repair, and overall logistics support required to keep the tank operational. A tank that is easier to maintain can reduce downtime and increase overall fleet readiness.

8.6 Cost-effectiveness

Assess the cost implications of the tank design, including both procurement and lifecycle costs. A cost-effective design should balance performance with affordability.

8.7 Comparison with Competing Designs

If applicable, comparison of the tank design is required with similar or competing vehicles from other manufacturers or nations, highlighting its strengths and advantages.

8.8 Recommendations for Future Improvements

Identify potential areas for further development. This could include suggestions for upgrades, technology integration, or improvements based on threats and requirements.

8.9 Overall Viability

Conclude with an assessment of whether the tank design is a viable option for procurement or further development and deployment within the armed forces.

References

1. Furmanek W, Kijewski J (2021) Constructional aspects for safe operation of 120 × 570 mm ammunition. Probl Mechatro Armament, Aviation Saf Eng 12, 4(46). ISSN 2081-5891
2. Newill JF, Gamer J, Soencksen K, Hoppel CPR. Launch dynamics of the 120-MM M83 1A1 heat training projectile. 10th U.S. Army gun dynamics symposium proceedings, ADA404787
3. Lin Y-H, Yang T-M, Li J-S, Kai-Tai L, Yeh T-F (2022) Preliminary study on characteristics of NC or HTPB-based high-energy gun propellants. Chem Eng 6:80
4. Kumar G, Tiwari PY, Marcopoli V, Kothare MV. A study of a gun-turret assembly in an armored tank using model predictive control. In: 2009 American control conference Hyatt regency riverfront
5. Narasimhan G, Sivaprasad N (1989) FEM analysis of gun tank turret. Def Sci J 39(3):257–268
6. Akçay M, Adil Yükselen M (2014) Unsteady thermal studies of gun barrels during the interior ballistic cycle with non-homogenous gun barrel material thermal characteristics. Isı Bilimi ve Tekniği Dergisi 34(2):75–81. J Thermal Sci Technol. ©2014 TIBTD Printed in Turkey ISSN 1300-3615

7. Pyka D, Bocian M, Jamroziak K, Kosobudzki M, Kulisiewicz M (2019) Concept of a gun barrel based on the layer composite reinforced with continuous filament. In: AIP conference proceedings 2078
8. Wang Z-M, Chun-dong H, Wang Y-X, Heng-chang L, Li J-S, Dong H (2021) Failure mechanism of gun barrel caused by peeling of Cr layer and softening of bore matrix. Metals 11:348
9. Li X, Mu L, Zang Y, Qin Q (2020) Study on performance degradation and failure analysis of machine gun barrel. Defence Technol 16:362e373
10. Zheng J, Li HJ, Wu B (2021) Fatigue failure and launch safety assessment of gun barrel. In: ICAMMT 2021 journal of physics: conference series, vol 1885, p 042027
11. Conroy PJ, Nuscal MJ, Chabalowskil C, Anderson W. Gun tube surface kinetics and implications. In: Defense Technical Information Center Compilation Part Notice ADP012467
12. Susantez C, Caldeira AB (2022) Heat transfer modelling and simulation of a 120 mm smooth-bore gun barrel during interior ballistics. Defence Sci J 72(1):30–39. https://doi.org/10.14429/dsj.72.16542. © 2022, DESIDOC
13. Conroy PJ, Nusca MJ, Chabalowski C, Anderson WR (2001) Initial studies of gun tube erosion macroscopic surface kinetics. Army Research Laboratory, Article July 2001
14. Gur Y, Azulay I, Touati D, Arad M (2007) Jump error and gun dynamics- a comparison between two types of 120 mm smooth bore tank guns, In: 23rd International symposium on ballistics Tarragona, Spain, 16–20 Apr 2007
15. McCall PL (2001) Measurements of gun tube motion and muzzle pointing error of main battle tanks. Shock Vibr 8:157–166 ISSN 1070-9622 (IOS Press)
16. Bose A, Dowding RJ. Swab JJ. Processing of ceramic rifled gun barrel. In: Materials and manufacturing processes. ISSN 1042-6914 print/1532-2475. https://doi.org/10.1080/10426910600609395
17. Yan C, Zhu C-G, Zhang M, Li Y (2023) Quantitative assessment method of muzzle smoke in a field environment. Am Chem Soc ACS Omega 8:7950–7955
18. Wei Z, Cheng Y, Wang Z, Lin Y. Simulation study on the impact response of barrels with different rifling profiles during bullet engraving. In: Hindawi modelling and simulation in engineering volume
19. Dubey A, Sharma PK (2022) Thermal study of 155 mm gun barrel—A review. Def Sci J 72(2):172–181. https://doi.org/10.14429/dsj.72.16625,2022,DESIDOC
20. Carlstedt A (2021) Modelling of electromechanical motors for turret and barrel control in MBT's. Degree project in vehicle engineering, second cycle, 30 credits Stockholm, Sweden
21. Kemao Z, Xiaojun M (1995) Method for improving the performance of electric drive of the tank turret. Defence Sci J 45(2):141–146. @ 1995, DESIDOC
22. Yuan S, Yao J, Deng W, Yang G, Ma X (2020) Active disturbance rejection adaptive control of tank turret-gun control systems. In: Proceedings of the 39th Chinese control conference 27–29 July 2020
23. Liu H-T, Song C, Cao Y, Zhang W-J, Wang D-J, Wu H-W (2021) A design of test equipment on gun control systems and autoloaders. AMTEI-2021 J Phys. https://doi.org/10.1088/1742-6596/2187/1/012018
24. Radhakrishnan R, Roopchand J, Hanumanna D (2003) Armoured vehicle structural design through modeling, impact analysis and virtual reality. In: SAE technical paper, 2003-28-0018, 22 Aug 2003
25. Balaban B (2019) Determination of impact loads for a tracked military vehicle during a crash scenario. In: 12th European LS-DYNA conference 2019, Koblenz, Germany
26. Karthick K, Malarvizhi S, Balasubramanian V (2021) Mechanical properties and microstructural characteristics of rotary friction welded dissimilar joints of rolled homogeneous armor steel and medium carbon steel. J Mech Behav Mater 30:171–178
27. Magier M, Zochowski P, Burian W. "Ur" type anti-tank rifle—A numerical analysis of armour penetration of a World War II tank. In: Problems of mechatronics armament aviation safety engineering. https://doi.org/10.5604/01.3001.0013.6487
28. Yang L, Xu J (2021) Analysis on the development of active protection system for tanks and armored vehicles. In: ISMTA 2020, journal of physics: conference series, vol 1855. IOP Publishing, p 012034. https://doi.org/10.1088/1742-6596/1855/1/012034

29. Madhu V, Balakrishna Bhat T (2011) Armour protection and affordable protection for futuristic combat vehicles. Defence Sci J 61(4):394–402 (DESIDOC)
30. Magier M (2019) Competition between tank armour systems and kinetic ammunition. Problemy Techniki Uzbrojenia. https://doi.org/10.5604/01.3001.0012.8313.
31. Naeem K, Hussain A, Malik AQ, Abbas S, Ahmad I, Farrukh S. A comparative numerical and experimental study of light weight materials for neutralizing explosive reactive armour. Central Eur J Energ Mater. ISSN 1733-7178; e-ISSN 2353-1843
32. Li X-D, Yang Y-S, Lv S-T (2014) A numerical study on the disturbance of explosive reactive armors to jet penetration. Defence Technol 10:66–75 (ScienceDirect)
33. Yeap S, Baxevanakis KP, Roy A (2022) A study on the effectiveness of explosive reactive armour against the penetration of long-rod projectiles. J Mech Eng Sci (SAGE Publications)
34. Rasheed MF, Wu C, Raza A (2019) Effect of explosive reactive armour cover plate on interaction of ERA and explosively formed projectile. In: Hindawi shock and vibration, vol 2019, Article ID 6093621, 10 p
35. Haskins PJ, Cook MD, Curtis JP, Stubberfield J, Cheese P, Lee PR. Experimental and modelling studies on explosive reactive armour initiation mechanisms. In: 23rd International symposium on ballistics Tarragona, Spain, 16–20
36. Fras T. Experimental and numerical study on a non-explosive reactive armour with the rubber interlayer applied against kinetic-energy penetrators—The 'Bulging Effect' Analysis". https://doi.org/10.3390/ma14123334
37. Kasanya B, Hussain S, Lect. Tanabi H, Lect. Ghaziani M, Lect. Latifi-Navid M. Non-explosive reactive armor (NERA). Department of Mechanical Engineering, University of Turkish Aeronautical Association
38. Pal RS, Gautam OP, Mohit K, Tripathi DN, Singh RK (2008) Development of radiation shielding materials and NBC pads for infantry combat vehicle and tank. In: International nuclear information system, radiation protection and dosimetry (S61) IARPNC-2008: 28. IARP national conference on management of nuclear and radiological emergencies, Jodhpur, India
39. Wisniewski A, Pirszel J (2021) Protection of armoured vehicles against chemical, biological and radiological contamination. Science Direct Defence Technol 17:384–392
40. Dhyani H, Bharati S, Thakare VB, Singh VV, Meher D, Boopathi M (2022) Technology trends and future opportunities in development of NBC protective clothing. Defence Life Sci J 7(2)
41. Kończak J (2020) Maneuverability of tracked vehicle at the border of traction between tracks and ground. In: Research Gate, Jan 2020. Springe, AISC 1032. https://doi.org/10.1007/978-3-030-27687-4_24
42. Piancastelli L, Cassani S, Calzini F, Pezzuti E. Mobility improvement of heavy tracked vehicles—The 'PAN' tank experience. ARPN J Eng Appl Sci
43. Zhang Y, Qiu M, Liu X, Li J, Song H, Zhai Y, Hu H. Research on characteristics of tracked vehicle steering on slope. In: Hindawi mathematical problems in engineering, vol 2021, Article ID 3592902
44. Jia W, Liu X, Zhang C, Qiu M, Zhang Y, Quan Q, Sun H (2022) Research on steering stability of high-speed tracked vehicles. In: Hindawi mathematical problems in engineering, vol 2022, Article ID
45. Ilie CO, Barothi L, Marinescu M, Giurgiu IT (2022) Aspects of electric transmission implementation on a battle tank. AITS 2021, IOP conference series: materials science and engineering, vol 1220, p 012017. https://doi.org/10.1088/1757-899X/1220/1/012017 (IOP Publishing)
46. Sivakumar P, Reginald R, Venkatesan G, Viswanath H, Selvathai T (2017) Configuration study of hybrid electric power pack for tracked combat vehicles. Defence Sci J 67(4). https://doi.org/10.14429/dsj.67.11454
47. Qin B, Zeng R, Li X, Yang J (2021) Design and performance analysis of the hydropneumatic suspension system for a novel road-rail vehicle. MDPI Appl Sci 11:2221
48. Zając K, Kowal J Konieczny J (2022) Skyhook control law extension for suspension with nonlinear spring characteristics. Energies. https://doi.org/10.3390/en15030754
49. Franklin SJ. Design of meta-material tank track system with experimental testing and sensitivity analysis of additively manufactured meta-material backer. A thesis presented to the Graduate

School of Clemson University, requirements for the Degree Master of Science Mechanical Engineering
50. Allen P. Models for the dynamic simulation of tank track components. Ph.D. thesis, Academic year 2005–2006. Engineering Systems Department, Cranfield University
51. Campos LCA, Menegaldo LL (2018) A battle tank simulator for eye and hand coordination tasks under horizontal whole-body vibration. J Low Frequency Noise Vibr Active Control 37(1):144–155. The Author(s) (SAGE)
52. Ginchev D, Stavrev S. A low-cost battle tank simulator using unreal engine 4 and open-hardware microcontrollers. In: Proceedings of XXIX international scientific conference electronics—ET2020, Sozopol, Bulgaria
53. Stavrev S, Ginchev D (2020) Towards a cost-efficient gunner controller for a modular battle tank simulator. In: Gate—Conference paper, Oct 2020. https://doi.org/10.1109/ICAI50593.2020.9311298
54. Wang P, Rui X, Liu F, Wang G, Yu H, He B, Gu J. Generation mechanism and control of high frequency vibration for tracked vehicles. Int J Mech Syst Dyn 7
55. Krylov VV (2011) Ground vibrations from tracked vehicles theory and applications. In: Proceedings of the 8th international conference on structural dynamics. In: De Roeck G, Degrande G, Lombaert G, Muller G (eds) EURODYN 2011 Leuven, Belgium, 4–6 July 2011
56. Hryciów Z, Malachowski J, Rybak P, Wisniewski A (2021) Research of vibrations of an armoured personal carrier hull with FE implementation. MDPI—Materials, Nov 2021. https://doi.org/10.3390/ma14226807
57. Ramamurthy NV, Vinayagam BK, Roopchand J (2018) Comfort level refinement of military tracked vehicles crew through optimal control study. Def Sci J 68(3):265–272. https://doi.org/10.14429/dsj.68.12002,2018,DESIDOC
58. Wang R, Yin Q, Yao M, Huang J, Li R, Gao Z, Wu S, Li Y, Wu J. Experimental investigation on ignition effects of fuel tank impacted by Bi_2O_3-reinforced PTFEAl reactive material projectile. MDPI-Metals
59. Althoff PS, Thien SJ (2005) Impact of M1A1 main battle tank disturbance on soil quality, invertebrates, and vegetation characteristics. Science Direct J Terramech 42:159–176
60. Kim S, Giachetti R, Park S (2018) Real options analysis for acquisition of new technology—A case study of Korea K2 Tank's powerpack. MDPI Sustain 10:3866. https://doi.org/10.3390/su10113866
61. Yang S, Chen H, Gao L, Qi B, Guo P, Deng J (2017) Study of spatial distribution characteristics for dust raised by vehicles in battlefield environments using CFD. IEEE Access XX
62. Haltovsky A, Shemar A, Schwarz A, Gur E (2021) The refractive periscope—A novel concept. In: 4th International conference on renewable energy and environment engineering IOP conference series: earth and environmental science, vol 897. IOP Publishing, p 012019. https://doi.org/10.1088/1755-1315/897/1/012019
63. Dziubak T (2021) Theoretical and experimental studies of uneven dust suction from a multicyclone settling tank in a two-stage air filter. MDPI Energies 14:8396
64. Sharoni AH, Bacon LD (1997) The future combat system (FCS)—Technology evolution review and feasibility assessment-1. In: ARMOR—July-August 1997
65. Sharoni AH, Bacon LD (1997) The future combat system (FCS)—Technology evolution review and feasibility assessment-2. In: ARMOR—September-October 1997

An Observer-Based Solution for Structural Health Monitoring of Mechanical Systems Subjected to Unknown Inputs



H. Jeevan Rao, Shrishail B. Sollapur, C. Devaraj Varma, Dheeraj K. Gara, S. Singh, and Sumit Sharma

Abstract The mechanical structure forms a crucial element of any engineered system as it determines the operational life of the system. For instance, the service life of an aircraft is decided by the properties of the airframe and the wings, and continuous loads acting on these structures can cause deterioration in their structural integrity. It thus becomes crucial to monitor the "health" of the structure to ensure that phenomena such as cracks can be quickly detected, and suitable corrective actions can be taken. This process is termed structural health monitoring (SHM), and it has received significant attention by industry. The SHM system involves the observation of a system over time using periodically sampled dynamic response measurements from an array of sensors and analyzing these measurements to determine the current health of the system. Traditionally, SHM has been conducted using techniques which require the system to be idle. In addition, the SHM of larger structures will require a proportionally large number of sensors to be used at certain locations in the structure. Thus, there is a need for an in-situ SHM solution which uses fewer sensors. The in-situ constraint thus requires that the structure health be monitored even in the presence of unknown inputs. To solve these problems, in this work, an unknown input observer (UIO)-based SHM solution is provided. This approach uses results from control theory and is demonstrated for a cantilever beam structure approximated as a set of two coupled spring-mass systems. It is assumed that the displacement and velocity of only one of these masses, on which the unknown input acts, are measured, and the states of the other mass are estimated based on these measurements. The advantages and limitations of the UIO-based in-situ solution are highlighted.

H. J. Rao (✉) · S. Singh
Amity Institute of Aerospace Engineering, Amity University Uttar Pradesh, Noida, India
e-mail: hjrao@amity.edu

S. B. Sollapur · D. K. Gara
Internatinal Institute of Aerospace Engineering, Jain University, Bangalore, India

C. D. Varma
School of Computer Science and Engineering, Jain (Deemed-to-be University), Bangalore, India

S. Sharma
Department of Mechanical Engineering, Amity University Uttar Pradesh, Noida, Noida, India

© The Author(s), under exclusive license to Springer Nature Singapore Pte Ltd. 2024

S. Singh et al. (eds.), *Recent Advances in Aerospace Engineering*, Lecture Notes in Mechanical Engineering, https://doi.org/10.1007/978-981-97-1306-6_48

Keywords Structural health monitoring (SHM) · Cantilever beam · Aircraft · Sensors · Measurement devices

1 Introduction

The usability of any engineered system is dependent on the properties of the structure which is used to construct it. For instance, the service life of an aircraft is decided by the properties of the airframe and the wings such as its ability to withstand sustained designed loads. In an aircraft, its important structure is its wing. Drastic and unexpected loads acting on the wings can cause deterioration in its structural integrity. Thus, if the wing's "health" is not monitored, then it may fail resulting in a catastrophe. It thus becomes crucial to monitor the health of the structure of such mechanical systems to ensure that phenomena such as cracks can be quickly detected, and suitable corrective actions can be taken. Such damage causes changes to the material and/or geometric properties of a structure, which adversely affect the system's performance. This process is termed structural health monitoring (SHM), and it has received significant attention by industry. Thus, the SHM system involves the observation of a system over time using periodically sampled dynamic response measurements from an array of sensors, the extraction of damage-sensitive features from these measurements, and the statistical analysis of these features to determine the current state of system health. Traditionally, SHM has been conducted using visual techniques, but these procedures require the system to be idle. To reduce such idle times, newer technologies were sought. Research in these domains led to SHM solutions termed as impedance-based, non-destructive evaluation using vibration signatures, limit strain measurement, data fusion method, inverse method, etc. In general, industrial SHM solutions consist of the following subsystems.

1. Portable test rig capable of long-term monitoring.
2. Sensors and measurement devices.
3. Wired/wireless data acquisition systems.
4. Rugged embedded software for continuous monitoring software.
5. Advanced analysis and signal processing tools.

It becomes evident from this list of equipment, which could be expensive and sensitive, that the SHM process could potentially become uneconomical. As a result, monitoring is done only at discrete intervals, whose duration may become dependent on system availability or the designer's judgment. In addition, the SHM of larger structures will require a proportionally large number of sensors to be used at certain locations in the structure. Although such a system is commonly used, there may be instances when a defect, such as a crack, can occur at a location where a sensor may not be present. The primary motivations of this work are to develop an in-situ SHM system which can be easily integrated with the structure and more importantly, which minimizes the number of sensors used. The need for an in-situ system is to allow for the continuous monitoring of the structure and as is evident, the use of fewer sensors

leads to an economical solution. To solve both these problems, in this work, a model-based SHM solution is provided and demonstrated for a cantilever beam structure, where the displacement and velocity of any point on the beam can be estimated with only corresponding measurements at a single location. The in-situ solution allows for SHM to be carried out even when the structure is subject to unknown inputs. Providing this feature in an SHM system forms the main contribution of this work. As an observer-based SHM solution is the focus of this work, existing results in literature are briefly described and differentiated from the results presented in this work. A survey of other techniques used in SHM can be found in [1]. The use of observers for state estimation has been prevalent for many decades. In the context of linear time-invariant (LTI) systems, which is also the class of systems considered in this work, initial results were presented in [2]. These results were then extended to the case when the LTI system is subjected to unknown inputs, which led to the term unknown input observer (UIO). A survey of developments in UIO, as well as a formal definition of the observer, can be found in [3], and some recent advances have been presented in [4]. UIOs have been extensively used in industrial applications such as rolling mill monitoring [5] and fault diagnosis [6].

The present work involves the use of UIOs for the estimation of the states of a mechanical system with more than 1-DOF subjected to unknown inputs with the measurement of only a few of the states. The UIO design is based on the results presented in [7]. In addition, limitations of the use of this approach for mechanical systems are also highlighted. A lumped parameter approximation of the continuous E-B cantilever beam is used as an illustration. The E-B beam is approximated using a 2-DOF spring mass system, and the UIO is designed to estimate the states of the second mass when only states of the first mass are measured. The unknown input is assumed to be acting on the first mass. The necessary conditions for the estimation of the states of the second mass are highlighted. These results are directly applicable as a viable SHM system as only a few sensors are required to estimate the remaining states of a larger mechanical structure, and it can also be implemented in-situ.

2 Problem Formulation

An aircraft wing, which forms the main background subject of this work, can be modeled as a Euler–Bernoulli (E-B) cantilever beam, as shown in Fig. 1. To deriving an SHM solution for this mechanical structure, the beam is assumed to be long, slender, and uniform. The transverse displacements of such a beam can be derived by applying Newton's laws to an infinitesimally small element of the beam.

From the free-body diagram of an element of the beam, as shown in Fig. 2, performing a force balance in the z-direction leads to

$$V - (V + \mathrm{d}V) + f(x,t)\mathrm{d}x = \rho A \mathrm{d}x \frac{\partial^2 w(x,t)}{\partial t^2} \tag{1}$$

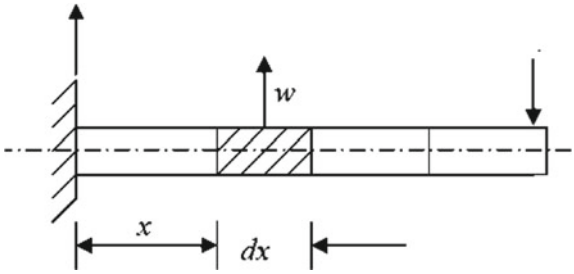


Fig. 1 Element of the E-B beam

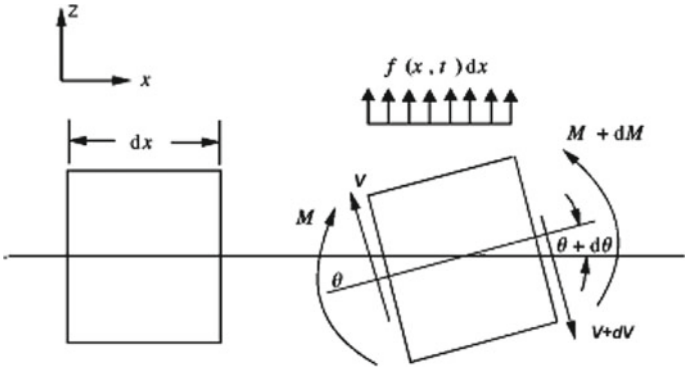


Fig. 2 Forces and moments acting on an element of the E-B beam

where $\rho A\ \mathrm{d}x$ is the mass of the element, $V(x,t)$ is the shear force, and $f(x,t)$ is the unknown external force per unit length of the beam. From the basics of E-B beam theory, the shear force acting on face of the element is related to the material stiffness by the relation.

$$V(x,t) = \frac{\partial M(x,t)}{\partial x} = EI\frac{\partial^2 w(x,t)}{\partial x^2} \tag{2}$$

where $M(x,t)$ is the internal bending moment, E is the young's modulus, and I is the second moment of inertia. Thus, from Eq. (1), the shear forces are related to the material stiffness given by Eq. (2). Using this relation, the interaction between a pair of elements of the E-B beam can be approximated by a pair of spring-mass stems, as shown in Fig. 3, where m is the mass of each element, and k is the stiffness of the spring. As the beam is assumed to be uniform, the parameters m and k are assumed to be the same.

To illustrate the issues for the implementation of a UIO for the E-B beam, the number of elements is restricted to two, and the unknown force is assumed to act only on the free end of the beam. Denoting the displacement and the time derivative of the free end of the beam as x_1, $\dot{x}_1$, respectively, and that of the second element by x_2, $\dot{x}_2$, respectively, the dynamic equations for this system are given by

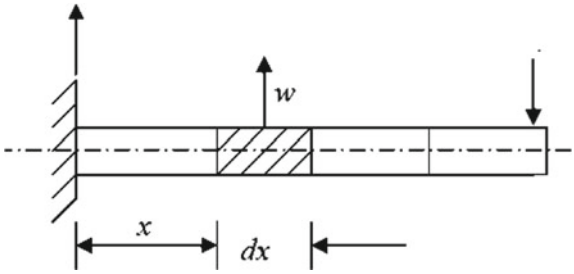


Fig. 3 Discretizing the E-B beam

$$\begin{aligned} m\ddot{x}_1 + kx_1 - kx_2 &= F \\ m_2\ddot{x}_2 + (2k)x_2 - kx_1 &= 0 \end{aligned} \tag{3}$$

Having introduced the mechanical system under study, the problem is formulated as follows: Estimate the states $x_2,\ \dot{x}_2$, when the unknown force F is acting on element 1 and the states of element 1 are measured. This problem can be justified in the context of SHM as having to estimate the transverse displacement of any element of the E-B beam when the beam is subjected to unknown inputs and measurements of the states of only a few elements of the beam are available. The UIO design is presented for this system in the following cases:

- When only the displacement x_1 is measured.
- When only the derivative $\dot{x}_1$ is measured.
- When both $x_1, \dot{x}_1$ are measured.

3 Methodology

3.1 System Parameters

The system dynamics presented in Eq. (3) is rewritten in a form amenable for the design of the UIO. Following [6], these equations are expressed as

$$\begin{aligned} \dot{x} &= Ax + DF \\ y &= \mathrm{C}x \end{aligned} \tag{4}$$

where $x = \begin{bmatrix} x_{P1} & x_{V1} & x_{P2} & x_{V2} \end{bmatrix}^T$, $x_{P1,2}$ are the displacements of the two elements, $x_{V1,2}$ are their velocities, y consists of all the measured states, and the matrices are given by

$$A = \begin{bmatrix} 0 & 1 & 0 & 0 \\ \frac{-k}{m} & 0 & \frac{k}{m} & 0 \\ 0 & 0 & 0 & 1 \\ \frac{k}{m} & 0 & 2\frac{-k}{m} & 0 \end{bmatrix}, D = \begin{bmatrix} 0 \\ \frac{1}{m} \\ 0 \\ 0 \end{bmatrix} \tag{5}$$

The matrix denoted by C is expressed in the form.

$$C = \begin{bmatrix} c_1 & 0 & 0 & 0 \\ 0 & c_2 & 0 & 0 \end{bmatrix} \tag{6}$$

where the coefficients $c_{1,2}$ are used to denote which states are measured. As mentioned earlier, three cases of outputs are considered:

- Case 1: $c_1 = 1, c_2 = 0$ implies that only the displacement of element 1 is measured.
- Case 2: $c_1 = 0, c_2 = 1$ implies that only the velocity of element 1 is measured.
- Case 3: $c_{1,2} = 1$ implies that both displacement and velocity of element 1 are measured.

The UIO is now designed for this system.

3.2 UIO Design

From [6], the UIO is selected in the form.

$$\begin{aligned} \dot{z} &= Nz + Ly \\ \hat{x} &= z - Ey \end{aligned} \tag{7}$$

where the matrices N, L, E are designed to make the state estimate error, defined by

$$e = z - x - Ey \tag{8}$$

tend to zero asymptotically. This can be achieved by evaluating the error dynamics.

$$\dot{e} = Ne + (NP + LC - PA)x - PDF \tag{9}$$

from which, by selecting the UIO matrices N, L, E such that.

$$(NP + LC - PA) = 0, PD = 0 \tag{10}$$

then, the error dynamics Eq. (9) reduces to $\dot{e} = Ne$. Now, the matrix N can be selected to be Hurwitz in such a way that its eigenvalues can also be chosen to achieve the

desired rates of convergence. Now, the matrices N, L, E, and P are calculated such that 10 holds. First, to determine E, the matrix P is selected in the form $P = I_n + EC$, where I_n is the $n \times n$ identity matrix. Now, since $(I_n + EC)D = 0$, the matrix E is given in the general form as

$$E = -D(CD)^{+} + Y(I_p - (CD)\big(CD)^{+}\big) \tag{11}$$

where Y is an arbitrary matrix of appropriate dimension, I_p is the $p \times p$ identity matrix, and $(CD)^{+} = (\big(CD)^T(CD)\big)^{-1}(CD)^T$ is the pseudo-inverse of the matrix CD. With this choice of the matrix P, the matrix N is given by

$$N = PA - (L + NE)C \tag{12}$$

By defining $K = L + NE$, which leads to

$$N = PA - KC \tag{13}$$

the matrix K can be selected to make N in Eq. (13) as a Hurwitz matrix using conventional approaches such as pole-placement. The matrix K can be selected in the form.

$$K = \begin{bmatrix} k_1 & k_2 \\ k_3 & k_4 \\ k_5 & k_6 \\ k_7 & k_8 \end{bmatrix} \tag{14}$$

Prior to selecting the matrices K and Y, it should be examined whether the system matrices, defined in Eqs. (5) and (6), satisfy the necessary UIO design conditions. As shown in [6], these conditions are as follows.

1. $\text{rank}(CD) = \text{rank}(D) = m$, where m is the number of unknown inputs, and n is the system order. In this case, $m = 1, n = 4$. Now, from Eqs. (5) and (6), the product $CD = \begin{bmatrix} 0 & \frac{c_2}{m} \end{bmatrix}^T$, and hence, the UIO can be implemented for this mechanical system only if $c_2 \neq 0$. Thus, Case 1 as described before need not be considered.
2. $\text{rank}(P) = n - m$. To show that this condition holds, first the matrix Y is selected as

$$Y = \begin{bmatrix} y_1 & y_2 \\ y_3 & y_4 \\ y_5 & y_6 \\ y_7 & y_8 \end{bmatrix} \tag{15}$$

It will be shown that the constants y_i, $i = 1 \ldots 8$ can be chosen such that the closed-loop error dynamics has desirable properties. Now, from the system

parameters, the matrix $(CD)^+ = \begin{bmatrix} 0 & 0 \\ 0 & 1 \end{bmatrix}$. This leads to

$$E = \begin{bmatrix} y_1 & 0 \\ y_3 & -\frac{1}{c_2} \\ y_5 & 0 \\ y_7 & 0 \end{bmatrix} \Rightarrow EC = \begin{bmatrix} y_1c_1 & 0 & 0 & 0 \\ y_3c_1 & -1 & 0 & 0 \\ y_5c_1 & 0 & 0 & 0 \\ y_7c_1 & 0 & 0 & 0 \end{bmatrix} \tag{16}$$

which results in

$$P = \begin{bmatrix} 1 + y_1c_1 & 0 & 0 & 0 \\ y_3c_1 & 0 & 0 & 0 \\ y_5c_1 & 0 & 1 & 0 \\ y_7c_1 & 0 & 0 & 1 \end{bmatrix} \tag{17}$$

Thus, the constant c_1 can be chosen to yield $rank(P) = 3$. It should be highlighted that the matrix P will always satisfy $\text{rank}(P) = 3$ for any $c_2 \neq 0$. This implies that, for the given system dynamics, to design the UIO, it is necessary to measure both the position as well as its time-derivative. Now that the necessary conditions have been identified, and attention is placed on the nature of the matrix N, which decides the dynamics of the error estimates. This matrix has the form

$$N = \begin{bmatrix} -k_1c_1 & (1 + y_1c_1 - k_2c_2) & 0 & 0 \\ -k_3c_1 & (y_3c_1 - k_4c_2) & 0 & 0 \\ -k_5c_1 & (y_5c_1 - k_6c_2) & 1 & 0 \\ -(\alpha - k_7c_1) & (y_7c_1 - k_8c_2) & -2\alpha & 1 \end{bmatrix}, \ \alpha = \frac{k}{m}$$

The eigenvalues of N are computed by solving $|\lambda I - N| = 0$. It can be shown that these eigenvalues are the roots of the quartic polynomial.

$$\left(\lambda^2 + 2\frac{k}{m}\right)\begin{pmatrix} \lambda^2 + (k_1 + k_4 - y_3)\lambda \\ +(k_1(k_4 - y_3) + k_3(1 + y_1 - k_2)) \end{pmatrix} = 0 \tag{18}$$

By solving this equation, the eigenvalues are given by

$$\lambda_{1,2} = \pm j\sqrt{2\frac{k}{m}}, \lambda_{3,4} = -\frac{b}{2} \pm \frac{1}{2}\sqrt{b^2 - 4d} \tag{19}$$

where $b = (k_1 + k_4 - y_3), d = (k_1(k_4 - y_3) + k_3(1 + y_1 - k_2))$. From these results, it becomes evident that only $\lambda_{3,4}$ can be selected by choosing the elements of the K and Y matrices, and in fact, the eigenvalues $\lambda_{1,2}$, which have zero real parts, are independent of these elements. This implies that the estimation errors will never

converge for non-zero initial values, thus reducing the applicability of the UIO for this class of systems.

The reason for introducing the Y matrix also becomes evident from Eq. (18). The constants $y_{1,3}$ can now be selected to obtain the desired rates of convergence. Although this result indicates that the UIO design cannot be carried forward for the given class of systems, by making a "realistic" modification to the mechanical system, the proposed UIO design can indeed be implemented. This modification and the resulting UIO design are presented in the next section. Finally, to complete the UIO design, the matrix L is determined. From Eq. (13) and the other derivations, this matrix is given by

$$L = \begin{bmatrix} (k_1 - y_3(1 + c_1 y_1)) & k_2 + \frac{(1+y_1 c_1)}{c_2} \\ (k_3 - y_3^2 c_1) & k_4 + \frac{y_3 c_1}{c_2} \\ 0 & 0 \\ \alpha y_5 & 0 \end{bmatrix}$$

3.3 Modifying the Structure: Introduce Damping

The system given by Eq. (5) is purely conservative in nature, i.e., it has no dissipative elements. Most mechanical systems will have a dissipative element, for instance, in the form of viscous or material damping. Now, to examine whether the UIO can be applied to such real systems, a damper is added in parallel with each spring of the system shown in Fig. 3. Now, the system will be as shown in Fig. 4.

With the addition of the damping elements, the equations of motion are

$$\begin{aligned} m\ddot{x}_1 - kx_2 + kx_1 + c\dot{x}_1 - c\dot{x}_2 &= F \\ m\ddot{x}_2 - kx_1 + 2kx_2 - c\dot{x}_1 + 2c\dot{x}_2 &= 0 \end{aligned} \tag{20}$$

With this modification, it can be shown that the conditions described previously are still satisfied and hence the UIO can be implemented. As can be seen, the damping elements change only the matrix A of the system. Hence, the derivation of the other matrices remains the same. Now, the eigenvalues of the matrix N are calculated by

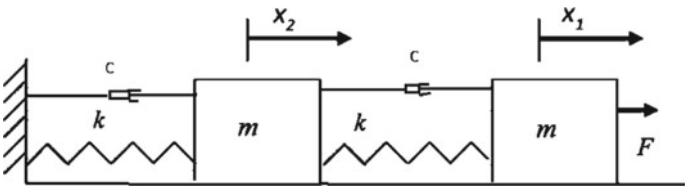


Fig. 4 Adding damping elements to the mechanical structure

solving

$$\left(\lambda^2 + 2\frac{c}{m}\lambda + 2\frac{k}{m}\right)\begin{pmatrix}\lambda^2 + (k_1 + k_4 - y_3)\lambda \\ +(k_1(k_4 - y_3) + k_3(1 + y_1 - k_2))\end{pmatrix} = 0 \tag{21}$$

to yield

$$\lambda_{1,2} = -\frac{c}{m} \pm \sqrt{\frac{c}{m}^2 - 2\frac{k}{m}}, \lambda_{3,4} = -\frac{b}{2} \pm \frac{1}{2}\sqrt{b^2 - 4d} \tag{22}$$

where b and d are as given in Eq. (19). This result indicates that all eigenvalues have non-zero negative real parts, thus implying convergence of the estimates to their real values. However, it should be noted that, even in this case, only $\lambda_{3,4}$ can be placed by selecting the observer matrices.

4 Results and Discussions

The simulation results of implementing the UIO are presented. The cases of the conservative system as well as its modified form are considered. The system parameters are chosen as $m = 5\,\text{kg}$, $k = 30\,\text{N/m}$. For the system modified with the introduction of damping, a damping coefficient of $c = 4.5\,\frac{\text{N}}{\text{m/s}}$. With these parameters, the natural frequencies of the mechanical system are 1.78, 0.68 rad/s. . Thus, to avoid resonant conditions, the unknown input force (units of *Newton*) is selected as $F = 0.5\sin(5t)$. For the cases of conservative and non-conservative systems, as was described in detail earlier, the K and Y matrices are selected as

$$K = \begin{bmatrix} k_1 & k_2 \\ k_3 & k_4 \\ 0 & 0 \\ 0 & 0 \end{bmatrix}, \; Y = \begin{bmatrix} y_1 & 0 \\ y_3 & 0 \\ 0 & 0 \\ 0 & 0 \end{bmatrix} \tag{23}$$

These matrices are selected to decide the eigenvalues of the matrix N. The matrix Y is initially set to zero. Thus, from Eq. (19), the constants $k_{1\ldots4}$ are selected so that the error dynamics has properties as listed in Table 1.

Table 1 Types of closed-loop error dynamics; $Y = 0$

Necessary condition: $(k_1 + k_4) > 0$	
Type of response	Choice of $\boldsymbol{k}_{1\ldots4}$
Under-damped	$\left((k_1 + k_4)^2 < 4(k_1k_4 + k_3(1 - k_2))\right)$
Critically damped	$\left((k_1 + k_4)^2 = 4(k_1k_4 + k_3(1 - k_2))\right)$
Over-damped	$\left((k_1 + k_4)^2 > 4(k_1k_4 + k_3(1 - k_2))\right)$

For simplicity, $k_1 = k_4 > 0$ is chosen. With this choice, selecting the remaining parameters k_2, k_3 also becomes simple, For instance, to have an over-damped type of response, the parameters k_2, k_3 are selected to satisfy $k_3(1 - k_2) < 0$. In addition, the following cases are also considered:

Case 1: $(k_1 + k_4) < 0.68$, i.e., the real parts of the eigenvalues are selected to be smaller than the lowest natural frequency of the system. The parameters for this case are shown in Table 2.

Simulation results are shown for these choices of parameters for both the conservative and the modified systems; note that the latter is a non-conservative system. The results are shown in Figs. 5, 6, and 7

As can be seen in the figures, for the conservative system, the states x_{P2} and x_{V2} can never be estimated. On the other hand, for the non-conservative system,

Table 2 Selection of K matrix parameters when $(k_1 + k_4) < 0.68$

Under-damped condition	$k_1 = k_4 = 0.3;\ k_2 = -0.2;\ k_3 = 0.2$
Critically damped condition	$k_1 = k_4 = 0.3;\ k_2 = 1;\ k_3 = 0.2$
Over-damped condition	$k_1 = k_4 = 0.3;\ k_2 = 2;\ k_3 = 0.03$

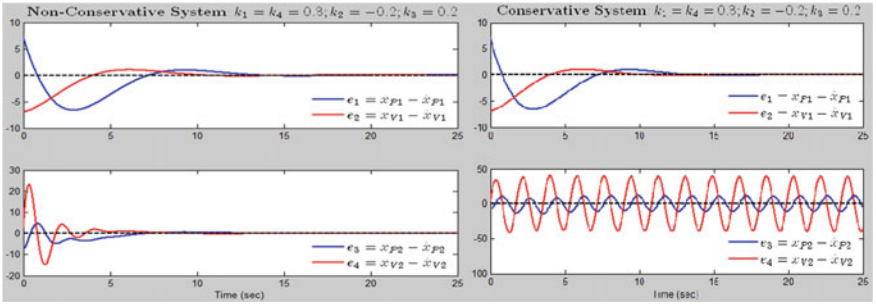


Fig. 5 Dynamics of error estimates for the under-damped case and $(k_1 + k_4) < 0.68$

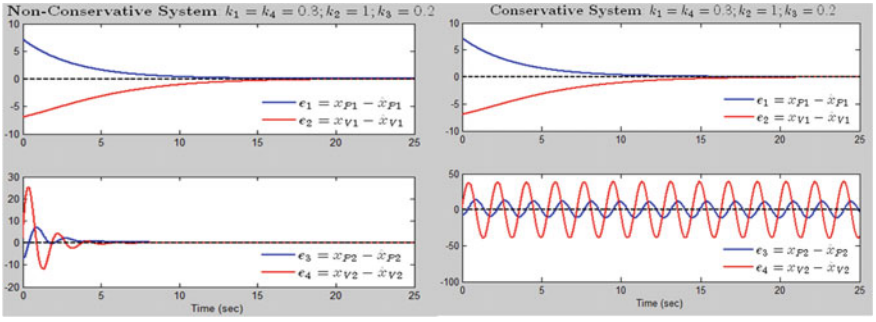


Fig. 6 Dynamics of error estimates for the critically damped case and $(k_1 + k_4) < 0.68$

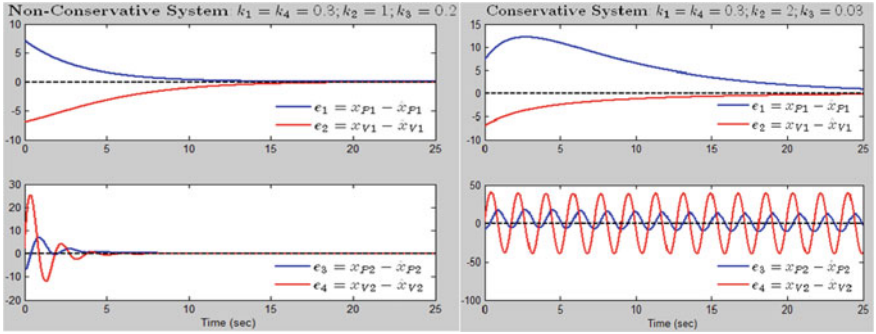


Fig. 7 Dynamics of error estimates for the over-damped case and $(\boldsymbol{k}_1 + \boldsymbol{k}_4) < 0.68$

although the estimates of these states converge to their real values, their rates of convergence are dependent only on the system parameters and cannot be changed using the K matrix. Thus, for a system which is lightly damped and has a higher stiffness, the rates of convergence of the estimates of x_{P2} and x_{V2} to the actual values will be higher. In addition, the rates of convergence of the estimates of the states x_{P1} and x_{V1} as decided by the choices of the parameters $k_{1\ldots4}$ also become evident from these figures. The oscillatory nature of the response for the under-damped case can be seen in Fig. 5 and the absence of oscillations can be seen for the cases of critical and over-damped responses. In these simulations, as $k_1 = k_4$ is selected, to obtain a stable over-damped response, the parameters k_2, k_3 are selected to satisfy $4k_3(k_2 - 1) < (k_1 + k_4)^2$.

Case 2: $(k_1 + k_4) \gg 0.68$, i.e., the real parts of the eigenvalues are selected to be larger than the lowest natural frequency of the system (Table 3).

The simulation results for this case are shown in Figs. 8, 9, and 10. As the only difference between this case and Case 1 is that the values of k_1, k_4 are selected to be higher, the rates of convergence of the estimates of x_{P1} and x_{V1} to the actual values will be higher. The steady-state characteristics remain the same.

Finally, the effect of introducing the matrix Y is presented. As can be observed from Eq. (21), two eigenvalues can be placed by selecting $\boldsymbol{Y}$ and $\boldsymbol{K}$ values. As an illustration, $\boldsymbol{Y}$ is chosen as

Table 3 Selection of K matrix parameters when $(\boldsymbol{k}_1 + \boldsymbol{k}_4) >> 0.68$

Under-damped condition	$k_1 = k_4 = 0.9;\ k_2 = -0.2;\ k_3 = 0.5$
Critically damped condition	$k_1 = k_4 = 0.9;\ k_2 = 1;\ k_3 = 0.5$
Over-damped condition	$k_1 = k_4 = 0.9;\ k_2 = 2;\ k_3 = 0.2$

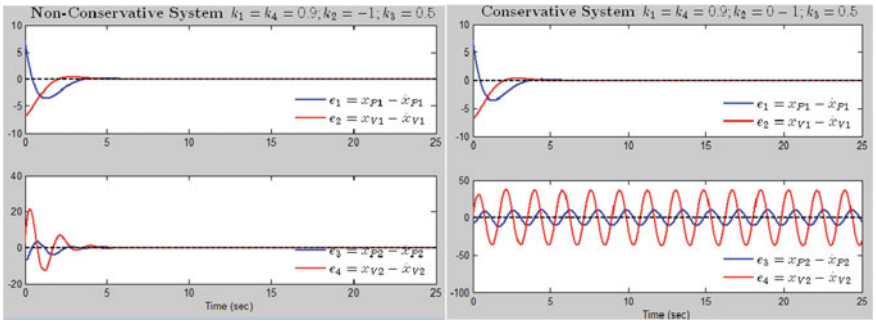


Fig. 8 Dynamics of error estimates for the under-damped case and $(k_1 + k_4) >> 0.68$

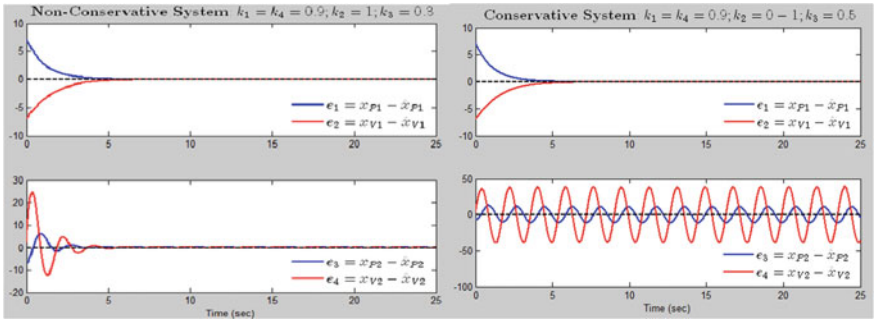


Fig. 9 Dynamics of error estimates for the critically damped case and $(k_1 + k_4) >> 0.68$

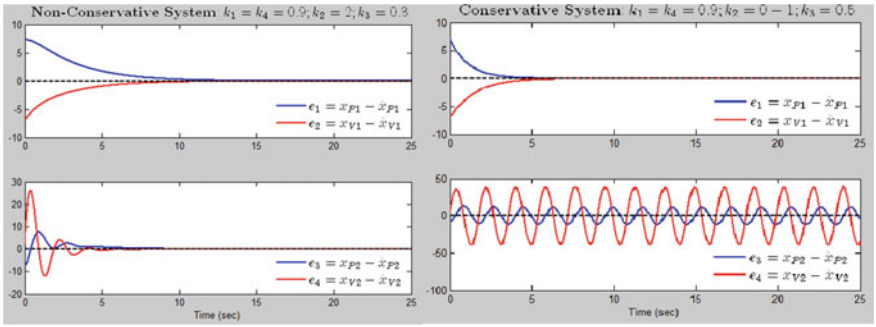


Fig. 10 Dynamics of error estimates for the over-damped case and $(k_1 + k_4) >> 0.68$

$$Y = \begin{bmatrix} 1 & 0 \\ -1.2 & 0 \\ 0 & 0 \\ 0 & 0 \end{bmatrix}$$

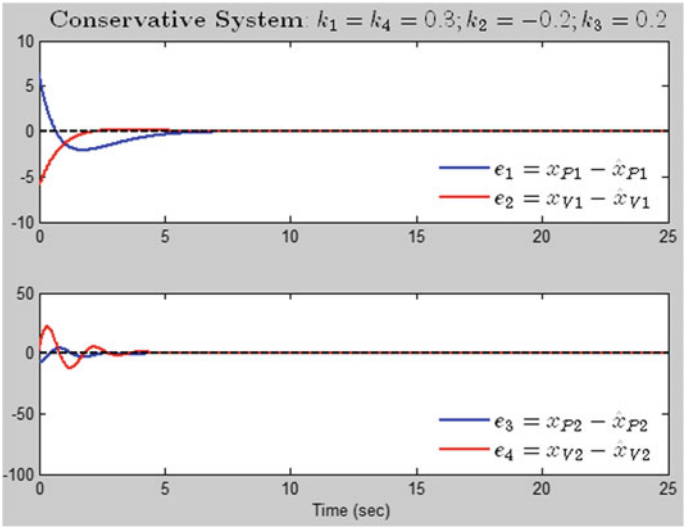


Fig. 11 Plot for the error estimates for under-damped system with Y values

and the results are shown in the following Fig. 11.

5 Discussions

The implementation of the presented UIO design on the considered mechanical structure has its advantages and limitations. While the unknown states can be estimated even in the presence of unknown inputs, the estimation procedure requires the mechanical structure to be non-conservative. This requirement is not very crucial as most real mechanical structures do have this property. In addition, estimation requires the measurement of position as well as velocity of the element on which the unknown force is acting. This requirement may give the impression that additional sensors are required for the UIO implementation. Although this is true, it can be observed that having two sensors in one location is preferable to having several position sensors in the mechanical structure. The proposed UIO design has the added advantage that it can be implemented even when the system parameters are not exactly known; a nominal dynamic model suffices. Thus, there is no need for complicated system identification procedures which have to be performed for state estimation, which is usually the case for the design and implementation of the conventional Luenberger observers. As has been shown in the results, the dynamics of some of the error estimates can be tuned to have the desired rates of convergence. This feature provides guidelines for implementation of the UIO in the discrete domain, as now the eigenvalues can be selected based on the sampling rates available. The problem of estimating the unknown states of a mechanical structure subjected to unknown

inputs has been studied. This problem has been solved with the implementation of the unknown input observer (UIO), which in this case is designed to be in full order. The study [8] reveals that the full observer has certain advantages over the Luenberger reduced order observer with respect to system output matrix. This implies that the UIO presented in this work is a significant contribution to the study of UIO. The closed-loop convergence properties of the UIO have been extensively analyzed, and the requirements for the successful implementation of the UIO have been highlighted. As the proposed UIO can be easily implemented on inexpensive and small microcontrollers, this solution, when viewed from the perspective of SHM, can be termed to be truly in-situ.

Funding Not applicable.

References

1. Chen J (1995) Robust residual generation for model-based fault diagnosis of dynamic systems. PhD Dissertation, University of York, Department of Electronics
2. Guemes A (ed) (2006) Proceedings of the Third European Workshop on Structural Health Monitoring. DEStech Publications Inc
3. Kothamasu R, Huang SH, VerDuin WH (2006) System health monitoring and prognostics—a review of current paradigms and practices. Int J Adv Manuf Technol 28:1012–1024
4. Luenberger D (1967) Canonical forms for linear multivariable systems. AC-12, 290–293
5. Luenberger DG (1971) An introduction to observers. IEEE Trans Automat Cont, 596–602
6. Mohamed Darouach MZ (2006) Full-order observer for linear system with unknown inputs. IEEE Trans Autom Control 39(3):606–609
7. Theilliol D, Mahfouf M, Sauter D, Gama MA (2006) Actuator fault detection, isolation method and state estimator design for hot rolling mill monitoring. In: 6th IFAC Symposium on Fault Detection, Supervision, and Safety of Technical Processes. Elsevier, Beijing, China
8. Tsui C-C (1996) A new design approach to unknown input observers. IEEE Trans Autom Control 41:464–468

Combined Effects of External and Nozzle Exit Flows on the Jet Acoustic Power Levels of Chevron Nozzles for Transonic Aircraft



Arsalan Ahmad, Dekkala Vinay, Shubhangi Sundaria, Sobia Raza, Maansi Srivastasva, Tanisha Singh, Sagnik Saha, and V. R. S. Kumar

Abstract The issue of jet noise pollution from major airports has become increasingly significant. Recent research has indicated that incorporating a geometry-optimized chevron nozzle can effectively reduce jet acoustic power levels. Herein, we conduct a diagnostic investigation into the acoustic power levels of four different chevron nozzles. In silico studies are performed using a validated steady three-dimensional density-based k-ε turbulence model. Our findings reveal that among the four chevron nozzles (sharp, square, flat, and round edge), the implementation of a round-edged chevron proves to be the most effective design choice for mitigating jet noise in transonic aircraft. This design reduces the acoustic power level by 10% when compared to the base model of a classical high-subsonic/transonic nozzle (without chevron), while still maintaining the benefits of momentum thrust. The results of this study contribute to advancements in aero-acoustic research and provide valuable insights for the design optimization of chevron nozzles for transonic aircraft.

Keywords Aero-acoustics research · Chevron nozzles · Noise pollution · Design and optimization of nozzles · Mach number · Acoustic power level

A. Ahmad · D. Vinay (✉) · S. Sundaria · S. Raza · M. Srivastasva · T. Singh · S. Saha · V. R. S. Kumar
Amity Institute of Aerospace Engineering, Amity University Uttar Pradesh, Noida 201313, India
e-mail: vinay0408200@gmail.com

V. R. S. Kumar
e-mail: vrskumar@amity.edu

© The Author(s), under exclusive license to Springer Nature Singapore Pte Ltd. 2024

S. Singh et al. (eds.), *Recent Advances in Aerospace Engineering*, Lecture Notes in Mechanical Engineering, https://doi.org/10.1007/978-981-97-1306-6_49

1 Introduction

Transonic chevron nozzles are specialized exhaust nozzles designed to reduce noise emissions and enhance performance in transonic flow regimes. They are particularly relevant in aerospace applications, where noise regulations and efficiency requirements are of paramount importance [1–15]. In aerodynamics, the term "transonic" refers to the speed range near the speed of sound (~0.7–1.2). The main objective of a transonic chevron nozzle is to suppress shock-associated noise, which is a significant source of noise in transonic flows. These nozzles feature chevron-shaped notches or serrations along the trailing edge of the nozzle exit, similar to subsonic chevron nozzles. However, in transonic chevron nozzles, the design and arrangement of the chevrons are optimized for transonic flow conditions. The specific mechanisms by which transonic chevron nozzles reduce noise can be attributed to several factors, viz. shockwave interaction control, boundary layer disruption, flow expansion, and compression. When an aircraft moves through the transonic range, the airflow over its surface undergoes a transition from subsonic to supersonic speeds due to streamtube compression and Sanal flow choking [19–36]. This transition causes a significant reduction in lift and an increase in acoustic power level due to possible shock wave generation. These shock waves can lead to increased drag, loss of control, and other aerodynamic challenges at the nozzle exit. Therefore, in this pilot paper we have carried out diagnostic studies on the combined effects of nozzle jet flows and the external flows on the jet acoustic power levels of chevron nozzles for transonic aircraft.

Jet noise has become a significant concern in aero-acoustics research areas due to noise regulations around major airports and rocket launching stations, driven by environmental considerations. Within jet nozzles, there are three primary sources of noise: aerodynamics noise, noise from craft systems, and engine and mechanical noise. Extensive analysis of existing literature reveals that a substantial portion of engine noise is attributed to the jet noise emitted through the exhaust nozzle. Despite numerous studies conducted in recent decades, accurately predicting and reducing the acoustic levels of various exhaust nozzle jets remains an active and ongoing area of research. It is well-established that the high-velocity jet exiting the engine encounters inherent instability in its shear layer, resulting in the formation of swirling ring-like vortices. These vortices subsequently deteriorate into turbulent sources of jet noise at the nozzle exit. Various methods have been proposed in scientific literature to mitigate jet engine noise without compromising other critical design parameters of propulsive systems. In summary, jet noise has become a significant focus in aero-acoustics research due to noise regulations and environmental concerns. The jet noise emitted through exhaust nozzles is a major contributor to engine noise, and efforts to accurately predict and reduce this noise continue to be an active area of investigation. Understanding the inherent instability and turbulence within the jet flow and exploring methods for noise mitigation using chevron nozzles are key objectives in aero-acoustic research.

The chevron notches alter the shockwave pattern and its interaction with the turbulent boundary layer. This control helps to mitigate shock-associated noise by reducing the intensity and frequency of shockwave-related disturbances. The chevron geometry disrupts the boundary layer flow, promoting enhanced mixing and reducing the growth of instabilities. This disruption reduces the generation of noise due to boundary layer interactions. The chevron notches create controlled flow expansions and compressions, which help to manage the shockwave structure and reduce its adverse effects on noise generation. A literature review reveals that numerous experimental and numerical studies have been conducted to investigate the acoustic and aerodynamic performance of chevron nozzles. These studies often employ computational fluid dynamics (CFD) simulations, wind tunnel testing, and acoustic measurements to evaluate the effectiveness of different chevron configurations and optimize nozzle designs. The development and implementation of transonic chevron nozzles have shown promising results in reducing noise levels and improving overall propulsion system efficiency in transonic flow conditions. These nozzles have been studied and applied in various aerospace applications, including aircraft engines, rocket motors, and other high-speed propulsion systems. In summary, transonic chevron nozzles are designed to mitigate shock-associated noise and improve performance in transonic flow regimes. Through careful chevron design and optimization, these nozzles effectively control shockwave interactions, disrupt the boundary layer, and manage flow expansions and compressions. Continued research and development in this field aim to further enhance the noise reduction capabilities and overall efficiency of transonic propulsion systems.

The subsonic chevron nozzle is an innovative exhaust nozzle design employed in aircraft engines to enhance performance and reduce noise emissions. The subsonic chevron nozzle incorporates chevron-shaped lobes on the nozzle's inner surface, disrupting the exhaust flow and altering its acoustic characteristics. These lobes are spaced evenly around the circumference of the nozzle, typically angled backward. The primary advantage of the subsonic chevron nozzle is its ability to significantly reduce aircraft noise levels, particularly during take-off and landing. The vortex shedding and mixing induced by the chevron lobes help to break up and disperse the noise-generating exhaust flow. The subsonic chevron nozzle has gained significant attention in recent years as a promising solution to mitigate jet noise in aircraft engines (see Fig. 1). This study report aims to evaluate the current state of research and development regarding high-subsonic/transonic chevron nozzles and propose a cogent design option. The article provides an overview of the design principles, performance characteristics, and challenges associated with these nozzles. Transonic chevron nozzles are designed with the objective of reducing jet noise without compromising the thrust performance of the aircraft engine. The chevron geometry, typically consisting of notches or lobes on the nozzle edges, introduces controlled mixing of the exhaust gases with ambient air, resulting in reduced noise levels. The optimization of chevron shape, number of lobes, and arrangement plays a crucial role in achieving the desired noise reduction, which we have attempted herein.

As stated earlier, numerous studies have been conducted to investigate the performance characteristics of high-subsonic/transonic chevron nozzles [1–18, 37–52].



Fig. 1 Chevron nozzle in Honeywell's Falcon 20

These studies employ both experimental and numerical techniques to assess parameters such as acoustic power levels, thrust efficiency, and flow characteristics. The findings suggest that properly designed chevron nozzles can effectively reduce jet noise by altering the exhaust flow pattern and enhancing mixing with the surrounding air. Moreover, they demonstrate that chevron nozzles can maintain or even improve thrust efficiency compared to conventional nozzles. While high-subsonic/transonic chevron nozzles show promise in reducing jet noise, several challenges remain. One major challenge is the complex interaction between the chevron geometry and the overall engine performance. Optimal design requires a balance between noise reduction and maintaining thrust efficiency, which demands comprehensive multidisciplinary analyses. Additionally, the manufacturing and integration of chevron nozzles into existing engine systems pose practical challenges that need to be addressed.

Future research directions should focus on further optimizing the chevron geometry, considering factors such as chevron angle, depth, and distribution. Advanced computational tools and experimental techniques can contribute to a better understanding of the underlying flow physics and aid in the design optimization process. Furthermore, investigating the impact of chevron nozzles on other performance parameters, such as emissions and fuel efficiency, would provide a more comprehensive assessment of their viability in practical applications. The high-subsonic chevron nozzle holds promise as an effective solution for reducing jet noise in aircraft engines. The design optimization of subsonic/supersonic chevron geometry and its impact on noise reduction and thrust performance have been extensively studied. However, further research and development are needed on transonic chevron nozzles to address challenges related to engine integration, multidisciplinary analysis, and comprehensive performance assessment. With continued efforts, high-subsonic/transonic chevron nozzles have the potential to contribute significantly to quieter and more efficient aircraft operations in the future. Herein, we conduct a diagnostic investigation of acoustic power levels and momentum thrust of four different chevron nozzles using three-dimensional in silico methodology.

2 In Silico Methodology

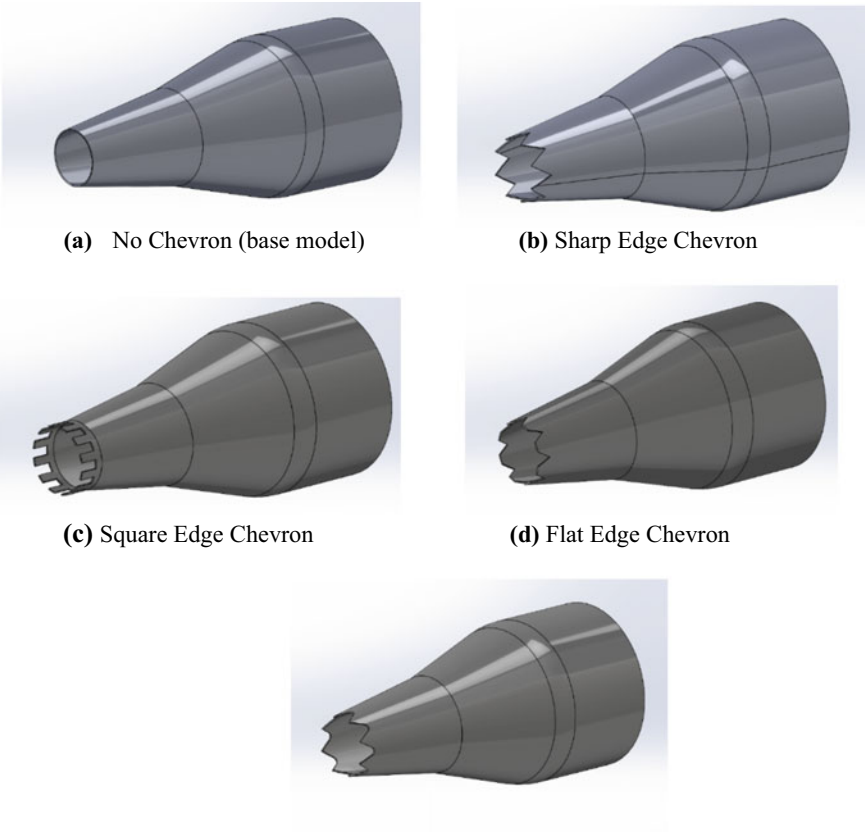
This paper focuses on the combined effects of external and the nozzle jet flows on the jet acoustic power levels of transonic chevron nozzles. We have carried out a detailed studies on the jet characterization and geometry optimization of chevron nozzles using a three-dimensional (3D) steady density-based standard k-ε turbulence model with standard wall functions. The standard k-ε model is widely utilized in practical engineering flow calculations and has become a commonly used approach. The standard k-ε model is classified as a two-equation turbulence model, enabling the determination of both the turbulent length scale and time scale through the solution of two separate transport equations. It is a semi-empirical model, with its equations derived based on phenomenological considerations and empirical data. The model equations for turbulence kinetic energy (k) and its dissipation rate (ε) are employed in the standard k-ε model. The transport equation for k is derived from the exact equation, while the transport equation for ε is derived using physical reasoning and does not closely resemble its mathematically exact counterpart. During the derivation of the k-ε model, the assumption is made that the flow is fully turbulent, and the effects of molecular viscosity are considered negligible. Therefore, the standard k-ε model is valid only for fully turbulent flows. In the context of this paper, the authors have employed the standard k-ε model to conduct jet acoustic characterization and optimize the geometry of chevron nozzles. This approach provides valuable insights into the acoustic behavior of the jets and allows for the optimization of nozzle designs to reduce noise emissions. However, it is important to note that the validity of the standard k-ε model is limited to fully turbulent flows, and its results should be interpreted accordingly in the context of the study. The transport equations for turbulence kinetic energy, k, and its rate of dissipation, ε, are employed to obtain their respective values. These equations, which govern the evolution of k and ε within the turbulent flow, are as follows:

$$\frac{\partial}{\partial t}(\rho k) + \frac{\partial}{\partial x_i}(\rho k u_i) = \frac{\partial}{\partial x_j}\left[\left(\mu + \frac{\mu_t}{\sigma_k}\right)\frac{\partial k}{\partial x_j}\right] + G_k + G_b - \rho\varepsilon - Y_M + S_k \quad (1)$$

$$\frac{\partial}{\partial t}(\rho \varepsilon) + \frac{\partial}{\partial x_i}(\rho \varepsilon u_i) = \frac{\partial}{\partial x_j}\left[\left(\mu + \frac{\mu_t}{\sigma_\varepsilon}\right)\frac{\partial \varepsilon}{\partial x_j}\right] + C_{1\varepsilon}\frac{\varepsilon}{k}(G_k + C_{3\varepsilon}G_b) - C_{2\varepsilon^0}\frac{\varepsilon^2}{k} + S_\varepsilon \quad (2)$$

In the numerical study, a fully implicit finite volume scheme was employed to solve the compressible Navier–Stokes equations. The viscosity of the fluid was determined using the Sutherland formula. The geometric variables and material properties of the nozzle were known beforehand. The initial wall temperature and inlet temperature were specified, and a no-slip boundary condition was imposed at the solid

walls. The working fluid was assumed to be an ideal gas. The conventional high-subsonic nozzle was selected as a base model (see Fig. 2a) for achieving the transonic exit Mach number. For the diagnostic investigation of acoustic power level and momentum thrust, idealized physical models consisting of four different shapes of chevron nozzles (sharp, square, flat, and round edge) have been chosen (see Fig. 2b–e). This selection allows for studying the combined effects of external and nozzle exit flows on jet acoustic power levels. These models will provide insights into the acoustic characteristics and thrust generated by each chevron nozzle design, helping to understand their performance and potential applications.



(a) No Chevron (base model)

(b) Sharp Edge Chevron

(c) Square Edge Chevron

(d) Flat Edge Chevron

(e) Round Edge Chevron

Fig. 2 (**a**–**e**) Idealized physical models of various nozzles

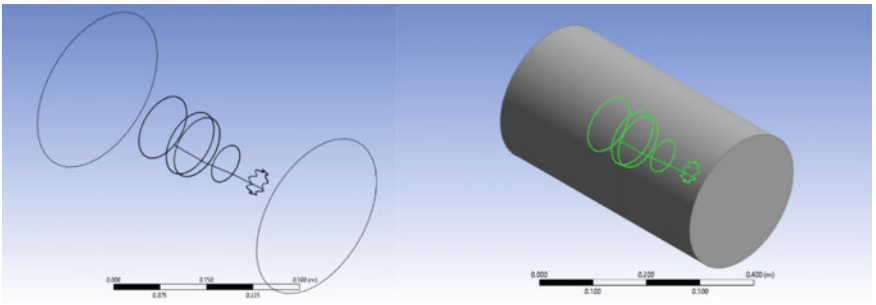
3 Results and Discussion

A high-subsonic chevron nozzle does not inherently create transonic flow at the exit. The primary function of a high-subsonic chevron nozzle is to reduce noise emissions and improve performance in high-subsonic flow regimes. In order to create transonic flow at the nozzle exit, additional design modifications and considerations are typically required. These modifications could include adjusting the nozzle geometry, incorporating divergent–convergent sections, or implementing specific flow control mechanisms. The design of a nozzle capable of generating transonic flow at the exit is a complex task that involves optimizing various parameters such as throat area, expansion ratio, and the curvature of the nozzle contours. Additionally, careful consideration must be given to factors such as shockwave placement, boundary layer control, and flow expansion/compression. Creating transonic flow at the nozzle exit is often desired in certain applications, as it allows for better aerodynamic performance and efficiency in supersonic or near-supersonic regimes. However, it is important to note that achieving transonic flow requires specific design features and considerations beyond those associated with a high-subsonic chevron nozzle. Of late, Kumar et al. [23] established conclusively through series of publications that the streamtube compression and Sanal flow choking leads to transonic condition and shock wave generation. When exhaust gases pass through the high-subsonic chevron nozzle, the chevron lobes create vortices that interact with the exhaust plume and external flows. This interaction results in the mixing of high-velocity and low-velocity flow regions, effectively reducing noise levels by redistributing and dissipating the energy in the exhaust stream. The vortex action within the chevron nozzle promotes better mixing of exhaust gases with ambient air, resulting in improved combustion efficiency and reduced fuel consumption. By enhancing mixing and combustion efficiency, the subsonic chevron nozzle contributes to a reduction in pollutant emissions, making it an environmentally friendly solution.

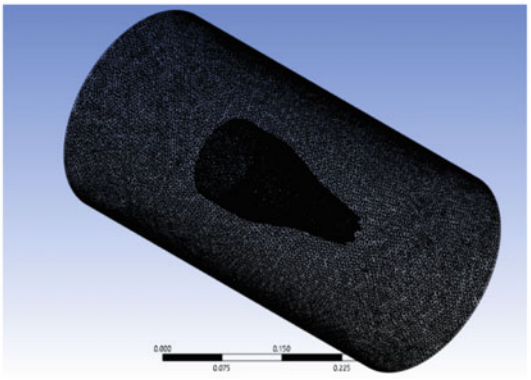
A high-subsonic chevron nozzle is a specialized type of exhaust nozzle used in jet engines to mitigate noise emissions and enhance performance. It incorporates chevron-shaped notches or serrations along the trailing edge of the nozzle exit. These notches disrupt the exhaust flow and induce a beneficial mixing process, resulting in noise reduction and improved thrust characteristics. The primary objective of a subsonic chevron nozzle is to reduce jet noise, particularly during take-off and landing phases, where noise regulations are more stringent. As seen from our self-explanatory in silico results (See Figs. 3, 4, 5, 6, and 7)) the chevron design helps to reduce the intensity and total characteristics of the noise generated by the engine exhaust. Figures 6 and 7 clearly indicate that the round-edged chevron nozzle exhibits a notable decrease in the overall acoustic power level by 10% compared to the base model (without chevrons). Importantly, this reduction in acoustic power level is achieved without any compromise in the momentum thrust generated by the nozzle. These findings suggest that the round-edged chevron design could be a promising option for mitigating acoustic noise while maintaining efficient thrust performance in the nozzle system. The specific mechanisms by which a high-subsonic chevron

nozzle reduces noise can be attributed to several factors, mixing enhancement, flow separation control, acoustic interference, streamtube compression, and shock wave generation. The application of chevron nozzles has demonstrated significant noise reduction in aircraft engines. It has become an integral part of noise reduction strategies employed in commercial aviation to comply with noise regulations around airports. Additionally, these nozzles have been studied for their potential application in other propulsion systems, including gas turbines and industrial exhausts. In summary, high-subsonic/transonic chevron nozzles are engineered to minimize jet noise through various mechanisms, including enhanced mixing, flow separation control, and acoustic interference, streamtube compression effects. Their implementation in jet engines has proven effective in reducing noise emissions during critical phases of flight, contributing to quieter and more environmentally friendly aviation operations.

The issue of jet noise pollution from major airports has garnered significant attention in recent times. Extensive research has demonstrated that incorporating a geometry-optimized chevron nozzle can effectively reduce jet acoustic power levels. To further explore this, we conducted a diagnostic investigation to analyze

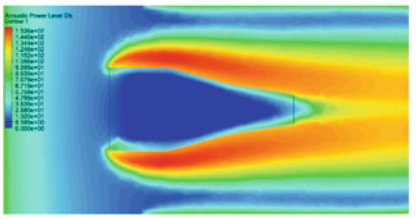


(a) Physical model in the computation domain

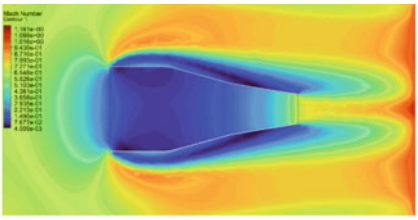


(b) Model with wireframe meshes

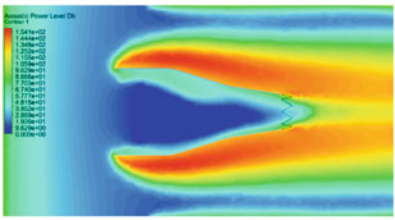
Fig. 3 (**a**, **b**) Physical model and grid system in the computational domain



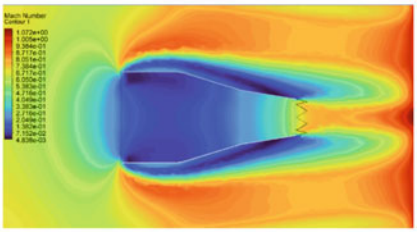
(a) Acoustic power level (base model)



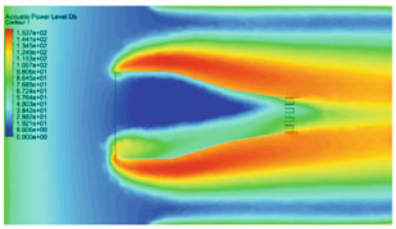
(f) Mach number contour (base model)



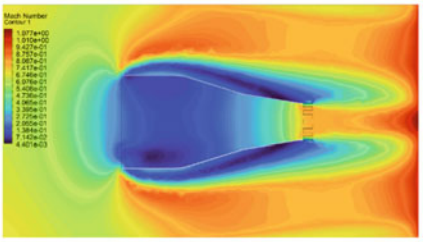
(b) Acoustic power level (sharp edge chevron)



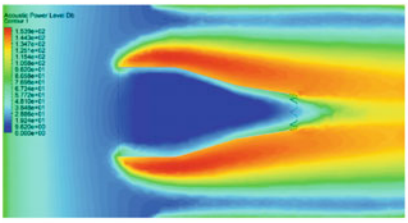
(g) Mach number contour (sharp edge chevron)



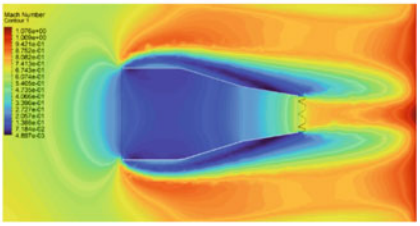
(c) Acoustic power level (Square edge chevron)



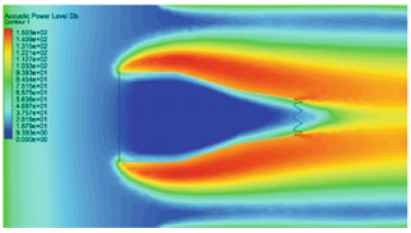
(h) Mach number contour (Square edge chevron)



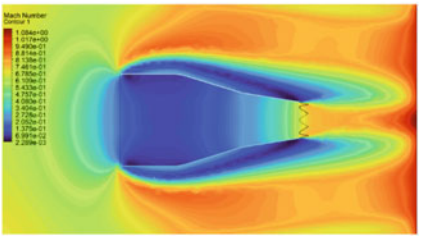
(d) Acoustic power level (Flat edge chevron)



(i) Mach number contour (Flat edge chevron)

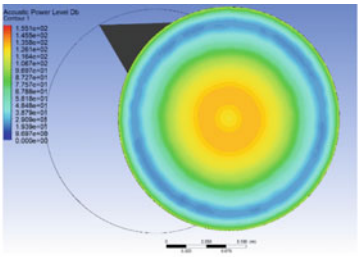


(e) Acoustic power level (Round edge chevron)

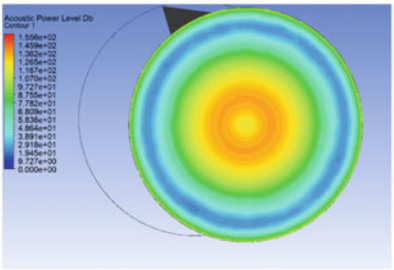


(j) Mach number contour (Round edge chevron)

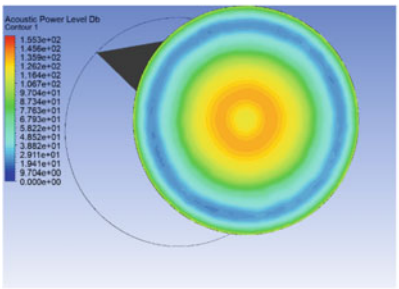
Fig. 4 Comparison of the acoustic power levels and Mach number variations of various types of nozzles



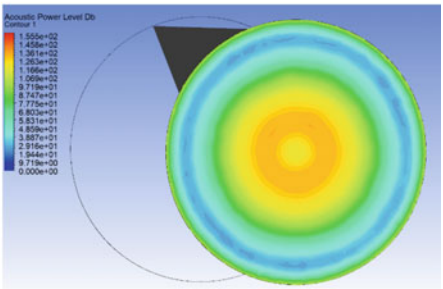
(a) Acoustic power level at the nozzle exit of the base model



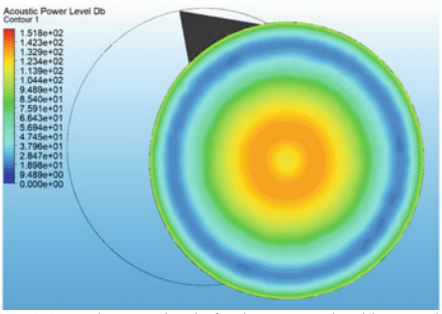
(b) Acoustic power level with a sharp edge



(d) Acoustic power level with a flat edge



(c) Acoustic power level with a square edge



(e) Acoustic power level of a chevron nozzle with a round edge

Fig. 5 (**a**–**e**) Comparison of the acoustic power levels at the exit of various types of nozzles

the acoustic power levels of four different chevron nozzle designs. In this study, we utilized in silico simulations employing a validated steady three-dimensional density-based k-ε turbulence model. Our findings highlight the superior effectiveness of the round-edged chevron nozzle among the four designs (sharp, square, flat, and round edge) in mitigating jet noise in transonic aircraft. Implementing the round-edged chevron nozzle resulted in a remarkable 10% reduction in the acoustic power level (see Fig. 6) when compared to the base model of a classical high-subsonic/transonic nozzle (without chevron). Importantly, this reduction in noise is achieved without compromising the advantages provided by momentum thrust (see Fig. 7).

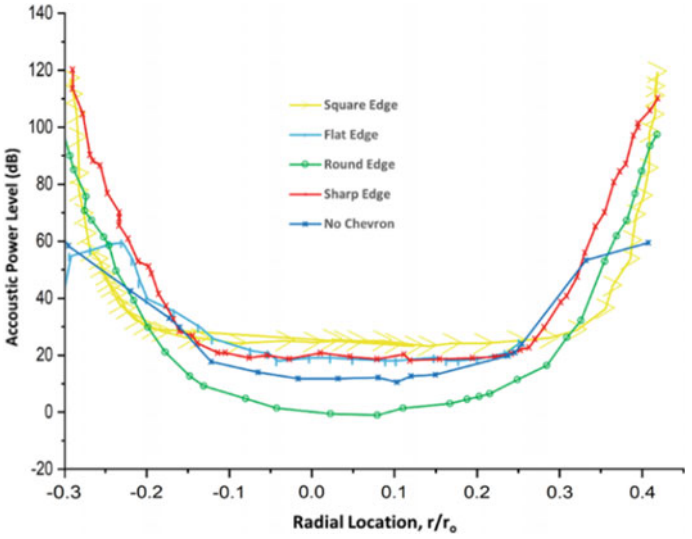


Fig. 6 Comparison of the average acoustic power levels at the exit of various types of nozzles

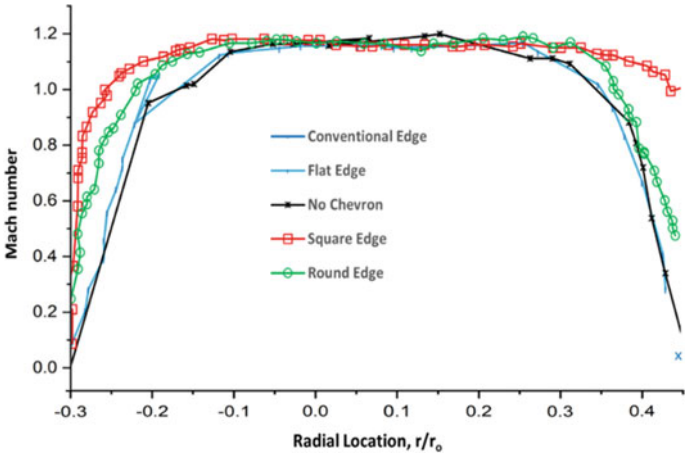


Fig. 7 Comparison of the average Mach number at the exit of various types of nozzles

The outcomes of this study contribute to the advancement of aero-acoustic research and offer valuable insights for optimizing the design of chevron nozzles for transonic aircraft. The utilization of concepts such as streamtube compression and Sanal flow choking has further enhanced the understanding of the nozzle's performance. By adopting round-edged chevron nozzles, aircraft manufacturers and researchers can make significant progress in addressing the issue of jet noise pollution and improving

the overall acoustic performance of aircraft engines. This research paves the way for more refined designs and potential noise reduction strategies in the aviation industry.

4 Concluding Remarks

The issue of jet noise pollution from major airports has gained considerable attention in recent times. Researchers have shown that incorporating a geometry-optimized chevron nozzle can effectively reduce jet acoustic power levels. In this study, we conducted a diagnostic investigation to analyze the acoustic power levels of four different chevron nozzles. In silico simulations were performed using a validated steady three-dimensional density-based k-ε turbulence model. Our findings highlight that among the four chevron nozzle designs (sharp, square, flat, and round edge), the implementation of a round-edged chevron proves to be the most effective in mitigating jet noise in transonic aircraft. This particular design choice resulted in a noteworthy reduction of 10% in the acoustic power level when compared to the base model of a classical high-subsonic/transonic nozzle (without chevron). Importantly, this reduction in noise is achieved without compromising the advantages provided by momentum thrust. The outcomes of this study contribute to the advancement of aero-acoustic research and offer valuable insights for the design optimization of chevron nozzles for transonic aircraft using the concept of streamtube compression and Sanal flow choking. By employing round-edged chevron nozzles, aircraft manufacturers and researchers can make significant progress in addressing the issue of jet noise pollution and improving the overall acoustic performance of aircraft engines. Admittedly, the high-subsonic/transonic chevron nozzle finds applications in various aircraft engines, including commercial airliners, regional jets, and military aircraft. It is particularly advantageous for aircraft operating in noise-sensitive areas, such as airports located near residential communities. The chevron lobes modify the exhaust jet's pressure distribution, optimizing thrust performance and potentially improving aircraft engine efficiency. The chevron nozzle design requires careful consideration of geometric parameters to reduce streamlines compression, including lobe size, spacing, and angle, to achieve optimal performance. Fabricating and maintaining the chevron nozzle may present challenges due to its intricate design and potential susceptibility to erosion and wear. The high-subsonic/transonic chevron nozzle represents a promising advancement in aircraft engine technology, offering substantial noise reduction, improved efficiency, and environmental benefits. While challenges exist, continued research and development in nozzle design and manufacturing processes can help optimize its performance and overcome limitations.

References

1. Ahmad A (2023) Design optimization of Chevron nozzle. AIAE NTCC-BTech-TR-AA-A3705519017, Undergraduate Project Report, Amity Institute of Aerospace Engineering, Amity University Uttar Pradesh, New Delhi NCR, India, May
2. Uzun A, Hussaini MY (2009) Simulation of noise generation in near-nozzle region of a Chevron nozzle jet. AIAA J 47:8. https://doi.org/10.2514/1.36659
3. Lyrintzis AS (2003) Surface integral methods in computational aeroacoustics: from the (CFD) near-field to the (acoustic) far field. Int J Aeroacoust 2(2):95–128
4. Sathyaprabha R, Vigneshwaran S, Manishaa R, Vivek S, Ajith S, Mani S, Kumar VRS (2016) Design of environmental friendly Chevron nozzles for lower stage rockets. In: 52nd AIAA/SAE/ASEE Joint Propulsion Conference, AIAA Propulsion and Energy Forum (AIAA 2016-4910). https://doi.org/10.2514/6.2016-4910
5. Sivabalan M, Lee DJ, Kumar VRS (2015) Jet acoustic characterization and geometrical optimization of Chevron nozzles using 3D k-ε model. In: 51st AIAA Joint Propulsion Conference, Florida, AIAA-2015-3884
6. Kanmaniraja R, Freshipali R, Abdullah J, Niranjan K, Balasubramani K, Kumar VRS (2014) 3D numerical studies on jets acoustic characteristics of Chevron nozzles for aerospace applications. Int J Mech, Aerospace, Indust Mech Eng 8(9)
7. Xu X, He J, Li X, Hu FQ (2015) 3-D jet noise prediction for separate flow nozzles with pylon interaction. In: AIAA SciTech, 53rd AIAA Aerospace Sciences Meeting, 5–9 January, Florida, AIAA 2015-0512
8. Bridges J, Brown CA (2004) Parametric testing of chevrons on single flow hot jets. AIAA-2004-2824
9. Zaman KBMQ, Bridges JE, Huff DL (2010) Evolution from 'tabs' to 'Chevron technology'—a review. In: Proceedings of the 13th Asian Congress of Fluid Mechanics, 17–21, Dhaka, Bangladesh
10. Massey SJ, Elmiligui AA, Hunter CA et al (2006) Computational analysis of a Chevron nozzle uniquely tailored for propulsion airframe aeroacoustics. In: 12th AIAA Aeroacoustic Conference, AIAA-2006-2436
11. Uzun A, Hussaini MY (2007) Noise generation in the near-nozzle region of a Chevron nozzle jet flow. In: 13th AIAA/CEAS AeroacousticConference, Rome, AIAA-2007-3596
12. Shur ML, Spalart PR, Strelets MK, Garbaruk AV (2007) Analysis of jet-noise-reduction concepts by large-eddy simulation. Int J Aeroacoust 6(3):243–285
13. Birch SF, Lyubimov DA, Secundov AN, Yakubovsky KY (2003) Numerical modeling requirements for coaxial and Chevron nozzle flows. In: 9th AIAA/CEAS Aeroacoustic Conference and Exhibit, South Carolina, AIAA-2003-3287. Crunteanu D, Cojan P-C (2013) Accoustic characteristics of the flow over different shapes of nozzle Chevron. INCAS Bull 5(3):53–59 ISSN 2066-8201
14. Saiyed N (2000) Separate flow nozzle test status meeting. NASA/TM 2000-210524
15. Saiyed N, Mikkelsen KL, Bridges J (2000) Acoustics and thrust of separate-flow exhaust nozzles with mixing devices for high-bypass-ratio engines. NASA/TM 2000-209948
16. Engblom WA, Khavaran A, Bridges J (2004) Numerical prediction of Chevron nozzle noise reduction using WIND-MGBK methodology. AIAA Paper 2004-2479
17. Birch SF, Lyubimov DA, Maslov VP, Secundov AN (2006) Noise prediction for chevron nozzle flows. AIAA Paper 2006-2600
18. Blaisdell GA, Lyrintzis AS, Sullivan JP (2011) Preliminary design and computational analysis of an ejector nozzle with chevrons. In: 49th AIAA Aerospace Sciences Meeting including the New Horizons Forum and Aerospace Exposition, Florida
19. Panchal D, Kumar VRS (2022) Demonstration of Sanal flow choking and streamtube flow choking causing deflagration to detonation transition in internal flow systems. The 2022 AIAA Aviation Forum—Flow Visualization Showcase, 3D Animation of Velocity Contour with Superimposed Streamlines. https://www.youtube.com/playlist?list=PLOl5RDXeYOMBvblsy4A5El6ugPkulwKIx

20. Kumar VRS et al (2023) Coherent explanation of aerodynamic lift and threshold condition of drag divergence using the concept of Sanal flow choking. AIAA Aviation 2023 Forum, 12–16 June, San Diego, CA, AIAA 2023-3754. https://doi.org/10.2514/6.2023-3754
21. Kumar VRS, Sankar V, Chandrasekaran N, Rafic SARM (2019) Discovery of Sanal flow choking, Patent Application No. 201841049355, Chennai, India, Date of online publication: January 4
22. Kumar VRS, Sankar V, Chandrasekaran N, Sukumaran A et al (2020) Sanal-flow-choking: a paradigm shift in computational fluid dynamics code verification and diagnosing detonation and hemorrhage in real-world fluid-flow systems. Glob Chall 4
23. Kumar VRS, Sankar V, Chandrasekaran N, Saravanan V, Sukumaran A, Rajendran V et al (2022) Universal benchmark data of the three-dimensional boundary layer blockage and average friction coefficient for *in silico* code verification. Phys Fluids 34. https://doi.org/10.1063/5.0086638
24. Kumar VRS, Sankar V, Chandrasekaran N et al (2018) A closed-form analytical model for predicting 3D boundary layer displacement thickness for the validation of viscous flow solvers. AIP Adv 8:025315. https://doi.org/10.1063/1.5020333
25. Kumar VRS, Sankar V, Chandrasekaran N, Rafc SARM, Sukumaran A, Radhakrishnan PK, Choudhary SK (2021) Discovery of nanoscale Sanal flow choking in cardiovascular system—exact prediction of the 3D boundary-layer-blockage factor in nanotubes. Nat Scient Rep, Date: 29 July. https://doi.org/10.1038/s41598-021-94450-8 (Note: Retraction challenges)
26. Kumar VRS, Sundararam BR, Radhakrishnan PK, Chandrasekaran N, Choudhary SK, Sankar V, Sukumaran A, Rajendran V, Rafic SARM, Panchal D, Raj Y, Shrivastava S, Oommen C, Jayaraman A, Deveswaran R, Bharath S (2022) *In vitro* prediction of the lower/upper-critical biofluid flow choking index and *in vivo* demonstration of flow choking in the stenosis artery of the animal with air embolism. Phys Fluid 34(9). https://doi.org/10.1063/5.0105407
27. Kumar VRS et al (2023) In silico demonstration of Sanal flow choking and/or streamtube flow choking in 3D reacting flows causing detonation and explosions. In: The 2023 AIAA SciTech, January 23, AIAA 2023-1102
28. Kumar VRS et al (2023) Sanal flow choking and/or sonic-fluid-throat effect reconfirms the Chapman–Jouguet condition of detonation propagation and ceases. AIAA Aviation 2023 Forum, 12–16 June, San Diego, CA, AIAA 2023-4416. https://doi.org/10.2514/6.2023-4416
29. Kumar VRS, Shankar SG, Saravanan A, Lenin C, Santhosh Kumar N, Sathyan P (2014) Phenomenological introduction of propulsion aspect of external flow choking at wing in ground effect. In: 50th AIAA/ASME/SAE/ASEE Joint Propulsion Conference, U.S.A, 2014, Paper No. AIAA-2014-3772. https://doi.org/10.2514/6.2014-3772
30. Vignesh S, Vivek S, Shankar SG, Ajith S, Mani S, Kumar VRS (2016) Studies on boundary layer blockage and external flow choking at moving wing in ground effect. In: 52nd AIAA/SAE/ASEE Joint Propulsion Conference, Propulsion and Energy Forum, Salt Lake, USA, AIAA 2016-4803. https://doi.org/10.2514/6.2016-4803
31. Kumar VRS, Saravanan V, Srinivasan V, Shankar SG, Mani S, Sankar V, Krishnamoorthy D et al (2021) The theoretical prediction of the boundary layer blockage and external flow choking at moving aircraft in ground effects. Phys Fluid 33(3). https://doi.org/10.1063/5.0040440
32. Vignesh S, Vivek S, Shankar SG, Hemasai ND, Kumar VRS (2016) Studies on external flow choking at moving wing at opposed wind flow in ground effect. In: 2016 Applied Aerodynamics Conference—Evolution & Innovation Continues—The Next 150 Years of Concepts, Design and Operations, Conference Programme & Proceedings, 19–21, July. Bristol, UK
33. Shrivastava S, Raj Y, Kumar VRS, Rajendran V, Dekkala V, Sharma S, Sharma R (2023) Investigation of streamtube flow choking and unchoking on the aerodynamic performance of transonic aircraft. AIAA Aviation 2023 Forum 2023, p 3755
34. Kumar VRS, Vinay D, Sharma R, Sharma S, Rajendran V, Sarswat R, Raj Y, Shrivastava S, Panchal D, Sharma A (2023) Phenomenological introduction of standoff distance of sonic ring impelling entropy waves and aerodynamic heating of hypersonic vehicles. In: 25th AIAA International Space Planes and Hypersonic Systems and Technologies Conference 2023, pp 3070-c1

35. Kumar VRS et al (2021) The physics of detonation chemistry: a radical theory in predicting the deflagration to detonation transition, environmental and supernova explosions. AIAA Propulsion and Energy 2021 Forum, AIAA 2021–3242
36. Kumar VRS, Sankar V, Chandrasekaran N, Saravanan V, Natarajan V, Padmanabhan S, Sukumaran A et al (2018) A closed-form analytical model for predicting 3D boundary layer displacement thickness for the validation of viscous flow solvers. AIP Adv 8:025315
37. Choi H, Moin P (1994) Effects of the computational time step on numerical solutions of turbulent flow. J Comput Phys 113(1):1–4
38. Uzun A, Hussaini MY (2010) High-fidelity numerical simulations of a round nozzle jet flow. In: 16th AIAA/CEAS conference, p 4016
39. Mohan NKD, Karabasov SA, Graham O, Dowling AP, Hynes TP, Tucker PG (2013) Reduced-order jet noise modelling for chevrons. In: 18th AIAA/CEAS conference, p 2083
40. Uzun A, Hussaini MY (2007) Noise generation in the near-nozzle region of a chevron nozzle jet flow. In: 13th AIAA/CEAS conference, p 3596
41. Zaman KBMQ (2011) Effect of nozzle exit conditions on subsonic jet noise. In: 17th AIAA/CEAS conference, p 2704
42. Andersson N, Eriksson L-E, Davidson L (2004) A study of Mach 0.75 jets and their radiated sound using large-eddy simulation. In: Proceedings of the 10th AIAA/CEAS Aeroacoustics Conference and Exhibit, Chalmers University of Technology, Gotenborg, Sweden, 10–12 May, p 3024
43. Andersson N, Eriksson L-E, Davidson L (2005) Investigation of an isothermal Mach 0.75 jet and its radiated sound using large-eddy simulation and Kirchhoff surface integration. Int J Heat Fluid Flow 26:393–410 [CrossRef]
44. Engblom W, Khavaran A, Bridges J (2004) Numerical prediction of chevron nozzle noise reduction using WIND-MGBK methodology. In: Proceedings of the 10th AIAA/CEAS Aeroacoustics Conference, NASA, Cleveland, OH, USA, 10–12 May, p 2979
45. Lindblad D, Sherwin SJ, Cantwell CD, Lawrence J, Proenca A, Ginard MM, Aeroacoustic analysis of a closely installed chevron nozzle jet using the high-order discontinuous Galerkin method
46. Schlinker RH, Simonich JC, Shannon DW, Reba RA, Supersonic jet noise from round and Chevron nozzles: experimental studies
47. Schlinker RH, Liljenberg SA, Polak DR, Post KA, Chipman CT, Stern AM (2007) Supersonic jet noise source characteristics and propagation: engine and model scale. In: 14th AIAA/CEAS Aeroacoustics Conference, Rome, Italy, 2007, AIAA 2007-3623
48. Massey SJ, Thomas RH, Abdol-Hamid KS, Elmiligui AA (2003) Computational and experimental flow field analyses of separate flow Chevron nozzles and pylon interaction. AIAA 2003–3212
49. Brown CA, Bridges J (2006) Acoustic efficiency of Azimuthal modes in jet noise using Chevron nozzles. AIAA-2006-2654
50. Opalski AB, Wernet MP, Bridges JE (2005) Chevron nozzle performance characterization using stereoscopic DPIV. In: AIAA Paper 2005-444
51. Bridges J, Brown CA (2004) Parametric testing of Chevrons on single flow hot jets. NASA/TM—2004–213107
52. Balusamy S, Rajendran V, Aloy AM, Sankar V, Kumar VRS (2021) In silico and in vitro experiments on Chevron nozzles with enhanced momentum thrust using streamtube expansion waves, AIAA 2021-3357. AIAA Propulsion and Energy 2021 Forum, August 9–11. https://doi.org/10.2514/6.2021-3357